University College London
Department of Chemical Engineering

www.chemeng.ucl.ac.uk/

Investigations on the Transition between Stratified and Non-stratified Horizontal Oil-water Flows

Talal Khamis Al-Wahaibi

A thesis submitted in fulfilment of the requirements of the degree of Doctor of Philosophy of the University of London and the Diploma of University College London

September 2006

Copyright Notice

University College London

Department of Chemical Engineering

Investigations on the Transition between Stratified and Non-stratified Horizontal Oil-water Flows

t.al-wahaibi@ucl.ac.uk

Published by: Talal Al-Wahaibi

Department of Chemical Engineering

University College London

Torrington Place

London WC1E 7JE

September 2006

www.chemeng.ucl.ac.uk/

Abstract

The work presented in this thesis aims to investigate experimentally and theoretically the transition from *stratified* to *non-stratified* horizontal oil-water flows and to improve the understanding of the *dual continuous* pattern, where both phases retain their continuity at the top and bottom of the pipe respectively but there is dispersion of one phase into the other. Two experimental facilities were used in this study; a 38 mm ID stainless steel test section in a pilot scale flow facility and a 14 mm ID acrylic test section in a small flow facility running with water and oil (5.5 mPa s viscosity and 828 kg/m^3 density) as test fluids. A high speed video camera was employed to examine wave characteristics and flow development, capture mechanism of drop formation and determine the onset conditions of drop entrainment and the *dual continuous* pattern in both facilities. In the 38 mm ID test section, a conductivity probe was also used to investigate wave structures before and at the onset of entrainment. A high frequency impedance probe was used to find the phase distribution of the oil-water flow while the local drop velocity and chord length distributions were measured using a dual impedance probe. In the 14 mm ID test section, the influence of adding polymer in horizontal oil-water flows was also investigated.

While the flow pattern map developed by Lovick and Angeli (2004a) was used for the 38 mm ID test section, a new flow pattern map was constructed for the 14 mm ID pipe. *Dual continuous* flow was found to occur for a smaller range of superficial velocities in the small test section compared to the large one. Visual observations from the two test sections revealed that no drops are formed when interfacial waves are absent. In addition *annular* flow with oil flowing at the core was observed in both pipes for low oil velocities and relatively high water velocities. The results from the high speed pictures and the conductivity probe showed that the amplitudes of the waves are increased as the superficial velocities of the two phases increase and as a result the required superficial water velocity, U_{sw}, for the onset of entrainment decreases as the superficial oil velocity, U_{so}, increases. The model suggested by Trallero (1995) for the transition from *stratified* to *non-stratified* flow failed to predict the experimental results. Moreover, the high speed video images and the conductivity probe results showed that the amplitudes of the waves found at 2 m from the inlet are smaller than those observed

at 7 m. When drops and the onset of entrainment were observed at 7 m from the inlet, these were not observed at 2 m from the inlet, which means that all drops forming downstream the pipe resulted from the waves. In the large pipe, the presence of a bend after the inlet section (T-junction) resulted in larger drops than when no bend was present (Y-junction). The high speed images also revealed that drops formed as a result of the relative movement between the oil and water phases. The faster phase will undercut the other one until a drop is detached from the wave crest.

The entrained fractions during *dual continuous* flow, or the fraction of one phase dispersed into the continuum of the other were calculated from the phase distribution data obtained with both inlet configurations (T-junction and bend and Y-junction). The entrained fraction of water in oil ($E_{w/o}$) increased as the input water flow rates increased at constant superficial oil velocity. Similarly, the entrained fraction of oil in water ($E_{o/w}$) increased as the oil flow rates increased at a constant water superficial velocity. Moreover, the entrained fractions when the bend was used were higher than those obtained without it.

From the chord length measurements in *dual continuous* flow, chord length and drop concentration were found to decrease with increasing distance from the interface while the number density of large drops decreased as U_{sw} increased at each U_{so}. Also, oil drops were in general larger than water drops. Drop velocity measurements also revealed that water drops were faster than the velocity of the upper layer while oil drops could be either slower or faster than the velocity of the lower layer. The results showed that average chord length L_{32} was almost constant for the oil drops while it tended to decrease for the water drops as the respective layer velocity increased.

In the 14 mm ID pipe, the addition of a polymer in the oil-water flow had a significant effect on the flow patterns and pressure drop. The transition from *stratified* to *non-stratified* patterns was clearly delayed and the pressure drop was found to decrease after adding the polymer. The wavy interface in the *stratified*, *dual continuous* and *annular* flows was damped when polymer was present. The interfacial and water wall shear stress were also found to decrease after the addition of the polymer.

Theoretically a model was developed based on Kelvin-Helmholtz (KH) instability to predict whether waves in *stratified wavy* flow with certain amplitudes and lengths are

stable or not. The model compared well with the Viscous KH correlation developed by Trallero (1995) and with some experimental results. The model was extended to predict the onset velocities of entrainment by including an empirical wave amplitude and length. The prediction agreed well with the experimental onset velocities from a number of studies. Based on a balance between drag force and surface tension on the crests of the waves, another equation was developed to predict the critical wave amplitude and length required for drop formation. This equation was used together with the stability equation to define three regions in a wave amplitude against length graph. These are; stable wave region; unstable wave region, where waves are unstable but drops may not form because waves need to grow more before drops can detach; drop entrainment region. The model agreed well with the experimental results. Finally, an entrainment model to predict the fraction of one phase entrained into the other during *dual continuous* flow, that was based on a balance between rate of drop entrainment and rate of drop deposition. The model was modified with experimental data from the current study and was then validated against data from literature. The comparison was reasonable in many cases.

Acknowledgment

Words can not express my deep gratitude and appreciation to Dr. Panagiota Angeli for all the discussions and recommendations she has given me as my supervisor. Her knowledge, personal guidance, encouragement, enthusiasm and interest has helped a lot to complete this project. I really learnt a lot from her.

I would like to give my special thanks to Karolina Ioannou and Bin Hu with them I shared the enjoyment of working in the rig. I would like to thank Karolina again not only for the fruitful and stimulating discussion and co-operation related to oil-water flow studies but also for helping me even in printing, binding and submitting the thesis.

I can not forget my friend Jason Lum and his smile. He taught me everything in the rig without complaining and he was always willing to help regardless of the circumstances. Jason you will be always in my memory.

I am also indebted to the technicians in the mechanical workshop of the department for offering the support to different parts of the project. They always like to help and give ideas when ever we need to build any thing.

Special thanks to my friends and colleagues in London; Adel Al-Ajmi, Yahya Al-Wahaibi, Abdul-Aziz Al-Hashmi, Mohammed Al-Gharbi, Sultan Al-Mahrouqi, Nabil Al-Belushi, Hamad Al-Shuraiqi, Carlos Amador, Wael Salman, Nan Shao, Sarah Germana, Cristina Jimenez, Kashif Zahoor and Jia Sun for many hours spent in discussions.

I am very grateful to Sultan Qaboos University for their continuous and generous financial support throughout this project. I would also like to thank the EPSRC Instrument Pool for providing the high speed camera and for providing financial support to drag reduction experiments.

Finally, and most deeply, I thank my wife for her encouragement, understanding and support that has enabled to achieve an ambition. A doctoral study is, by nature, a lonely journey. Now the destination has been reached, we can resume normal family life again. Mohammed and Al-Waleed will doubtless appreciate a more relaxed father.

Contents

List of Figures

Chapter 3:

Chapter 5:

Chapter 6:

Chapter 9:

Appendix D: Phase Distribution

List of Tables

CHAPTER 1

Introduction

1.1 Background

Liquid-liquid flows occur in various major applications in the petroleum and chemical industries. In the petroleum industry as an example, oil-water flows appear in both the wellbore and the flowline in horizontal and inclined pipes. This flow occurs due to the presence of formation water or water breakthrough in the well in later years of production. In offshore production or production in remote areas, the reservoir fluids (oil and water) will have to be transported through flowlines with substantial lengths prior to their separation.

Therefore, it is very important to understand the flow behavior of oil-water mixtures so oil can be transported in an efficient way and separation facilities can be designed in a better way. Fundamental understanding of such flows will also help the understanding of more complex three and four phase flows in the presence of gas and/or solids.

The basic difference between single phase and two phase flow is the appearance of interfaces in two phase flow. The term flow pattern refers to the geometrical distribution of the two phases in the pipe. Each flow configuration has a particular spatial distribution of the interface, resulting in different flow characteristics such as velocity, holdup profiles and pressure drop.

Flow patterns are normally determined by visual observations from which data are mapped on a two dimensional plot where the axes are normally superficial or mixture velocities or phase fraction. Such plots are called flow pattern maps. Flow pattern maps are important because the flow in each pattern has specific hydrodynamic characteristics. Based on them models for pressure drop and hold-up can be developed

for each pattern. Knowledge of the flow pattern map of a two-phase system can help therefore predict important flow parameters.

Any flow pattern in a given two-phase flow system depends on operational parameters such as liquid flow rates, geometrical variables (pipe diameter and inclination angle) and the physical properties of both phases such as liquid densities and viscosities.

Oil-water flow patterns are classically grouped into two categories:

Segregated flow: both phases (oil and water) retain their continuity at the top and bottom of the pipe. Two main flow patterns are recognized under this category according to Lovick and Angeli (2004a):

Stratified flow pattern (ST)

In this pattern (which occurs at relatively low oil and water superficial velocities), the two phases are separated by gravity, where the denser phase (water) flows at the bottom of the pipe while the lighter phase (oil) flows at the top. The *stratified* flow pattern is subdivided into *stratified smooth* (*SS*), where the liquid-liquid interface is smooth and *stratified wavy* (*SW*) at which stable waves form on the interface.

Dual continuous flow pattern (DC)

In this pattern, both phases are continuous but with entrainment in the form of dispersed drops of one phase into the other (Fig. 1.1). This flow occurs in inclined as well as horizontal flow at different mixture velocities; i.e. Scott, 1985, Trallero, 1995, Vedapuri et al., 1997, Alkaya, 2000, Lum et al., 2004 and Lovick and Angeli, 2004a. The *dual continuous* flow pattern is basically a *stratified* flow but with mixing at the interface. The beginning of this mixing is the onset of this pattern. Additionally, as the mixture velocity increases, the mixing increases and so does the degree of dispersion.

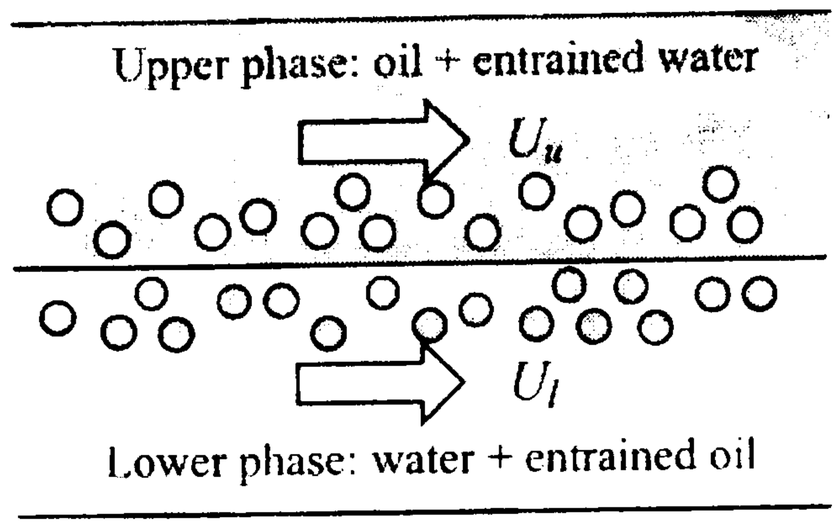

Fig. 1.1 Schematic diagram of *dual continuous* flow by Lovick and Angeli (2004a)

Dispersed flow: where one phase is found to be dispersed while the other is continuous. Two main flow patterns are found in this category:

Oil-in-Water Dispersion (Do/w)

Oil-in-water dispersion occurs at relatively low oil superficial velocities in which water is the continuous phase while oil is the dispersed one. At the lower mixture velocities, most of the drops are located near the upper pipe wall. When the mixture velocities increase, the oil drops are distributed more uniformly in the entire cross sectional area of the pipe. This pattern can be subdivided into two other patterns (according to Angeli and Hewitt, 2000a). *Stratified mixed flow* (*SM*) appears when the dispersed phase occupies the top of the pipe leaving a layer of water at the bottom free of drops. Trallero (1995) called this pattern *dispersed oil in water with water layer*. Fully *dispersed* flow appears when water is continuous while the dispersed oil distributes uniformly across the pipe cross section.

Water-in-Oil Dispersion (Dw/o)

At high oil velocities, oil becomes the continuous phase while water disperses in it. The dispersion again can be located at a part of the pipe (bottom) or be dispersed through the entire cross sectional area of the pipe.

Within the available literature, the *dual continuous* pattern has been reported under different names in a number of works mainly concerned with experimentally observed flow pattern boundaries in liquid-liquid flows (Guzhov et al, 1973, Cox, 1985, Scott, 1985, Trallero, 1995, Nädler and Mewes, 1997, Vedapuri et al., 1997, Angeli and Hewitt, 2000a, Lum et al., 2004 & 2006; for a comprehensive review see Lovick and Angeli, 2004a). This pattern is common for a wide range of mixture velocities and phase fractions especially with low viscosity oils. In contrast to flow pattern transition observations, limited information exists on parameters such as pressure drop and hold up during *dual continuous* flow, while the modelling attempts are even less (Guzhov and Medvedev, 1971, Vedapuri et al., 1997, Lovick, 2004). The most important issue in analyzing this pattern is the prediction of the fraction of one phase dispersed into the other (*entrained fraction*). Accurate prediction of the entrained fraction is critical to effectively model pressure drop and hold up in this regime.

It has been suggested that drop entrainment from one phase into the other happens when drops detach from the waves of a *stratified wavy* flow (Trallero, 1995). Therefore, to be

able to predict entrained fraction, the conditions should be investigated that lead to drop entrainment into the opposite phase such as mechanism of drop detachment from the waves, phase velocities and structure of the wavy interface at the onset of entrainment. Waves affect the rate of entrainment from one phase into the other as well as the pressure drop because they cause roughening of the interface. Understanding entrainment would require a complete investigation of the characteristics of the interfacial waves. There are currently no published studies on wave characteristics at the onset of *dual continuous* flow.

The focus of this thesis is to investigate and predicte the transition between *stratified* and *non-stratified* flow (in particular the *dual continuous* flow) in order to improve the understanding of the *dual continuous* pattern.

Also, findings in the gas-liquid literature (Oliver and Young Hoon, 1968, Al-Sarkhi and Hanratty, 2001(a,b), Soleimani et al., 2002), suggest that addition of very small amounts of polymers in the flows damps the waves in the gas-liquid interface and delays the transition from *stratified* to *annular* and *slug* flow patterns. Similarly to single phase flows, these polymers also reduce the frictional pressure drop and for this reason they are called drag reducing polymers (DRP). This observation motivated the investigations carried out as part of this project (where the transition between *stratified* and *dual continuous* flows is studied) of the influence of DRP on the transition between *stratified* and *non-stratified* horizontal oil-water flows.

1.2 Aims

This study aims to improve understanding of the transition between horizontal *stratified* and *non-stratified* liquid-liquid flows through experimental investigations and theoretical modeling.

This research has two parts; experimental and theoretical. The objectives of the experimental work are as follows:

- To investigate the transition between *stratified* and *non-stratified* flows and its associated phenomena (e.g. wave structure, onset of entrainment and mechanism of drop formation).

- To obtain quantitative information using a conductivity probe on wave structure such as amplitude and wavelength before and at the onset of entrainment.
- To investigate the entrained fraction of each phase into the other from phase distribution measurements and the drop size distribution from chord length measurements in the *dual continuous* pattern.
- To investigate the effect of drag reducing polymers on flow pattern boundaries and several flow characteristics in oil-water flows.

The objectives of the theoretical work are:

- To derive a model based on Kelvin-Helmholtz (K-H) instability to predict the transition between stable and non-stable wavy *stratified* flow. The model can be used to predict wave amplitude required to destabilize a wave at a certain wavelength. The model is then extended to predict the onset of entrainment and to validate it against wide range of experimental data.
- To develop a model that predicts the critical amplitude of the waves required for drop formation based on the mechanism of drop formation.
- To derive a model that predict the entrained fraction of oil in water and water in oil and to check the validity of the model against experimental data.

1.3 Thesis Structure

The thesis is structured as follows. Chapter 2 reviews the available literature in liquid-liquid flows. Due to the limited information available in liquid-liquid, some of the literature from gas-liquid flows has also been included. The literature covers topics such onset of entrainment, mechanism of drop formation, wave structure measurements, entrained fraction, drop size distribution and drag reduction. The description of the experimental facilities, instrumentation and techniques used are given in chapter 3. The instrumentation and the techniques used to capture the mechanism of drop detachment, wave structure measurements, phase distribution and chord length are described in detail.

In chapter 4, wave structure, flow development and onset of entrainment obtained from visual observation in two different experimental facilities (38 mm ID stainless steel pipe and 14 mm ID acrylic pipe) using a high speed video camera are given. Measurements

of the wave structure using a conductivity probe before and at the transition between *stratified* and *non-stratified* flows are also reported. In the 38 mm ID test section, the oil-water flow is investigated at 2 and 7 m from the inlet while the effect of bend at the inlet on the onset of entrainment is also presented.

Chapter 5 presents a model (based on K-H instability) that predicts the transition between stable and non-stable waves in *stratified* flow and the critical amplitude required to initiate instability for certain wavelength. The model is validated against the experimental data described in chapter 4. The model is further extended to predict the onset of entrainment which is compared with different experimental data was. Chapter 6 contains the experimental results of the mechanism of drop formation and the model developed to predict the required wave amplitude for drop detachment.

Experimental measurements of entrained fraction of each phase into the other, chord length distribution, drop velocity and drop size distribution are given in chapter 7. The effect of different inlet geometries on the measured entrained fraction has also been studied. A model that predict the entrained fraction of each phase into the other is described in chapter 8. The model is derived based on a physical understanding together with experimental entrainment data. The correlation obtained is validated against independent entrainment data from a number of investigators.

Chapter 9 demonstrates the effect of drag reducing polymers on oil-water flows in a horizontal 14 mm ID acrylic pipe. Flow patterns boundaries, pressure drop and hold-up have been investigated and compared in flows with and without polymer. Finally, conclusions drawn from this work and recommendations for future plans are given in chapter 10.

CHAPTER 2

Literature Review

In this chapter, a review of the published literature in horizontal oil-water flows is presented. Section 2.1 focuses on studies covering the *dual continuous* pattern. The mechanism of drop formation in both gas-liquid and liquid-liquid flows is discussed in section 2.2. Section 2.3 reports refers to work on the onset of entrainment in *dual continuous* liquid-liquid flow and gives a summary of correlations from gas-liquid *annular* flow investigations that predict the onset of entrainment. Experimental work in liquid-liquid and gas-liquid flows on the wave structures is given in section 2.4. Section 2.5 presents the entrained fraction literature for both gas-liquid and liquid-liquid flows. Drop size distribution in liquid-liquid flows is discussed in section 2.6. Literature on the effect of drag reducing polymers on both single and multiphase flows is presented in section 2.7. Finally, a summary is given in section 2.8.

2.1 Dual Continuous Flow

During the simultaneous flow of two liquids, several flow patterns can be distinguished. At low superficial oil and water velocities the flow is *stratified*. When the flow rates increase, interfacial waves appear which are initially long compared to the pipe diameter. Such waves will become more disturbed and shorter in terms of wavelength as the flow rates increase. The reported wavelengths are roughly twice the pipe diameter (Trallero, 1995). Along the waves, water droplets will form in the oil layer and oil droplets will appear in the water layer. This pattern is known as *dual continuous* flow (Lovick and Angeli, 2004a). In this study, the transition between the *stratified wavy* and the *dual continuous* patterns is defined as *onset of entrainment*. The transition is considered to have happened when one or more drops of one phase are found to flow continuously within the opposite phase.

As in gas-liquid flows, the mechanism of drop formation in liquid-liquid is still not known. The literature on mechanism of drop formation is given in section 2.2 for both liquid-liquid and gas-liquid flows. Once a drop is formed in the other phase, inertial forces will try to disperse it throughout the cross section of the pipe. Gravity or buoyancy, on the other hand, will try to keep the drop in its original phase. At low mixture velocities, mixing is restricted around the interface. As the mixture velocity increases, mixing increases and the degree of dispersion of one phase into the other also increases.

The *dual continuous* pattern as shown in Fig 1.1 has been reported under different names in a number of works mainly concerned with experimentally observed flow pattern boundaries in liquid-liquid flows (Guzhov et al, 1973, Cox, 1985, Scott, 1985, Trallero, 1995, Nädler and Mewes, 1997, Vedapuri et al., 1997, Soleimani, 1999, Angeli and Hewitt, 2000a, Elseth, 2001, Lum et al., 2004, Raj, et al., 2006; for a comprehensive review see Lovick and Angeli, 2004a). For example, Angeli and Hewitt (2000a) described this pattern as *three-layer* flow while Trallero (1995) described it as a *stratified* flow with mixing at the interface. In this project, the *dual continuous* flow is given to describe the pattern in accordance to Lovick and Angeli (2004a). A detail summary of the researchers that have observed the *dual continuous* pattern in their experimental studies is given in Table 2.1.

Oglesby (1979), Arirachakaran et al. (1989) and Valle and Kvandal (1995) observed the dual pattern as well. However, they noted a thin film of water flow which forms annulus around the pipe wall with an oil continuous dispersion flowing in the middle. This was observed at low oil and high water superficial velocities. Valle (2000) attributed that to the wetting properties of the transparent glass section used in the above experiments.

Authors	Pipe ID (mm)	Pipe Material	Oil Properties			Dual Continuous boundaries		Observed dual cont. flow patterns	Flow pattern identification method
			μ (mPa s)	ρ (kg/m^3)	σ (mN/m)	Min Mixt. vel. Oil %	Max Mixt. vel Oil %		
Guzhov et al. (1973)	39.4	Steel	21.8	896	44.8	0.3m/s 30-90%	1.6m/s 70-90%	Sep. flow with disp. at int. and water or oil/water bottom layer, emulsion of water/oil & oil/water	Visual observation
Malinoswky (1975)	38.4	Steel	4.6	850	22.3	0.6m/s 55%	2m/s 55%	Do/w & w/o	Visual observation
Laflin and Oglesby (1976)	38.4	Steel	4.94	828	22.3	0.5m/s 43-64%	1.2m/s 58%	Segregated, Do/w & w/o	Visual observation
Oglesby (1979)	41		32	868	30.1		1.4m/s 74%	Semi segregated, Semi mixed	
Cox (1985)	50.1	Acrylic	1.38	754		0.7m/s 30-76%	1m/s 30-76%	Stratified bubble	Visual observation
Scott (1985)	50.1	Acrylic	1.38	754		0.7m/s 30-76%	1m/s 30-76%	Stratified bubble	Visual observation
Trallero (1995)	50.1	Acrylic	29.6	850	36	0.25m/s, 5-95%	>3m/s 50-62%	ST & MI, Do/w & Dw/o	Visual observation
Valle and Kvandal (1995)	37.5	Glass	2.3	794	37.3	0.85-0.9m/s 24-68%	1.7m/s >64% <28%	Stratified wavy-entrain. Stratified wavy with oil and water dispersed zones	Conductivity and sample probes
Nädler and Mewes (1997)	59	Perspex	22-35	841		0.3m/s 20-95%	1.6m/s 60%	Stratified with mixing at int., Layers of w/o & w or w/o, o/w & w	Conductivity probe

Vedapuri et al. (1997)	101.2	Plexi-glass	2.0			0.4m/s 20-80%	1.4m/s 20-80%	Semi-segragated, Semi-mixed	Isokinetic probe
Angeli (1996)	24.3	St. Steel	1.6	801	17.0	0.3m/s 32-77%	1.3m/s 66%	Stratified wavy/drops, Three-layer	Mainly visual observation-Impedance probe
Angeli and Hewitt (2000a)	24	Acrylic	1.6	801		0.3m/s 33%	1.6m/s 50%		
Soleimani (1999)	24.3	St. Steel	1.6	801	17.0	0.5m/s 20-85%	1.5m/s 62-66%	Stratified wavy/drops, Three-layer	Visual obs. Impedance probe-Gamma densitometer
Elseth (2001)	56.3	St. Steel	1.6	790	43	0.7 m/s 15 %	2.5 m/s 45-60%	ST & MI, Do/w & Dw/o	Visual obs. Gamma densitometer
Lovick and Angeli (2004a)	38.0	St. Steel	5.5	828	39.4	0.8 m/s 10-90 %		Dual continuous	Visual Obs. Impedance probe
Raj et al. (2005)	25.4	Acrylic	1.2	787	45	0.6m/s 30%	2.2m/s 50%	Three-layer stratified	Visual Obs.

Table 2.1. Summary of studies carried out at the *dual continuous* flow pattern

Trallero (1995) reported that as the mixture velocity increased the dispersion in each phase in *dual continuous* flow which is located initially at the interface also increased. Also, the dispersion in each phase became more uniformly distributed as the velocity increased. In the *dual continuous* pattern, he estimated the diameter of the observed drops between 1-12 mm while they decreased to 2-3 mm when both phases became fully dispersed *Dw/o* & *Do/w*).

Dual continuous flow is common for a wide range of mixture velocities and phase fractions especially with low viscosity oil. In contrast, limited information exists on the behaviour of other parameters such as pressure drop and hold up during this pattern, while even less modelling attempts exist mainly focusing on the prediction of pressure gradient and hold up (Guzhov and Medvedev, 1971, Vedapuri et al., 1997, Lovick, 2004). The most important issue in analyzing this pattern is the prediction of the fraction of one phase into the other (*entrained fraction*). Accurate prediction of the entrained fraction is critical to effectively model pressure drop and hold up. Therefore, measurement of the onset of drop formation on the oil-water interface, understanding the mechanism responsible of such formation, measurement of wave structure at the onset and being able to predict them are crucial to understand *dual continuous* flow. Such investigation provides the fundamentals to theoretically model this pattern.

2.2 Mechanism of Drop Formation

At the transition between *stratified wavy* and *dual continuous* flows, drops start forming. Identifying the mechanism of drop formation will lead to accurate prediction of this transition. In the open literature, drop formation mechanism is still not known for liquid-liquid flows. On the other hand, extensive studies have been done in gas-liquid flows and especially *annular* ones.

2.2.1 Gas-liquid flows

In gas-liquid flows, several possible mechanisms have been identified for drop formation. For example, Woodmansee and Hanratty (1969) investigated the mechanism responsible for the removal of droplets from the liquid surface in an *annular* flow using high speed camera. They found that atomization mainly occurs by the removal of small

wavelets which exist on the top of roll waves in the liquid film. By analyzing the pictures, Woodmansee and Hanratty (1969) postulated that drops formed as a result of Kelvin-Helmholtz instability where the destabilizing force is the pressure variation caused by the compression of the gas streamlines at the crest of the wavelets. A similar mechanism was found later by Azzopardi (1983), who also observed a second mechanism where the crest of the roll waves was stretched and thin ligaments were torn from the liquid film.

Ishii and Grolmes (1975) summarized, as shown in Fig. 2.1, five basic types of entrainment mechanisms observed experimentally by different researchers. Shearing off roll wave crests by gas phase (Type I) is the most common one in *annular* two-phase flow. The second mechanism is when the gas phase undercuts the liquid film. The third mechanism occurs when the liquid film contains bubbles which burst when they are released to the surface. The fourth type of entrainment is caused by the impingement of the liquid drops to the film interface. Entrainment as described in mechanism number five occurs when the countercurrent flow reaches flooding conditions (for a comprehensive review, see also Wallis, 1969 and Hewitt and Hall-Taylor, 1970).

Moreover, entrainment of drops was found to result from the disturbance waves which occurred in *annular* flow. Hewitt and Hall-Taylor (1970) reported that the relation between disturbance waves and entrainment was clearly described by several investigators using visual observations and photographic techniques. Azzopardi and Whalley (1980) conducted an artificial wave experiments from which drops were found to form from the disturbance waves.

Fig 2.1 Different entrainment mechanism in gas-liquid summarized by Ishii and Grolmes (1975)

2.2.2 Liquid-liquid flows

In liquid-liquid flows, the mechanism of drop formation is still not known. Guzhov et al. (1973) reported that the relative movement of the two liquid phases develops a vortex motion at the boundary of the two liquids which penetrate in each phase so drops will form. Trallero (1995) pointed out that Kelvin-Helmholtz instability (K-H) may predict the onset of droplet formation. He mentioned that K-H instability will make the wavy disturbance on the interface to grow in amplitude and such waves will break even with small shear velocities when the flow of the liquids is laminar.

2.3 Onset of Entrainment

The majority of studies in identifying and predicting the onset of entrainment in multi-phase flow have been carried out for two-phase gas-liquid flows.

2.3.1 Gas-liquid flows

Extensive studies have been done for both measuring and correlating the onset of entrainment on two-phase gas-liquid flow especially for the *annular* pattern. Wallis (1969), Hewitt and Hall-Taylor (1970) and Nigmatulin (1991) reviewed the existing experimental and analytical work on the inception of liquid entrainment. The review of Hewitt and Hall-Taylor (1970) summarizes the various experimental data and correlations. The summary showed large discrepancies between the different correlations. The differences were due to the different methods used in defining the onset of entrainment.

An example of the correlations developed empirically for the onset of entrainment in gas-liquid flow is that by Ousaka and Kariyasaki (1992):

$$P = 135\,\mathrm{Re}_{Lf}^{-0.912} \tag{2.1}$$

where Re_{Lf} is the liquid film Reynolds number and

P is defined as $\quad P = \dfrac{j_g \mu_{Lf}}{\sigma}$ (2.2)

where j_g is the gas volumetric flux, μ_{Lf} is the liquid film viscosity and σ is the surface tension.

A more mechanistic equation was developed by Ishii and Grolmes (1975) based on Type I mechanism (see Fig. 2.1) for the onset of entrainment. They said that for film Reynolds number greater than 160, the shearing off mechanism of roll waves is the primary means of droplet entrainment in co-current *annular* flow. They believed that for entrainment to occur the drag force resulting from the high shear flow of gas must be higher than the surface tension trying to stabilize the wave. Based on this balance, the onset of liquid entrainment was found to be

$$\frac{\mu_{Lf} j_g}{\sigma}\sqrt{\left(\frac{\rho_g}{\rho_{Lf}}\right)} \geq 11.78 N_\mu^{0.8}\,\mathrm{Re}_L^{\frac{-1}{3}} \quad for\ N_\mu \leq \frac{1}{15} \tag{2.3}$$

where ρ_g is the gas density, ρ_{Lf} is the liquid density, N_μ is the viscosity number and Re_L is the total liquid Reynolds number.

The viscosity number is defined as $N_{\mu} = \frac{\mu_{Lf}}{(\rho_{Lf}\sigma\sqrt{(\frac{\sigma}{g\Delta\rho})^{\frac{1}{2}}}}$ (2.4)

and the total liquid film Reynolds number as $\mathrm{Re}_L = \frac{\rho_{Lf} j_L D_{Lf}}{\mu_{Lf}}$ (2.5)

The above equation is valid in the range $160 < \mathrm{Re}_L < 1635$. Above this number, another equation was developed for the onset of entrainment.

2.3.2 Liquid-liquid flows

In liquid-liquid flows, several investigators have identified the boundary of *dual continuous* flow while experimentally investigating flow patterns. Theoretically, there are no published studies on the prediction of the onset of drop formation in liquid-liquid flows. Stability analysis has been used to predict the limit of stable wavy *stratified* flow (Brauner and Molaem Maron, 1992a&b and Trallero, 1995) (see section 2.3.2.2). Trallero (1995) reported that his model may be used to predict the onset of drop formation.

2.3.2.1 Experimental studies

Lovick and Angeli (2004a) gave a summary of the work on *dual continuous* flow pattern at which they described the minimum and maximum boundary where the pattern occurred. Most of the works done described just the onset or the boundary of the pattern without further investigating it. For example, Cox (1985) and Scott (1985) found the onset of droplet formation at the interface which indicates the start of *stratified bubble* flow. This is equal to the onset of *dual continuous* flow. A decrease in the wave amplitudes was observed at the start of the *stratified bubble* flow (onset of *dual continuous* flow). At the lower oil fractions, slight differences on the transition between *stratified* to *stratified bubble* flow were observed by the two investigators for the same flow system and fluids. Such differences could be due to the definition used by each investigator to find the onset and to the uncertainty which normally accompanies flow pattern classification using visual observation.

Valle and Kvandal (1995) observed the onset of *stratified wavy* with entrainment at a mixture velocity of about 0.85 m/s which is equivalent to the onset of entrainment in *dual continuous* flow. To detect it they used wall mounted conductivity probes and a sampling tube.

Lovick and Angeli (2004a) detected the onset at 0.80 m/s mixture velocity with visual observation. Figs. 2.2, 3 and 4 demonstrate the transition between *stratified* and dual flow pattern, i.e. the onset of the dual flow pattern by different investigators.

Angeli and Hewitt (2000a) observed experimentally flow patterns in both stainless steel and acrylic pipes using the same fluid properties and pipe diameter. They found that the onset of *dual continuous* flow occurred at slightly lower mixture velocities for the stainless steel pipe than for the acrylic one.

Fig. 2.2 Experimental results on the initial boundary of *dual continuous* flow pattern, in horizontal oil-water flow, D=3.94 cm, $\mu_o/\mu_w = 21.8, \rho_o/\rho_w = 0.898, \sigma = 44.8$ dynes/cm, Guzhov et al. (1973)

Fig. 2.3 Experimental results on the initial boundary of *dual continuous* flow pattern, in horizontal oil-water flow, D=3.75 cm, $\mu_o/\mu_w = 2.3$, $\rho_o/\rho_w = 0.79$, $\sigma = 37.3$ dynes/cm, Valle and Kvandal (1995)

Fig. 2.4 Experimental results on the initial boundary of *dual continuous* flow pattern, in horizontal oil-water flow, D=5.01 cm, $\mu_o/\mu_w = 29.60$, $\rho_o/\rho_w = 0.85$, $\sigma = 36$ dynes/cm, Trallero (1995)

The effect of oil viscosity on dual flow pattern is not clear due to the different fluid properties and pipe materials used in the different studies. However, it can be noted that for high viscosity oils, the onset appeared at lower velocities compared to low viscosity oils (see Figs. 2.2, 3 and 4).

2.3.2.2 *Predictive models*

Brauner and Moalem Maron (1992a) conducted a linear stability analysis of stratified liquid-liquid flows. In this analysis, they included the effect of surface tension due to wave curvature. In addition, the conditions required for real characteristics were also investigated. The stability and well-posedness analyses gave two transition lines, the zero neutral stability (ZNS) line and the zero real characteristics (ZRC) line. Brauner and Moalem Maron (1992b) used the two lines to predict the transition from *stratified* to other flow regime. These referred mainly to the *stratified*, *annular* and *stratified-dispersed* flow regimes. The ZNS line represents the transition from *stratified smooth* to *stratified wavy* while the ZRC predicts an upper bound for the existence of the *stratified wavy* configuration.

Trallero (1995) conducted a theoretical study for predicting the transition between *stratified* and *non-stratified* flow of water and low viscosity oil based on Kelvin-Helmholtz (KH) stability analysis and using the two-fluid model. The study was done as part of his extensive work on predicting flow pattern transitions. Such analysis determines whether the interface is stable for one-dimensional two-phase flow.

Based on his analysis, a VKH stability equation (Eq 2.6) was developed theoretically for long waves. The equation was derived based on continuity and momentum equations of two phase flow. Inside the VKH stability line the flow is considered stable *stratified* while outside it, the flow is unstable with wavy interface or *stratified* flow with mixing at the interface may form (*dual continuous* flow). Trallero (1995) compared the model with his data and some other published data as shown in Fig. 2.5. The comparison showed a reasonable fit with the data. Trallero (1995) stated that the onset of *dual* flow pattern may be found when the VKH equation is equal to zero. However, the model failed to predict the data of Valle and Kvandal (1995) if used to predict the onset of drop formation.

The viscous KH criterion developed by Trallero (1995) is given by:

$$(C_v - C_{iv}) + \frac{\rho_w \rho_o}{\rho^2 H_w H_o}(U_w - U_o)^2 - \frac{(\rho_w - \rho_o) A g \cos\theta}{\rho S_i} - \frac{\sigma A k^2}{\rho S_i} + \frac{\rho_i (U_w - U_o)^2 C_s A}{\rho}\left(\frac{1}{A_w} + \frac{1}{A_o}\right) < 0 \qquad (2.6)$$

where ρ_o, ρ_w, ρ_i and ρ are oil, water, corresponding phase and total densities respectively, U_o and U_w are the in-situ oil and water velocities respectively, H_o and H_w are the oil and water hold-up respectively, A_o, A_w and A are oil, water and total cross sectional area respectively, S_i is the interfacial length, k is the wave number and C_s is the sheltering coefficient.

or it can be written as

$$J_\eta + J_u - J_g - J_\sigma + J_s < 0 \qquad (2.7)$$

where the first term J_η is the viscous term, J_u is the velocity term which destabilises the wave while the third gravity (J_g) and fourth surface tension (J_σ) terms will tend to stabilize the interfacial waves. The last term (J_s) is known as the sheltering effect which is used to incorporate the wave effects into the model.

Fig. 2.5 Comparison of the theoretical VKH stability line with experimental data (points), in horizontal, (D=5.01 cm, $\mu_o/\mu_w = 29.60$, $\rho_o/\rho_w = 0.85$, $\sigma = 36$ dynes/cm), Trallero (1995)

In the first term, C_v is the wave velocity and C_{iv} is the critical wave velocity. They are expressed as follows respectively:

$$C_v = \frac{\left(\frac{\partial F}{\partial H_w}\right)_{Usw,Uso}}{\left(\frac{\partial F}{\partial U_{so}}\right)_{Usw,Hw} - \left(\frac{\partial F}{\partial U_{sw}}\right)_{Uso,Hw}} \tag{2.8}$$

$$C_{iv} = \frac{\rho_w U_w H_w + \rho_o U_o H_o}{\rho_w H_w + \rho_o H_o} \tag{2.9}$$

The derivatives in Eq. 2.8 can be evaluated numerically by perturbing H_w, U_{so} and U_{sw} by small amounts in Eq. 2.10.

Eq. 2.10 is the two-fluid model derived for smooth interface.

$$F = -\frac{\tau_w S_w}{A_w} + \frac{\tau_o S_o}{A_o} + \tau_i S_i \left(\frac{1}{A_w} + \frac{1}{A_o}\right) - (\rho_w - \rho_o) g \sin\theta \tag{2.10}$$

where τ_w, τ_o, τ_i are the water, oil and interfacial shear stresses respectively and S_w, S_o are the water and oil wall wetted perimeter.

Fairuzov et al. (2000) investigated experimentally the flow pattern transitions for oil-water mixtures in large diameter pipe for horizontal pipelines. The experimental results for the transitions between *stratified* and *non-stratified* flow were compared with the viscous Kelvin-Helmholtz and inviscid Kelvin-Helmholtz (IKH) criteria. The comparison showed that the theoretical prediction by VKH analysis agreed reasonably with the experimental results while IKH overpredicted the transition boundary especially at equal phase velocity.

2.4 Measurements of Waves Structures

The growth and development of wave structures at the interface in liquid-liquid pipe flows is important for understanding the transition to *dual continuous* flows (onset of entrainment). Waves affect the rate of entrainment from one phase into the other as well as the pressure drop because of the roughening of the interface. Understanding entrainment would therefore require a complete investigation of the characteristics of the interfacial waves. There are currently no published studies on describing the characteristics of the waves at the onset of *dual continuous* flow. However, there are

very few published studies in the core-*annular* flow pattern of highly viscous oils that discuss interfacial wave structure (Oliemans, 1986; Miesen et al., 1992; Bai, 1995; Bannwart, 1998; Bai and Joseph, 2000). In these cases, all measurements of interfacial waves were obtained with visual observation using high speed video camera. In the investigations, Bannwart (1998) measured wavespeed and volume fraction in core *annular* flow and employed kinematic wave theory to describe interfacial waves. The theory was used satisfactorily to describe wave speed, slip ratio and volumetric fraction of the core. Thus, Bannwart (1998) developed a technique to determine the core fraction from wavespeed measurements. The comparison with the direct hold-up measurements showed a good agreement.

Bai (1995) and Bai and Joseph (2000) also investigated interfacial waves in vertical core *annular* flow. In their investigation, they used high speed video cameras to identify the interfacial wavelength and quick closing valves to measure oil hold-up.

For gas-liquid flow extensive literature exists on the structure of waves at the interface of thin films. Depending on the application, detail information of the characteristics of the interface is needed. However, the interface differs significantly according to the flow rates of gas and liquid. The properties of the waves have been measured by either photographing the liquid film through the transparent pipe wall or by continuous film thickness recording with conductivity probes (Azzopardi, 1997). Hewitt and Hall Taylor (1973) and Azzopardi (1997) described the properties of the waves and their link to entrainment. Since the aim of this work is to measure the structure of the waves in liquid-liquid flows, only few examples are cited from the area of gas-liquid. Jurman et al. (1988) used parallel wire conductance probe to measure the waves in a rectangular channel. The measurements of wavelength and speed of waves were compared with the predictions of linear theory.

Andritsos et al. (1988) investigated the effect of liquid viscosity on the initiation of *slug* from *stratified* flow using a conductance probe. Fan et al. (1993) employed both photographic and instrumental methods (conductance probes) to investigate how a *slug* evolves in a *stratified* flow. They reported that the growth of the waves can result to a breaking wave or to a wave that touches the upper wall of the pipe and fills the whole

cross section. Ng et al. (2004) examined the axial evolution of interfacial structures in wavy stratified two-phase pipe flow using conductance probes along the test section.

2.5 Entrained Fraction

One of the main features in *dual continuous* flow is the existence of entrainment of oil in the water phase and water in the oil phase. Knowledge of the entrained fraction in each phase is important for the accurate calculation and prediction of pressure drop and hold-up. In spite of the common occurrence of this pattern in liquid-liquid flows, very limited amount of work exists both experimentally and theoretically. The entrained fraction is a result of the rate of entrainment and rate of deposition. Most available information comes from gas-liquid flows. Below the gas-liquid literature is reviewed first and the few available attempts on liquid-liquid are discussed next.

2.5.1 Gas-liquid flows

All the works conducted to model entrainment were mainly done for *annular* gas-liquid flow in either horizontal or vertical pipes. Azzopardi (1997) in his review concluded that all the predictive methods for the rate of entrainment are still empirical. Researchers began to model the entrained fraction since it is a more stable parameter to measure and to correlate. However, it gives a considerable error when applying to certain transient conditions (Ishii and Mashima, 1989). Some other investigators attempted to model the rate of entrainment which represents the mass transfer better at the wavy interfaces and worked well at the transient conditions which are very critical for nuclear reactors (Kataoka et al., 2000).

In vertical flows, several correlations were developed to predict entrained fraction in *annular* gas-liquid flow. Most correlations were empirical or semi-empirical that contained at least one or more empirical terms. Paleev and Filipovich (1966) developed a dimensionless empirical equation by fitting the experimental data. This equation is given by

$$E = 0.015 + 0.441 \log\left[\frac{\rho_g}{\rho_{Lf}}\left(\frac{\mu_{Lf} j_g}{\sigma}\right)^2 \times 10^4\right] \tag{2.11}$$

One of the main disadvantages in the correlation is that the effect of pipe diameter and liquid flow rate were not taken into account. Hewitt and Hall-Taylor (1970) summarized different entrained fraction correlations that were developed by different investigators, some dimensional and others dimensionless. In the summary, they showed that these correlations were giving good prediction just over limited ranges of experimental conditions.

Entrainment can be predicted theoretically from the balance between the rate of entrainment (R_A) and the rate of deposition (R_D). The rate of deposition is a linear function on the droplet concentration and can be expressed as follows (Dallman et al., 1979, Pan and Hanratty, 2002a&b):

$$R_D = k_D C_D = k_D\left(\frac{W_{Le}}{Q_g S}\right) \tag{2.12}$$

where k_D is the deposition rate constant, C_D is the droplet concentration, Q_g is the volumetric flow of the gas, S is the ratio of drop velocity to gas velocity and W_{Le} is the droplet mass flow rate.

At equilibrium, R_A=R_D

$$E = R_A \frac{Q_g S}{k_D W_L} \tag{2.13}$$

where, $E = \frac{W_{Le}}{W_L}$ (2.14)

and W_L is the total liquid mass flow rate.

The first attempt to develop a simple mechanistic model for predicting entrained fraction using this approach in *annular* flow was by Hutchinson and Whalley (1973). In their study, the rate of deposition was given by

$$R_D = k_D C \tag{2.15}$$

and the entrainment rate was written as

$$R_A = k_A C_e \tag{2.16}$$

where k_A is the mass transfer coefficient and C_e is the equilibrium concentration which has been correlated by

$$C_e = C_e\left(\frac{\tau_i \delta}{\sigma}\right) \tag{2.17}$$

where τ_i is the interfacial shear and δ is the film thickness.

This model encountered some difficulties when applying. The data exhibit considerable scattering around the trend which makes hard to formulate a correlation for C_e, taking also into consideration that parameter δ and C_e are not measured in some experiments.

Dallman et al. (1979) included the effect of pipe diameter (D) while developing the entrained fraction equation. In their approach, a linear relation of the rate of entrainment was obtained first empirically. This equation was balanced with the rate of deposition for fully developed conditions from which an entrained fraction was developed as follows

$$\frac{E/E_M}{1-(E/E_M)} = \frac{k_A D U_g^3 S(\rho_g \rho_{Lf})^{0.5}}{4k_D} \tag{2.18}$$

where E_M is the maximum entrained fraction.

The above equation showed that E/E_M is strongly dependent on gas velocity (U_g) and independent on liquid mass flow rate (W_L). However, Hay et al. (1996) showed from the measurements of R_A and R_D that k_A and k_D change with W_L.

Applying the above approach and using the experimental results published by different investigators, Pan and Hanratty (2002a) developed a correlation from entrainment measurements of liquids with viscosities close to that of water based on Eq. 2.18. They examined the effect of liquid flow (W_L), gas density, surface tension, pipe diameter and gas velocity from the published experimental results using the following equation:

$$\frac{E}{E_M} = f\left[\frac{(U_g - U_{gc})^2 (\rho_g \rho_{Lf})^{0.5} D}{\sigma}\right] \tag{2.19}$$

This equation was fitted linearly with the published data and the following was obtained:

$$\frac{E/E_M}{1-(E/E_M)} = A_1 \frac{(U_g - U_{gc})^2 (\rho_g \rho_{Lf})^{0.5} D}{\sigma} \tag{2.20}$$

where $A_1 = 6 \times 10^{-5}$

The above equation showed weaker effects of surface tension and gas density when compared to the one obtained by Paleev and Filipovich (1966). For further enhancing the entrainment correlation and based on physical understanding, Pan and Hanratty (2002a) derived an equation for k_D. This relation offered more reliable correlation for entrainment rather than assuming k_D/S is proportional to U_g.

A different approach was employed to model the entrained fraction by Ishii and Mishima (1989). They used the model developed by Ishii and Grolmes (1975) for the onset of entrainment and assumed that all the excess liquid above the onset of entrainment velocity will be entrained as shown in the equation below.

$$1 - E_{th} = \frac{j_{Lf}}{j_L} = \frac{\mu_{Lf}}{\rho_{Lf} D_{Lf} j_L} \left(11.78 N_\mu^{0.8} \frac{\sigma}{\mu_{Lf} j_g} \sqrt{\left(\frac{\rho_{Lf}}{\rho_g} \right)} \right)^3 \tag{2.21}$$

where E_{th} is the theoretical entrainment limit if all the excess liquid was entrained and j_{Lf} is the liquid film volumetric flux. E_{th} was found to be much greater when compared with the experimental data. From the equation, E is a function of dimensionless gas flux ($j_g^* \approx j_g / (\sigma g \Delta\rho / \rho_g^2)^{1/4}$) and Re_L. To improve the prediction, the effect of droplet inertia in the gas core was included by modifying j_g^*. Accordingly, by plotting the entrained fraction against different Reynolds numbers, the gas core inertia near the interface increased by a factor of $\left(\frac{\Delta\rho}{\rho_g} \right)^{1/3}$ due to the droplets.

Furthermore, it is known that E depends also on the droplet concentration. Consequently, they introduced a dimensionless hydraulic diameter (D^*) to take into account the effect of droplet concentration. Such addition made the entrained fraction

equation to be function of j_g^*, Re_L and D^*. Therefore, by fitting the data, an equation was developed for the entrained fraction for fully developed flow. This is:

$$E_\infty = \tanh(7.25\times10^{-7} We^{1.25}\,\mathrm{Re}_L^{0.25}) \tag{2.22}$$

where E_∞ is entrained fraction at equilibrium and We is the effective Weber number for entrained and it is given by

$$We = \frac{\rho_g j_g^2 D_{Lf}}{\sigma}\left(\frac{\Delta\rho}{\rho_g}\right)^{1/3} \tag{2.23}$$

Another approach based again on defining the critical liquid film velocity below which there is no entrainment was developed by Hewitt and Govan (1990). The developed equation calculates the mass entrained rate per unit perimeter. The equation only applies when the liquid film velocity is greater than the critical one.

Schadel et al. (1990) carried out a comprehensive study based on some theoretical understanding of the process and using experimental data to develop correlations for the rate of entrainment, rate of deposition and the entrainend fraction for upward *annular* flow. In this work, the mass flow rates of the droplets (W_{Le}) were measured and then the concentrations were calculated. Such measurements were achieved by injecting salt solution in the film so the concentration of the film was measured with several conductance probes located at different points from the injection point. A mass balance was performed on the salt from which the following equation was derived:

$$\frac{d\ln\alpha}{dz} = \frac{-\pi DR_D}{W_L}\frac{1}{E(1-E)} \tag{2.24}$$

where $\alpha = \dfrac{C_F - C_{MC}}{C_{MC}}$, C_F is the concentration of the salt and C_{MC} is the mixing cup concentration which was determined for each measurement with a pair of wall electrodes by taking a liquid sample from the separator.

They calculated the entrained fraction by plotting $ln\alpha$ vs. z which gives a straight line, the slope of which is $\dfrac{-\pi DR_D}{W_L}\dfrac{1}{E(1-E)}$ and the intercept at $z = 0$ gives $(C_{F0} - C_{MC})/C_{MC}$ which can be used to calculate the entrained fraction.

It was found that applying the published entrained fraction correlations at transient conditions might lead to some errors and only a reliable entrainment rate equation can predict the entrainment behavior at such conditions. Kataoka et al. (2000) attempted to develop a reliable correlation that can predict the entrainment rate from the liquid film. A mass balance equation at the interface at steady state was derived which was based on the deposition rate and the entrained fraction. This equation was expressed as:

$$R_A = \frac{D\rho_{Lf} j_{Lf}}{4}\left(\frac{\partial E}{\partial z}\right) + R_D \tag{2.25}$$

The deposition rate, R_D, was given by $R_D = k_D C$ and k_D was found from the correlation developed by Paleev and Filippovich (1966). The entrained fraction was given by Eq. 2.22 which was developed by Ishii and Mishima (1989).

Kataoka et al. (2000) developed a model for the pipe entrance and equilibrium regions. The entrainment rate correlation for the fully developed region is expressed as

$$\frac{R_A D}{\mu_{Lf}} = 6.6\times10^{-7}\,\mathrm{Re}_L^{0.74}\,\mathrm{Re}_{Lf}^{0.185}\,We^{0.925}\left(\frac{\mu_g}{\mu_{Lf}}\right)^{0.26} \tag{2.26}$$

where Re_{Lf} is the liquid film Reynolds number.

Holowach et al. (2002) developed a correlation for entrainment rate which was based on physical argument. A control volume analysis was performed (see Fig. 2.6) and the entrainment rate for the droplets was expressed by

$$R_A = \frac{V_{entr,w}\rho_{Lf} N_{w,cv}}{A_{cv}\tau_{w,cv}} \tag{2.27}$$

Fig. 2.6 Entrainment control volume by Holowach et al. (2002)

The entrainment rate as it can be noted from the equation depends on the volume of liquid removed from each wave ($V_{entr,w}$), the number of waves in the control volume ($N_{w,cv}$), the area of the control volume (A_{cv}) and the period of the entrainment phenomena in the control volume ($\tau_{w,cv}$). The droplet entrainment results from Kelvin-Helmoholtz instability as showed by Woodmansee and Hanratty (1969), Holowach et al. (2002) performed an interfacial stability calculation from which the critical wavelength was calculated. To get the other parameters required for finding the entrainment rate, they performed force balances on a sine wave to determine the maximum amount of liquid that can be entrained from one wave.

Once the critical wavelength and the volume of the entrained wave were found, all the other parameters can also be calculated. The entrainment rate predicted by the model is significantly higher than that measured, so to determine the average droplet entrainment rate, Holowach et al. (2002) compared his model with the experimental data published by Hewitt and Pulling (1969) and Keeys et al. (1970). A correlation was produced for the average entrainment rate, which is expressed as

$$R_A = 0.0311 \mathrm{Re}_{Lf}^{1.67} \left(\frac{\rho_{Lf}}{\rho_g} \right)^{7/8} N_\mu^3 \frac{V_{entr,w} \rho_{Lf} (\overline{U_{gc}} - \overline{U_{Lf}})}{\lambda^3 \{1 - \alpha_1\}^{1/2}} \tag{2.28}$$

where U_{gc} is the gas core velocity and U_{Lf} is the liquid film velocity and λ is the wavelength.

This equation showed a good agreement when compared to some other experimental data (Fig. 2.7).

Kelvin-Helmholtz instability analysis was also utilized by Lopez de Bertodano (2001) to get a relation for the entrainment rate. The relation was found to be as follows:

$$\frac{R_A D}{\mu_{Lf}} \alpha \, We_g \, \mathrm{Re}_{Lf} \frac{U_g}{U_{Lf}} \sqrt{\frac{\rho_g}{\rho_{Lf}}} \tag{2.29}$$

where We_g is the gas Weber number and it is given by $We_g = \frac{\rho_g j_g^2 D}{\sigma}$.

The above relation is approximately similar to the rate of entrainment equation which was developed by Kataoka and Ishii (1982). The differences between them are that the appearance of velocity ratio and the absence of viscosity ratio in Eq. 2.29. Also, Eq 2.29 is a function of Re_{Lf} instead of Re_L $(1\text{-}E)^{0.2}$. Consequently, based on Eq. 2.29, Dallman et al. (1979) and Kataoka and Ishii (1982) equations, the following relation was suggested which combines the strong points of both correlations.

$$\frac{R_A D}{\mu_{Lf}} = f\left(We_g \, \mathrm{Re}_{Lf} \frac{\rho_g}{\rho_{Lf}} \frac{\mu_{Lf}}{\mu_g}\right) \tag{2.30}$$

Based on the above well-chosen dimensionless numbers, experiments were designed to measure the entrainment rate for air-water loop and a Freon loop. Doing so, a new dimensionless correlation was developed and given by

$$\frac{R_A D}{\mu_{Lf}} = \frac{k_A'}{4}(\mathrm{Re}_{Lf} - \mathrm{Re}_{Lfc}) We_g \left(\frac{\rho_g}{\rho_L}\right)^{1/2} \tag{2.31}$$

where Re_{Lfc} is the critical liquid film Reynolds number.

The above correlation showed a good agreement when compared with the old and new experimental data.

Fig. 2.7 Predicted and experimental entrainment data by Holowach et al. (2002)

For *annular* gas-liquid phase flowing in horizontal pipes, the liquid film at the bottom is usually thicker than that at the top. In comparison to vertical flows, McCoy and Hanratty (1977) concluded that the distribution of the liquid film in the horizontal pipes is not the same. They suggested that the deposition mechanism in horizontal flows can be different than that for vertical flows due to the effect of gravity on droplet deposition.

Wicks and Dukler (1960) developed for horizontal flow a dimensionless entrainment correlation which is given by

$$R_A = \frac{We_c\left(\frac{j_{Lf}}{j_g}\right)}{\left(\frac{dp}{dz}\right)_g W_{Le}} \tag{2.32}$$

where $\left(\frac{dp}{dz}\right)_g$ is the pressure gradient for the gas phase and We_c is the critical Weber number

This equation was correlated in terms of Martinelli parameter (X)

$$\left(X = \left[\left(\frac{dp}{dz}\right)_{Lf} / \left(\frac{dp}{dz}\right)_g\right]\right) \tag{2.33}$$

$\left(\frac{dp}{dz}\right)_{Lf}$ is the pressure gradient for the liquid phase

One of the early attempts to develop a correlation for *annular* flow in horizontal pipes was carried by Dallman et al. (1984) based on the equations derived for vertical flows (see Eq. 2.18). The entrainment equation for vertical flows, with $\frac{k_A}{4k_D}$ = constant, failed to predict the measuring entrainment data for air and water flowing in horizontal 2.54 cm pipelines. This is because the effect of gravity on the deposition was not taken into account while it is important for horizontal flows. A new empirical correlation was developed by fitting the data as shown in Fig. 2.8. The empirical equation is given by

$$\frac{E}{1-\frac{W_{Lfc}}{W_L}} = \frac{3.6\times10^{-8}\left[\left(D-2\langle m\rangle\right)\rho_g^{1/2}\rho_{Lf}^{1/2}U_g^3\right]^{1.5}}{1+3.6\times10^{-8}\left[\left(D-2\langle m\rangle\right)\rho_g^{1/2}\rho_{Lf}^{1/2}U_g^3\right]^{1.5}} \tag{2.34}$$

where W_{Lfc} is the critical liquid film mass flow rate and 3.6×10^{-8} is a dimensional constant.

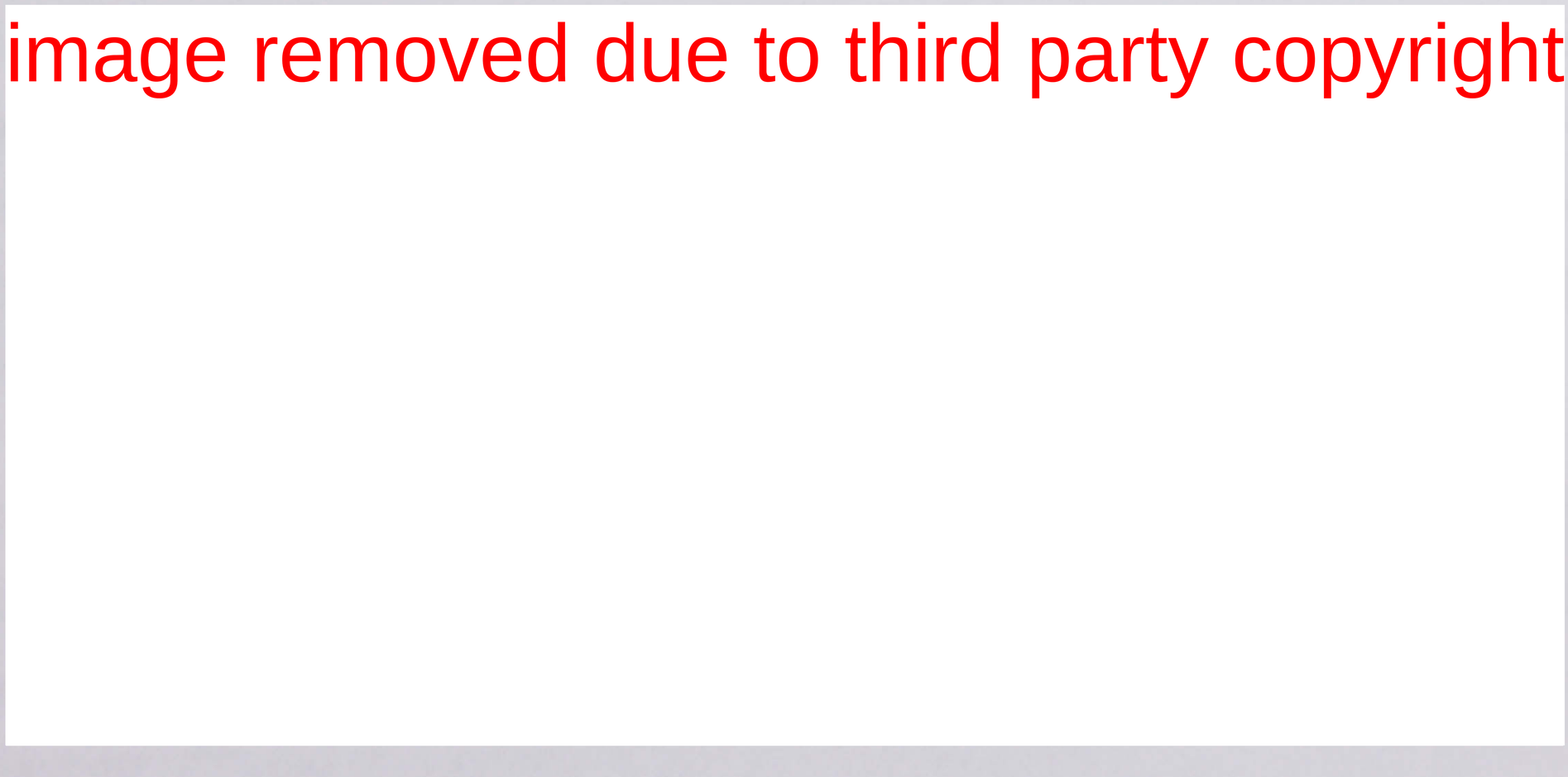

Fig. 2.8 Correlations for entrainment measurements by Dallman et al. (1984)

Williams et al. (1996) modified Eq. 2.18 derived by Dallman et al. (1979) for vertical pipes so it could be used for horizontal flows. Such modification was managed by conducting experiments to measure the entrainment for air and water flowing in a horizontal 9.53 cm pipe. They observed a stratification of drops which could be related

to the influence of gravity. A theoretical derivation was done in parallel with the entrainment measurements to get an equation for k_D in respect to fluid turbulence and gravitational settling. This equation is expressed as follows

$$k_D = \frac{g\rho_{Lf}D}{\mu_g}\left(\frac{\sigma}{\rho_g U_g^2 f_s}\right)\left\langle\frac{C_w}{C_B}\right\rangle \tag{2.35}$$

$$\text{where } \left\langle\frac{C_w}{C_B}\right\rangle = \frac{1}{\pi}\int_0^{\pi}\frac{C_w}{C_B}\cos(\theta)d\theta \tag{2.36}$$

and C_w is the concentration at the wall, C_B is the bulk concentration and f_s is the friction factor for flow over smooth wall.

Their work could be considered as the first attempt that includes the effect of settling gravity which is significant in horizontal flow.

As a continuation of the work done by Williams et al. (1996), Pan and Hanratty (2002b) developed an entrained fraction equation for *annular* flow in horizontal pipes in a similar manner to the one derived by Dallman et al. (1979) for vertical pipes for fully developed conditions ($R_A = R_D$). For the entrainment rate, they used two empirical equations; the first one was obtained for horizontal pipes at low gas velocities. The correlation found by Dallman et al. (1979) for vertical pipes at high gas velocities was used for the second one. This is because the gravity will be less significant at high velocities and equations derived for vertical flows could be applied.

For the deposition rate, they derived a general relation by conducting a theoretical study of particle turbulence. Pan and Hanratty (2002b) showed that R_D relation worked well at large and small gas velocities. Applying the definition which states that entrainment is the result of R_A and R_D, the following relation was developed:

$$\frac{E/E_M}{1-(E/E_M)} = 0.05\left(\frac{U_g}{U_{gc}}\right)^3\left(\frac{U_g}{U_{gc}}\right)^{(1+m)/(2-m)} \tag{2.37}$$

where m is the average film height around the pipe circumference.

2.5.2 Liquid-liquid flows

Modeling the entrainment of one phase into the other is important to understand and analyze the *dual continuous* flow pattern. In spite of the importance of knowing the entrained fraction of one phase into the other, only Valle (2000) has attempted to develop correlations for the entrained fraction based on the rate of entrainment and the rate of deposition. The entrained fraction can then be applied into other equations to improve the prediction of pressure drop

The model Valle (2000) on entrainment rate was based on a balance between three forces acting on a drop. These are gravity force (F_g), drag force (F_D), and driving force (F_T) due to turbulent fluctuations as shown below respectively:

$$F_g = \frac{\pi}{6} d^3 (\rho_c - \rho_d) g \cos\theta \tag{2.38}$$

where d is the drop diameter, ρ_c is the continuous phase density and ρ_d is the dispersed phase density.

$$F_D = \frac{\pi}{8} d^2 C_d \rho_c v_d |v_d| \tag{2.39}$$

where C_d is the drag coefficient and v_d is the initial drop velocity normal to the interface.

$$F_T = \frac{\pi}{4} d^2 \rho_c \langle v'^2 \rangle \tag{2.40}$$

where $\langle v'^2 \rangle$ is the mean of the square of the velocity fluctuations v'.

Valle (2000) described that the initial drop velocity (v_d) can be found by balancing the above three terms as expressed below

$$\frac{\pi}{8} d^2 C_d \rho_c v_d^2 = (F_T - F_g) \tag{2.41}$$

In addition to that, he suggested that for a certain location in the pipe, the volumetric entrained drop flux could be given as

$$R_A(y) = \frac{\pi}{6} d_{init}^3 n_d v_d \tag{2.42}$$

where n_d is the number of drops at the interface and d_{init} is the initial drop diameter.

The initial drop diameter was set equal to d_{50}-value combined with the d_{95}-value where the d_{50}- value is estimated from the Rosin-Rammler distribution function while the d_{95}-value is found from the Hinze (1955) model. It is important to note that the calculated diameter is an assumed number and did not represent the actual initial drop diameter at the liquid-liquid interface.

By combining the equations, Valle (2000) expressed the rate of entrainment as

$$R_A = C_1 . \frac{d_{init}}{\lambda}\left[\left\langle \hat{v}^{'+2} \right\rangle U^{*2} - \frac{2}{3} d_{init} . \frac{|\rho_c - \rho_d|}{\rho_c} . g\cos\theta\right]^{0.5} \tag{2.43}$$

where U^* is the friction velocity and $v^{'+} = \frac{v'}{u_*}$.

C_1 is a constant which takes into account the number of unstable interfacial waves that form drops and the interaction between the formation and the entrainment of drops in each phase. Valle (2000) assumed a value of 0.1 for C_1.

For the rate of deposition, several forces acting on the drop, Valle (2000) considered three forces. These are the displacement force which is the force required to displace the continuous phase between the drop and the interface, the gravity force and the drag force. By obtaining a balance between them, the rate of deposition was found to be:

$$R_D(y) = \frac{\pi}{6} d^3 n_d v_{df} \tag{2.44}$$

v_{df} is the final velocity for a drop in the oil-water interface for the relevant drop sizes and is given by:

$$v_{df} = \frac{dh_m}{dt} = \frac{2(1+2m)F_g h_{cr}}{3\pi\mu_c d^2} \tag{2.45}$$

where h_{cr} is the critical distance between the drop and the interface and it is assumed to be equal to 0.1μm, μ_c is the continuous phase viscosity and m is the mobility parameter.

Valle (2000) used the entrainment and deposition rates to describe the entrained fraction concentrations at the interface by conducting a material balance between them. The results were used to develop equations that can calculate the superficial velocities of the

continuous phases with entrained opposite phase as shown below in terms of the in-situ phase fractions.

$$U_{sco} = \frac{U_{so} - U_{sw}(\frac{E_{co}}{E_{dw}})}{1 - \frac{E_{do}E_{dw}}{E_{cw}E_{co}}} \tag{2.46}$$

$$U_{scw} = \frac{U_{sw} - U_{so}(\frac{E_{cw}}{E_{do}})}{1 - \frac{E_{do}E_{dw}}{E_{cw}E_{co}}} \tag{2.47}$$

where U_{sco} is superficial velocity when oil is the continuous phase, U_{scw} is the superficial velocity when water is the continuous phase E_{ci} is the in-situ phase fraction of continuous phase i, E_{di} is the in-situ phase fraction of dispersed phase i and i is either oil (o) or water (w).

These equations were used in parallel with the two-fluid model to enhance the prediction of pressure drop. The mixture liquid properties of each separate zone in the two-fluid model were calculated as a function of the entrained fractions of the drops. The predicted pressure drops though did not fit the experimental data as shown in Fig. 2.9. The entrained fractions were not tested against some experimental data.

Fig. 2.9 Predicted and experimental pressure drop at (a) 1.17 m/s and (b) 0.87 m/s mixture velocities by Valle (2000)

Experimentally, Valle and Kvandal (1995) conducted a study of stratified oil/water to investigate the dispersion characteristics and phase distribution related to the measured pressure drop. As a part of this study, they measured the entrained fractions of the droplets in the continuous phase at different mixture velocities as shown in Fig. 2.10. They assumed that above 50% oil, the continuous phase is oil while below it; it is water. The onset of droplet formation was found at mixture velocities of about 0.85 m/s. To predict the pressure drop, they used the two-fluid model at different mixture velocities. It is worth noticing that at low oil superficial velocity, (*stratified* flow without entrainment) the standard two-fluid model agreed well with the predicted pressure drop as shown in Fig. 2.11. On the other hand, for mixture velocities equal to 1.0 and 1.5 m/s (*dual continuous* flow), the two-fluid model was unable to predict the pressure drop when compared with the experimental data (Fig. 2.12).

Lovick and Angeli (2001) calculated the entrainment of one phase into the other during *dual continuous* flow from phase distribution measurements obtained by an impedance probe. They reported that the initiation of entrainment was observed around 0.8 m/s mixture velocity. These measurements were then included in the two-fluid model to enhance the prediction of pressure drop. However, the model still over predicted the experimental pressure drop data. Such over prediction could be attributed to the increase in the dispersion viscosity models used for the upper and lower layers of *dual continuous* flow.

Fig. 2.10 Entrained fraction at different mixture velocities for 0.40 oil volume fraction, by Valle and Kvandal (1995)

Fig. 2.11 Predicted and experimental pressure drop at 0.25 m/s mixture velocity, by Valle and Kvandal 1995

Fig. 2.12 Predicted and experimental pressure drop at 1.5 m/s mixture velocity, by Valle and Kvandal 1995

Soleimani (1999), Elseth (2001) and Hussain (2004) measured the vertical local volume fractions across the pipe cross section. These data can be transformed to calculate the entrained fraction of each phase into the other if the interface location is known.

2.6 Drop Size Distribution

The majority of work on drop sizes in multiphase flow has been conducted for two-phase gas-liquid flows especially for flows of air and water (Simmons and Azzopardi, 2001). However, two-phase systems in the oil and chemical industries may consist of

dispersions of two immiscible liquids. Knowledge of drop size and drop size distribution are important factors that determine rheology and stability of a dispersion. They also have a very significant effect upon equipment performance. Several studies have been carried out to model the size and the distribution of the dispersed phase in the continuous phase. However, there is very limited amount of data from pipe line flow due to the complex nature of the experiments. Thus, most research in this area has been carried out in stirred vessels with researchers trying to construct models for both drop break-up and coalescences. Break-up and coalescence will determine the final drop size distribution in a dispersed flow system. While most of the works looked at this phenomena separately, a few tried to combine them using population balances (Valentas et al., 1966; Tsouris and Tavlarides, 1994; Hu, 2006).

2.6.1 Drop break-up

The first fundamental work that assumed drop break-up in a turbulent flow field was conducted by Kolmogorov (1949) and Hinze (1955). Hinze (1955) reported that viscous stress or dynamic pressure force exerted by the continuous phase on the drops is responsible of drop deformation. He assumed that this force (τ) will try to deform the drop while surface tension on the other hand (σ) will try to maintain the drop as a sphere. The surface tension force was assumed to be of the magnitude σ/d (where d is the drop diameter). Due to its deformation, internal flow can be set inside the drop which will cause both viscous stresses and dynamic pressure forces. The dynamic pressure forces will cause flow velocities of the order of $(\tau/\rho_d)^{0.5}$ while viscous stresses inside the drop will be of the order of

$$\frac{\mu_d}{d}\sqrt{\frac{\tau}{\rho_d}} \tag{2.48}$$

where ρ_d is the dispersed phase density and μ_d is the dispersed phase viscosity.

According to Hinze, three forces will act on the drop and two dimensionless groups can be calculated. A generalized Weber number (We) is a result of the balance between the external forces trying to deform the drop and the surface tension trying to resist the deformation:

$$We = \frac{\tau d}{\sigma} \tag{2.49}$$

The second one is the viscosity group which stabilizes the drop. The dimensionless number which accounts for the dispersed phase viscosity is expressed as

$$N_{vi} = \frac{\mu_d}{\sqrt{\rho_d \sigma d}} \tag{2.50}$$

Hinze (1955) argued that since only two dimensionless groups described the phenomenon the following relation can be found

$$We_{\text{crit}} = C_1(1 + \varphi(N_{vi})) \tag{2.51}$$

where C_1 is constant, We_{crit} is the critical Weber number that gives the maximum drop size (d_{max}) that can resist break-up in a turbulent flow field and the function φ decreases to zero as N_{vi} goes to zero.

According to Hinze viscosity is normally not significant in turbulent flows. He mentioned that external viscous forces can only be important if the drops are small compared to the length scale of the viscous flow which is given by the Kolmogoroff length scale (the length scale of turbulence which gives Reynolds number equal to one). Thus, the deformation of drops was attributed to the dynamic pressure forces caused by changes in the velocity over a distance equal to the drop size and given by

$$\tau = \rho_c \Delta v^2 \tag{2.52}$$

where Δv is the velocity difference across the drop.

The estimation of this velocity difference will require an understanding of the turbulent flow field of the continuous phase. The turbulent field can be considered homogenous and isotropic at length scales that are small compared to the length scale l_e of the energy containing eddies (Hinze, 1955). For the small length scales, the eddies structure will depend on both the viscosity of the continuous phase and the rate of the energy dissipation per unit mass (ε). For high Reynolds number, the eddies structure will depend mainly on ε and the velocity difference can be written as follows:

$$\Delta v^3 = C_1 \varepsilon l \tag{2.53}$$

where the length scale l is defined as $l_k << l << l_e$

In pipe flow a value of $l_e \approx 0.1D$ (where D is the pipe diameter) is used (Hutchison et al., 1971; Kubie and Gardener, 1977). l_k is the Kolmogoroff length scale which is given by

$$l_k = \frac{(v_c^3)^{0.25}}{\varepsilon} \tag{2.54}$$

where v_c is the kinematic viscosity of the continuous phase.

Hinze (1955) assumed that the N_{vi} group is small in turbulent flows so the maximum drop size can be written as follows:

$$d_{\max}\left(\frac{\rho_c}{\sigma}\right)^{3/5} \varepsilon^{2/5} = C_2 \tag{2.55}$$

where C_2 is a constant. The above correlation was fitted to data from Clay (1940) and a value of 0.725 for C_2 was obtained. Experimental data from stirred vessels showed good fit to the above correlation (Sprow, 1976). The equation can be used also for pipeline if the mean energy dissipation per unit mass is used as follows:

$$\varepsilon_M = \frac{fU_c}{2D} \tag{2.56}$$

where f is the friction factor, U_c is the average axial velocity of the continuous phase and D is the pipe diameter. When Eq. 2.55 and 2.56 are combined (Kubie and Gardener, 1977; Karabelas, 1978), the following equation can be found

$$\left(\frac{d_{\max}\rho_c U_c^2}{\sigma}\right)\left(\frac{fd_{\max}}{4D}\right)^{2/3} = 0.369 \tag{2.57}$$

Karabelas (1978) argued that for pipeline flow, drop break-up may happen in the inertial sub-layer close to the wall. He attributed this to the decrease in the thickness of the buffer layer for high Reynolds numbers. This decrease made the lower boundary of the inertial sub-layer to be very close to the wall. Tenneks and Lumley (1972) reported that for pipe flow in the inertial sub-layer, the local energy rate per unit mass (ε_l) is inversely proportional to the distance from the wall (y_w):

$$\varepsilon_{l;} \approx \frac{U^{*3}}{Ky_w} \tag{2.58}$$

where K is the von Karman constant. Close to the wall ε_l will be larger than ε_M. However, at a certain distance from the wall ε_M will become equal to ε_l.

Karabelas (1978) assumed that d_{max} will appear between the beginning of the inertial sub-layer and the distance where $\varepsilon_M = \varepsilon_l$.

Kubie and Gardner (1977) argued that when $d > l_e$ the fluctuating turbulent velocity should be used instead of the velocity difference and Eq. 2.52 will become

$$\tau = \rho_c u_f^{'} \tag{2.59}$$

Hughmark (1971) assumed $u_f^{'}$ approximately equal to $1.3U^*$.

where U^* is the friction velocity and it can be found according to Massey (1989) as

$$U^* = (\frac{f}{8})^{0.5} U_c \tag{2.60}$$

Kubie and Gardner (1977) demonstrated that the maximum drop size from Eq. 2.49 in a pipe flow when the drops have sizes larger than the inertial turbulence subrange scale can be written as

$$\frac{f d_{\max} \rho_c U_c^2}{\sigma} = 5.53 \tag{2.61}$$

Sleicher (1962) found that the maximum drop size from his data did not agree with the Hinze model and proposed a new equation where a different viscosity group was used. The equation can be expressed as:

$$\left(\frac{d_{\max} \rho_c U_c^2}{\sigma}\right)\left(\frac{\mu_c U_c}{\sigma}\right)^{0.5} = 38\left(1+0.7\left(\frac{\mu_d U_d}{\sigma}\right)^{0.7}\right) \tag{2.62}$$

Brauner and Ullmann (2002) argued that the Hinze model is only applicable to dilute dispersions. While in concentrated dispersions the model failed to predict the max drop size because the inherent assumption that the turbulent kinetic energy flux of the continuous phase is greater than the surface energy generation by drop break-up is no

longer valid. Thus, they proposed a new correlation for high concentration dispersions which is given by:

$$d_{\max} = 2.22 C_H \left(\frac{\rho_c U_c^2 D}{\sigma}\right)^{-0.6} \left(\frac{\rho_m}{\rho_c (1-\phi_d)} f\right)^{-0.4} \left(\frac{\phi_d}{1-\phi_d}\right)^{0.6} \tag{2.63}$$

where ρ_m is the mixture density, C_H is a tunable constant and ϕ_d is given by

$$\phi_d = \frac{U_{sd}}{U_{sd} + U_{sc}} \tag{2.64}$$

where U_{sd} is the dispersed phase superficial velocity and U_{sc} is the continuous phase superficial velocity.

A comprehensive summary about drop break up models was given by Hu (2006).

2.6.2 Drop coalescence

In order for coalescence of drops to take place in a turbulent flow field, first they must collide. Sufficient time is required for the drops to remain in contact, which will allow the continuous phase film entrapped between the drops to reach a critical thickness where it ruptures and the two drops join. Before coalescence, turbulent eddies of the continuous phase may take apart the contacted drops. The drainage of the film of the continuous phase between the contacted drops depends on different parameters (eg. temperature, vibrations, surfactants, fluid properties). This makes the modeling of such phenomenon difficult as reported by Valentas et al. (1966) and Thomas (1981).

Similar to drop break up, Shinnar (1961) suggested that drop coalescence happens in the inertial sub-range of turbulence. When drops collide, they exert an attraction force to each other. Shinnar (1961) assumed that this force depends on the size of the drops. According to this, the adhesion energy for two drops of equal diameter can be expressed as

$$E_a = A(h_o)d \tag{2.65}$$

where h_o is the film thickness,

$$A(h_o) = \frac{1}{2}\pi \int_{ho}^{\infty}\int_{h}^{\infty} f(h)\delta(h)\delta \,,$$

and $f(h)$ is the attraction force per square centimeter between two infinite parallel surfaces separated by distance h.

Also, he reported that the kinetic energy of two drops with equal diameters (d) that are in relative movement to each other is proportional to $\rho_c v^2 d^3$. The coalescence of the drops can be prevented by keeping the kinetic energy higher than the adhesion force. Therefore, there will be a minimum diameter d_{min} for which separation of drops after collision is still possible. This d_{min} can be described by the following equation:

$$\frac{\rho_c v^2 d_{\min}^2}{A(h_o)} = C_3 \tag{2.66}$$

where C_3 is a constant. Coalescence is not possible if drops have diameter larger than the minimum defined in the above equation.

Although Thomas (1981) regarded that drop coalescence occurred in the inertial sub-range of the turbulent flow field (similar to Shinnar, 1966), he argued that adhesion energy is not important for coalescence. Instead, he believed coalescence depends on the time that the drops remain in contact. For this reason, he provided an equation to calculate the time required for the film between two drops to drain to the critical thickness. The equation can be given as

$$t = \frac{3}{32\pi} \mu_c F \left(\frac{d}{\sigma h_r} \right)^2 \tag{2.67}$$

where F is the force pressing the drops together and h_r is the thickness of the continuous phase film between the drops where rupture will occur.

Angeli (1996) and Hu (2006) presented extensive summary of the drop coalescence literature used for dispersed system.

2.6.3 Drop size distribution

As there is a large number of profiles that can characterize a drop size distribution it is easier to compare drop size distributions using characteristic mean diameters. The d_{max} which was discussed before might be very large if the distributions have a long tail. For this case, d_{95} could be used. This is defined as the diameter that is larger than the 95%

of the cumulative number of drops. Mean diameters that are normally used are the linear mean diameter (d_{10}) and the Sauter mean diameter (d_{32}) which are defined as follows:

$$d_{10} = \frac{\sum_{j=1}^{n} d_j}{n} \tag{2.68}$$

$$d_{32} = \frac{\sum_{j=1}^{n} d_j^3}{\sum_{j=1}^{n} d_j^2} \tag{2.69}$$

where n is the of drops measured (Pacek et al., 1998)

Few investigators have attempted to develop mathematical models that can predict drop size distribution in a turbulent flow field (Angeli, 1996). On the other hand, a number of investigators have presented experimental drop size distribution in turbulent pipe flow despite the fact that most of them concentrated on dilute dispersion. Ward and Knudsen (1967) investigated both drop size and velocity distribution in downward vertical liquid-liquid flow. In their study, they used a dispersed volume up to 35%. The dispersion was made in a stirred vessel and then pumped to the test section. The authors used photographic technique to measure the drop size and found that the Sauter mean diameter varied as the 0.4 power of the dispersed phase concentration. Sleicher (1962) in his experimental study used an inlet nozzle to form drops while studying the stability of artificially formed drops. He found that the maximum drop size decreased as the velocity increased. Further investigation of this relation by Su and Hanzevack (1988) concluded that the drop size is linearly decreased with the increase in velocity. Recently, Angeli and Hewitt (2000) and Lovick and Angeli (2004) found that the effect of mixture velocity on drop size is less strong. Sleicher (1962) conducted his measurement close to the wall where there is a greater shear and this could explain the difference in the result.

Collins and Knudsen (1970) investigated drop size of three different oils (with viscosities 1.1, 8.6 and 15.6 mPa s) in water for vertical downward flow. The oil is injected into the flowing water which resulted in a certain drop size distribution at the inlet. A second distribution then appeared as the flow developed along the pipe as a

result of the turbulent flow. They found that none of the commonly used distribution laws could represent their data. The distribution near the nozzle could be approximated by log-normal distribution while drops formed further down as result of turbulence diverged from the log normal one. The study showed that the length of time for the drops to break-up into their final distribution increases as the viscosity of oil increases. Collins and Knudsen (1970) found that the model developed by Sleicher (1962) was able to predict the maximum stable drop diameter found in their experiments.

Kubie and Gardner (1977) conducted experiments in horizontal pipes by injecting the dispersed phase into the continuous one using four different injector types. The results showed a small effect on the final drop distribution. The measurements were taken by photographing the flow through the pipe wall. They found that the d_{max} value could be predicted by Eq. 2.61.

Karabelas (1978) described two of the most common standard distributions shapes. These are the Rosin-Rammler and the log normal distributions given respectively as follows:

$$V_{cum} = \exp\left(-\left(\frac{d}{d^*}\right)^n\right) \tag{2.70}$$

and

$$y(d) = \frac{\varphi}{\sqrt{2\pi\delta^2}}\exp\left[\frac{-1}{2\delta^2}(\ln(d-\zeta))^2\right] \tag{2.71}$$

where V_{cum} is the cumulative volume fraction, n is the slope of the plot, d^* is the diameter corresponding to V_{cum} =0.3679, δ, φ, ζ are parameters of the log normal distribution with δ affecting the distribution height and ζ affecting the distribution width.

The Rosin-Rammler distribution can be used for any characteristic diameter and for d_{95} the equation becomes:

$$V_{cum} = \exp\left(-2.996\left(\frac{d}{d_{95}}\right)^n\right) \tag{2.72}$$

His experiments were conducted to study water dispersion in oil in a horizontal pipe. The drops were first introduced via injection tube. The drop distributions were measured using both dispersed phase sampling and photographic technique. Karabelas (1978) reported that the data from Collins and Knudsen (1970) as well as his data could be satisfactorily fitted by a Rosin-Rammler or an upper limit log-normal distribution. As in other works, coalescence was not present in the study since 0.2% of dispersed phase volume fraction was used. Karabelas found that the parameter n was almost constant and varied between 2.3 and 2.9 for the conditions investigated.

Using a laser back-scatter technique, chord length distributions were measured in a horizontal flow by El-Hamouz and Stewart (1996). A static mixer was used to form the drops before entering the test section. The measurements showed that chord length increased as drops moved further from the mixer. This could represent coalescence in the test section rather than drop break-up.

Angeli and Hewitt (2000b) used an endoscope located inside the flow to measure drop size distribution generated from turbulent flow. The experimental results revealed that d_{max} decreased as the continuous phase velocity increased. Also, water drops in the oil phase appeared to have smaller mean drop sizes compared to oil drops in water. They also found a strong effect of pipe wall material on the drop size distribution.

Simmons et al. (2000) compared two different optical techniques, backscatter (Par-Tec 300C) and diffractions (Malvern 2600) techniques to investigate drop size distribution. Their results reflect a decrease in d_{32} with increasing mixture velocity. Simmons and Azzopardi (2001) used the same laser techniques to study drop size distributions for both vertical upward and horizontal flows. The authors argued that Rosin-Rammler distribution is not physically sound since it does not have a mathematical upper-cut off which means that it has a tail to infinite drop sizes. For this reason, the upper limit log normal function was used that fitted the experimental results well. Also, the maximum drop diameter was found to agree with the theory of Hinze (1955) for dilute dispersions but not for concentrated ones.

Lovick and Angeli (2001) designed a dual impedance probe (see chapter 3) to measure the chord length distributions. Using this probe, Lovick and Angeli (2004a) measured

drop size distribution in horizontal oil-water flows along a vertical diameter. Most of the conditions investigated were in the *dual continuous* regime. The experimental results revealed that drop size decreased with increasing distance from the interface (Fig. 2.13). Also, a slight effect of velocity on the maximum and median chord lengths was found. They explained this by arguing that higher velocities would tend to decrease drop size but also increase the amount of one phase entrained into the other which favours larger drop sizes. In all the cases water drops were found faster than the upper layer while oil drops could be either faster or slower than the lower layer. None of the available correlations on maximum drop size was able to predict their results.

Using the same oil, Hu (2006) studied chord length distributions for horizontal, downward and upward vertical flows with the dual impedance probe developed by Lovick (2004). He found more large oil drops in the pipe central region for both downward and upward flow. Also, the measurements showed smaller water drops in oil compared to oil drops in water. By averaging the local measurements of drop chord length over the pipe cross-section, Hu (2006) found that the possibility of the probe to intersect large chords increases as the dispersion fraction increases. Using a method to transform chord length to drop size (see section 2.6.4), Hu (2006) showed that d_{32} of the oil drops increases significantly as the dispersion of oil in water increases for both downward and upward flows.

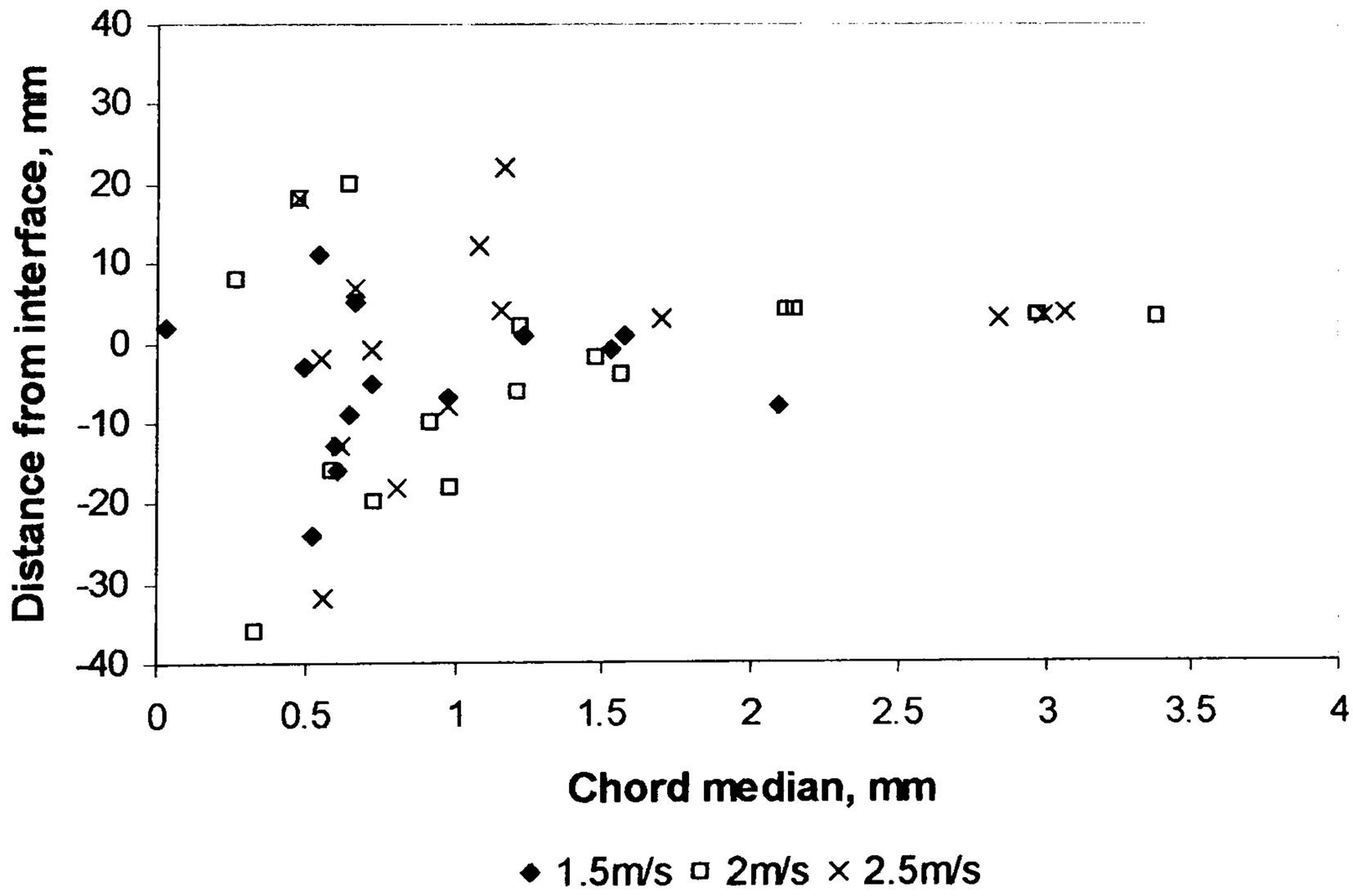

Fig. 2.13 The effect of the distance from the interface on chord length medians for all mixture velocities and input oil concentrations

2.6.4 Transformation of chord length distribution to drop size distribution

In this work, a dual impedance probe (Lovick, 2004) is used to obtain chord length distribution (CLD) (see section 3.3.3). Therefore, to get a drop size distribution (DSD), the measured chord length distribution needs to be transformed.

A number of models have been proposed for converting a chord length distribution to drop size one. For example, probability apportioning method (PAM and PAM2) (see Simmons et al., 1999 and Langston et al., 2001), finite element method (FEM) (see Simmons et al., 1999) and FBRM model (for extensive review see Lovick and Angeli, 2004 and Hu 2006). Lovick and Angeli (2004) and Hu (2006) showed that none of them is suitable for chord length data measured from impedance probe. Therefore, Hu et al. (2006) developed analytically a rigorous relationship between the distribution of chord lengths from a point sensor and the corresponding distribution of drop sizes in liquid-liquid dispersion. To develop the equation, they assumed spherical drops that move with the same velocity and are uniformly distributed. Also, they assumed that maximum chord length (L_{max}) is equal to the maximum drop diameter (d_{max}). The relationship derived is given by

$$\begin{bmatrix} C(1,1) & \cdots & C(1,N-1) & C(1,N) \\ C(2,1) & \cdots & C(2,N-1) & C(2,N) \\ \vdots & \ddots & \vdots & \vdots \\ C(M-1,1) & \cdots & C(M-1,N-1) & C(M-1,N) \\ C(M,1) & \cdots & C(M,N-1) & C(M,N) \end{bmatrix} \begin{bmatrix} P(1) \\ P(1) \\ \vdots \\ P(N-1) \\ P(N) \end{bmatrix} = \begin{bmatrix} G(1) \\ G(1) \\ \vdots \\ G(M-1) \\ G(M) \end{bmatrix} \tag{2.73}$$

where M is the number of chord length groups, N is the number of drop diameter groups, $G(i)$ is the number density of chords and $P(j)$ is the fraction of drops in the j^{th} drop group.

This equation can be written as

$$[C][P] = [G] \tag{2.74}$$

where the matrix $[C]$ contains the coefficients $C(i,j)$ used for the forward calculation of the CLD $[G]$ from the DSD $[P]$.

To do the backward calculation and find the DSD knowing CLD, the equation needs to be solved for P:

$$[P]=[C]^{-1}[G] \tag{2.75}$$

Further details about the development of the relationship between drop size distribution and chord length can be found in Hu et al. (2006) and Hu (2006).

The above equation (Eq. 2.75) gave negative solutions when used for experimental chord lengths distribution that have some noisy errors. To avoid this problem, additional smoothing equations were added in matrix [C] to reduce the noisy errors which result from the experimental measurements. By adding the smoothing equations, Eq. 2.75 becomes

$$\begin{bmatrix} C \\ C^s \end{bmatrix}[P]=\begin{bmatrix} G \\ 0 \end{bmatrix} \tag{2.76}$$

where $\lfloor C^s \rfloor$ is the coefficient matrix for the smoothing equations.

To evaluate the method, Hu et al (2006) compared the drop size distributions obtained from converted experimental chord length measurements with drop size data obtained experimentally with a high speed video camera. The comparison showed a good agreement.

2.7 Drag Reduction

The addition of small amounts of additives as low as parts per million (ppm) can greatly reduce frictional resistance in a flowing fluid and the phenomenon is known as drag reduction. Theses additives can be grouped into polymers, surfactants and fibers. Surfactants cause drag reduction by reducing the surface tension of a liquid. Fibers which look like long cylinders orient themselves in the direction of the flow which results in a reduction of the turbulent friction factor of the fluid. The formal discovery of drag reduction using polymers is attributed to Toms (1948) during experiments on the degradation of polymers in pump. To date hundreds of papers have been published in the area of drag reduction in single phase flow while few papers can be found for multiphase flow.

2.7.1 Single phase flow

As mentioned above, Toms (1948) initiated one of the most interesting findings in single phase turbulent flows by discovering a reduction of the frictional resistance during flow with added polymers. Warholic et al. (1999) observed a drag reduction in single phase turbulent flow with concentrations as low as 0.2 ppm. Until today, single phase drag reduction is still subject of intense research.

Recently, Wei and Willmarth (1992) and Warholic et al. (1999) used laser Doppler velocimetry (LDV) to study and describe how the turbulence properties differ in the presence of polymers from those of pure fluids. A general review of drag reduction is given by Lumley (1969) and recently by Gyr and Bewersdorff (1995) and Manfield et al. (1999).

Although huge amount of work on drag reduction in single phase flows available in the literature, a complete satisfactory model that explains the mechanism by which macromolecules such as polymers reduce the friction is still not available. However, a number of theories have been proposed to explain the mechanism. Lumley (1969) suggested that the stretching of the randomly coiled polymers will increase the effective viscosity which will damp the small turbulent eddies. Such scenario will cause a thickening to the viscous sub layer and as a result drag reduction. Several experimental investigations support the theory by showing that polymers increase the thickness of the viscous sub layer (Astria, 1969 and Fortuna and Hanratty, 1971). De Gennes (1990) argued that drag reduction is caused by elastic properties of the polymer. This argument was supported by observations which showed that drag reduction occurs in experiments where polymers are active at the centre of the pipe. At the centre of the pipe, viscous forces are not very important.

Recent studies attribute drag reduction to the change of turbulence properties by the added polymers. Warholic et al. (1999) suggested different mechanisms depending on the drag reduction percentage. At low drag reduction (< 35%), the dimensionless mean streamwise velocities (root-mean square of the streamwise velocity fluctuation non-dimensionalised against frictional velocity) show a logarithmic relation for a distance away from the wall compared to the Newtonian fluids. This could be due to the increase of the thickness of the viscous wall layer (see also Astria, 1969 and Fortuna and

Hanratty, 1971). Also, it has been suggested that the logarithmic velocity law will be obeyed until a critical value of the wall shear stress is reached above which the dimensionless velocity will change between that of a Newtonian fluid shifted by a constant term upward and of a maximum drag reduction asymptote at a certain concentration of the drag reducing agent (Hoyt, 1986). At large drag reduction (55 – 69 %), the mean velocity profile does not show a logarithmic relation and instead the dimensionless turbulence intensities appear to be lower than those for Newtonian fluids while Reynolds stresses are found to be approximately zero throughout the test channel. The polymer stresses, however, (resulting from the interaction of turbulence with the polymer chains) appeared in the whole channel and turbulence was produced by the interaction of polymer additives with the fluctuating flow field; as a result the velocity field would be different than that in Newtonian flow. Decrease in Reynolds stresses and in normal velocity fluctuations has also been reported by a number of investigators (Luchik and Tiederman, 1988 and Wei and Willmarth, 1992). Warholic et al. (1999) showed that drag reduction would depend on the mixed concentration of the polymer in the test section, the method of polymer injection and the inconsistencies in the preparation of the concentrated polymer solutions that is injected into the pipe. Choi and Jhon (1996) showed that drag reduction depends on the concentration of the polymer but beyond the maximum effective concentration, drag reduction can also decrease.

Warholic et al. (1999) suggested that the drag reducing polymers interfere with the wall vortices that sustain turbulence in Newtonian fluids. The vortices which appear as streaks starting near the wall and then rise periodically through the buffer layer to the turbulent core. The drag reducing polymers, however, destroy these vortices and as a result the degree of turbulent transfer to the core decreases. Brooke and Hanratty (1993) reported that these vortices recreate themselves in a process which can be followed for several generations. The destruction of one of them would have a strong impact and could justify the large effects of even very small amounts of polymers in turbulence (Warholic et al., 1999).

2.7.2 Multi-phase flow

In contrast to the huge amount of work available on drag reduction in single phase flows, the influence of drag reducing polymers (DRP) on multiphase flows has not

received so much attention. All the publications describe mainly the reduction in pressure drop. Recently, the addition of polymers to multiphase flows has been found to change flow patterns in addition to effects on pressure drop. Unfortunately, few publications are available discussing the change in flow patterns and they are mainly on gas-liquid flow.

The first experiments on drag reduction in gas-liquid flows were reported by Oliver and Young Hoon (1968) who used 1.3% polyethylene oxide (PEO) aqueous solution and air. They found that in *slug* flow the liquid exhibited considerably less circulation while in *annular* flow wave formation was damped resulting in a smoother liquid film. Greskovich and Shrier (1971) first used the term DRP in multiphase systems and found drag reduction that could reach 40% during *slug* air-water flow. Since then drag reduction has been documented by a number of investigators in a variety of systems with differing results (Otten and Fayed, 1976; Thwaites et al., 1976; Sylvester and Brill, 1976). During *slug* flow Rosehart et al. (1972) for example found higher drag reduction than in single phase while Saether et al. (1989) found lower drag reduction. A comprehensive review of drag reduction with additives in multiphase flows up to 1999 was given by Manfield et al. (1999) where it was concluded that understanding of the effect of drag reducing agents on multiphase flows is insufficient. In publications that appeared after this review Al-Sarkhi and Hanratty (2001a and b) investigated the influence of a co-polymer of polyacrylamide and sodium acrylate on *annular* air-water flow in 9.53 cm ID and 2.54 cm ID pipes. The observed drag reduction was attributed to the reduction of interfacial waves which cause drop formation and help the liquid to spread around the pipe as an annulus. The maximum drag reduction was found when all the liquid was flowing at the bottom of the pipe in a *stratified* manner with relatively smooth interface. Drag reduction up to 63% was observed in the small pipe which was greater than the maximum drag reduction measured in the large pipe (48%).

In one of the first publications that specifically addressed the effect of DRP on flow pattern boundaries Soleimani et al. (2002) investigated the transition from *stratified* to roll waves and to *slug* flow in a 2.54 cm ID pipe. The experimental results showed that small wavelengths at the interface in *stratified* flow were damped which led to decreased interfacial friction. The critical liquid film thickness was increased for transition to roll waves due to the decrease in the interfacial friction factor and to *slug*

flow due to suppression of turbulence in slugs. Similarly, in a large pipe with 9.53 cm ID the amplitude of interfacial waves in *stratified* flow was decreased and at low gas velocities the transition to *slug* flow was delayed to higher liquid velocity (Baik and Hanratty 2003). Al-Sarkhi and Soleimani (2004) found in gas-liquid flow with DRP in a 2.54 cm ID horizontal pipe changes in the flow pattern boundaries (se Fig. 2.14) and a sharp decrease in the interfacial shear stress. The maximum drag reduction appeared when the *slug*, *pseudo slug* and *annular* flow regimes changed to *stratified* flow after the addition of the polymer as was also seen by Al-Sarkhi and Hanratty (2001a and b). In a recent study Mowla and Naderi (2006) experimented with polyalpha-olefin in the oil phase during oil-air *slug* flow. Smooth and rough pipes of different diameters were used and drag reduction varied from zero to about 40% for some experimental conditions (see Fig. 2.15). An optimum polymer concentration of 18 ppm was found for the different pipes investigated. However, higher drag reduction was encountered in the rough pipe, where turbulence is increased, than in the smooth one. In agreement with the work by Al-Sarkhi and Hanratty (2001a and b), drag reduction was found to be higher in the smaller than in the larger pipe.

Fig. 2.14 Flow pattern map in 2.54 cm pipeline during air-water flow for polymer concentration 0 and 50 ppm (Al-Sarkhi and Soleimani, 2004)

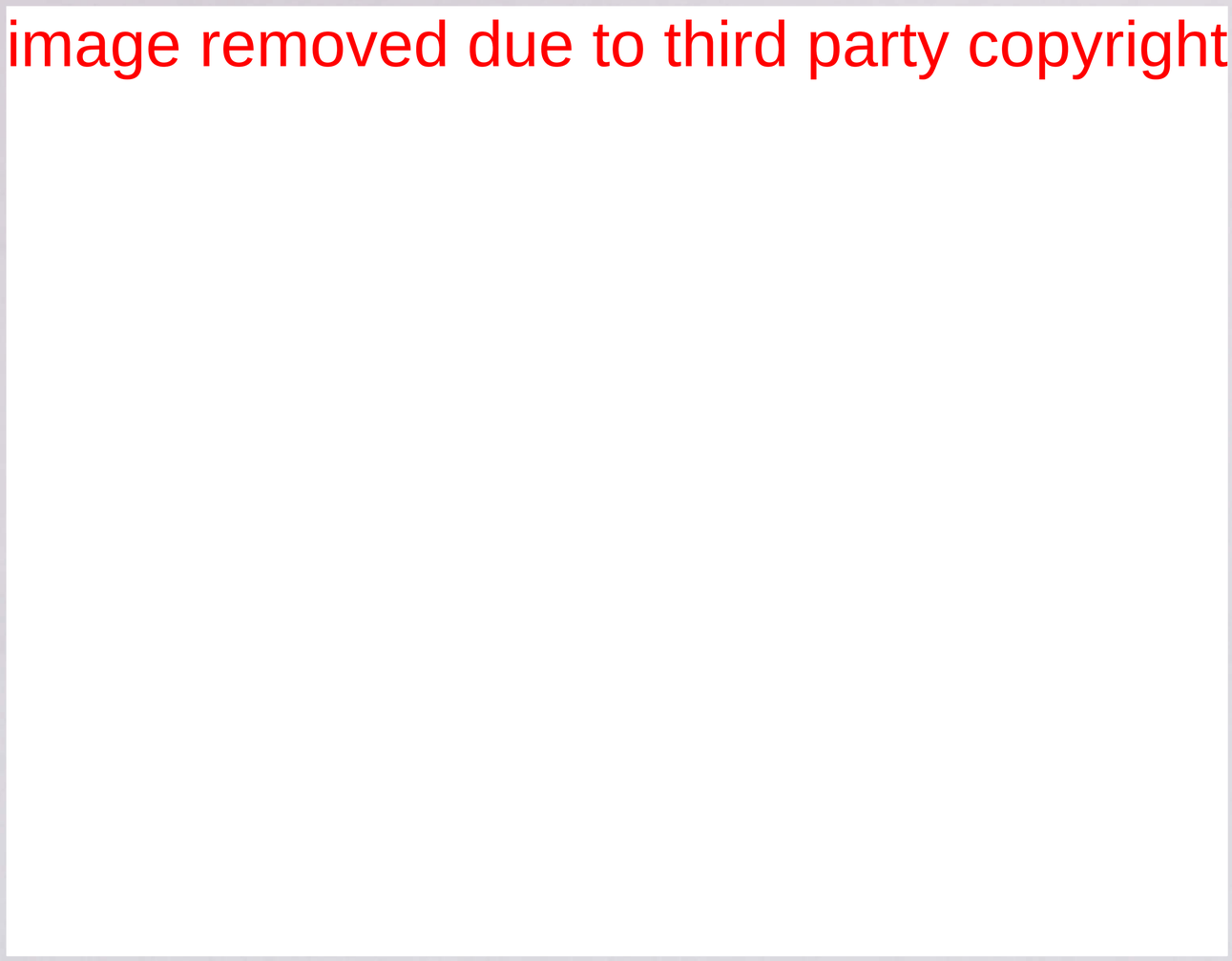

Fig. 2.15 Variation of percentage drag reduction (%DR) versus DRP concentration in a rough pipe during air-oil flow (Mowla and Naderi, 2006)

2.8 Summary

The literature survey showed that limited amount of information is available on both the onset of entrainment and entrained fraction in the *dual continuous* pattern experimentally and theoretically. Based on the above, there is a need for a model that can predict the onset of entrainment in liquid-liquid flow. Also, the mechanism of drop formation in liquid-liquid is still not known. Valle (2000) developed a model based on rate of entrainment and rate of deposition to calculate the entrainment of each phase into the other, but this model was not validated against experimental data and contains a number of unknown parameters. Apart from the work of Valle and Kvandal (1995) and Lovick (2004), no entrained fraction data has been reported in the literature. Also there is no information on wave structures. In addition most work on drop size distribution is from dispersed flows although *dual continuous* flow occurs for a wide range of conditions. There is currently no work available on the effect of drag reducing polymers in liquid-liquid flows.

Based on the above, the aim of the thesis is to improve understanding of the transition between horizontal *stratified* and *non-stratified* (particularly *dual continuous* flow) liquid-liquid flows through experimental investigations and theoretical modeling and to investigate the effect of drag reducing polymers on flow pattern boundaries and several flow characteristics in oil-water flows.

CHAPTER 3

Instrumentation and Experimental Methods

Currently there is insufficient information on entrained fraction, drop size and onset of entrainment in dual continuous flow while there are no studies on wave structure at the onset of this pattern. Therefore, there is a need of experiments to identify the mechanism and the onset of drop formation, investigate the structure of the waves at onset and measure the entrained fraction in *dual continuous* flow. This chapter describes in detail the experimental facilities, instrumentations and methods used to achieve the above objectives. Section 3.1 describes the testing fluids used in this study. Two experimental facilities are used for the experiments, a pilot scale with 38 mm ID stainless test section and a smaller scale with 14 mm ID acrylic test section. A detailed description of the facilities is given in section 3.2. Section 3.3 demonstrates the instrumentation and techniques employed to visualize the flow, measure phase distribution, chord length distribution and wave structure in the pilot scale facility while section 3.4 describes the instrumentation and techniques used in the small scale facility to again observe flow development but also study the effect of drag reducing polymers in horizontal oil-water flows. Finally, section 3.4 provides a short summary of the chapter.

3.1 Working Fluids

A model Oil and tap water were used as test fluids. The oil (EXXSOL D140) was supplied by Exxon Chemicals. The average properties of the fluids and test conditions are:

- Oil
  - Density, $\rho_o = 828\ kg/m^3$, Viscosity, $\mu_o = 5.5\ cp @ 25^\circ C$

- Water
  - Density, $\rho_w = 1000\ kg/m^3$, Viscosity, $\mu_w = 1\ cp @\ 25^\circ C$
- Surface tension, $= 27.6\ mN/m @\ 25^\circ C$
- Oil-water interfacial tension $= 39.6\ mN/m @\ 25^\circ C$

The viscosity of the oil was measured using a Contraves 155 rheometer for different range of temperatures. The surface and interfacial tension were measured using a Kruss Processor Tensiometer K-12.

3.2 Experimental Flow Facilities

The experimental facilities used in this work are located in the Department of Chemical Engineering at the University College London. Two experimental facilitates are used; a pilot scale rig with a 38 mm ID stainless steel test pipe in and a smaller scale rig with a 14 mm ID acrylic test pipe.

3.2.1 Pilot scale facility (38 mm ID stainless steel test section)

Figs. 3.1 and 3.2 show a schematic diagram and photograph respectively of the oil-water experimental setup. The experimental rig was designed to run single or two phase mixtures of oil and water both horizontally and with some inclination.

3.2.1.1 Description of the rig

The test loop is made up of three main parts. These are the oil and water handling facilities, test section and the oil-water separation equipment. The oil-water handling system consists of two fiberglass storage tanks (one for oil and the other for water) of 880 liters capacity, two centrifugal pumps and two armoured variable area flow meters. The storage tanks contain baffles which enhance the separation of any contaminating phase in the tank and reduce the possibility of the contaminating phase entering the pump. The baffles are also used to reduce the vortices that may appear in the tanks. Such phenomena might introduce air in the liquid sucked by the pumps.

While conducting the experiments, the operating temperature should be kept around 25°C. This was done by constantly draining and refilling the water tank. Also, a cooling coil could be fitted in the oil tank to maintain a constant temperature.

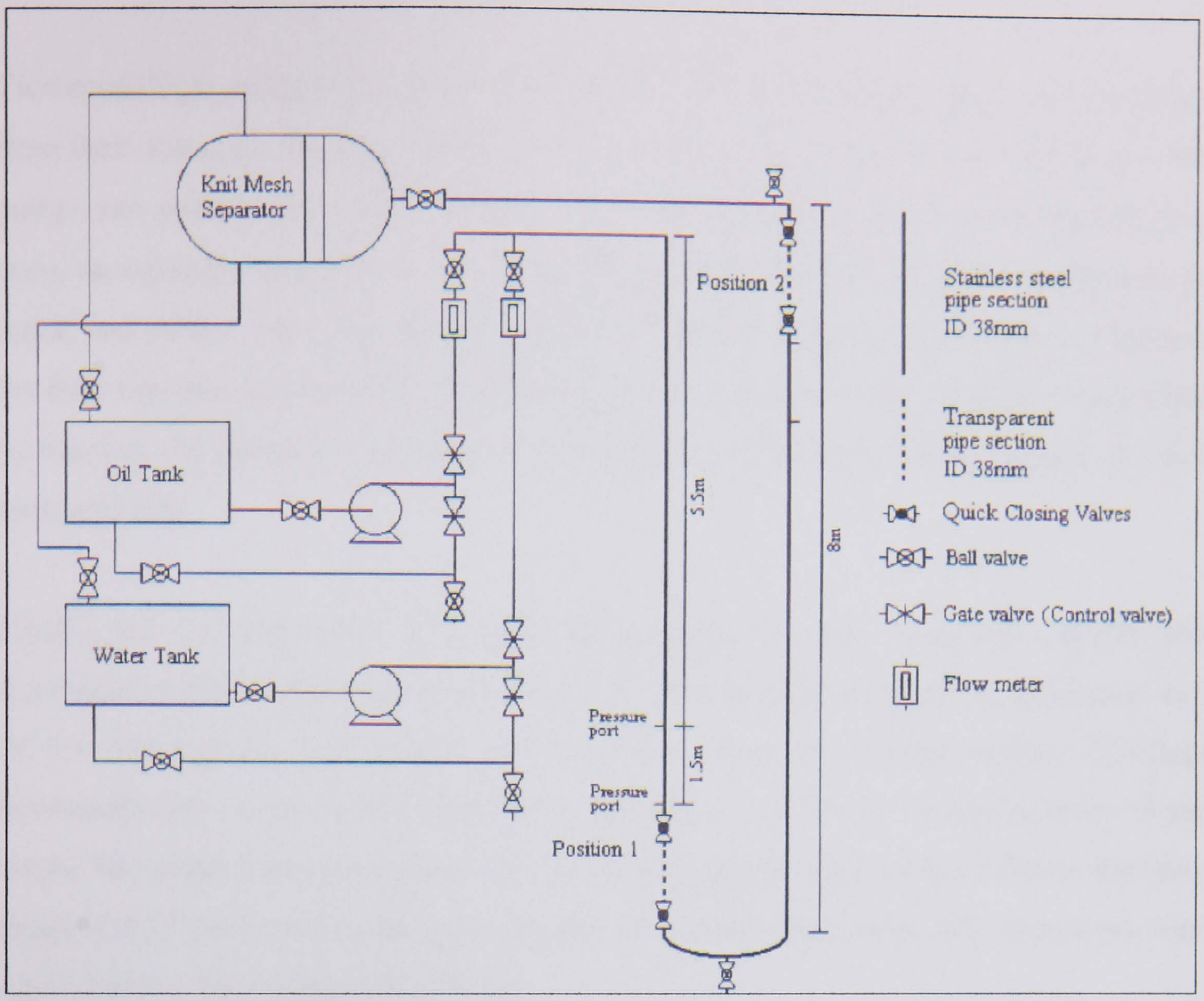

Fig 3.1 Schematic diagram of the pilot scale oil-water experimental flow facility

Fig 3.2 Photograph of the pilot scale oil-water experimental flow facility

Two centrifugal pumps (Ingersoll-Dresser CPX200) are used to pump the oil and water from their storage tanks separately to the test pipe via two variable area flowmeters. The pumps can generate flow at 240 l/min and 450 kPa. Since the pumps have specific flow rates, recycle pipe sections were made to allow part of the flow to go back to the storage tanks, and control the oil and water flow rates this way. Gate valves are used to regulate the flow into the recycle part and the test sections. Excessive heat generation may result by leaving the valves too closed so care must be taken when handling them to avoid such problem.

Finally, the oil and water flow rates are metered via two armoured variable area flowmeters (ABB Instrumentation 10A5400). The two flowmeters are connected to a PC for data logging. Large and small flowmeters were used in this project. The large flowmeters have 0-240 l/min range, with an accuracy of 1% full scale for both oil and water. The small flowmeters have 2% full scale accuracy. The oil small flowmeter has a range of 0-20 l/min while the water one has a range of 0-6.5 l/min. All flowmeters were calibrated for the corresponding fluid.

The test section is made of 38 ID stainless steel 316 pipe. It consists of two eight-meter long parts connected via U-bend. Each part is made of two-meter and one-meter sections connected with tri-clamp fittings which provide a near seam free connection. Instrumentation was made so that it could be put in between the different pipe sections and also connected with tri-clamps to the rest of the pipe. This allowed instrumentation to be put at different locations along the pipe.

The oil and water join through a T-junction (see Fig. 3.3) before entering the test section. The water phase is allowed to enter from the bottom while the oil joined from the top to reduce the effect of mixing of the two phases.

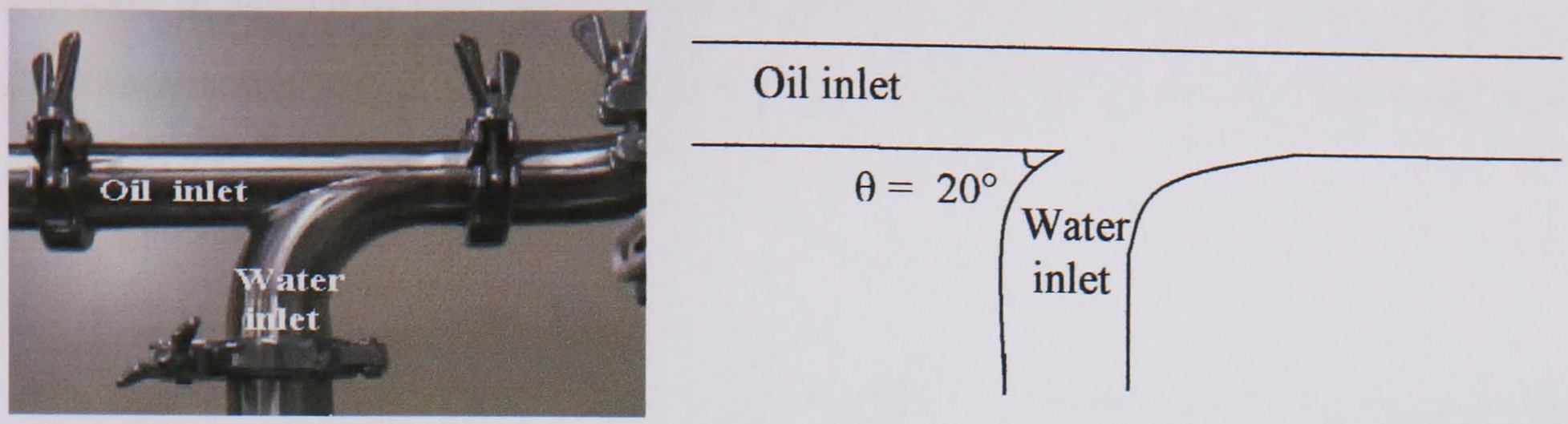

(a) (b)

Fig 3.3 Test inlet section (a) Photograph (b) Schematic diagram

Two one-meter long transparent acrylic pipes are used for flow visualization. For this work one was located before the U-bend, 7 m from the entrance while the other is located at the end of the test section before the inlet to the separator. But, they can also move between any two steel lengths along the pipes. Each transparent section is equipped with Quick Closing Valves (QCV) at both ends to trap the oil-water mixture between them. The trapped mixture can be drained to a graduated cylinder to measure the in-situ volume fraction of the phases.

Finally, the two-phase flow of oil and water will return to the separation equipment which consists of one horizontal separator vessel that can handle up to 800 liters of fluid. The separator contains a KnitMesh coalescer (DC9201, KnitMesh Ltd) located approximately half way along its length to improve the separation of the mixture. The mesh has a large surface area that is composed of two different materials (one plastic and one metal) with different surface energies. The materials help the coalescence of the two phases since each one is wetted by only one phase. The turbulence of the inlet mixture is reduced by this mesh and as a result the drops will have sufficient time to settle by gravity in the second part of the separator oil exits from the top of the separator and goes to the oil storage tank while water exits from the bottom of the separator to the water tank.

All the experimental information was acquired with a data acquisition program. The software used is HPVee. The data from the flow meters, the pressure transducer and the conductivity probe were recorded simultaneously at a sampling rate of 10 Hz. The measurements of the wavelengths and amplitudes by the new conductivity probe were recorded at a sampling rate of 500Hz. Finally, another computer with custom-made

software in MS-DOS was used for the logging of the data from the impedance and the dual impedance probes. The logging frequency varied in this case as it is the same as the sampling frequency.

3.2.1.2 Modification to the loop

Although the T-junction (see Fig. 3.3) was designed to reduce the effect of mixing since water entered beneath the oil phase, the 90° elbow immediately downstream and before the test section may increase the mixing. Also, the elbow may affect the stratification of the flow by forming drops of both phases as a result of the mixing. Therefore, a new inlet section was designed to allow the phases to be introduced into the test section as a *stratified* flow.

Fig. 3.4 shows a schematic diagram of the new inlet configuration of the two liquids. In the new design each phase flows alone through the bend. In the test section, oil enters from the top with an angle of 15° from the horizontal test section at which the water is flowing. The new entrance section avoids generation of drops due to the mixing at the inlet. Also, it is believed that such configuration will lead to more reliable results for the measurements of the onset of entrainment, wave structures and entrained fraction. As there is no mixing at the inlet in this case, wave formation, droplet formation and entrainment will be resulting purely from the relative motion of oil and water layers.

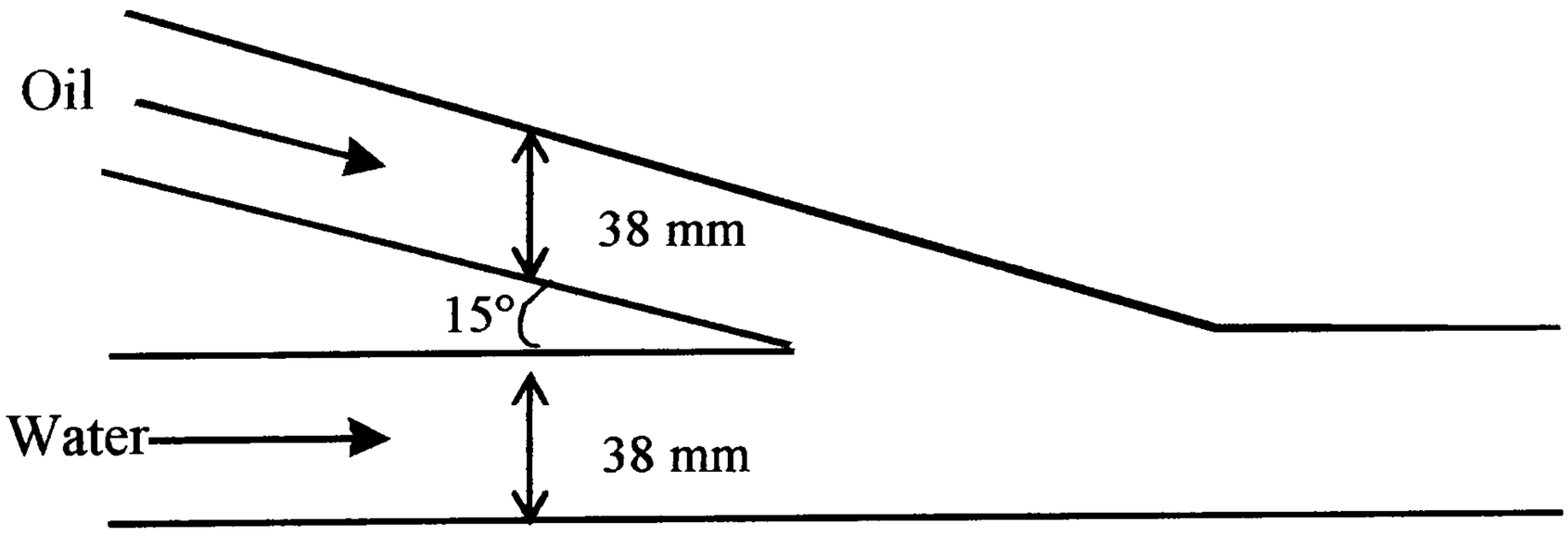

Fig 3.4 New inlet section

3.2.1.3 View box

To reduce optical distortion due to the curvature of the pipe, a view box was designed and placed around the transparent section used for visual observation. This section is composed of a rectangular box made from acrylic as shown in Fig. 3.5. Glycerin was

selected to fill the box since its refraction index is close enough to the indices of water, oil and acrylic which minimized any refraction problems.

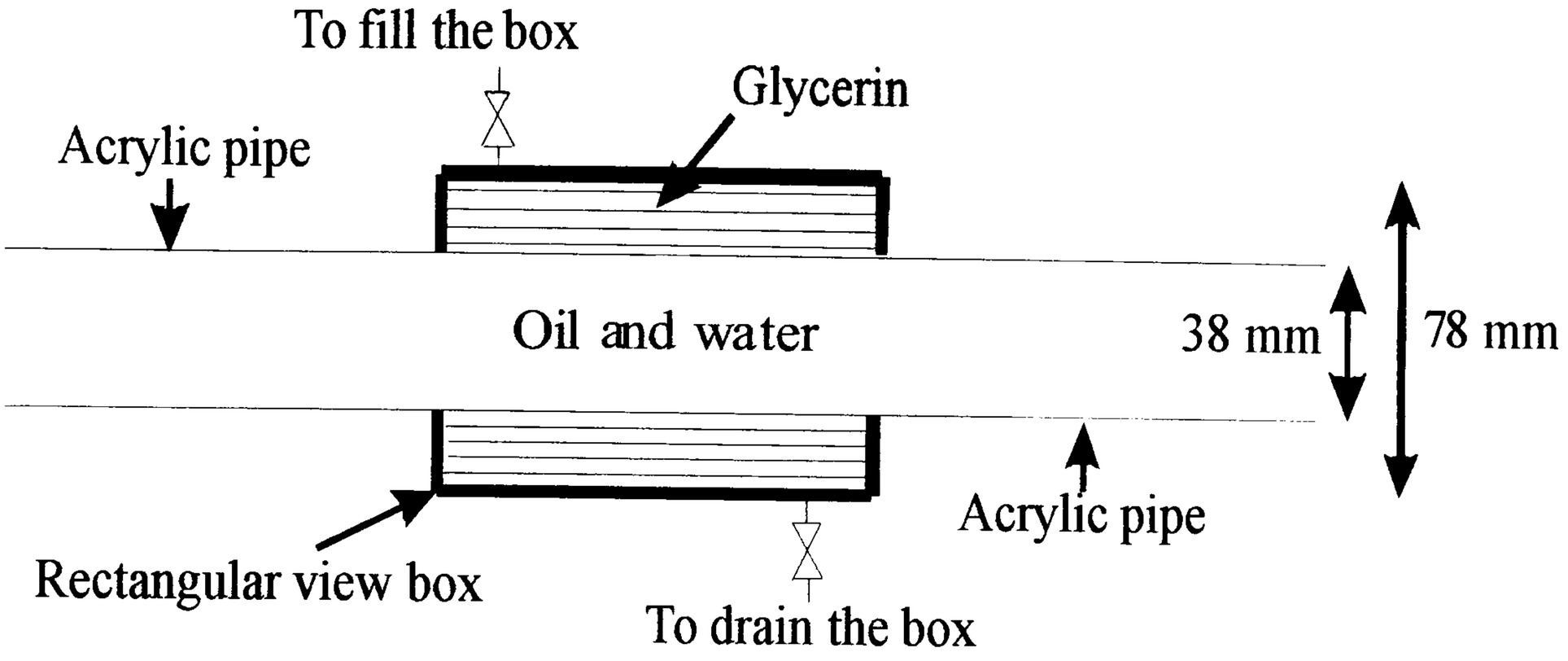

Fig 3.5 Viewing section

3.2.2 Small scale facility (14 mm ID acrylic pipe)

The a small scale experimental flow facility was built for the purpose of this project in the Department of Chemical Engineering at UCL. The experimental set-up is described in Section 3.2.2.1 and a schematic diagram and photograph of the set-up is shown in Figs. 3.6 and 3.7 respectively.

The facility consists of three main parts; the oil and water handling system, test section and the separation equipment. The handling system consists of two plastic storage tanks. Each tank has a total volume of approximately 15 litres, one for oil and one for water. Due to the small size of the tanks, the water tank was constantly filled with water to keep running the experiments. Water in the separator was normally drained while keeping oil in the separator. Two centrifugal pumps capable of generating a flowrate of 12 litres/min at 300 kPa each are used to pump the fluids. As the pumps have a fixed flowrate, recycle pipes have been installed to allow each fluid return back to its storage tanks and help regulate the flow. The flow of each fluid to the recycle pipe and the test section is controlled by gate valves. The two pumps are used to pump the oil and water from their storage tanks separately to the test pipe via two variable area flowmeters one for each phase. The flowmeters were calibrated the respective phase. The oil flowmeter has a range of 0-4.2 l/min while the water one has a range of 0-7.5 l/min, the accuracy of both is 1% full scale.

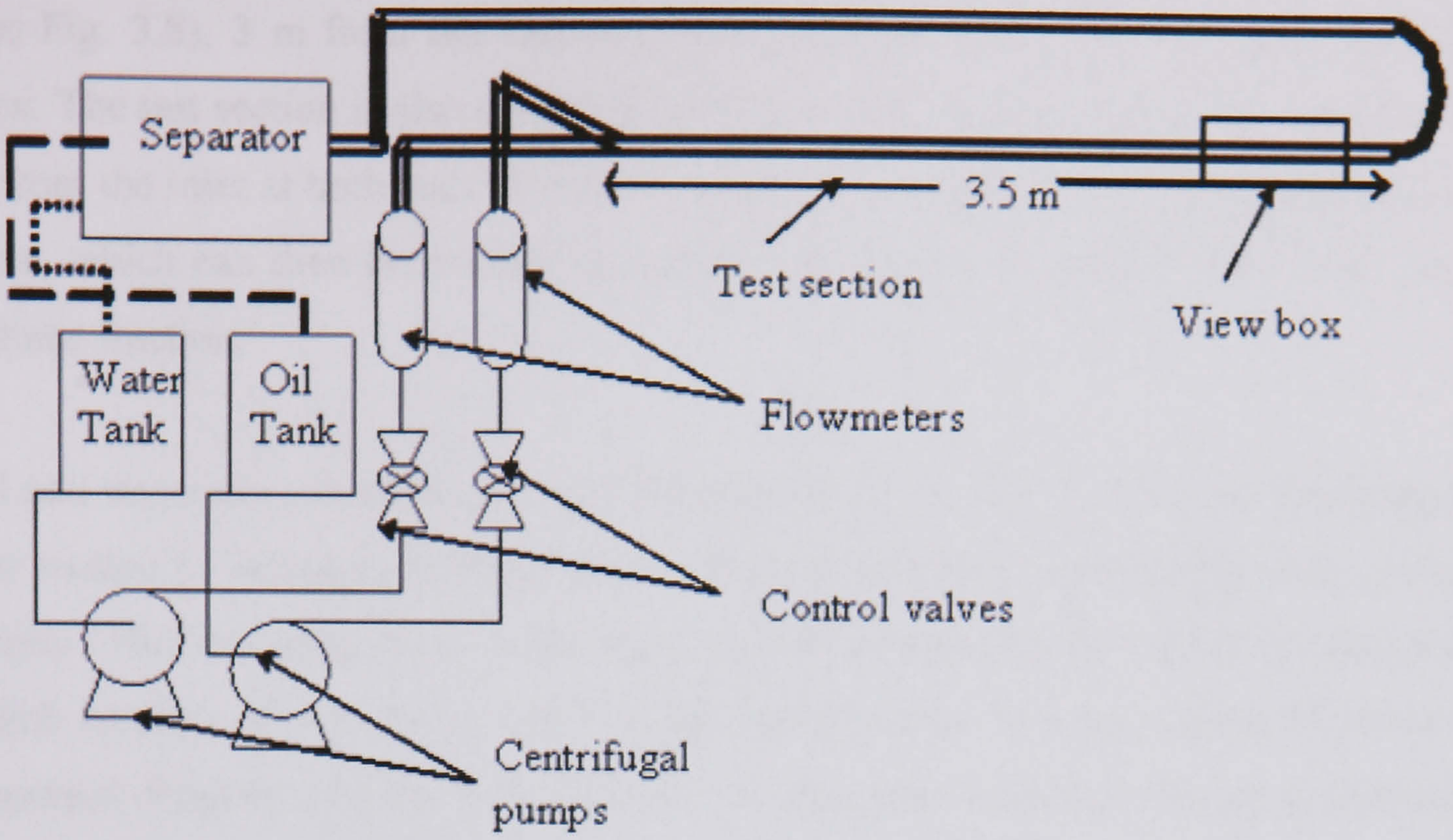

Fig 3.6 Schematic diagram of the small scale oil-water experimental flow facility

Fig 3.7 Photograph of the small scale oil-water experimental flow facility

The test section is made up of 14 mm diameter, 3.5 m long acrylic pipe at the front while PVC pipe is used after the U-bend to return the mixture to the separator. A view

box filled with glycerin is used for flow visualization towards the end of the test section (see Fig. 3.8), 3 m from the entrance, to get the maximum possible fully developed flow. The test section is also equipped with Quick Closing Valves (QCV) located at 2.5 m from the inlet at both ends. The QCV are used to trap the oil-water mixture between them, which can then be drained to a graduated cylinder to measure the in-situ phase volume fraction.

Oil and water are joined through a Y-junction as shown in Fig. 3.9 before entering the test section to introduce a better stratification of the flow and minimize any entrance effects. The two-phase flow of oil and water will return to the separation equipment which consists of one plastic tank that can handle up to 15 litres. The tank allows the dispersed drops to coalesce and the phases to separate via gravity. The oil is allowed to flow back from the separator to the oil tank while water is let to the rain. New water was constantly introduced in the water tank.

The flow rates of both oil and water were measured by taking the reading of the flow meters while an inverted manometer filled with water and located at the end of the test section was used to measure the pressure drop.

Fig 3.8 View box used in the small scale facility

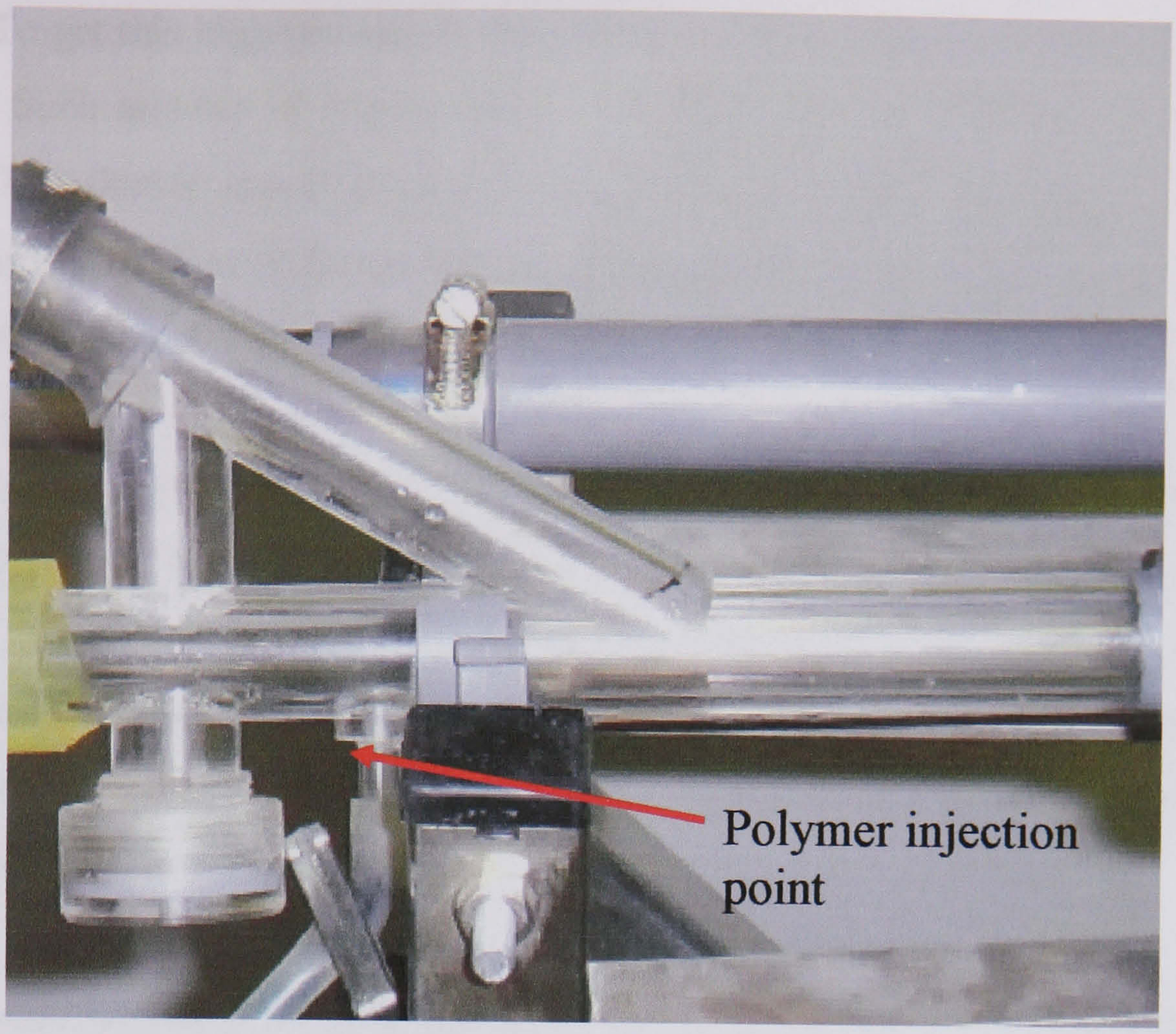

Fig 3.9 Test section inlet in the small scale facility

3.3 Measuring Methodologies and techniques in the 38 mm ID Stainless Steel Pipe

In this section a description of all the instrumentation and methods used to conduct experiments in the pilot scale facility is given. High speed video camera is used for visual observation. Impedance and dual impedance probes are used to measure phase and chord length distribution respectively. Finally, a wire conductivity probe is also implemented to measure the structure of the oil-water wavy interface.

3.3.1 Visual observation

Visual observation is used to identify the conditions for the onset of entrainment in *dual continuous* flow and the mechanism of the entrainment. Observations were done with a high-speed video camera (provided by EPSRC). The camera was located in front of the view box, at the end of the first eight meter part of the test section to get the maximum possible fully developed flow. Thus, the flow of oil and water could be monitored and recorded.

The high speed video camera is a Photron Ultima APX system that can record up to 120000 fps. Maximum resolution of 1024 x 1024 can be obtained if 2000 fps or less is

selected. To get this high resolution, the maximum frames that can be recorded per run are 6000. Such number of frames allows recording time of 3 seconds if 2000 fps is selected. The shutter speeds of the system is between 10ms and 4μs. In this work, 500f/s was selected as a frame rate and 6000 frames were recorded per run. Such number of frames allows recording time of 12 seconds of flow which increase the chance of capturing the droplet removal mechanism from waves while it also makes the analysis more representative. The recorded pictures could be viewed before downloading them in a Pentium 4 PC with a 3.2GHz processor, 1 Gb RAM, 111 Gb hard drive. The PC is connected to the video processor via a Firewire cable. Once the downloading was completed, another record of the flow could then be made. The downloading time is 3s for 100 images. Thus, 3 minutes were needed to download the recorded 6000 frames.

Several conditions were investigated for the study of the onset of entrainment starting from a mixture velocity of 0.55 m/s (Lovick and Angeli, 2004, observed the onset of *dual continuous* flow at 0.80 m/s mixture velocity). A mixture velocity of 0.55 m/s was selected to make sure that the conditions where the first drops appear are captured as well as the structure of the waves before entrainment. The experiments were conducted starting from oil superficial velocity 0.05m/s to 0.55m/s, with an increment of 0.05 m/s. The water superficial velocity from 0.55 m/s was increased at each oil superficial velocity until entrainment was observed and going further up to mixture velocity equal to 0.90-1.10 m/s where the *dual continuous* flow was fully established. The mechanism and the onset of entrainment were identified by carefully analyzing the recorded pictures using Photron FASTCAM Viewer.

Both the old inlet (T-junction with bend) and the new inlet (Y-junction) sections were employed to identify the onset of entrainment. These results were used to investigate the effect of different inlets geometries on the onset. The high speed video camera was also used to study the flow 2 m from the inlet at the measured onset velocities using the new inlet section only. This would reveal the way flow develops along the pipe.

3.3.2 Measurement of entrained fraction

The entrained fraction was measured in dual continuous flow using the local impedance probe designed by Lovick (2004). The probe can measure the local volume fractions in the pipe cross section.

The impedance probe measures the differences in capacitance and/or resistance between the two phases. The probe is composed of two electrodes connected to an electrical circuit. If the electrodes are in the oil phase, the resistance value is large and no signal can be recorded. Different configurations have been used extensively in research of both gas-liquid and liquid-liquid flows (Das and Pattanayak, 1993, Angeli, 1996, Soleimani, 1999). However, the most common configuration is to have both electrodes on a single coaxial wire. This configuration depends a lot on the geometry of the probe tip since it is the part that pierces the droplets.

Using a sharp pointed tip as shown in Fig. 3.10 can pierce the droplets more easily which increase the chance of measuring even smaller droplets compared to a blunt tip. However, it gives a spread electrical field which will be more prone to the errors from wall effects. On the other hand, a blunt tip gives better results close to the pipe wall.

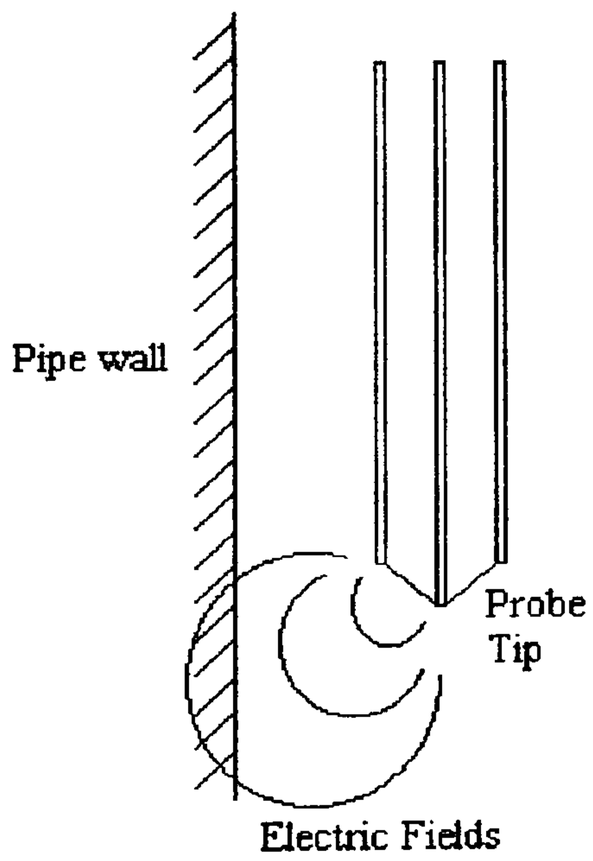

Fig. 3.10 Electrical field around impedance probe tip

Lovick (2004) designed an impedance probe based on the work of Das and Pattanayak (1993). This probe is used in this project to measure the phase distribution from which the entrained fraction can be calculated. The probe was constructed in the Department

of Chemical Engineering at the University College London. The basic principle of the probe is the ability of detecting the difference in the electrical impedance between the oil and water. The electronics have a variable AC frequency, but measurement were taken when the current was flowing in one direction only. This method prevents the possibility of getting different results from each direction (Das and Pattanayak, 1993). Alternating current was selected so polarization and electrolysis effects could be avoided. However, there is a chance of having an electrolytic-attack on the tip.

The electrodes used for the probe consists of a semi-rigid coaxial wire with inner and outer electrode. The inner electrode has a diameter of 0.2 mm of silver coated copper. The outer electrode has a diameter of 0.9 mm solid copper. The two electrodes are separated by an insulator and the whole wire is coated with a heat shrink insulator which makes the total outside diameter 1.4 mm (Fig. 3.11). The outer insulator leaves 0.5 m tip free that is exposed to the flow. A photograph of the impedance probe used in this project is given in Fig. 3.12.

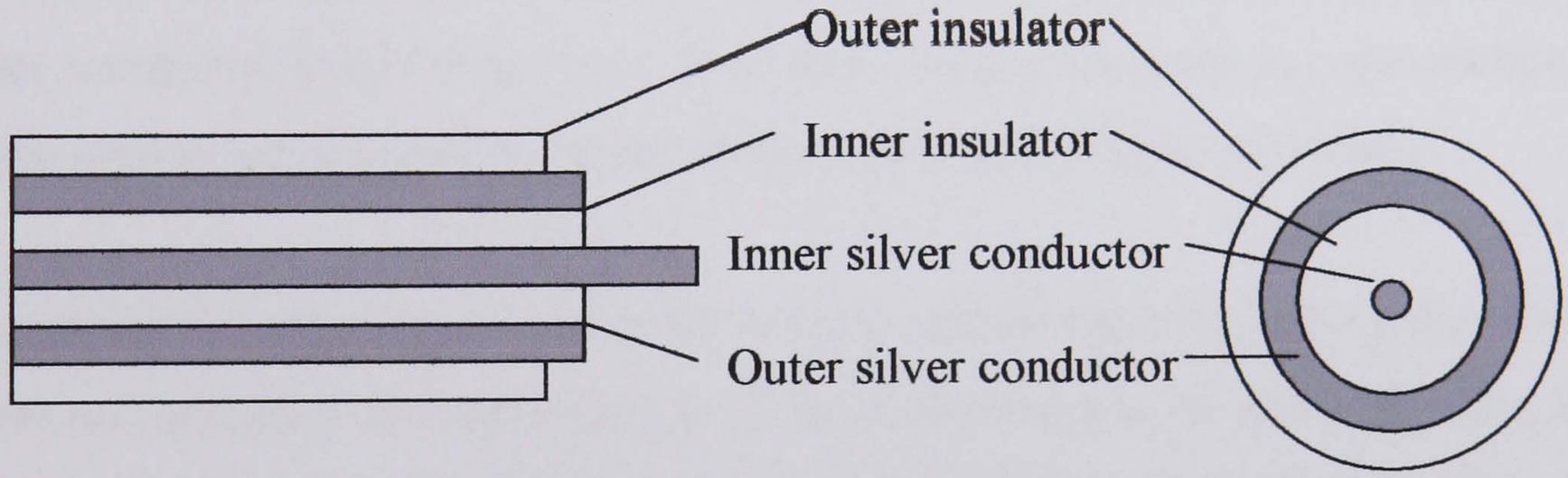

Fig. 3.11 The electrodes used for the high frequency impedance probe

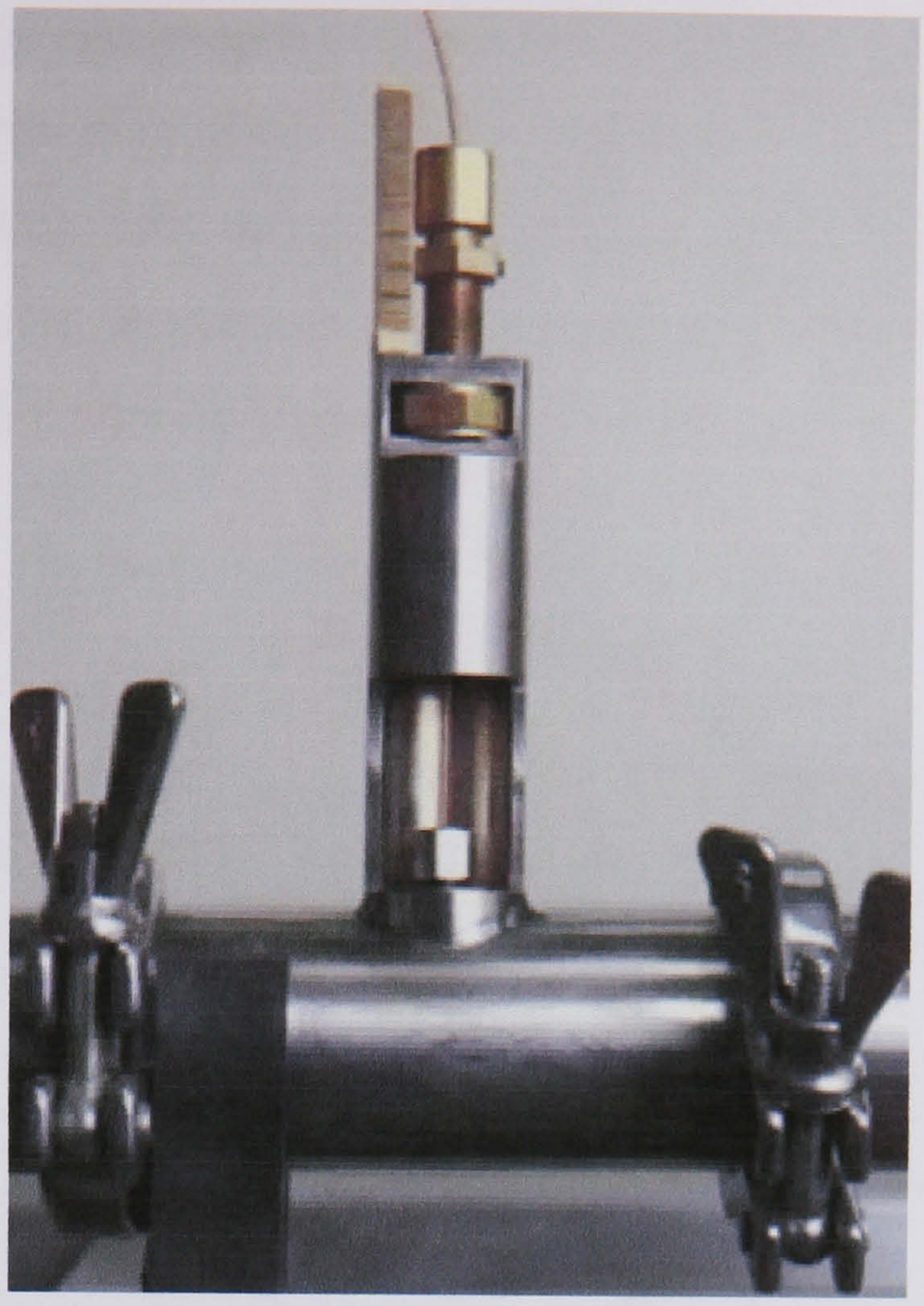

Fig. 3.12 Photograph of the impedance probe mounting between two sections of pipe

The smallest droplet diameter that can be measured is basically equal to the diameter of the inner conductor which is 0.2 mm. Minimum distance between the two conductors should be used so measurements can be taken as close as possible to the wall.

Before running the experiments, the water value should be found by putting the probe in the water and adjusting the signal (band) of the oscilloscope to its minimum. The same thing should be repeated with 100% oil but by setting the signal to the maximum. The width of the band enhances the determination of the percentage of each phase. Therefore, setting the band width to the maximum allows a greater difference between the impedance of the phases to be achieved. The percentages of the oil are then calculated at any point in the pipe cross section by knowing the counts for both 100% water and 100% oil. A count that represents the time at which the probe is in the oil is also measured. Therefore, since the duration of the total cycle is known, the percentage of oil can then be calculated.

Most of the experiments were conducted at a sampling rate of 20 kHz and 60,000 samples were recorded. These values were selected based on the work done by Lovick (2004). Lovick (2004) in his PhD thesis described the procedures that have to be

followed while taking measurements. He mentioned that the time counter is turned on and off depending on the state of the capacitor rather than by a predetermined value of impedance. The capacitor will not charge when the probe is in the oil so the time counter starts. The count continues until the probe is surrounded by water which charges the capacitor and stop the time counter.

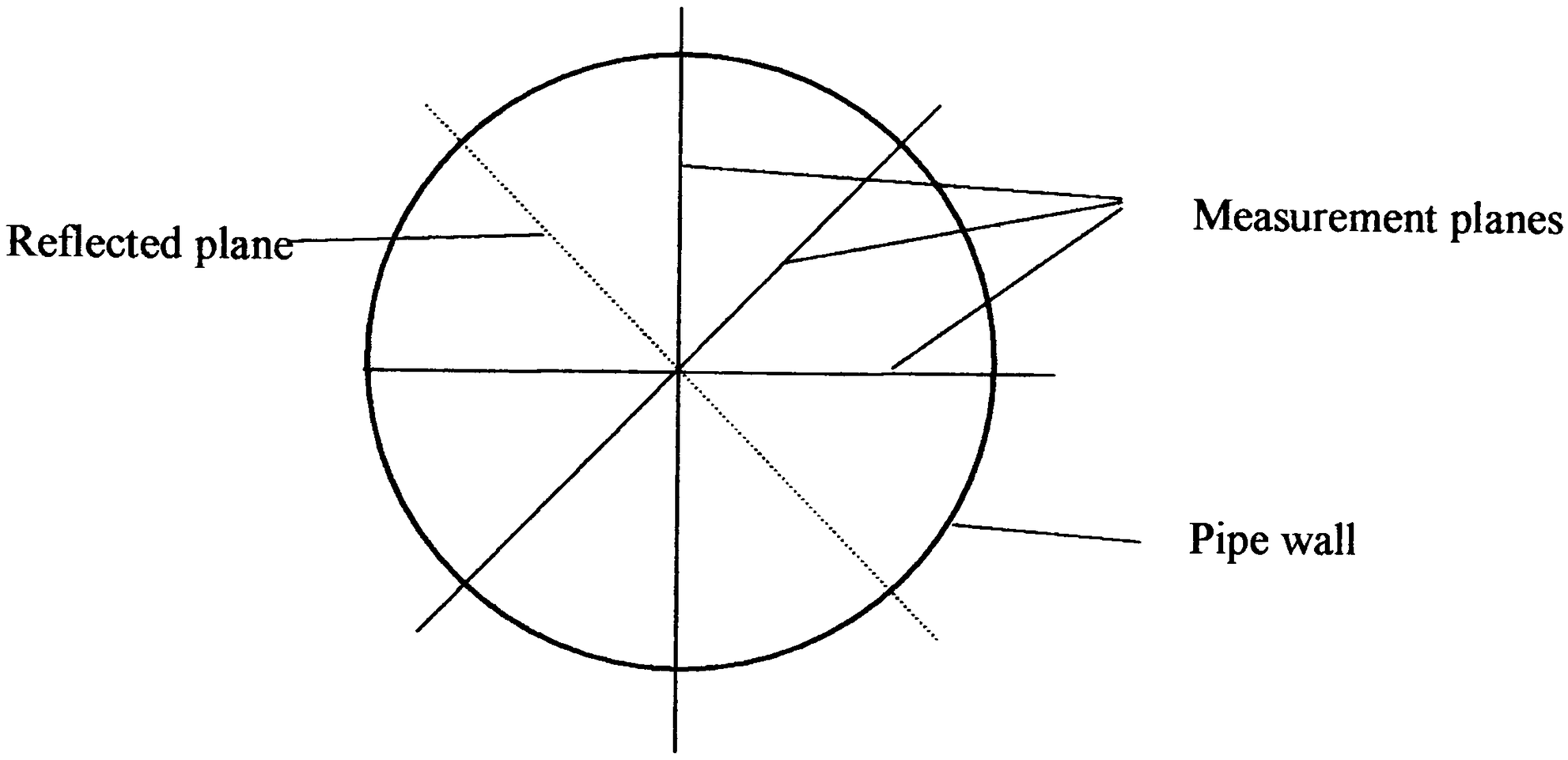

Fig. 3.13 Measurement planes for impedance probe

The local in-situ phase fractions were measured in the horizontal, vertical and 45° degree from the horizontal at intervals of 2 mm as shown in Fig. 3.13. Symmetry was assumed so the local volume fraction values at 135° degree from the horizontal were assumed to be equal to those measured at 45°. Also, the left hand side of the horizontal was assumed to be equal to the right hand side. Therefore, 10 locations were only measured in the horizontal while 20 locations were measured for the vertical and the 45° degree from the horizontal. The data measured at the above locations were integrated over the whole pipe cross sectional area to find the average volume fractions of the two phases using a FORTRAN program developed by Lovick (2004).

The average volume fractions were plotted using MATLAB to get the phase distribution graph. From the graph, the entrained fraction of each phase into the other was calculated by counting the number of the squares of a certain colour. Each colour represents a percentage of oil. Each oil percentage that is in the water phase as an example was then multiplied by the number of squares representing this percentage. The summations of all

the percentages in the water phase were divided by the total number of squares for that phase. The result of this division is the entrained fraction of the oil in the water phase. The same thing was repeated in the oil phase to get the entrained fraction of water in the oil. The oil phase was found to lose its continuity around 68% oil and the phase changes from oil continuous to water continuous.

Both the T-junction and the Y-junction were used when measuring the phase distribution. The results were used to investigate the entrance effect on the entrained fraction.

3.3.3 Measurement of drop size

Lovick (2004) developed a dual impedance probe (see Fig. 3.14). The probe was installed in the pilot scale facility described in section (3.2.1) to measure drop velocity and drop size distribution in oil-water *dispersed* flows. For detail description of the probe see Lovick (2004). The dual impedance probe was used in this project to obtain the drop size distribution in *dual continuous* horizontal oil-water flows.

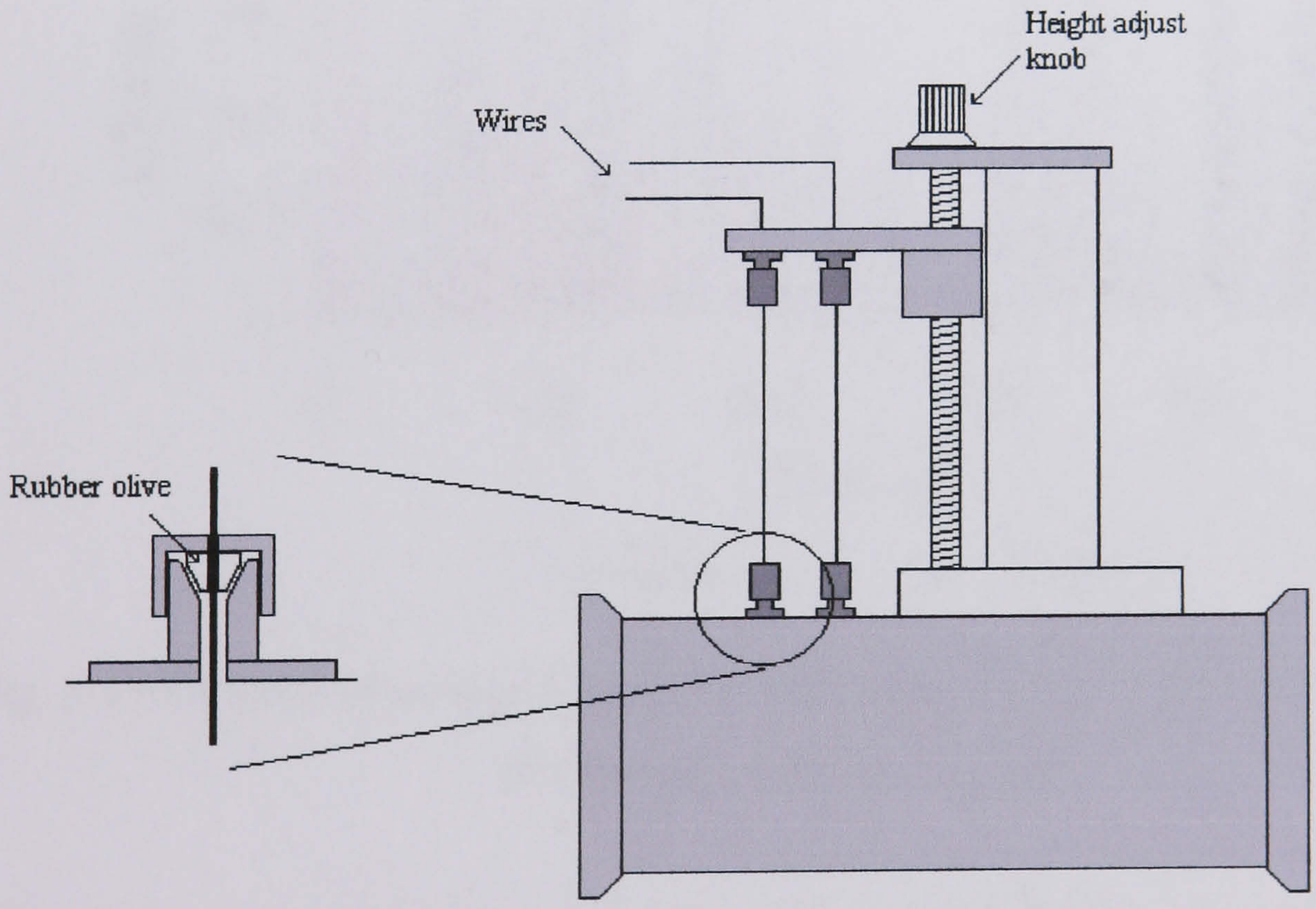

Fig. 3.14 Schematic of dual impedance probe

The dual impedance probe consists of two impedance probes working independently. Each impedance probe measures the differences in capacitance and/or resistance

between the two phases. Detailed description of each single impedance probe is given in section 3.3.2. The distance between the two impedance probes is 10 mm and they are placed one behind the other in the flow direction. The two probes are designed in such a way so they can move together along the same diameter in the pipe cross section. To each probe, an alternating current with frequencies between 2-45 kHz can be applied via a signal controlling box.

Most of the experiments were conducted with a frequency between 35 kHz. Measurements were taken every 2mm along a vertical diameter to give a total of 20 sample locations. The output signals from the two probes are then saved in a PC at a total number of 120,000 from each location by a FORTRAN program. An example of the signals from the dual impedance probe at U_{so} = 1.4, U_{sw} = 1.1 m/s is presented in Fig. 3.15.

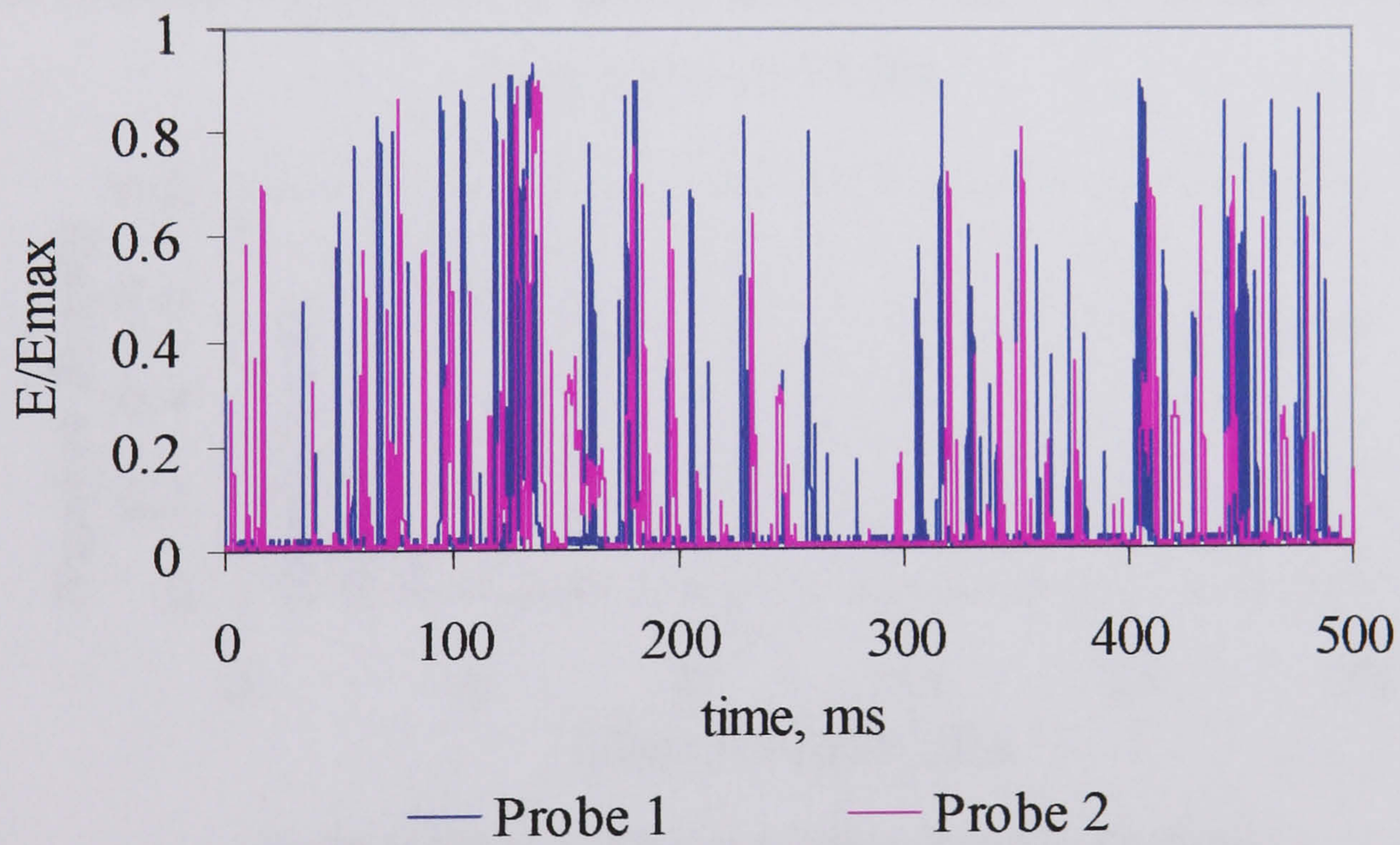

Fig. 3.15 Dimensionless signal from dual impedance probe, 14 mm from the top of the pipe at U_{so} = 1.4, U_{sw} = 1.1 m/s

The data from the two probes was then cross-correlated (see Fig. 3.16) to obtain the average time delay for the drops passing through both probes. Since the distance is known to be 10 mm, the average drop velocity can be calculated by dividing the 10 mm with the average time delay. When the drop velocity is found, the chord length of the drops can be calculated from the signal of either probe by multiplying the drop velocity

by the time duration that each dispersed phase drop is in contact with the sensor. The chord length of the drops is found using a program developed by Hu (2006). Finally, chord length distributions for each location are found by summarizing all the drops in recorded signals as shown in Fig. 3.17.

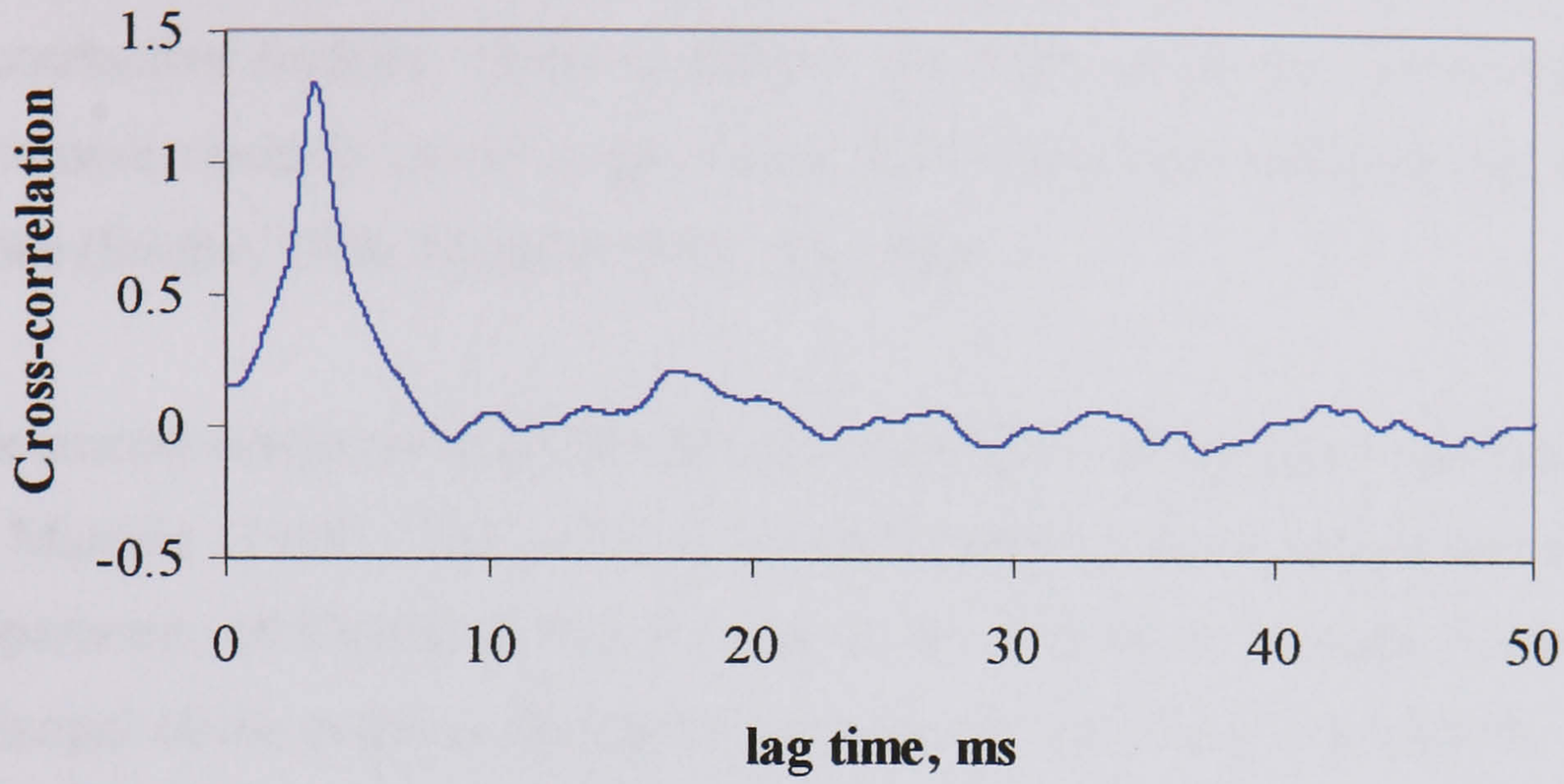

Fig. 3.16 Cross-correlation function against lag time, 14 mm from the top of the pipe at U_{so} = 1.4, U_{sw} = 1.1 m/s

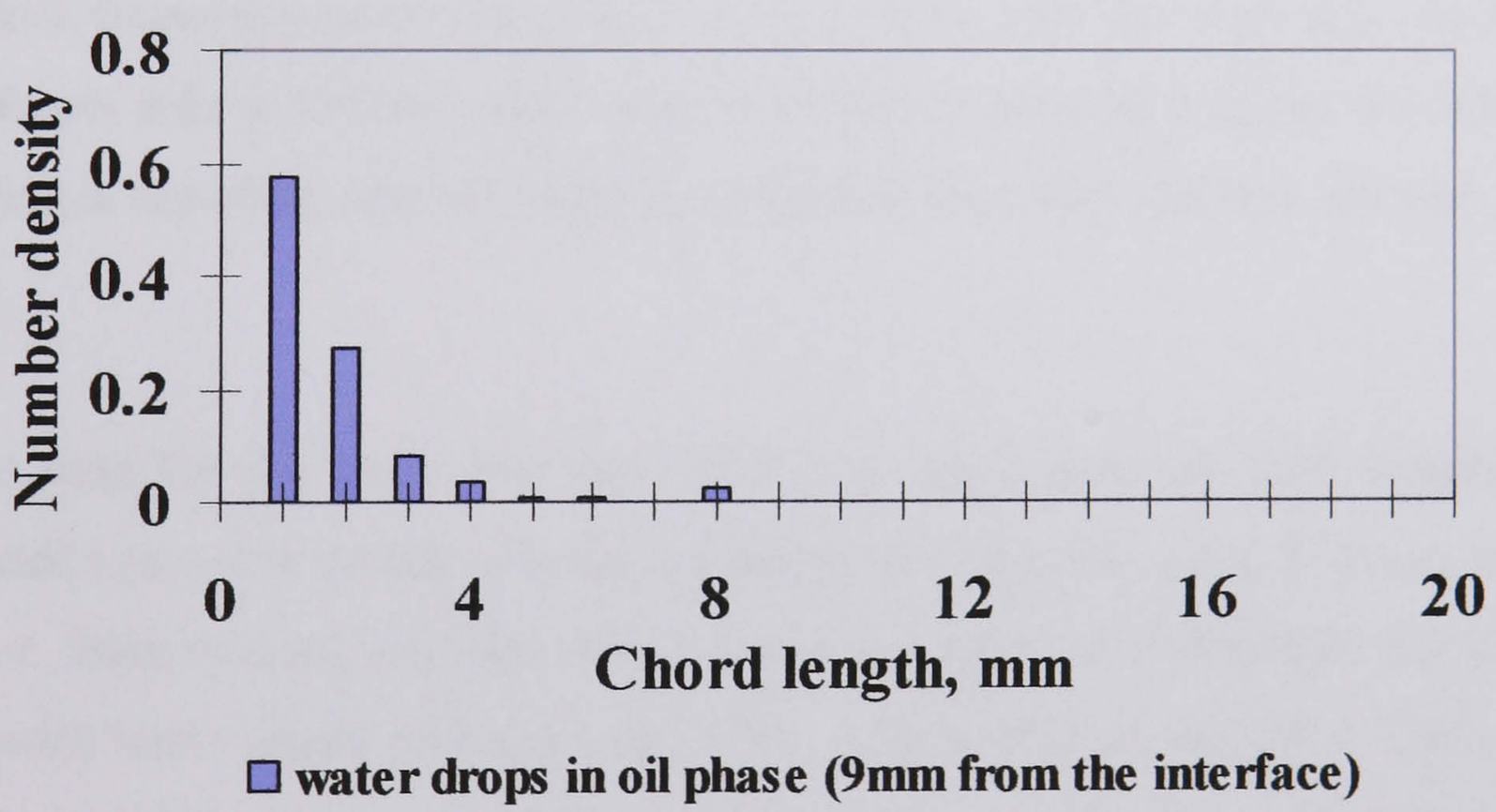

Fig. 3.17 Chord length number density, 14 mm from the top of the pipe at U_{so} = 1.4, U_{sw} = 1.1 m/s

3.3.4 Measurement of wave amplitudes and lengths

Wave structures were measured with a wire conductivity probe before and at the onset of entrainment to see how waves develop until they form drops. The results are also used to validate the model developed in chapter 5 and 6.

The conductivity probe measures the resistance or conductance of the water layer in separated oil-water flow. The probe is composed of a pair of parallel wires which act as electrodes and connected to an electrical circuit. The two wires are stretched across the test section, perpendicular to the flow direction. In an oil-water system, the water acts as a conductive medium which completes the electrical circuit between the two wires. Extensive research exists in gas-liquid flow using this configuration of conductivity probe (Srichai, 1994, Manolis, 1995, Ng, 2002).

The current conductivity probe that was designed for this project was based on the work of Manolis (1995). The probe was constructed in the mechanical workshop in the Department of Chemical Engineering at the University College London. The basic principal of the probe is the ability to measure water layer thickness by measuring the resistance or conductance between the two wires. The electrical conductance varies with the thickness of the water layer. The thicker the water, the larger the electrical conductance. The electrical circuit measures the conductance across the two wires. The master clock frequency of the electronic box used in this project is 50 kHz. As there are 5 channels per side in the box, each channel is therefore being sampled for 20% of the time, giving a sampling rate of 5 kHz per channel. Note that the box has two sides of channels.

The wires used for the probe are made of 0.5mm thick stainless-steel. Stainless steel was selected since it is harder to break compared to platinum wires. The two wires are 5mm apart. 2mm spacing was also tried but wrong signals were obtained. The changing in signal with water height was also weak when a 2mm spacing was used. The wires are stretched across the pipe cross section, perpendicular to the flow, passing vertically across the pipe. The bottom parts of the wires were clamped and sealed to prevent any water from getting into contact with the wires in the region outside the test section. The top of the wires are free to be connected to the electronics. Two caps at the upper part of each wire were used to stretch the wires and keep them in tension. The two caps were connected with screws so the wires can be stretched by pushing the two caps apart. PTFE plugs were used to prevent any leakage from the tube to the outer section of the probe and a silicone rubber was also used to prevent the liquid paths around the two wires from getting out.

The probe mounting is shown in Fig. 3.18. The whole mounting is located on a separate short acrylic pipe section, approximately 8 cm long, with the same internal diameter as the test section. It can therefore be placed in between two pipe lengths of the test section and can measure the interface fluctuation at any distance from the inlet. Measurements were made at 2 and 7m from the inlet.

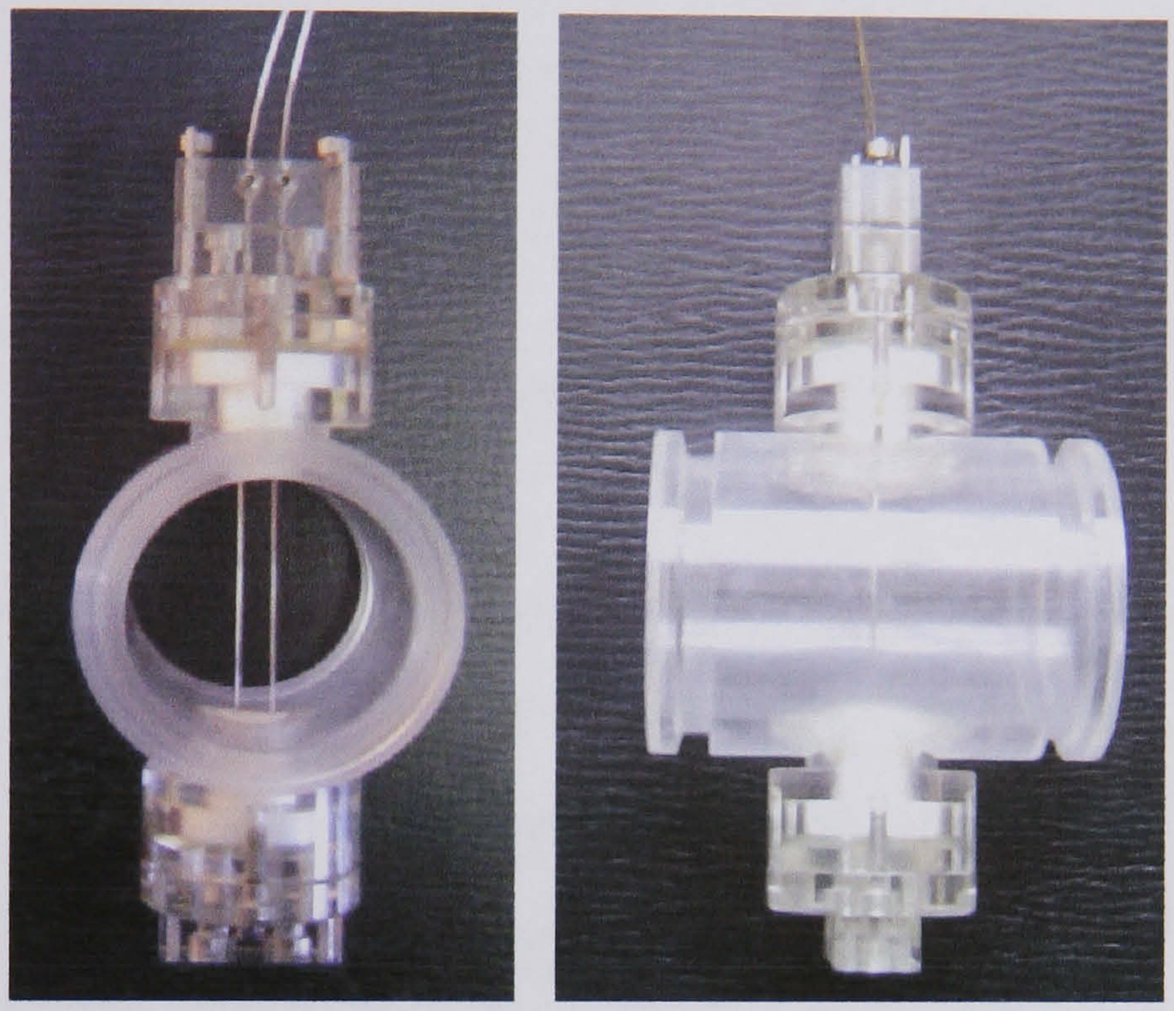

Fig. 3.18 Photograph of the conductivity probe

Before running the experiments, a calibration of the voltage against the water height was necessary since the recorded signals are in the form of voltages. The calibrations were performed offline initially. The probe assembly was fitted between two pipe sections with known overall volume. 100% oil was introduced initially to this volume and the corresponding voltage acquired at the sampling frequency of 500 Hz was recorded. The recorded voltage which is almost zero represents zero water height. The percentage of oil was then decreased by 10% while that of water was increased by 10% until the calibration section was filled with 100% water. The volume of oil and water were measured before and after the addition and the corresponding voltage was also recorded. The height of the water was measured from the hold up calculated from the volume of oil and water at each percentage. The voltage and the height at each percentage were recorded. The same procedure was repeated starting from 100% water until 100% oil. The interface between the oil and water was allowed to quieten before a new measurement was taken. A reasonable gain was selected to have a reasonable range

of voltage. Fig. 3.19 shows the calibration curve for calculating the height of the water interface. The calibration curve was obtained by fitting a polynomial to the calibration points. The polynomial equation is given by

$$h_w = 0.507\ V^2 + 5.15\ V - 0.1896 \qquad (3.1)$$

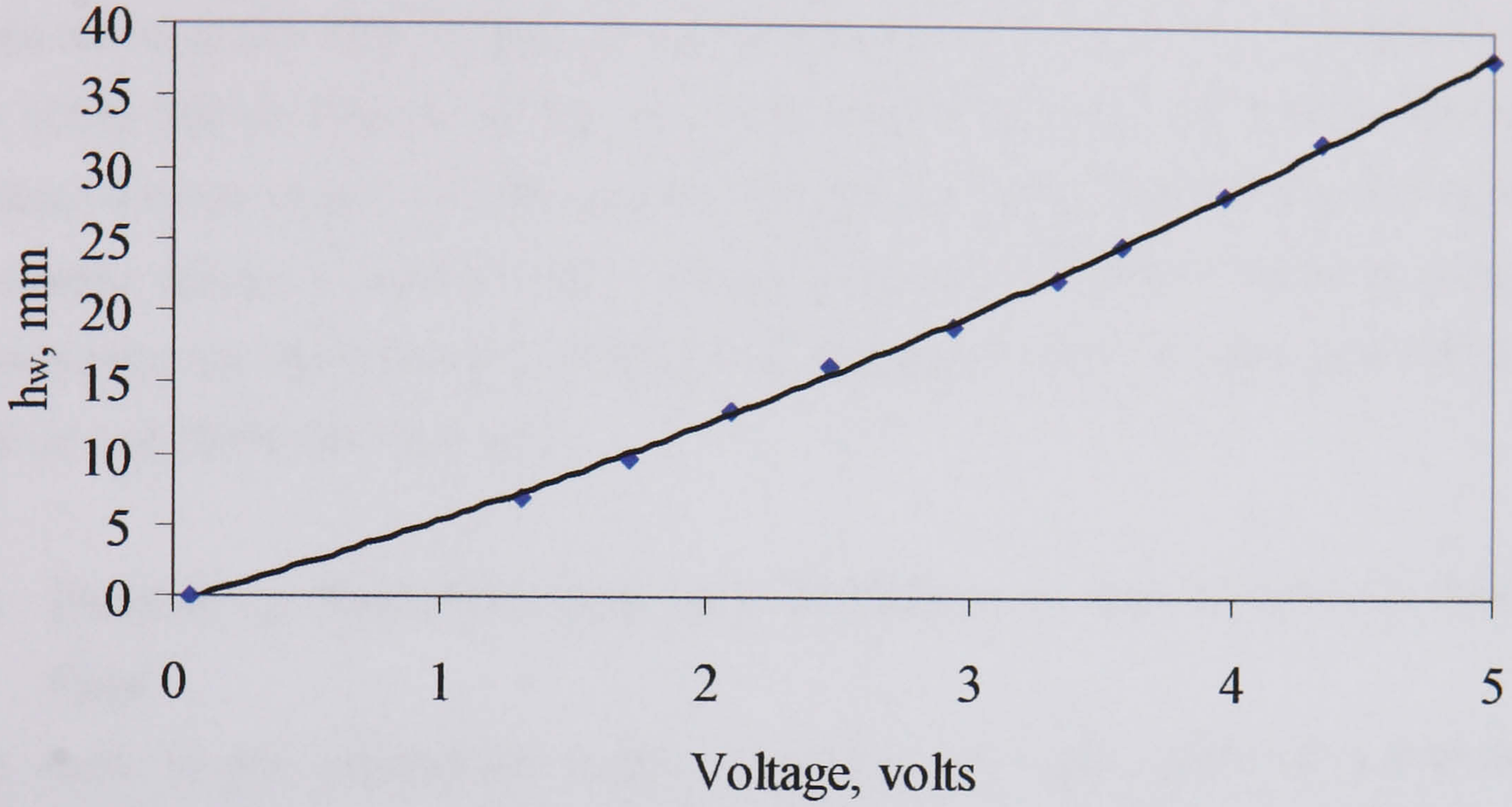

Fig. 3.19 Calibration chart for conductivity probe

All the experiments were conducted at a sampling rate of 500 Hz and 6000 samples were recorded per run. Investigations of the interface fluctuation took place at the onset velocities. The onset velocities obtained using the high speed video camera (section 3.2) were used. The measurements were done for the whole set of the experimental onset velocities found as described in section 3.3. Also, measurements were taken below the onset velocities at certain superficial oil velocities and increasing superficial water velocities until the entrainment onset velocities. Using the onset velocities, the same measurements were done 2 m from the inlet. The output signals were recorded as voltages that correspond quickly to the fluctuation of the height of the water interface. The calibration equation was used to transform voltage into height. From the interface height variation the wave amplitudes and lengths were calculated. MATLAB was used to average the raw data (3 points) to remove strange shapes that may occur in the waves as a result of noise without losing any essential information.

All the measurements were conducted in one week to avoid the problem of getting inaccurate results from the conductivity measurements. Ng (2002) discovered a reduction in the measured voltage signals with time. The reduction was due to a porous layer that was found to form on the stainless steel wires and affects the voltage output. It was found that the voltage signal for a pipe full of water decreased from 3V to 1V over a period of 19 experimental days. This problem was also observed in our experiment but it was not so severe. The voltage signals were decreased from 5V to 4.5V when the pipe was 100% full with water for the one week used to run the experiments. Since the problem was not severe, correction to the voltages was made by assuming that the same percentage change occurred to all voltages measured. Therefore, before running the experiments, the corresponding voltage was measured when the pipe was 100% full with oil and 100% full with water.

3.4 Measuring Methodologies and Technique in the 14 mm ID Acrylic Pipe

The work in the small-scale facility involved two main types of experimental investigations. The first part of the experiments involves visual observation using photographic technique. The second part aims to investigate the effect of adding drag-reducing polymers on horizontal oil-water flows.

3.4.1 Visual observation

Visual observation was used in the small pipe to identify the flow patterns formed and investigate the mechanism of drop formation. A high-speed video camera provided by EPSRC was used which was located in front of the view box at the end of the test section.

Kodak high-speed video (KODAK HS 4540) was used for visualization experiments. This system can record at up to 4500 fps with a full size picture and up to 40500 fps with a reduced picture. The system will record 3072 full frames with a maximum resolution of 256x256 pixels. Thus, 0.66 s of recording time is available if 4500 f/s is selected as a speed rate. More recoding time can be obtained if a slower speed rate is chosen.

In these experiments, 125 f/s was selected as a frame rate. This frame rate allowed recording time of approximately 25s. The recorded images could be viewed with the provided monitor before downloading them via the supplied PC which is 300MHz Pentium II. The downloading speed to the PC is very slow and takes approximately 1 s for 1 picture. Once the downloading was completed, another record of the flow could be made.

Several conditions were tested and recorded starting from superficial oil velocity of 0.09 m/s up to 0.44 m/s with an increment of 0.07 m/s. The water superficial velocities were increased at each oil superficial velocity starting from 0.10 m/s up to 0.80 m/s with an increment of 0.10 m/s. After each run, the recorded pictures were downloaded for further investigations. The flow patterns and the mechanism of drop formation were identified by carefully analyzing the recorded pictures using Photron FASTCAM Viewer.

3.4.2 Drag reduction measurements

The effect of adding small amounts of drag reducing polymer to a horizontal oil-water flow was investigated experimentally in the small flow facility. The objective is to reduce the frictional pressure drop and to visualize the effect on flow patterns. Measurements were made with high-speed video camera and U-tube manometer to investigate the effect on flow patterns and pressure drop respectively.

3.4.2.1 Preparation of the polymer

The polymer used in this study is Magnafloc 1011 manufactured by Ciba Specialty Chemicals. Magnafloc 1011 is a co-polymer of polyacrylamide and sodium acrylate which was provided in a powder form. The powder was mixed with deionized water in a tank with a stirrer. This was done by slowly adding the Magnafloc powder into the water tank with gentle mixing. When all required powder had been added into the tank, the solution was kept agitated at a low speed for 2 h with marine type impeller (Fig. 3.20). After that, the solution was left at rest for a day to allow the polymer to hydrate in the solution. In this study, a fixed master solution of 1000 ppm is used for all the measurements. This was prepared by adding 5 g of polymer into 5 l of deionized water.

Fig. 3.20 Stirrer used to mix the polymer solution

3.4.2.2 Polymer injection system

A polymer injection system is used to inject the master solution into the test section. The injection system consists of a pump, reservoir and an injection point. The pump is used to deliver the polymer solution from a reservoir into the inlet section. The pump used in this study is a PTFE diaphragm pump (MASTERFLEX-Model No. 07090-42 manufactured by Cole-Parmer Instrument Company). The pump can work continuously against back pressure up to 50 psig with accuracy better than 2 % dispensed volume. The diaphragm pump is lined-up with MASTERFLEX L/S variable speed drive to control the flow rate of the injected polymer solution via peristaltic tubing (see Fig. 3.21). The polymer solution was kept in the reservoir from which it was pumped. The reservoir is a 5 l tank that used to store the 1000 ppm master solution. To avoid pulsation, the outlet tube of the pump is connected to a pulse dampener (MASTERFLEX L/S pulse dampener). The outlet from the dampener is attached to the injection point.

Fig. 3.21 MASTERFLEX L/S pump used to deliver the pump from the master solution reservoir to the 14 mm ID flow loop (PTFE diaphragm pump, MASTERFLEX L/S variable speed drive and peristaltic tubing)

The flow rate of the injected polymer is controlled by the variable speed of the pump. Using the 1000 ppm master solution, the pump is calibrated for different variable speeds. With this concentration, the pump can deliver between 40-400 ml/min with an accuracy of 2%. The calibration chart is given in Fig. 3.22. The polymer solution was injected into the flow loop by introducing the master solution into the water through a hole with a 3 mm diameter. The hole is located at the bottom of the pipe 10 cm upstream of the Y junction where oil and water are mixed.

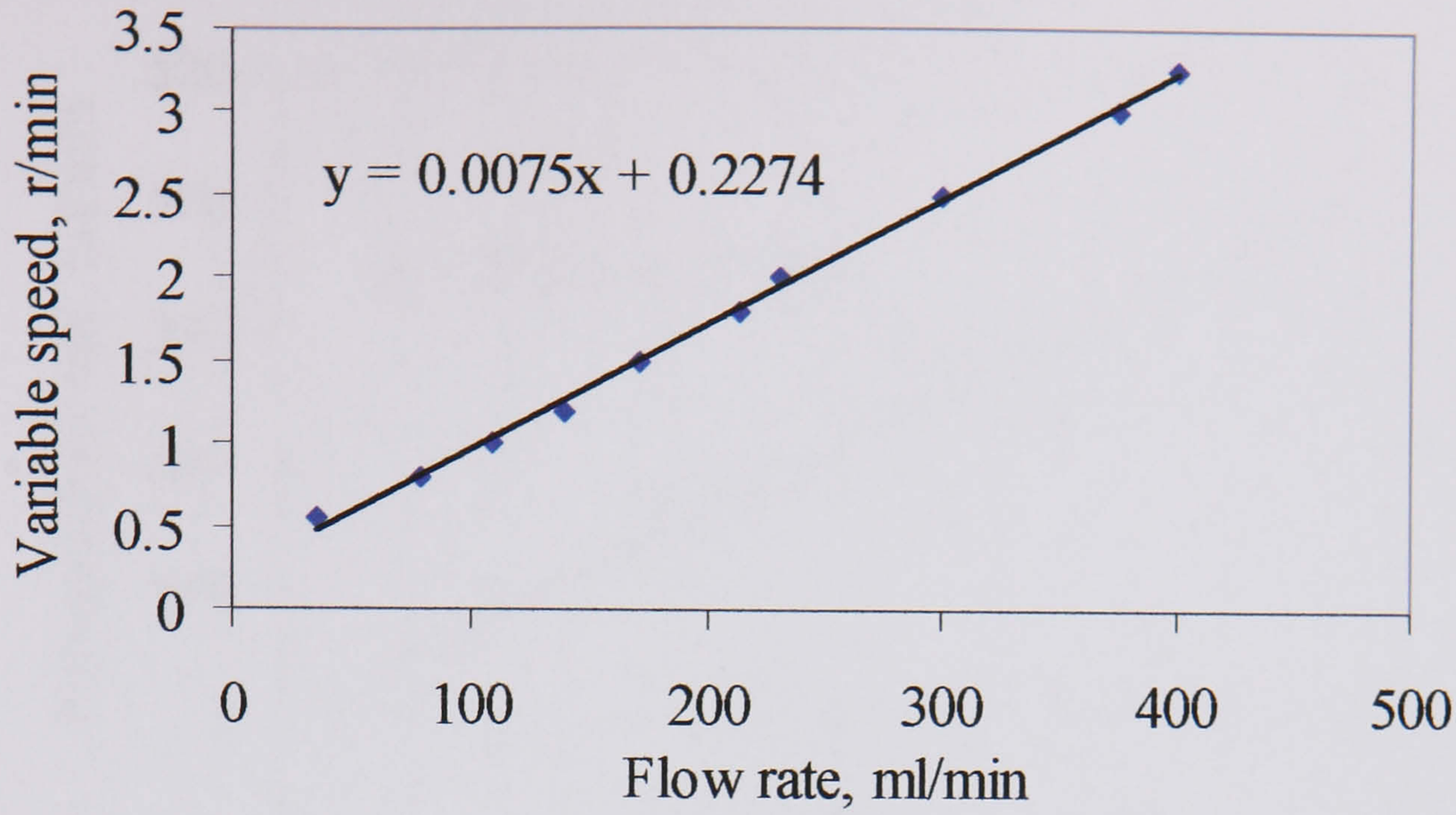

Fig. 3.22 Calibration chart of the MASTERFLEX L/S pump for 1000 ppm of polymer solution

3.4.2.3 Experimental Procedure

Before running the experiments, calibration of the polymer flow rates is required at different water flow rates to obtain fixed amount of polymer concentration inside the loop (20 and 50 ppm). At each water flow rate, certain polymer flow rate should be delivered by the pump to obtain the desired polymer concentration in the pipe. As mentioned earlier, the pump flow rate is regulated by the variable speed of the pump. Fig. 3.23 shows a chart for the required polymer flow rate required to achieve 50 ppm concentration in the pipe at different water flow rates when 1000 ppm of master polymer solution is used.

An experimental run started by passing a given flow rate of oil through the system. Water at a given flow rate was then introduced into the flow loop. The flow rates of oil and water were adjusted to the predetermined values. The flow pattern observed in the view box was recorded using the high-speed video camera (see section 3.4.1). A U-tube manometer was used to measure the pressure drop over 0.7m. The first pressure tap was located 2.5 m from the inlet section.

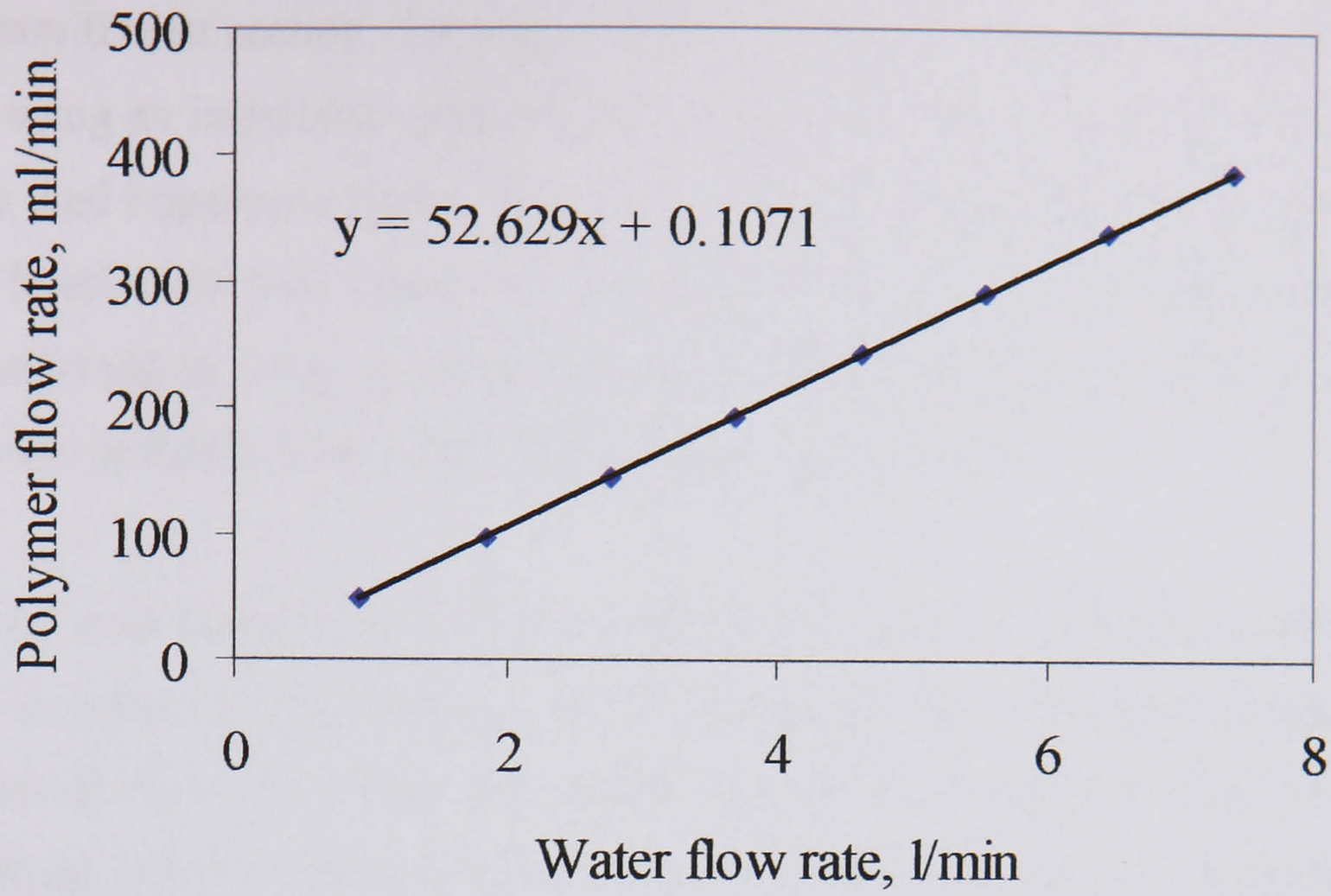

Fig. 3.23 Calibration chart of the polymer flow rate required to achieve concentration of 50 ppm inside the flow loop when 1000 ppm of polymer solution is used

At this condition of oil and water flow rates; a predetermined polymer flow rate was injected through the small hole to achieve 50 ppm of polymer concentration in the flow loop. After the addition of the polymer the pressure drop was also measured and the flow pattern was recorded to investigate the effect of polymer on flow patterns. During the experiments, the water was drained from the separator while the oil outlet from the separator was closed to avoid mixing with the oil tank. After each run, the oil was allowed to settle in the separator while downloading the recorded pictures before a new run could be made. The oil flow rate was varied from 0.09 m/s – 0.44 m/s at given water flow rate to provide a matrix of data. When the flow rate of water was changed the flow rate of the injected polymer solution was changed accordingly to achieve 50 ppm.

3.5 Summary

This chapter demonstrates the experimental flow facilities, instrumentations and techniques employed in this work to study the transition from wavy stratified to dual continuous pattern in horizontal oil-water flows and obtain information of flow characteristics in these patterns. In the pilot scale facility (38 mm ID stainless steel test section), high-speed video camera was used to measure the onset velocities of entrainment and observe the flow before and after the onset (2 and 7 m from the inlet).

Also, measurements of phase distribution, drop size and wave structures were obtained in the 38 mm ID test section. The phase distribution of the pipe cross sectional area was measured using an impedance probe while velocity and chord length of the drops were given by a dual impedance probe. The phase distribution was then used to calculate the entrained fraction of each phase into the other while the chord length measurements were transformed to drop size distributions. A wire conductivity probe was used to measure wave structure before and at the onset of entrainment.

In the small scale facility (14 mm ID acrylic test section), a high speed video camera was used to obtain a flow pattern map of the conditions investigated, identifying the onset of entrainment and capture the mechanism of drop formation. Also, the effect of drag reducing polymer on horizontal oil-water flows was studied. Magnafloc 1011 which is a co-polymer of polyacrylamide and sodium acrylate (provided in a powder form) was used to prepare 1000 ppm of master solution. The high speed camera was used to monitor the flow while measurements of pressure drop were taken before and after the addition of the polymer.

CHAPTER 4

Experimental Investigation of the Transition between *Stratified* and *Non-stratified* Flow and Associated Phenomena in Oil-Water Horizontal Pipeline Flow

In this chapter, the results from experimental investigations of the transition between *stratified* and *non-stratified* flows (mainly transition to *dual continuous* flows) and associated phenomena in co-current horizontal oil-water flows are reported. Section 4.1 discusses the phenomena visually observed using high speed video camera in the two different experimental facilities with 38 mm ID stainless steel and 14 mm ID acrylic test pipes respectively. The onset velocities obtained in the two test sections are presented and compared in section 4.2. Section 4.3 demonstrates the wave structures before and at the onset of entrainment obtained by the conductivity probe at 2 and 7 m from the inlet. A summary is given in section 4.4

4.1 Visual Observation

High speed recording was implemented to monitor the flow prior and after the transition from *stratified* to *non-stratified* flows and especially to *dual continuous*. Two different cameras were used. A Photron Ultima APX system (see section 3.3.1) was used in the 38 mm ID stainless steel pipe while a Kodak high-speed video (KODAK HS 4540) was used in the 14 mm ID acrylic pipe.

4.1.1 Pilot scale facility (38 mm ID stainless steel pipe)

In the 38 mm ID test section, flow visualization experiments were carried out by monitoring and recording the oil-water flow through the view box described in section 3.2.2. The view box is placed at two meters and at seven meters from the test section inlet. The aim is to investigate how the waves develop and when the drops form at the two locations. All the observations were made using the modified inlet section (Y-junction) which was designed to minimize entrance effects (see section 3.2.1.2). The flow was also monitored for different inlet geometries (oil and water are joined through a T-junction and flow through a 90° bend before entering the test section as described in section 3.2.1.1). The flow pattern map for the latter inlet section was developed by Lovick and Angeli (2004).

4.1.1.1 Observations at 7 m from the inlet

At 7 m from the inlet (185 D), fully developed flow was assumed to be reached. The recorded pictures revealed a number of flow characteristics. For example, no entrainment was found when interfacial waves were absent. It appears that drop formation depends on two main factors, wave amplitude and the relative velocities between the two phases. Waves are found to grow in amplitude as the flow rates of oil and water increase until they attain a critical height where drop formation is possible (*onset of entrainment*). No drops could be observed when the amplitudes of the waves were less than 2 mm.

For the *stratified* flow (prior to the transition to *dual continuous* flow), the amplitudes of the waves are found to increase as both superficial oil and water velocities increase. For example, at U_{so} = 0.10 m/s, the amplitudes grow as U_{sw} increases. However, at higher oil velocity (U_{so} = 0.30 m/s) the observed amplitudes are larger than those found at lower oil velocity (U_{so} = 0.10 m/s) for the same water velocity (U_{sw} = 0.45 m/s). This comparison is shown in Fig. 4.1. Thus, the largest amplitude is found at higher oil and water velocities. This is why the required superficial water velocity to initiate drops decreases as the oil velocity increases. For instance, while drops were first observed at U_{sw} = 0.50 m/s for U_{so} = 0.10 m/s, drops was found to form at U_{sw} = 0.40 m/s for U_{so} = 0.30 m/s (see the discussion in section 4.2).

Moreover, the lengths of the waves at the onset velocities were found to be relatively larger when the two phases travel at similar velocities than when they have different velocities. For example, at U_{so} = 0.40, U_{sw} = 0.40 m/s the observed wavelengths are larger than those observed at U_{so} = 0.10, U_{sw} = 0.50 m/s.

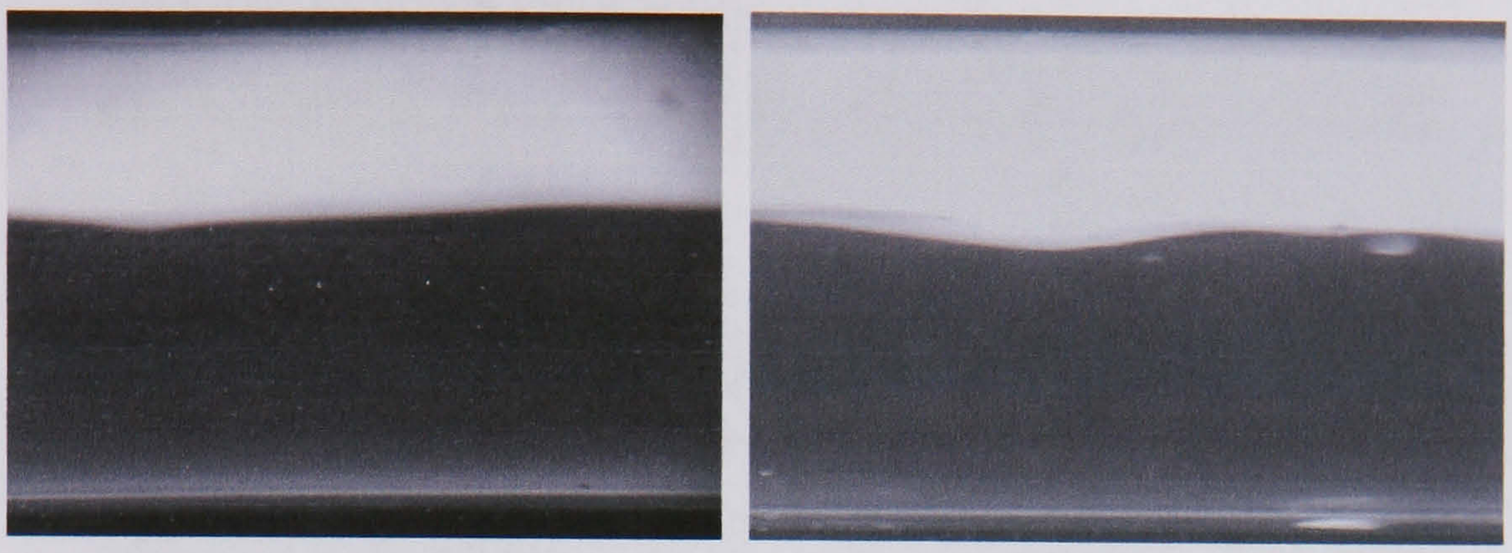

(a) (b)

Fig. 4.1 Wave amplitudes at (a) U_{so} = 0.10, U_{sw} = 0.45 m/s and (b) U_{so} = 0.30, U_{sw} = 0.45 m/s in the 38 mm ID test pipe, 7 m from the inlet section (Y- junction inlet section).

Fig. 4.2 shows the effect of increasing the water superficial velocity at U_{so} = 0.10 m/s when the modified inlet section is used (Y-junction). From the pictures, it is clear that the amount of drops entrained increases as the superficial water velocity increases. The effect of increasing U_{sw} at U_{so} = 0.10 m/s is also obtained when the oil and water are introduced through a T-junction followed by bend as shown in Fig. 4.3. Interestingly, larger drops are observed when the flow goes through a bend in comparison to those found while using the Y-junction. It is possible that the bend mixes the two fluids and encourages formation of drops larger in size. This could also explain the entrained fraction results presented in chapter 7 which show that the entrained fractions with the T-junction are higher than those with Y-junction.

U_{sw} = 0.45 U_{sw} = 0.50 U_{sw} = 0.60

Fig. 4.2 The effect of increasing water superficial velocity at U_{so} = 0.10 m/s in the 38 mm ID test pipe, 7 m from inlet section (Y- junction inlet section)

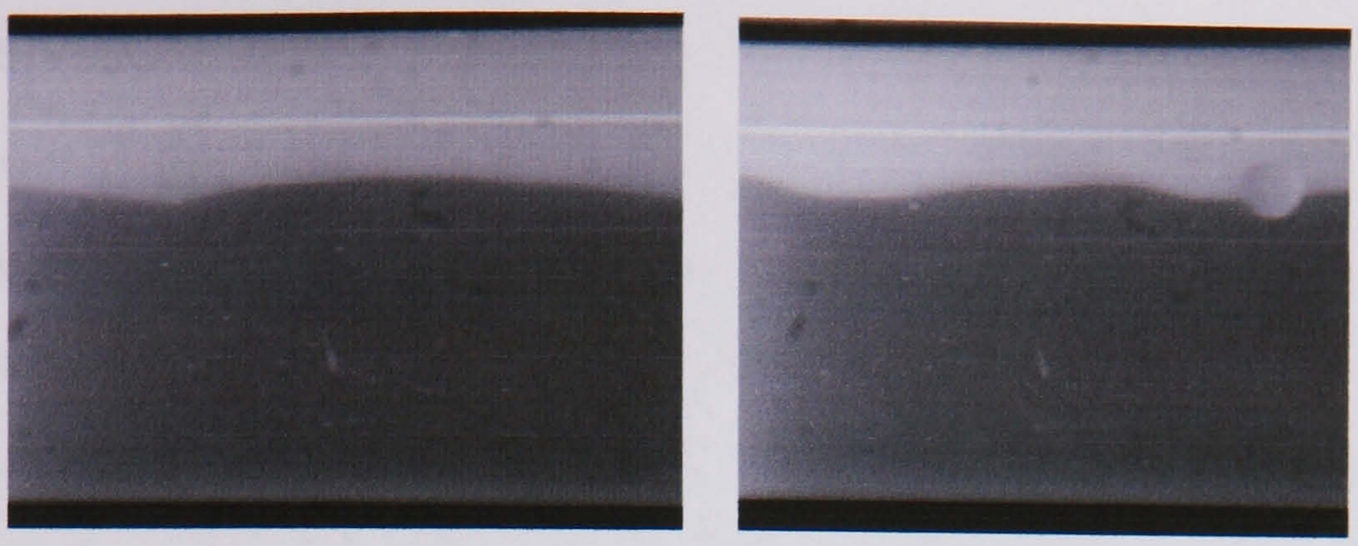

$U_{sw} = 0.45$ $U_{sw} = 0.50$

$U_{sw} = 0.55$ $U_{sw} = 0.60$

Fig. 4.3 The effect of increasing the water superficial velocity at $U_{so} = 0.10$ m/s in the 38 mm ID test pipe, 7 m from inlet section (T- junction inlet section with bend)

The flow pattern map of the test fluids used is developed by Lovick and Angeli (2004) as shown in Fig. 4.4. The map was found when the T-junction with bend is used for the inlet test section.

Fig. 4.4 Flow pattern map as developed by Lovick and Angeli (2004) in the 38 mm ID test pipe, 7 m from inlet section (T- junction inlet section with bend)

4.1.1.2 Observations at 2 m from the inlet

The flow characteristics were also investigated two meters from the inlet uisng the Y-junction as the inlet. The pictures revealed that no drops were found at this location at the onset velocities obtained 7 m from the inlet. This means that all the drops found downstream the pipe have been produced from the waves only as they propagate through it. Also, it means that the new inlet section introduces a better stratification to the flow and diminishes entrance effects. Drops were observed at higher superficial water velocities than those found at 7 m from the inlet, for all the tested superficial oil velocities. For example, at $U_{so} = 0.20$ m/s, onset of entrainment was observed at $U_{sw} = 0.45$ m/s while at 2m from the inlet drops started to form at $U_{sw} = 0.70$m/s. Further increase of the water superficial velocities did not increase drop formation significantly (see Fig. 4.5). Instead, the waves just became more disturbed. At the highest water velocity ($U_{sw} = 0.90$ m/s), the flow became *annular*.

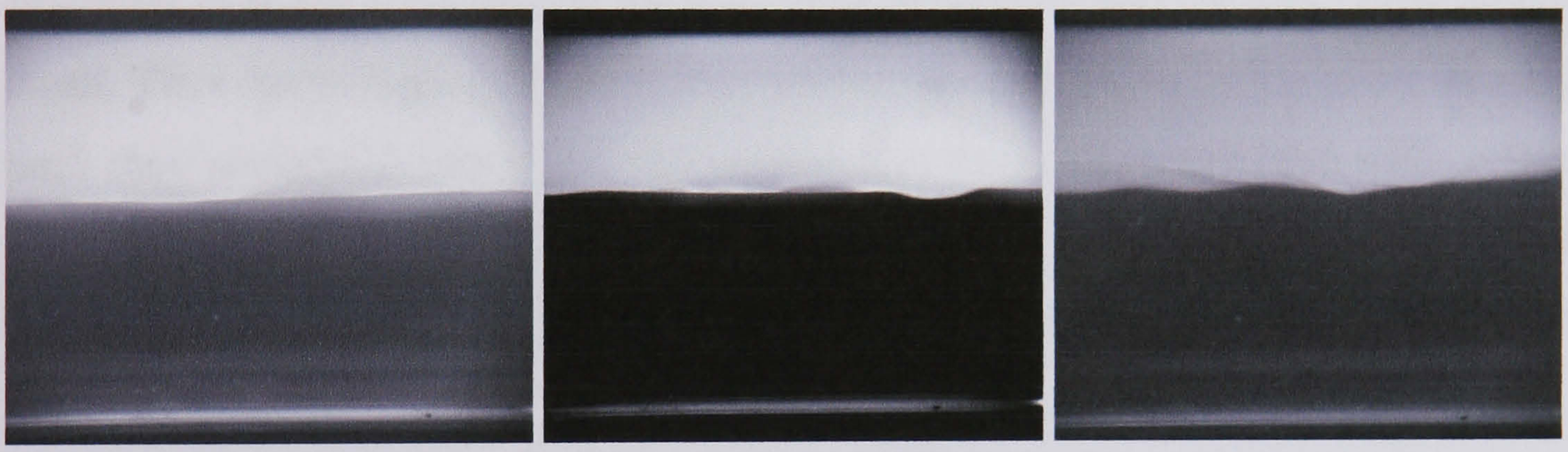

$U_{sw} = 0.40$ m/s $U_{sw} = 0.50$ m/s $U_{sw} = 0.60$ m/s

$U_{sw} = 0.70$ m/s $U_{sw} = 0.80$ m/s $U_{sw} = 0.90$ m/s

Fig. 4.5 The effect of increasing the water superficial velocity at $U_{so} = 0.20$ m/s in the 38 mm ID test pipe, 2 m from inlet section (Y-junction inlet section)

From the pictures it appears that close to the inlet the amplitudes of the waves are smaller and the interface in several cases is smooth with small wavelets (see Fig. 4.5 at $U_{sw} = 0.40 - 0.60$ m/s). These waves would grow in amplitude and may decrease in

wavelength as they propagate downstream the pipe and eventually reach critical amplitude at which drop formation becomes possible due to the relative movement of oil and water. On the other hand, the small waves which appear as ripples in the interface may just decay as they move through the pipe (see the discussion in chapter 5 and 6). Also, although the interface became highly disturbed at higher water superficial velocities (U_{sw} = 0.70 – 0.90 m/s), drop formation did not increase significantly. Obviously either the amplitude had not reach the critical size required for drop formation or the wave deformation necessary for drops to form had not developed yet which will happen further downstream (see Fig. 4.2).

4.1.1.3 Annular flow pattern

From the visual observations and by careful analysis of the pictures, *annular* flow pattern was clearly observed at low oil superficial velocities and high water superficial velocities (see Fig. 4.6). At low oil superficial velocities, the thickness of the oil layer is small. Thus due to high difference in velocities, the amplitudes of the water waves grow until they manage to bridge the test section and touch the upper pipe wall to form an annulus. Table 4.1 shows the onset of this pattern that was observed 7 m from the inlet. This pattern was only seen when oil and water were introduced through the Y-junction.

U_{so}, m/s	U_{sw}, m/s
0.05	0.75
0.10	0.80
0.15	0.85
0.20	0.90

Table. 4.1 The onset of the *annular* flow in the 38 mm ID test pipe, 7 m from inlet section (Y-junction inlet section)

This pattern was found at both 2m and 7m from the inlet which suggests that *annular* flow exists along the whole pipe. At each superficial oil velocity, the *annular* flow, once formed, continued to exist as the water superficial velocities increased. However, the water annulus became thicker while the oil layer became more dispersed. The occurrence of *annular* flow was also reported by Oglesby (1979), Arirachakaran et al. (1989) and Valle and Kvandal (1995) at low oil and high water superficial velocities.

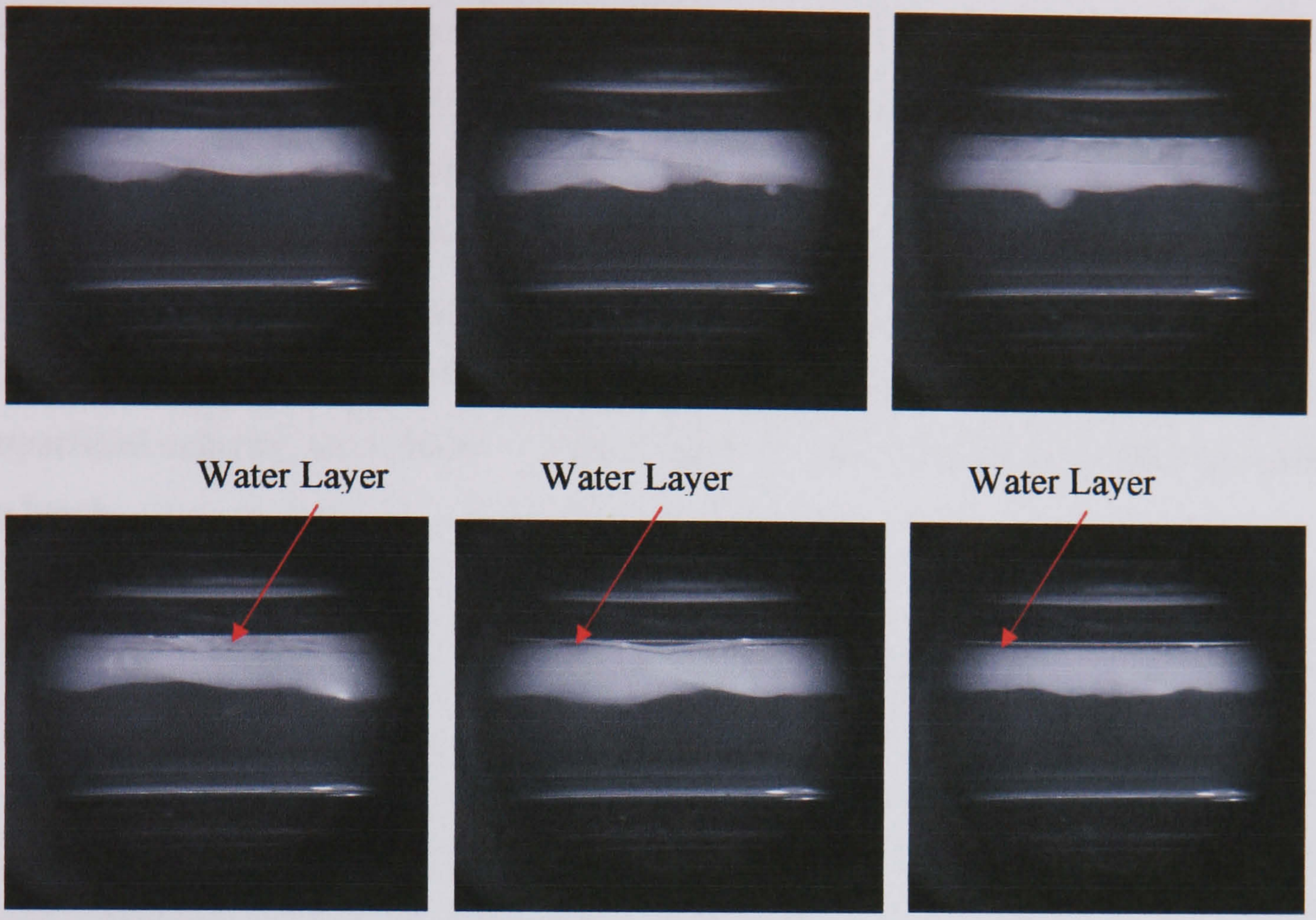

Fig. 4.6 The formation of *annular* flow at U_{so} = 0.10, U_{sw} = 0.80 m/s flow in the 38 mm ID test pipe, 7 m from inlet section (Y-junction inlet section)

4.1.2 Small scale facility (14 mm ID acrylic pipe)

The flow pattern map obtained in the small scale experimental system (14 mm ID acrylic pipe), described in section 3.2.2, is presented in Fig. 4.7 in terms of oil and water superficial velocities. All flow visualization measurements were made through the viewing box which was placed towards the end of the test section, 3 m from the entrance, to get the maximum possible fully developed flow. A range of oil and water superficial velocities were investigated. The oil and water flow rates were adjusted to the desired condition and time was allowed for steady conditions to be established. Once steady state was reached, high speed images were taken at each measurement.

Five flow patterns were identified for the range of conditions investigated. These are *stratified* (*stratified smooth, SS and stratified wavy, SW*), *dual continuous* (*DC*), *annular* (*AN*), *slug* (*SG*) and *bubbly* (*Bb*). The visual observation and the analysis of the pictures showed clearly that no drops form when they are no waves or when the wave amplitudes are small. At U_{so} = 0.09-0.23 m/s, oil *slug* (*SG*) (oil drops larger than the

pipe diameter) or elongated *bubble* (*Bb*) (oil drops less than the pipe diameter) patterns form as the water velocities increase instead of the *dual continuous* pattern which was observed in the 38 mm ID stainless steel horizontal pipe. This could be attributed to the decrease in the thickness of the oil layer as that of the water layer increases; with increasing water velocity, its turbulence increases and breaks the oil layer. In addition, the oil tends to wet the pipe and cover a large cross sectional area relative to its volume. Therefore, as the ratio of oil to water decreases as a result of the increase in water superficial velocity, the tendency of the oil layer to wet a large area of the pipe causes it to break.

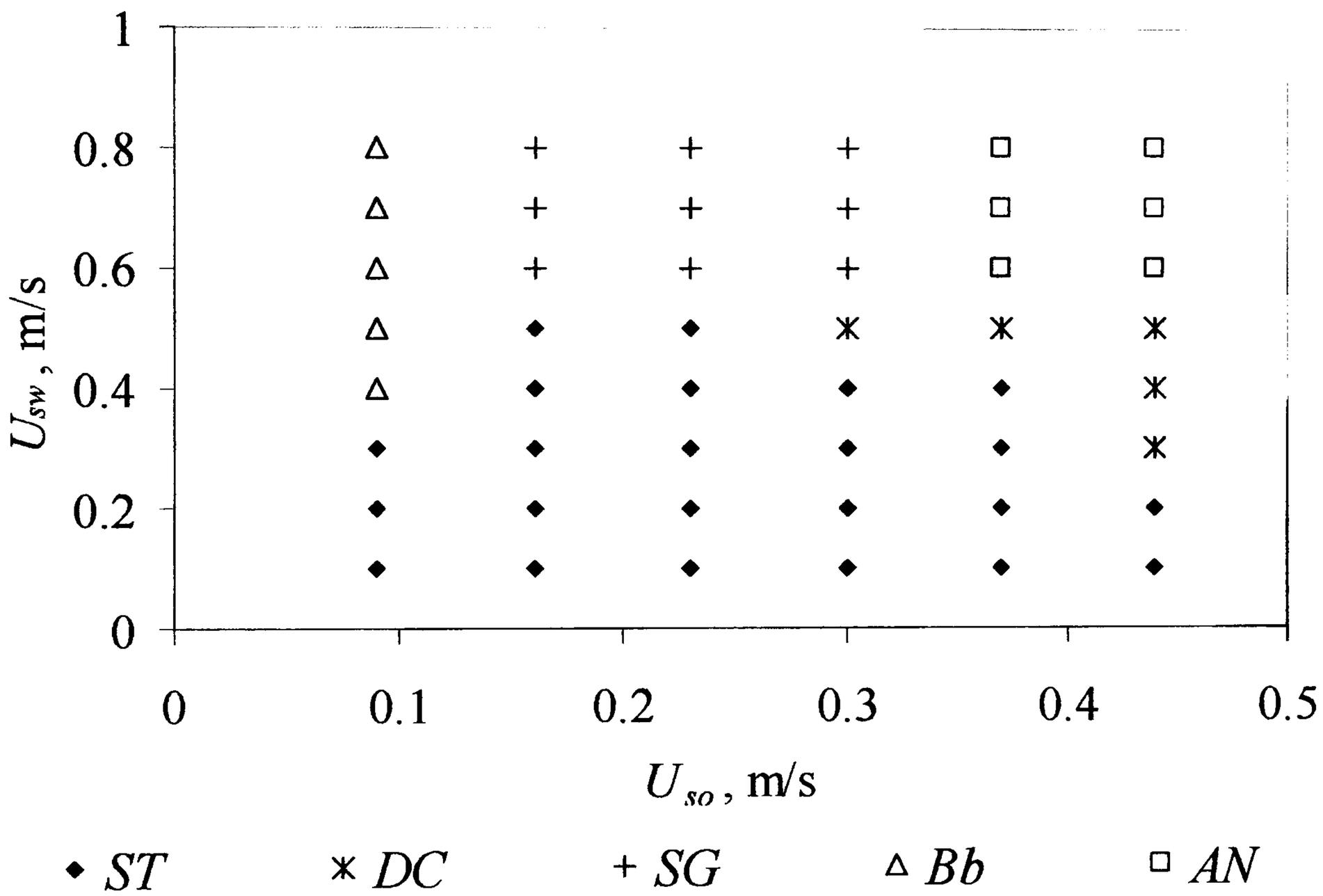

Fig. 4.7 Flow pattern map for oil-water flow (14 mm ID acrylic test section). Flow patterns: *ST* (*stratified smooth* or *wavy*), *DC* (*dual continuous*), *SG* (*slug*), *Bb* (*bubble*) and *AN* (*annular*).

At higher oil velocity, the oil layer preserves its continuity and drops form at the interface as the water velocity increases for a constant oil velocity. This is due to the increase in the amplitudes of interfacial waves. At these conditions the oil layer is thick enough and an increase in the water velocity instead of breaking the oil layer will increase the relative movement between the two phases that causes wave growth and

eventually drop formation. It is noted that waves should reach a finite height before drop formation is possible. As the water velocities further increase, the height of the water interface increases so some of the waves in the water phase may touch the upper pipe wall and give *annular* flow.

The effect of increasing water velocity at U_{so} = 0.09 m/s, where transition to *bubble* flow occurs is shown in Fig. 4.8. At U_{sw} = 0.1 m/s, the flow is *stratified* and the interface is smooth. As U_{sw} increases, the interface becomes more wavy with small amplitude waves. At U_{sw} = 0.4 m/s, the flow changes from *stratified* to *oil-bubbles-in-water*. Further increase in the water superficial velocity causes the *bubbles* to become smaller.

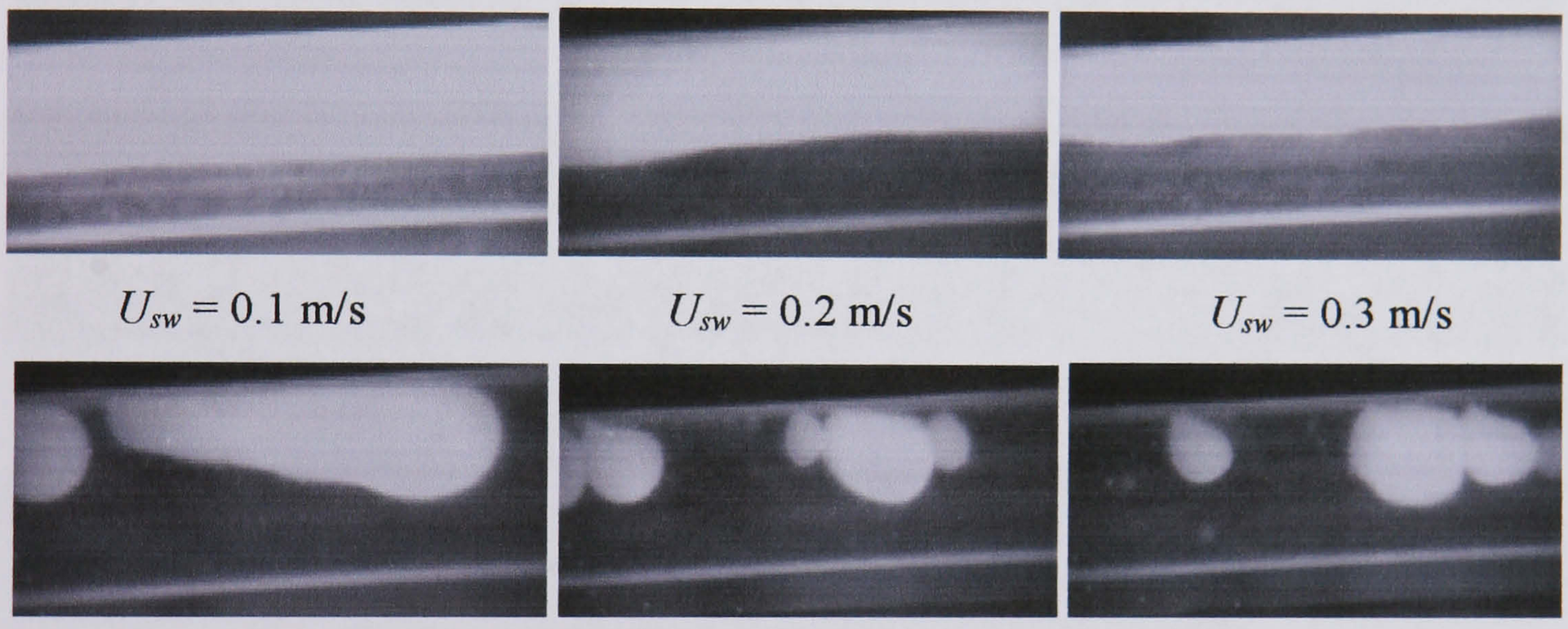

U_{sw} = 0.1 m/s U_{sw} = 0.2 m/s U_{sw} = 0.3 m/s

U_{sw} = 0.4 m/s U_{sw} = 0.6 m/s U_{sw} = 0.8 m/s

Fig. 4.8 Transition from *stratified* to *bubble* flow with increasing water velocity at U_{so} = 0.09 m/s in the 14 mm ID acrylic test section (the upper phase is oil while the lower phase is water). Flow direction is from left to right.

Fig. 4.9 demonstrates the effect of increasing water superficial velocity at U_{so} = 0.23 m/s, where transition to *slug* flow takes place. It is clear from the images that the *stratified* flow is wavier than that at U_{so} = 0.09 m/s. Also, the amplitudes of the waves increase as U_{sw} increases. This shows again that the amplitudes of the waves increase as the superficial velocities of oil and water increase and the highest amplitude in the *stratified* region should be found at the highest U_{so} and U_{sw} before transition to another pattern. At U_{sw} = 0.60 m/s, the pattern changes from *stratified* to *slug*. However, the *slugs* appear to be very long and in some cases they look like *stratified* flow but with discontinuity in the oil layer.

In general, *slug* flow only appears at the higher water velocities; there the water turbulence will be increased and the interface will be wavier. The probability of the waves to touch the upper pipe wall and break up the thin oil layer will be higher. The slug length seems to decrease with decreasing oil to water ratio. At high water velocities the increased water turbulence will tend to break the large *oil slugs* and shorter ones will be formed. Also the slug length decreases as the oil velocities decrease, because with reduced oil velocity the amount and the thickness of the oil layer decreases and it makes it easier to break.

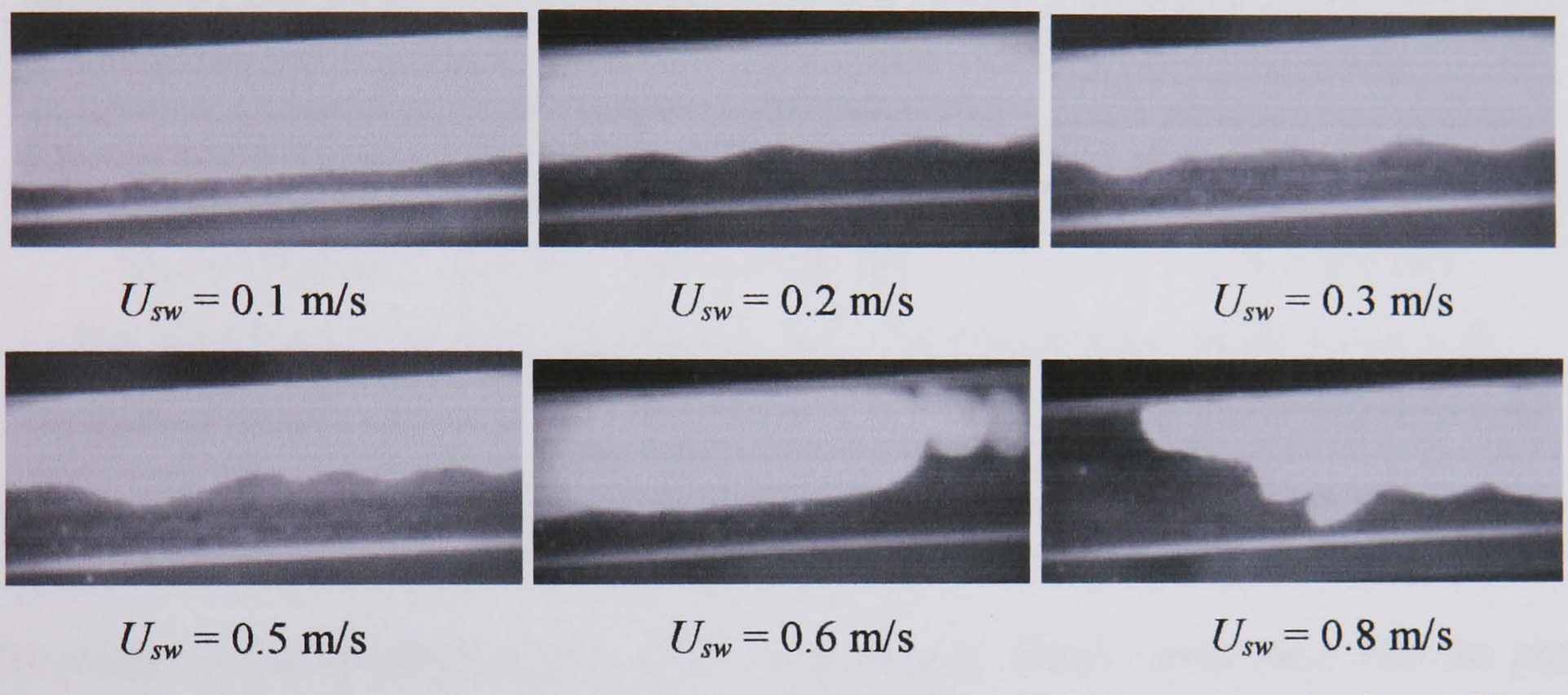

Fig. 4.9 Transition from *stratified* to *slug* flow with increasing water velocity at U_{so} = 0.23 m/s in the 14 mm ID acrylic test section (the upper phase is oil while the lower phase is water). Flow direction is from left to right.

The effect on the flow pattern of increasing the water velocity at U_{so} = 0.44 m/s, where drop formation and transition to *dual continuous* and *annular* flows occur, is shown in Fig. 4.10. The interface becomes even more wavy at U_{so} = 0.44 m/s for the same water velocities (see Fig. 4.8 and 4.9). At U_{sw} = 0.3 m/s, *dual continuous* pattern appears and some drops of oil are entrained in the water phase. This pattern extends up to U_{sw} = 0.5 m/s and then *annular* flow is observed for the higher water velocities. In *annular* flow, a thin layer of water is seen at the top of the pipe, the interface is disturbed and drops of oil are visible within the water. The flow appears to be more disturbed as the water velocities increase.

In general, *dual continuous* flow appeared only for a limited range of conditions in the 14 mm ID pipe in contrast to the large (38 mm ID) test section where it dominated at

medium oil and water superficial velocities (see Fig. 4.4). In the small pipe diameter, the growing waves can touch the upper wall more easily due to the small thickness of the oil layer and such things will result into either *slug* or *annular* flows

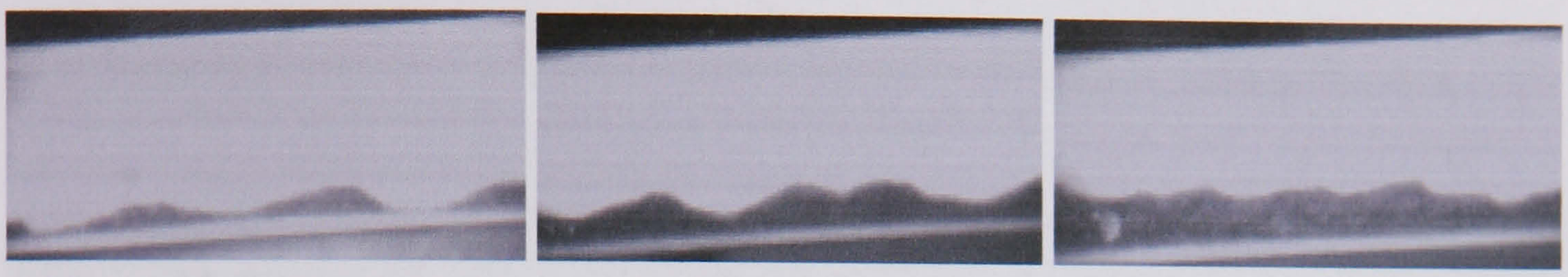

U_{sw} = 0.1 m/s U_{sw} = 0.2 m/s U_{sw} = 0.3 m/s

U_{sw} = 0.5 m/s U_{sw} = 0.6 m/s U_{sw} = 0.8 m/s

Fig. 4.10 Transition from *stratified* to *dual continuous* and *annular* flows with increasing water velocity at U_{so} = 0.44 m/s in the 14 mm ID acrylic test section (the upper phase is oil while the lower phase is water). Flow direction is from left to right.

The waves at the interface can be either short or long. Short waves (less than the pipe diameter with very small amplitude) normally decay as they propagate along the test section (Fig. 4.11) while long waves (normally longer than the pipe diameter) grow due to instability (see chapter 5) and they may form drops (Fig. 4.12). Long waves, therefore, appear to be the source of drop formation.

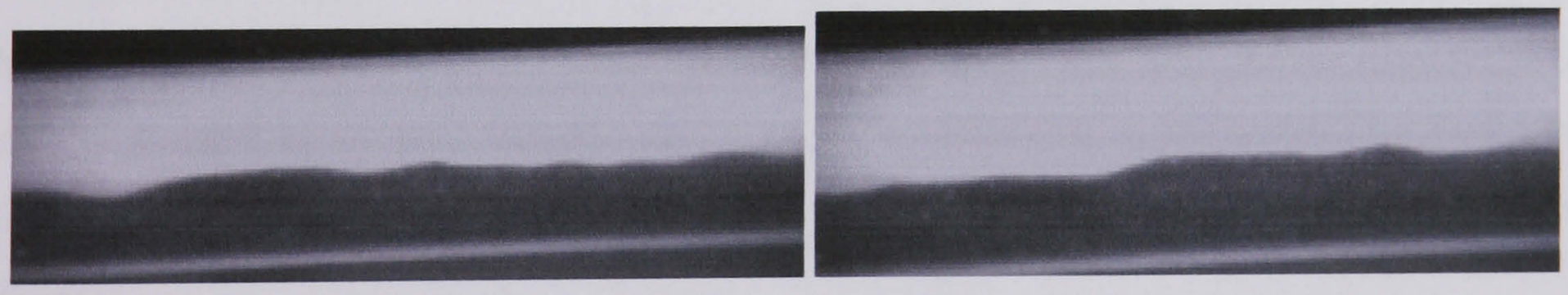

t = 0 s t = 0.016 s

t = 0.032 s t = 0.048 s

Fig. 4.11 Propagation and decay of short waves along the test section at U_{so} = 0.23 m/s, U_{sw} = 0.40 m/s in the 14 mm ID acrylic test section. Flow direction is from left to right.

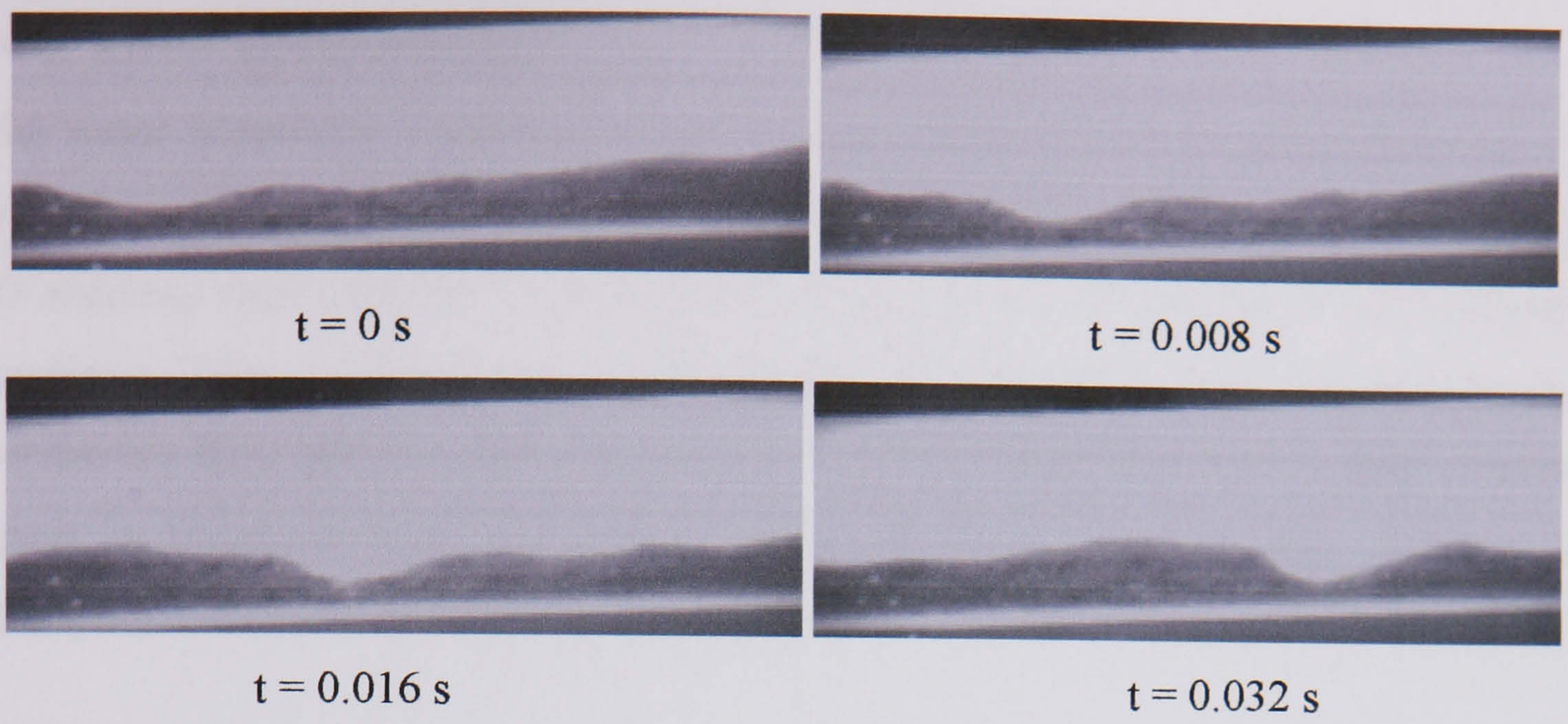

Fig. 4.12 Propagation of long waves along the test section at U_{so} = 0.37 m/s, U_{sw} = 0.30 m/s in the 14 mm ID acrylic test section. Flow direction is from left to right.

Several investigators have also reported the occurrence of *annular* flow at low oil and high water superficial velocities (Oglesby, 1979, Arirachakaran et al., 1989, Valle and Kvandal, 1995 and the present work in the 38 mm ID pipe). The only difference is that *annular* flow in these other studies was observed at relatively higher superficial water velocities. This could be due to the small diameter pipe used here which will increase the probability of the water waves to touch the upper pipe wall and form an annulus. At the lower oil velocities, *slug* flow formed instead.

Similar to the current work in the 14 mm ID, Charles at al. (1961) and Russell et al. (1959) also found oil *slug* and *bubble* flow in their studies. Charles et al., however, did not report any *stratified* flow as they used fluids with the same density. This could be due to the same fluids density used. The *bubble* and *slug* flow observed by Charles et al. and by Russell et al. and current work could be attributed to the small diameter pipe used in all these cases which increases the chance to form slugs (see the discussion above).

Apart from the works of Charles at al. (1961) and Russell et al. (1959), none of the other studies available in the literature have reported *bubble* or *slug* flow. This could be mainly due to the pipe diameter and the oil viscosity used. For example, although Angeli and Hewitt (2000) worked in a smaller diameter pipe (25.4 mm similar to the diameter used by Russell et al.,1959), they did not observe *slug* flow perhaps because of the lower viscosity oil used (1.6 cp) compared to that by Russell et al. (1959) (16 cp).

4.2 Onset of Entrainment

The water superficial velocities, U_{sw}, at which droplets are first observed in the oil-water interface at different oil superficial velocities, U_{so}, were investigated in the 38 mm ID stainless steel (section 4.2.1) and the 14 mm ID acrylic (section 4.2.2) horizontal pipelines. These velocities are considered to be the onset velocities for the *dual continuous* flow pattern. Onset is considered to have happened when a drop of either phase is found to flow continuously in the opposite phase (usually close to the interface).

4.2.1 38 mm ID stainless steel pipe

In the 38 mm ID stainless steel pipe, two different inlet geometries (a T-junction followed by a 90° bend and a Y-junction) (see chapter 3, section 3.2.1.1 and section 3.2.1.2) were used to investigate the onset velocities for entrainment. This demonstrated the effect of precise inlet geometry on flow pattern transitions which is normally ignored.

4.2.1.1 Inlet section: T-junction with 90° bend

From Fig. 4.13, it is obvious that for onset of entrainment the water superficial velocities decrease as the input oil flow rates increase. This could be because the wave amplitudes increase as the superficial oil velocities increase so as a result the required water velocity to from drops decreases (see also discussion in section 4.1).

Lovick and Angeli (2004) found the onset of *dual continuous* flow pattern at 0.80 m/s mixture velocity using visual observation. Using the same fluids and the same experimental system in the present study slightly different results are found. The comparison is demonstrated in Fig. 4.14. The differences could be attributed to the definition of onset of drop entrainment. In this study, onset is taken to happen when even one drop appears to flow continuously. This was possible to establish with the high speed video camera used. In the study by Lovick and Angeli (2004), flow patterns were only observed visually and quite a few drops has to be present to establish onset of entrainment. This explains the slightly higher U_m found compared to the current study.

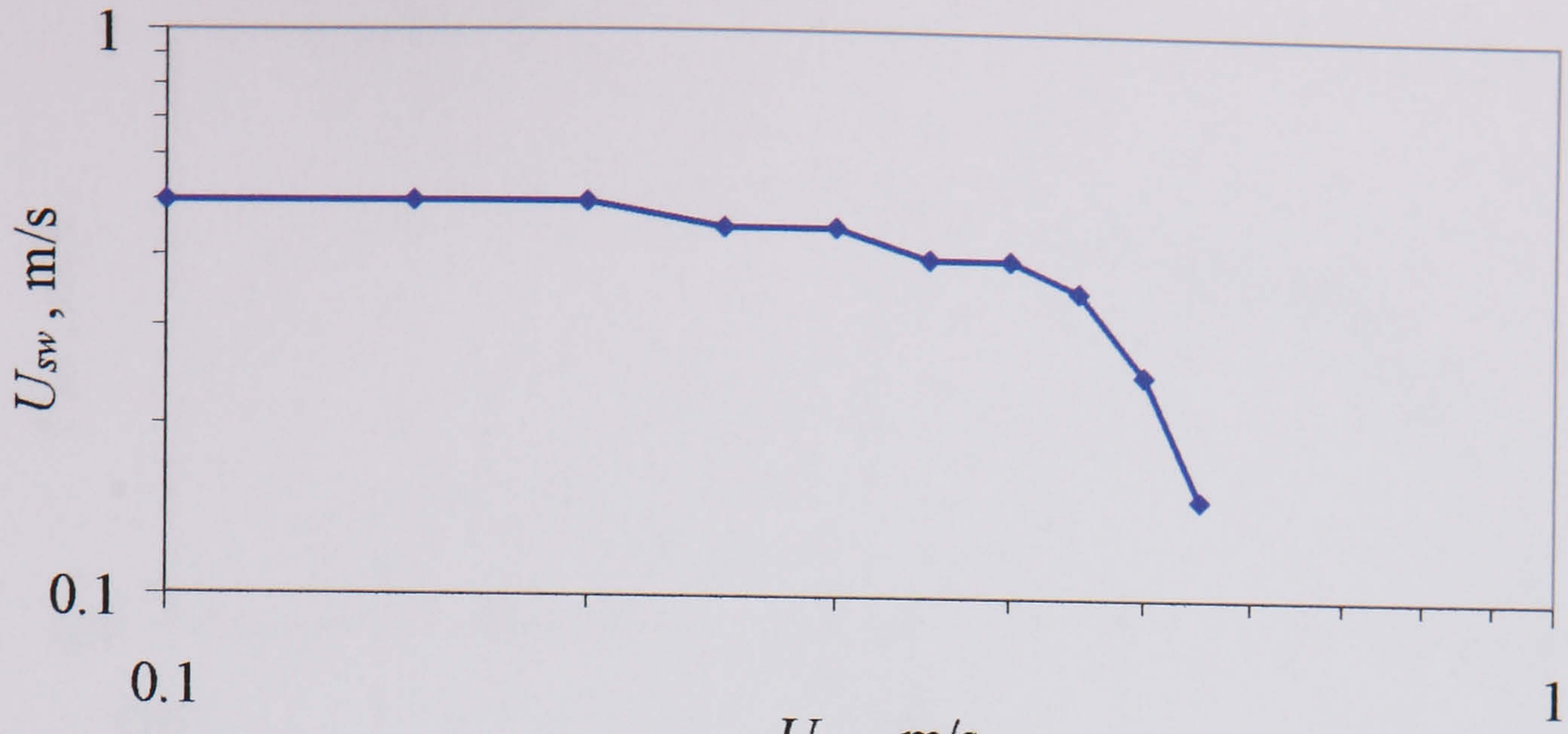

Fig. 4.13 Onset velocities for *dual continuous* flow pattern in the 38 mm ID test pipe, 7 m from inlet section (T- junction inlet section with bend)

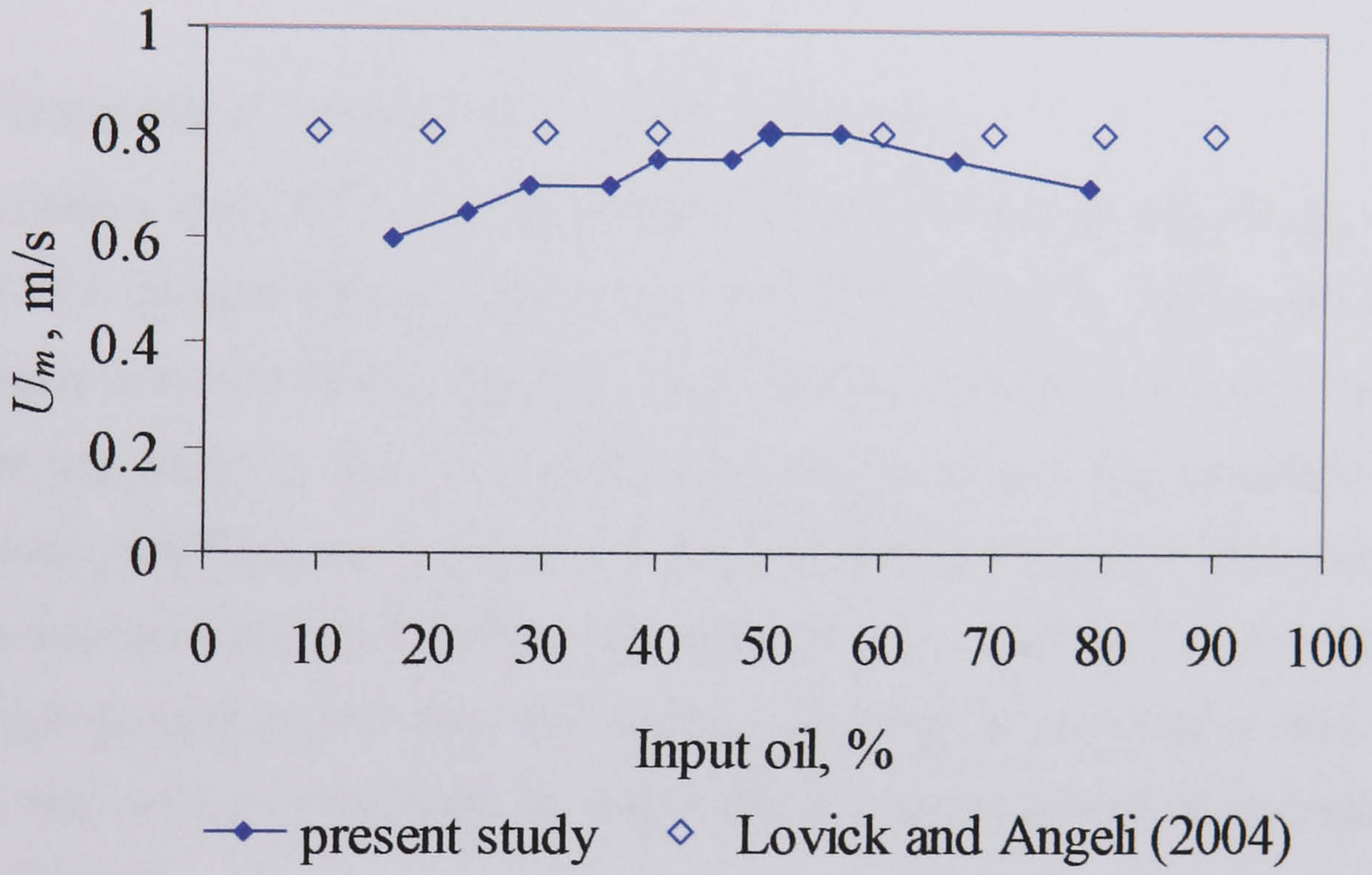

Fig. 4.14 Comparison between the onset velocities of *dual continuous* flow pattern in the 38 mm ID test pipe, 7 m from inlet section (T- junction inlet section with bend)

4.2.1.2 Inlet section: Y-junction

The velocities at the onset of entrainment were also obtained using the modified inlet section (Y-junction). The superficial water velocities U_{sw} at which drops were first observed forming in the flow at certain oil superficial velocity U_{so} are shown in Fig. 4.15. The results showed that as the flow rate of the oil increases, the water velocity required to form drops decreases.

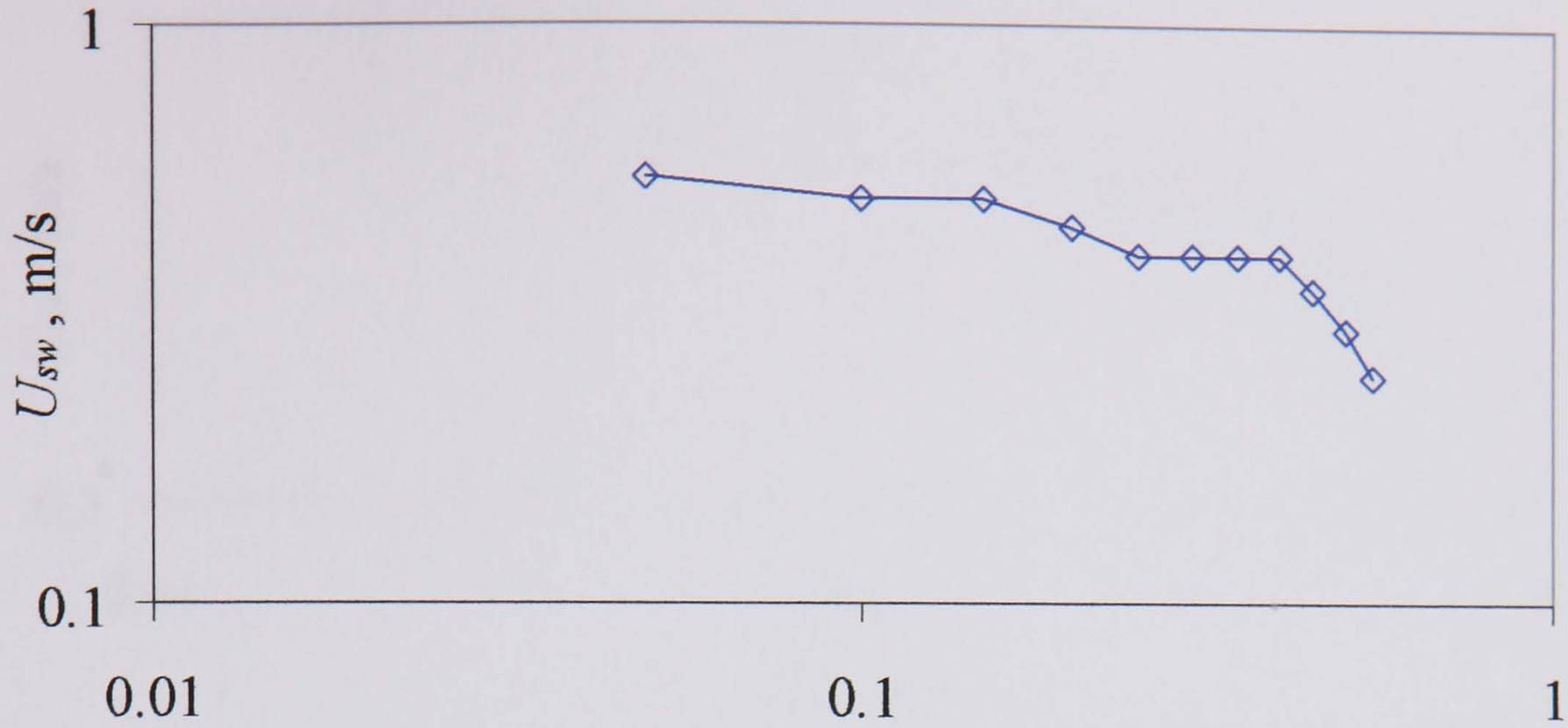

Fig. 4.15 Onset velocities for *dual continuous* flow pattern in the 38 mm ID test pipe, 7 m from inlet section (Y- junction)

4.2.1.3 Comparison between the two inlet sections

Fig. 4.16 shows that there is no significant difference between the onset velocities measured with the two different inlets apart from the highest U_{so}. This could be due to the low onset velocities so any drop that may form due to mixing in the 90° bend after the T-inlet will settle. At the two highest oil velocities though, and especially at U_{so} = 0.55 m/s there is difference. At U_{so} = 0.55 m/s for example, drops are observed at U_{sw} = 0.25 m/s when there is no bend in the inlet while they are found at U_{sw} = 0.15 m/s when the fluids go through a bend. The early appearance of drops in the latter case could be caused by the mixing in the bend. It seems that the drops formed in the bend do not settle downstream.

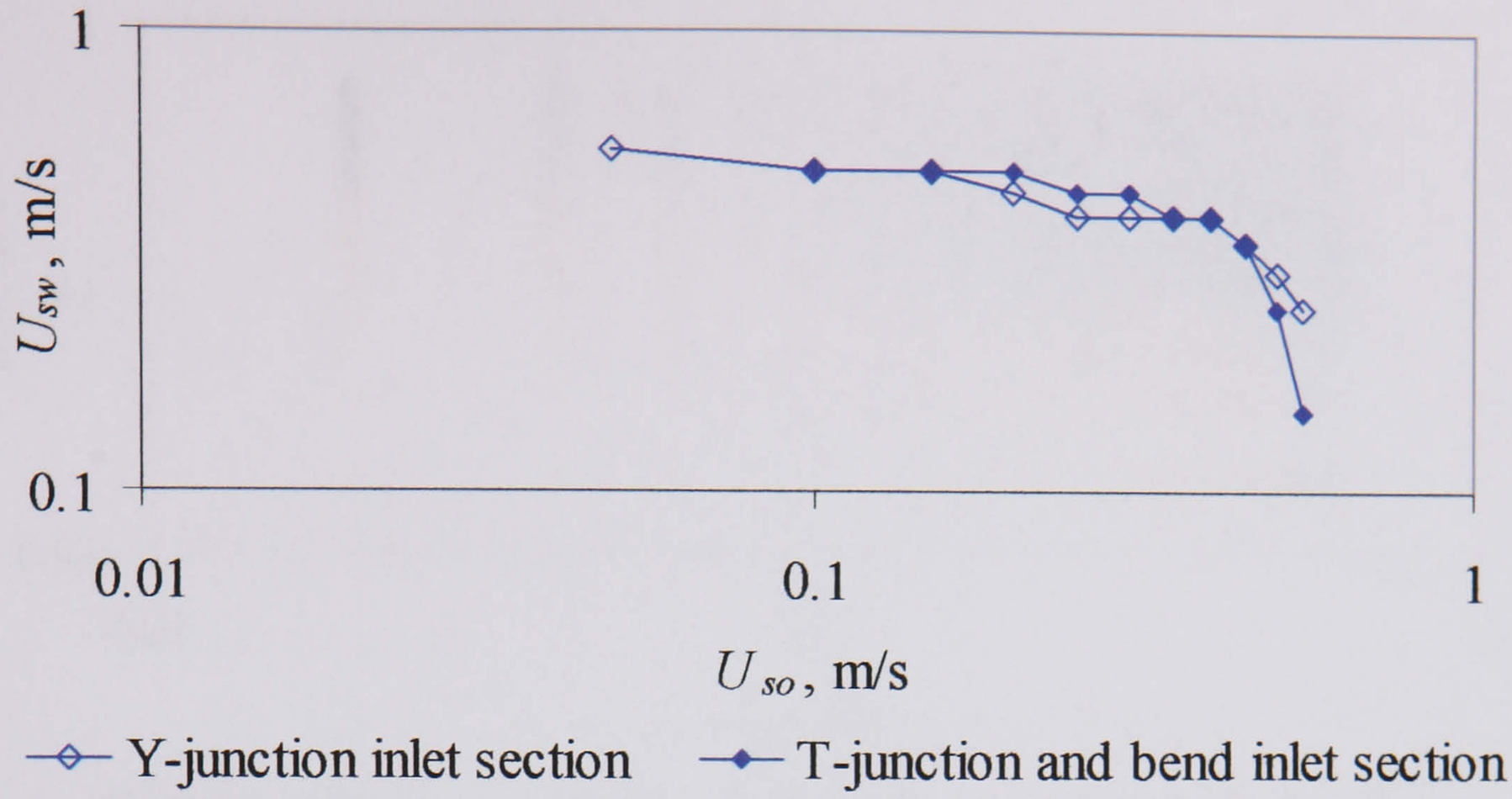

Fig. 4.16 Comparison between the onset velocities of *dual continuous* flow pattern in the 38 mm ID test pipe, 7 m from inlet section (Y and T junction)

4.2.1.4 Comparison with the model by Trallero (1995)

In his theoretical study of flow pattern boundaries, Trallero considered that the VKH equation (see section 2.3.2.2) will determine the transition between stable *stratified* flow and either unstable *stratified* with wavy interface or some other flow pattern and may be used to predict onset of entrainment. However, the predictions of this model did not agree with the onset conditions found in the present work as shown in Fig. 4.17. In chapter 5, a new model is developed based on K-H instability to better predict the onset of entrainment.

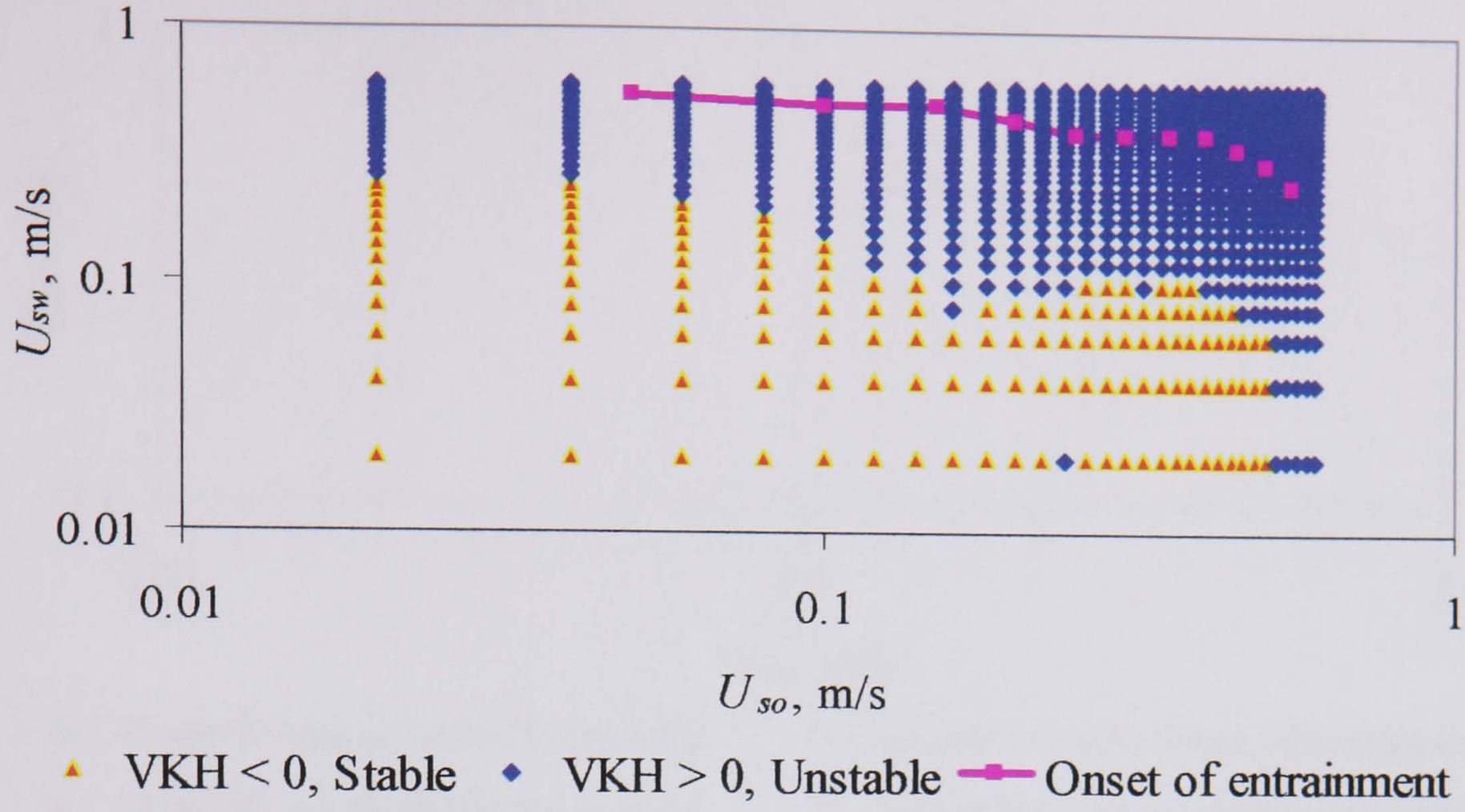

Fig. 4.17 Comparison between Trallero model (points) and the onset velocities (line) found in the 38 mm ID test pipe, 7 m from inlet section of the present study using the Y-junction.

4.2.2 14 mm ID acrylic pipe

The onset velocities for drop formation were also measured in the 14 mm ID acrylic pipe. Oil and water are introduced through a Y-junction, where oil comes from the top and water from the bottom in a manner similar to the introduction of the fluids described in section 4.2.1.2 in the large pipe.

As discussed in section 4.1.2, *dual continuous* flow exists for a small range of conditions and it changes to *slug* or *annular* flow at higher U_{sw}. *Stratified* flow also changes to either *bubble* or *slug* flow without going through *dual continuous* with increasing U_{sw} (see Fig. 4.7). Thus onset velocities (transition from *stratified* to *dual continuous*) were observed only for a few conditions. Fig. 4.18 shows a comparison between the onset velocities obtained in the 14 mm ID acrylic and the 38 mm ID stainless steel (with Y-junction inlet) pipes. As expected, the water superficial velocities decrease as the oil superficial velocities increase. At U_{so} less than 0.4 m/s, the onset of drop formation in the 38 mm ID pipe appears at lower U_{sw} than that in the 14 mm ID. On the other hand, at U_{sw} greater than 0.40 m/s the U_{sw} at the onset in the 38 mm ID stainless steel pipe are higher than those in the 14 mm ID acrylic pipe.

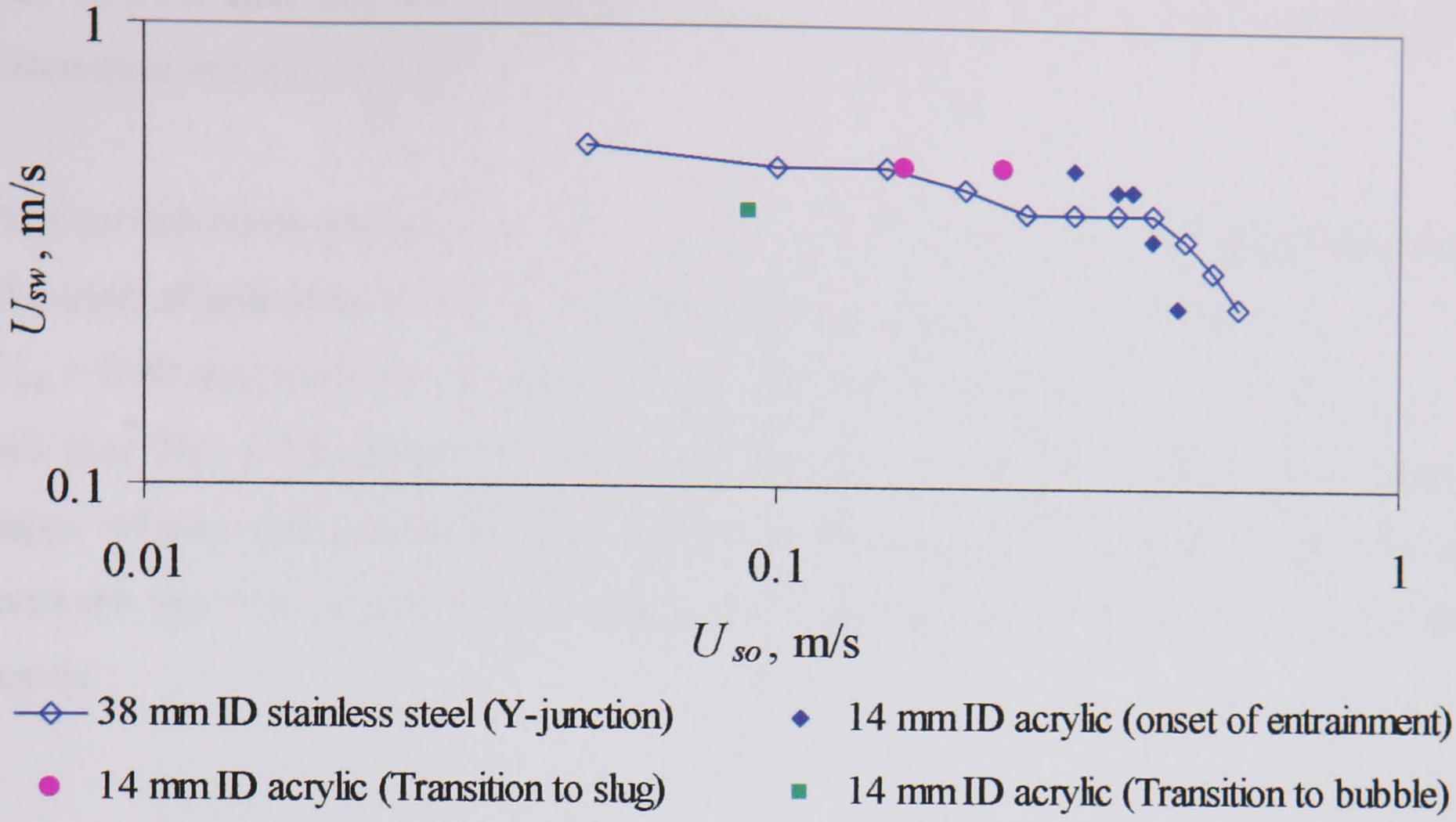

Fig. 4.18 Comparison between the onset velocities of *dual continuous* flow pattern in the 38 mm ID stainless steel pipe and 14 mm ID acrylic pipe

4.3 Experimental Wave Characteristics at the Onset of Entrainment in the 38 mm ID Test Section

Wave characteristics were studied with the conductivity wire probe (see section 3.3.4) in the 38 mm ID stainless steel test section. Investigations were varied out both at 7m from the inlet and close to it at 2m. In all cases the Y-junction inlet was used that minimize entrance effects.

4.3.1 At 7 m from the inlet

4.3.1.1 Growing waves

From the different cases investigated experimentally, three were selected to show how waves grow from a *stratified* regime up to the onset of entrainment. Fig. 4.19 shows the development of the height of the water layer (h_w) at U_{so} = 0.20 m/s with increasing water velocity until drop formation is observed. For U_{sw} = 0.20 m/s, the amplitude of the waves is no more than 1 mm while as the water velocity increases to U_{sw} = 0.40 m/s, the amplitude increases to around 2 mm. At U_{sw} = 0.45 m/s, where entrainment is observed, the amplitude of the waves further increases and in some cases it may reach 4 mm. It

can be said that the wave amplitude increases as the water velocity increases (see discussion in section 4.1).

At a certain wave amplitude a large velocity difference between the phases can result in the onset of entrainment while a smaller difference may not. For example, at $U_{so} = 0.20$, $U_{sw} = 0.40$ m/s waves have amplitudes (2 mm) equal to those at $U_{so} = 0.05$, $U_{sw} = 0.55$ m/s (see Fig. 4.19). However, drops will only form in the latter case where there is a large velocity difference between the phases and not in the former where the shear between the two phases is not enough to detach a drop from such small amplitude waves.

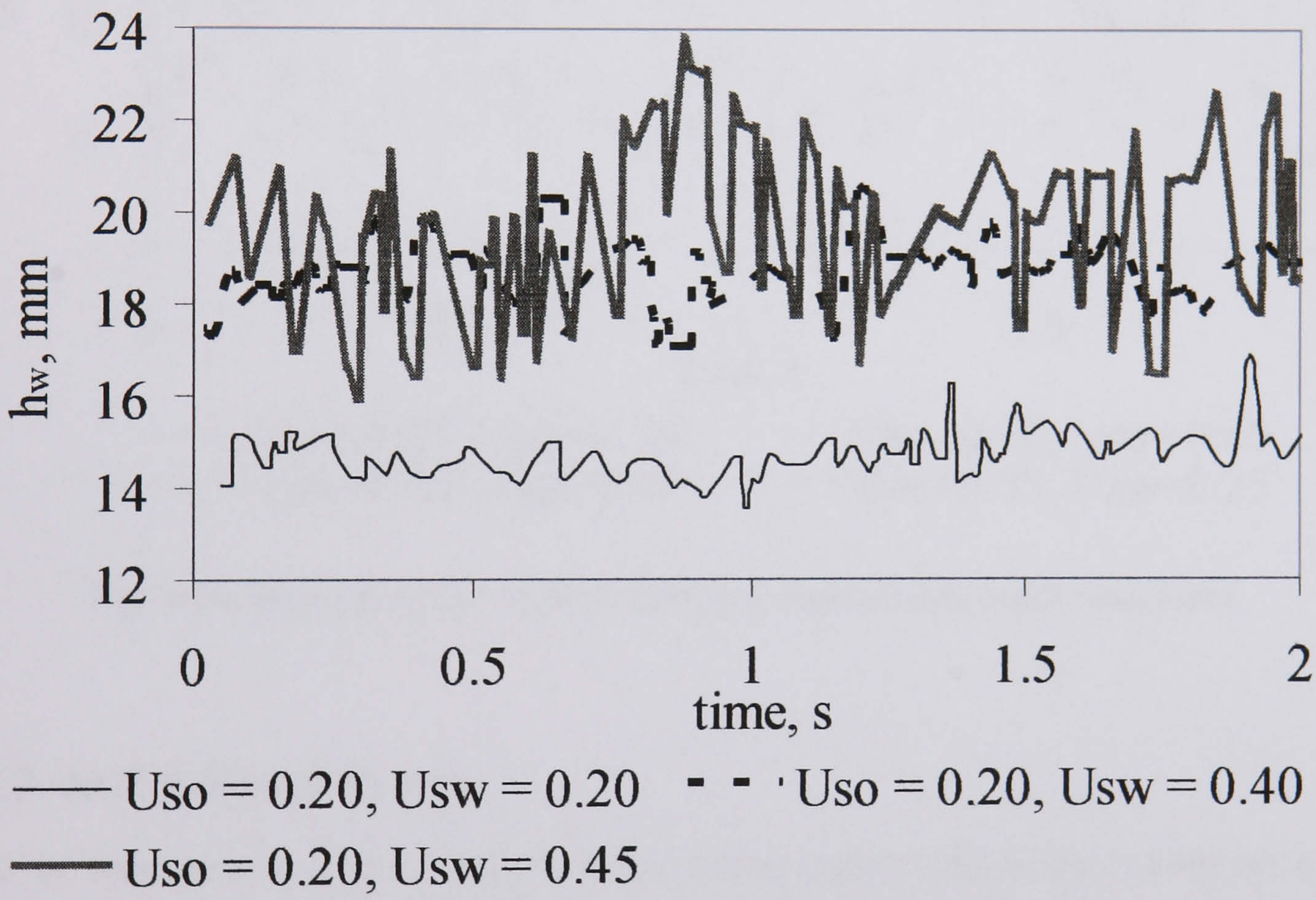

Fig. 4.19 Effect of increasing U_{sw} on wave amplitude at $U_{so} = 0.20$ m/s (38 mm ID stainless steel pipe, 7 m from the inlet, Y-junction)

4.3.1.2 Structure of the waves at the onset of entrainment

At the onset of entrainment, four conditions were selected to show the difference in wave structure. These are shown as time series of the interface height in Fig. 4.20. At $U_{so} = 0.40$, $U_{sw} = 0.40$ m/s the highest wave amplitudes that would lead to drop formation are slightly higher than at $U_{so} = 0.20$, $U_{sw} = 0.45$ m/s and $U_{so} = 0.55$, $U_{sw} =$

0.25 m/s and these are slightly higher than at $U_{so} = 0.05$, $U_{sw} = 0.55$ m/s. As was also shown in chapter 5 for the low viscosity oil at small velocity differences, the shear between the two phases is small and waves have to grow to a large amplitude before drop formation is possible. It is also clear that the wavelength increases as the velocity difference between the two phases decreases.

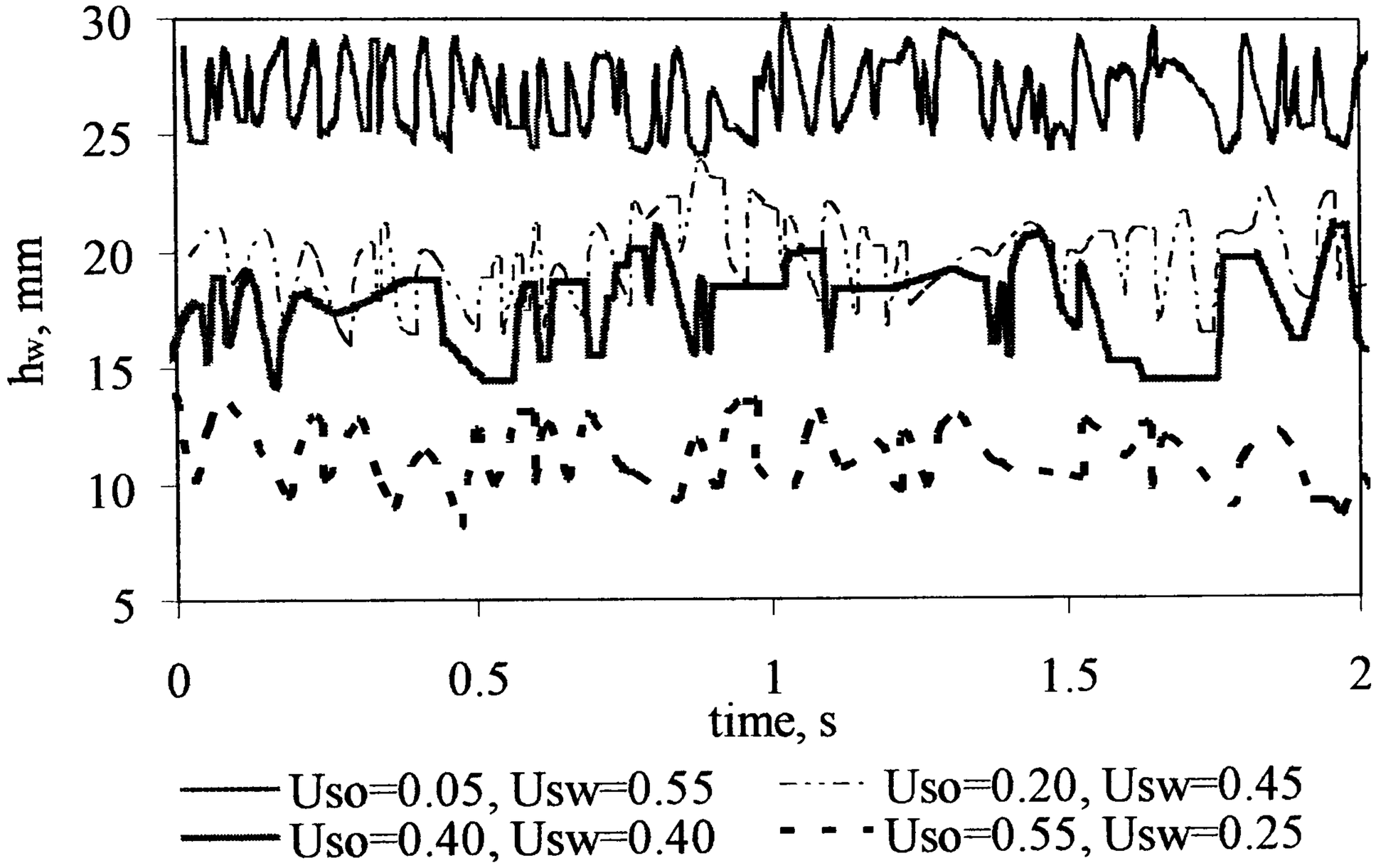

Fig. 4.20 Wave structure at four different entrainment onset conditions

4.3.2 At 2 m from the inlet

At 2 m downstream of the inlet, the wave characteristics were also measured at the onset velocities to see the development of the waves. The results reveal an interesting behaviour. The amplitudes of the waves increase as the superficial oil velocities increase (see Fig. 4.21). For the wavelength, there is no general trend but it could be said that wavelengths decrease as the slip velocity between the phases decreases as shown in Fig. 4.21 which is opposite to the results obtained 7 m from the inlet (see section 4.3.1.2 and Fig. 4.20).

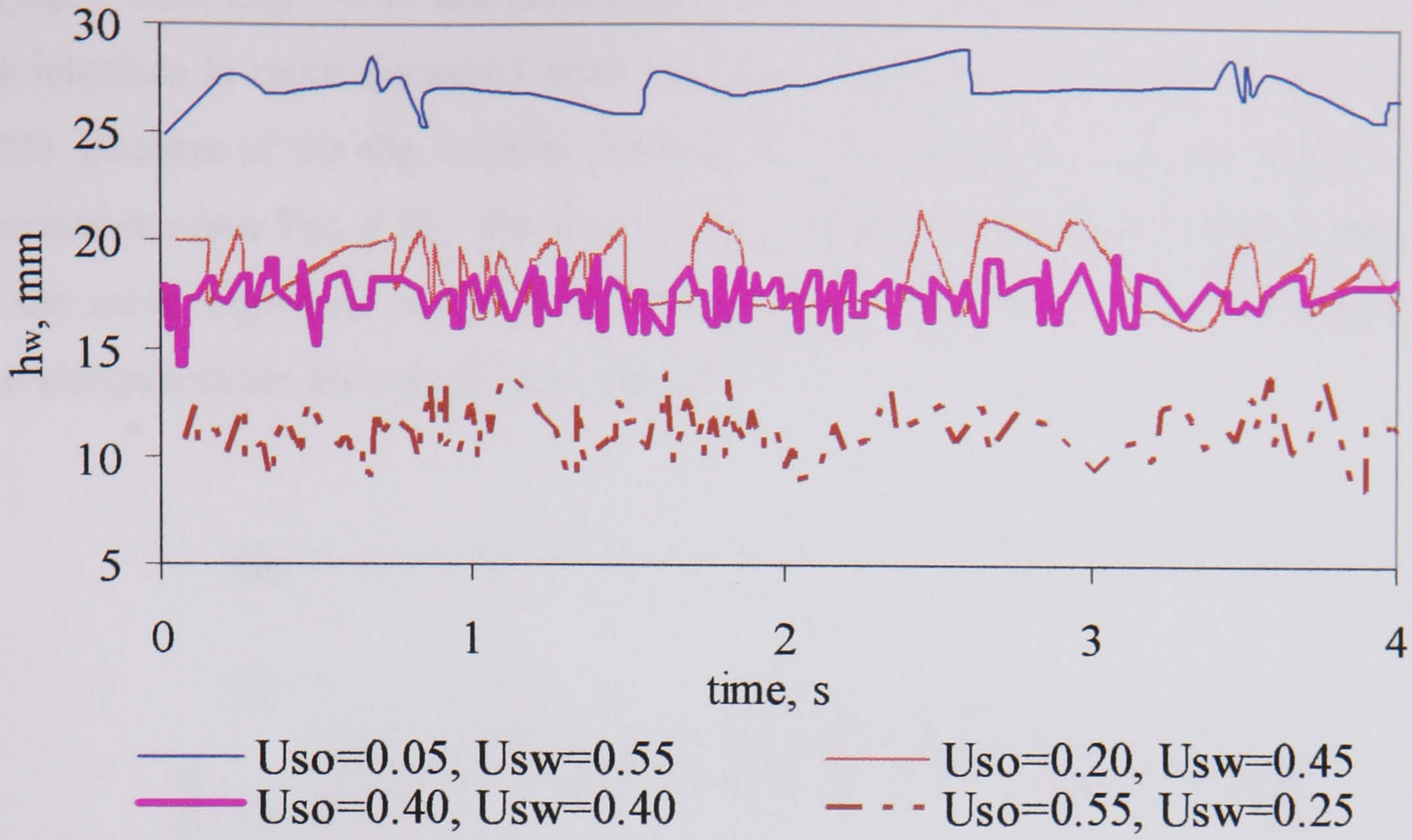

Fig. 4.21 Wave structure at the entrainment onset conditions (2m from inlet)

At U_{so} = 0.05, U_{sw} = 0.55 m/s (case 1), the oil layer is in laminar flow. When the two fluids join therefore the interface will not be very disturbed and this is reflected to the long wave lengths and short amplitudes seen in Fig. 4.21. The large velocity difference between the phases though will make the waves to grow faster further downstream (Fig. 4.22). In this case the amplitude to wavelength ratio is the highest.

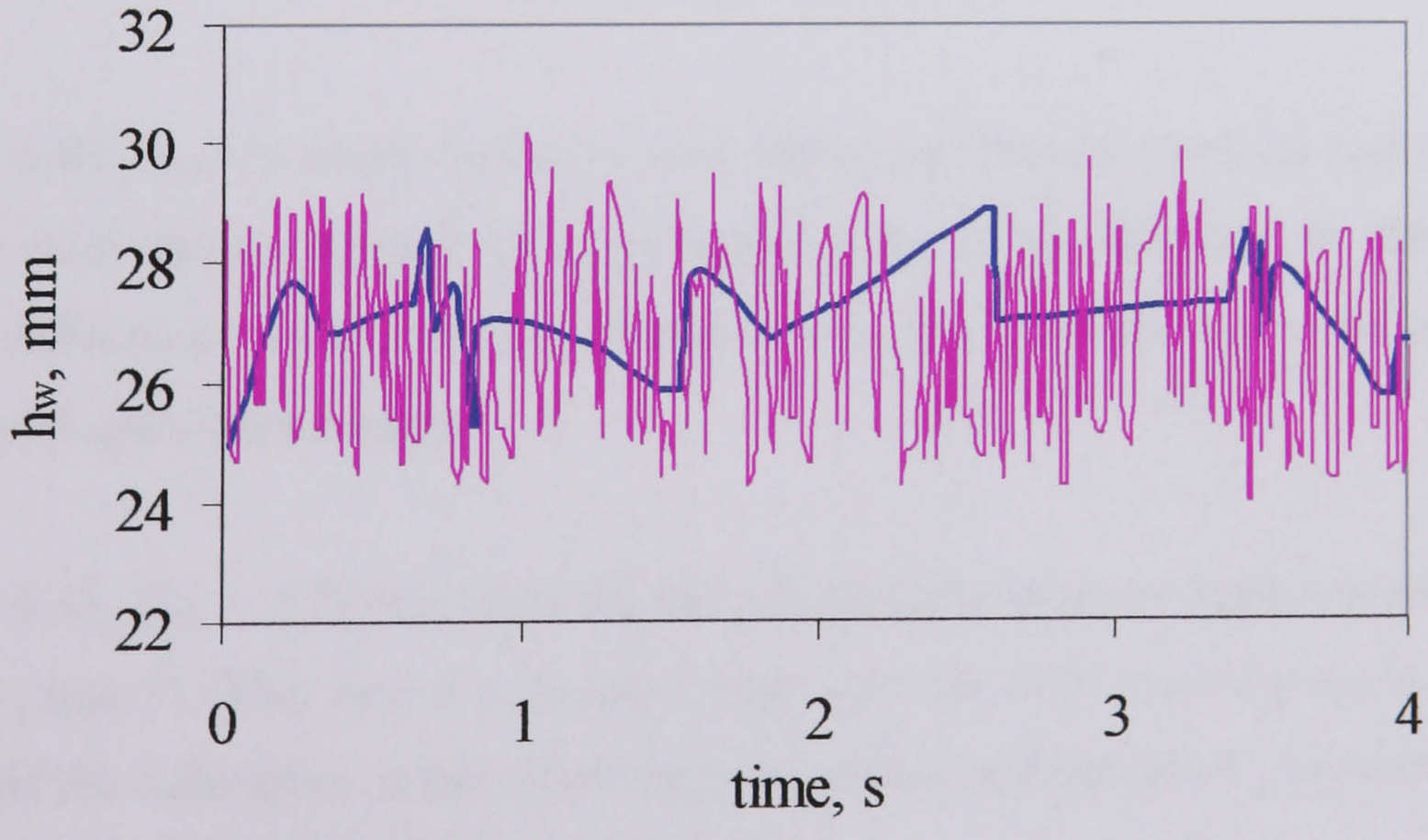

Fig. 4.22 Comparison between the wave structure results 2 and 7 m from the inlet at U_{so} = 0.05, U_{sw} = 0.55 m/s.

At $U_{so} = 0.20$, $U_{sw} = 0.45$ m/s (case 2), the oil layer is now turbulent and for this reason the interface is more disturbed after the inlet comparing with the previous case (Fig. 4.22). Because of the slip velocity between the two phases the waves will grow further downstream (see Fig. 4.23). Because the slip velocity is less than in case 1, the growth of the wave amplitude is also less (compare Fig. 4.22, 4.23). Also, the amplitudes to wavelengths ratios are smaller than case 1.

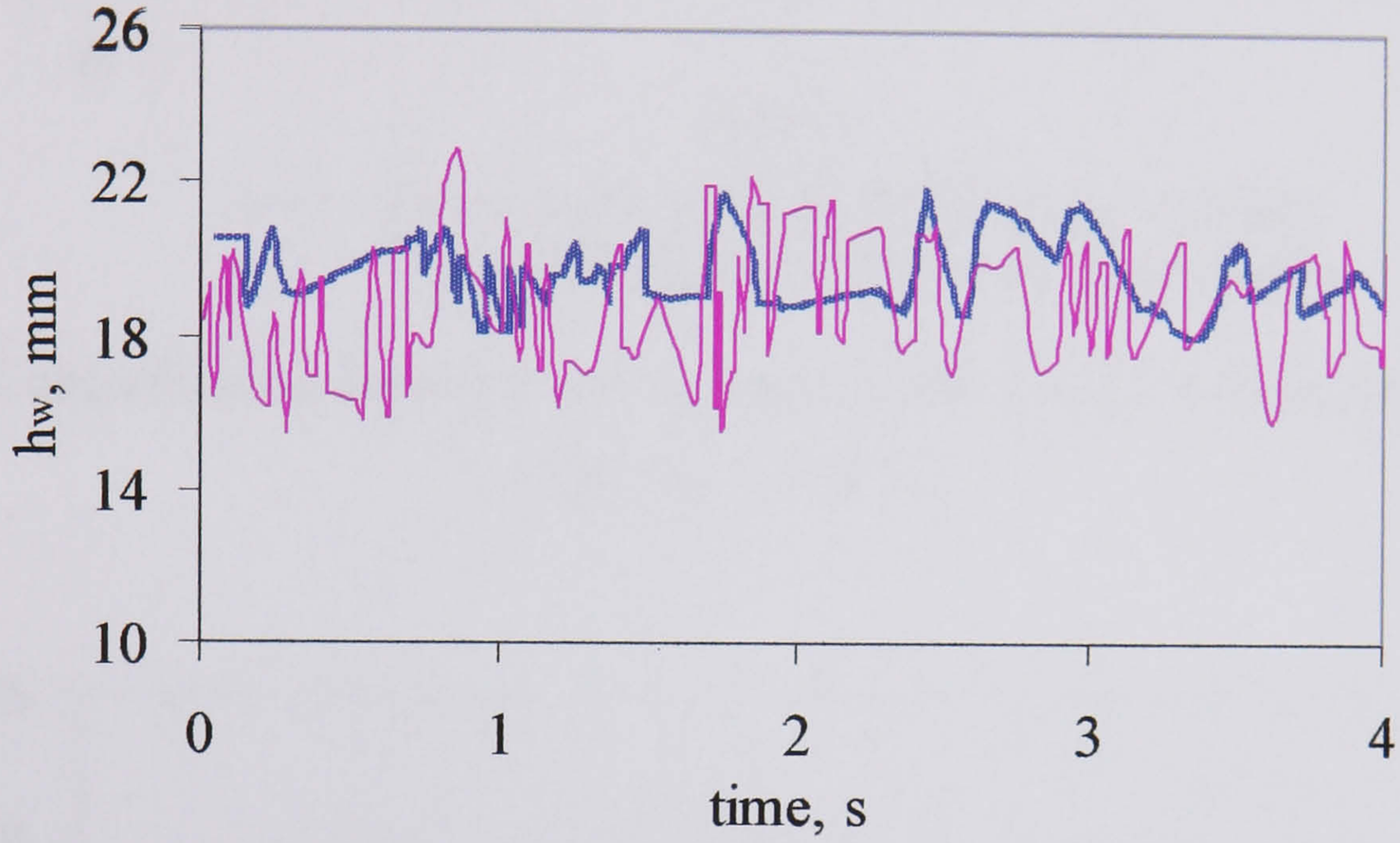

Fig. 4.23 Comparison between the wave structure results 2 and 7 m from the inlet at U_{so} = 0.20, U_{sw} = 0.45 m/s.

At $U_{so} = 0.40$, $U_{sw} = 0.40$ m/s (case 3), both layers are turbulent and for that reason just after the inlet the interface is quite disturbed (Fig. 4.24). However in this case the velocity difference between the two phases is very small and the waves do not seem to grow significantly downstream.

At $U_{so} = 0.55$, $U_{sw} = 0.25$ m/s (case 4), the wavelengths increase again compared to the previous (case 3). This time U_{so} is quite high (see Fig. 4.25) but the decrease in U_{sw} means that the turbulence in the water layer is reduced and the wave amplitudes are less than in case 3 but higher than in the other two cases.

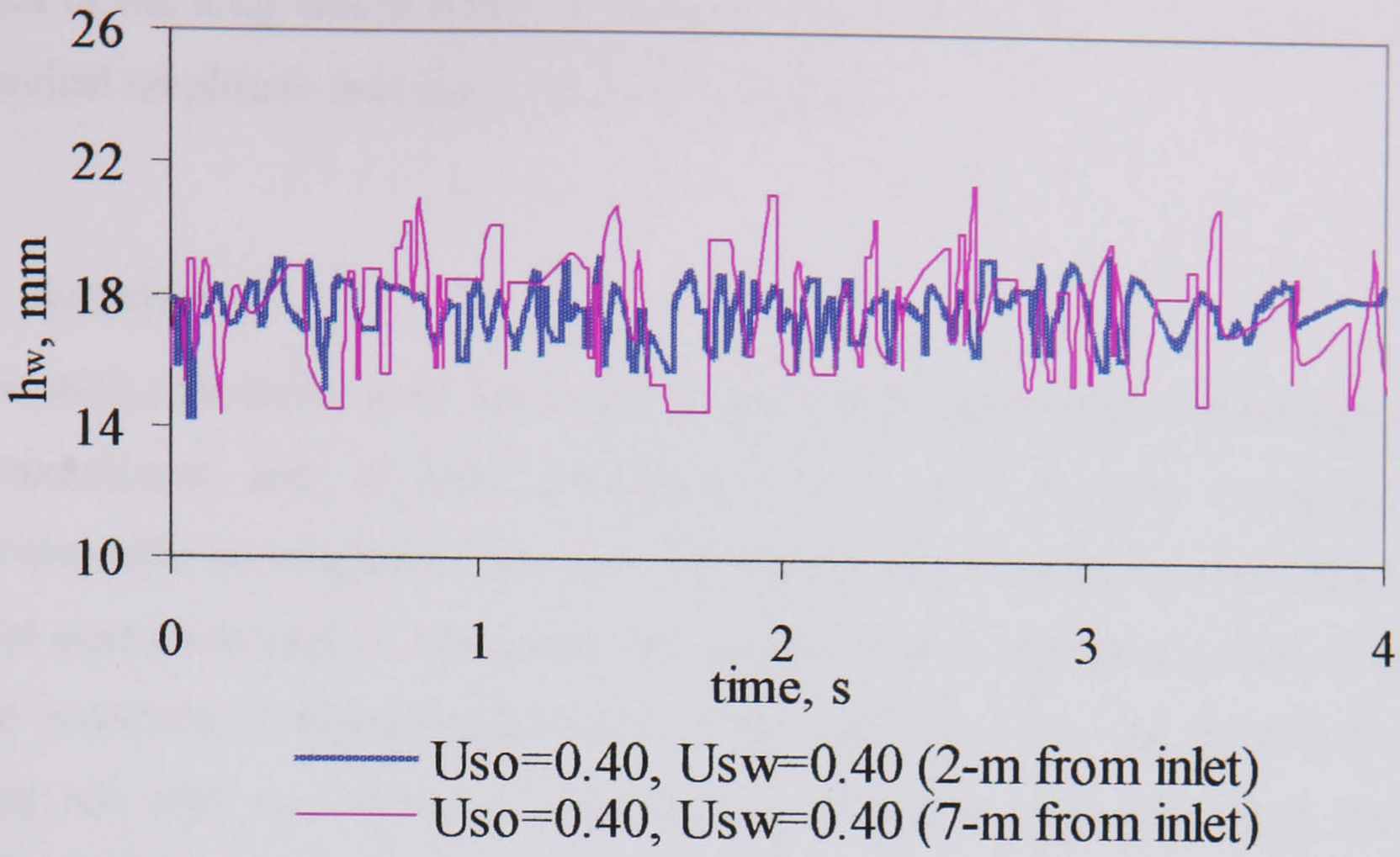

Fig. 4.24 Comparison between the wave structure results 2 and 7 m from the inlet at U_{so} = 0.40, U_{sw} = 0.40 m/s.

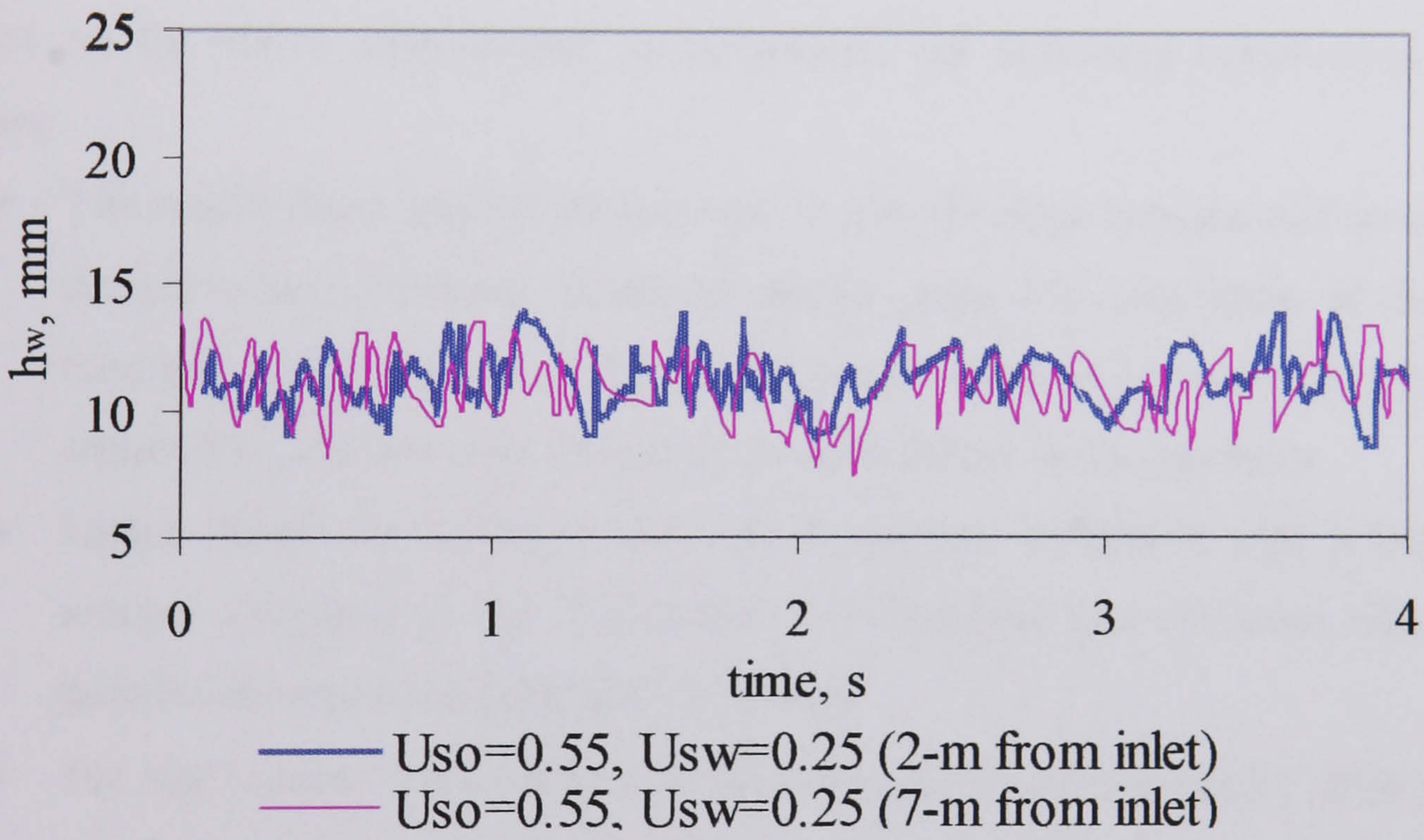

Fig. 4.25 Comparison between the wave structure results 2 and 7 m from the inlet at U_{so} = 0.55, U_{sw} = 0.25 m/s.

In general it appears that at 2 m from the inlet, the amplitudes are always less than at 7 m from the inlet (see Fig. 4.22, 23, 24 and 25). The wavelengths on the other hand at 2 m from the inlet are relatively longer. These measurements agree with the visual observations discussed in section 4.1. Such evidence and the discussion above showed that along the pipe, the relative movement between the oil and the water results in the

growth of the long waves which will increase in height until some of the waves reach the critical amplitude necessary for drop formation.

4.4 Summary

In this study, transition between *stratified* and *non-stratified* flow (particularly the onset of entrainment and of *dual continuous* flow) in horizontal oil-water flow is experimentally investigated. Two test sections (38 mm ID stainless steel and 14 mm ID acrylic pipes) are used to investigate the transition and wave characteristics before and at the transition to *non-stratified* flows. The experiments in the 38 mm ID pipe are carried out with two different inlet sections (Y-and T-junctions). High speed video images and a conductivity probe are used to investigate the wave structures at 2 and 7 m from the inlet. In the 14 mm ID, high speed camera was also used to obtain a flow pattern map and study the waves characteristics at different experimental conditions.

Based on the above experimental investigations, the following conclusions can be drawn:

- The results from both the 38 mm and 14 mm ID pipes indicate that no drops are formed when interfacial waves are absent. Also, the amplitudes of the waves increase as both the superficial oil and water velocities increase. As a result the required U_{sw} for the onset of entrainment decreases as U_{so} increases.
- Larger drops are observed with the T-junction combined with a bend inlet section compared to the Y-junction. It is believed that the bend after the T-junction increases the mixing of the phases.
- The high speed video images and the conductivity probe results show that the amplitudes of the waves found at 2 m from the inlet are smaller than those observed at 7 m from the inlet. Drops therefore and onset of entrainment appeared at 7 m while for same conditions could not be seen at 2 m. This reflects that all drops found 7 m from the inlet are formed from the waves.
- *Annular* flow pattern is observed at low oil and high water superficial velocities.
- The effect of inlet geometry on the onset of entrainment at 7 m from the inlet is almost negligible.
- In the 14 mm ID pipe, *dual continuous* occurs at a small range of superficial velocities compared to the large pipe. At low oil velocities, *stratified* flow

changes to either *slug* or *bubble* flows (due may be to the small thickness of the oil layer).

- The VKH equation developed by Trallero (1995) failed to predict the onset of entrainment.

CHAPTER 5

Stability Analysis and Prediction of the Onset of Drop Entrainment in Horizontal Oil-Water Flow

In this chapter, a stability equation is developed based on Kelvin-Helmholtz analysis to predict the transition between *stratified* and *non-stratified* flow in horizontal oil-water pipes. The equation is then extended to predict the onset velocities of entrainment. A brief introduction of previous investigations with K-H instability is given in section 5.1. Section 5.2 describes the mathematical equations and model development. Section 5.3 discusses the model results while section 5.4 shows a comparison between the model and experimental results. The model is then extended in section 5.5 to predict the onset of entrainment. A summary of the chapter is given in section 5.6.

5.1 Introduction

In gas-liquid flow, several investigators postulated that liquid droplet entrainment into the gas phase occurred as a result of Kelvin-Helmholtz instability. Woodmansee and Hanratty (1969) reported that droplet entrainment in *annular* film flow primarily results from such instability where the destabilizing force is the pressure variation caused by the compression of the gas streamlines at the crests of the wavelets. This instability criterion has been widely used for the transition between *stratified* and *slug* patterns in gas-liquid flow. Two types of Kelvin-Helmholtz (KH) instability have been considered; in the viscous KH one (VKH), shear stresses are included (Wallis, 1969; Lin and Hanaratty, 1986; Barnea, 1991; Barnea and Taitel, 1993, 1994) while in the inviscid KH

theory (IKH) the shear stress terms are neglected (Taitel and Dukler, 1976; Mishima and Ishii, 1980).

In liquid-liquid flow, Trallero (1995) suggested that KH instability will cause any wavy disturbances on the interface of *stratified* flow to grow in amplitude; such waves will break to form drops even with small shear velocities when the flow of the liquids is laminar. In his theoretical study of flow pattern boundaries, Trallero considered that the VKH equation will determine the transition between stable *stratified* flow and either unstable *stratified* with wavy interface or some other flow pattern and may be used to predict onset of entrainment. However, his model results did not agree with the experimental findings from Valle and Kvandal (1995) and from the present work when used to predict the onset of drop formation.

In this present study, the KH stability analysis is implemented to develop an equation for the wave amplitude required to destabilize the wave at a certain wavelength. This equation will then be extended to predict onset of entrainment and the transition from *stratified* to *dispersed* patterns for a large number of systems reported in the literature.

5.2 Model Development

5.2.1 Formulation of the problem

When the flow rates of oil and water increase, interfacial waves appear which are initially long compared to the pipe diameter. These waves will grow until they reach a certain wavelength and amplitude at which point their crests will break and drops will start forming. The phase velocities at which the waves will break are called the onset velocities.

A finite solitary sinusoidal wave is considered at the interface between two fluids (oil and water) in a moving coordinate system as shown in Fig. 5.1. The term a denotes the amplitude while λ represents the wavelength. The coordinate system is moving in the positive x-direction with the wave which means that the wave is stationary while oil and water are moving relative to the wave velocity. The densities of the fluids are different

while both fluids are taken to be incompressible and inviscid. The wave is assumed to be two-dimensional that propagates with speed C_v and the wave shape does not change.

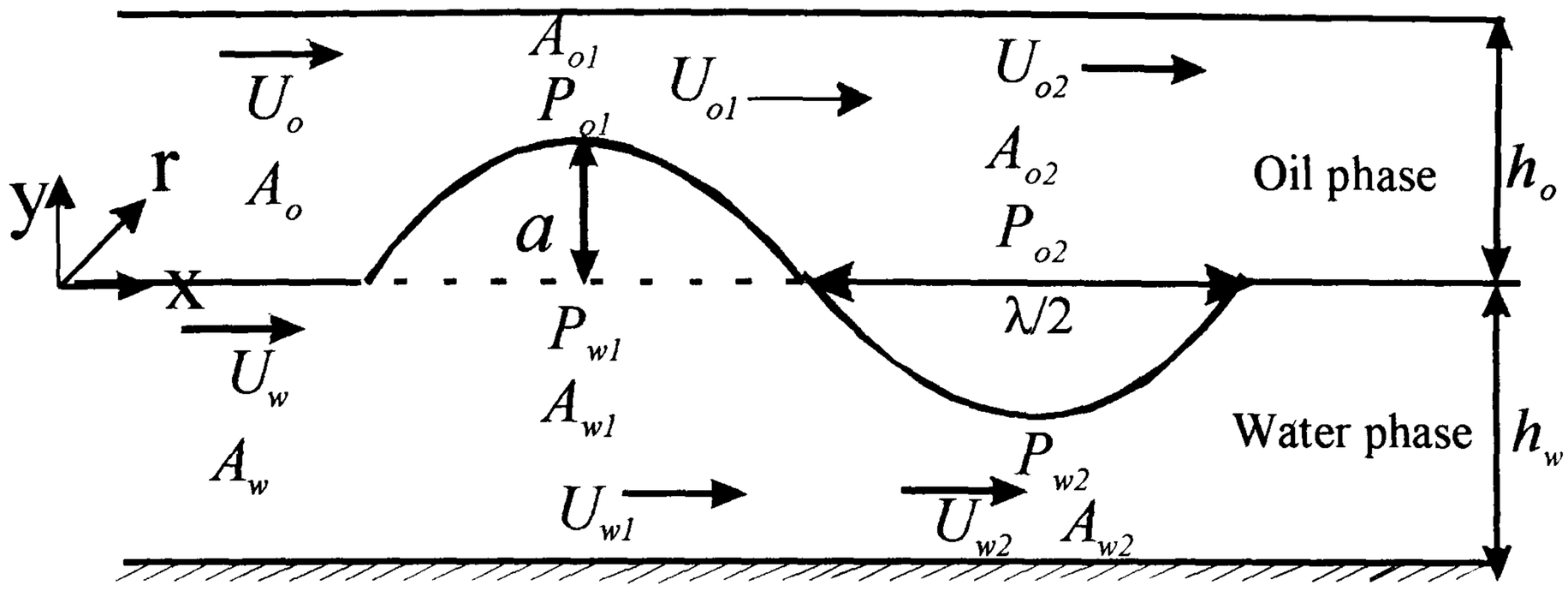

(a)

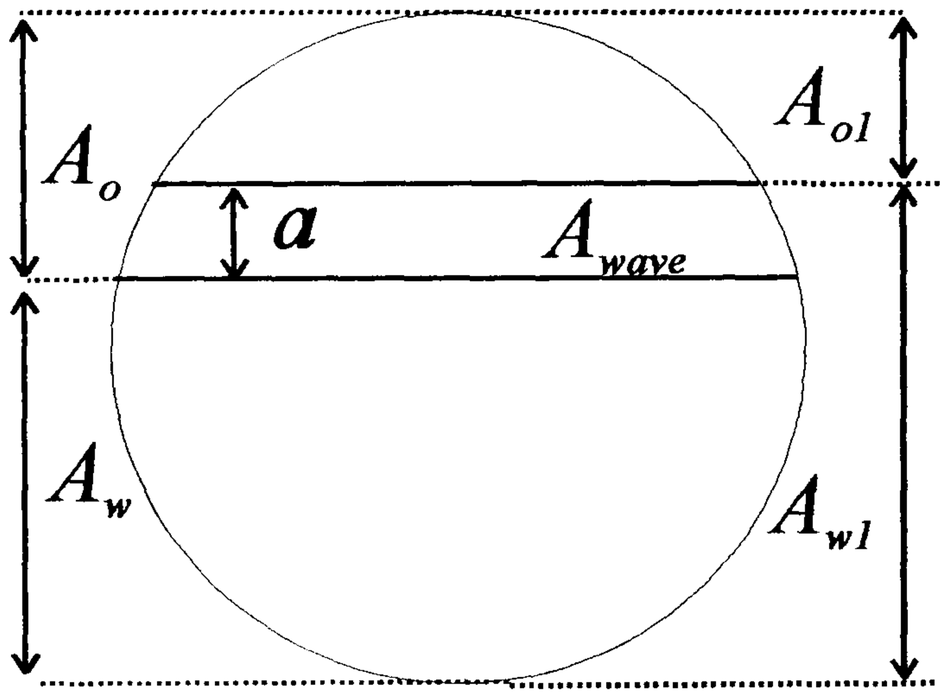

(b)

Fig. 5.1 Schematic diagram of a sinusoidal wave at the onset of entrainment (a) Side view (b) Cross sectional view

From the continuity equation (see Fig. 5.1):

$$(U_w - C_v)A_w = (U_{w1} - C_v)A_{w1} = (U_{w2} - C_v)A_{w2},$$
$$(U_o - C_v)A_o = (U_{o1} - C_v)A_{o1} = (U_{o2} - C_v)A_{o2} \tag{5.1}$$

$$(U_{w1} - C_v) = (U_w - C_v)\left(\frac{A_w}{A_{w1}}\right), \quad (U_{w2} - C_v) = (U_w - C_v)\left(\frac{A_w}{A_{w2}}\right) \tag{5.2}$$

$$(U_{o1} - C_v) = (U_o - C_v)\left(\frac{A_o}{A_{o1}}\right), \quad (U_{o2} - C_v) = (U_o - C_v)\left(\frac{A_o}{A_{o2}}\right) \tag{5.3}$$

where,

$$A_{o1} = A_o - A_{wave}, \quad A_{o2} = A_o + A_{wave} \tag{5.4}$$

$$A_{w1} = A_w + A_{wave}, \quad A_{w2} = A_w - A_{wave} \tag{5.5}$$

The equation of the sinusoidal wave is given in terms of a and λ as

$$y = a\sin\left(\frac{2\pi x}{\lambda}\right) \tag{5.6}$$

The interface is assumed to be flat in the r-direction.

According to the stability analysis, the relative movement of the two liquids will create a suction pressure force that acts below and above the interface and makes the waves grow in amplitude. Bernoulli's equation above and below the interface is used to get expressions for the pressure:

$$\frac{P_o}{\rho_o} = -\frac{1}{2}(\nabla\phi_o)^2 - gy + K_o, \quad \frac{P_w}{\rho_w} = -\frac{1}{2}(\nabla\phi_w)^2 - gy + K_w \tag{5.7}$$

where, $\nabla\phi$ is the velocity potential that is assumed to exist, K is Bernoulli's constant for both phases, P is the pressure, ρ is the density and the subscripts o and w represent the oil and water phases respectively.

5.2.2 Pressure suction force calculation

For simplicity, the velocity is assumed to change in the x-direction and at each position x uniform velocity is assumed within each phase, so that

$$\nabla\phi = \frac{\partial\phi}{\partial x} = U_x = U \tag{5.8}$$

where U is the phase velocity.

The pressure variation above the interface causing the wave to grow is given by Bernoulli's equation with the moving coordinate system:

$$P_{o,1} - P_{o,2} = \frac{1}{2}\rho_o\left[\left(U_{o,2} - C_v\right)^2 - \left(U_{o,1} - C_v\right)^2\right] - 2ga\rho_o \tag{5.9}$$

Below the interface, the pressure variation is given by:

$$P_{w,1} - P_{w,2} = \frac{1}{2}\rho_w\left[\left(U_{w,2} - C_v\right)^2 - \left(U_{w,1} - C_v\right)^2\right] - 2ga\rho_w \tag{5.10}$$

The stability conditions for inviscid *stratified wavy* flow at the onset of entrainment can be found by balancing the normal stresses (pressure) across the interface with the

surface tension. At the crest of the wave shown in Fig. 5.1, the stability equation is given by

$$P_{o,1} - P_{w,1} = -\sigma\left(\frac{1}{R_1} + \frac{1}{R_2}\right) \tag{5.11}$$

At the trough of the wave, the pressure across the interface is expressed as

$$P_{o,2} - P_{w,2} = +\sigma\left(\frac{1}{R_1} + \frac{1}{R_2}\right) \tag{5.12}$$

Since two-dimensional waves are assumed in this study, R_1 is the curvature radius of a plane curve and R_2 is infinite. That is,

$$\frac{1}{R_1} = \frac{\left|\frac{d^2y}{dx^2}\right|}{\left(1+\left(\frac{dy}{dx}\right)^2\right)^{3/2}}, \quad \frac{1}{R_2} = 0. \tag{5.13}$$

As curvature is defined the inverse of the radius of curvature $\left(\kappa = \frac{1}{R}\right)$. For the sinusoidal wave assumed, the curvature can be calculated as

$$\kappa = \frac{\left|-\frac{4\pi^2 a}{\lambda^2}\sin(\frac{2\pi x}{\lambda})\right|}{\left(1+\left(\frac{2\pi}{\lambda}\cos(\frac{2\pi x}{\lambda})\right)^2\right)^{3/2}} \tag{5.14}$$

Since the balance of forces is done at the peak of the wave, the curvature is calculated at that point where it actually has its maximum value. This maximum curvature is calculated by Eq (5.14) at $x = \frac{\lambda}{4}$:

$$\kappa_{\max} = \frac{4\pi^2 a}{\lambda^2} \tag{5.15}$$

Subtracting Eq (5.12) from Eq (5.11) will give

$$\left(P_{o,1} - P_{o,2}\right) - \left(P_{w,1} - P_{w,2}\right) = -\frac{2\sigma}{R} \tag{5.16}$$

By substituting Eq (5.9) and Eq (5.10) into Eq (5.16), the following expression can be obtained

$$\left[\frac{1}{2}\rho_o\left[\left(U_{o,2}-C_v\right)^2-\left(U_{o,1}-C_v\right)^2\right]-2ga\rho_o\right]-$$
$$\left[\frac{1}{2}\rho_w\left[\left(U_{w,2}-C_v\right)^2-\left(U_{w,1}-C_v\right)^2\right]-2ga\rho_w\right]=-2\frac{\sigma}{R} \tag{5.17}$$

$$\frac{1}{2}\rho_w\left[\left(U_{w,2}-C_v\right)^2-\left(U_{w,1}-C_v\right)^2\right]+\frac{1}{2}\rho_o\left[\left(U_{o,1}-C_v\right)^2-\left(U_{o,2}-C_v\right)^2\right]$$
$$-2ga\left(\rho_w-\rho_o\right)-2\frac{\sigma}{R}=0 \tag{5.18}$$

Substituting Eq (5.2), (5.3) and (5.15) into Eq (5.18) will result in Eq (5.19) that predicts the critical wave amplitude for certain wavelength at which the waves in *stratified* flow become unstable.

$$\frac{1}{2}\rho_w\left[\left(U_w-C_v\right)^2\times\left(\left(\frac{A_w}{A_{w2}}\right)^2-\left(\frac{A_w}{A_{w1}}\right)^2\right)\right]+$$
$$\frac{1}{2}\rho_o\left[\left(U_o-C_v\right)^2\times\left(\left(\frac{A_o}{A_{o1}}\right)^2-\left(\frac{A_o}{A_{o2}}\right)_v\right)^2\right]-2ga\left(\rho_w-\rho_o\right)-\frac{8\pi^2 a}{\lambda^2}\sigma=0 \tag{5.19}$$

In this equation U_w and U_o are the in-situ velocities for water and oil respectively for the flat interface, C_v is the continuity wave velocity as described by Wallis (1969) and analysed in section 5.2.3. The two-fluid model (section 5.2.4) in a non-moving coordinate system is used to calculate the in-situ phase velocities, U_w and U_o for flat interface. This is a reasonable assumption considering that the amplitudes of both the wave crest and trough are equal and the average interface height will be the same as that of the undisturbed interface. It is important to note that the continuity Eq. (5.1) is used to calculate the in-situ velocities in the moving coordinate system.

The terms in Eq (5.19) comprise the stability criterion for the Kelvin-Helmholtz analysis. The relative velocities will amplify any disturbance on the interface while gravity and surface tension forces will tend to reduce the unstable growth of the wave. The critical amplitude required to initiate instability at certain oil and water superficial velocities is determined when the sum of the three forces is equal to zero. Below zero, the waves are stable (they will decay) while above zero the waves become unstable and drops may form.

5.2.3 Wave velocity calculation using the two-fluid model

Wallis (1969) presented a general relationship for wave velocity which is the derivative of the liquid flux with respect to its in-situ hold-up. The above wave velocity can be estimated directly from the equilibrium conditions of the two-fluid model. The derivative of the water flux (U_{sw}) with respect to its in-situ holdup (H_w) is

$$C_v = \left(\frac{\partial U_{sw}}{\partial H_w}\right)_{(U_{sw}+U_{so})} = \frac{\left(\frac{\partial F}{\partial H_w}\right)_{Usw,Uso}}{\left(\frac{\partial F}{\partial U_{so}}\right)_{Usw,Hw} - \left(\frac{\partial F}{\partial U_{sw}}\right)_{Uso,Hw}} \tag{5.20}$$

where, U_s is the superficial velocity, the subscripts o and w represent the oil and water phases respectively and F is defined by equation (5.21).

The derivatives in equation (5.20) can be evaluated numerically by perturbing H_w, U_{so} and U_{sw} in a two-fluid model with smooth interface by small amounts (+ or – 1%).

5.2.4 Calculation of phase velocities using the two-fluid model

By considering smooth equilibrium horizontal *stratified* flow, taking the momentum balance on each phase and equating the pressure drop in the two phases, the following equation is derived (Trallero, 1995).

$$F = -\frac{\tau_w S_w}{A_w} + \frac{\tau_o S_o}{A_o} + \tau_i S_i \left(\frac{1}{A_w} + \frac{1}{A_o}\right) = 0 \tag{5.21}$$

where τ_w, τ_o, τ_i are the water, oil and interfacial shear stresses respectively. The wall shear stresses, τ_w and τ_o are expressed in terms of the corresponding fluid friction factors, f_w and f_o:

$$\tau_w = f_w \frac{\rho_w U_w^2}{2}; \; f_w = m\,\mathrm{Re}_w^{-n} = m\left(\frac{D_w U_w \rho_w}{\mu_w}\right)^{-n} \tag{5.22}$$

$$\tau_o = f_o \frac{\rho_o U_o^2}{2}; \; f_o = m\,\mathrm{Re}_o^{-n} = m\left(\frac{D_o U_o \rho_o}{\mu_o}\right)^{-n} \tag{5.23}$$

where the friction factors are Fanning type and the pipes are considered smooth. The coefficient m and the exponent n are equal to 0.046 and 0.2 for turbulent flow and to 16 and 1.0 for laminar flow respectively.

D_w and D_o are the equivalent hydraulic diameters. Their values are based on which phase is faster. Therefore, they can be defined as follows,

$$D_w = \frac{4A_w}{(S_w + S_i)}; D_o = \frac{4A_o}{(S_o)} \; for \; U_w > U_o \tag{5.24}$$

$$D_o = \frac{4A_o}{(S_o + S_i)}; D_w = \frac{4A_w}{(S_w)} \; for \; U_w < U_o \tag{5.25}$$

$$D_o = \frac{4A_o}{(S_o)}; D_w = \frac{4A_w}{(S_w)} \; for \; U_w \approx U_o \tag{5.26}$$

where the parameters S_i, S_o, S_w, A_o and A_w are defined in Table 5.1.

In this study, the interfacial shear stress is given by

$$\tau_i = f_i \frac{\rho_i (U_o - U_w)|U_o - U_w|}{2}; f_i = m\,\mathrm{Re}_i^{-n} = m\left(\left(\frac{S_i}{\pi}\right)\frac{U_i \rho_i}{\mu_i}\right)^{-n} \tag{5.27}$$

$$\text{where } \rho_i, U_i, \mu_i = \begin{Bmatrix} \rho_w, U_w, \mu_w \; if \; U_w > U_o \\ \rho_o, U_o, \mu_o \; if \; U_w < U_o \end{Bmatrix} \tag{5.28}$$

When the ratio of the two phase velocities is between 0.98 and 1.05 (Brauner and Moalem Maron, 1989) then there is no interfacial shear stress and both phases are assumed to flow as in an open channel. In this case the hydraulic diameters are calculated by Eq (5.26).

Using the two-fluid model equation, the in-situ water and oil velocities can be calculated.

Parameter	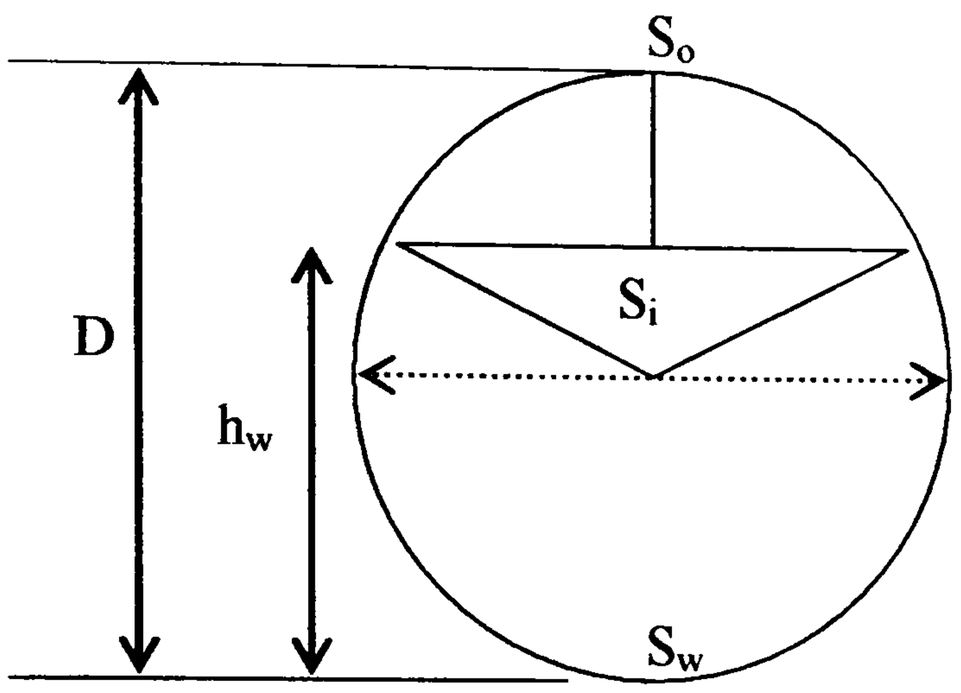
Interfacial length (S_i)	$D \times \left(1-\left(2\frac{h_w}{D}-1\right)^2\right)^{0.5}$
Wall perimeter of oil phase (S_o)	$D \times \cos^{-1}\left(2\frac{h_w}{D}-1\right)$
Wall perimeter of water phase (S_w)	$\pi D - S_o$
Cross sectional area of the pipe	$\frac{\pi}{4}D^2$
Area oil phase (A_o)	$\frac{D}{4} \times (S_o - S_i \times (2\frac{h_w}{D}-1))$
Area water phase (A_w)	$A_w = A - A_o$
Oil hold-up (H_o)	A_o / A
Water hold-up (H_w)	A_w / A
In-situ oil velocity (U_o)	U_{so} / H_o
In-situ water velocity (U_w)	U_{sw} / H_w

Table 5.1. Geometric parameters used in the two-fluid model

5.2.5 Comparison with the Trallero (1995) VKH equation

Assuming very long wavelength (λ=100**D*) and small amplitude (0.001**D*), the stability Eq. (5.19) should give similar predictions to the VKH analysis developed by Trallero (1995). The VKH equation determines the transition between stable *stratified* flow and either unstable *stratified* with wavy interface or some other flow pattern. As can be seen in Figs. 5.2 and 3 indeed the two developments give very similar predictions.

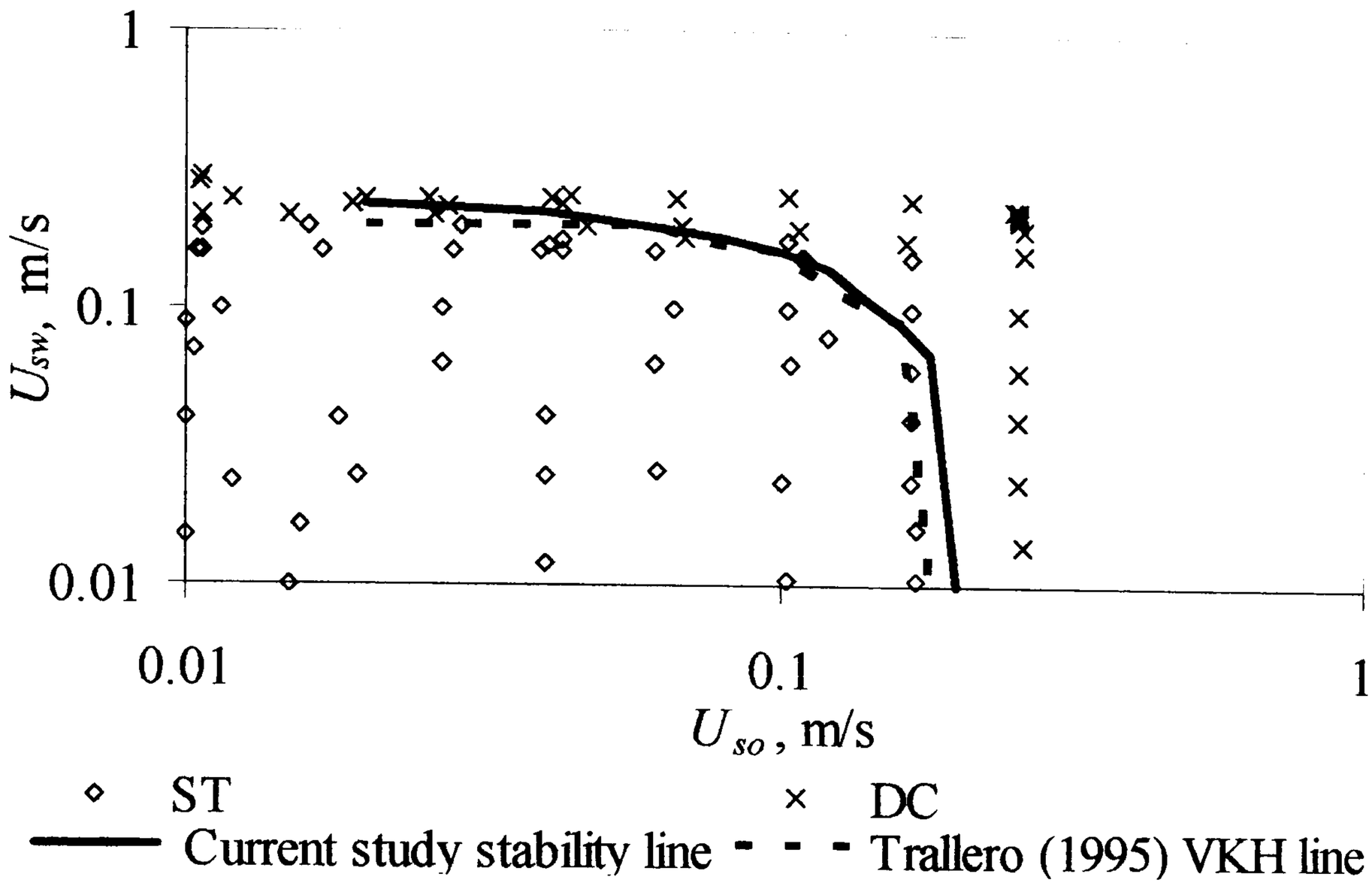

Fig. 5.2 Comparison between the stability line developed in the present study (Eq. 5.19) and the VKH line developed by Trallero (1995) using the experimental input parameters by Trallero (1995). Flow patterns: *ST* (*stratified*), *DC* (*dual continuous*).

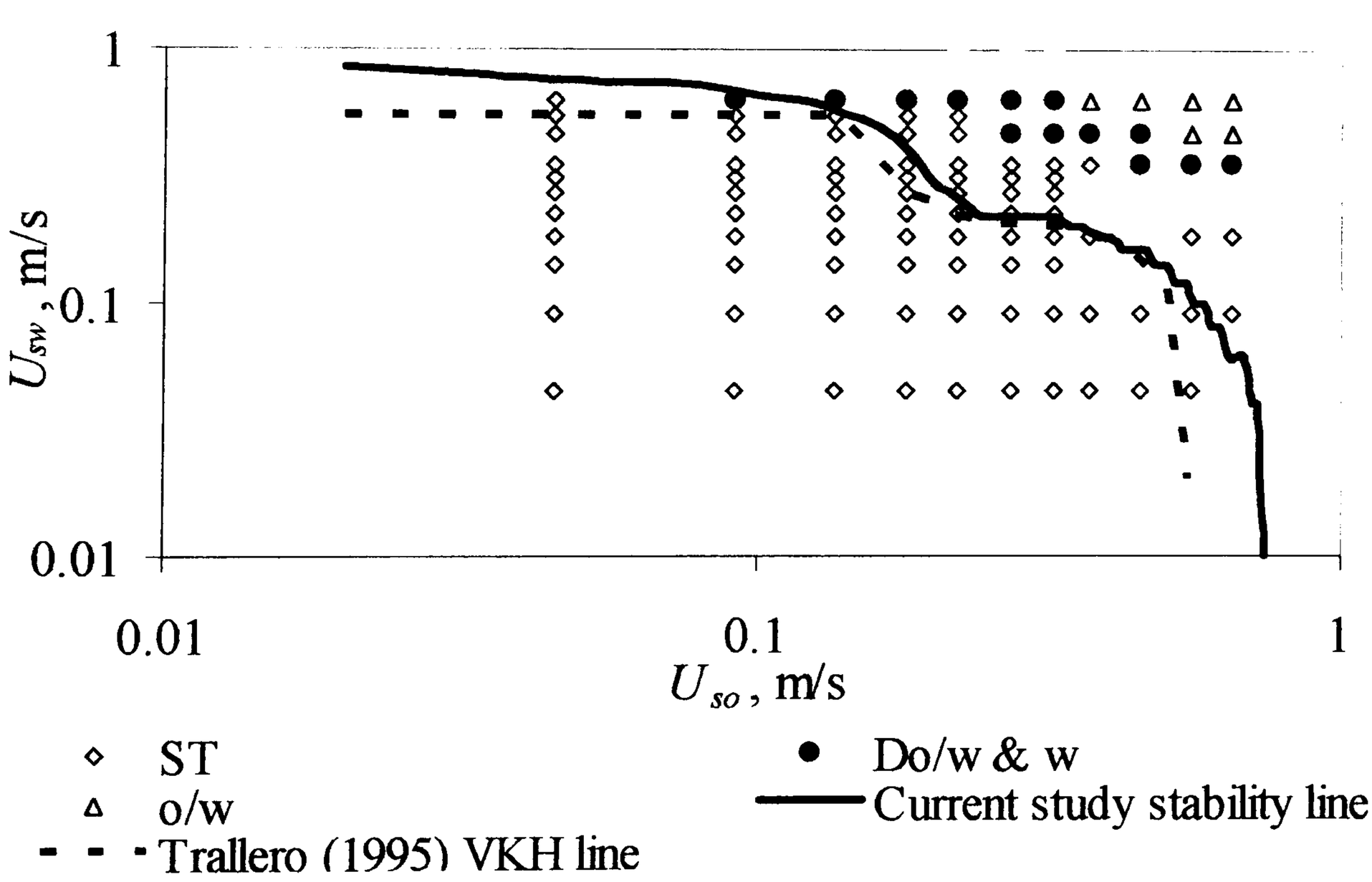

Fig. 5.3 Comparison between the stability line developed in the present study (Eq. 5.19) and the VKH line developed by Trallero (1995) using the experimental input parameters by Cox (1985). Flow patterns: *ST* (*stratified*), *Do/w & w* (*dispersed oil in water and water layer*), *Do/w* (*dispersed oil in water*).

5.3 Discussion of the Model Results

The critical amplitude for different wavelengths obtained by the stability Eq. (5.19) is shown in Fig. 5.4 for different water superficial velocities at U_{so} = 0.05 m/s, for the test fluids and pipe diameter (38 mm ID) used in this study (see section 5.3). The oil and water in-situ velocities required for Eq. (5.19) were found by the two-fluid model (as described in section 5.2.4). The flow is considered to be stable *stratified* if the amplitudes of all the waves fall below the stability line while it is unstable if amplitudes of some waves fall above the stability line; these waves may eventually form drops. At velocities higher than the entrainment onset velocity or where *dual continuous* flow is fully established, almost all the waves are expected to fall above the stability line.

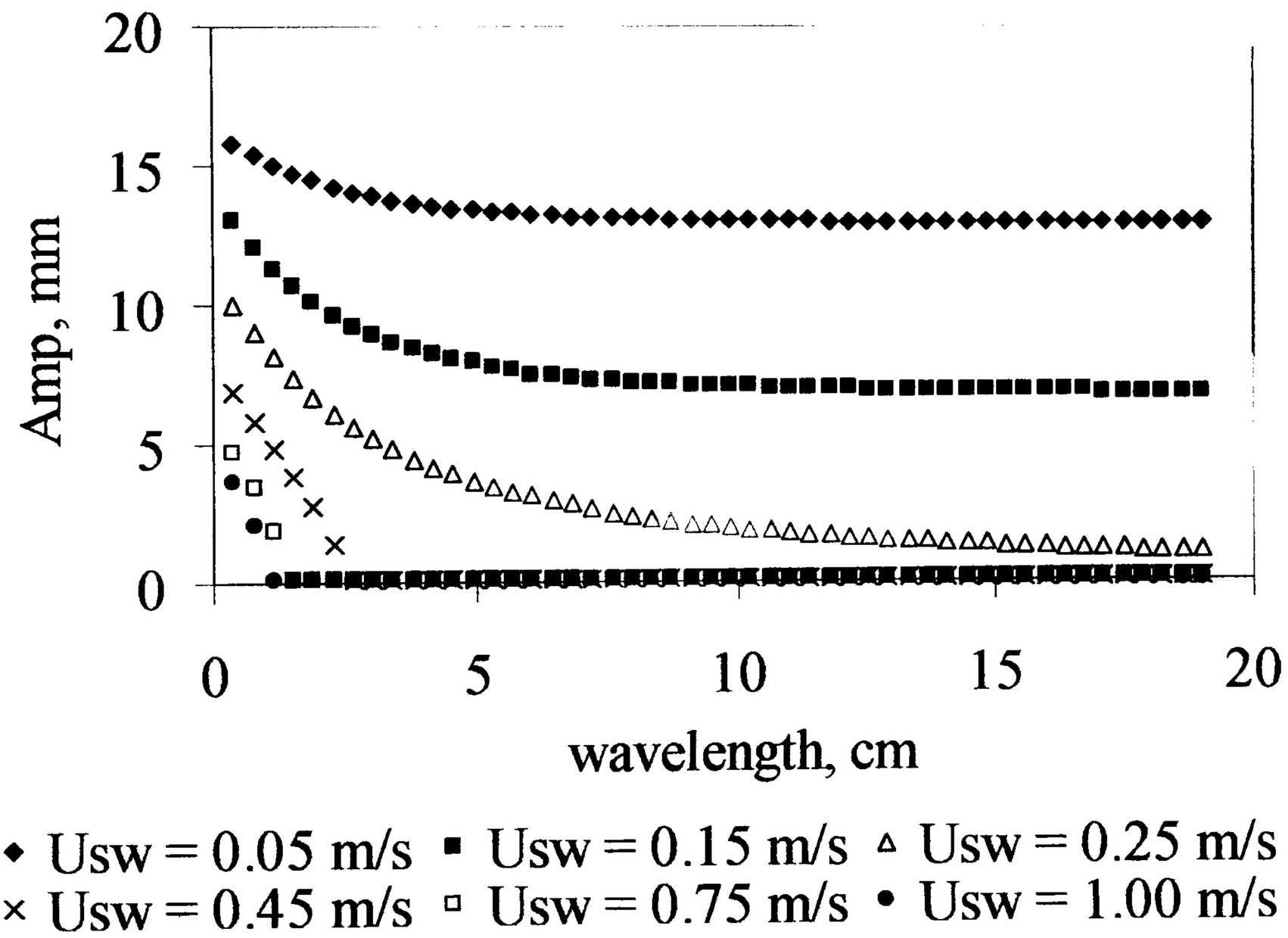

Fig. 5.4 Critical wave amplitude required to initiate instability for a certain wavelength at U_{so} = 0.05 m/s and different superficial water velocities (Present Study, 38 mm ID test section)

From Fig. 5.4, it can be noted that at the lower water velocities (U_{sw} = 0.05, U_{sw} = 0.15 m/s), the required critical amplitudes that the waves should reach to become unstable are high (almost half the pipe diameter). Thus, all the waves are expected to fall underneath the stability line. In other words, all the disturbances that exist in the oil-water interface will decay and the flow will remain *stratified* (*stratified smooth* or

stratified with small amplitude waves). As the water velocities increase, the critical amplitudes decrease. The initiation of unstable waves is expected to occur between U_{sw} = 0.25 and U_{sw} = 0.45 m/s since at the latter velocity some waves will definitely fall above the stability line. Finally, at even higher water velocities (U_{sw} = 0.75, U_{sw} = 1.00 m/s), most disturbances in the oil-water interface will be unstable so most or all the waves will grow to form drops.

Fig. 5.5 shows the stability lines at three different conditions selected from the flow pattern map of Trallero (1995) (see Table 2.1 for the values of relevant parameters). The first point was chosen at U_{so} = 0.10, U_{sw} = 0.10 m/s where flow is *stratified*. At this condition it is clear that the required amplitudes for the waves to become unstable are very high which means that waves at this condition are not expected to cross the stability line and are stable. At the transition between *stratified* and *dual continuous* flows (U_{so} = 0.10, U_{sw} = 0.18 m/s), any disturbance with wavelength greater than 2 times the diameter (equal to about 10 cm) will become unstable and will grow to form drops. The last condition is selected from the *dual continuous* region at U_{so} = 0.10, U_{sw} = 0.30 m/s where the stability line further shifts to the left. Thus, most of the waves at this condition are unstable and drop formation will be further enhanced.

Another interesting finding is that with the high viscosity oil used by Trallero (29.6 mPa s) the onset of drop formation and transition to *dual continuous* flow, at U_{sw} = 0.18 m/s for U_{so} = 0.10 m/s, coincides with the appearance of the unstable waves according to the stability line (Fig. 5.5). On the other hand, with the low viscosity oil used in the present work (5.5 mPa s), the onset of drop formation and transition to *dual continuous* flow for U_{so} = 0.05 m/s appeared at higher U_{sw} (U_{sw} = 0.55 m/s), than the predicted transition to unstable waves according to Fig. 5.4 (transition between U_{sw} = 0.25 m/s and U_{sw} = 0.45 m/s). This could be attributed to the large viscosity difference between the two layers in the former case which further destabilizes the wave and increases the shear between the two phases that helps drop detachment, compared to the latter case.

From the model results (Figs. 5.4 and 5.5) and at small wavelengths, it can be seen that the amplitude decreases as the wavelength increases. This is because the effect of surface tension which tends to stabilize the waves decreases with increasing wavelength

(see equation (5.19)). For short waves, surface tension opposes wave growth so that short waves need larger amplitudes before they become unstable. When the flow is stratified (U_{so} = 0.05, U_{sw} = 0.15 from Fig. 5.4 and U_{so} = 0.10, U_{sw} = 0.10 from Fig. 5.5), the amplitudes are high so for the entire range of wavelengths all the disturbance (waves) are expected to decay. As the velocity of the water increases (U_{so} = 0.05, U_{sw} = 0.45 from Fig. 5.4 and U_{so} = 0.10, U_{sw} = 0.18 from Fig. 5.5), a critical wavelength (λ_c) appears below which all the waves are stable. For longer wavelengths the stabilizing effect of surface tension becomes very small, and even small disturbances become unstable. As the velocities increase further the critical wavelength decreases until the flow becomes unstable for the entire range of wavelengths. This normally happens at high velocities where the *dual continuous* flow is fully established and a large amount of drops exists in both phases.

Fig. 5.5 Critical wave amplitude required to initiate instability for a certain wavelength at U_{so} = 0.10 m/s and different superficial water velocities (Trallero, 1995)

The effect of viscosity on the critical amplitudes at different wavelengths at U_{so} = 0.05, U_{sw} = 0.25 m/s is shown in Fig. 5.6 where the rest of the parameters are from the system used in the present study. The results reveal that the critical amplitudes to initiate instability decrease as the oil to water viscosity ratio increases. This agrees with

published experimental results which show that the onset velocities for drop formation (onset of *dual continuous* flow) decrease as the viscosity ratio increases (Lovick and Angeli, 2004a). From Fig. 5.6 at viscosity ratio equal to 1 the flow is expected to be *stratified* since the critical amplitudes are high and all the waves will fall below the stability line. Published data actually show that for viscosity ratio close to 1 (see Cox, 1985 and Angeli and Hewitt, 2000a, and Table 2.1 for the fluid properties) the flow is *stratified* at the same oil and water superficial velocities. For viscosity ratio between 5 and 10, the critical amplitudes are generally high so most waves are considered to be stable. Only waves with long lengths (greater than 20 cm), if they exists, they may fall above the stability line and become unstable. However, in the present study where a 5.5 viscosity ratio was used, *stratified* flow was found at these superficial velocities.

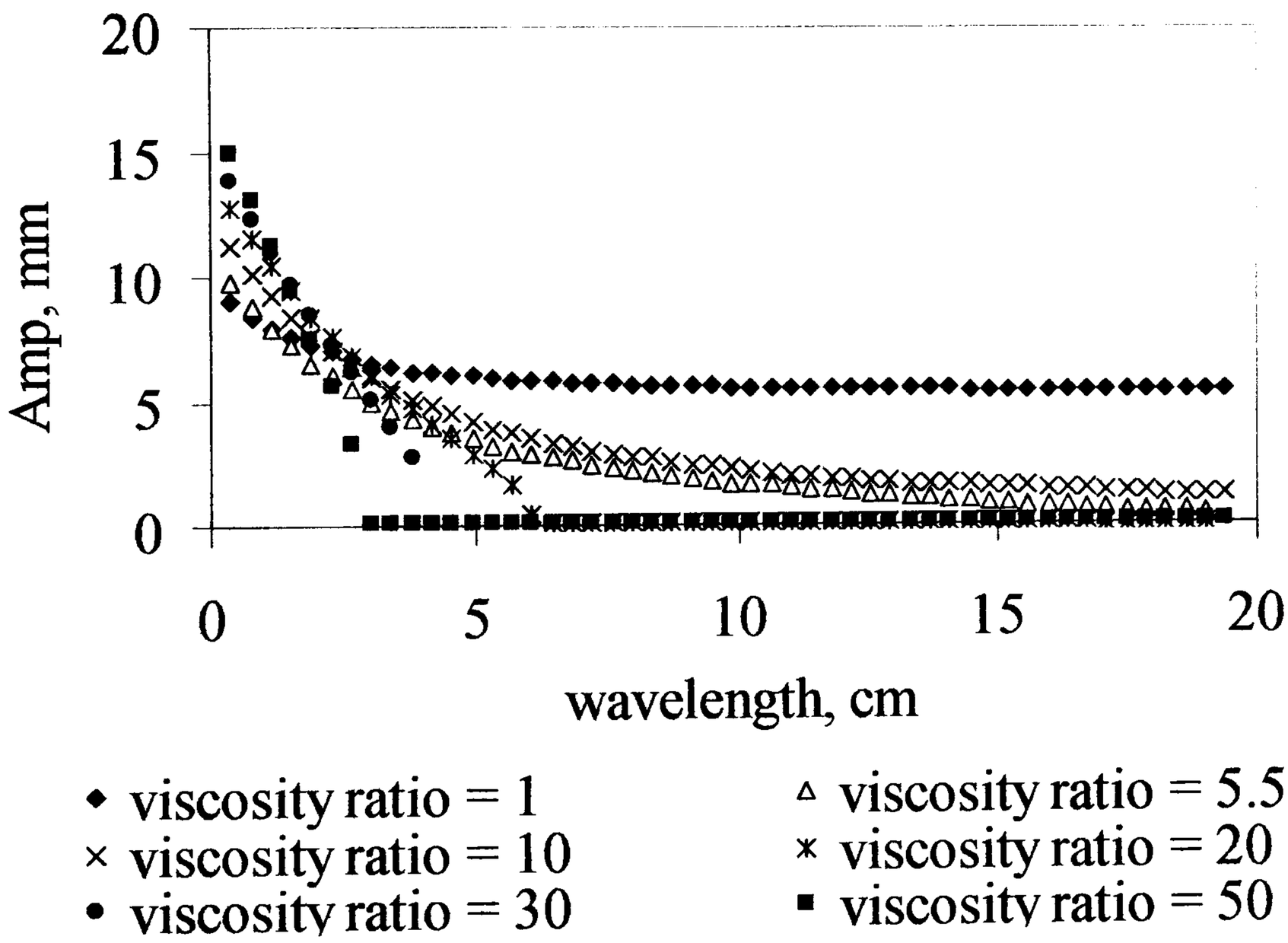

Fig. 5.6 Effect of oil to water viscosity ratio on the critical wave amplitude required to initiate instability for a certain wavelength at $U_{so} = 0.05$, $U_{sw} = 0.25$ m/s

Finally, for the high viscosity ratios (20-50) the stability line further decreases and the *stratified* flow is expected to be unstable. Guzhov et al. (1973) (see Table 2.1 for the fluid properties) for a viscosity ratio close to 20 actually found for these superficial velocities a transition between *stratified* and *dispersed oil in water and water layer* flows, which agrees with the model results. Also for viscosity ratio close to 30, Trallero

(1995) observed *dual continuous* flows for the same condition which again agrees with the predictions of the stability line.

The stability lines for the systems used by three investigators that cover a range of viscosity ratios are shown in Fig. 5.7 for U_{so} = 0.10 m/s and U_{sw} at the experimentally found entrainment onset velocities. It can be seen that at the onset of drop formation the dimensionless critical wavelength (λ_c) required for the waves to be unstable decreases as the viscosity of oil decreases.

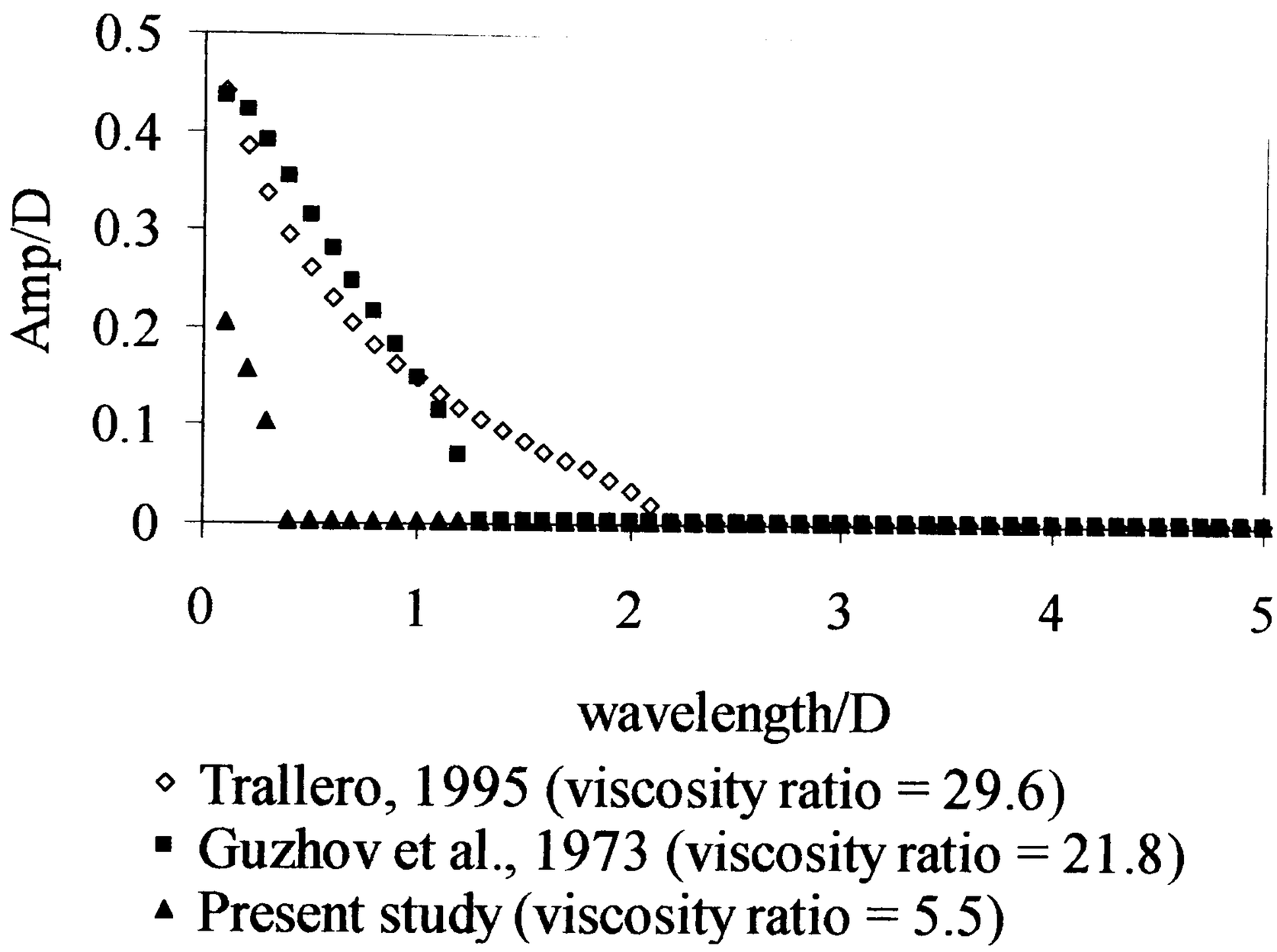

Fig. 5.7 Critical wave amplitude required to initiate instability for a certain wavelength at the entrainment onset velocities of U_{so} = 0.10 m/s from three different studies

The critical amplitudes for the current system at wavelength equal to the pipe diameter (3.8cm) are shown in Figs. 5.8a and b against the difference between the in-situ velocities of the two phases (*slip velocity*) at U_{so} = 0.05 and 0.15 m/s respectively for different viscosity ratios. It can be seen that as (U_w-U_o) increases the critical amplitude first reaches a maximum and then decreases at high slip velocities. This is because at high slip velocities, the relative movement between the two layers is also high so smaller amplitude waves can more easily become unstable compared to lower slip velocities. At high slip velocities, the critical amplitudes become zero and this indicates

that instability will occur even for very small disturbances at the oil-water interface. It was also found that apart from the slip velocity the oil layer velocity can affect drop formation. For example at U_{so} = 0.05 m/s (Fig. 5.8a), a higher amplitude is required than at U_{so} = 0.15 m/s (Fig. 5.8b) to destabilize the wave for the same slip velocity because in the latter case the oil layer velocity is higher and probably increases the destabilization effect.

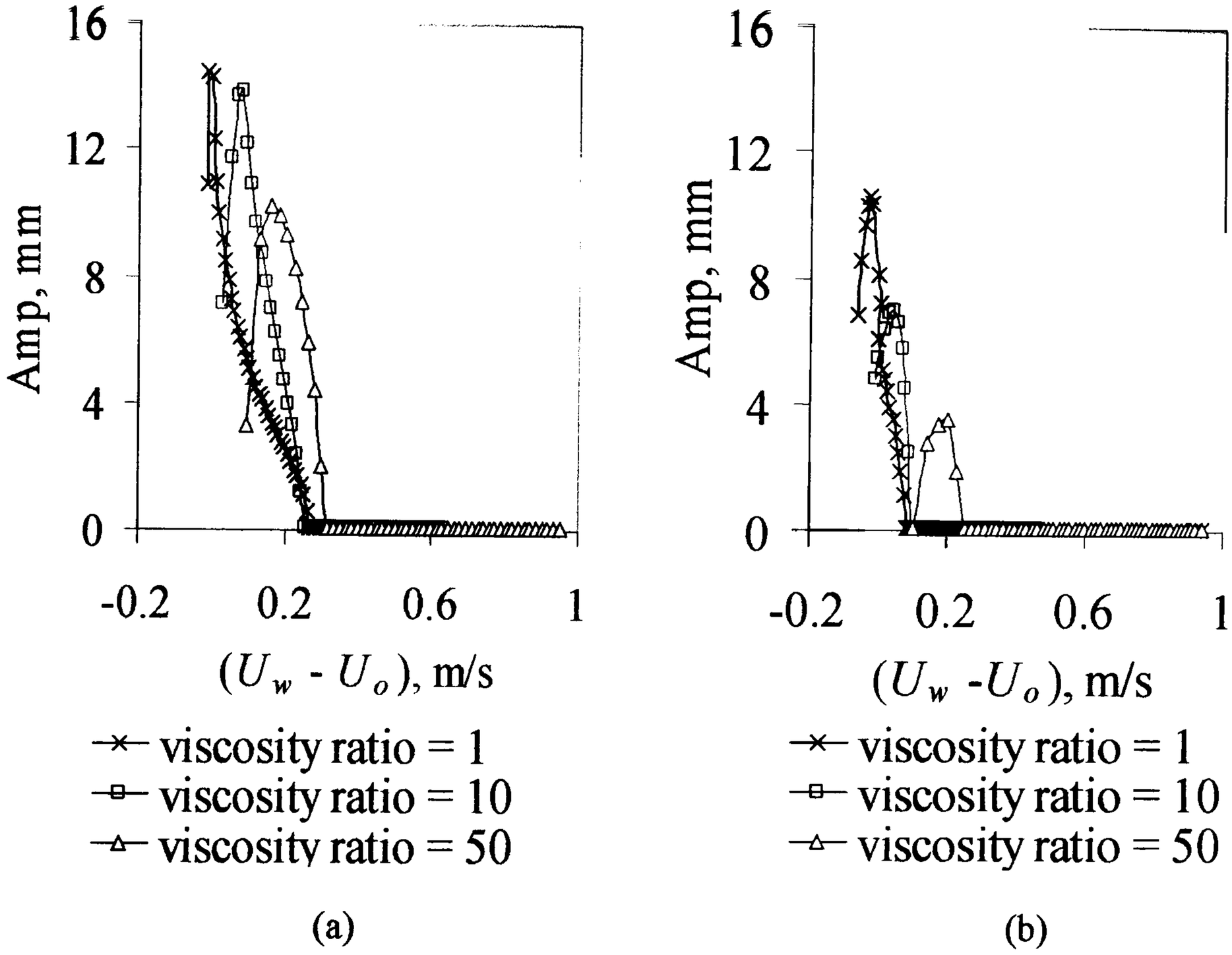

Fig. 5.8 Critical wave amplitude required to initiate instability against slip velocity at (a) U_{so} = 0.05 m/s, (b) U_{so} = 0.15 m/s for different oil to water viscosity ratios (D = 3.8 cm, ρ_o/ρ_w=0.828, σ = 39.6 dynes/cm)

From Fig. 5.8a and b, it is clear that the maximum amplitude shifts towards the right as the viscosity of the oil increases. For the low viscosity oils (viscosity ratio = 1) the amplitude reaches its maximum value when both liquids travel roughly at the same velocity (slip velocity close to 0) while for the higher viscosity oils (viscosity ratio equal to 10 and to 50), the maximum amplitude is achieved when the oil velocity is lower than that of the water. Two main factors are responsible of destabilizing *stratified* flow, namely velocity and viscosity difference between the two phases. For oils with low

viscosities similar to that of water the effect of viscosity is diminished and the velocity difference is the main destabilizing factor. As a result, when both fluids move with approximately the same velocity (slip velocity close to zero), the amplitude has to increase to a maximum before waves become unstable. As the oil viscosity increases viscous effects also contribute to the destabilization of the flow in addition to inertial effects and the maximum wave amplitude appears at higher slip velocity.

5.4 Comparison with Experimental Wave Characteristics at the Onset of Entrainment

5.4.1 Growing waves

In chapter 4, the results from the conductivity probe showed how waves grow from a *stratified* regime up to the onset of entrainment. Fig. 4.18 (section 4.3.1) shows the development of the height of the water interface (h_w) at U_{so} = 0.20 m/s with increasing water velocity until drop formation is observed.

The experimental data from Fig. 4.18 are shown against the stability lines predicted by the model in Fig. 5.9. Two stability lines can be drawn based on wave velocity and hold-up that are either calculated as shown in sections 5.2.3 and 5.2.4 respectively or experimentally measured. Using the experimental values at U_{so} = 0.20, U_{sw} = 0.20 m/s, all waves fall below the stability line (see Fig. 5.9a) which indicates that all waves are stable (they will decay). When the model values are used for the stability line, some waves are found above the stability line and they will be unstable. At U_{so} = 0.20, U_{sw} = 0.40 m/s few waves fall above both stability lines (Fig. 5.9b) which means that these waves are unstable and drops may or may not form from them; according to the visual observations, however, no drops were found at these conditions (see section 4.2.1). At the onset of entrainment at U_{so} = 0.20, U_{sw} = 0.45 m/s, many waves are found above the stability lines (Fig. 5.9c). These waves are unstable and will break to form drops. From the above, waves should reach a critical amplitude and length for entrainment to start. However, the stability model can only predict whether the interface is stable and not whether drops will form. Another criterion should be implemented based on the mechanism of drop formation from wave crests to indicate whether drops will form from unstable waves.

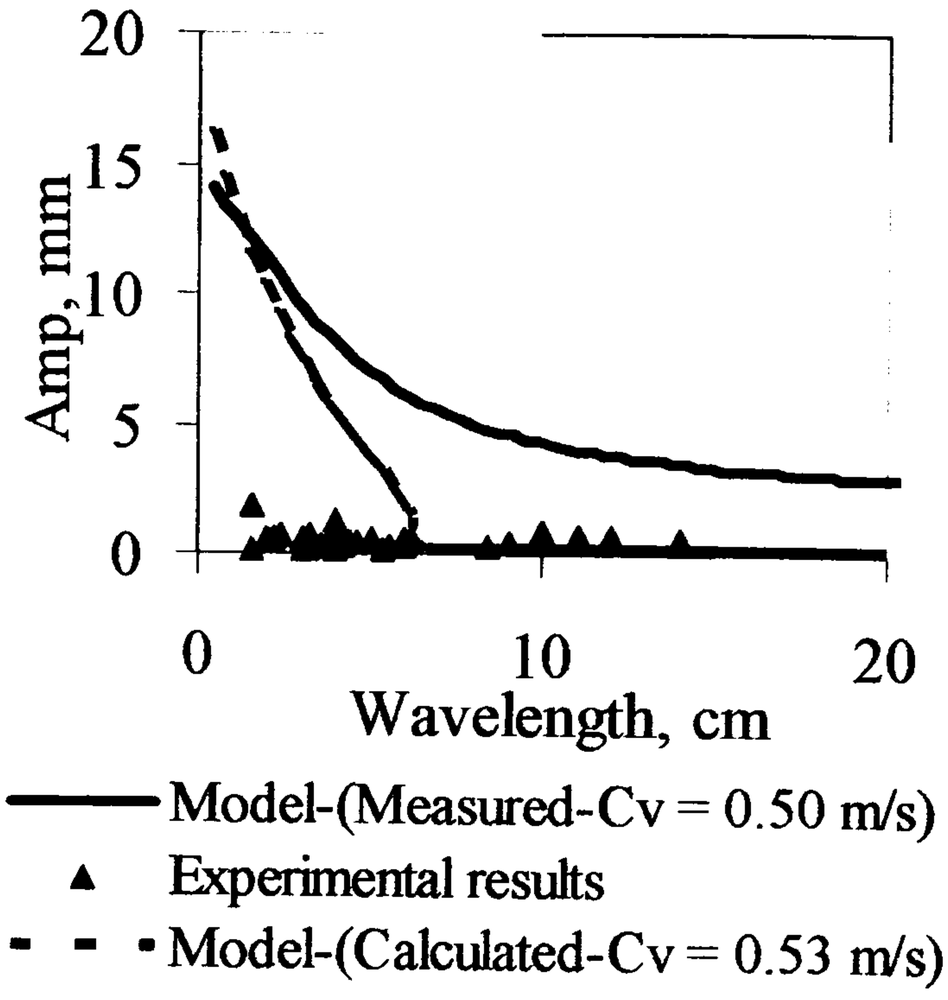

(a)

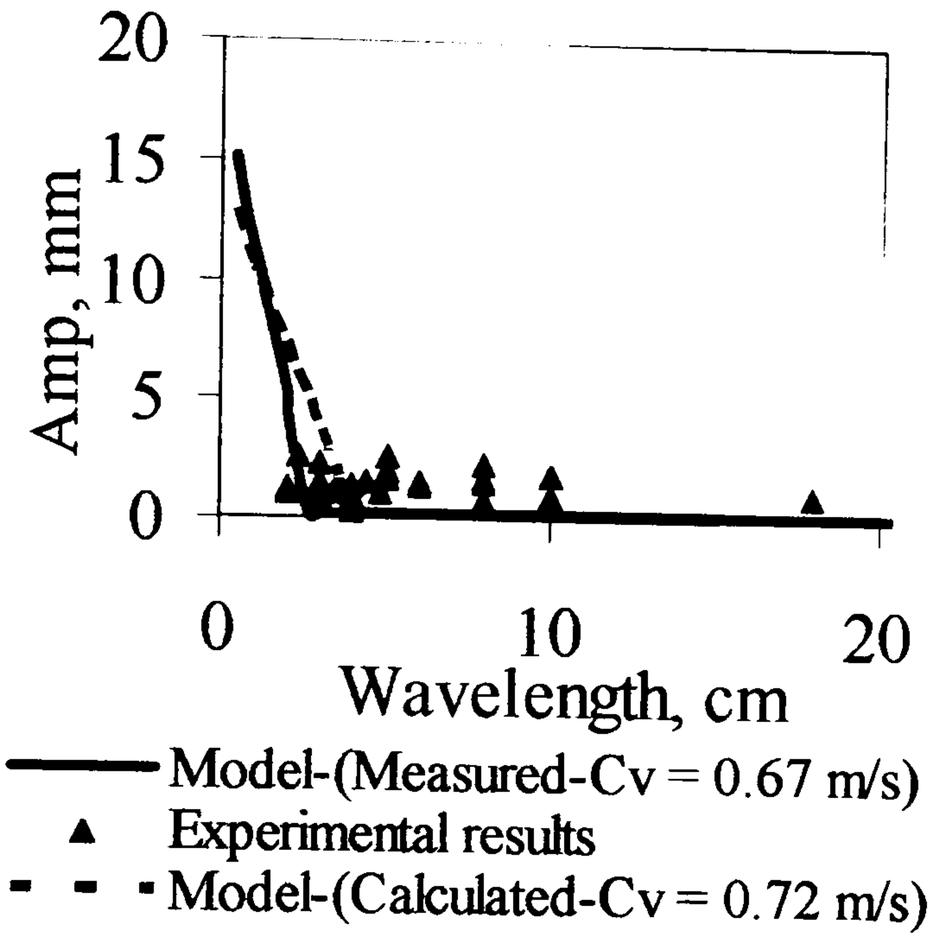

(b)

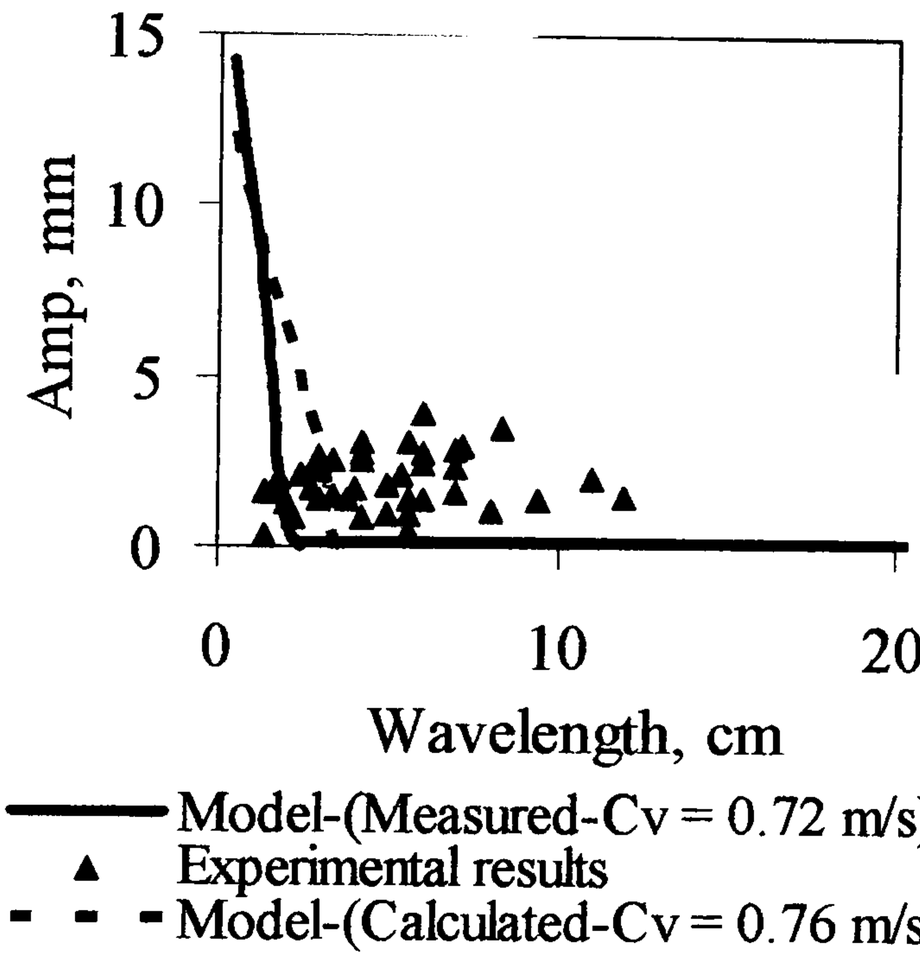

(c)

Fig. 5.9 Comparison between model (lines) and experimental (points) results; (a) U_{so} =0.20, U_{sw}=0.20 m/s, (b) U_{so}=0.20, U_{sw}=0.40 m/s, (c) U_{so}=0.20, U_{sw}=0.45 m/s

5.4.2 Structure of the waves at the onset of entrainment

In section 4.3.1, four conditions were selected to show the difference in wave structure at the onset of entrainment. These are shown as time series of the interface height in Fig. 4.19. The experimentally measured amplitudes and lengths of the waves at the four selected different onset conditions are plotted against the model predictions in Fig.5.10. Waves with a range of amplitudes and lengths will be present in the flow. However, the waves are considered to be unstable if they fall above the stability lines. The results in Fig 5.10 show that in all cases where entrainment was observed experimentally, a large

number of waves had characteristics above the stability lines. It can also be seen that there is a critical wavelength below which the waves are stable. In general and according to both stability lines, waves with length less than 0.5 the pipe diameter (D = 3.8 cm) are stable because the required amplitudes to initiate instability are very high and cannot be reached.

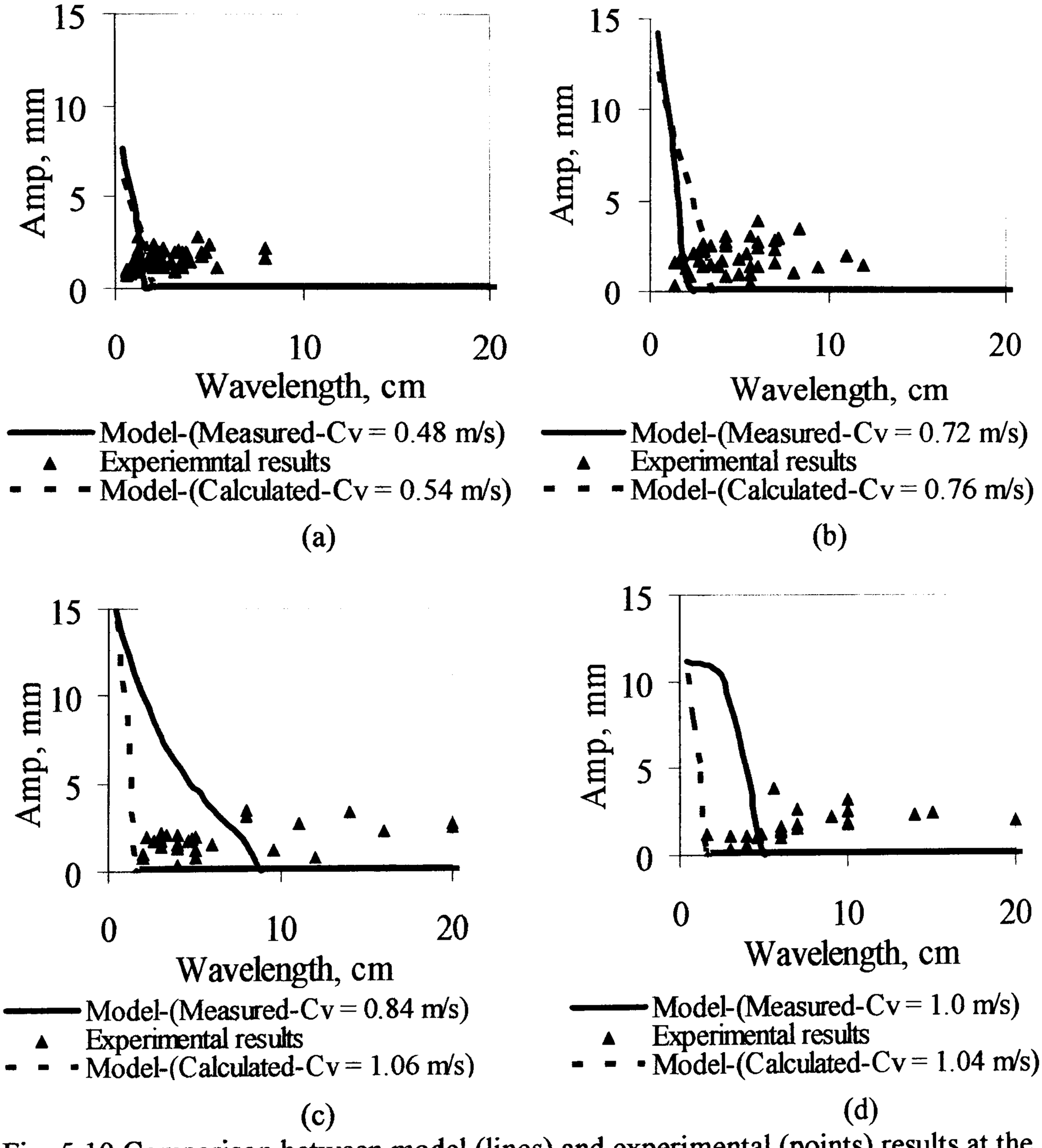

Fig. 5.10 Comparison between model (lines) and experimental (points) results at the onset of entrainment; (a) U_{so} =0.05, U_{sw}=0.55 m/s, (b) U_{so}=0.20, U_{sw}=0.45 m/s, (c) U_{so}=0.40, U_{sw}=0.40 m/s, (d) U_{so}=0.55, U_{sw}=0.25 m/s

5.5 Prediction of the Onset of Entrainment

The onset of entrainment in horizontal liquid-liquid flow happens when a disturbance at the oil-water interface grows until it acquires a critical amplitude and wavelength where it becomes unstable and drops form. The beginning of instability will not necessarily coincide with drop formation. To predict the onset of entrainment the required wavelength and amplitude for drop formation should be known. These can be used in Eq. (5.19) to find the velocities of the two phases at the onset of entrainment. Critical wavelengths based on experimentally found onset velocities are shown in Fig. 5.7 for a range of oil viscosities. The stability lines show that the dimensionless critical wavelength decreases as the oil viscosity increases. In this paper and for simplicity, the critical wavelength is selected to be 0.5 times the diameter for oil viscosity less than 10 and equal to 2 times the diameter for oil viscosity higher than that (see Fig. 5.7). The critical amplitude is assumed to be 0.05 times the diameter, which is the average of all the amplitudes from the experimental results at entrainment onset conditions in this study (1.7 mm). However, it is important to note that in order to predict the entrainment onset velocities precisely a relationship between the required amplitudes to form drops and wavelengths should be established.

Figs. 5.11-17 show the comparisons between the predicted and experimental entrainment onset velocities for the current work (from both the 38 and 14 mm ID test section) and that by Guzhov et al. (1973), Cox (1985), Valle and Kvandal (1995), Trallero (1995) and Nädler and Mewes (1997). In Figs. 5.11 and 5.14, the comparison was made between the experimental onset velocities and the predicted ones. In the case of the other investigators, where the onset velocities were not measured directly, the transition between *stratified wavy* and *dual continuous* flow (see Table 2.1 for original flow pattern names) in their flow pattern maps was used for the comparison. As can be seen in all cases where higher viscosity oils are used the comparisons between predictions and experiments are satisfactory.

For the present work (both the small and the large pipes) and that by Cox (1985) and Valle and Kvandal (1995) the comparisons showed either an overprediction or an underprediction of the experimental results. In general, however, the predictions are very good taking into account the diversity of conditions used in the various works but

most importantly the ambiguity that exists in defining the transitions between the different flow patterns. Our own work also indicated that variations in the inlet geometry of the test pipe can affect the entrainment velocities and the small discrepancies between the model predictions and the experimental data may reflect these variations.

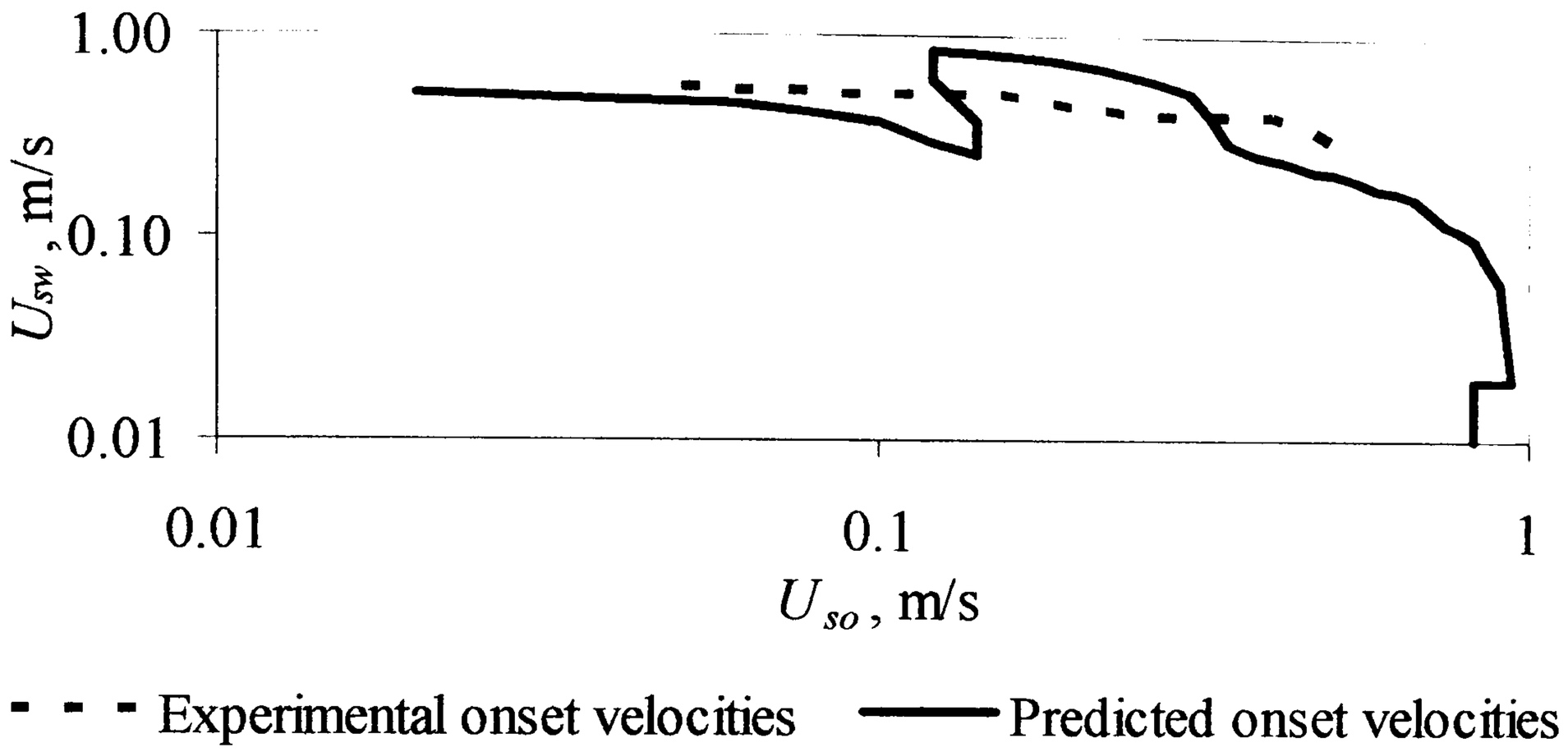

Fig. 5.11 Comparison between the predicted and the experimental onset velocities from the present work

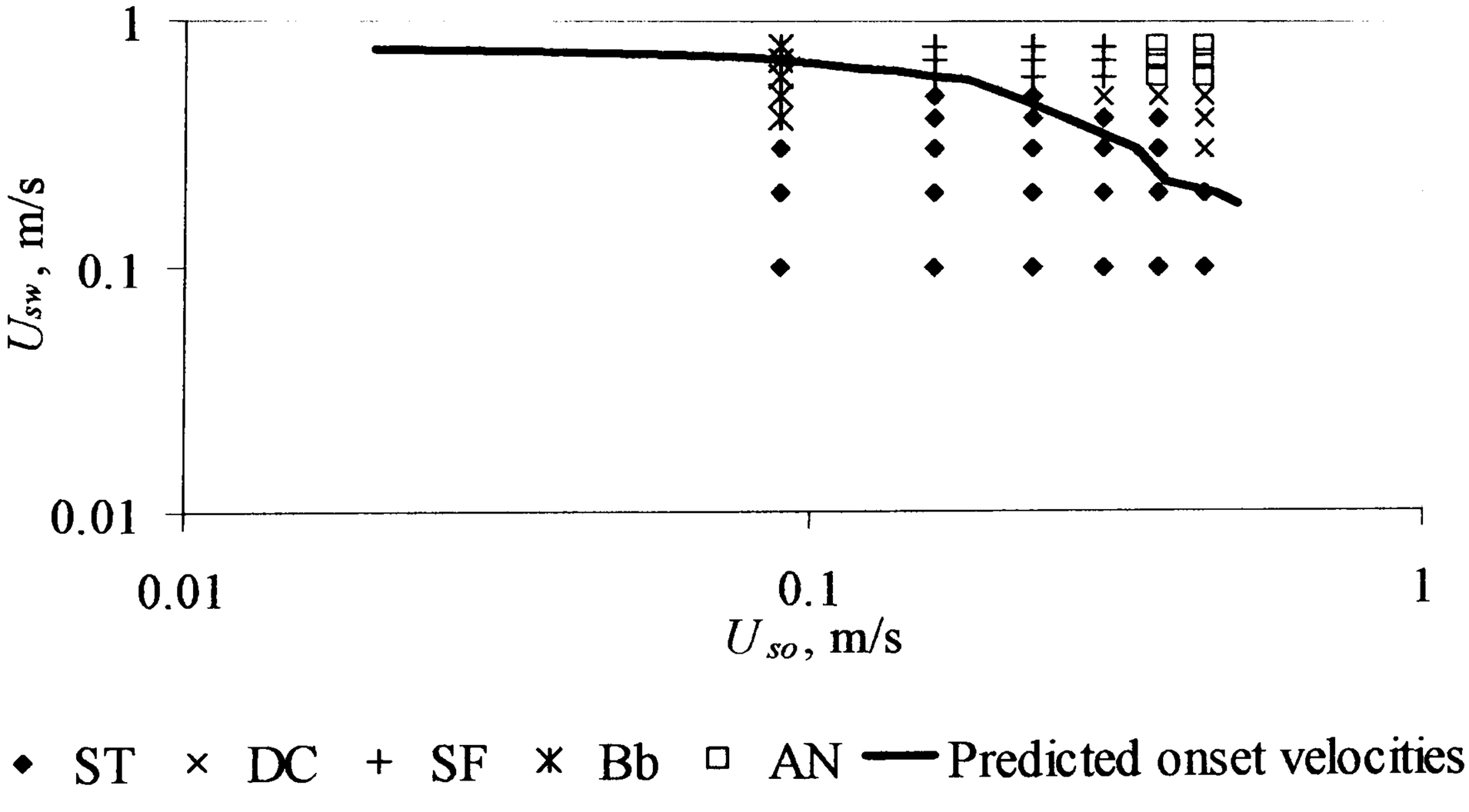

Fig. 5.12 Comparison between the predicted onset velocities (line) and the experimental results from the 14 mm ID pipe. Flow patterns: *ST* (*stratified*), *DC* (*dual continuous*), *SF* (*slug* flow), *Bb* (*Bubble*), *AN* (*annular*)

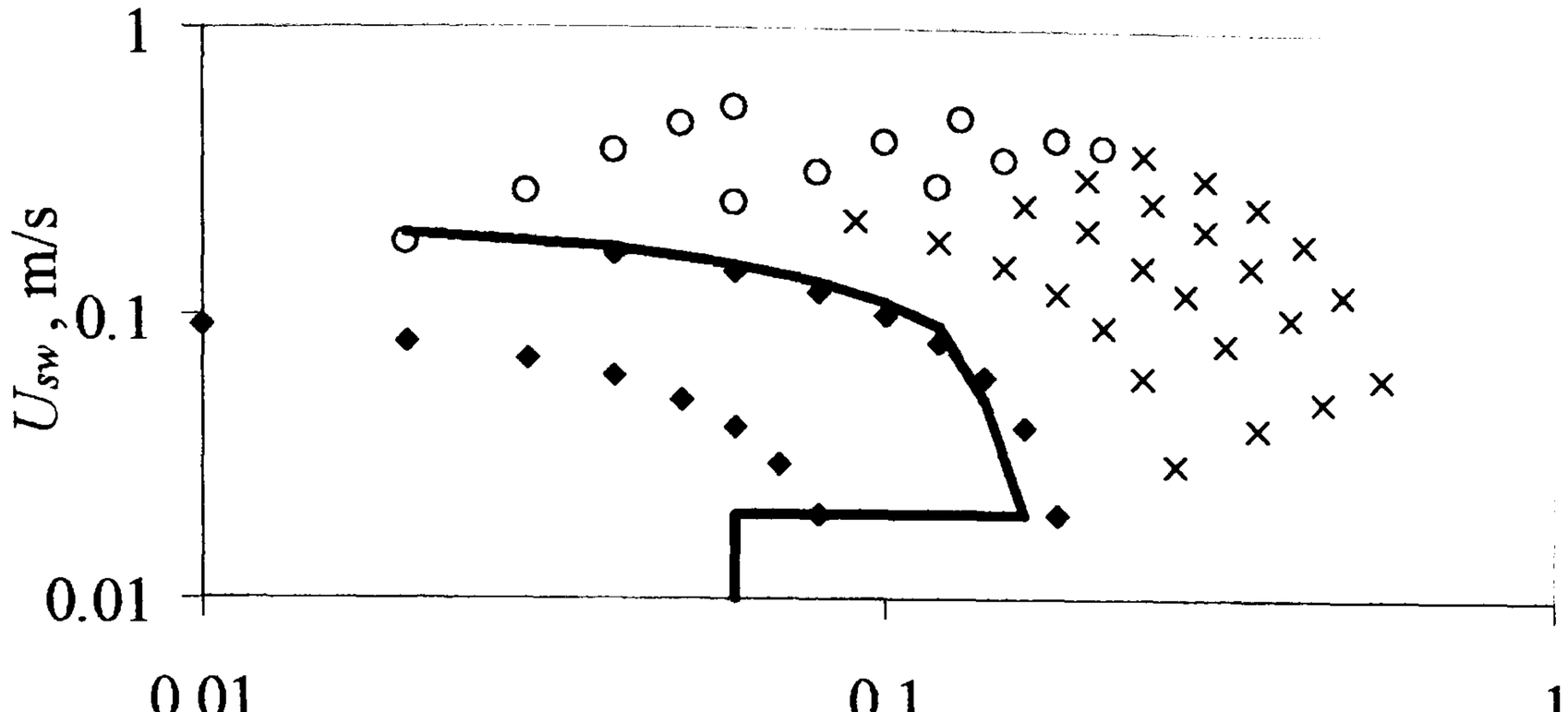

Fig. 5.13 Comparison between the predicted onset velocities (line) and the experimental results of Guzhov et al. (1973). Flow patterns: *ST* (*stratified*), *DC* (*dual continuous*), *Do/w & w* (*dispersed oil in water and water layer*)

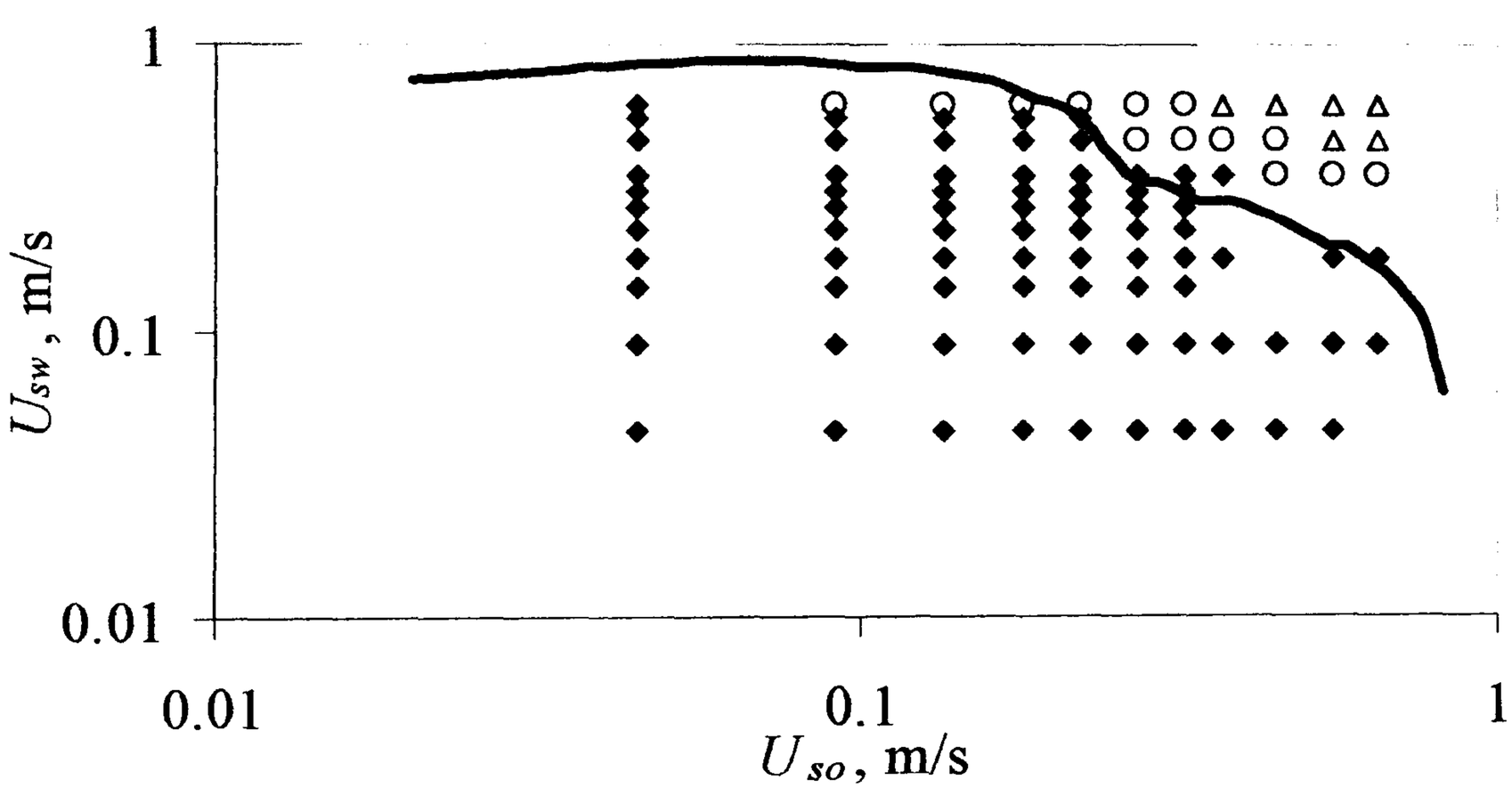

Fig. 5.14 Comparison between the predicted onset velocities (line) and the experimental results of Cox (1985). Flow patterns: *ST* (*stratified*), *Do/w & w* (*dispersed oil in water and water layer*), *Do/w* (*dispersed oil in water*).

Fig. 5.15 Comparison between the predicted and the experimental onset velocities of Valle and Kvandal (1995)

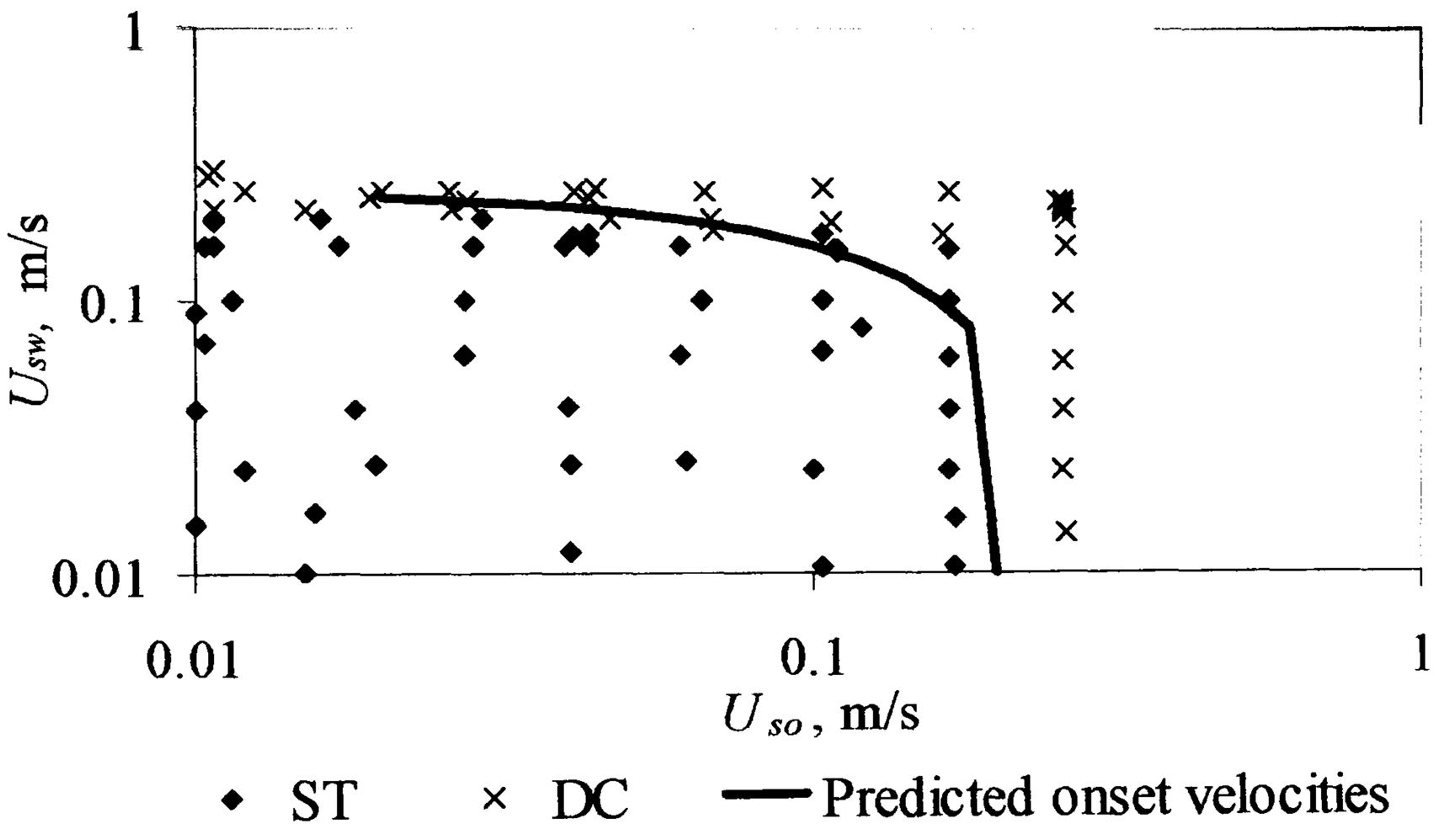

Fig. 5.16 Comparison between the predicted onset velocities (line) and the experimental results of Trallero (1995). Flow patterns: *ST* (*stratified*), *DC* (dual continuous).

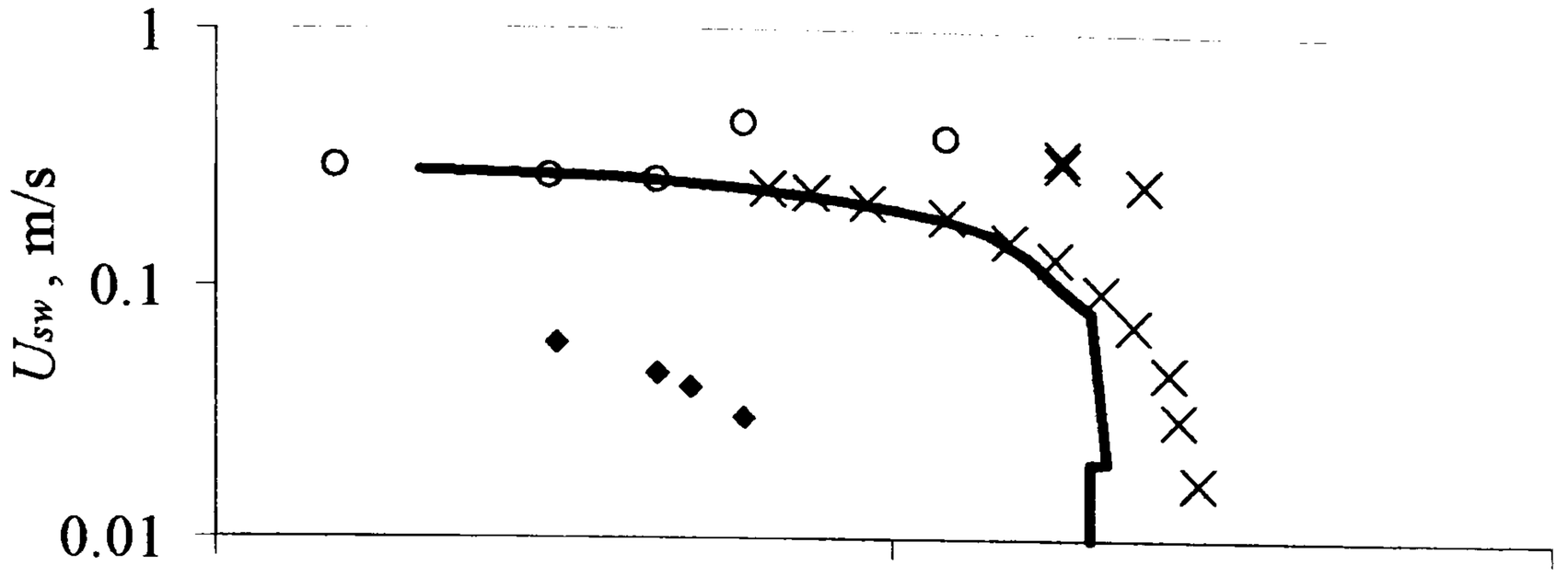

Fig. 5.17 Comparison between the predicted onset velocities (line) and the experimental results of Nädler and Mewes (1997). Flow patterns: *ST* (*stratified*), *DC* (*dual continuous*), *Do/w & w* (*dispersed oil in water and water layer*)

5.6 SUMMARY

A criterion for the transition between *stratified* stable and unstable liquid-liquid flows was derived theoretically based on K-H instability and finite wavelength that relates critical amplitude and wavelength at the onset of instability. The model predicts well the VKH line developed by Trallero (1995) assuming very long wavelength. The model satisfactory predicts whether waves with certain amplitudes and lengths are stable or not. According to the model the required amplitudes and lengths to form drops decrease as the superficial water velocity increases for a given superficial oil velocity. At higher water velocities, any disturbance in the oil-water interface will become unstable.

In comparison with experimental results it was found that the onset of drop formation with higher viscosity oils coincides with the appearance of unstable waves, while with lower viscosity oils, the onset of drop formation appears at higher velocity than the transition to unstable waves. The results reveal that critical amplitudes to initiate instability decrease as the viscosity ratio increases. This agrees with published experimental results which show that onset velocities for drop formation decrease as the viscosity ratio increases. It was also found from the model that for low viscosity oils the critical amplitude to initiate instability acquired maximum value at almost zero slip

velocity while for high viscosity oils the maximum value was reached for water velocity higher than the oil one.

The interfacial wave characteristics that were studied experimentally in section 4.3 before and at the onset of entrainment showed satisfactory agreement when compared with the model predictions.

The stability model can predict transition from stable to unstable waves but not the conditions for drop formation. Another criterion should be implemented based on the mechanism of drop formation to determine whether unstable waves will form drops. However, the required amplitudes and lengths of the waves for drop formation would need to be above the critical ones for transition to instability. Based on this and on current experimental data an empirical amplitude and wavelength were selected to predict the onset of entrainment and the transition from *stratified* to other mixed flow regimes. These predictions agreed well with experimental observations from a number of studies using both low and high viscosity oils.

CHAPTER 6

Mechanism of Drop Formation in Horizontal Oil-Water Flows

The mechanism of drop formation in the *dual continuous* of horizontal oil-water flows in the 14 mm ID acrylic pipe is presented in this chapter. A model is developed based on the drop formation mechanism to predict the critical amplitude of the waves required for drop formation. The model is then used together with the stability equation developed in chapter 5 to locate the region of unstable wave amplitudes and lengths that lead to drop formation. Section 6.1 provides a short introduction about the problem. The experimental results demonstrating the mechanism of drop formation are given in section 6.2. The mathematical equations and model development are presented in section 6.3. Section 6.4 shows a comparison between the model and the experimental results while section 6.5 demonstrates further validation of the model with experimental results. Finally, a summary is given in section 6.6.

6.1 Introduction

Based on the Stability analysis described in chapter 5, it is found that there is a critical wavelength below which no drops will form due to the stabilizing effect of interfacial tension (see Eq. 5.19). In *stratified* flow, waves must become unstable before drops can detach from them while stable waves decay. However, the stability criterion equation (Eq. 5.19 in chapter 5) can only determine if waves are stable or not and does not predict whether an unstable wave with certain length will give a drop or it has to grow more in amplitude for a drop to form. For this, the mechanism of drop detachment needs to be known which, combined with the K-H instability, can be used to predict the

critical wave amplitudes and lengths necessary for drop formation and the onset of entrainment in the oil-water interface.

In this work, an experimental investigation is conducted to observe the conditions and mechanism leading to drop formation in horizontal liquid-liquid flows using a high speed video camera (see section 3.4.1). Based on the experimental findings, a model is developed that relates amplitudes and lengths of waves necessary for drop detachment. Combined with the wave stability criterion given by Eq. (5.19) (see section 5.2), the region of unstable wave amplitudes and lengths that lead to drop formation is defined. The model predictions are then compared with experimental wave characteristics obtained before and at the onset of drop entrainment.

6.2 Experimental Results

The visual observation and the analysis of the pictures showed clearly that no drops form when they are no waves or when the wave amplitudes are small. The careful analysis of the high speed pictures showed how drops detach from waves. Fig. 6.1 shows a deformed wave (6.1a) that keeps deforming (6.1b). Later, the crest of the wave starts to roll (6.1c), ready to detach. It is believed that drop formation becomes possible when the drag force acting on the wave crest, that resulted from the relative movement between the two phases, exceeds the retaining force of surface tension. From Fig. 6.1, it is clear that the water phase which moves at a higher velocity than oil starts to push or undercut the oil phase until drop breakage becomes possible. The deformed crest of the oil wave on the other hand will undercut the water phase. Both phases are believed to be responsible for the drop detachment.

In Fig. 6.2 an already deformed wave that has rolled and is undercut again by the water phase is shown. Pictures 6.2c and 6.2d show the detachment of the oil drop from the wave. Another example of wave deformation is shown in Fig. 6.3. From these pictures the following sequence of events for drop formation is deduced: waves deform under the influence of drag force resulting from the velocity difference between the two phases while surface tension force tends to preserve their original shape. When a deformed wave becomes flat on one side (See Fig. 6.1b) surface tension acts only on the curved side of the wave. At this point the wave is considered to reach its critical

condition and if drag force exceeds surface tension, the wave will deform further and drops will detach, otherwise the wave will return to its original form (see Fig. 6.4). This mechanism of drop formation is similar to the breakdown of disturbance waves by undercutting as described by Hewitt and Hall-Taylor (1970) and Ishii and Grolmes (1975). The difference in liquid-liquid flows is that both phases are believed to undercut each other and both oil and water drops may form as a result.

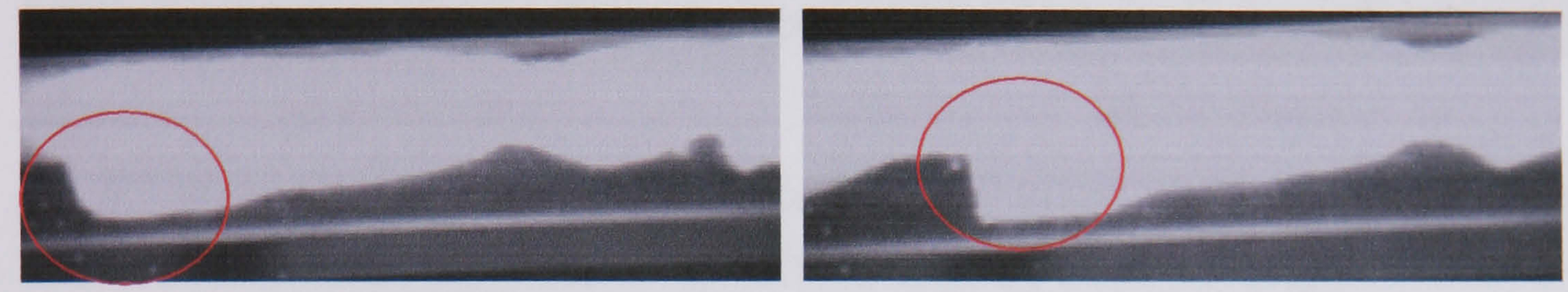

(a) t = 0 s (b) t = 0.008 s

(c) t = 0.024 s (d) t = 0.04 s

Fig. 6.1 Wave deformation caused by the relative movement of the two phases (U_{so} = 0.44 m/s, U_{sw} = 0.70 m/s). Flow direction is from left to right.

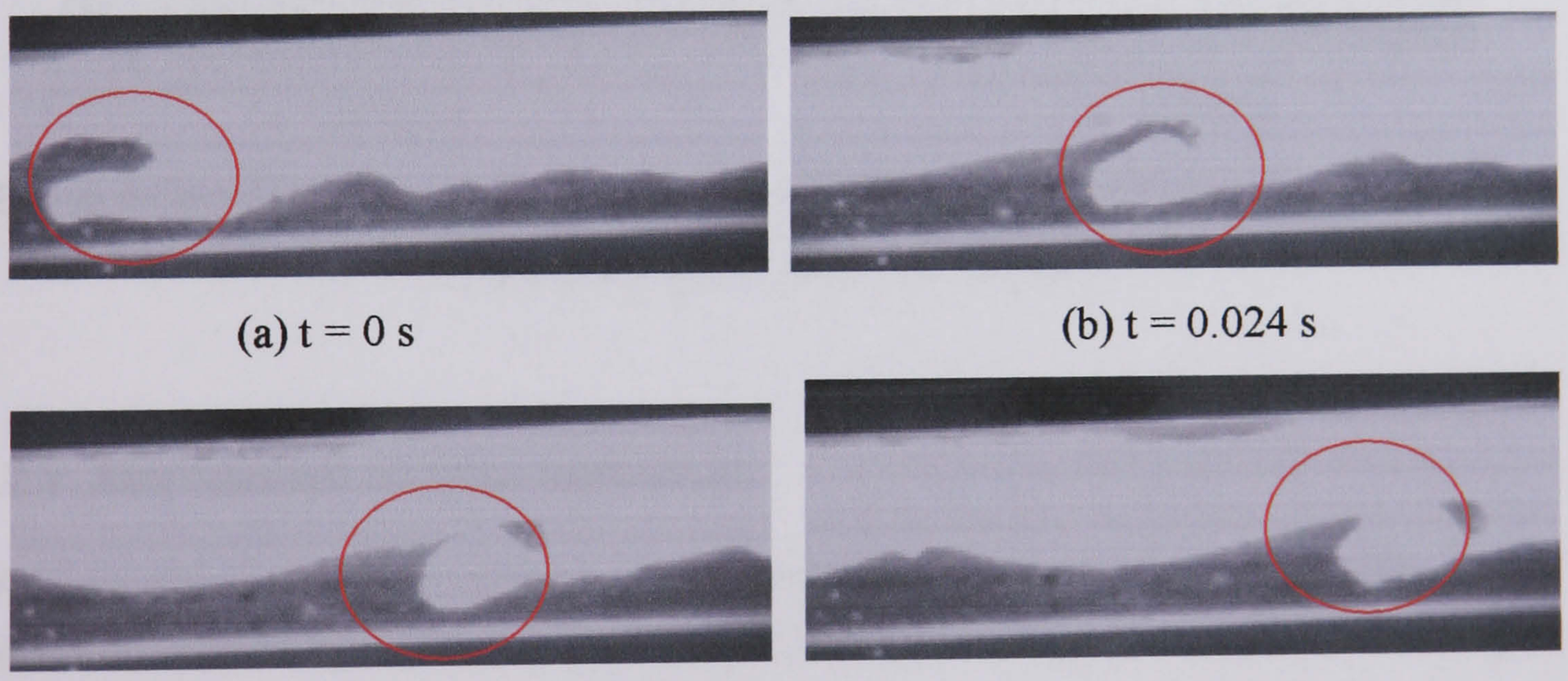

(a) t = 0 s (b) t = 0.024 s

(c) t = 0.032 s (d) t = 0.040 s

Fig. 6.2 Drop detachment from wave crest caused by the relative movement of the two phases (U_{so} = 0.44 m/s, U_{sw} = 0.50 m/s). Flow direction is from left to right.

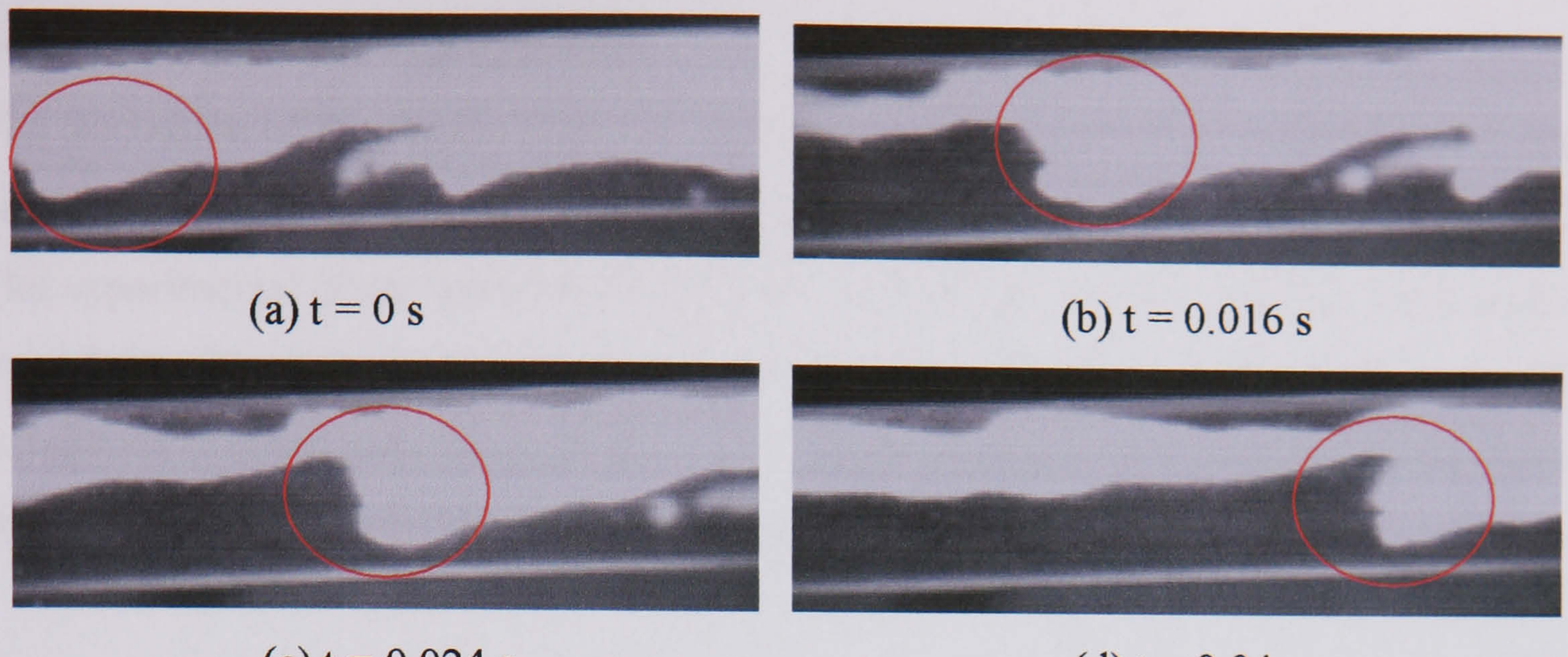

(a) t = 0 s (b) t = 0.016 s

(c) t = 0.024 s (d) t = 0.04 s

Fig. 6.3 Wave deformation caused by the relative movement of the two phases (U_{so} = 0.37 m/s, U_{sw} = 0.70 m/s). Flow direction is from left to right.

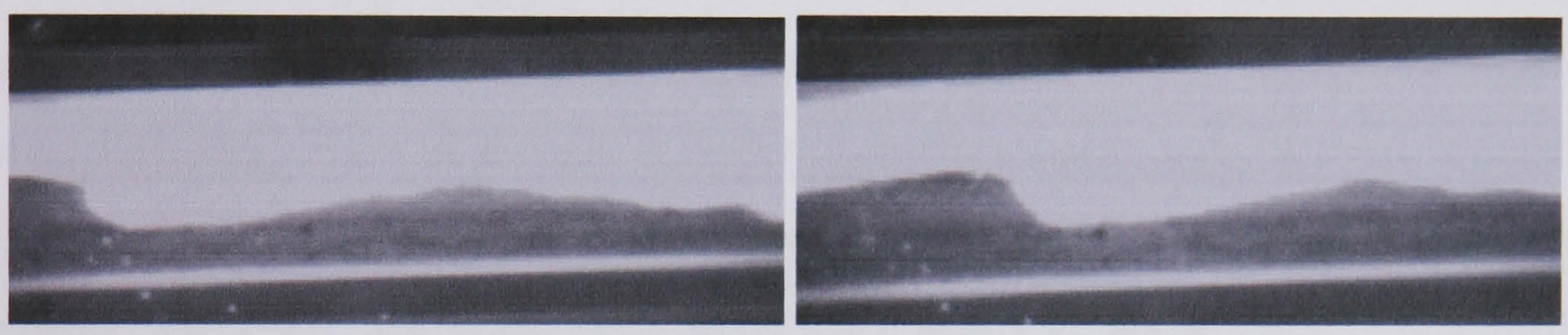

t = 0 s t = 0.008 s

t = 0.024 s t = 0.032 s

Fig. 6.4 Deformed wave returns to its original form (U_{so} = 0.37 m/s, U_{sw} = 0.50 m/s). Flow direction is from left to right.

6.2.1 Mechanism of drop formation

Based on the above the following mechanism is suggested for drop formation. Kelvin-Helmholtz instability will cause the wavy disturbance on the oil-water interface to grow in amplitude while interfacial tension and gravity will tend to stabilize it. When the destabilizing forces are greater than the stabilizing ones, waves become unstable. These unstable waves will continue to grow. Drops will eventually detach when the drag force acting on the wave crest that tends to deform it, becomes greater than the surface tension force that tends to prevent wave deformation.

6.3 Development of the Model

The discussion of the results from the stability equation in chapter 5 showed that at the onset of entrainment, some waves become unstable due to Kelvin-Helmholtz instability. The experimental observations in Section 6.2 showed that in this case the wave crests may form drops depending on the wave deformation as a result of the relative movement between the phases (Figs. 6.1-3). In this section a force balance on the wave crest is implemented to model drop detachment.

In gas-liquid *annular* flow a balance between drag and surface tension forces has been used to describe wave deformation and drop detachment. Ishii and Grolmes (1975), Kataoka et al. (1983) and Holowach et al. (2002) have employed this force balance on a wave crest when developing their models of droplet removal. According to Ishii and Grolmes (1975) entrainment occurs when the drag force on the liquid wave resulting from the high shear flow of the gas is higher than the surface tension force that tends to stabilize the wave; based on this a criterion for the inception of droplet entrainment was suggested. The same technique was applied by Kataoka et al. (1983) to develop an equation for droplet size distribution in *annular* two-phase flow.

Holowach et al. (2002) used the force balance method to determine the maximum volume of liquid that can be entrained from a wave. Combined with the critical wavelength calculated from interfacial stability using the inviscid pressure stress analysis, a correlation for the rate of entrainment in vertical *annular* two-phase flow was obtained. The force balance was performed on a three-dimensional sine wave. The maximum amount of liquid that can be entrained from the wave crest occurs when the sum of forces acting on the wave crest along the axis of the flow is zero. In other words,

$$\vec{F}_d + \vec{F}_g + \vec{F}_\sigma = 0 \tag{6.1}$$

where $\vec{F}_d$ is the drag force, $\vec{F}_g$ is the gravitational force and $\vec{F}_\sigma$ is the surface tension force.

In this study a force balance on the wave crest at the onset of entrainment is considered in a way similar to that suggested by Ishii and Grolmes (1975), Kataoka et al. (1983) and Holowach et al. (2002). It is, however, assumed that the drag force results from the difference in velocities between the oil and water phases rather than just the shearing

action of one of them, and that both phases can form drops. A finite two-dimensional sinusoidal wave (Fig. 6.5) is considered at the oil-water interface and a force balance is performed on the wave along the axis of the flow at the onset of entrainment (when the drop is about to form). For entrainment to occur, it is assumed that the drag force acting on the wave should exceed the resisting force of surface tension:

$$\vec{F}_d \geq \vec{F}_\sigma \tag{6.2}$$

In the development below oil waves are considered and oil drops are expected to form. This is because experimentally it is easier to observe oil wave deformation and oil drop formation. The force balance on the trough of the waves is illustrated in Figs. 6.5 and 6.

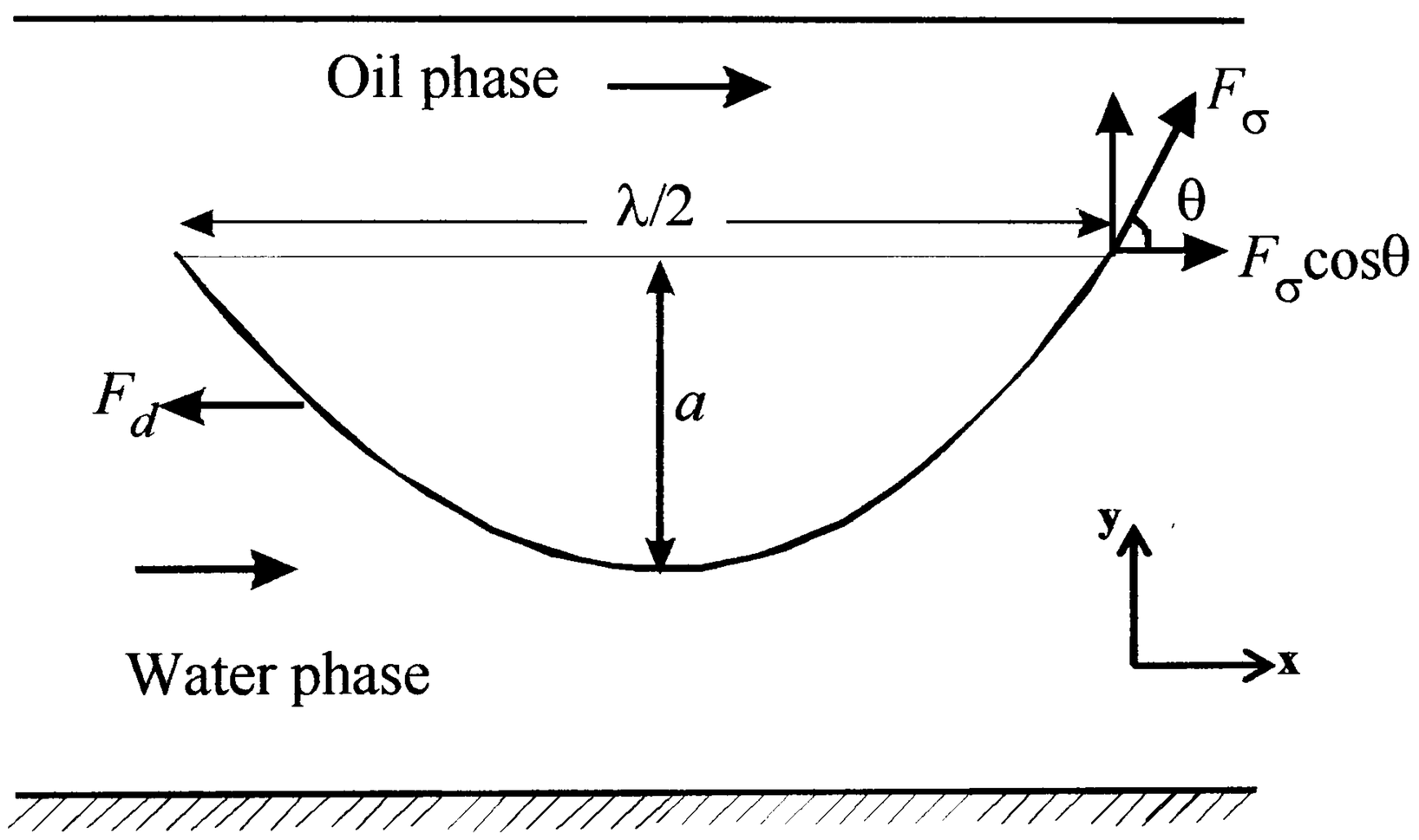

Fig. 6.5 Force balance on a two-dimensional sinusoidal wave on the oil-water interface (oil phase wave crest is pushed or undercut by the faster water-phase).

The drag and surface tension forces are assumed to act on the whole wave. The drag force is calculated by knowing the drag coefficient, the effective area normal to the flow on which it acts and the relative velocities between the two phases. On the other hand, surface tension forces in the flow direction do not have an effect for a symmetrical wave (as in Fig. 6.5). This is because the forces in the x-direction cancel out. When the wave starts to deform, surface tension on the rear of the wave tries to pull it back to its original form (Fig. 6.6). The highest effect of surface tension is expected when the front of the wave becomes flat before break-up.

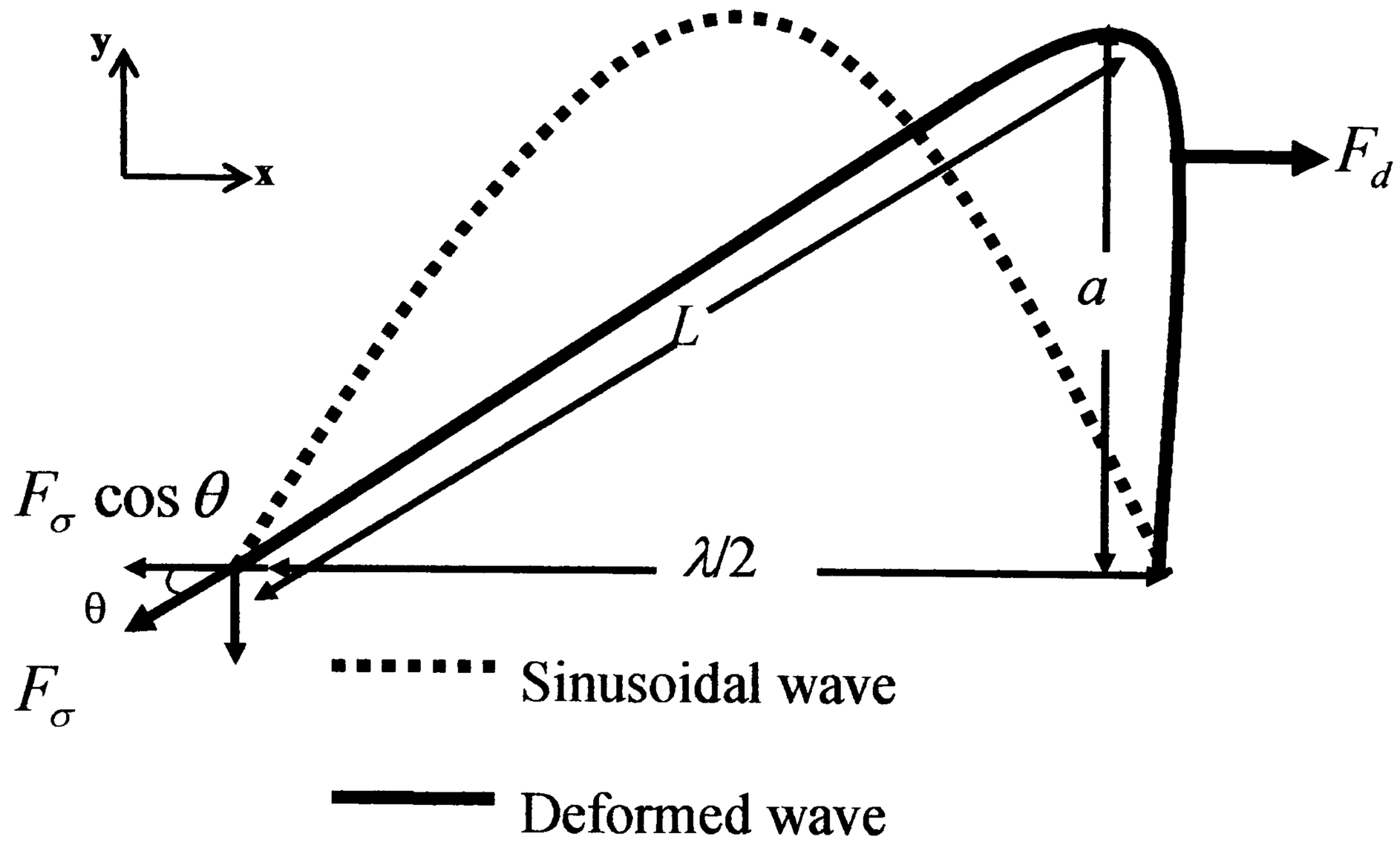

Fig. 6.6 Force balance on a deformed two-dimensional wave on the oil-water interface.

6.3.1 Drag force calculation

At the onset of entrainment, the drag force from the relative movement of the two phases (oil and water) tries to deform the wave. The drag force is given in terms of the drag coefficient C_d and the relative velocity between oil and water. For oil drop formation the oil wave area and the density of the water are used and the drag force becomes:

$$F_d = C_d A_{oil\ wave} \rho_w \frac{(U_w - U_o)^2}{2} \tag{6.3}$$

The relative velocity between oil and water is used instead of the wave velocity because it is believed that the velocities of both phases are responsible for wave breakage. For water drop formation, the density of water is replaced by the density of oil and the water wave area is used instead of the oil one in the drag force equation:

$$F_d = C_d A_{water\ wave} \rho_o \frac{(U_w - U_o)^2}{2} \tag{6.4}$$

The drag force is assumed to act on the whole wave to deform it, so the area A_{wave} is the cross sectional wave area normal to the flow (See section 5.2.1, Fig. 5.1b).

$$A_{oil\ wave} = (A_w - A_{w2}) = (A_{o2} - A_o) \tag{6.5}$$

To estimate the drag coefficient C_d, the results by Kataoka et al. (1983) are used. They related the drag coefficient to a critical Weber number for the volume median drop diameter entrained ($C_d = We/8$), based on the mechanism of shearing off the crest of roll waves in gas-liquid *annular* flow. This Weber number was then correlated to Reynolds numbers, viscosities and densities of the two phases from a wide range of experimental data. The following correlation for the drag coefficient was finally suggested:

$$C_d = 286\,\mathrm{Re}_{Lf}^{1/6}\,\mathrm{Re}_g^{-2/3}\left(\frac{\rho_g}{\rho_{Lf}}\right)^{1/3}\left(\frac{\mu_g}{\mu_{Lf}}\right)^{-2/3} \tag{6.6}$$

where Re_{Lf} and Re_g are the Reynolds numbers for the liquid film and the gas phase respectively.

As there are no data or correlations for the drag coefficient in liquid-liquid systems, the above equation was used initially in the current study. The equation was modified so that the gas Reynolds number is substituted by that of the faster phase (which in liquid-liquid systems can be either the oil or the water), while the density and viscosity of the gas are substituted by those of the upper (oil) phase and the density and viscosity of the liquid film are substituted by those of the lower (water) phase. In the case of oil drop formation water is the faster phase.

$$C_d = 286\,\mathrm{Re}_{slower\ phase}^{1/6}\ \mathrm{Re}_{faster\ phase}^{-2/3}\left(\frac{\rho_{upper\ phase}}{\rho_{lower\ phase}}\right)^{1/3}\left(\frac{\mu_{upper\ phase}}{\mu_{lower\ phase}}\right)^{-2/3} \tag{6.7}$$

where Re is given by

$$\mathrm{Re}_i = \frac{U_i D_i \rho_i}{\mu_i} \tag{6.8}$$

and i represents the respective phase, U is the in-situ phase velocity, D is the hydraulic diameter, ρ is the phase density and μ is the phase viscosity.

6.3.2 Surface tension force calculation

Surface tension on the other hand tries to resist deformation and to maintain the wave geometry. For a drop to break up, the sinusoidal wave deforms due to drag force and

becomes flat at its front side (see also Figs. 6.1b and 6.3c). This is assumed to be the maximum deformation that the surface tension force can handle, beyond which the wave will break to form a drop. At this point a drop will form if the drag force is greater than surface tension otherwise the wave will return to its original shape (see Fig. 6.4). Such deformation of the wave makes the surface tension force in the x-direction to act only on the rear side of the wave while it is almost zero at the front flat side as shown in Fig. 6.6. To calculate the surface tension force for a deformed wave, the shape of the wave is assumed to be triangular. This shape agrees with the experimental observations of deformed waves with flat fronts (see Fig. 6.1b and 6.3c) and it is also easy to handle.

The surface tension force acting along the slope on the rear side of the wave can be analyzed into two components (Fig. 6.6), one in the x-axis along the flow and the other in the y-axis normal to the flow. Since the force balance is in the direction of the flow (x-axis), only the net surface tension force acting on the wave in the x-direction is considered. This net surface tension force is the sum of all the forces along the length of the wave contact line with the interface. This is given in terms of interfacial tension (σ) and the length where the force acts upon. Since a two-dimensional wave is considered, the length where surface tension force acts will be the width of the pipe at the height of the interface, S_i, multiplied by 2. For the x-component of the force the angle θ between the surface tension force and the horizontal is also needed. The angle θ can be found from the Pythagorean Theorem for the assumed triangular wave (Fig. 6.6).

$$\cos\theta = \frac{(\lambda/2)}{L} \tag{6.9}$$

where $L = \sqrt{(a^2) + (\lambda/2)^2}$

The net surface tension force can then be expressed by

$$F_{\sigma,x-axis} = \sigma(2S_i)(\frac{\lambda/2}{L}) \tag{6.10}$$

For the wave to deform

$$\vec{F}_d \geq \vec{F}_\sigma \tag{6.11}$$

and from Eqs. (6.3) and (6.10), for oil drop formation Eq. (6.11) becomes:

$$C_d A_{oil\ wave} \rho_w \frac{(U_w - U_o)^2}{2} \geq \sigma(2S_i)(\frac{\lambda/2}{L}) \tag{6.12}$$

The same analysis can be applied to water waves and water drop formation.

6.3.3 Calculation procedures

In chapter 5, a new equation (Eq. 5.19) that separated the region between stable and unstable waves in *stratified* oil-water flow was developed with two unknowns, wavelength, λ, and wave amplitude, a. In a wave amplitude against wavelength graph, Eq. 5.19 is represented by a line (*stability line*) below which waves are stable while above it waves are unstable. Using the equation developed in this study (Eq. 6.12), another line (*entrainment line*) can be drawn in the same graph that defines the region where drag force is greater than surface tension force. In this region drop formation and entrainment will occur. The lines derived by the two equations are plotted in Fig. 6.7. The intersection of the two lines gives the minimum (*critical*) wavelength and amplitude below which no drops can form. The region above both the stability and entrainment lines will be known as the *entrainment region*. On the other hand, in the region between the two lines the waves are unstable but would have to grow more for drops to form (*unstable waves region*). Waves with characteristics below both lines will be stable (*stable waves region*).

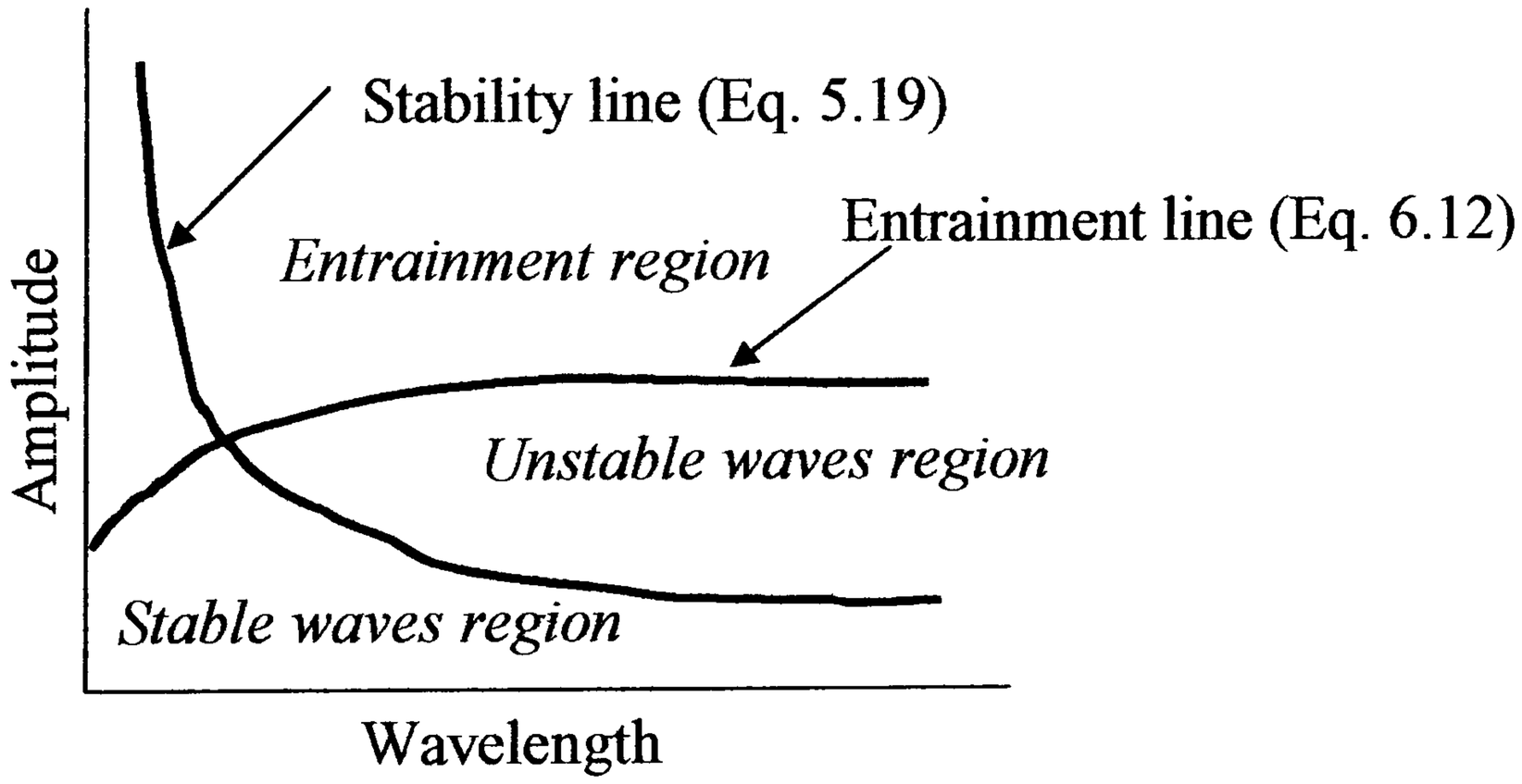

Fig. 6.7 The three regions of wave characteristics as defined by the stability line (Eq. (5.19)) and the entrainment line (Eq. (6.12)).

6.4 Comparison with Experimental Results

Experimental onset velocities together with Eqs. (5.19) and (6.12) are used to calculate critical wavelengths and amplitudes for the onset of entrainment. The experimental values were obtained in the pilot scale liquid-liquid flow system (see chapter 4). The

test section was a 38mm ID stainless steel pipe and measurements were conducted at 7m from the inlet (for a full description of these experiments see section 3.3). In the current system at the onset of entrainment oil drop formation was observed first. The onset phase velocities were found from the respective superficial velocities and phase hold up (see section 4.2). The input experimental parameters used for the calculations in this section are given in Table 6.1. The predicted critical wavelengths and amplitudes required to form drops at the different onset velocities, from the intersection of the entrainment and stability lines as shown in Fig. 6.7, are depicted in Fig. 6.8. Below these values no drops are expected to form. For example, at $U_{so} = 0.40$,$U_{sw} = 0.40$ m/s drops form from waves with length equal to 4.5 cm and amplitude equal to 5.4 mm. It can be seen that as the critical wavelength decreases the critical amplitude decreases as well.

U_{so}, m/s	U_{sw}, m/s	h_w, mm	C_v, m/s
0.05	0.55	28	0.48
0.20	0.45	20	0.72
0.40	0.40	16.7	0.84
0.55	0.25	11.3	1.00

Table. 6.1 Experimental input parameters at the onset of entrainment used for the calculation of critical wave characteristics

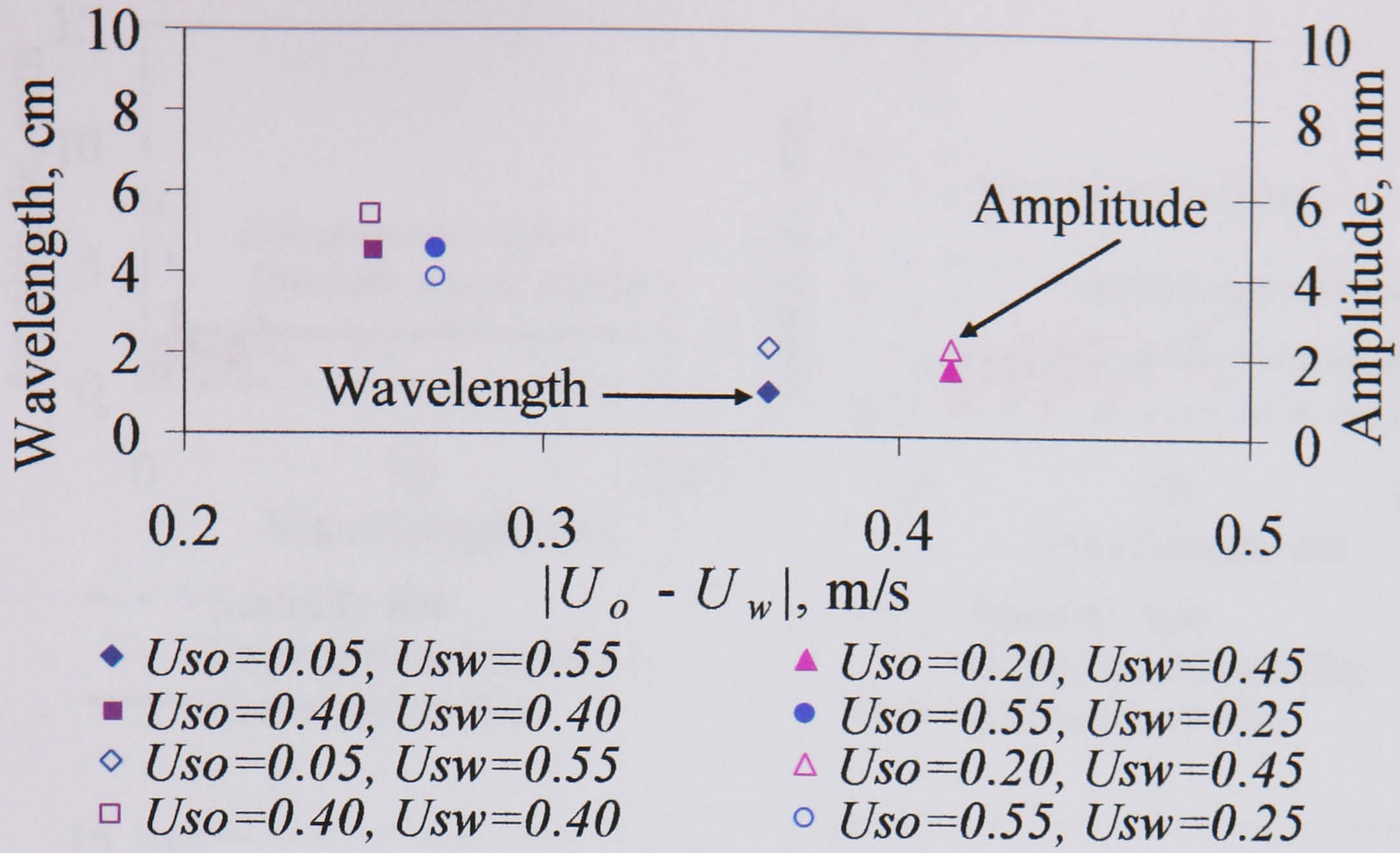

Fig. 6.8 Critical wave amplitudes (open marks) and lengths (full marks) required for drop formation at different entrainment onset velocities. All the superficial velocities are in m/s.

Wave characteristics at entrainment onset conditions obtained experimentally are compared in Fig. 6.9 with the stability and entrainment lines. Waves with characteristics above the entrainment line are unstable and also drag force is greater than surface tension which will lead to drop formation. Waves that fall between the two lines are considered to be unstable but they are not yet forming drops. These waves have to cross the entrainment line for drops to form. In agreement with the model there are waves above the entrainment line in most cases, suggesting that drops are forming, which is what was found by visual observation. Even in the case (Fig. 6.9c) where no measured waves are above the entrainment region, many waves are in the unstable region. As unstable waves propagate along the test section their amplitude and wavelength could change so that they may form drops. In addition, according to entrainment equation (Eq. 6.12) and the results shown in Fig. 6.9, there is always a finite amplitude that the wave has to reach before drop detachment becomes possible. This agrees with the experimental observations in section 4.1 which showed that no drops form when waves are absent or their amplitudes are small.

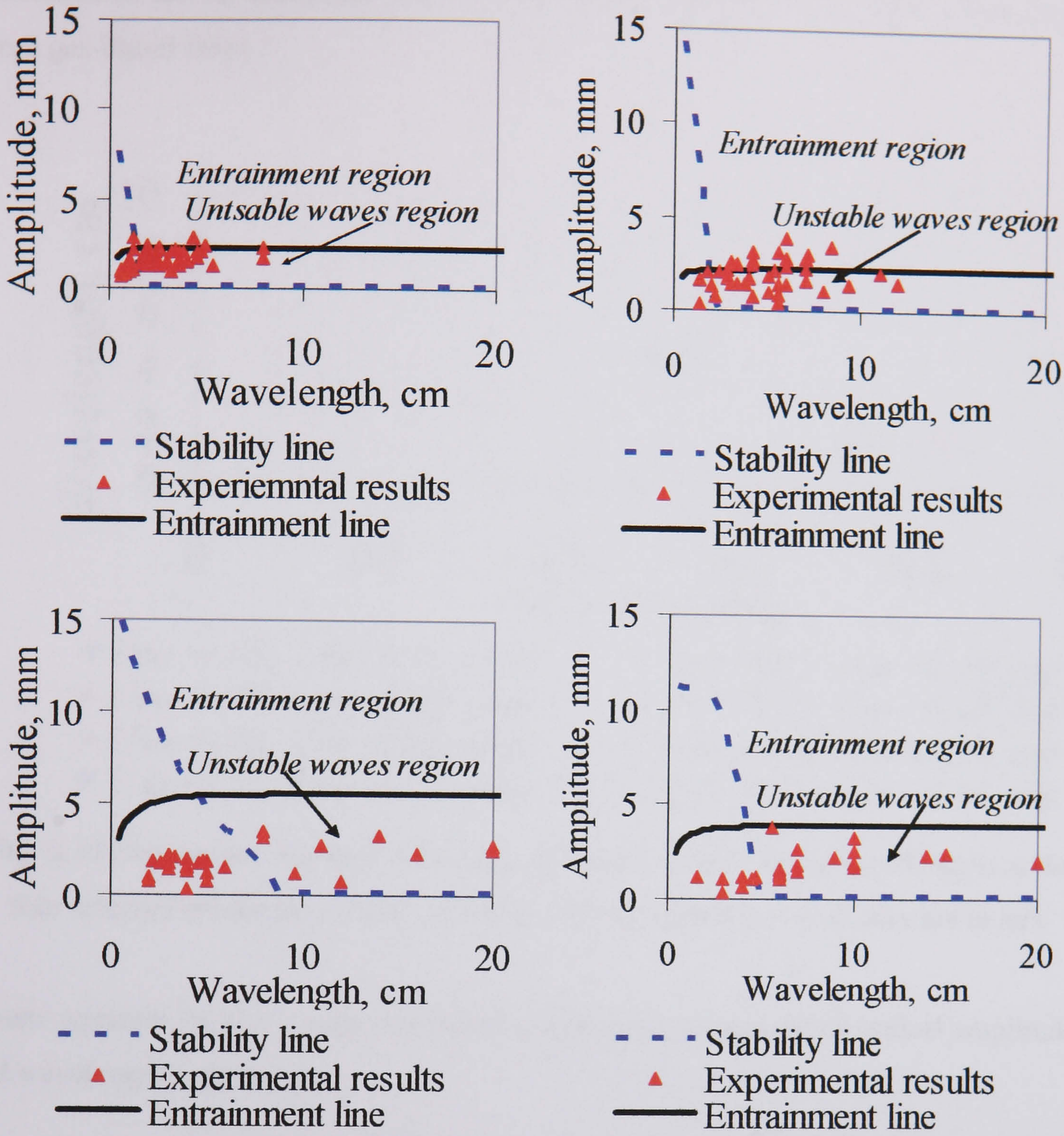

Fig. 6.9 Experimental wave characteristics at the onset of entrainment in relation to wave stability and entrainment lines; (a) U_{so} =0.05, U_{sw}=0.55m/s, (b) U_{so}=0.20, U_{sw}=0.45m/s, (c) U_{so}=0.40, U_{sw}=0.40 m/s, (d) U_{so}=0.55, U_{sw}=0.25 m/s.

It is more difficult to define the experimental critical amplitudes and wavelengths. Here they are taken as the minimum amplitudes and lengths that cross the stability line since no drops are expected to form below it. Thus at U_{so} =0.05, U_{sw}=0.55m/s the minimum experimental amplitudes and wavelengths will occur at 2.8 mm and 1.3 cm respectively. These experimental values are compared with the predicted ones in Fig. 6.10. The experimental values are slightly underpredicted for U_{so} =0.40, U_{sw}=0.40m/s, while they are predicted well for U_{so}=0.05, U_{sw}=0.55 m/s, U_{so}=0.20, U_{sw}=0.45 m/s and U_{so}=0.55, U_{sw}=0.25 m/s. The difference in the results of U_{so} =0.40, U_{sw}=0.40m/s could be

attributed to the C_d coefficient used for the calculation (Eq. 6.7), which was adjusted from gas-liquid flows.

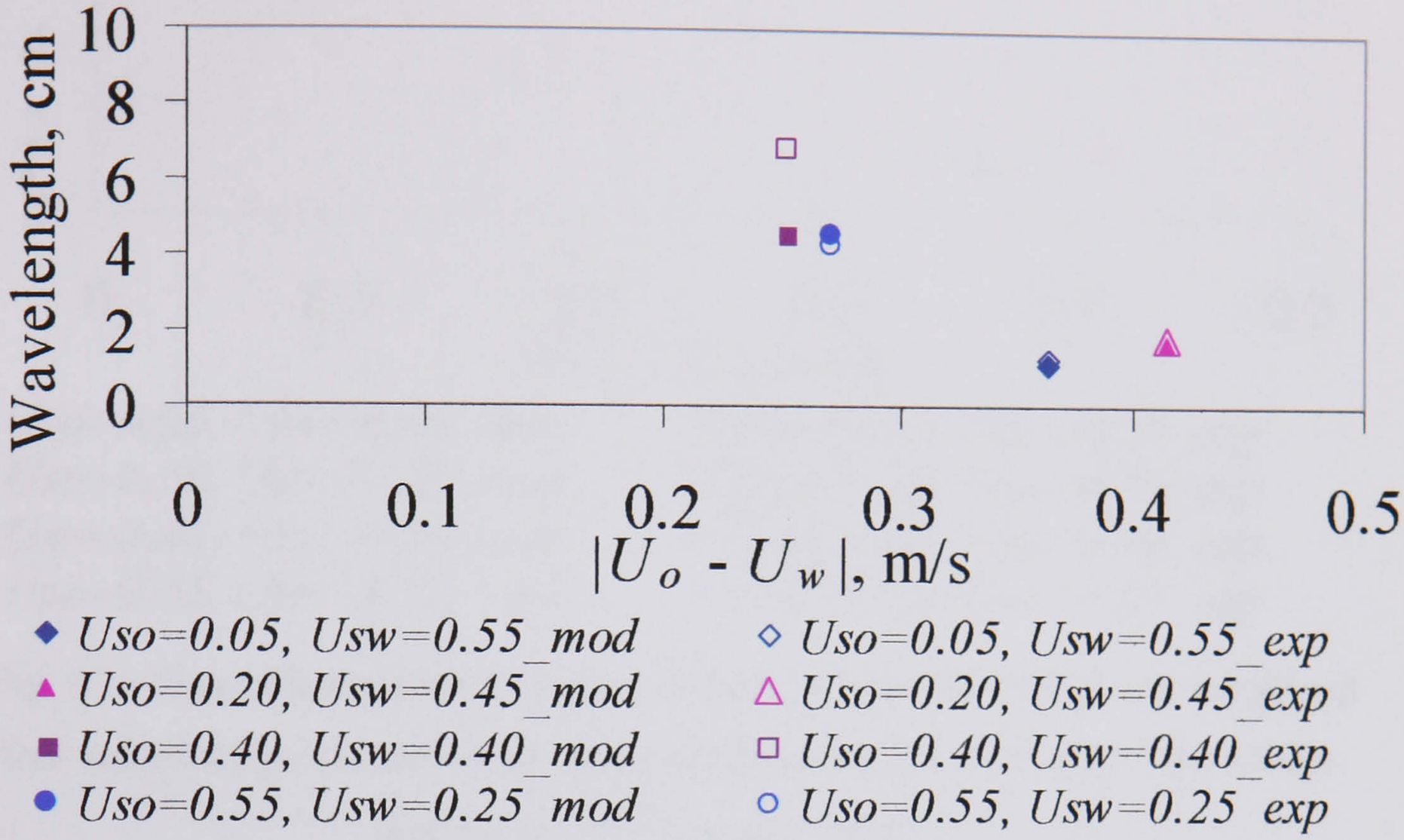

Fig. 6.10 Comparison between predicted and experimental critical wavelengths at the four selected entrainment onset velocities. All the superficial velocities are in m/s.

A new equation for C_d is suggested based on the above experimental critical amplitudes and wavelengths, given by:

$$C_d = 4.9\times10^{-8} \times \mathrm{Re}_o{}^{0.77} \times \mathrm{Re}_w{}^{0.86} \times \left(\frac{\mu_o}{\mu_w}\right) \tag{6.13}$$

In this equation compared to Eq. (6.7) the Reynolds numbers of the two phases and the viscosity ratio were retained to fit the experimental data but the density ratio was removed assuming that the effect of density is not very significant in liquid-liquid flows. Using this new equation for C_d, the model was able to predict even better the experimental critical wave characteristics, as shown in Fig. 6.11. In Fig. 6.12 the region where entrainment occurs using this new C_d equation is depicted. In all cases now waves appear at or above the entrainment line indicating drop formation.

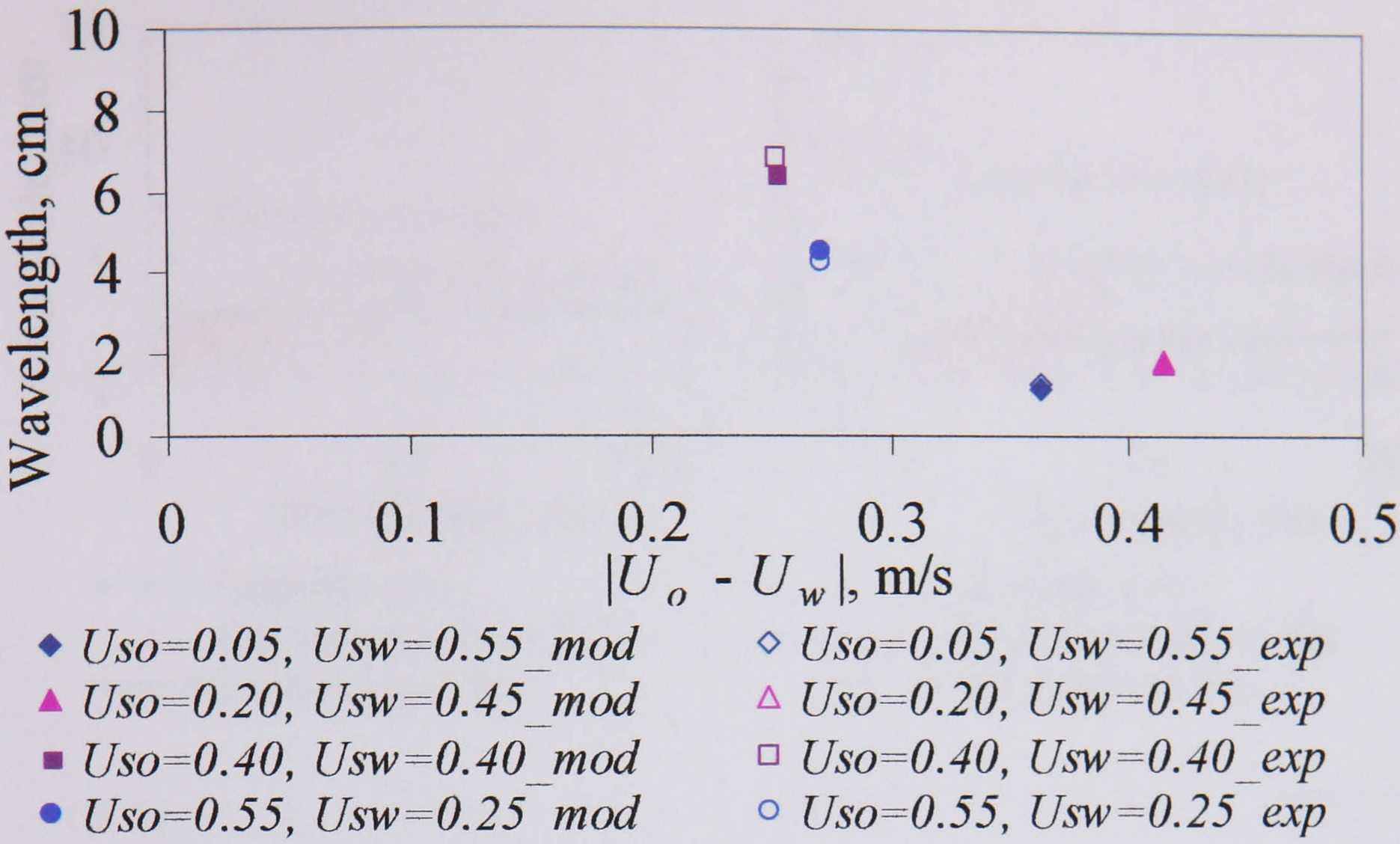

Fig. 6.11 Comparison between predicted and experimental critical wavelengths at the four selected entrainment onset velocities using the new C_d.(Eq. (6.13)). All the superficial velocities are in m/s.

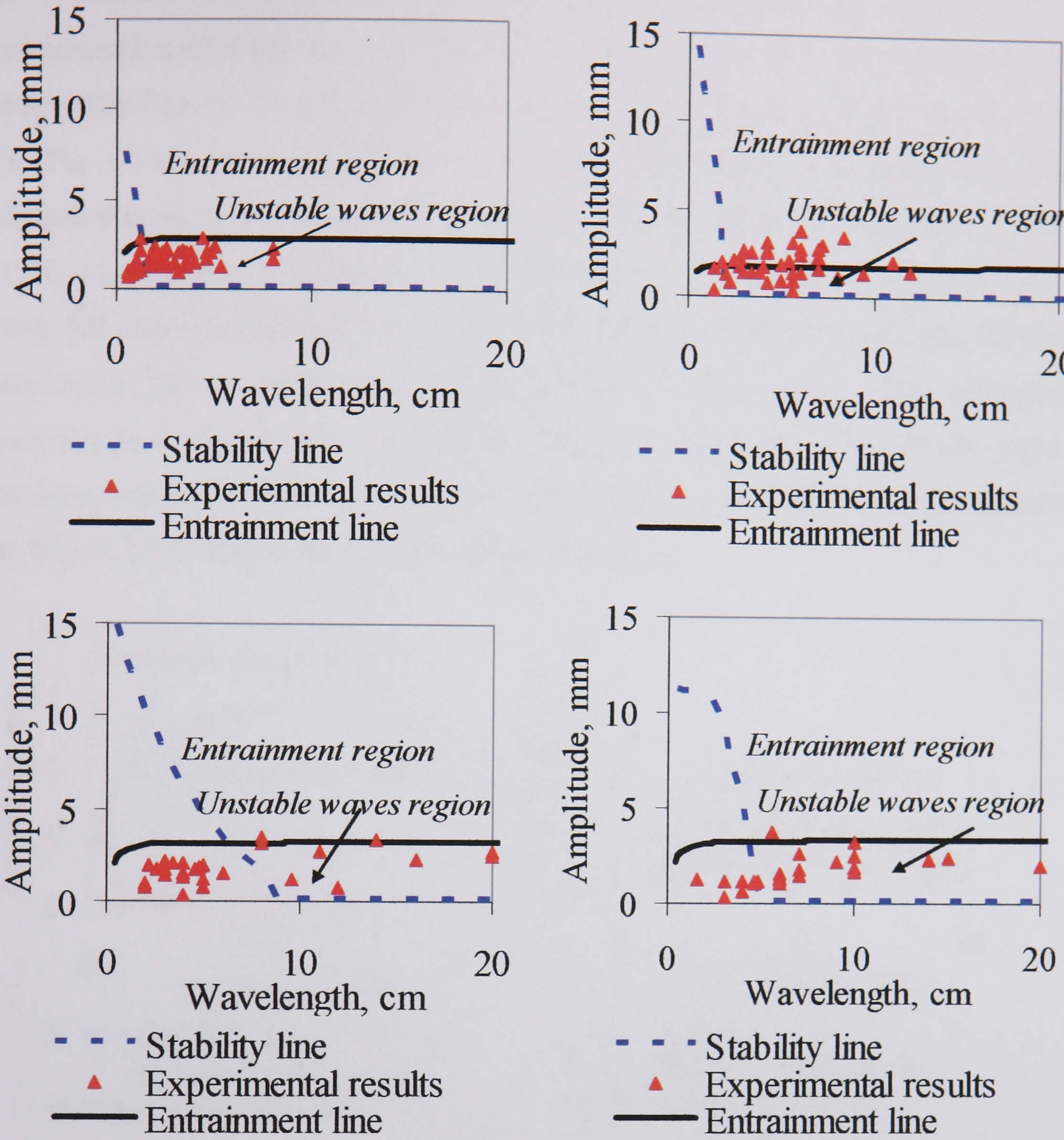

Fig. 6.12 Experimental wave characteristics at the onset of entrainment in relation to wave stability and entrainment lines when the new C_d (Eq. (6.13)) is used; (a) U_{so} =0.05, U_{sw}=0.55m/s, (b) U_{so}=0.20, U_{sw}=0.45m/s, (c) U_{so}=0.40, U_{sw}=0.40 m/s, (d) U_{so}=0.55, U_{sw}=0.25 m/s.

6.5 Model Validation Against Experimental Results

6.5.1 Flow pattern transitions

6.5.1.1 Stainless steel pipe (38 mm ID)

From the experimental results in the stainless steel, 38 mm ID test section, three conditions were selected to show the development of wave characteristics at U_{so} = 0.20 m/s with increasing water velocity as the boundary from *stratified* to *dual continuous*

flow is crossed. Waves were studied with a conductivity probe (see section 4.3). The experimental results are shown in Fig. 6.13 against the stability and entrainment lines predicted by Eqs. (5.19) and (6.12) respectively using the C_d (Eq. (6.13). For $U_{sw} = 0.20$ m/s (Fig. 6.13a), all waves fall below both the stability and entrainment lines which indicates that all waves are stable and they will not form drops (they will decay). At $U_{so} = 0.20$, $U_{sw} = 0.40$ m/s (close to the onset of entrainment) although a large number of waves fall above the stability line (Fig. 6.13b) and are unstable, few of them fall on the entrainment line so drops may or may not form from them. The experimental observations, however, did not show any drops at these conditions. At the onset of entrainment at $U_{so} = 0.20$, $U_{sw} = 0.45$ m/s, many waves are found above the entrainment line (Fig. 6.13c). These waves will break to form drops.

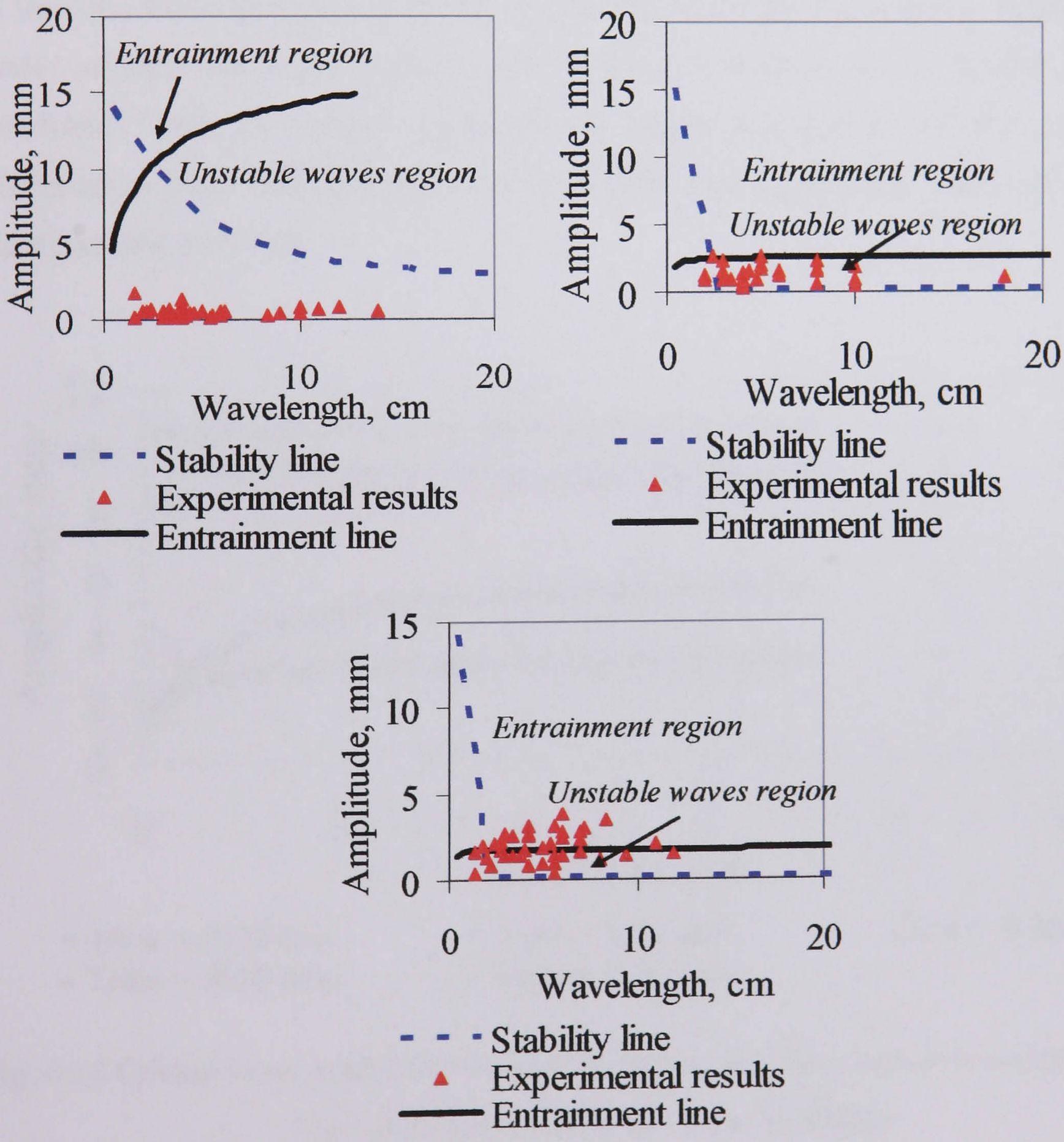

Fig. 6.13 Comparison between model (lines) and experimental (points) wave characteristics; (a) U_{so} =0.20, U_{sw}=0.20 m/s, (b) U_{so}=0.20, U_{sw}=0.40 m/s, (c) U_{so}=0.20, U_{sw}=0.45 m/s.

6.5.1.2 *Acrylic pipe (14 mm ID)*

From the results in the acrylic, 14 mm ID test section (see section 4.1.2), U_{so} = 0.23 and 0.44 m/s are chosen for different water velocities for the experimental system used in this study to validate the model. The measured interface height was used with Eq. 6.12 to predict the critical amplitude required to form drops at the above velocities. Fig. 6.14 shows the critical values required to form drops at U_{so} = 0.23, it is clear that required amplitudes decreases as the water velocities increase. All the amplitudes values are high so no drops are expected to form at the above conditions which agree with the experimental findings where *stratified* flow are observed at this conditions. At U_{so} = 0.23, U_{sw} = 0.50 m/s (just prior to the transition to *slug* flow), the required amplitude is about 3mm while the maximum amplitude observed using the high speed video camera is less than this value (around 2mm). However, it is clear also that any increase in the water velocity above the 0.50 m/s will result to a decrease in the critical predicted amplitude while the waves amplitude will continue growing and this indicates a transition to other flow pattern (could be *dual* by forming drops or *slug*) which is *slug* flow (see section 4.1.2).

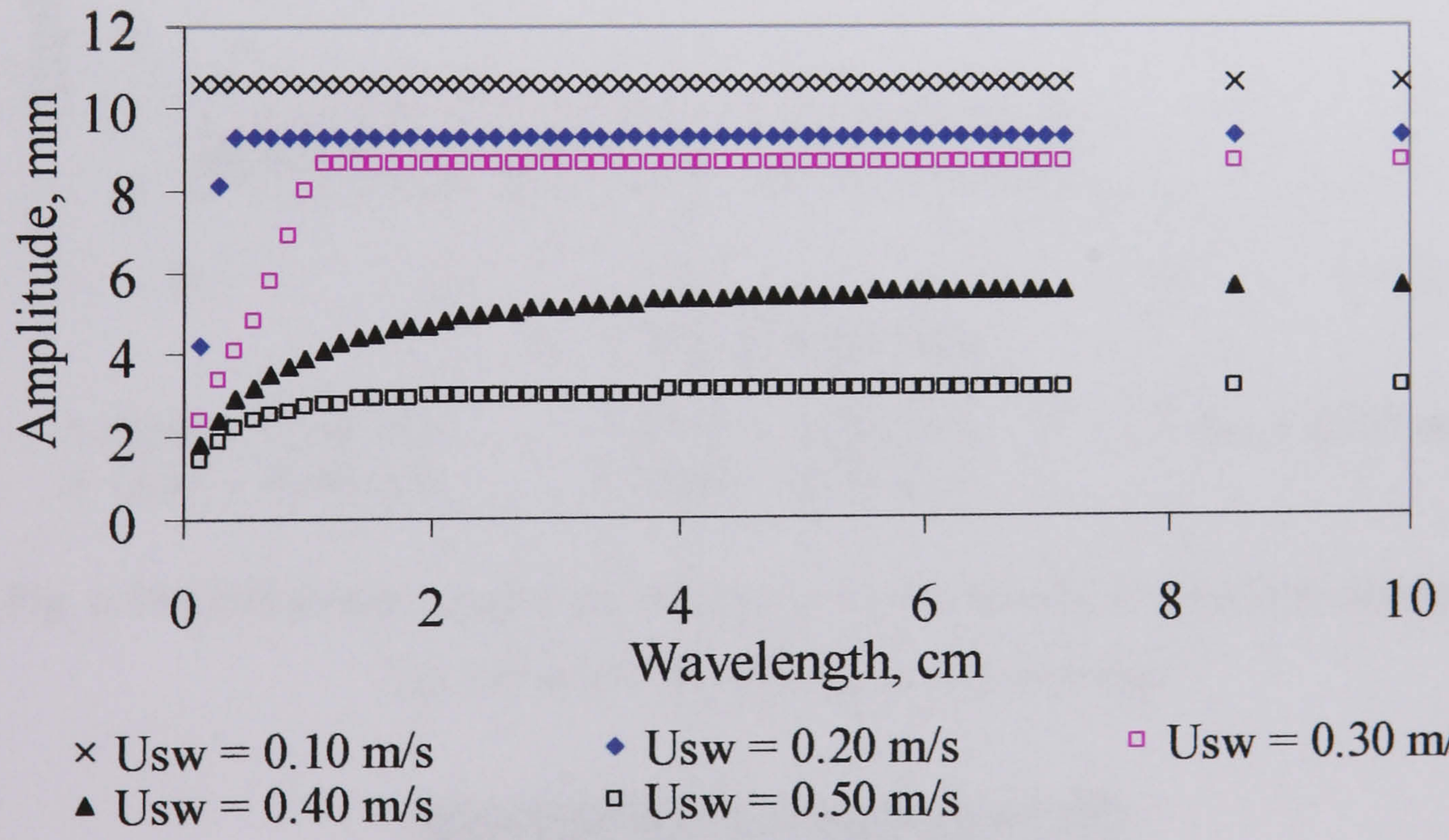

Fig. 6.14 Critical wave amplitude required to form a drop for a certain wavelength at the U_{so} = 0.23 m/s for different water velocities

For U_{so} = 0.44 m/s drop formation at the oil-water interface of *stratified* flow is found at U_{sw} = 0.30 m/s (see section 4.1.2). The measured interface height was used to find the

actual phase velocities required in Eq. (6.12) to calculate the entrainment line for the different water velocities (Fig. 6.15). It can be seen that the required amplitudes at U_{sw} = 0.10 and 0.20 m/s are extremely high so all the waves at these conditions are expected to fall below the entrainment line indicating *stratified* flow, as was also found experimentally (see section 4.1.2). The high speed pictures show that the maximum amplitudes observed at these conditions do not exceed 1.5 mm. At U_{so} = 0.44, U_{sw} = 0.30 m/s (where the onset of drop formation is found experimentally), the required amplitudes to form drops are around 2 mm. The pictures obtained using the high speed video camera reveal that some waves can reach such amplitudes (see Fig. 6.16) which means that some waves will reach the entrainment line and they will form drops. At higher water velocities (U_{sw} = 0.4 and 0.5 m/s) where more drops are found in the interface, the required amplitudes further decrease.

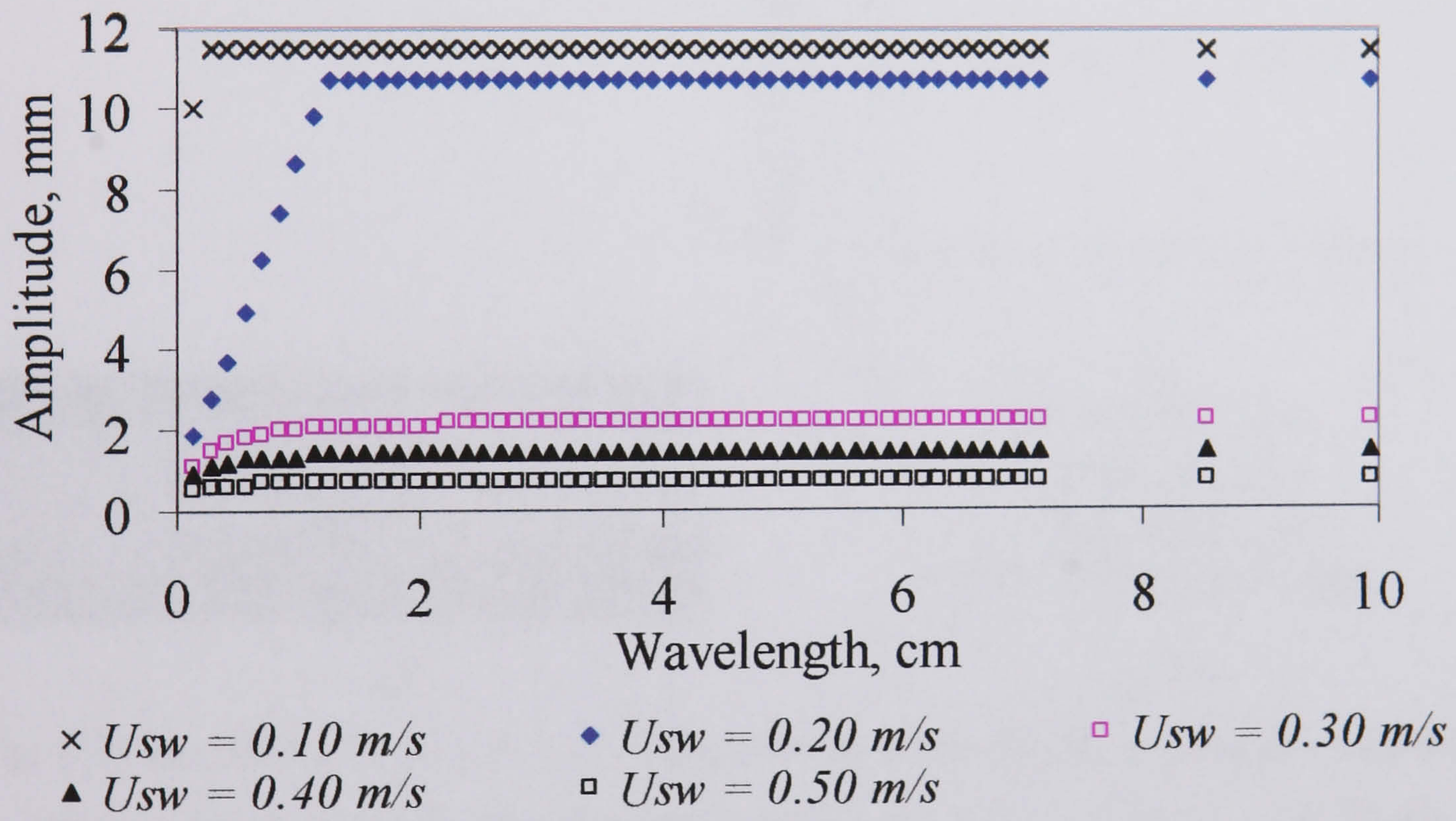

Fig. 6.15 Critical wave amplitude required to form a drop for a certain wavelength at U_{so} = 0.44 m/s for different water velocities

Fig. 6.16 Waves found experimentally to reach an amplitude of about 2mm at U_{so} = 0.44, U_{sw} = 0.30 m/s.

6.5.2 Validation against characteristics of waves that result in drop formation

During the experiments described in section 6.2 on the mechanism of drop formation, a number of cases were captured at which drops are detaching from wave crests of oil-water flow. Drops should form from wave crests when the amplitude and length of these waves fall in the entrainment region as defined in Fig. 6.7. Drops ready to detach from the tops of deformed oil waves are shown in Figs. 6.17a, 18a and 19a for three different conditions. As can be seen in Figs. 6.17b, 18b and 19b the amplitudes and lengths of these waves in all three cases do fall in the predicted entrainment region. The model is therefore able to predict the critical lengths and amplitudes at which waves are able to form drops.

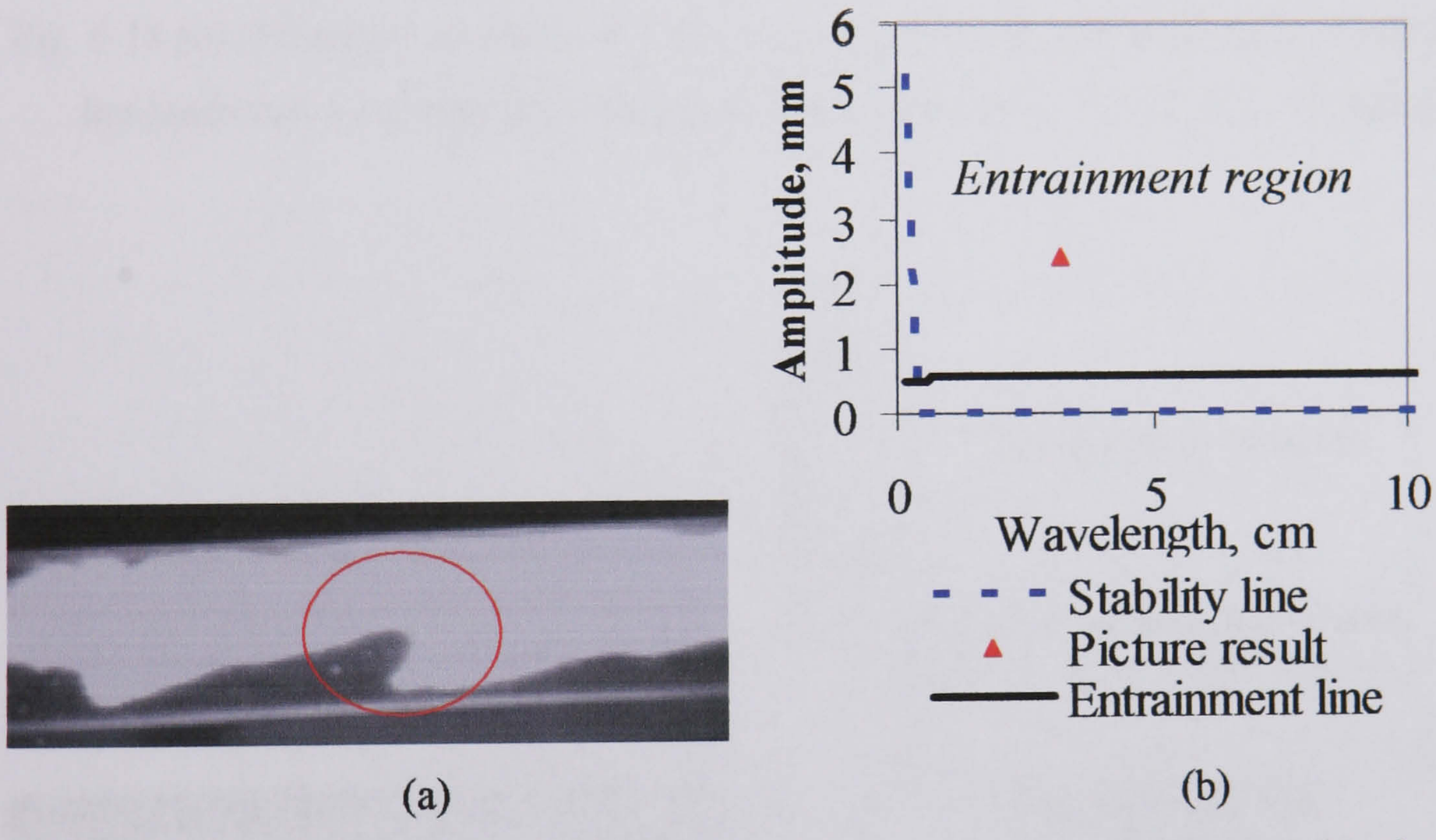

Fig. 6.17 (a) Deformed oil wave. (b) Measured wave amplitude and length in relation to the predicted wave stability and entrainment lines at $U_{so} = 0.44$, $U_{sw} = 0.70$ m/s.

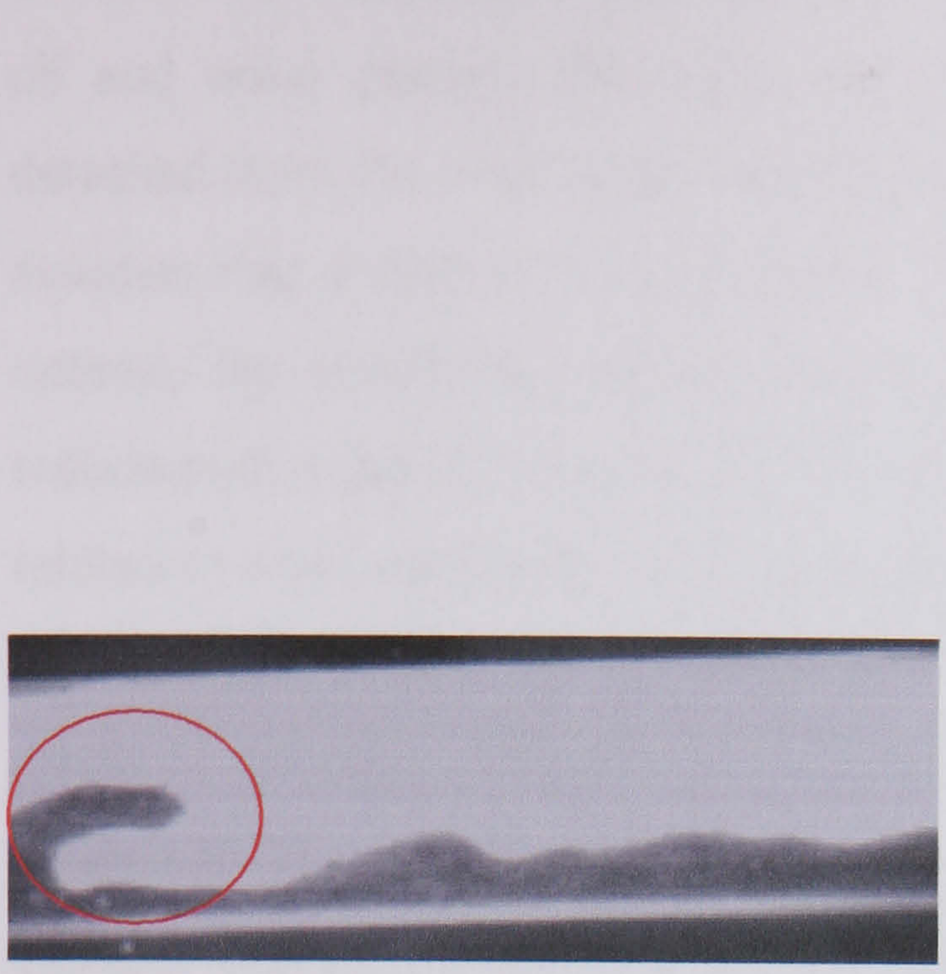

(a)

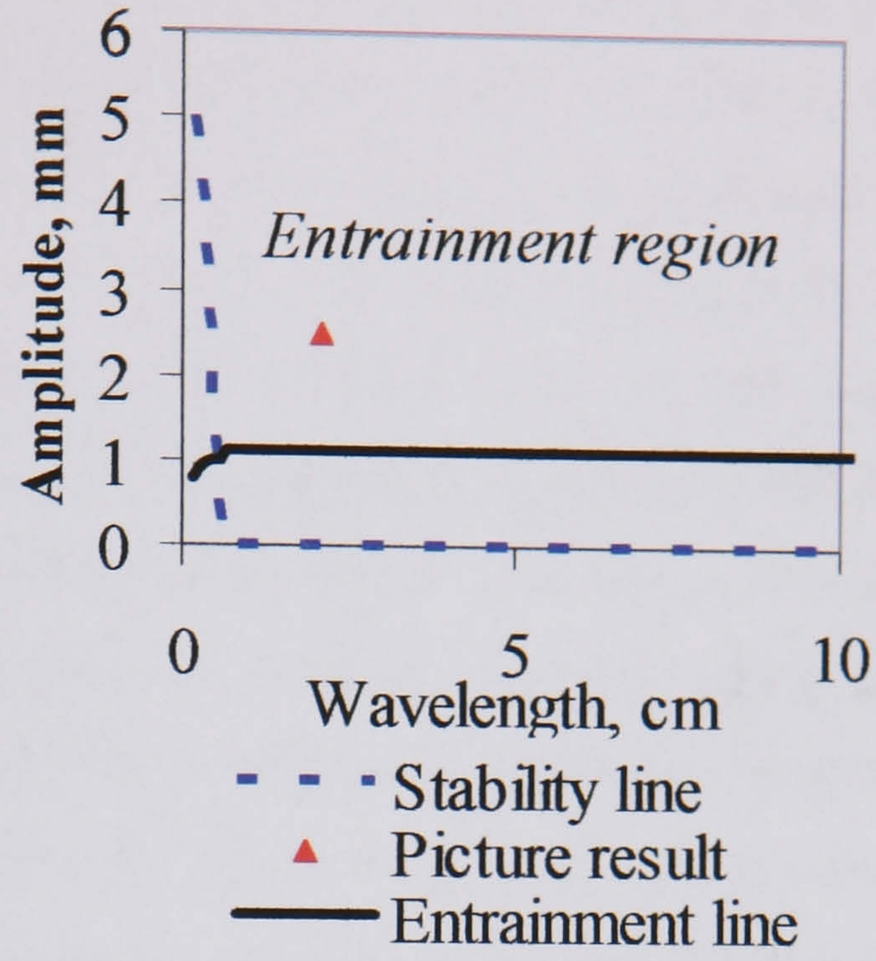

(b)

Fig. 6.18 (a) Deformed oil wave. (b) Measured wave amplitude and length in relation to the predicted wave stability and entrainment lines at $U_{so} = 0.44$, $U_{sw} = 0.50$ m/s.

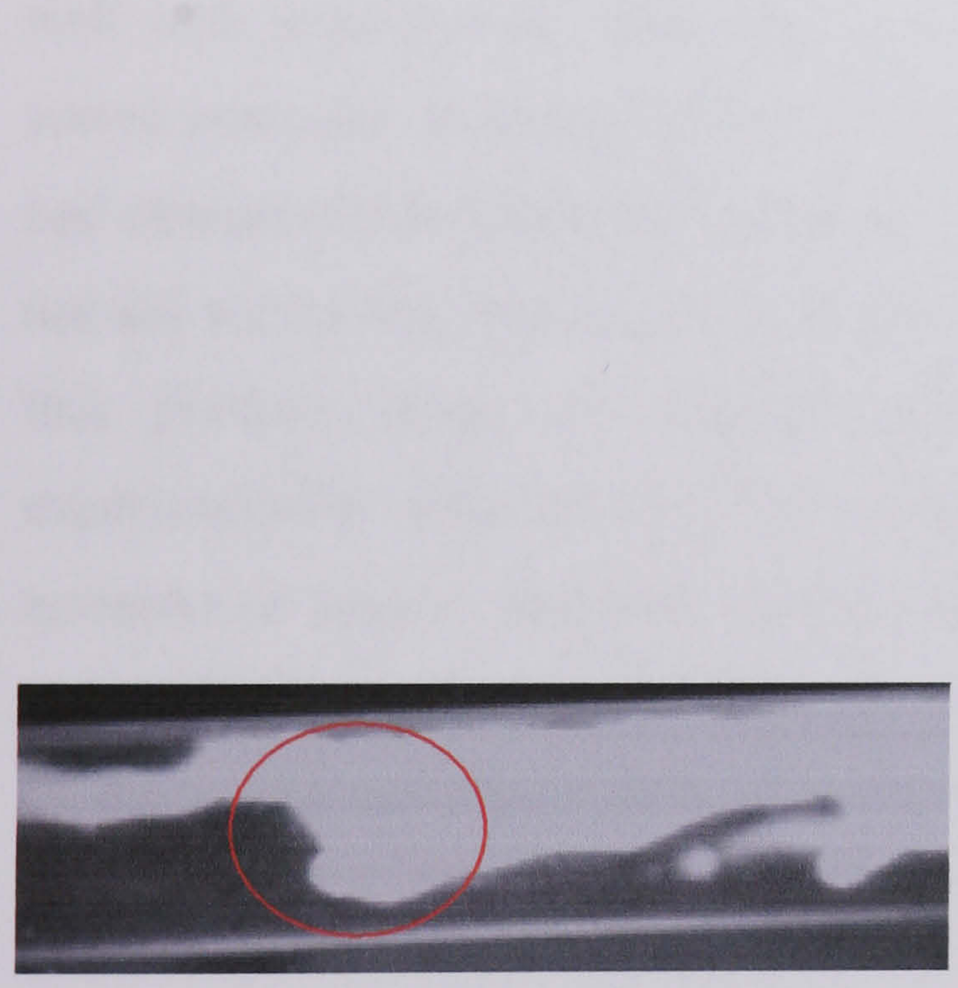

(a)

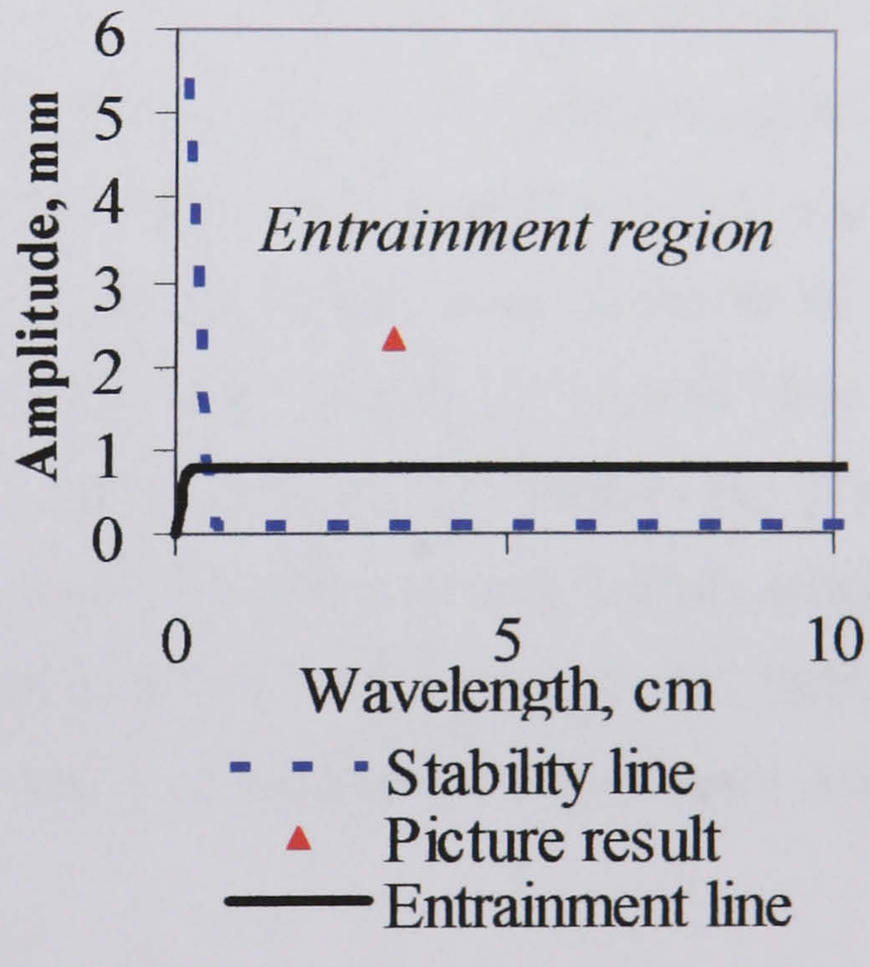

(b)

Fig. 6.19 (a) Deformed oil wave. (b) Measured wave amplitude and length in relation to the predicted wave stability and entrainment lines at $U_{so} = 0.37$, $U_{sw} = 0.70$ m/s.

6.6 Summary

The conditions and mechanism leading to drop formation from the wave crests in wavy *stratified* oil-water flow and to the transition to *dual continuous* flow were investigated

in this study. Drops were found to form as a result of the relative movement between the oil and water phases. The faster phase will undercut the other one until a drop is detached from the wave crest. Based on this observation a model was developed which assumes that a drop will detach from a wave when the drag force acting on the wave exceeds the stabilizing surface tension force in the flow direction. In the suggested entrainment equation (Eq. 6.12) the critical wave length for droplet formation was related to wave amplitude. This equation can be used together with Eq. (5.19) on wave stability (see chapter 5) to define three regions in a wave amplitude against length graph. In the region below both lines (*stable waves region*) the waves are stable and no drops can form. In the region above both lines (*entrainment region*) the waves are unstable and also drag force exceeds the surface tension force so that drops can form from the wave crests. Finally in the region between the two lines (*unstable waves region*) the waves are unstable but would need to grow further before any drops can detach from them. The critical minimum amplitudes and wavelengths required for drop formation, found from the intersection of the two lines (Eqs. (5.19) and (6.12)), agreed well with experimental data when a new correlation for the drag coefficient on the waves was used. In *stratified* flow it was found that all waves measured experimentally had characteristics below the entrainment line while in *dual continuous* flow some (but not all) waves had characteristics above the entrainment line; these would be the waves that produce drops. In addition amplitudes and lengths of waves that were experimentally observed to form drops were found to be within the predicted entrainment region. Thus the model can predict satisfactorily the critical amplitudes required to form drops at the onset of entrainment. Knowing the amplitudes and lengths of the waves, the model can predict the transition between *stratified wavy* and *dual continuous* flow.

CHAPTER 7

Entrained Fraction and Drop Size Distribution in the Dual Continuous of Horizontal Oil-Water Flows

This chapter describes the experimental results from the impedance and dual impedance probes during *dual continuous* flow. The local volume fractions obtained along a diameter vertically, horizontally and at 45° from the horizontal in a pipe cross section from the impedance probe are used to find the phase distribution. The results are then used to calculate entrained fraction of oil in water and water in oil as described in section 7.2. This section also presents the effect of inlet geometry on the entrainment of each phase into the other. Section 7.3 briefly shows chord length distributions obtained from the impedance probe and the effect of distance from the interface on them at different conditions. Drop size distributions resulting from transformation of the chord length distributions are presented in section 7.3. Finally, a summary is given in section 7.4.

7.1 Local Volume Fractions

7.1.1 Inlet section (T-junction with 90° bend)

The inlet section with the bend represents the old inlet section before the modification (see section 3.2.1.1). In this inlet geometry, the oil and water are introduced via a T junction and then flow through a 90° bend before entering the test section.

Fig. 7.1 to 7.4 show the local volume fraction in the pipe cross section for different water superficial velocities at a constant oil superficial velocity. In all cases *dual continuous* flow exists. The numbers along the abscissa are the fraction of the diameter

from the 0-wall position. Volume fraction equal to 1 indicates pure oil while 0 represents pure water.

All the figures demonstrate that the dispersion originates at the interface and the degree of dispersion at the interface increases as the superficial water velocity increases while it occupies more than 45% of the pipe at U_{so} = 1.10, U_{sw} = 1.10 m/s. It is interesting that at U_{so} = 1.10, U_{sw} = 0.80 m/s (Fig. 7.3) the pipe core is occupied by pure oil (see results for horizontal direction) while close to the wall the flow is water continuous (oil fraction < 68%). This indicates an oil-water interface that is curved upwards.

The integration of these local volume fractions gives the phase distribution of the whole pipe cross section (see appendix D.1). The entrained fractions of each phase into the other are then calculated assuming continuous water phase exists below 68% local oil percent. This assumption is based on experimental measurements on phase continuity using conductivity probe.

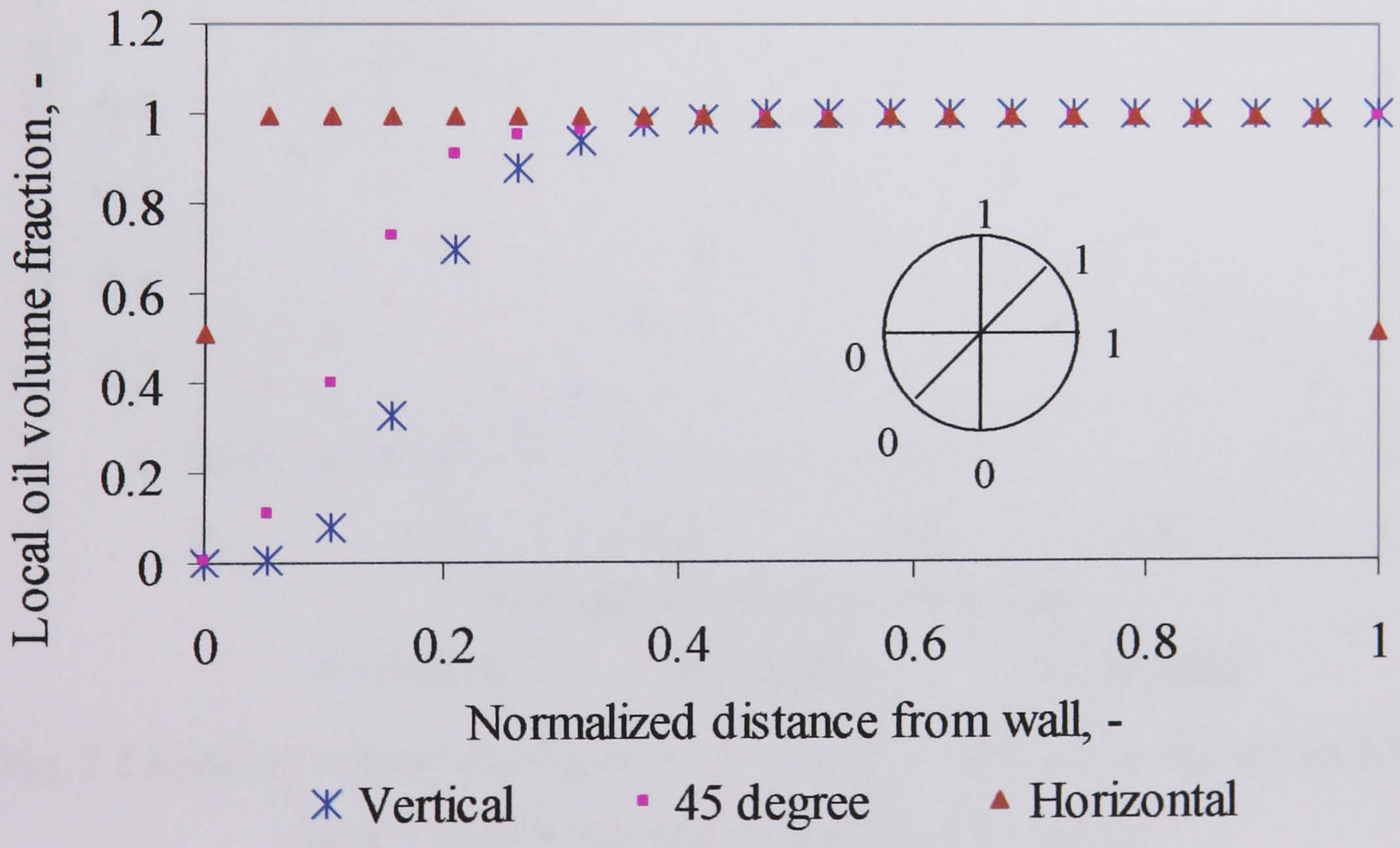

Fig. 7.1 Local volume fraction at U_{so} = 1.10, U_{sw} = 0.20 m/s in the 38 mm ID test pipe, 7 m from the inlet (T-junction inlet section).

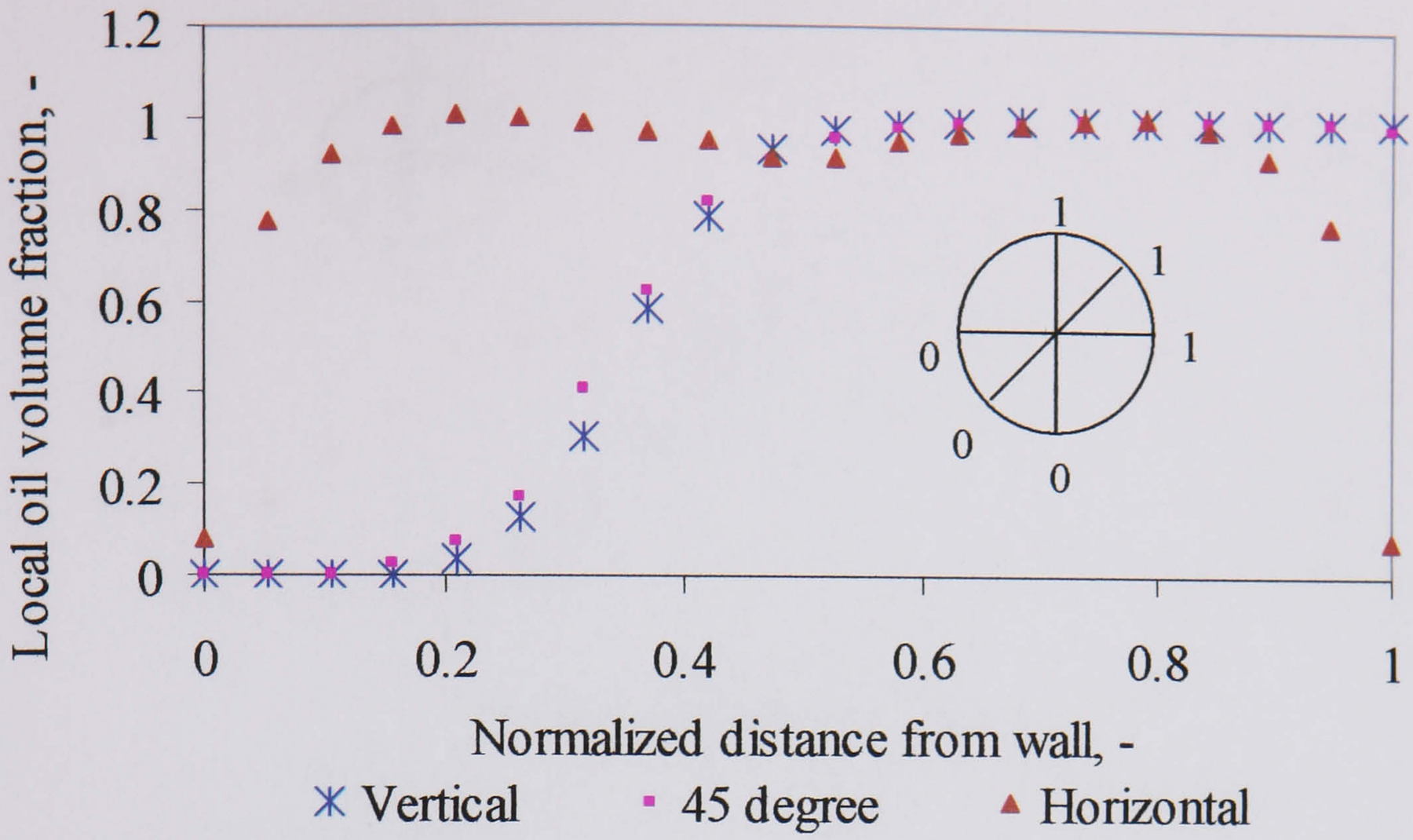

Fig. 7.2 Local oil volume fraction at U_{so} = 1.10, U_{sw} = 0.50 m/s in the 38 mm ID test pipe, 7 m from the inlet (T-junction inlet section).

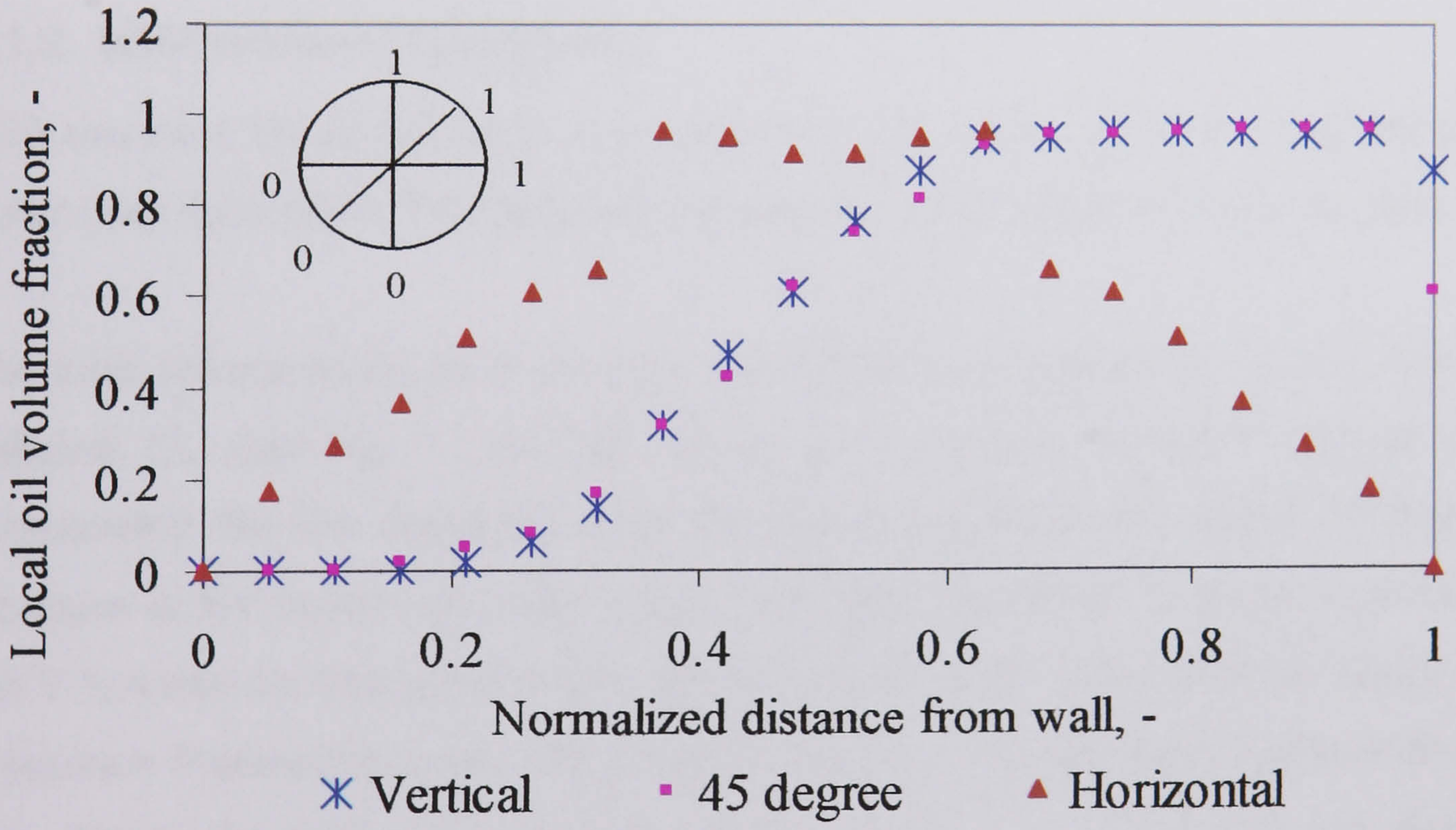

Fig. 7.3 Local oil volume fraction at U_{so} = 1.10, U_{sw} = 0.80 m/s in the 38 mm ID test pipe, 7 m from the inlet (T-junction inlet section).

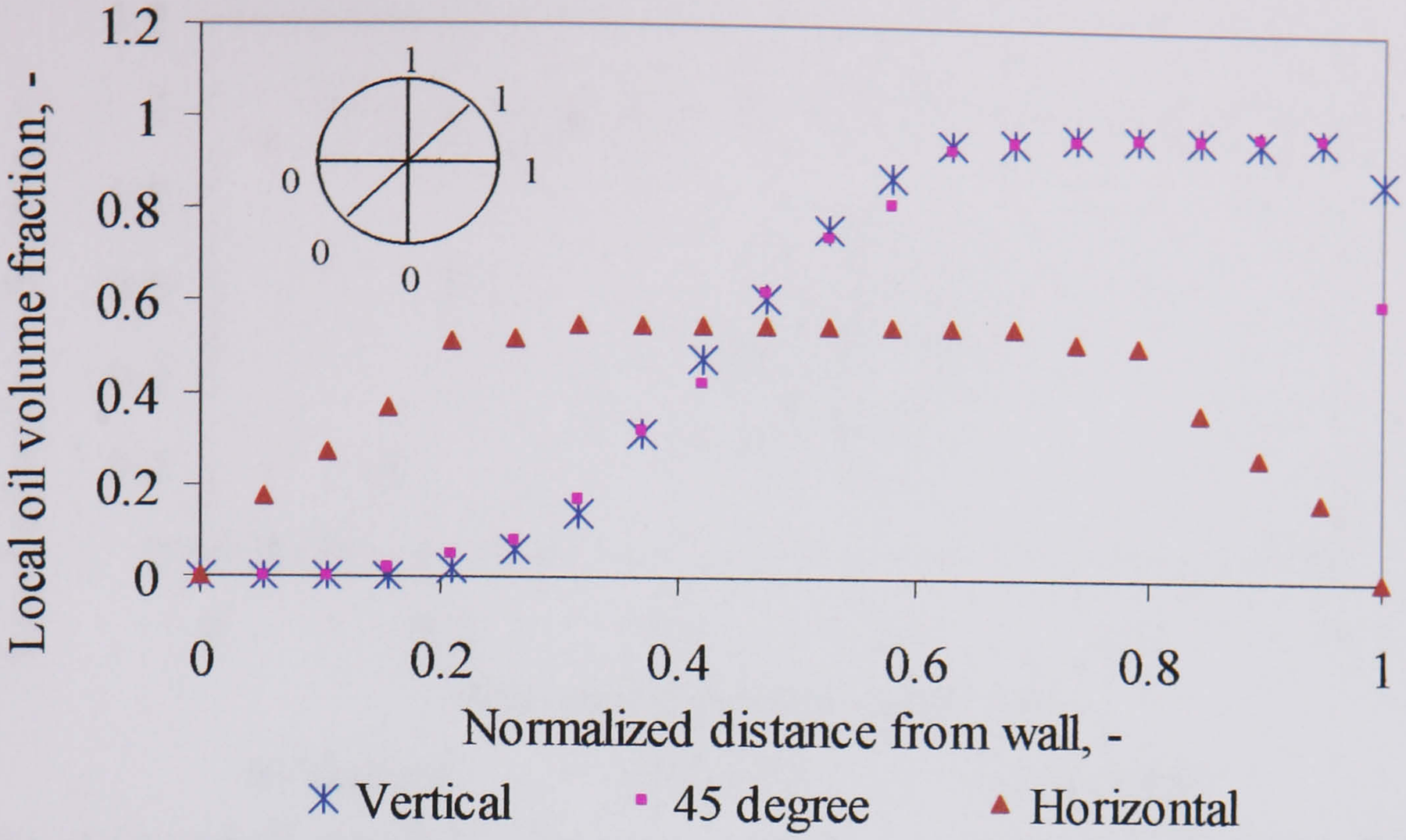

Fig. 7.4 Local oil volume fraction at U_{so} = 1.10, U_{sw} = 1.10 m/s in the 38 mm ID test pipe, 7 m from the inlet (T-junction inlet section).

7.1.2 Inlet section (Y-junction)

With this inlet, the oil and water are joined via a Y junction, the oil from the top and the water from the bottom. This geometry introduces a better stratification to the flow.

The local volume fractions in the pipe cross section are plotted at U_{so} = 1.10 m/s for different U_{sw} (see Fig. 7.5 to 7.8). Similar to T-junction (section 7.1.1), all figures demonstrate that the dispersion occurs at the interface and the degree of dispersion increases as the superficial water velocity increases. However, it can be seen that with the Y-junction the dispersion is less spread on both sides of the interface than with the T-junction followed by bend. This could be related to the increased mixing in the latter case due to the bend. For example, at U_{so} = 1.10, U_{sw} = 0.50 m/s, the dispersion occupies 20 % of the pipe cross section with the Y-junction (Fig. 7.6) while it occupies 25 % of the pipe with the T-junction (Fig. 7.2).

The phase distribution results of the pipe cross section for the conditions investigated are given in appendix D.2.

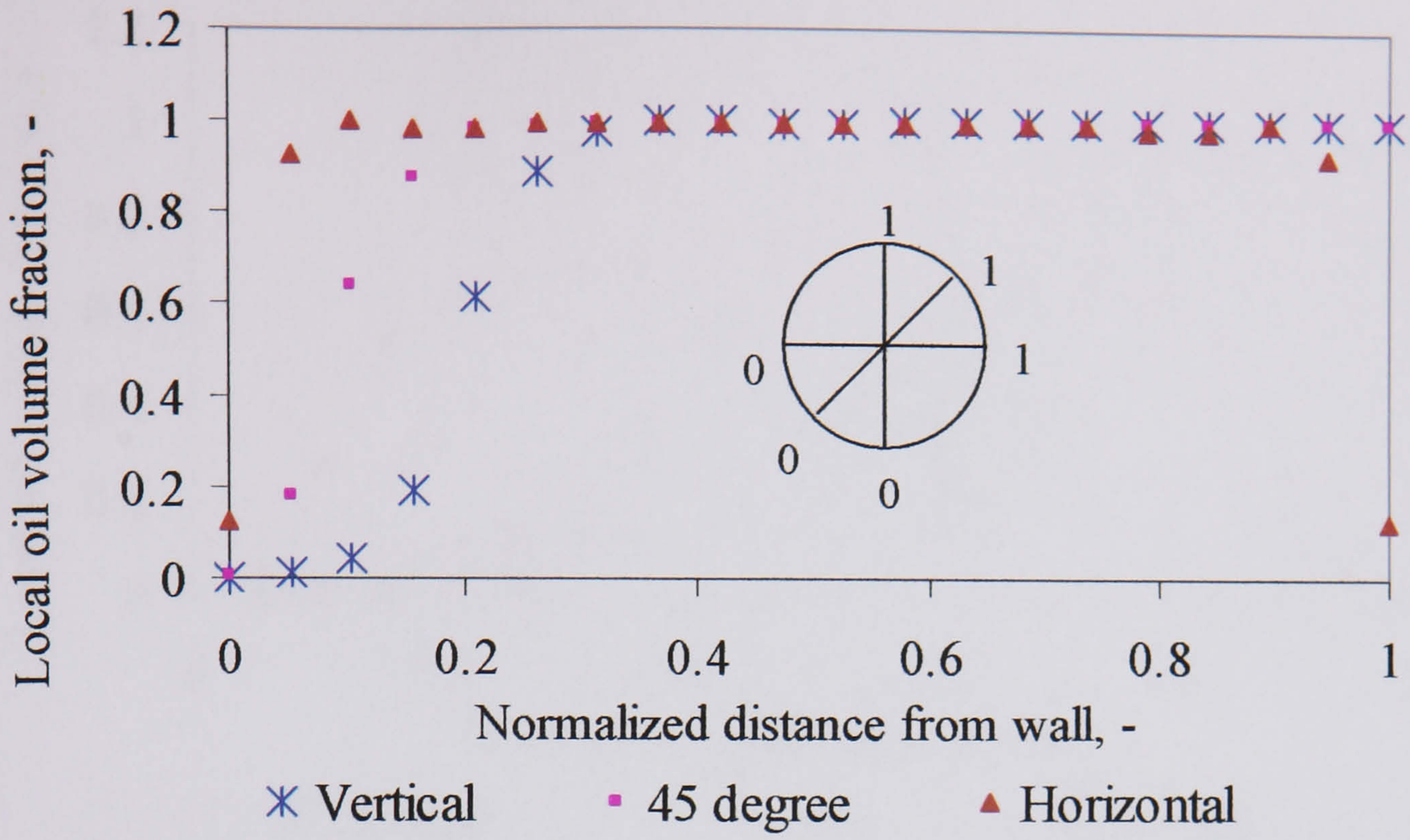

Fig. 7.5 Local oil volume fraction at U_{so} = 1.10, U_{sw} = 0.20 m/s in the 38 mm ID test pipe, 7 m from the inlet (Y-junction inlet section).

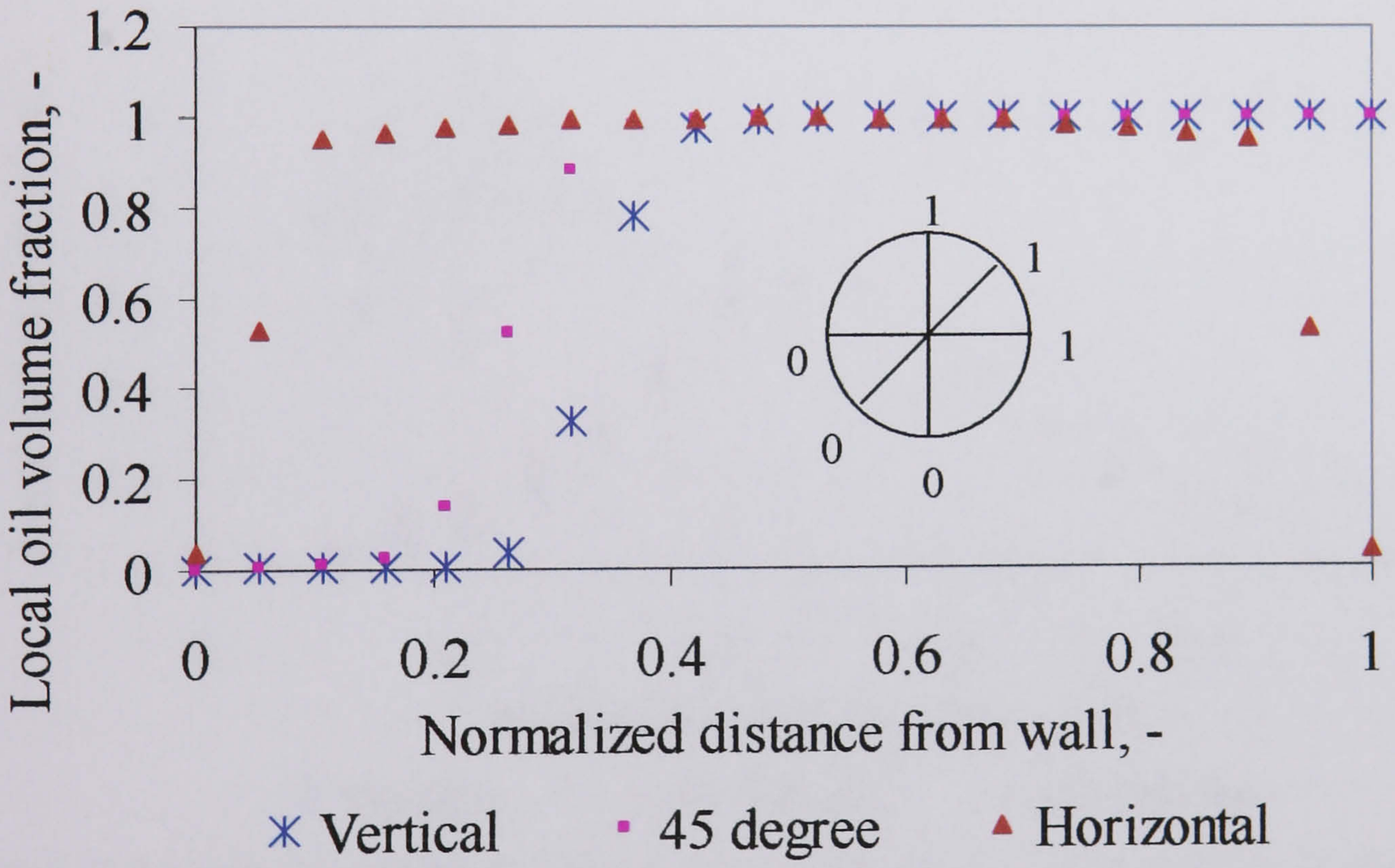

Fig. 7.6 Local oil volume fraction at U_{so} = 1.10, U_{sw} = 0.50 m/s in the 38 mm ID test pipe, 7 m from the inlet (Y-junction inlet section).

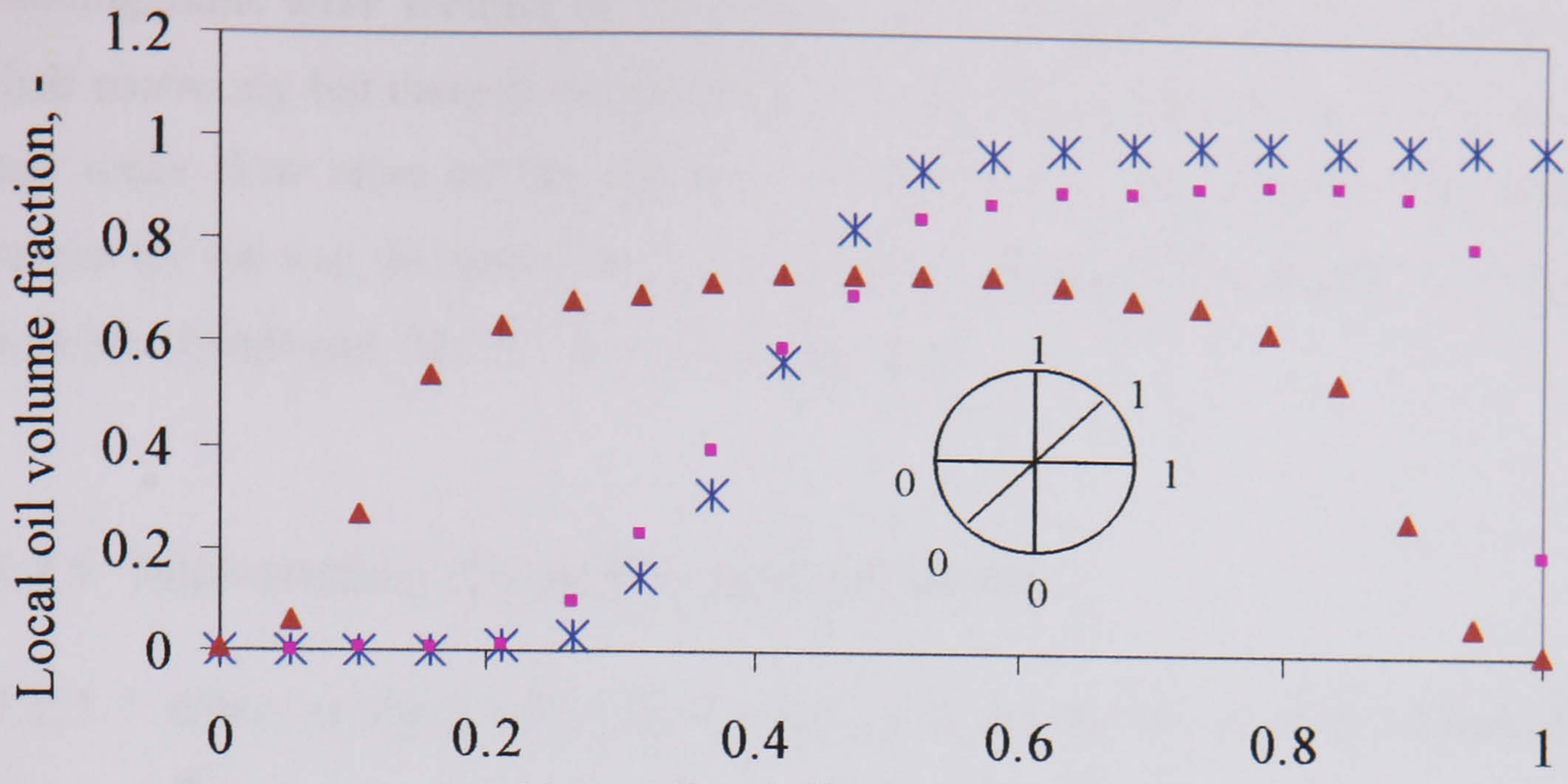

Fig. 7.7 Local oil volume fraction at U_{so} = 1.10, U_{sw} = 0.80 m/s in the 38 mm ID test pipe, 7 m from the inlet (Y-junction inlet section).

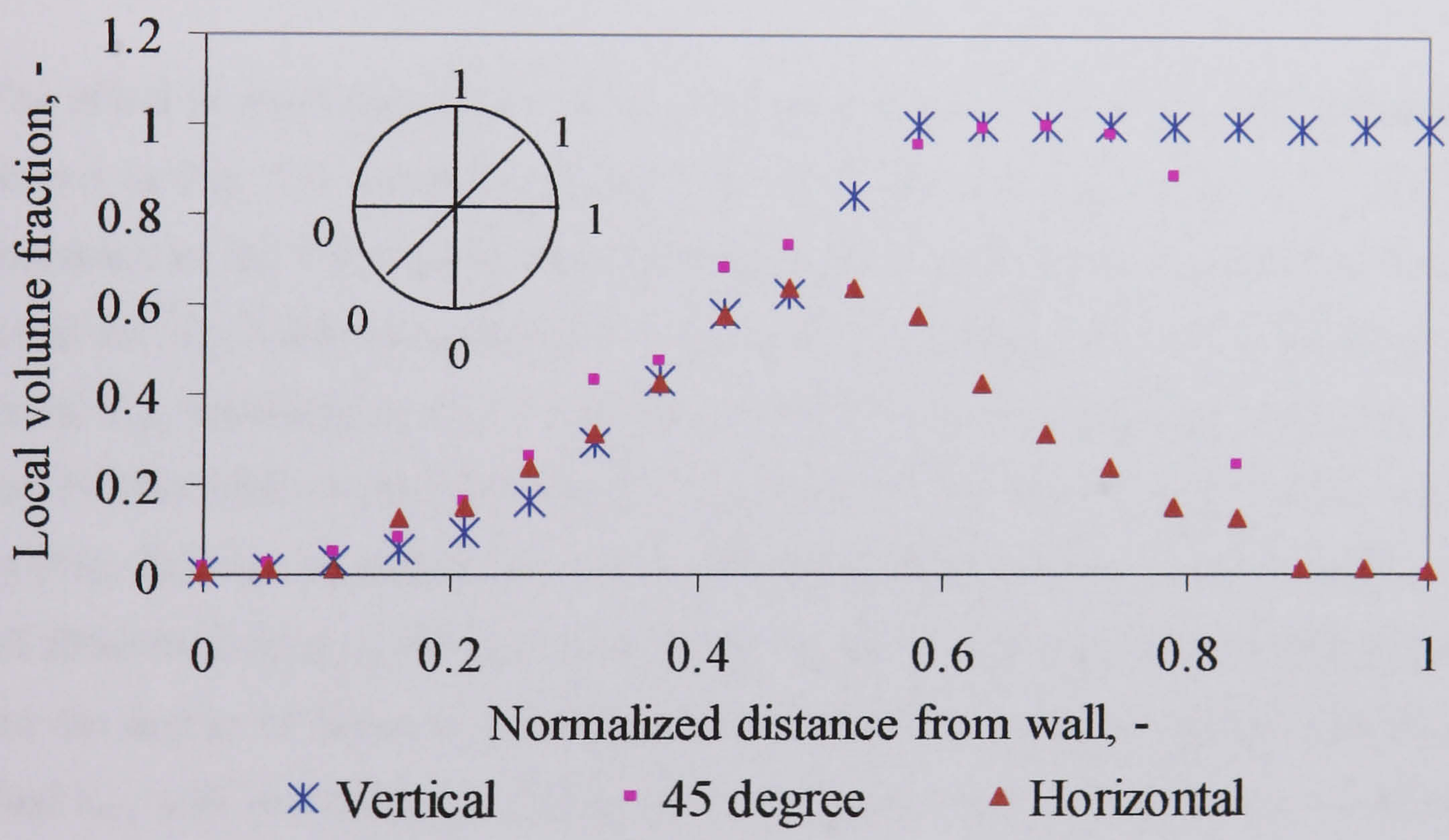

Fig. 7.8 Local oil volume fraction at U_{so} = 1.10, U_{sw} = 1.10 m/s in the 38 mm ID test pipe, 7 m from the inlet (Y-junction inlet section).

7.2 Entrained Fraction

The phase distributions at different conditions of oil and water superficial velocities were obtained by integrating the measured local volume fractions. From the phase distributions, entrained fractions of oil in water and water in oil are calculated. All

investigations were focused on the *dual continuous* pattern where both phases retain their continuity but there is interdispersion of one phase into the other. The effect of oil and water flow rates on the entrained fractions were also studied. The entrainment results for the two different inlet geometries are presented in sections 7.2.1 (T-junction with 90 ° bend) and 7.2.2 (Y-junction) respectively.

7.2.1 Inlet section (T-junction with 90° bend)

7.2.1.1 Effect of input water flow rates on entrainment of water in the oil phase ($E_{w/o}$)

The entrained fraction of water in oil, $E_{w/o}$, is defined as the mass flow rate of water drops (W_{wd}) divided by the total mass flow rate of the upper phase (W_u).

$$E_{w/o} = \frac{W_{wd}}{W_u} \tag{7.1}$$

The effect of input water flow rate on the entrainment of water in the oil phase ($E_{w/o}$) is shown in Fig. 7.9. From the graph, it is clear that entrained fraction of water ($E_{w/o}$) increases as the input water flow rate increases. However, it is noted that there is no trend for $E_{w/o}$ with oil superficial velocity. For example, at input water flow rate 34 l/min, $E_{w/o}$ measured at U_{so} = 0.80 m/s (5.7%) is less than that measured at U_{so} = 1.40 m/s (9.4%) while at the same time it is greater than the one measured at U_{so} = 1.10 m/s (4.9%). This can be attributed to two competing phenomena that determine $E_{w/o}$. As the oil flowrate increases the thickness of the oil layer increases (that would reduce $E_{w/o}$) but the degree of dispersion of water in oil increases (which would increase $E_{w/o}$). The final $E_{w/o}$ will be a balance of these two phenomena. For example at U_{so} = 0.80 m/s, the degree of dispersion is the lowest so it is normal to have a low $E_{w/o}$. At U_{so} = 1.10 m/s, although the amount of entrained water increases as a result of increased mixing, the thickness of the oil layer is now larger. Thus, the increase in the amount of entrained water is less compared to the increase in the oil volume. This is why the entrained fraction of water in oil decreases. At U_{so} = 1.40 m/s the increase in the amount of entrained water is more compared to the increase in the oil volume and $E_{w/o}$ has higher values than in the other two cases. In addition to those two effects, as water is entrained

into the oil, there are also oil drops that transfer to the water phase and their amount increases as the input water flow rates increase.

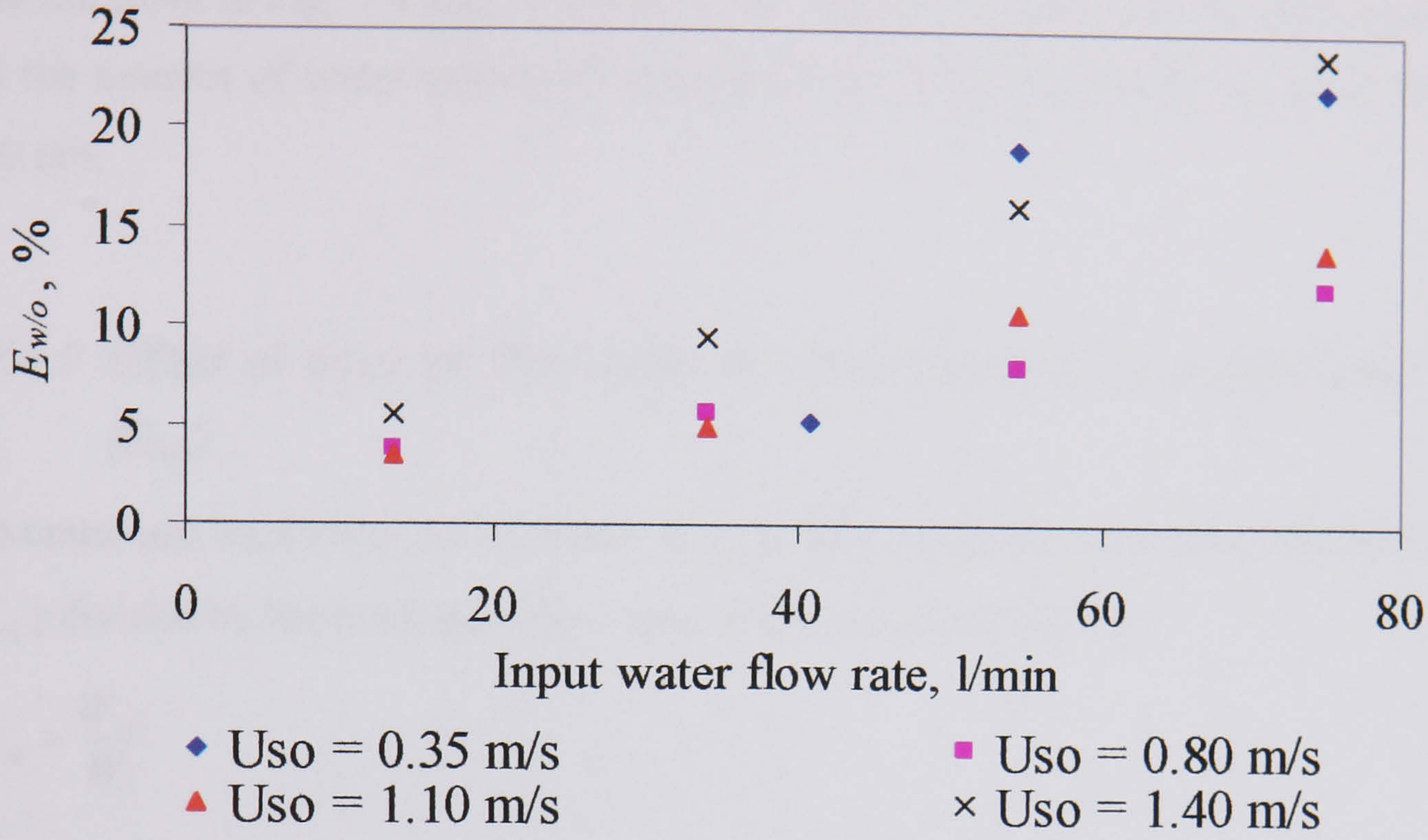

Fig. 7.9 Effect of input water flow rate on the entrainment of water in oil in the 38 mm ID test pipe, 7 m from the inlet (T-junction inlet section).

From the graph, it is noted that $E_{w/o}$ increase linearly with U_{sw} at U_{so} = 1.40 m/s while it increases logarithmically at U_{so} = 0.35 m/s. This because at U_{so} = 0.35 m/s, the thickness of the oil layer is small so any increase in the water flow rate will cause a sharp increase in the entrained fraction of water in oil (taking into consideration that the oil layer is decreasing also due to the oil drops transferring into the water phase). This increase levels out close to the transition to *Do/w* where any further increase in the water flow rate will make the oil to lose its continuity and will cause the pattern to change from *dual continuous* flow to *dispersed oil in water* (*Do/w*) flow. Note that oil is expected to lose its continuity around 68 % oil.

At U_{so} = 1.40 m/s, the total oil flow rate is high so the increase in water flow rate will cause an increase in the fraction of water entrained into oil. However, the increase in comparison to that of U_{so} = 0.35 m/s is less steep due to the larger volume of the oil layer at U_{so} = 1.40 m/s. In other words, although the amount of water entrained into the oil phase at U_{so} = 1.40 m/s is more compared to that at U_{so} = 0.35 m/s, the percentage increase is for U_{so} = 0.35 m/s due to the small thickness of the oil layer in the latter case.

At U_{so} = 1.40 m/s, the increase in the $E_{w/o}$ will continue with the same slope and a double dispersion layer (*Do/w* & *Dw/o*) is expected to appear before it will change to *dispersed oil in water* (*Do/w*) by further increasing the water flow rate. This can be seen from the trend in Fig. 7.9 and 7.10 where the amount of oil entrained to the water phase and the amount of water entrained into the oil phase are relatively the same for U_{so} = 1.40 m/s.

7.2.1.2 Effect of input oil flow rates on entrainment of oil in the water phase ($E_{o/w}$)

The entrained fraction of oil in water, $E_{o/w}$, is defined as the mass flow rate of oil drops (W_{od}) divided by the total mass flow rate of the lower phase (W_l).

$$E_{o/w} = \frac{W_{od}}{W_l} \tag{7.2}$$

Fig. 7.10 shows the effect of increasing the input oil flow rate on the entrainment of oil in water. The results reveal that $E_{o/w}$ increases as the oil flow rate increases at a constant water superficial velocity. Similar to $E_{w/o}$, there is no general trend for $E_{o/w}$ with respect to different water superficial velocities at constant oil flow rate. This is again depends on the relative increase of the water layer and the amount of oil drops entrained in water as the water flow rates increases.

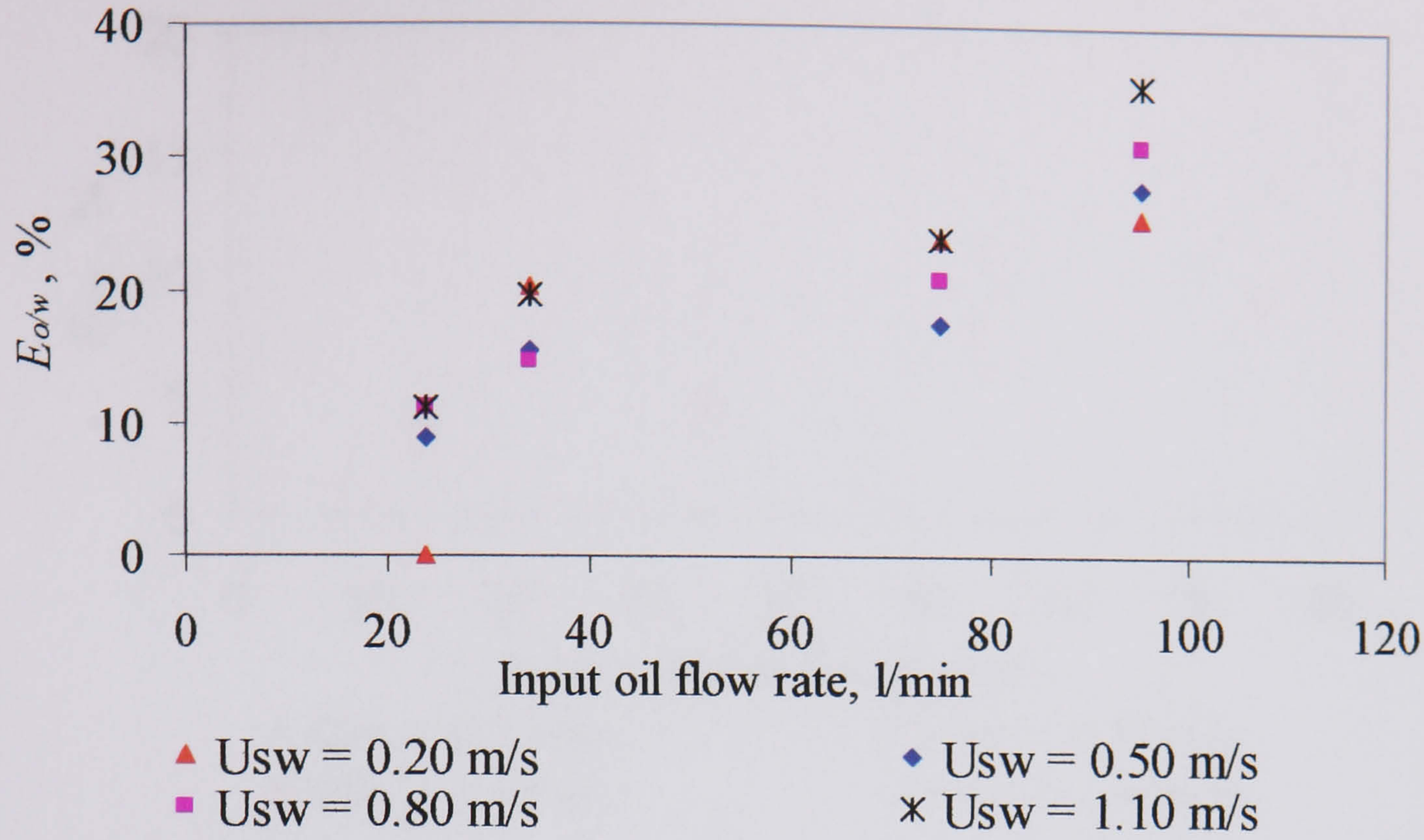

Fig. 7.10 Effect of input oil flow rate on the entrainment of oil in water in the 38 mm ID test pipe, 7 m from the inlet (T-junction inlet section).

7.2.2 Inlet section (Y-junction)

7.2.2.1 Effect of input water flow rates on entrainment of water in the oil phase ($E_{w/o}$)

The effect of water flow rate on $E_{w/o}$ when the Y-junction is used is plotted in Fig. 7.11. The same trend to that in section 7.2.1.1 is noted. $E_{w/o}$ increases as the input water flow rates increase for all the tested oil superficial velocities. Again there is no trend with U_{so}. However, the increase is less sharp in this section than that seen with the T-junction (section 7.2.1.1). The comparison between two inlet sections is given in section 7.2.3.

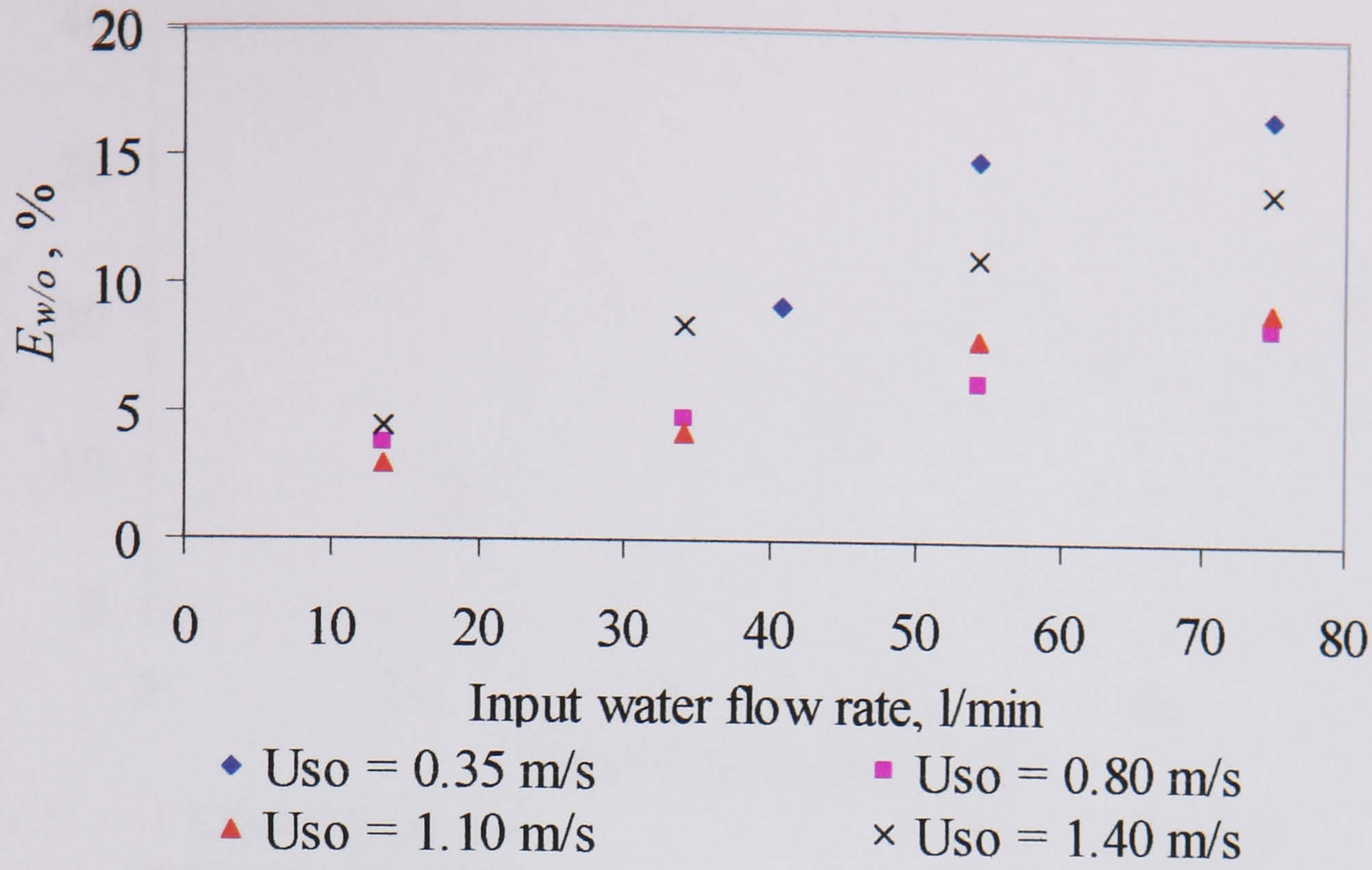

Fig. 7.11 Effect of input water flow rate on the entrainment of water in oil in the 38 mm ID test pipe, 7 m from the inlet (Y-junction inlet section).

7.2.2.2 Effect of input oil flow rates on entrainment of oil in the water phase ($E_{o/w}$)

A plot of the entrained fraction of oil in the water phase when the Y-junction is used with respect to input oil flow rates at different water superficial velocities is given in Fig. 7.12. $E_{o/w}$ is found to increase as the input oil flow rates increase for constant water superficial velocity.

Also, $E_{o/w}$ is found to increase as the water superficial velocities decrease at constant input oil flow rate. This is shown more clearly in Fig. 7.13 where $E_{o/w}$ is plotted against water flow rate for different oil superficial velocities. The results show that $E_{o/w}$ is initially with increasing water flow rate decreasing and then becomes relatively constant. The trend in this section is different than that in section 7.2.1.2 when a bend was used in the inlet section. A detail discussion of the difference in the results between the two inlets is given in section 7.2.3.

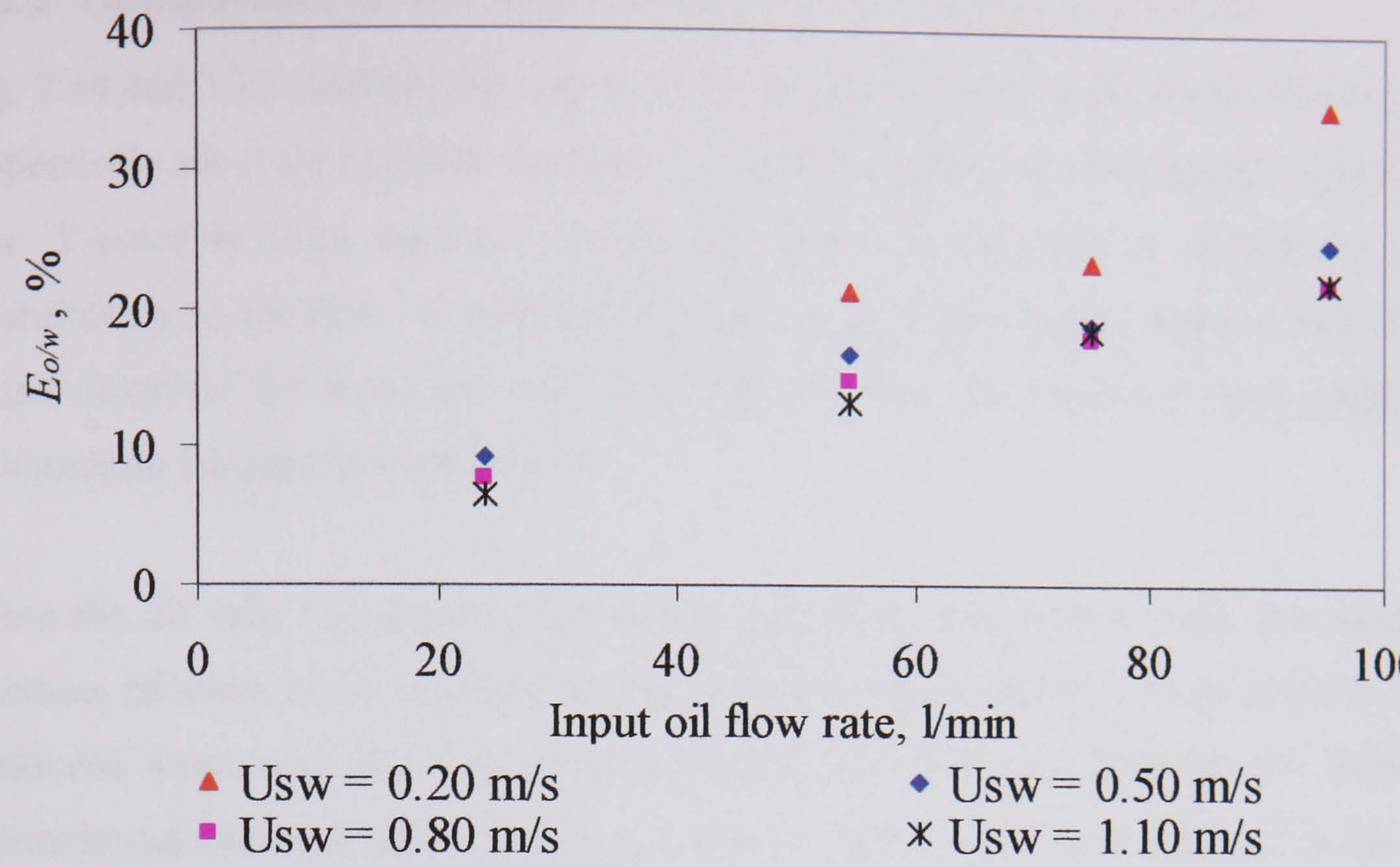

Fig. 7.12 Effect of input oil flow rate on the entrainment of oil in water in the 38 mm ID test pipe, 7 m from the inlet (Y-junction inlet section).

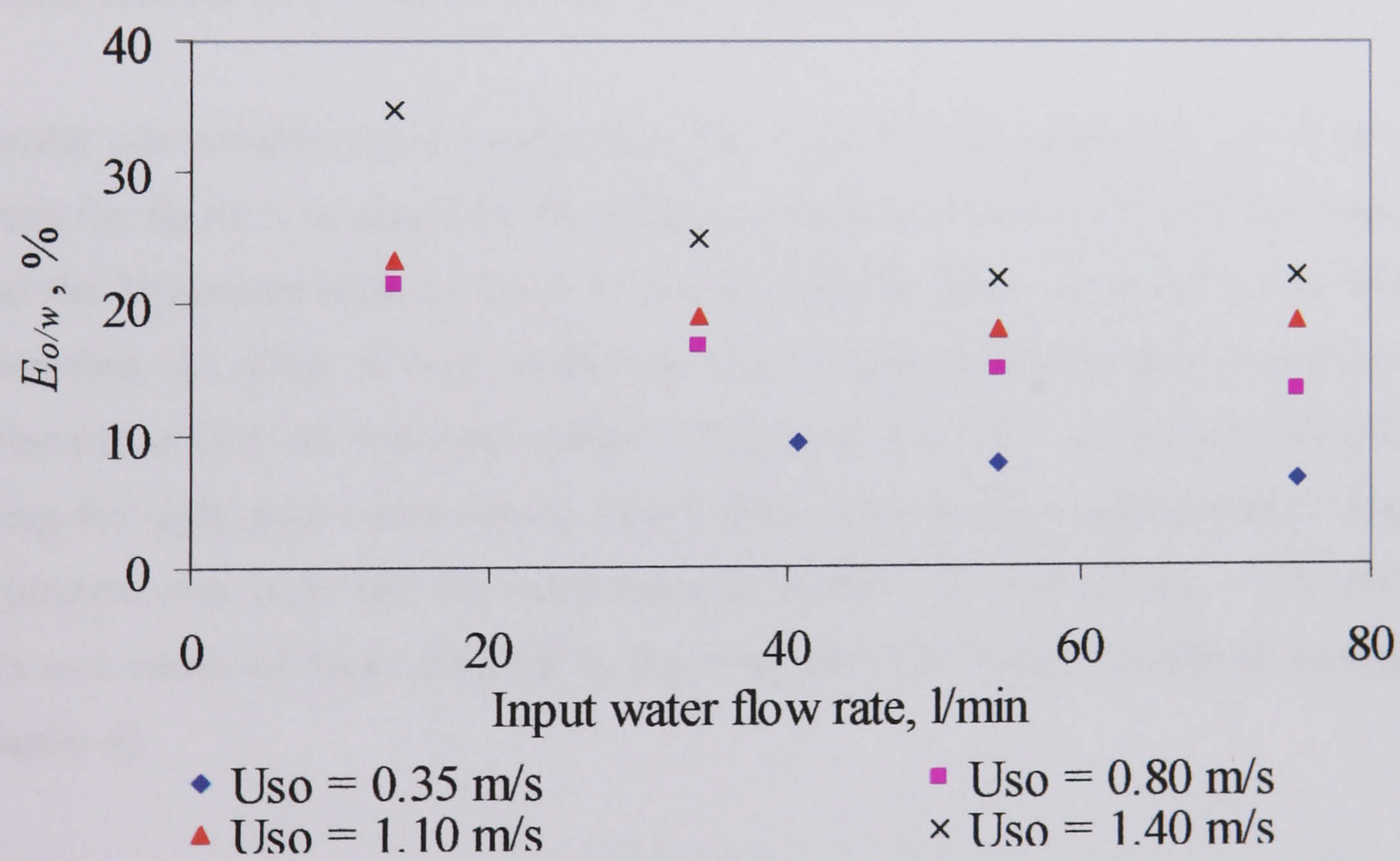

Fig. 7.13 Effect of input water flow rate on the entrainment of oil in water in the 38 mm ID test pipe, 7 m from the inlet (Y-junction inlet section).

7.2.3 Comparison of entrained fractions between the two inlets

Fig. 7.14 and 7.15 compare the entrained fractions of oil and water when oil and water respectively when the two inlet sections are used (T-junction with bend and Y-junction). The Y-junction inlet section without the bend proves that it introduces more stratification to the flow. In addition the high speed video images showed that all the drops observed 7m from the inlet were formed from the waves as they propagate downstream the pipe (see chapter 4).

When the old inlet (T-junction inlet section with bend) was used instead, the entrained fractions of water in oil as shown in Fig. 7.14 were found initially to be close to those measured when with the Y-junction. However, the difference between the values is increasing as the input water flow rates increase. This indicates that the bend in the inlet creates a mixing between the two liquids from which drops are forming. These drops persist downstream and cause the difference in entrained fractions between the two inlets measured at 7 m from the inlet. The amount of drops forming as a result of such mixing increase as the superficial oil velocity increases.

Similar observations can be made from Fig. 7.15 for the entrainment of oil in water. From the figure it is clear that the difference between the values from the Y-junction and the T-junction with the bend is increased as the input water flow rates increase. Therefore, the effect of bend on the entrained fraction becomes more obvious at high velocities of both oil and water phases. This agrees with the experimental observations using the high speed video camera where drops were found to appear earlier when the T-junction was used than the onset found from the Y-junction at U_{so} = 0.50 and 0.55 m/s as a result of drops forming in the bend after the T-junction due to mixing (see chapter 4).

The increase in the dispersion region around the interface in *dual continuous* flow has a big effect on flow pattern transitions boundaries especially from *dual continuous* to other *dispersed* flow patterns. The bend in the inlet increases the dispersion of each phase into the other and cause the transition to the *dispersed* pattern to happen earlier. For example, with the T-junction the entrained fraction of water in oil at input water flow rate of 75 l/min is equal to 24% for U_{so} = 1.40 m/s (Fig. 7.14). Further increase in the input water flow rate will make the oil phase to lose its continuity and *oil dispersed*

in water pattern will result. On the other hand, $E_{w/o}$ is much smaller when the Y-inlet is used at the same conditions (see Fig. 7.14) which delay the transition to *dispersed oil in water*.

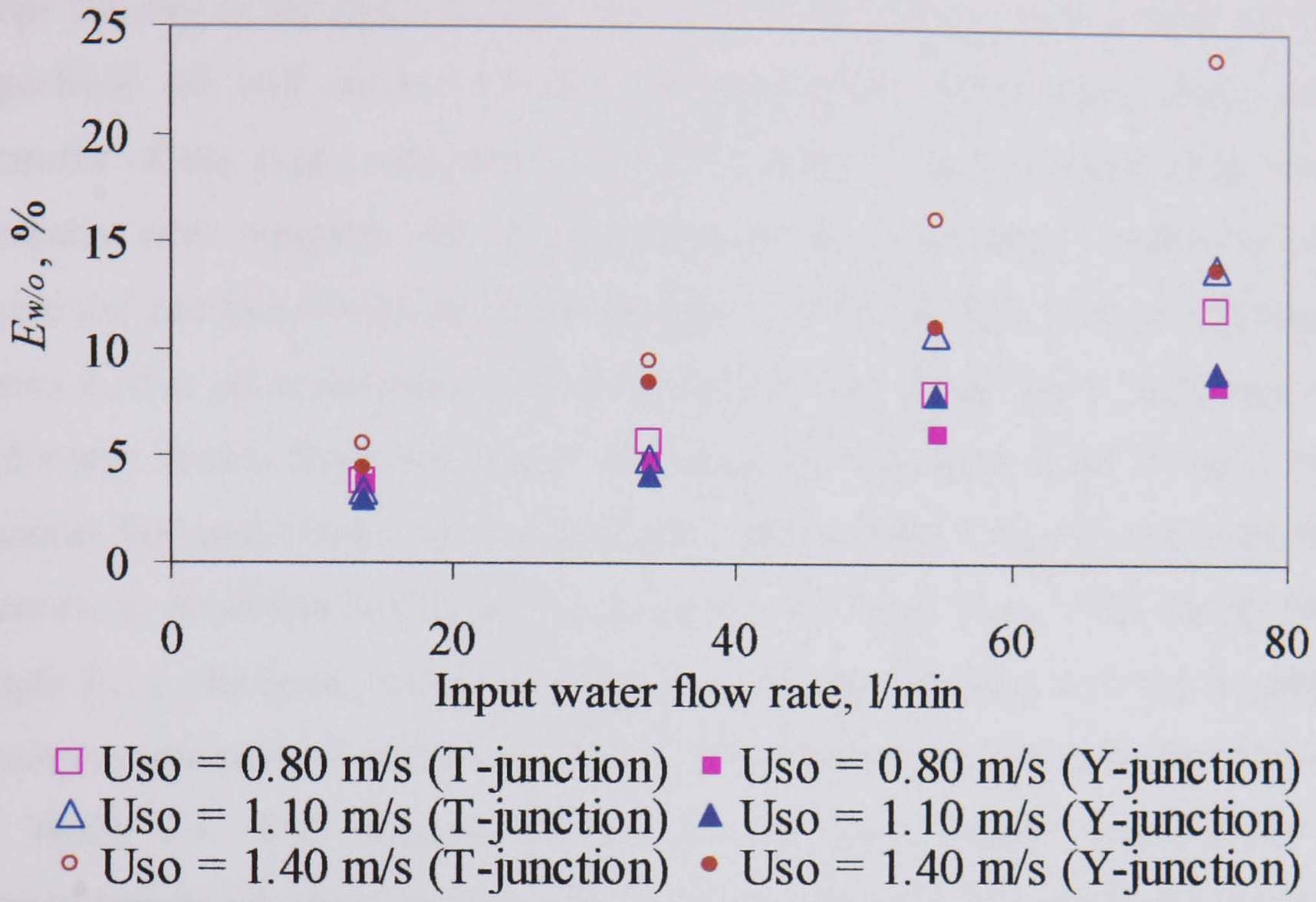

Fig. 7.14 Effect of inlet geometry on the entrained fraction of water in oil in *dual continuous* flow in the 38 mm ID test pipe, 7 m from the inlet.

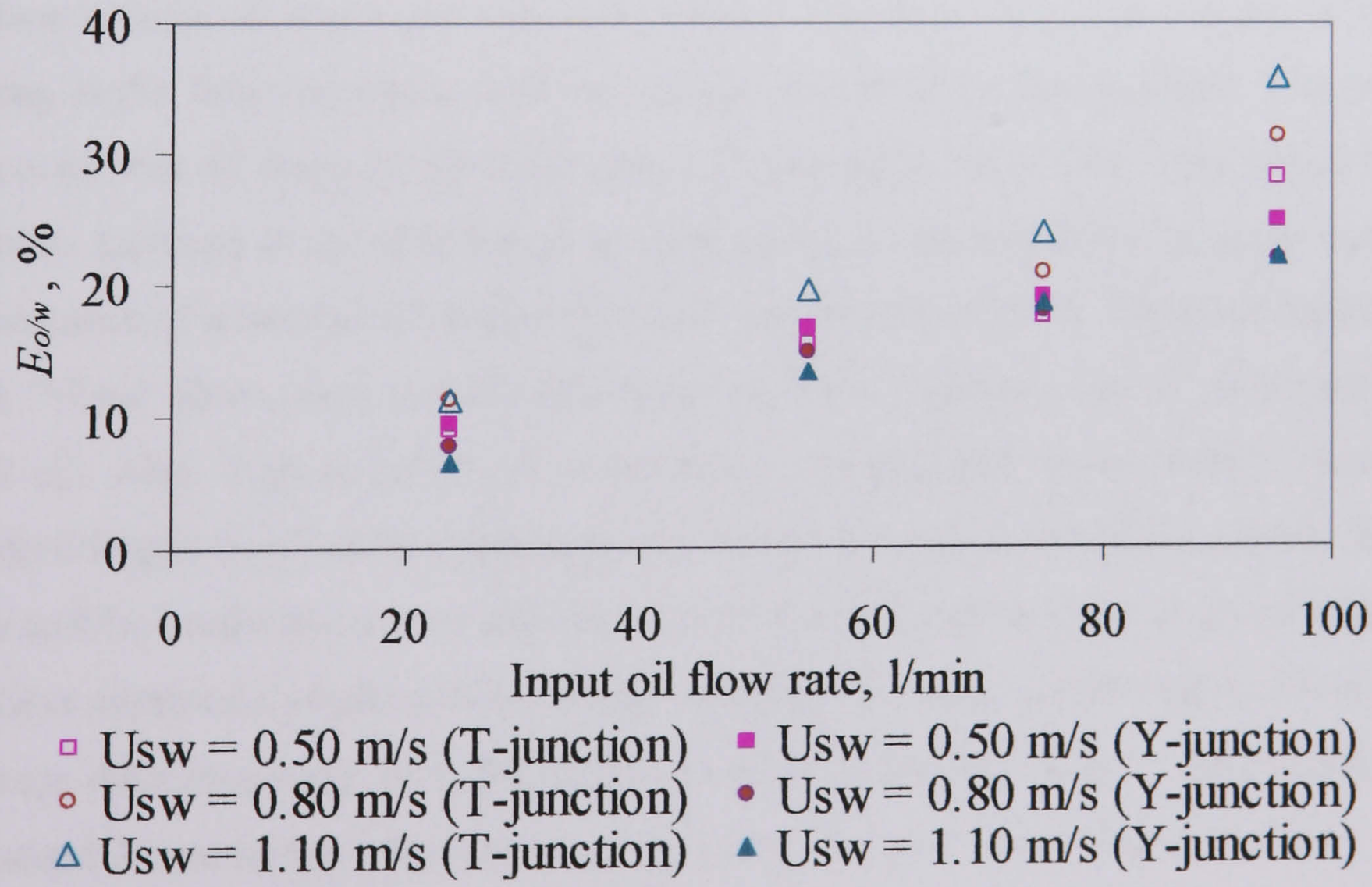

Fig. 7.15 Effect of inlet geometry on the entrained fraction of oil in water in *dual continuous* flow in the 38 mm ID test pipe, 7 m from the inlet.

7.3 Chord Length Distribution

Using the dual impedance probe as illustrated in section 3.3.3, drop velocities were found by cross-correlating the signals from the two sensors and chord lengths of the drops flowing in the pipe could be measured. Experiments were conducted at different superficial oil and water velocities. Measurements were taken along the vertical diameter of the pipe cross section, every 2 mm. At each oil and water velocity, 20 locations were sampled. All measurements were on the *dual continuous* pattern. To locate the interface it was assumed that below 68 %, the flow is water continuous while above it, it is oil continuous. This is because it was found that a dispersion of this oil and water inverts from one phase continuous to the other at 68 % input oil volume fraction. For each phase, all measurements taken below 3 mm from the interface were ignored, to avoid any inaccuracies caused by interfacial waves. The Sauter mean chord length (L_{32}), the linear mean chord length (L_{10}) and the drop velocity representing the measurements taken 7 m from the inlet at different locations from the interface are listed in Table 7.1. The number density of the chord length distributions of these measurements are given in Appendix E. At each location the number density decreases as chord size increases.

From Appendix E and Table 7.1, it is clear that drops are formed further away from the interface at high oil and water velocities than at low ones. Also, the number of drops existing in the flow decreases with increasing distance from the interface. The results also reveal that oil drops in the water phase are generally larger than water drops in the oil phase. Looking at the distribution in each location, the data from the probe indicate the existence of a number of large drops with length up to 20 mm. These are mainly oil drops. Visual observation showed that drops can have diameters up to 10-15 mm (see Fig. 7.16). Also, Trallero (1995) observed drops with diameter up to 12 mm. The tail in the chord length distribution extends up to 20 mm for many conditions especially for oil drops and for locations close to the interface. Since the probe measured chord length, it may have captured elongated drops which will result in larger chord lengths. The size of the drops decreases away from the interface and the maximum drop in some cases does not exceed 2 mm. Large drops are normally found at higher local volume fractions.

U_{so}, m/s	U_{sw}, m/s	h of int, mm	d from int, mm	Oil drops in water phase				Water drops in oil phase			
				Local vol. %	L_{32}	L_{10}	drop vel., m/s	Local vol. %	L_{32}	L_{10}	drop vel., m/s
0.35	0.80	25	3	2.1	8.04	3.83	1.03				
0.35	1.10	27	3	11.0	11.25	3.64	1.35	97.0	1.87	1.07	1.25
			5	3.1	7.65	2.40	1.39				
			7	2.5	3.58	1.60	1.37				
			11	2.3	3.52	2.23	1.33				
0.80	0.20	9	3	1.9	6.22	4.50	0.75				
0.80	0.50	15	3	3.8	12.23	5.50	1.39	98.0	8.89	3.48	1.47
0.80	0.80	19	3	9.0	12.77	6.32	1.59	97.8	2.78	1.47	1.56
			5	2.9	7.58	3.95	1.45	98.7	1.37	1.13	1.79
			7	2.0	6.99	2.44	1.40	98.8	1.96	1.25	1.64
0.80	1.10	21	3	27.9	11.24	5.23	2.06	94.0	7.92	1.75	2.02
			5	8.5	7.08	2.97	2.10	98.0	1.70	1.36	2.14
			7	4.5	3.88	2.13	2.08	99.0	1.35	1.10	2.10
			9	2.2	3.67	1.80	2.00				
			11	0.4	1.97	1.36	2.00				

Table 7.1: Drop velocity and average mean and linear chord length for oil drops in water and water drops in oil

U_{so}, m/s	U_{sw}, m/s	h of int, mm	d from int, mm	Oil drops in water phase				Water drops in oil phase			
				Local vol. %	L_{32}	L_{10}	drop vel., m/s	Local vol. %	L_{32}	L_{10}	drop vel., m/s
1.10	0.20	9	3	19.3	10.86	5.26	0.97	97.0	10.59	2.30	1.32
			5	4.1	9.61	4.35	1.00	99.0	3.25	1.90	1.30
			7	1.1	5.43	3.25	0.99				
1.10	0.50	13	3	19.0	10.59	3.70	1.56	97.0	5.73	2.01	1.69
			5	6.0	10.12	2.70	1.47	99.0	2.07	1.25	1.63
			7	1.0	4.45	2.24	1.23				
1.10	0.80	17	3	30.7	12.81	5..53	2.15	93.8	6.51	2.06	2.13
			5	14.2	11.04	5.13	2.02	97.0	3.07	1.51	2.13
			7	3.1	7.23	4.29	2.04	98.5	1.82	1.28	2.15
			9	1.3	5.44	3.01	1.98	99.0	1.68	1.35	2.16
1.10	1.10	23	3	23.6	8.03	1.32	2.50	84.0	2.04	1.25	2.50
			5	29.2	11.09	1.91	2.50	98.0	1.34	1.11	2.56
			7	16.3	10.31	2.50	2.73	99.0	1.30	1.08	2.50
			9	9.2	4.79	2.12	2.71				
			11	5.6	4.08	2.14	2.75				
			13	3.0	3.82	1.84	2.65				
			15	1.4	3.14	1.75	2.43				
			17	1.1	3.82	1.44	2.30				

Table 7.1 (*Cont.*) Drop velocity and average mean and linear chord length for oil drops in water and water drops in oil

U_{so}, m/s	U_{sw}, m/s	h of int, mm	d from int, mm	Oil drops in water phase				Water drops in oil phase			
				Local vol. %	L_{32}	L_{10}	drop vel., m/s	Local vol. %	L_{32}	L_{10}	drop vel., m/s
1.40	0.20	7	3	26.0	6.62	3.34	1.30	88.0	5.05	2.27	1.48
			5	7.4	8.70	2.72	1.32	90.0	3.82	2.38	1.48
			7					94.9	4.00	2.20	1.52
			9					97.0	3.25	1.99	1.58
			11					98.3	3.57	2.34	1.63
1.40	0.50	13	3	23.9	11.17	4.58	1.90	96.5	11.25	3.64	1.92
			5	11.3	8.90	3.82	1.91	99.0	4.55	2.20	1.94
			7	2.1	3.84	2.42	1.87				
			9	1.6	2.81	1.92	1.70				
1.40	0.80	15	3	38.7	13.08	4.69	2.20	83.0	7.45	2.59	2.38
			5	13.3	7.43	3.10	2.12	87.0	6.70	2.64	2.43
			7	7.6	6.27	2.38	2.17	93.0	4.55	2.21	2.46
			9	4.5	3.86	2.35	1.89	97.0	2.62	1.49	2.63
			11	3.7	2.87	1.51	1.82	98.2	2.50	1.41	2.69
			13					98.7	2.96	1.37	2.59
			15					98.4	1.91	1.26	2.38
1.40	1.10	17	3	47.2	10.93	4.30	2.67	79.9	8.09	2.49	2.73
			5	24.9	7.80	3.22	2.63	89.0	5.44	2.09	2.80
			7	11.1	7.12	2.40	2.50	93.7	4.39	1.76	2.97
			9	4.8	3.57	1.77	2.50	95.8	3.79	1.58	2.94
			11	2.9	2.88	1.68	2.34	98.1	1.64	1.23	2.89
			13	2.6	2.57	1.62	2.30	98.1	1.66	1.25	2.71
			15	1.3	2.19	1.38	2.27				

Table 7.1 (*Cont.*) Drop velocity and average mean and linear chord length for oil drops in water and water drops in oil

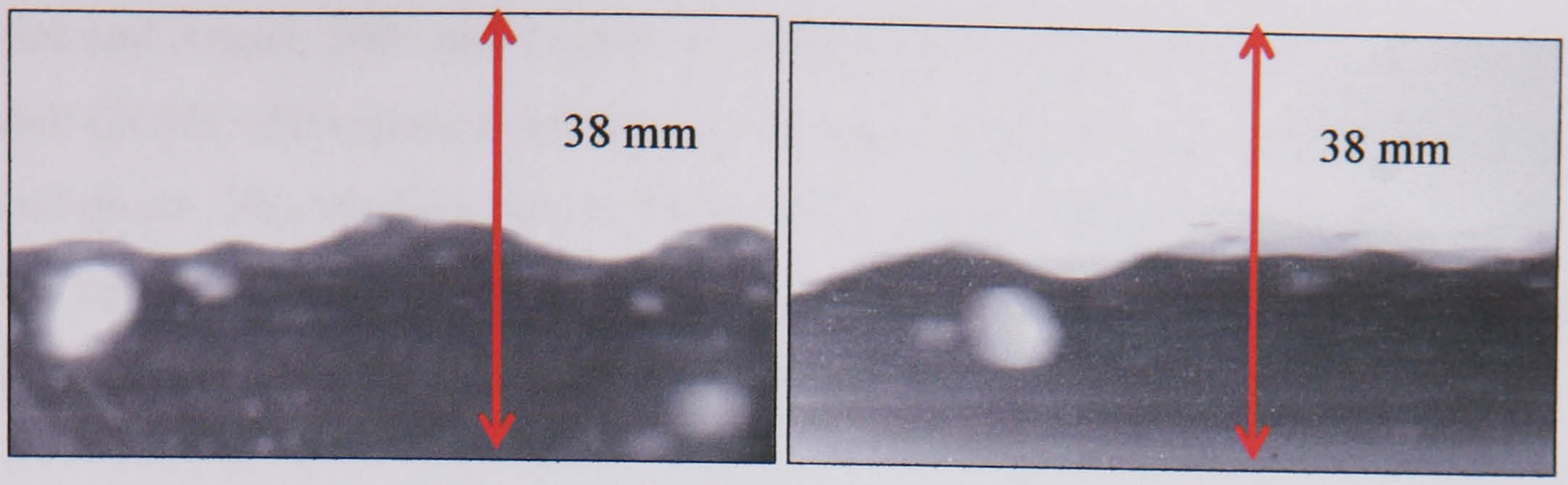

(a)

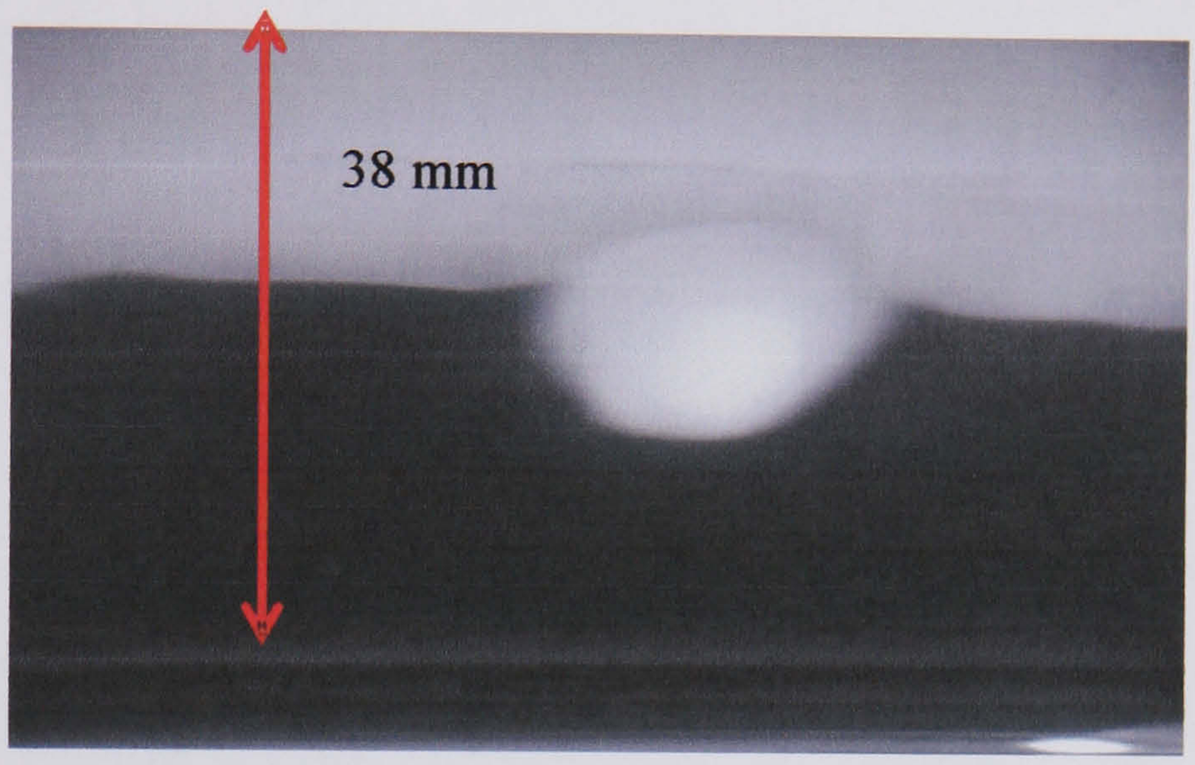

(b)

Fig. 7.16 Photographs showing drop sizes at (a) $U_{so} = 0.80$, $U_{sw} = 0.80$ m/s and (b) $U_{so} = 0.15$, $U_{sw} = 0.70$ m/s in the 38 mm ID test pipe, 7 m from the inlet

Fig. 7.17 and 7.18 show the effect of distance from the interface on the Sauter mean chord length (L_{32}) of oil drops in water (negative points below the zero) and water drops in oil (positive points above the zero) at $U_{so} = 1.1$ and 1.4 m/s respectively at different water superficial velocities. It can be seen that L_{32} decreases away from the interface for both oil drops in water and water drops in oil while, there are larger drops close to the interface for both phases. This is because close to the interface, the local volume fraction of the dispersed phase is high (see Table 7.1). Thus, the coalescence rate of the drops increases with concentration which will result in many large drops in the flow. Buoyancy effects will also tend to increase the number of large drops close to the interface.

Water drops appear to be smaller than oil drops in most cases. This is because oil can remain dispersed at higher fractions than water and this would favor larger drops compared to water ones (the oil lose its continuity at 68 % input oil fraction, see also

Lovick and Angeli, 2004 and Lum et al., 2006). This result contradicts with the work of Lovick (2004) who reported that there is no significant difference between water drops and oil drops. This could be due to the fact that Lovick (2004) ignored any drops larger than 5 mm. It is believed that this may distort the results especially for the oil phase where a large number of drops has diameter more than 5 mm.

From Fig. 7.17 and 18, it is clear that water drops in oil generally increase in size as the oil superficial velocity increases for certain water superficial velocity. The increase could be attributed to the increase in the amount of water entrained in the oil phase.

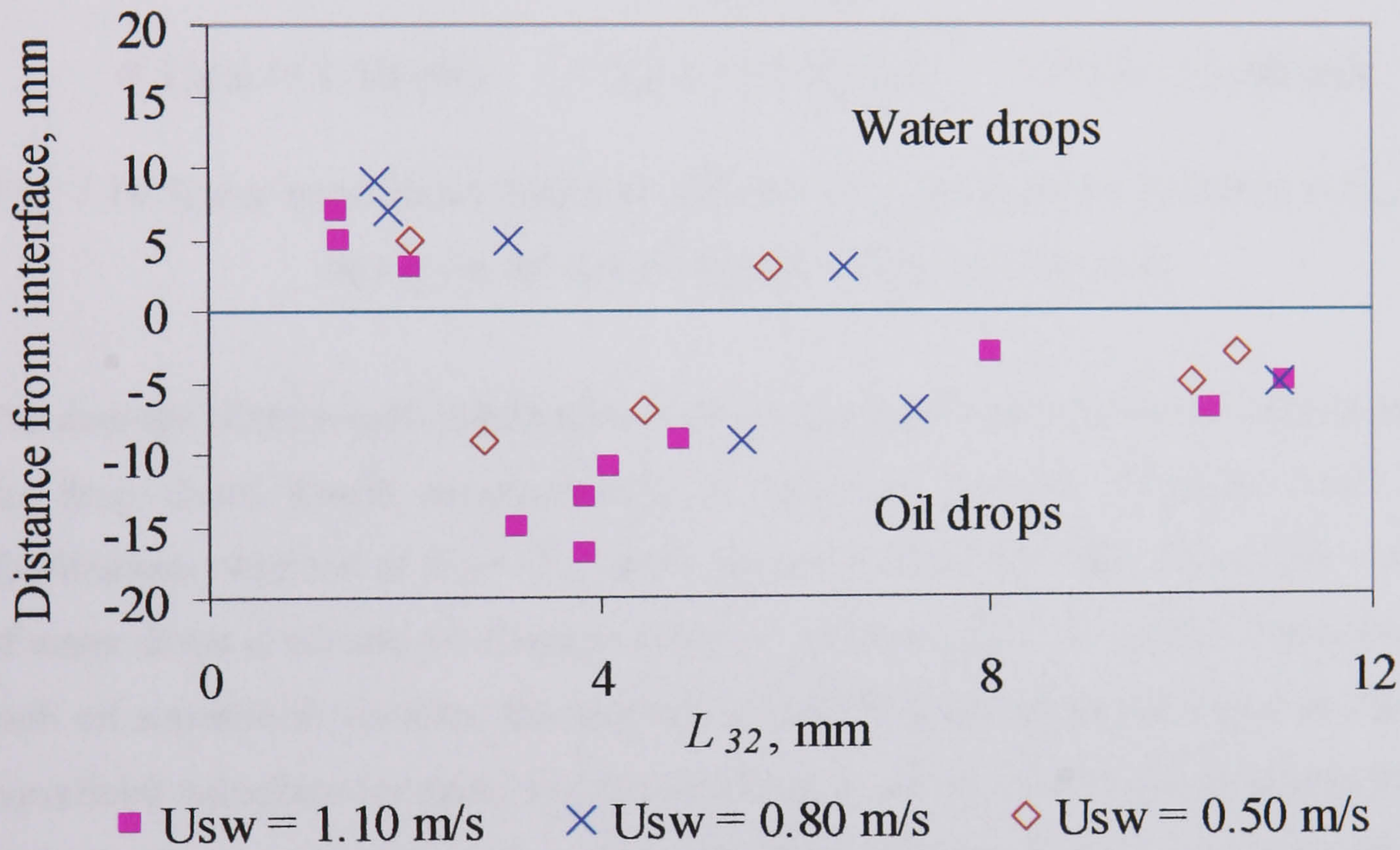

Fig. 7.17 Sauter mean chord length at different locations from the interface at U_{so} = 1.1 m/s for different U_{sw} in the 38 mm ID test pipe, 7 m from the inlet

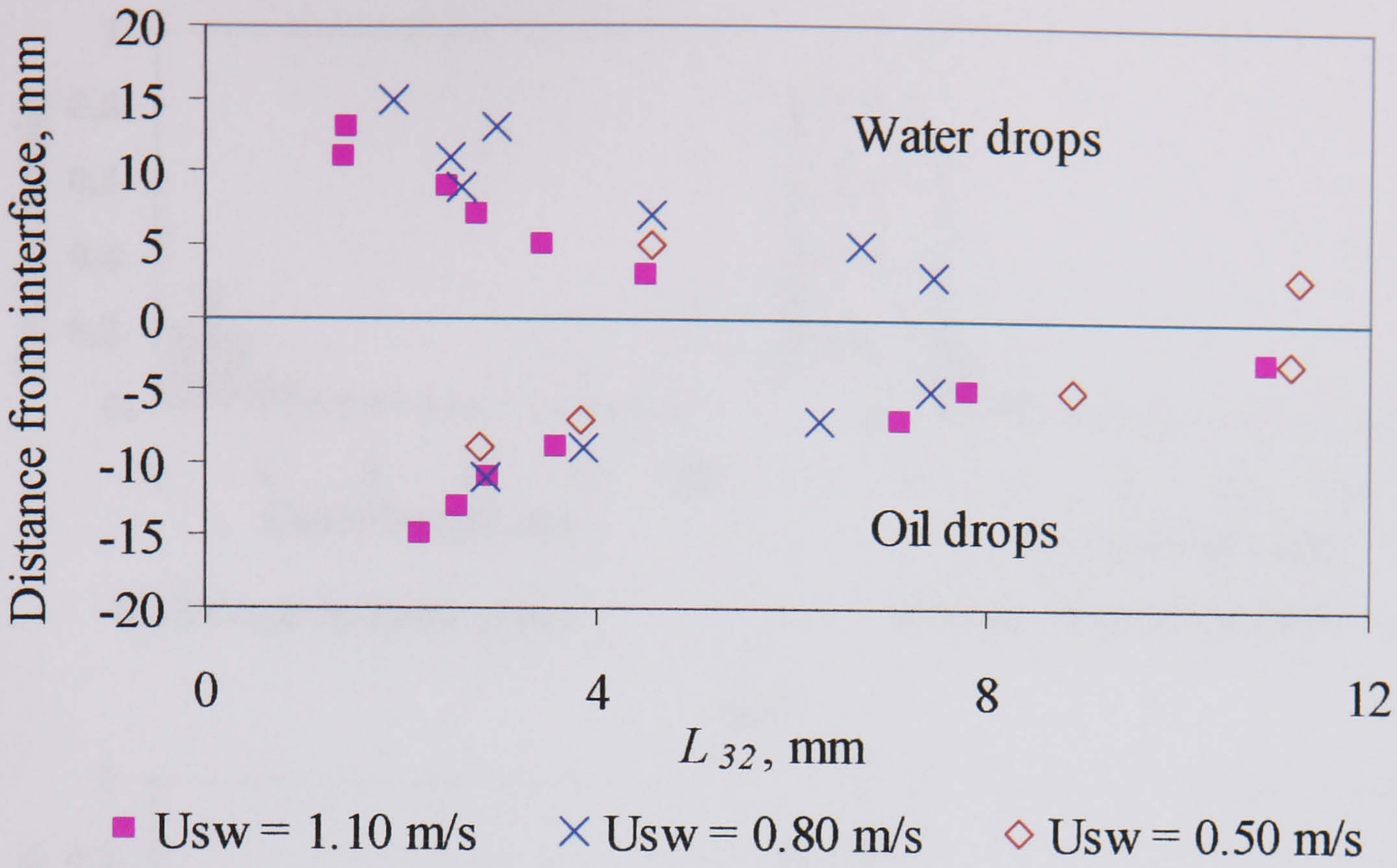

Fig. 7.18 Sauter mean chord length at different locations from the interface at U_{so} = 1.4 m/s in the 38 mm ID test pipe, 7 m from the inlet

The average chord length distribution over the pipe cross-section can be calculated from the drop chord length measurements at different locations. Average chord length distributions obtained at U_{so} = 1.1 and 1.4 m/s for different water superficial velocities of water drops in oil and oil drops in water are given in Fig. 7.19 and 20 respectively. At each oil superficial velocity, the number density of large drops decreases as the water superficial velocities increase. For the oil drops in water, smaller oil drops are found at U_{sw} = 1.10 m/s compared to U_{sw} = 0.50 and 0.80 m/s for both U_{so} = 1.10 and 1.40 m/s.

From the chord length distribution, it is clear that drops with chord length equal to 20 mm may exist in the flow especially for oil drops in water. These values originate either from large drops or elongated drops that have deformed in the flow. At this point it is important to note that the chord length measurements found using the dual impedance probe are biased towards larger drops (Hu, 2006). Thus, drops size are expected to be smaller than the corresponding chord lengths.

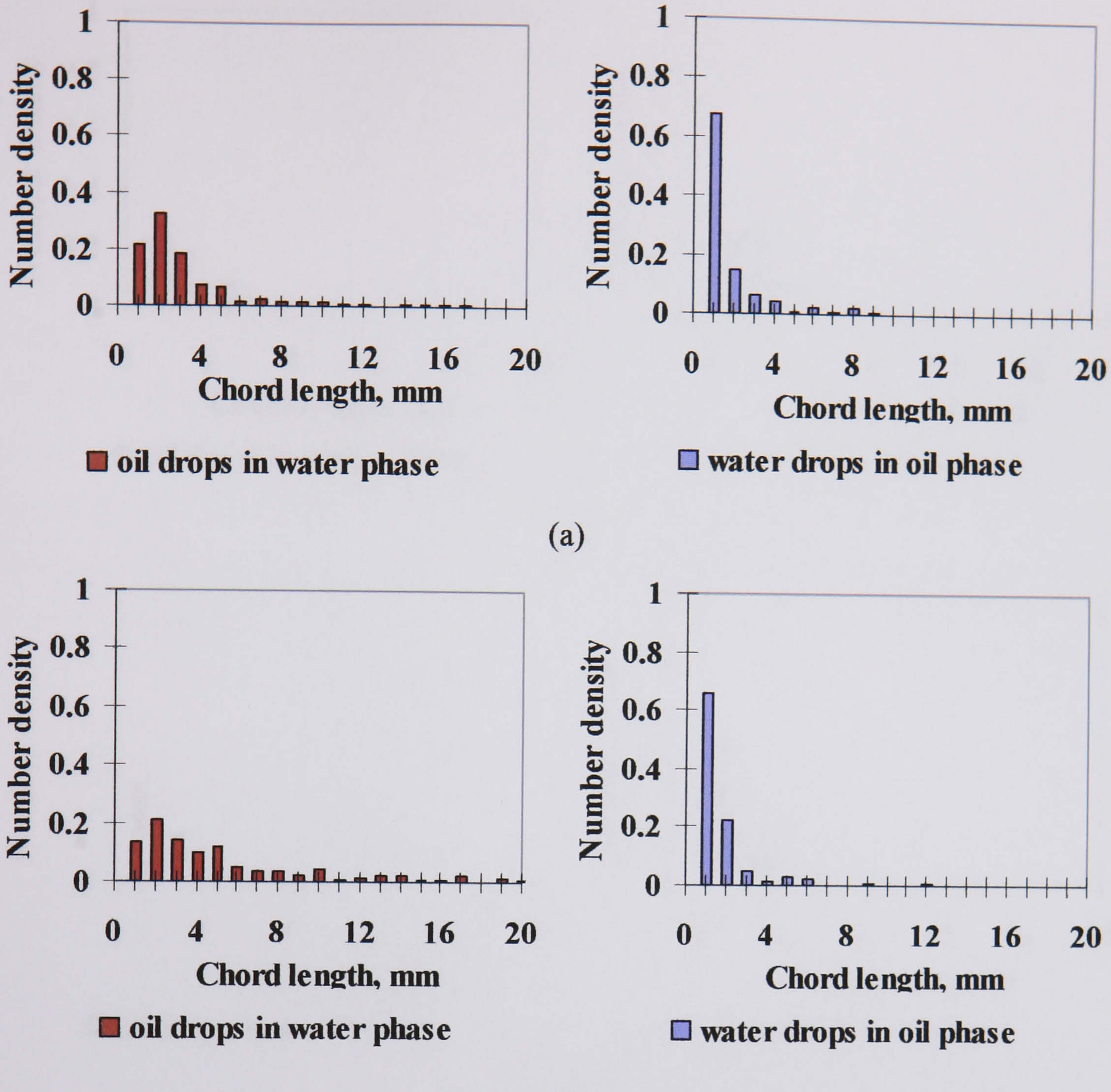

Fig. 7.19 Average chord length distributions of oil drops in water and water drops in oil at U_{so} = 1.10 m/s for (a) U_{sw} = 0.50 m/s, (b) U_{sw} = 0.80 m/s and (c) U_{sw} = 1.10 m/s in the 38 mm ID test pipe, 7 m from the inlet.

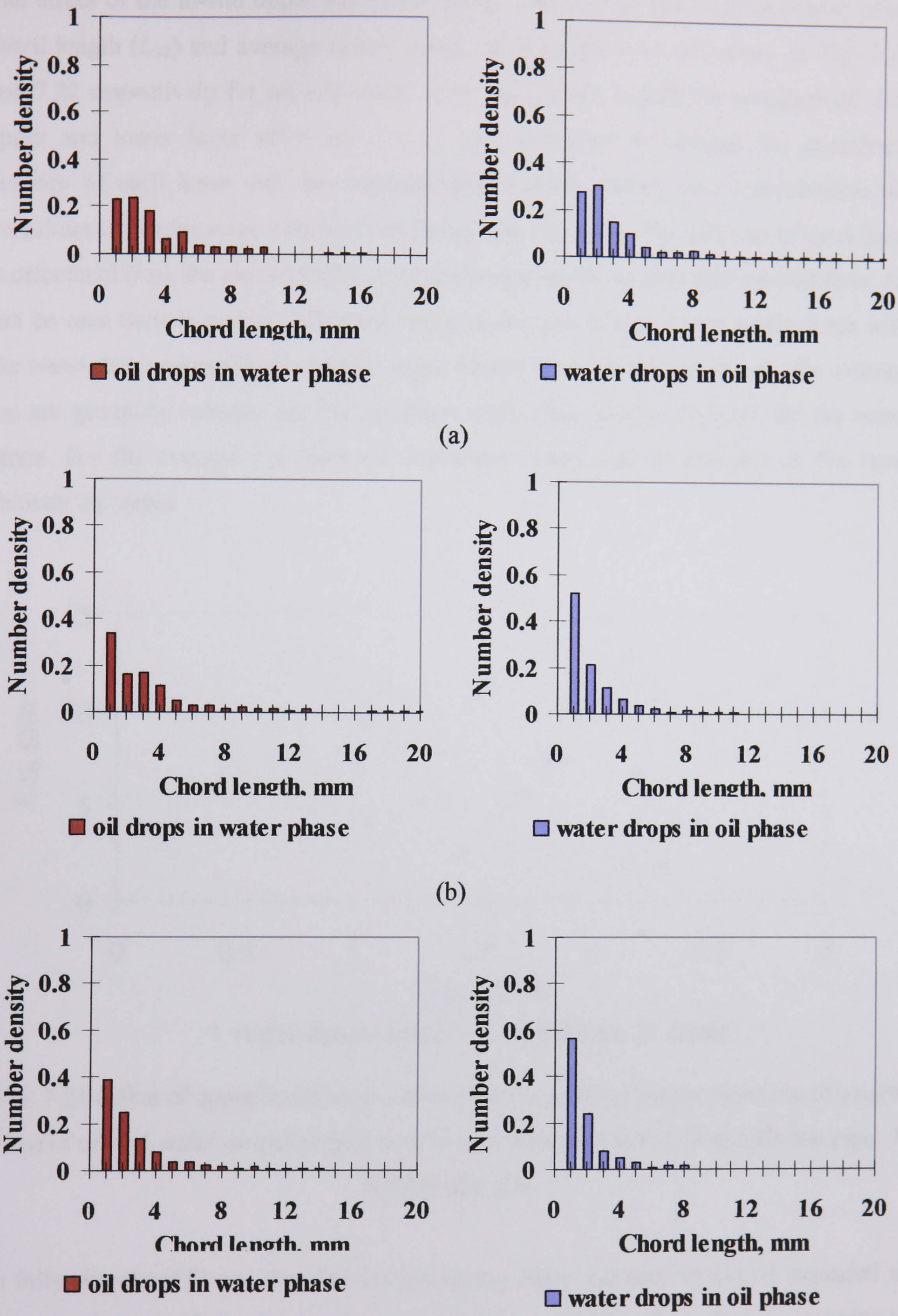

Fig. 7.20 Average chord length distributions of oil drops in water and water drops in oil at U_{so} = 1.40 m/s for (a) U_{sw} = 0.50 m/s, (b) U_{sw} = 0.80 m/s and (c) U_{sw} = 1.10 m/s in the 38 mm ID test pipe, 7 m from the inlet.

The effect of the in-situ upper and lower phase velocities on the average Sauter mean chord length (L_{32}) and average Linear mean chord length (L_{10}) are shown in Fig. 7.21 and 7.22 respectively for oil and water drops and all the conditions investigated. The upper and lower layer velocities (U_{layer}) are calculated by divided the superficial velocity of each layer with the corresponding hold-up taking into consideration the experimental entrainment values of one phase into the other. The hold-up of each layer is calculated from the experimental interface height assuming *stratified smooth* flow. As can be seen there is a clear difference between the size of the oil and water drops with the water drops generally the smaller ones. As the layer velocity increases, the average L_{32} are generally constant for the oil drops while they tend to decrease for the water drops. For the average L_{10}, both oil and water drops tend to decrease as the layer velocity increases.

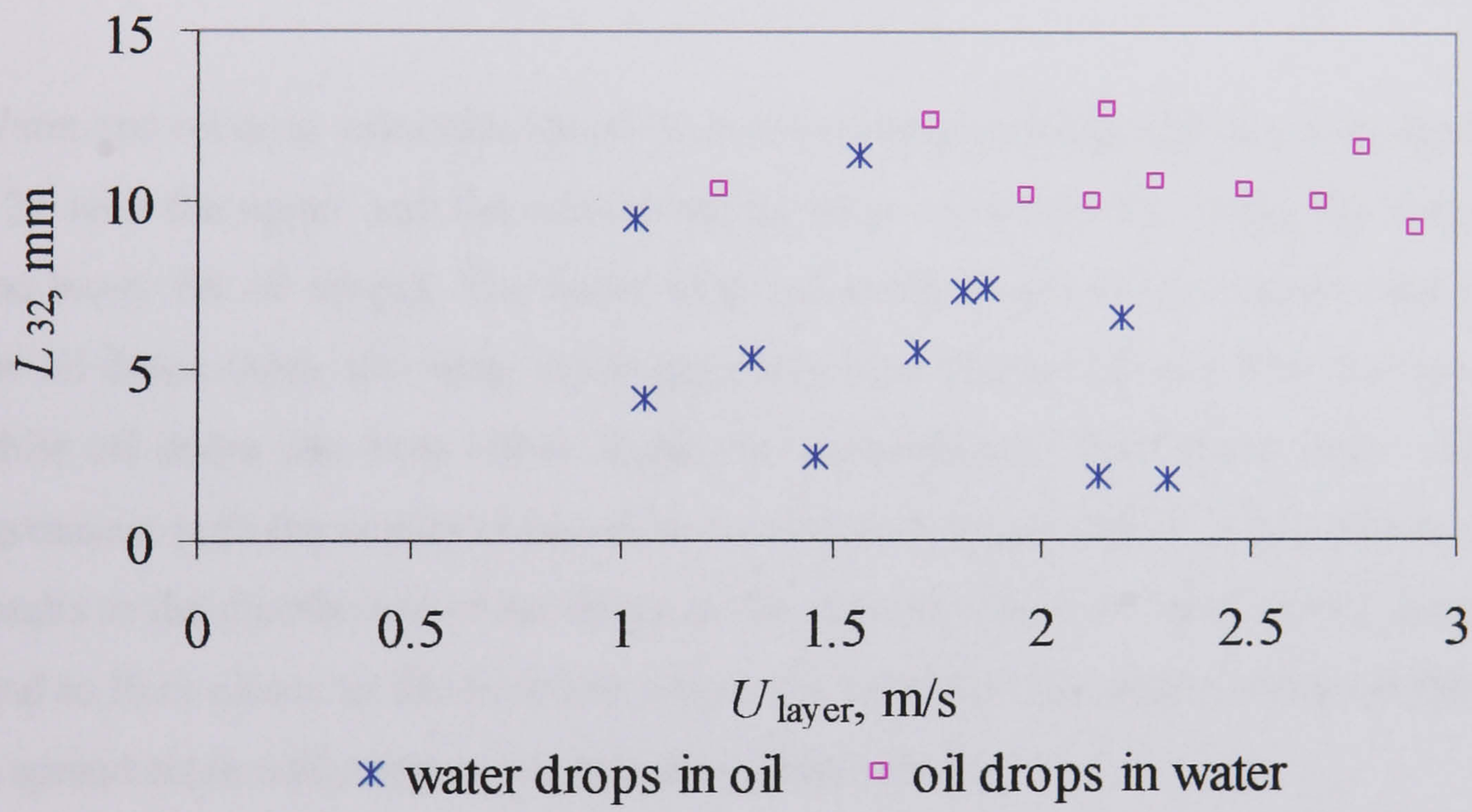

Fig. 7.21 Effect of upper/lower layer velocity on the average Sauter mean chord length (L_{32}) of oil and water drops for the conditions investigated in the 38 mm ID test pipe, 7 m from the inlet.

In fully *dispersed* flows, increase in continuous phase velocity would be expected to decrease the size of the dispersed drops. In *dual continuous* flow though, increase in velocity also increases the degree of entrainment. Larger entrainment means larger drops. As a result, the increase on the layer velocity does not necessarily result in smaller drops dispersed in that phase.

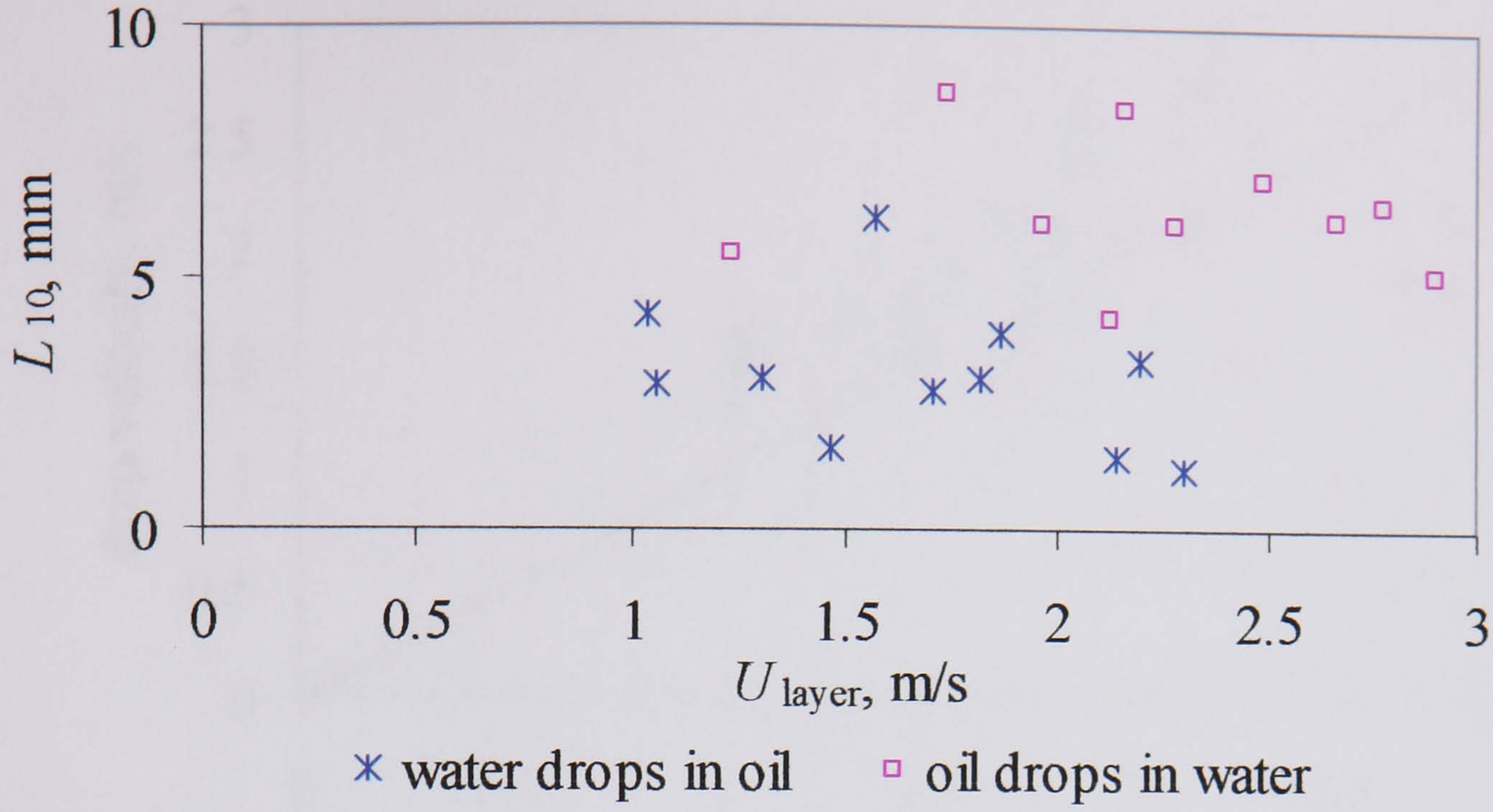

Fig. 7.22 Effect of upper/lower layer velocity on the average Linear mean chord length (L_{10}) of oil and water drops for the conditions investigated in the 38 mm ID test pipe, 7 m from the inlet.

Water and oil drop velocities found from the cross-correlation data are compared in Fig. 7.23 with the upper and the corresponding layer velocities (i.e. upper for water drops and lower for oil drops). The water drop velocities in general are higher than those of the oil drops. Also, the water drops generally have higher velocity than the upper layer while oil drops can have either higher or lower velocity than lower layer. This is an agreement with the results obtained by Lovick and Angeli (2004). They attributed these results to the distribution of the drops in the opposite phase. In other words, water drops tend to flow closer to the interface where the velocities are higher while oil drops tend to spread more uniformly in the opposite phase (see Fig. 7.17).

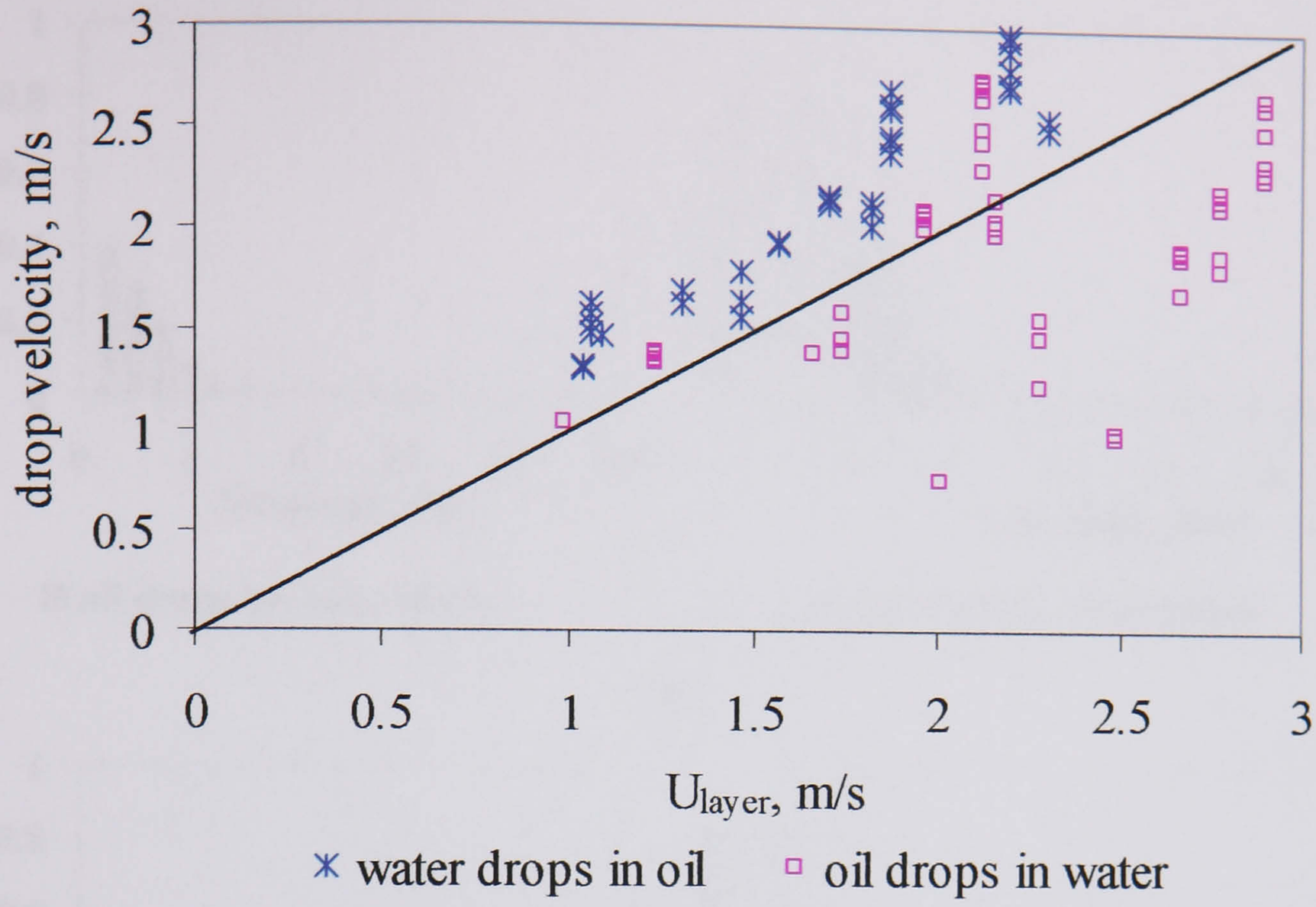

Fig. 7.23 Drop velocity of both water drops in oil and oil drops in water for all the conditions investigated during *dual continuous* horizontal oil-water flows in the 38 mm ID test pipe, 7 m from the inlet.

7.4 Drop Size Distribution

In this section, the measured chord length distributions were transformed to drop size distributions based on an algorithm developed by Hu et al. (2006) and discussed in section 2.6.4. The data presented in Figs. 7.19 and 20 as chord length distributions were converted to drop size distributions as shown in Figs. 7.24 and 25. The figures clearly reflect that chord length distributions are biased to larger sizes compared to drop size distributions. Also, the average Sauter mean diameters (d_{32}) for both oil drops in water and water drops in oil are calculated and shown below for different water and oil superficial velocities.

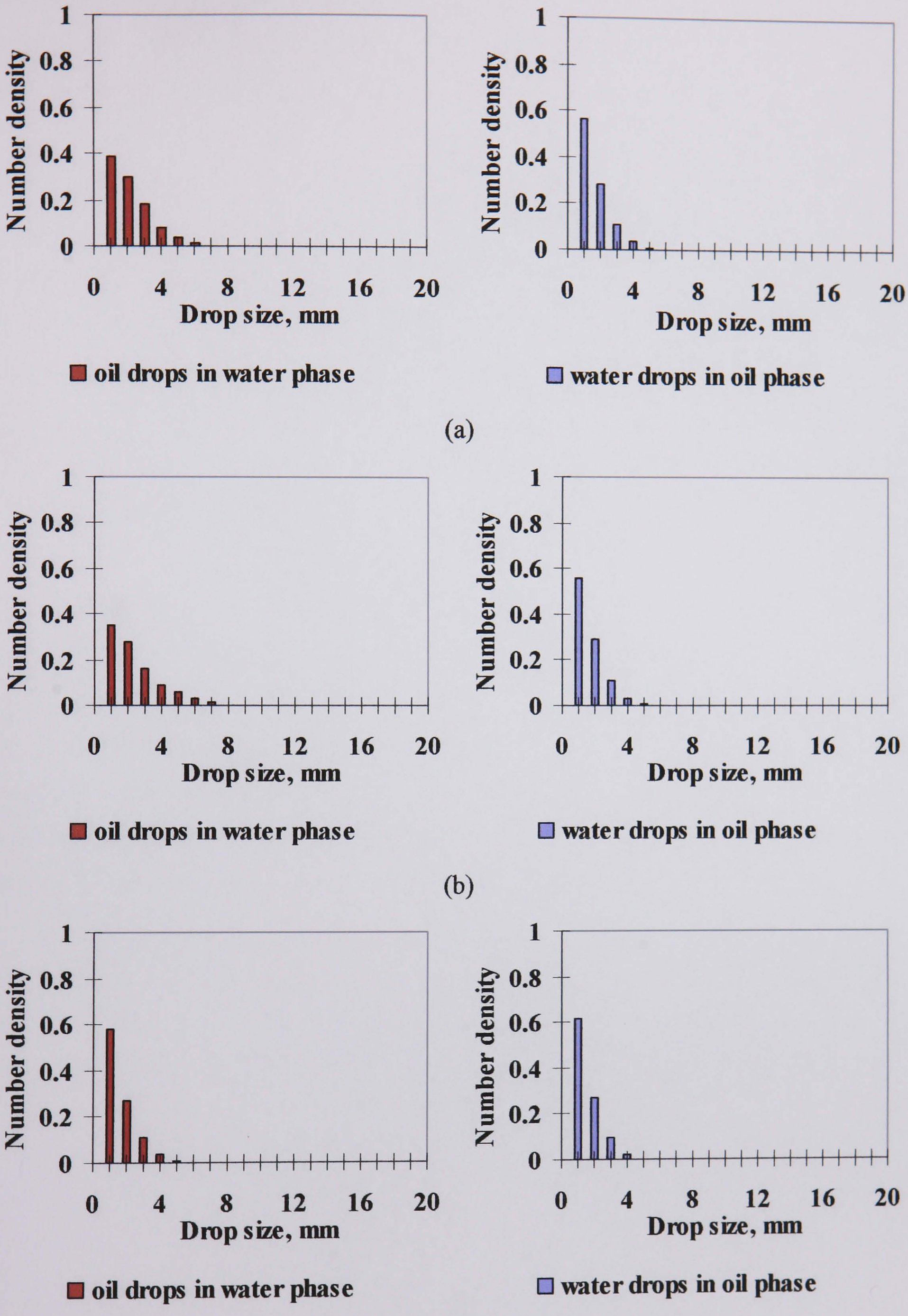

(a)

(b)

(c)

Fig. 7.24 Average drop size distributions of oil drops in water and water drops in oil at U_{so} = 1.10 m/s for (a) U_{sw} = 0.50 m/s, (b) U_{sw} = 0.80 m/s and (c) U_{sw} = 1.10 m/s. in the 38 mm ID test pipe, 7 m from the inlet

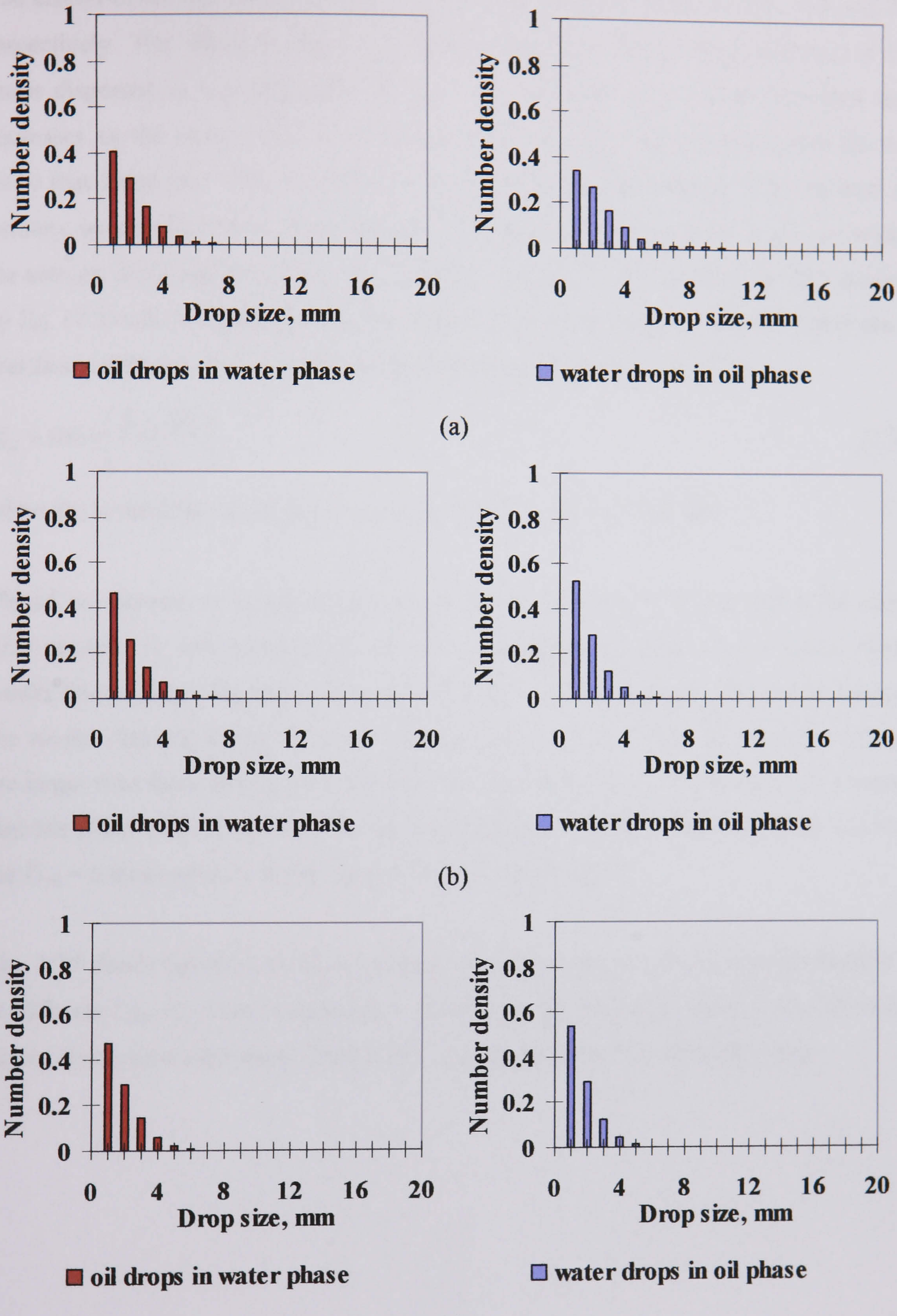

(a)

(b)

(c)

Fig. 7.25 Average drop size distributions of oil drops in water and water drops in oil at U_{so} = 1.40 m/s for (a) U_{sw} = 0.50 m/s, (b) U_{sw} = 0.80 m/s and (c) U_{sw} = 1.10 m/s in the 38 mm ID test pipe, 7 m from the inlet.

The effects of oil and water superficial velocity on d_{32} are shown in Figs. 7.26 and 27 respectively. The effect of water superficial velocity on the average diameter of oil drops dispersed in it is presented in Fig. 7.26. It would be expected that drop size decreases as the water velocity increases. However, the experimental results do not show that behaviour. This is attributed to two opposing phenomena. The increase in velocity would affect drop break up and decrease drop size. However, it also increases the amount of oil entrained from the oil phase into water. This is given by (E_o) defined by Eq. (7.3) which represents the percentage of oil flow rate entrained into water (note that this is different than oil entrainment in the water phase $E_{o/w}$, Eq. 7.2).

$$E_o = 100 \times \left(\frac{E_{o/w} Q_L}{Q_o} \right) \tag{7.3}$$

where Q_L is the flow rate of the lower layer and Q_o is the oil flow rate.

Therefore, increase in water velocity would tend to decrease drop size but at the same time increase E_o and consequently increase the dispersed in water oil fraction which would favour larger drops (increase the coalescence rate of drops). This would explain the results obtained in Fig. 7.26. For example, at U_{sw} = 0.20 m/s, the drop sizes found are larger than those at U_{sw} = 1.1 m/s and less than those at U_{sw} = 0.80 m/s. This means that the effect of E_o is greater than drop breakage due to the increase in water velocity for U_{sw} = 0.8 m/s while it is the opposite for U_{sw} = 1.10 m/s.

Fig. 7.27 shows the effect of oil superficial velocity on d_{32} of water drops dispersed in it at different U_{sw}. E_w is the percentage of water flow rate entrained into oil. Similar to the above, there is no clear trend of the effect of oil velocity on the water drop size.

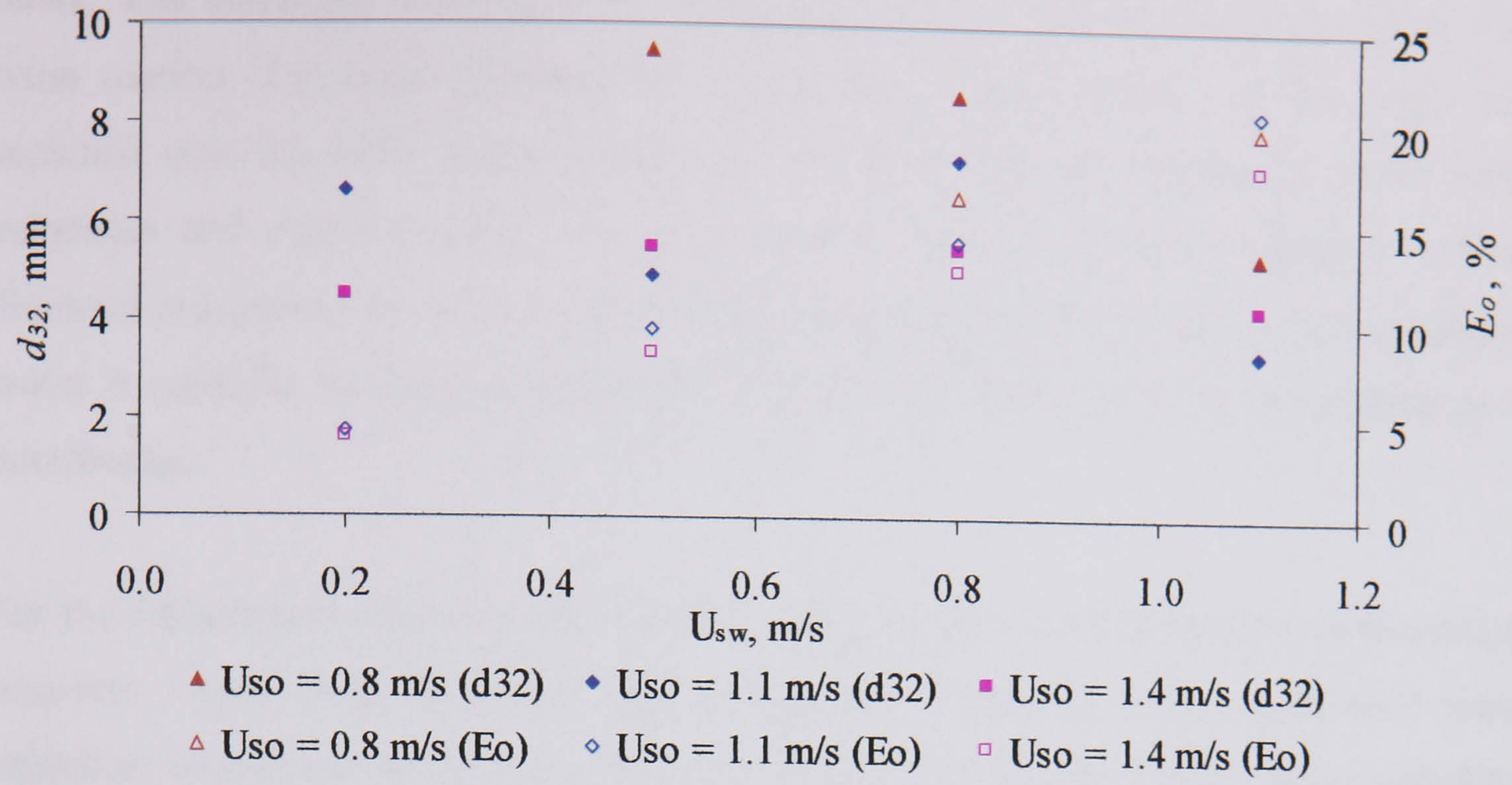

Fig. 7.26 Effect of superficial oil velocities on the Sauter mean diameter of oil drops in water at different U_{sw} in the 38 mm ID test pipe, 7 m from the inlet.

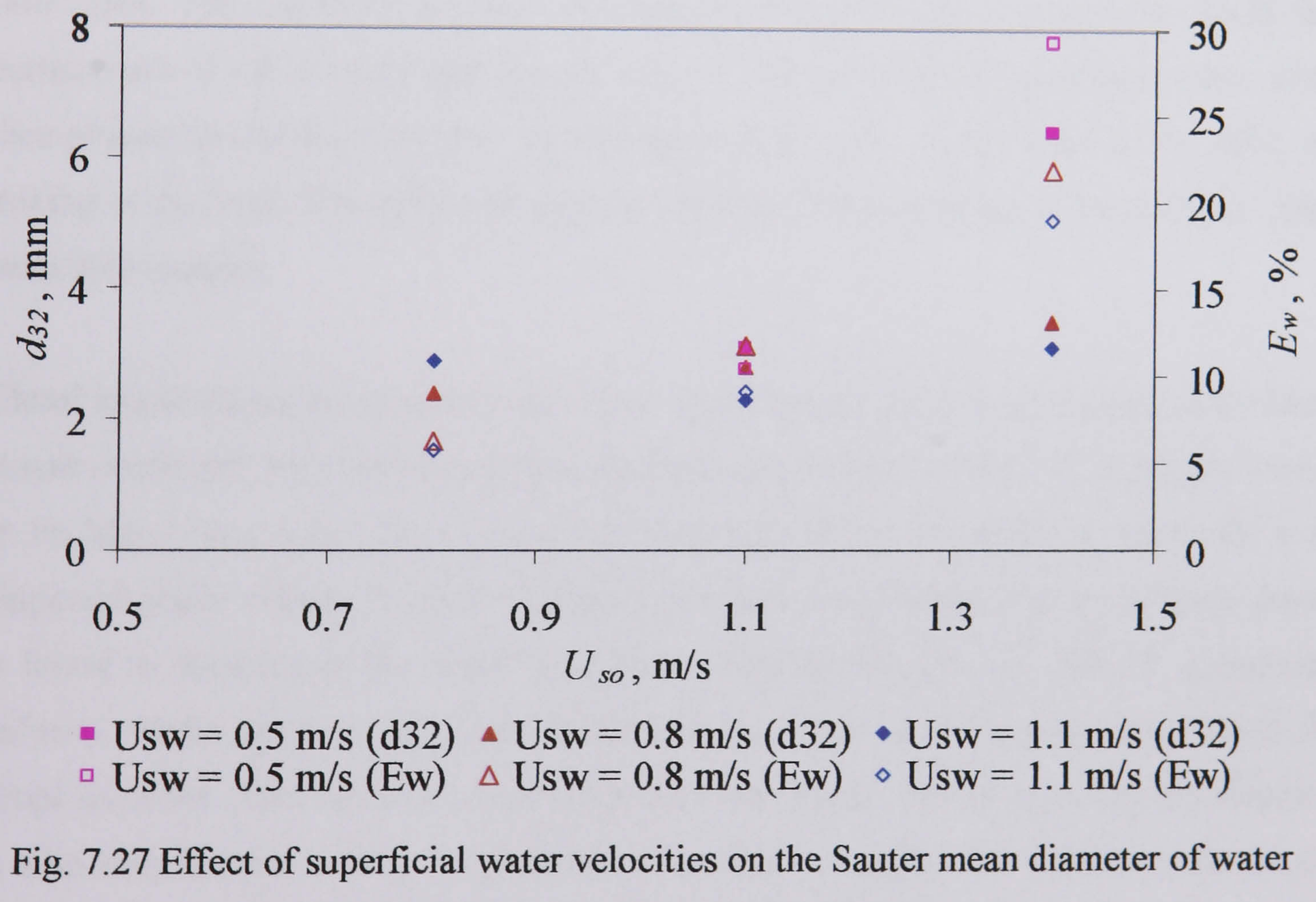

Fig. 7.27 Effect of superficial water velocities on the Sauter mean diameter of water drops in oil at different U_{so} in the 38 mm ID test pipe, 7 m from the inlet.

7.5 Summary

The entrained fraction of each phase into the other and the chord length and size of the entrained drops were studied in detail during *dual continuous* horizontal oil-water

flows. The entrained fractions were calculated from the phase distribution in a pipe cross section. The phase distribution is obtained by integrating over the pipe cross sectional area the local volume fractions measured with the impedance probe. Drop velocities and chord lengths were measured at different locations along a vertical diameter in a pipe cross section with the dual impedance probe. In all the measurements, water is consider continuous below 68 % oil while above that oil is considered to be continuous.

For the entrainment of each phase into the other, the degree of dispersion increases and occupies larger cross sectional area around the interface as the superficial water velocities increase at certain superficial oil velocity. The results show that the entrained fraction of water ($E_{w/o}$) increases as the input water flow rates increase while no trend is found with oil flow rate. The results also reveal that the amount of oil drops in water ($E_{o/w}$) increases as the input oil flow rates increase but there is no trend with input water flow rates. The entrained fraction was studied using two inlet geometries. Both the entrainment of oil in water and that of water in oil are found to be higher when after then phases join at the inlet they go through a bend. This is attributed to the effect of mixing in the bend. The difference between the two inlets increases as the oil and water velocities increase.

Chord length measurements indicated sizes up to 20 mm. Drop concentration and chord length decreased with increasing distance from the interface. Also, oil drops are found to be larger than water drops since oil tends to lose its continuity at relatively low dispersed phase volume fraction compared to water. The number density of large drops is found to decrease as the water superficial velocities increase at each oil superficial velocity. Water drops are in general faster than the velocity of the upper layer while oil drops could be either faster or slower than the lower layer. The chord length distribution is also transformed to drop size distribution using a method developed by Hu et al. (2006). The results show that the drop size distribution are shifted to smaller sizes compared to chord length distribution.

CHAPTER 8

Predictive Model of the Entrained Fraction in Horizontal Oil-Water Flows

Entrained fraction in *dual continuous* horizontal oil-water flows is studied based on a balance between the rate of entrainment and rate of deposition. In this chapter, section 8.1 emphasizes the importance of predicting entrained fraction in *dual continuous* flows. The development of the model and the mathematical equations are described in section 8.2. A comparison and discussion of the predicted entrained fraction of both oil in water and water in oil and experimental data from this study is presented in section 8.3. A comparison of the predicted entrained fraction with independent test data from the literature is shown in section 8.4. A conclusion is given in section 8.5.

8.1 Introduction

In previous chapters, the transition from *stratified/stratified wavy* to *dual continuous* flow in horizontal oil-water pipeline was studied. In this pattern, both oil and water maintain their continuity at the top and bottom of the pipe respectively but there is a dispersion of one phase into the other at various degrees (Fig. 8.1). The major issue in the analysis of the *dual continuous* pattern is the prediction of the fraction of one phase entrained into the other (*entrained fraction*). Accurate prediction of the entrained fraction is crucial to effectively model pressure drop and hold up in this regime.

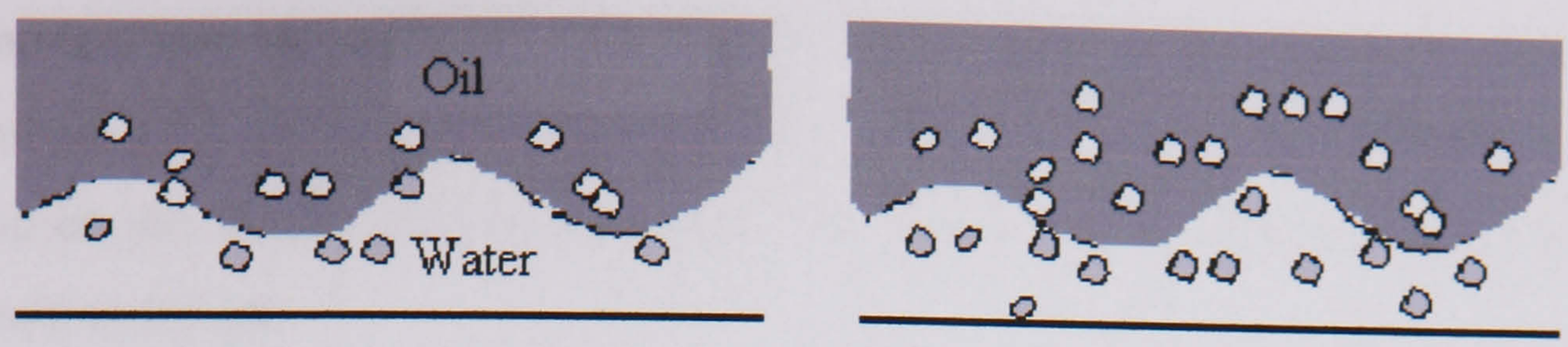

Dual continuous flow pattern

- Water drops
- Oil drops

Fig. 8.1 Sketch of the *dual continuous* flow pattern showing the distribution of oil and water drops

Despite its importance, only Valle (2000) has presented a model for entrained fraction which was based on the rates of drop entrainment and drop deposition. This model was used together with the two-fluid model to predict pressure drop during *dual continuous* flow. However, the entrainment correlations were not compared with experimental data (see section 2.5.2 for more details). Thus, the goal of the work in this chapter is to model the entrained fraction of oil in water and vice versa and to check the validity of the model against experimental data.

8.2 Model Development

The experimental results discussed in chapter 4 showed that no drops are observed when waves are absent from the oil-water interface. The work in chapter 5 suggested that Kelvin-Helmholtz instability will cause the wavy disturbance on the oil-water interface to grow in amplitude while interfacial tension and gravity will tend to stabilize it. When the destabilizing forces are greater than the stabilizing ones, waves become unstable. These unstable waves will continue to grow. Drops will eventually detach when the drag force acting on the wave crest that tends to deform it, becomes greater than the surface tension force that tries to prevent deformation (see chapter 6). Therefore, in the development of a physical model for entrained fraction of either oil or water into the opposite phase during *dual continuous* flow, the force balance on the wave crests for predicting the critical amplitude at which the waves form drops should be implemented. Photographs that clearly show the formation of drops are given in chapter 6.

Entrainment can be predicted theoretically from the balance between the rate of entrainment (R_A) and the rate of deposition (R_D). The rate of deposition is a linear function on the droplet concentrations (see the discussion in section 2.5) and it can be expressed as follow:

$$R_D = k_D C_D \tag{8.1}$$

where k_D is the deposition rate constant (m/s) and C_D is the droplet concentration (kg/m^3).

At equilibrium, R_A=R_D

Thus to predict the amount of entrainment of oil in water ($E_{o/w}$) and the amount of entrainment of water in oil ($E_{w/o}$), the rate of entrainment and deposition of each phase should be found.

8.2.1 Rate of entrainment

Since experimental observation showed that drops only form from waves, the rate of entrainment can be calculated if the volumes of entrainment swept off from the waves are known. The sketch in Fig. 8.2 shows a control volume of a pipe. The control volume consists of a number of waves ($N_{w,cv}$) on an axial length, *Ls*. The rate of entrainment of one phase into the other can be found by performing a control volume analysis on this length, *Ls*.

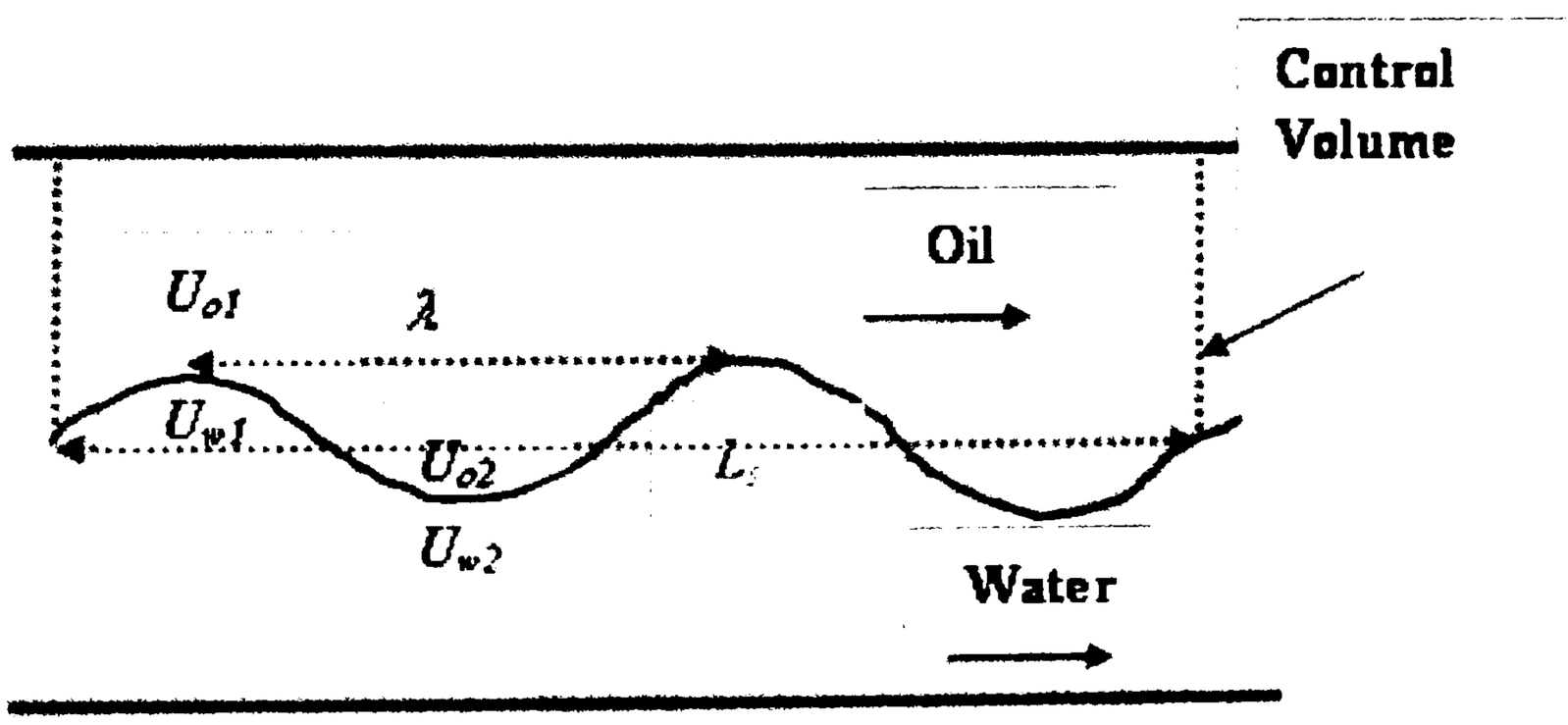

Fig. 8.2 Control volume of a pipe to calculate the entrainment rate of oil

The rate of entrainment is a function of the mass of entrained phase (mass of drops) that will detach from the waves per area of this control volume, A_{cv}, divided by the period of the entrainment phenomena in the control volume, $\tau_{w,cv}$. Thus the rate of entrainment of each phase can be given as (the effect of entrained drops on the waves is neglected):

$$R_A = \frac{V_{ent,w}\rho_{ent,w}N_{w,cv}}{A_{cv}\tau_{w,cv}} \tag{8.2}$$

where $V_{ent,w}$ is the volume of the entrained phase from each wave crest, $\rho_{ent,w}$ is the density of the entrained phase and $N_{w,cv}$ is the number of waves in the control volume. In the above it is assumed that all waves in the control volume will form drops.

The area of the control volume (A_{cv}) is expressed as (assuming that before the entrainment process no drops exist in the flow):

$$A_{cv} = Ls \times S_i \tag{8.3}$$

The number of waves in the control volume ($N_{w,cv}$) is given by:

$$N_{w,cv} = \frac{Ls}{\lambda} \tag{8.4}$$

To find the rate of entrainment of oil in the water phase, the period of entrainment phenomena in the control volume ($\tau_{w,cv}$) is calculated by dividing the wavelength by the difference between oil and water velocities at the trough of the wave where oil drops are expected to form. The oil velocity (U_{o2}) represents the velocity of oil above the wave trough while the water velocity (U_{w2}) characterizes the velocity of water below the wave trough. The equation is given by:

$$\tau_{w,cv} = \frac{\lambda}{|U_{w2} - U_{o2}|} \tag{8.5}$$

Thus the rate of entrainment of oil is expressed as:

$$R_{Ao} = \frac{V_{ent\_o,w}\rho_o|U_{w2} - U_{o2}|}{S_i \times \lambda^2} \tag{8.6}$$

On the other hand, the rate of entrainment of water can be written as

$$R_{Aw} = \frac{V_{ent\_w,w}\rho_w|U_{wl} - U_{ol}|}{S_i \times \lambda^2} \tag{8.7}$$

where the difference in velocities $(U_{wl} - U_{ol})$ is taken at the wave crest from where water drops are swept. U_{wl} represents the water velocity below the wave crest and U_{ol} the oil velocity above the wave crest.

8.2.2 Volume of the entrained wave

In chapter 6, a correlation was developed based on a force balance at the wave crest to predict the critical wave amplitude where waves will form drops. For the critical oil-wave amplitude, the equation is given by (see also Eq. (6.17) in chapter 6)

$$C_d \times A_{oil-waves} \times \rho_w \frac{(U_{w2} - U_{o2})^2}{2} \geq \sigma \times (2S_i) \times \frac{(\lambda/2)}{L} \tag{8.8}$$

While for the critical water-wave amplitude, the equation is given by

$$C_d \times A_{water-waves} \times \rho_o \frac{(U_{wl} - U_{ol})^2}{2} \geq \sigma \times (2S_i) \times \frac{(\lambda/2)}{L} \tag{8.9}$$

According to this equation the critical amplitudes at which drops start forming can be found using the experimental oil and water onset velocities. If a system is operating above the line representing the onset of entrainment in a graph of superficial oil and water velocities, then some oil will entrain into the water phase while some water drops will disperse in the oil phase. Once this happens new conditions will establish; where the required critical amplitudes to form drops are found to be lower than those calculated at the onset conditions. The difference in the volume of the waves at the onset conditions and at the new conditions after drops start forming will represent the entrained volume. To calculate the wave volumes it is assumed that at both conditions all waves have amplitudes equal to the critical amplitude for drop formation. Also for the calculation of the critical amplitudes from the above equations it is assumed that the wavelength is equal to 1 pipe diameter (see the discussion in chapter 6).

Based on the above assumptions, the volume of entrainment coming from each phase can be calculated at the onset of entrainment and the new condition assuming that the difference in amplitude will transfer to drops.

$$V_{ent,w} = V_{wave\_onset} - V_{wave\_new\,condition} \tag{8.10}$$

$$V_{wave} = \int_0^{\lambda/2} a\sin\left(\frac{2\pi x}{\lambda}\right)dx \times S_i = \frac{a\lambda}{2\pi}[\cos(0) - \cos(\pi)] \times S_i = \frac{a\lambda S_i}{\pi} \tag{8.11}$$

$$V_{ent,w} = \left(\frac{a\lambda S_i}{\pi}\right)_{wave\_onset} - \left(\frac{a\lambda S_i}{\pi}\right)_{wave\_new condition} \tag{8.12}$$

To simplify the calculations only one critical amplitude was used for the various sets of onset velocities, which was taken as the largest of all critical amplitudes obtained from the different onset velocities.

8.2.3 Rate of deposition

The deposition rate of oil drops in the water phase can be expressed as follows:

$$R_{Do} = k_{Do} C_{Do} \tag{8.13}$$

where k_{Do} is the deposition rate constant of the oil drops and C_{Do} is the concentration of oil droplets in the lower water phase, defined as (see section 2.5)

$$C_{Do} = \left(\frac{W_{od}}{Q_l S}\right) \tag{8.14}$$

where W_{od} is the mass flow rate of the oil drops, Q_l is the volumetric flow rate of the lower phase and S is the slip velocity between the oil drops and the water continuous phase. By assuming no slip between the dispersed and the continuous phase, $S = 1$.

Similarly, the deposition rate of water drops in the upper oil phase is defined as

$$R_{Dw} = k_{Dw} C_{Dw} \tag{8.15}$$

where k_{Dw} is the deposition rate constant of the water drops and C_{Dw} is the concentration of water droplets in the upper phase, given by

$$C_{Dw} = \left(\frac{W_{wd}}{Q_u S}\right) \tag{8.16}$$

where W_{wd} is the mass flow rate of the water drops, Q_u is the volumetric flow rate of the upper phase and S is the slip velocity between the water drops and the oil continuous phase.

Unfortunately, no correlation for the deposition rate constant in liquid-liquid flows is available in the literature. In this study, correlation of k_D/U^* found by McCoy and Hanratty (1977) in vertical annular gas-liquid flows is used to calculate the coefficient k_D. The equation is given by

$$k_D = 0.17U^* \tag{8.17}$$

where U^* is the friction velocity and is defined for oil drops in water as

$$U^* = \sqrt{\tau_w/\rho_w} \tag{8.18}$$

and for water drops in oil as

$$U^* = \sqrt{\tau_o/\rho_o} \tag{8.19}$$

8.2.4 Calculation of the entrained fraction of oil drops in the water phase ($E_{o/w}$)

The entrained fraction of oil in water $E_{o/w}$ is defined as the mass flow rate of the oil drops divided by the total mass flow rate of the lower water phase.

$$E_{o/w} = \frac{W_{od}}{W_{od}+W_{wc}} = \frac{W_{od}}{Q_l\rho_{mix}} = \frac{W_{od}}{Q_l[(1-E_{o/w})\rho_w + E_{o/w}\rho_o]} \tag{8.20}$$

At equilibrium the rate of entrainment is equal to the rate of deposition and by substituting Eq. (8.20) the following expression is found:

$$R_{Ao} = R_{Do} = k_{Do}\left(\frac{W_{od}}{Q_l}\right) = k_{Do}\frac{E_{o/w}\times Q_l[(1-E_{o/w})\rho_w + E_{o/w}\rho_o]}{Q_l} \tag{8.21}$$

Also, by substituting Eq. (8.6) for the rate of entrainment of oil into Eq. (8.21), the following equation is obtained:

$$\frac{V_{ent\_o,w}\rho_o|U_{w2}-U_{o2}|}{S_i\times\lambda^2} = k_{Do}\times E_{o/w}[(1-E_{o/w})\rho_w + E_{o/w}\rho_o] \tag{8.22}$$

8.2.5 Calculation of the entrained fraction of water drops in the oil phase ($E_{w/o}$)

The entrained fraction of water in oil $E_{w/o}$ is defined as the mass flow rate of water drops divided by the total mass flow rate of the upper oil phase. Similar to the above:

$$E_{w/o} = \frac{W_{wd}}{W_{wd} + W_{oc}} = \frac{W_{wd}}{Q_u \rho_{mix}} = \frac{W_{wd}}{Q_u [(1 - E_{w/o})\rho_o + E_{w/o}\rho_w]} \tag{8.23}$$

$$R_{Aw} = R_{Dw} = k_{Dw}\left(\frac{W_{wd}}{Q_u}\right) = k_{Dw}\frac{E_{w/o} \times Q_u [(1 - E_{w/o})\rho_o + E_{w/o}\rho_{wo}]}{Q_u} \tag{8.24}$$

$$\frac{V_{ent\_w,w}\rho_w |U_{wl} - U_{ol}|}{S_i \times \lambda^2} = k_{Dw} \times E_{w/o}[(1 - E_{w/o})\rho_o + E_{w/o}\rho_w] \tag{8.25}$$

8.3 Results and Discussions

From the above model, the entrained fractions of oil in water and water in oil were predicted for different input water fractions and using Eq. (8.17) for the k_D. The predictions were also compared with the flow patterns observed at these conditions.

8.3.1 Entrained fraction of oil drops in the water phase ($E_{o/w}$)

The model predictions of the entrained fraction of oil in water ($E_{o/w}$) are compared with the experimental data obtained in this work as shown in Fig. 8.3 using $k_D = 0.17U^*$ (Eq. (8.17)). It can be seen that the predictions did not match with the experimental values. This could be due to different reasons; however, the obvious one could be related to the k_D equation used in the calculation. Thus, the k_D equation (Eq. 8.17) must be corrected to better predict the entrainment data. This is done by implementing Eq. (8.22) to calculate k_D using the present study experimental entrained fraction data (see Table 8.1) and compared with those obtained using Eq. (8.17). The results are presented as a ratio of the predicted k_D using Eq. (8.22) divided by the calculated k_D using Eq. (8.17) plotted as a function of the superficial oil velocity divided by the mixture velocity (see Fig. 8.4). The results are plotted in log-log scale and show a trend of straight line. From Fig. 8.4, the corrected form of Eq. (8.17) for calculating the deposition rate constant of oil drops in the water phase (k_{Do}) is given as The gravity term is expected to

be important in liquid-liquid flows and it is in this case implicitly included in the k_{Do} equation which has been fitted to the experimental data:

$$k_{Do-corr} = 0.051\left(\frac{U_{so}}{U_m}\right)^{-2.08} U^* \tag{8.26}$$

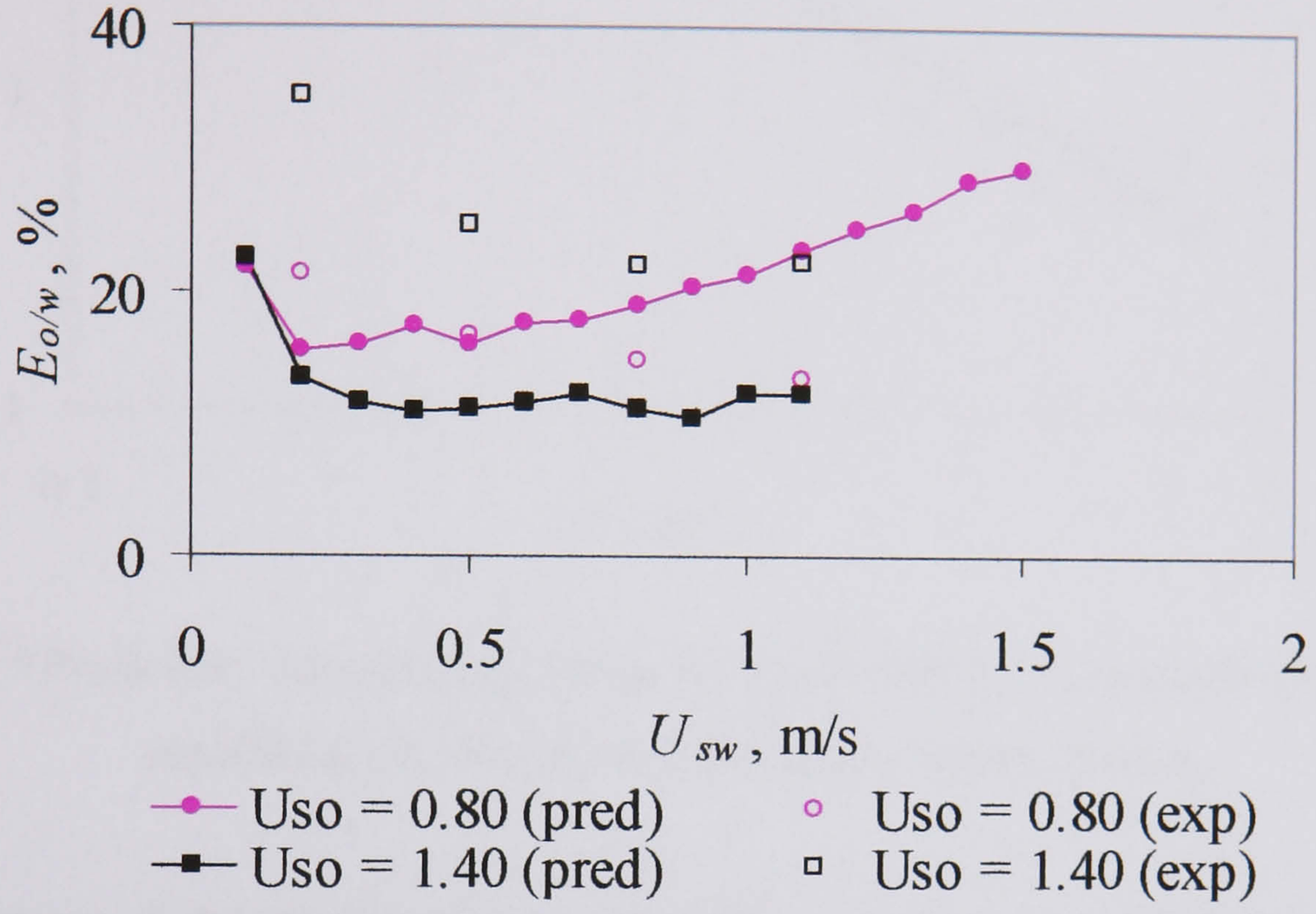

Fig. 8.3 Measured and predicted entrained fraction of oil in water ($E_{o/w}$) for the present study data using Eq. 8.22 and $k_D = 0.17U^*$ versus U_{sw}.

U_{so}, m/s	U_{sw}, /s	k_{Do}_Eq. 8.22, m/s	k_{Dw}_Eq. 8.25, m/s
0.35	0.60	0.030	0.012
0.35	0.80	0.051	0.007
0.35	1.10	0.085	0.007
0.80	0.20	0.006	0.124
0.80	0.50	0.011	0.071
0.80	0.80	0.018	0.047
0.80	1.10	0.030	0.026
1.10	0.20	0.006	0.237
1.10	0.50	0.010	0.113
1.10	0.80	0.013	0.042
1.10	1.10	0.016	0.033
1.40	0.20	0.005	0.212
1.40	0.50	0.007	0.074
1.40	0.80	0.009	0.042
1.40	1.10	0.012	0.021

Table 8.1 Predicted k_{Do} and k_{Dw} using Eq. 8.22 and 8.25 respectively and the experimental entrainment data.

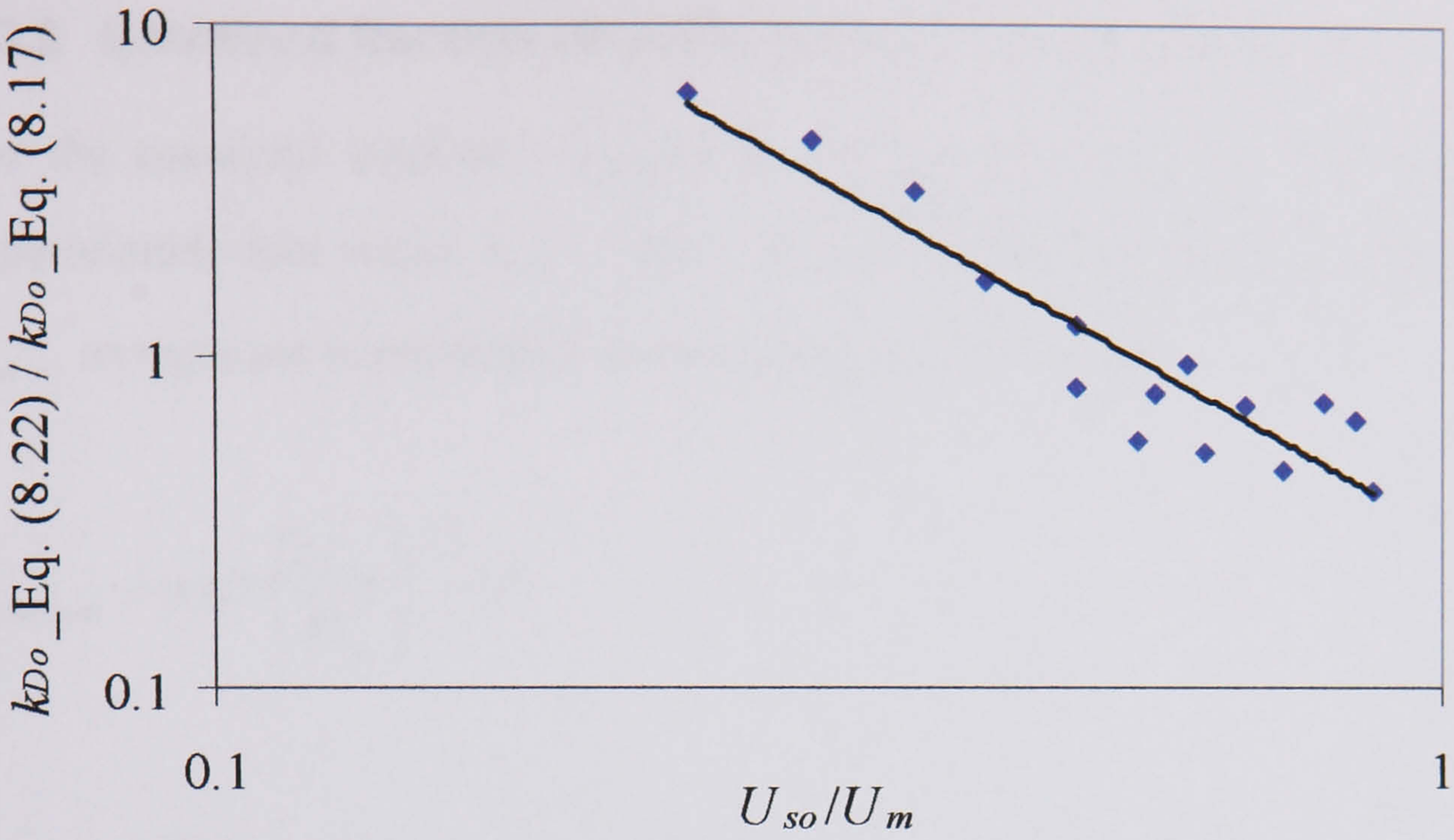

Fig. 8.4 Predicted / calculated k_{Do} using Eq. (8.22) and (8.17) respectively against superficial oil velocity divided by the mixture velocity

A comparison of the predicted $E_{o/w}$ using the corrected k_{Do} with the experimental results is presented in Fig. 8.5 for different water superficial velocities. It can be seen that using Eq. 8.26 gives better prediction. The average error of the proposed model is found to be 24 %. However, more data is indeed required to validate or even improve the model. Particularly a correlation for k_D based on liquid-liquid flows is needed.

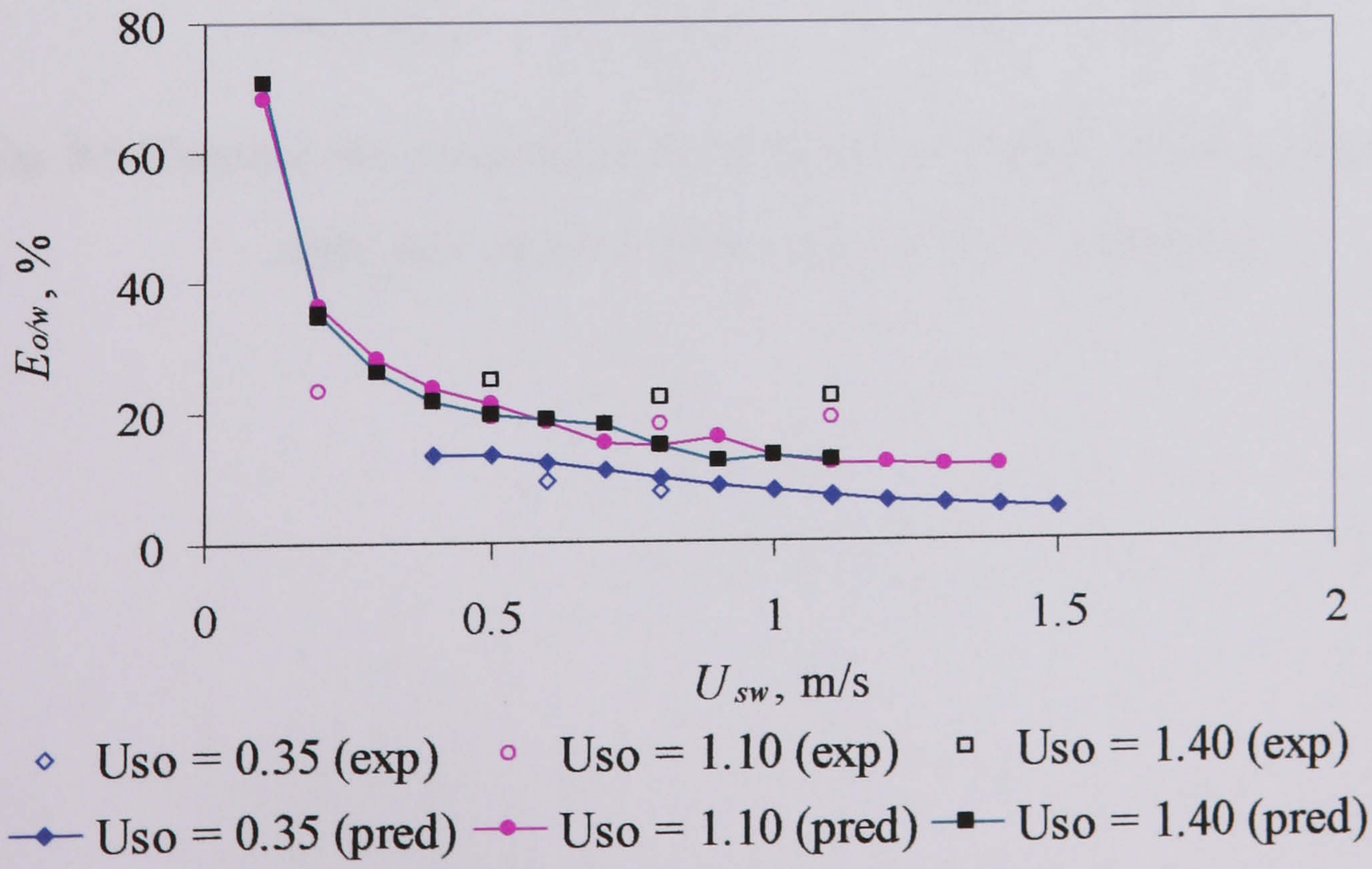

Fig. 8.5 Predicted and measured entrained fraction of oil in water ($E_{o/w}$) at different oil and water superficial velocities

8.3.2 Entrained fraction of water drops in the oil phase ($E_{w/o}$)

For the entrained fraction of water in oil, Fig. 8.6 presents the predicted and the experimental data when $k_D = 0.17U^*$ is used. Similar to the procedure followed for $E_{o/w}$, an equation is developed to correct k_{Dw} (see Fig. 8.7):

$$k_{Dw-corr} = 0.077\left(\frac{U_{sw}}{U_m}\right)^{-1.8} U^* \tag{8.27}$$

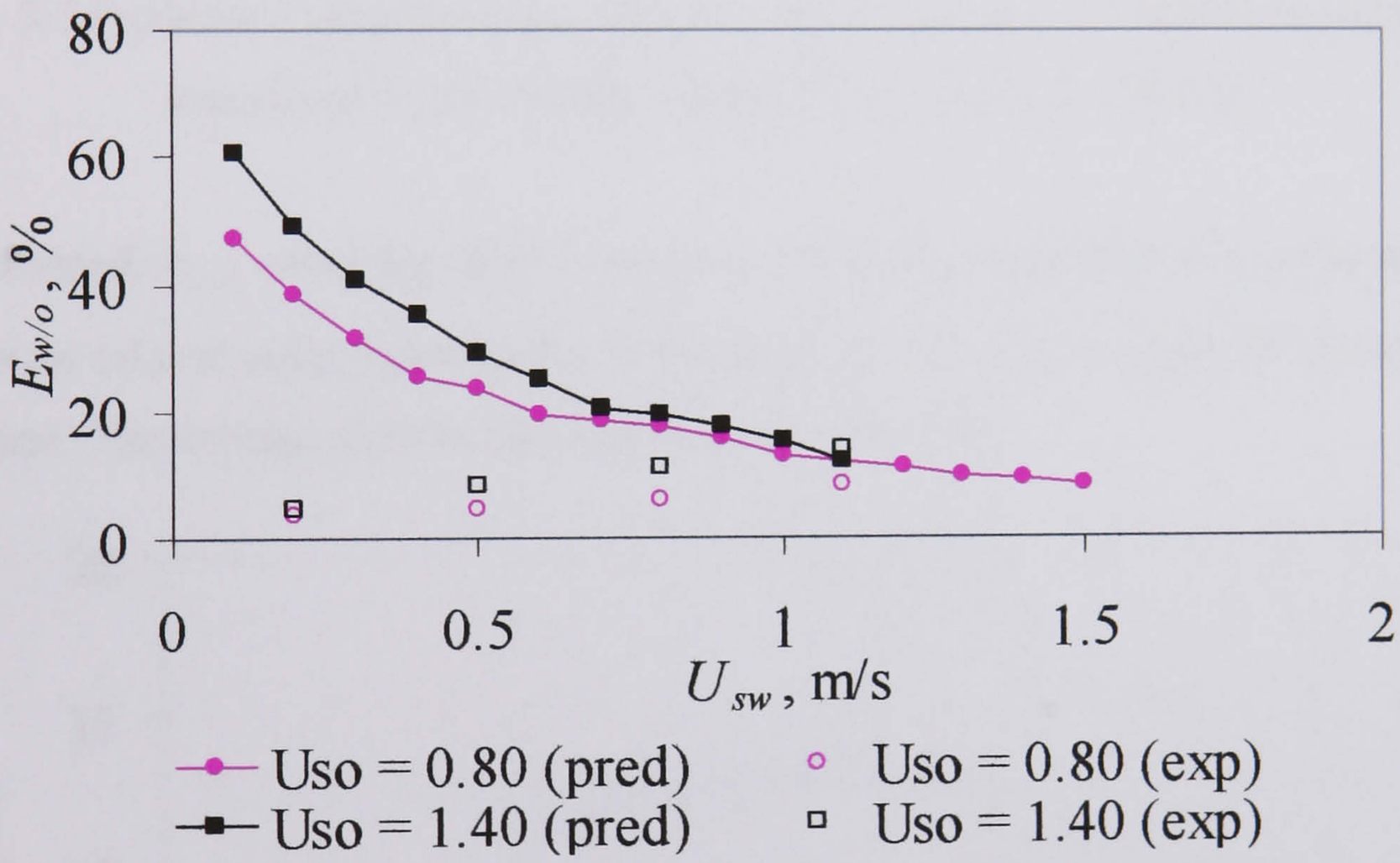

Fig. 8.6 Measured and predicted entrained fraction of water in oil ($E_{w/o}$) for the present study data using Eq. 8.25 and $k_D = 0.17U^*$ versus U_{sw}.

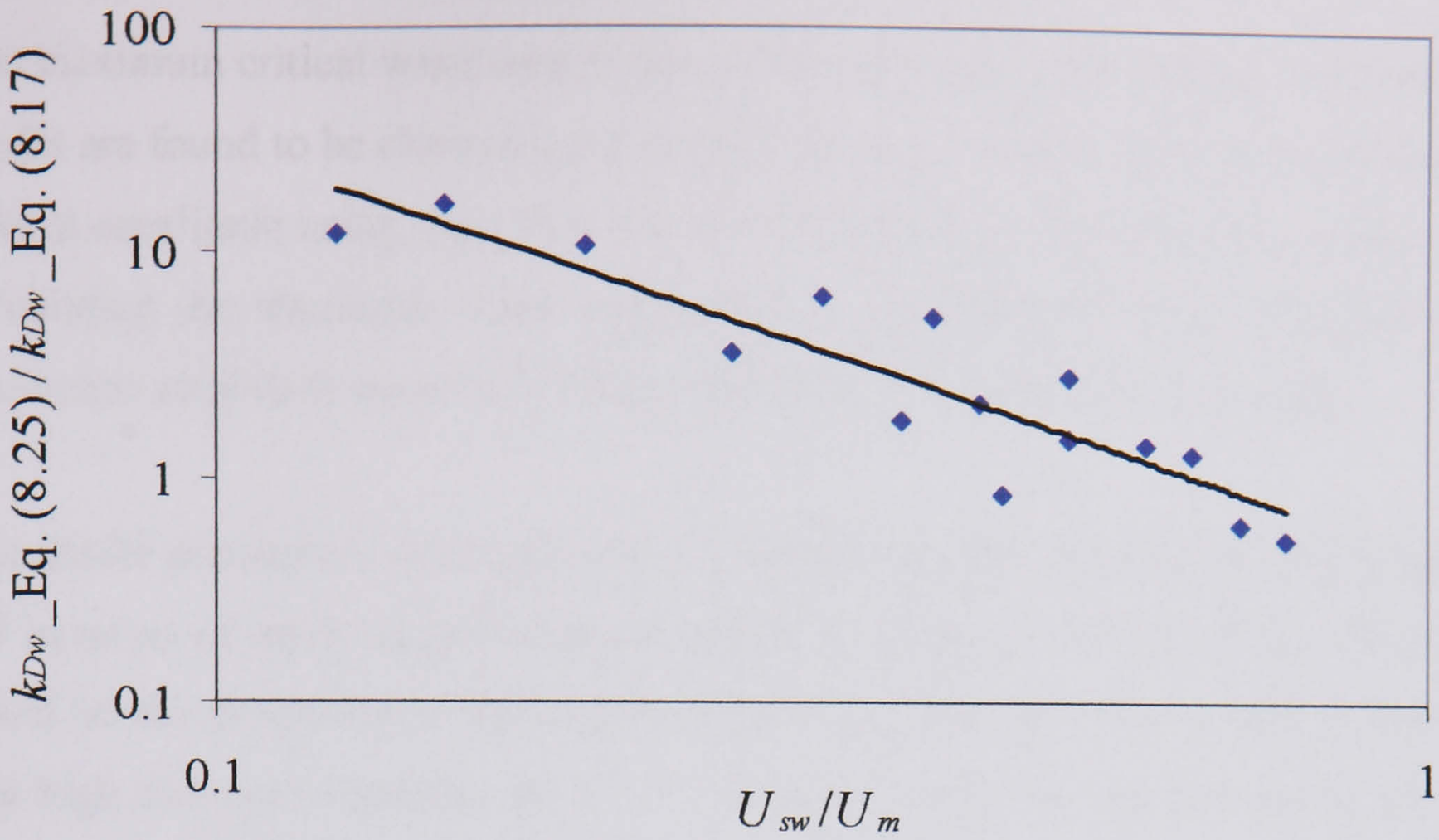

Fig. 8.7 Predicted / calculated k_{Dw} using Eq. (8.25) and (8.17) respectively against superficial water velocity divided by the mixture velocity

The corrected $E_{w/o}$ using Eq. 8.27 is compared with the experimental entrainment data at different oil and water superficial velocities in Fig. 8.8. The comparison shows better prediction. The average error in the predicted result is 30 %.

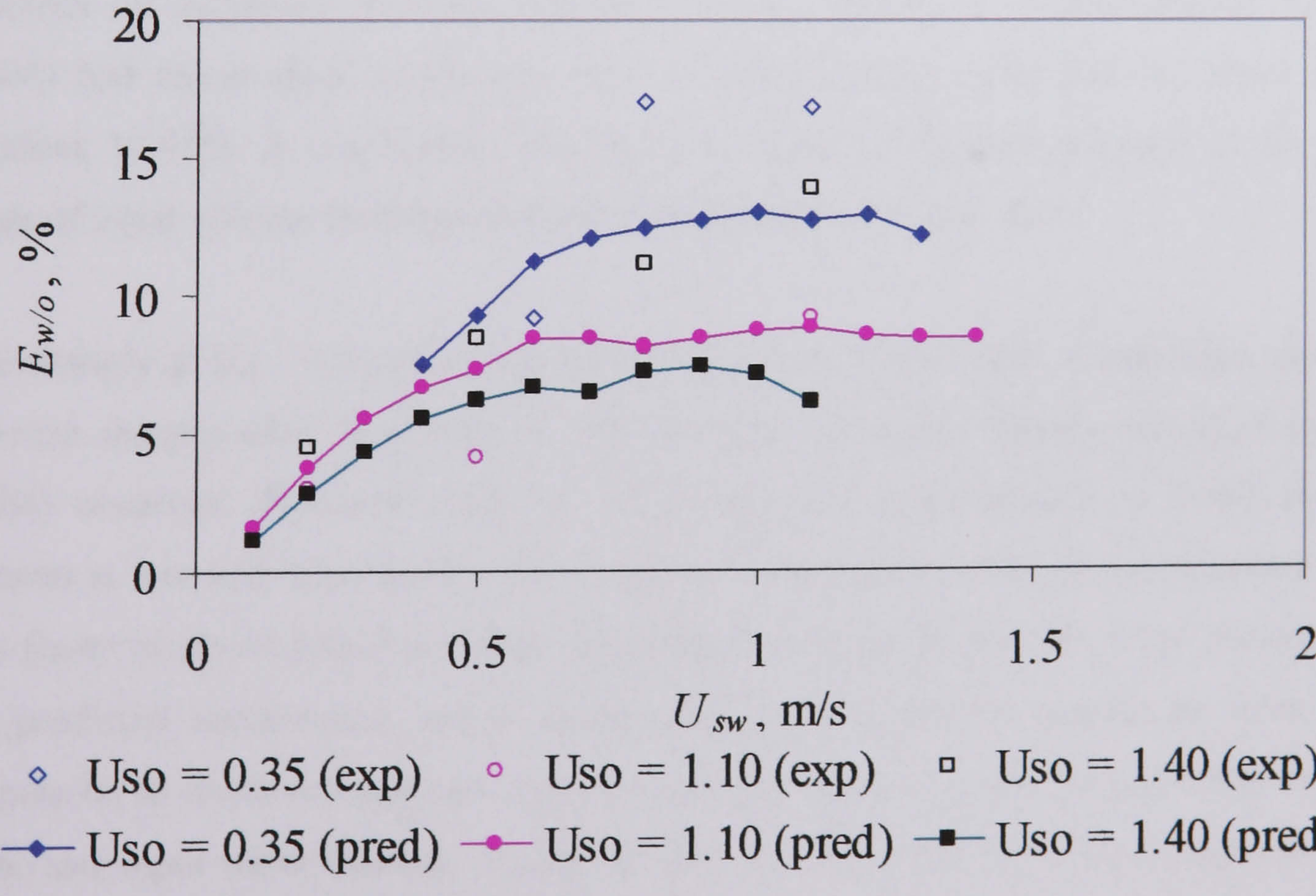

Fig. 8.8 Predicted and measured entrained fraction of water in oil ($E_{w/o}$) at different oil and water superficial velocities

8.3.3 Discussion of the results

The maximum critical wave amplitudes at the onset velocities needed in the entrainment model are found to be close to 0.1 times the diameter. This was found by calculating the critical amplitude using Eqs. (8.8 and 8.9) at different onset velocities. Thus, to avoid calculating the maximum wave amplitudes at the different onset velocities a critical maximum amplitude equal to 0.1 times the diameter was used for all cases.

The model predictions of entrainment of oil in water and water in oil are plotted in Fig. 8.9 in terms of input water fraction at different mixture velocities (U_m). The results are based on the properties of the test fluids used in this study. The trends vary at the low and high mixture velocities. At U_m = 1.0 and 1.5 m/s the entrainment of oil in water ($E_{o/w}$) with decreasing water fraction increases until it reaches around 70 and 50 % respectively at 10% input water. Above this point, the oil becomes continuous while the water becomes disperse since the oil is found to be continuous around 68 % oil.

Similarly, the entrainment of water in oil $E_{w/o}$ increases as the oil fraction decreases (water fraction increases) until it reaches 30 % (the point where the water becomes continuous) at input oil fraction 10% (90% input water fraction) and then the flow becomes *oil dispersed in wate*r instead of *dual continuous*. Experimentally Lovick (2004) had found *dual continuous* flow at these mixture velocities for input water fractions 10-90%. It can be seen that the model also predicts entrainment at the same range of input volume fractions indicating also *dual continuous* flow.

Interestingly at U_m = 2.0 and 2.5 m/s entrainment curves for both oil and water seem to increase sharply after they reach a critical value. At these mixture velocities Lovick (2004) observed *dispersed water in oil* (*Dw/o*) and *dispersed oil in water* (*Do/w*) patterns at low and high input water fractions respectively while *dual continuous* flow was found at the intermediate input fractions. It is possible that the sharp increases in the predicted entrainment curves could indicate flow pattern transitions from *dual contimuous* to *dispersed* regimes. For example the increase in the oil entrained fraction at the low input water fractions would indicate that the water layer has disappeared and no oil can therefore be entrained (transition from *dual continuous* to *Dw/o*) while the

increase in the water entrained fraction at high water fractions would mean that the oil layer has disappeared (transition from *dual continuous* to *Do/w*).

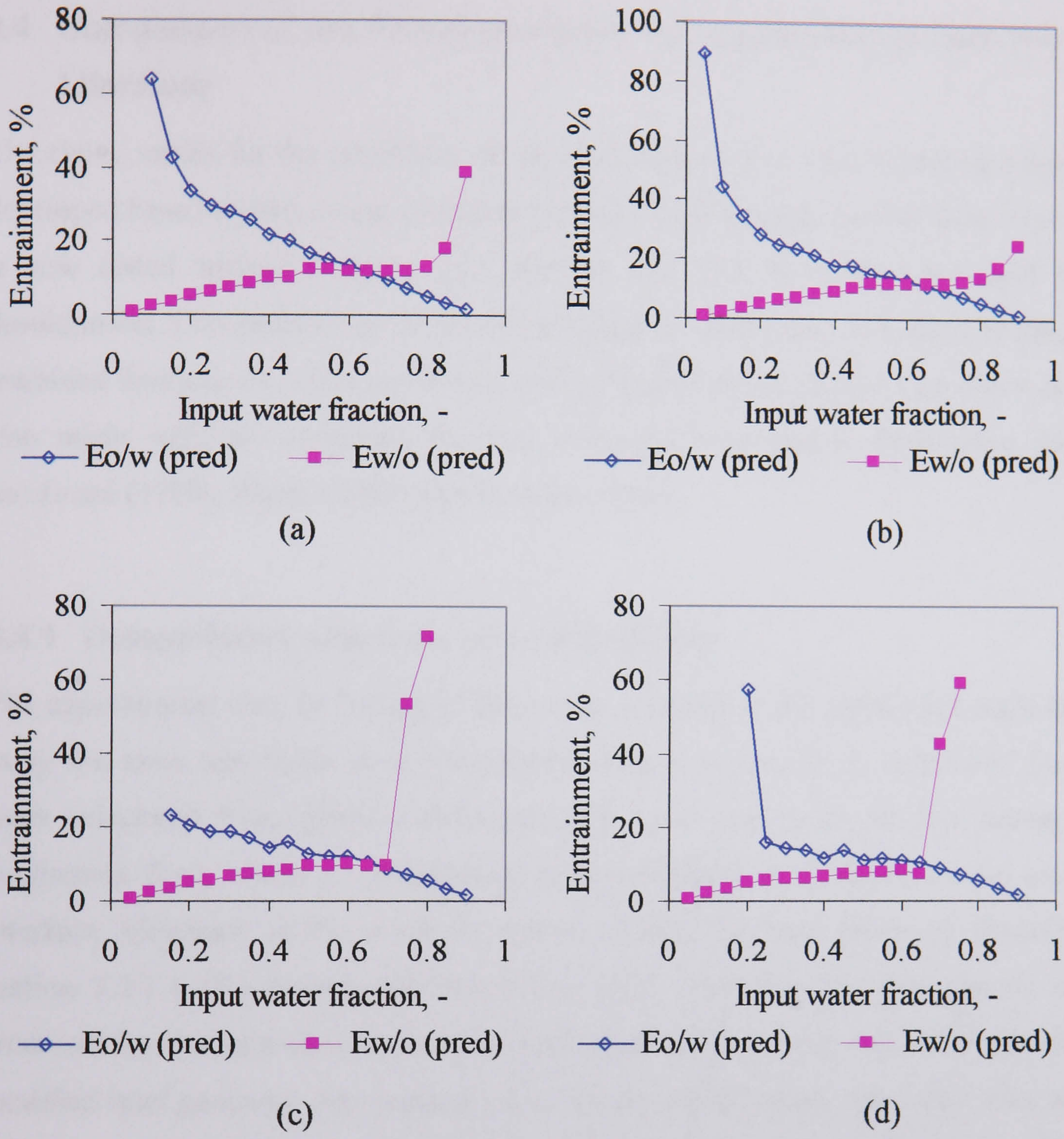

Fig. 8.9 Predicted entrained fraction of oil in water ($E_{o/w}$) and water in oil ($E_{w/o}$) at different input water fractions for (a) U_m = 1.0 m/s, (b) U_m = 1.5 m/s, (c) U_m = 2.0 m/s and (d) U_m = 2.5 m/s.

In addition the model shows the sharp increase in the oil entrainment curves to occur at 15 % and 25 % water fraction at mixture velocities of 2 and 2.5 m/s respectively. Experimentally Lovick (2004) found the transition from *DC* to *Dw/o* flow to occur at 20% water fraction for both mixture velocities. For the entrainment of water in oil, the sharp increase in the entrainment curve occurs at 70% for 2 m/s and 65 % for 2.5 m/s while experimentally the change from *DC* to *Dw/o* was found at 60 % for both mixture

velocities. Thus, the model presented above can be used to predict the transition between *dual continuous* and *dispersed* patterns.

8.4 Comparison of the Proposed Model with Experimental Data from the Literature

The above model for the prediction of entrained fractions in *dual continuous* flow was developed based on theoretical considerations and current experimental data. The model is now tested against different experimental data that have not been used for its development. Comparisons of the model predictions were made with directly measured entrained fractions by Valle and Kvandal (1995) and Lovick (2004). Comparisons were also made with the entrained fractions retrieved from phase distribution data by Soleimani (1999), Elseth (2001) and Hussain (2004).

8.4.1 Comparisons with Data by Lovick (2004)

The experimental data by Lovick (2004) were obtained in the same pilot scale facility using the same test fluids as in the present study (see chapter 3). Entrained fractions were calculated from phase distribution data in a pipe cross section during *dual continuous* flow, where a conductivity probe indicated the position of the oil-water interface. However, in the work by Lovick (2004) the inlet geometry described in section 3.2.1.1 (T-junction with bend) was used, while for the development of the entrained fraction correlations in the present study experimental data obtained with the modified inlet geometry (see section 3.2.1.2) were implemented. The latter inlet section provides a better stratification to the flow and reduces any mixing effects. The effect of inlet geometry on the entrained fraction was discussed in Section 7.1.4.

The comparison (see Fig. 8.10) shows a reasonable agreement between predicted and the experimental values taking also into consideration the ambiguity in calculating entrained fraction from local volume fraction data (2.5%).

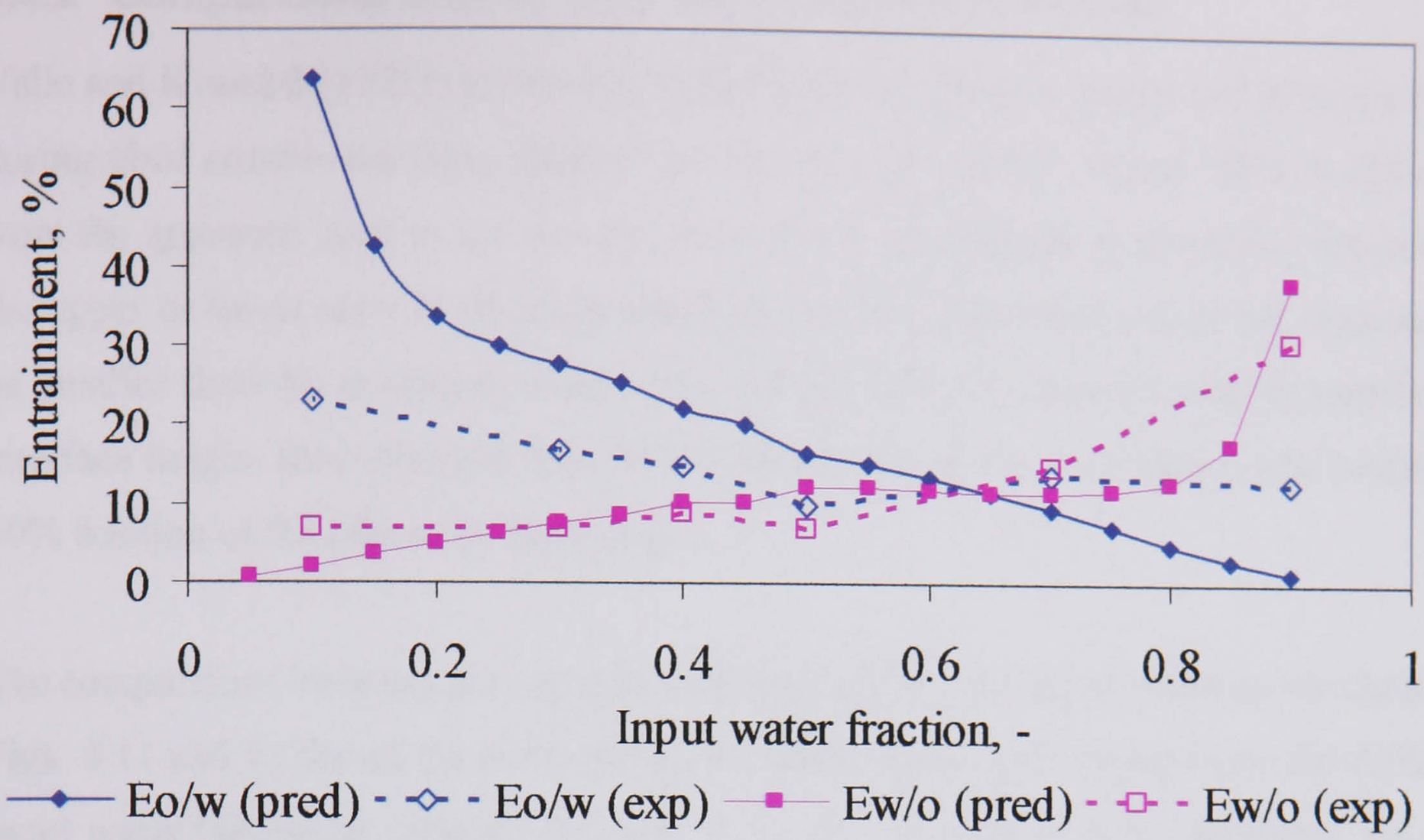

(a)

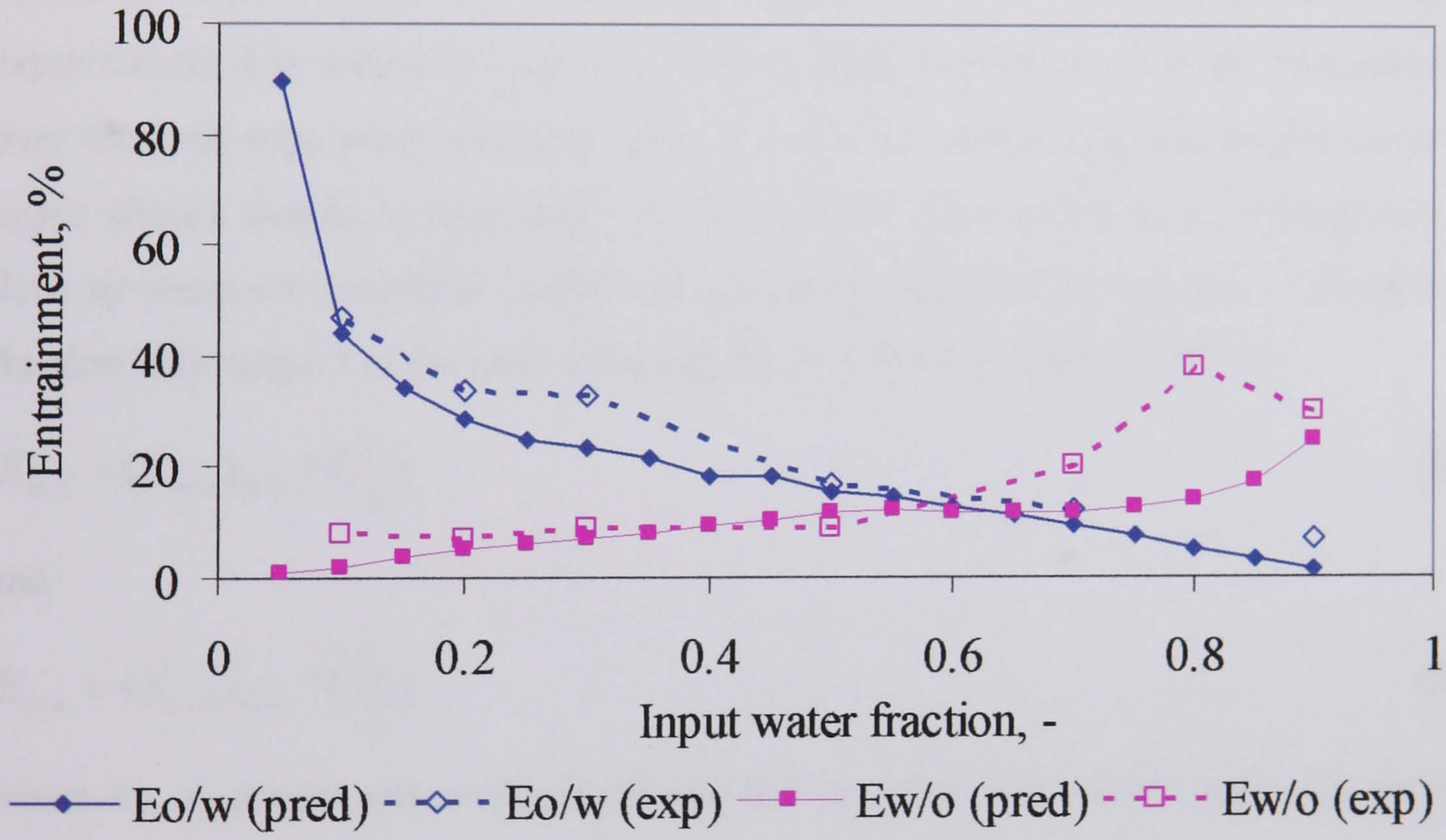

(b)

Fig. 8.10 Comparison between the predicted entrained fractions of oil in water ($E_{o/w}$) and water in oil ($E_{w/o}$) at (a) U_m = 1.0 m/s, (b) U_m = 1.5 m/s with the experimental data by Lovick (2004).

8.4.2 Comparisons with Data by Valle and Kvandal (1995)

Valle and Kvandal (1995) reported entrained fractions of oil in water and of water in oil during *dual continuous* flow relative to the total pipe cross section. This is different from the approach used in the current work where entrainment is given as a fraction of the upper or lower layer in the *dual continuous* flow. Thus, their results are expected to be smaller than the predicted ones. Also, as they did not measure experimentally the interface height, they assumed that the interface between the two phases was located at 50% fraction of the oil/water dispersion.

The comparisons between the experimental data and the model predictions are shown in Figs. 8.11 and 12 for oil drops in water and water drops in oil respectively for different input water fraction at mixture velocity of 1.5 m/s. As expected, the predicted $E_{o/w}$ and $E_{w/o}$ are found to be higher than the measured ones due to the different definition of the entrained fraction used by Valle and Kvandal (1995). Predictions closer to the experimental data would be expected if the predicted entrained fraction was calculated over the total pipe cross sectional area. For that the areas occupied by the lower and upper phases should be estimated. As there is no other information present this was done by using the two-fluid model and assuming smooth *stratified* flow. The entrained fraction with respect to the total cross section can thus be found as follows:

$$E_{w/o} = (E_{w/o})_{\text{mod}} * (\frac{A_o}{A}) \tag{8.28}$$

and

$$E_{o/w} = (E_{o/w})_{\text{mod}} * (\frac{A_w}{A}) \tag{8.29}$$

where A_w, A_o are the area of the water and the oil phase respectively assuming *stratified smooth.*

The new predictions are closer to the experimental entrained fractions as can be seen from Figs. 8.11 and 8.12. The assumption of smooth *stratified* flow in Eq. (8.33) above as well as the positioning of the interface at 50% phase fraction for the evaluation of the experimental entrained fractions would account for the discrepancies between model and experimental results.

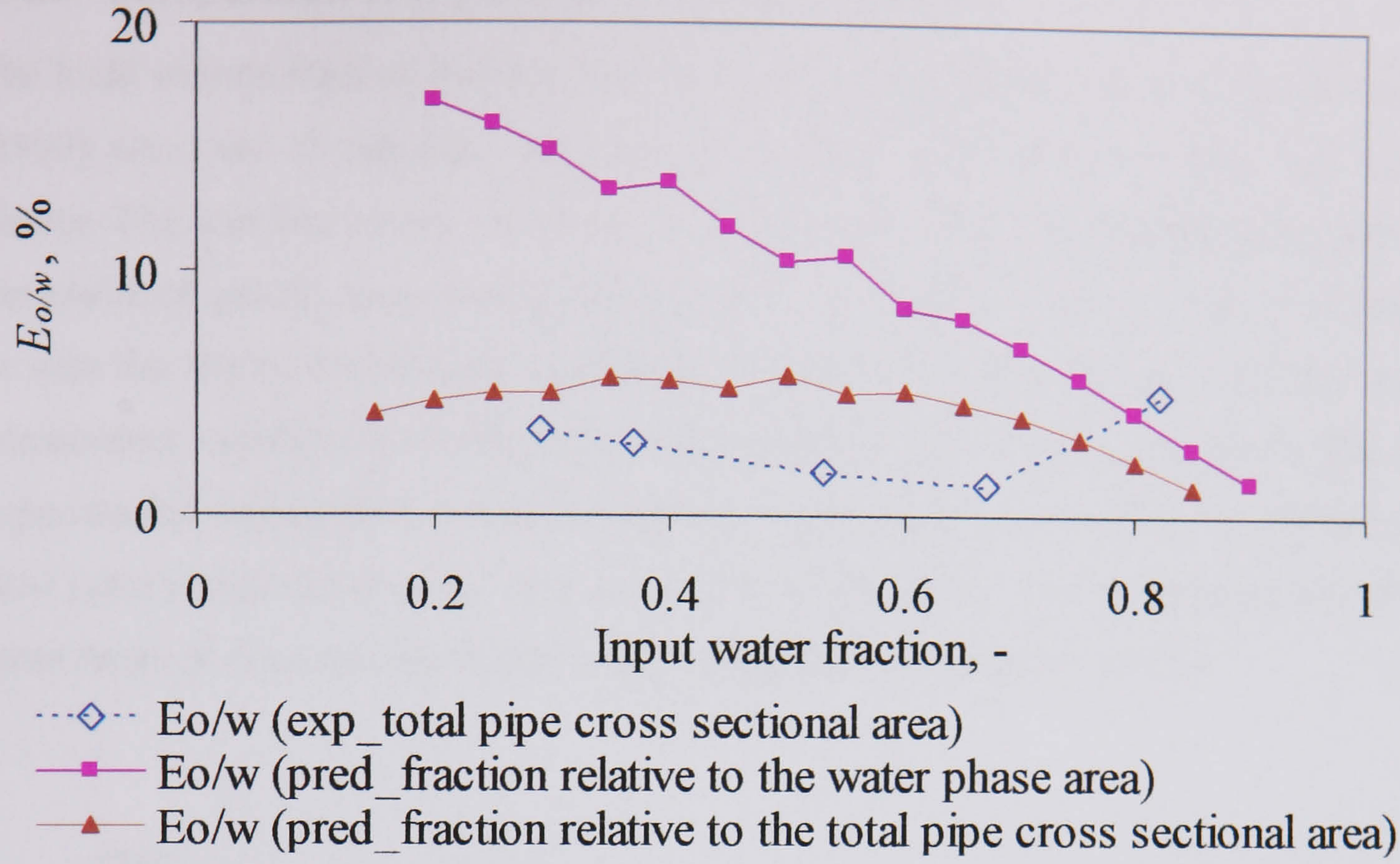

Fig. 8.11 Comparison between the predicted entrained fractions of oil in water ($E_{o/w}$) at U_m = 1.5 m/s with the experimental data by Valle and Kvandal (1995).

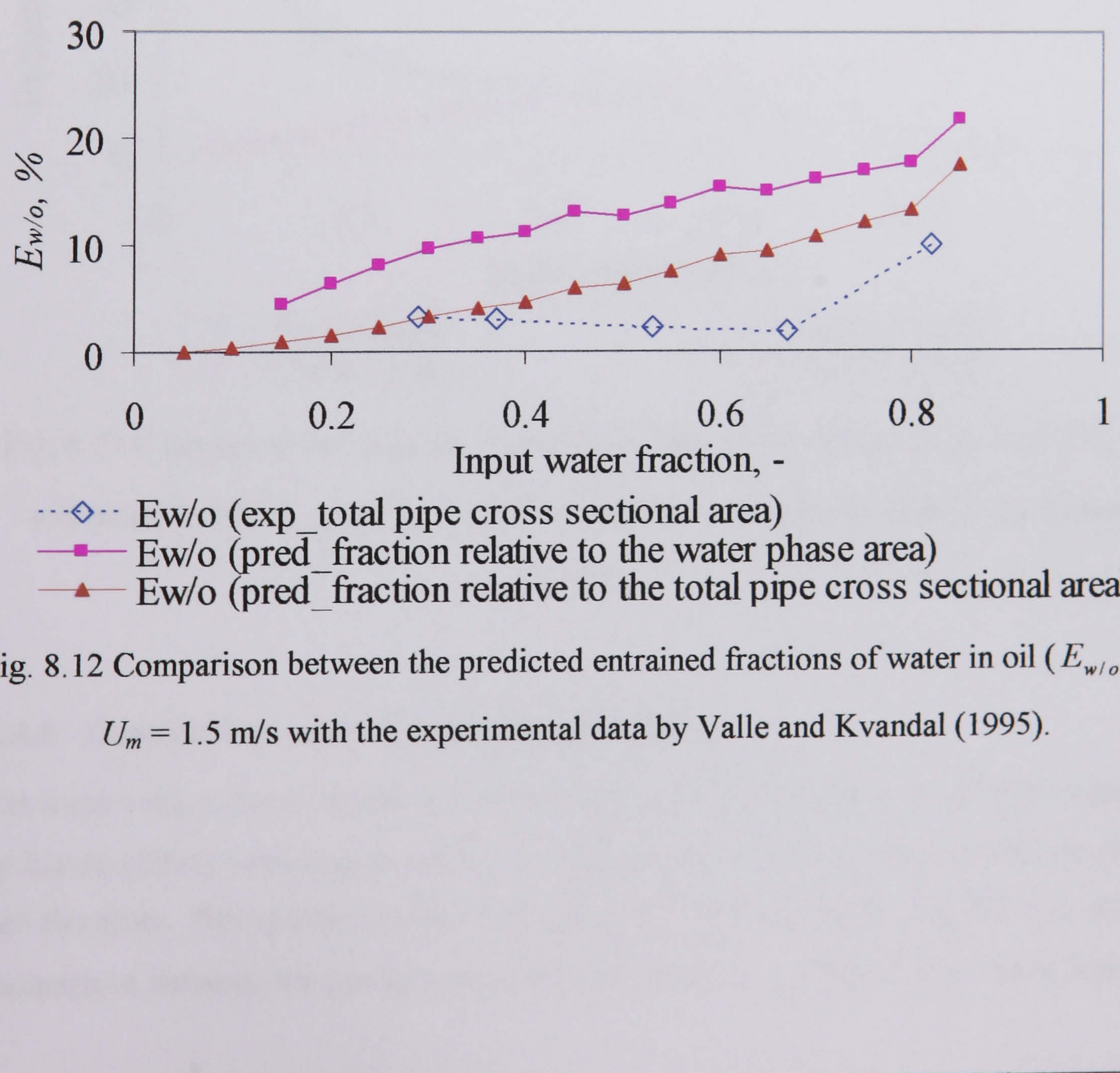

Fig. 8.12 Comparison between the predicted entrained fractions of water in oil ($E_{w/o}$) at U_m = 1.5 m/s with the experimental data by Valle and Kvandal (1995).

8.4.3 Comparison with Data by Soleimani (1999)

The local volume fraction distribution over a pipe cross section measured by Soleimani (1999) was used to calculate the average entrained fraction in the upper and lower phases. The interface height was taken at 35 % input water. The comparisons between the predicted and the experimental values at U_m = 1.25 m/s is shown in Figs. 8.13. It can be seen that the oil entrainment experimental values are under predicted while the water entrainment experimental values are over predicted. It is clear that both model and experimental entrainment curves follow the same trends. Also, at U_m = 1.25 m/s, the flow pattern map shows a *DC* only as well the model which predicts entrainment at the same range of input volume fractions indicating also *dual continuous* flow.

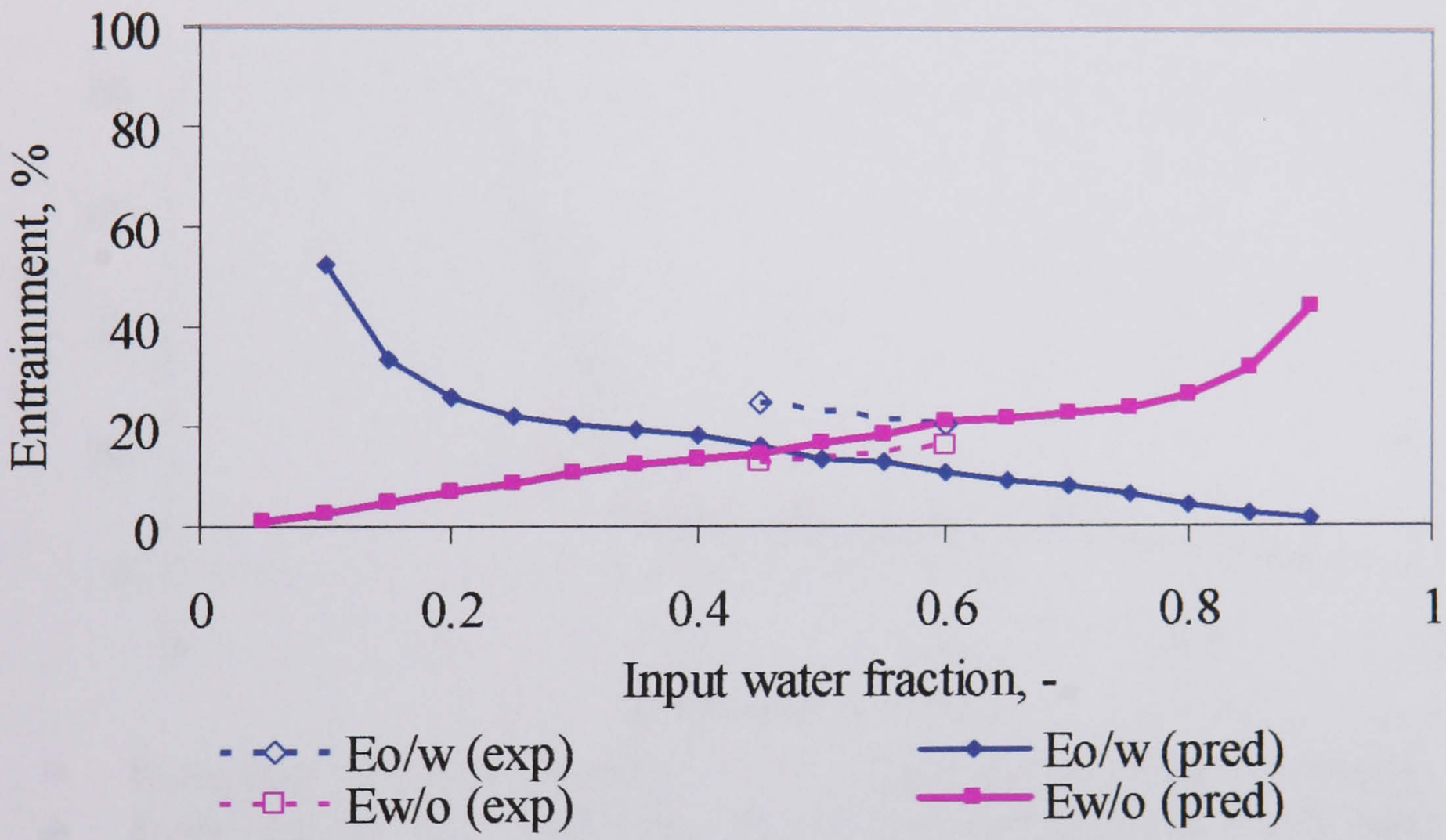

Fig. 8.13 Comparison between the predicted entrained fractions of oil in water ($E_{o/w}$) and water in oil ($E_{w/o}$) at U_m = 1.25 m/s with the experimental data by Soleimani (1999).

8.4.4 Comparison with Data by Elseth (2001)

The local volume fractions along a vertical diameter of the pipe cross section measured by Elseth (2001) were area averaged to yield average entrained fractions of one phase into the other. The interface height was taken at 50 % input water. Fig. 8.14 presents a comparison between the predicted and the calculated $E_{o/w}$ against input water fraction

at different mixture velocities. The model slightly under predicts the experimental data for most cases. However, both experimental and model entrained fraction curves exhibit similar trends of increasing $E_{o/w}$ as the input water fraction decreases. Also, similar to the experimental results the predicted values reflect a general increase in $E_{o/w}$ as the mixture velocity increases. In the predicted entrainment curves there is a sharp increase in the entrained fraction after a maximum which, as discussed in Section 8.3.3 could indicate transition between *dual continuous* and *Dw/o* patterns. This sudden increase occurs at 40 % for U_m = 2.0 m/s and at 35 % for U_m = 1.5 and 1.67 m/s. Interestingly the flow pattern map by Elseth (2001) also showed transition from *dual continuous* to *Dw/o* at 30 % input water fraction for U_m = 2.0 m/s, at 25 % for U_m = 1.67 and at 20 % for U_m = 1.5 m/s.

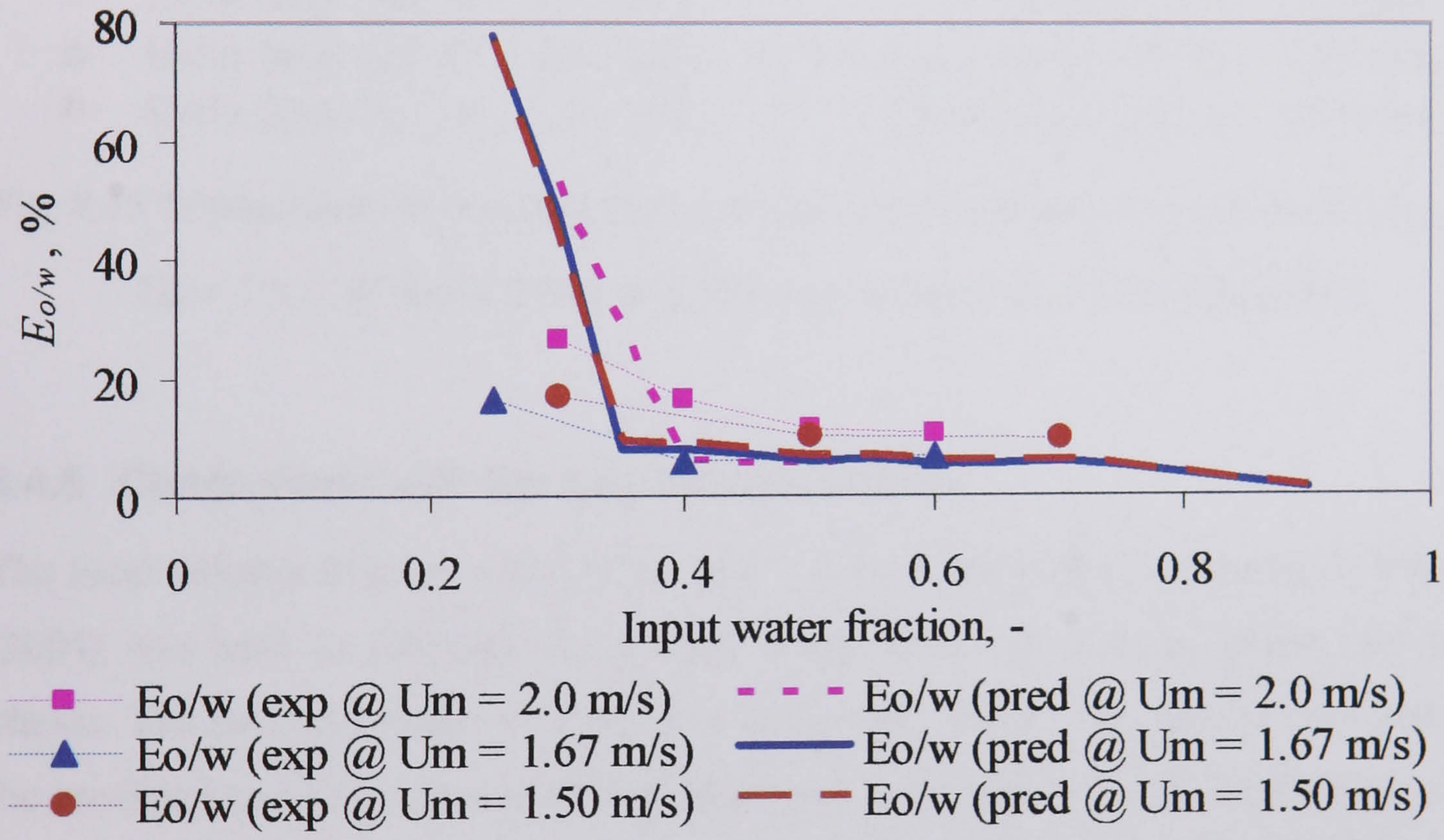

Fig. 8.14 Comparison between the predicted entrained fractions of oil in water ($E_{o/w}$) at U_m = 1.5, 1.67 and 2.0 m/s with the experimental data by Elseth (2001).

The comparison between experimental and predicted $E_{w/o}$ can be seen in Fig. 8.15. In this case there is reasonable agreement between model and predictions taking also into account the uncertainty in both calculating and measuring the entrained fraction (only vertical volume fraction was used for calculation). The predicted curves indicate transition (sharp increase) between *dual continuous* and *Do/w* at 70 % input water for U_m = 1.67 and 2.0 m/s and at 75 % for U_m = 1.5 m/s. From the flow pattern map by

Elseth (2001), this transition happens at 65 % input water for U_m = 2.0 m/s and at 70 % for U_m = 1.5 and 1.67 m/s.

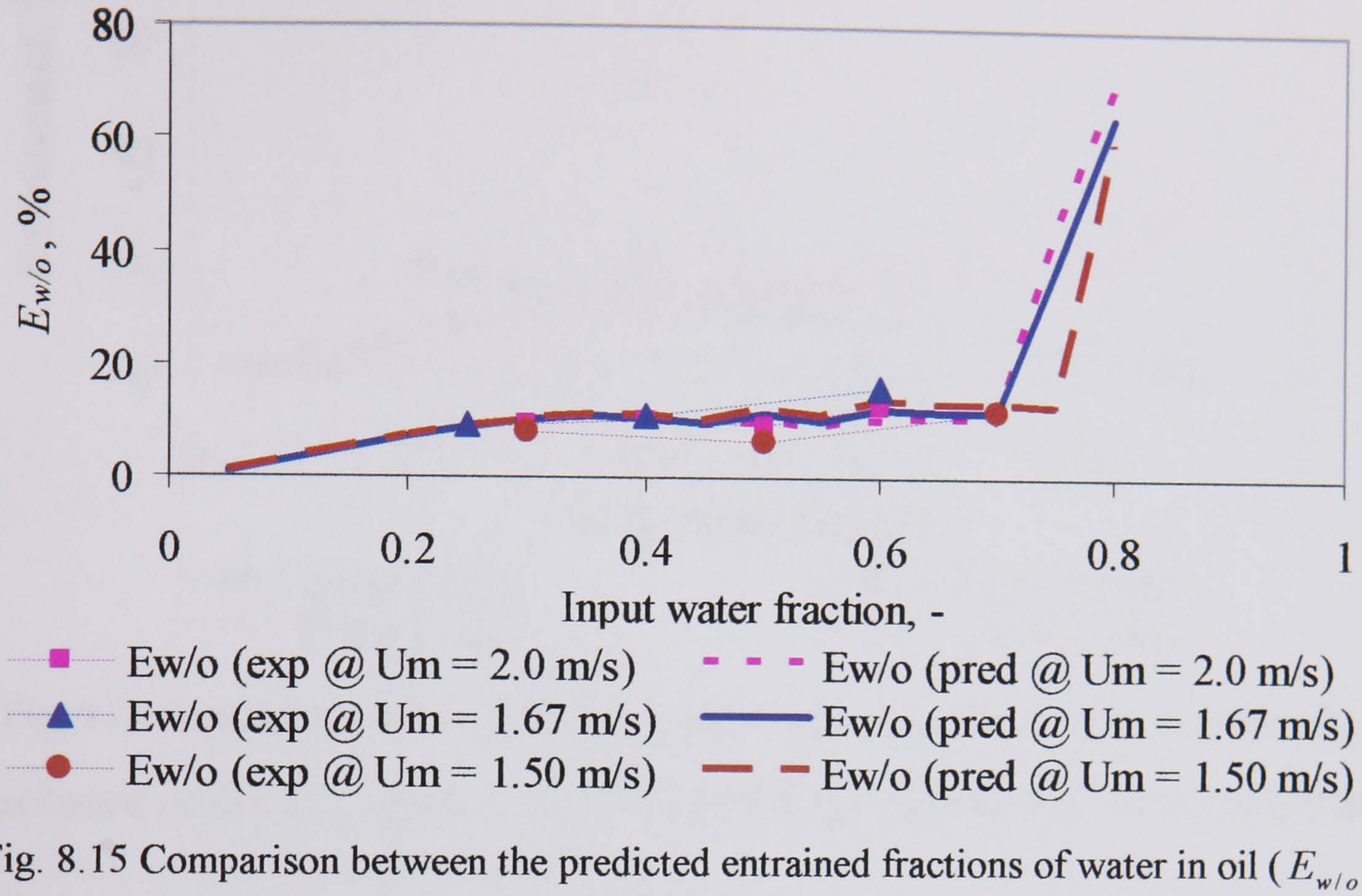

Fig. 8.15 Comparison between the predicted entrained fractions of water in oil ($E_{w/o}$) at U_m = 1.5, 1.67 and 2.0 m/s with the experimental data by Elseth (2001).

8.4.5 Comparison with Data by Hussain (2004)

The local volume fraction distribution over a pipe cross section measured by Hussain (2004) was used to calculate the average entrained fraction in the upper and lower phases. The interface height was taken at 35 % input water. The comparisons between the predicted and the experimental values at U_m = 1.67 and 2.17 m/s are shown in Figs. 8.16 and 8.17 respectively. It can be seen that the experimental values are under predicted while both model and experimental entrainment curves follow the same trends. Also, at U_m = 1.67, a transition between *DC* and *Dw/o* flow is predicted by the model at 20 % input water while the flow pattern map produced by Hussain (2001) indicates transition to *Dw/o* at 35 % and to *Do/w* at 70 % input water from *dual continuous* flow. Furthermore, the model predicts a transition to *Dw/o* at 30 % input water and to *Do/w* at 80 % input water at U_m = 2.17 m/s, while in the map by Hussein (2001) the transition to Dw/o occurs at 35 % and to Do/w at 70 % input water fraction for the same mixture velocity.

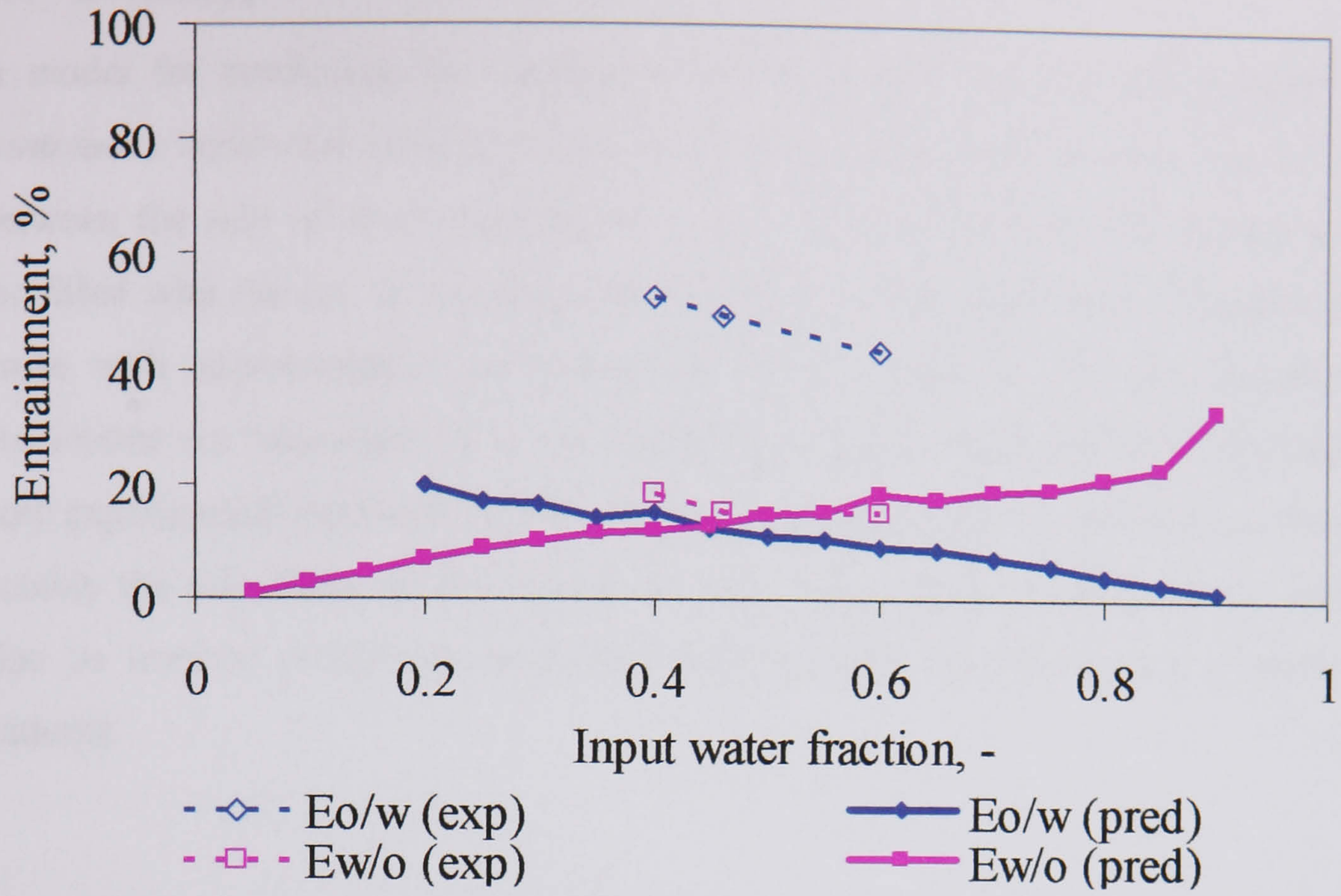

Fig. 8.16 Comparison between the predicted entrained fractions of oil in water ($E_{o/w}$) and water in oil ($E_{w/o}$) at U_m = 1.67 m/s with the experimental data by Hussain (2004).

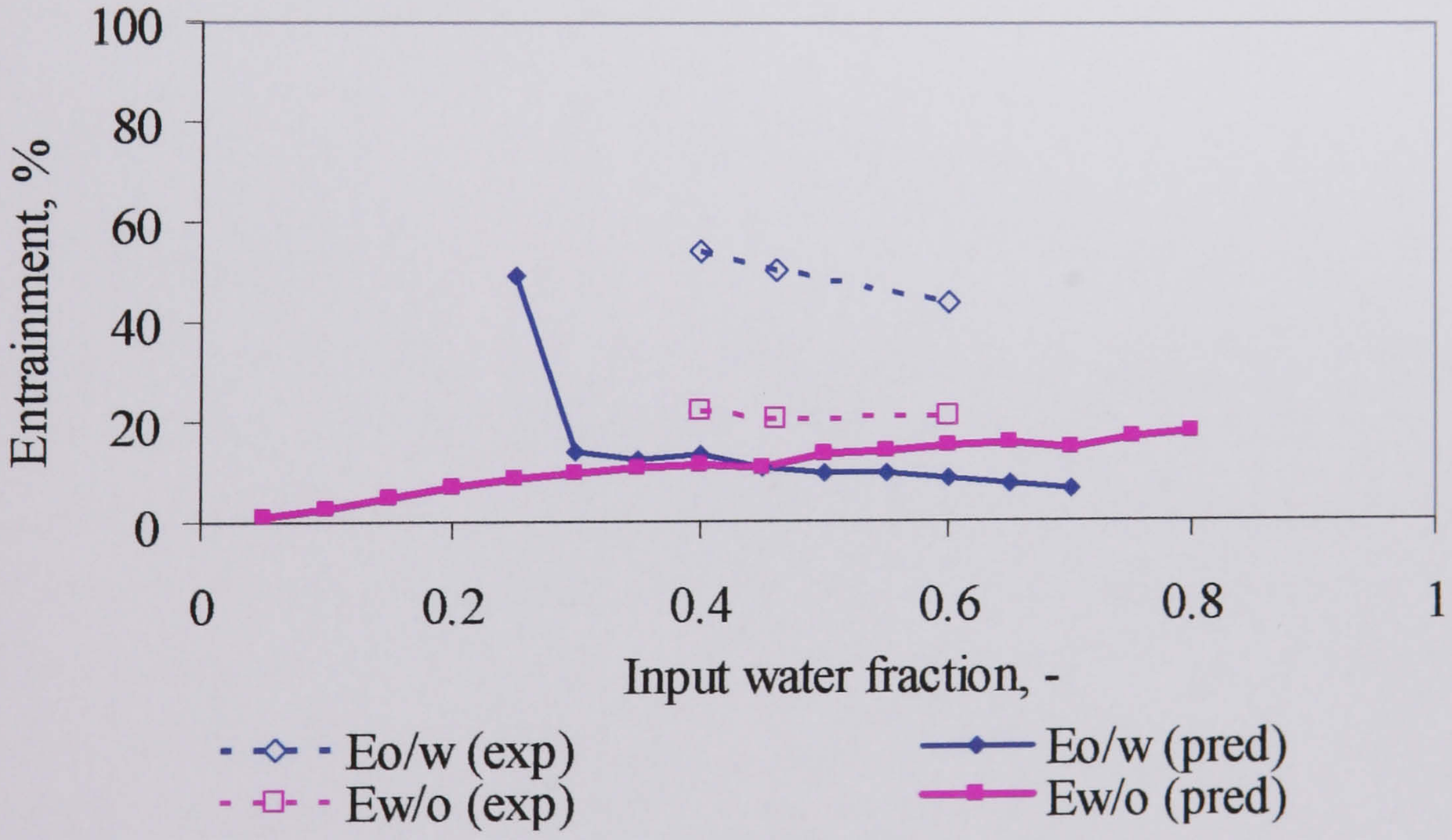

Fig. 8.17 Comparison between the predicted entrained fractions of oil in water ($E_{o/w}$) and water in oil ($E_{w/o}$) at U_m = 2.17 m/s with the experimental data by Hussain (2004).

8.5 Summary

A model for predicting the entrainment of one phase into the other phase in *dual continuous* horizontal oil-water flows is developed theoretically based on the balance between the rate of drop entrainment and of drop deposition. The model is further modified with the use of experimental data from the present work. Comparisons were made with experimentally determined entrained fractions from the literature. The predictions are reasonable in many cases taking into consideration the uncertainties in both experimental entrained fraction measurements and in the model development (most notably the calculation of the deposition rate). It was demonstrated that the model can also be used to predict the transition between *dual continuous* and *dispersed* flow patterns.

CHAPTER 9

Effect of Drag Reducing Polymer on Oil-Water Flows in a Horizontal Pipe

The effect of drag reducing polymers on flow patterns transitions in horizontal oil-water flows was experimentally investigated. Section 9.1 introduces the term *drag reduction*, its importance in multiphase flows and the methods followed in this investigation. The effect of drag reducing polymer on the onset of entrainment, flow pattern transitions and pressure drop is discussed in section 9.2. Hold-up measurements and the interfacial and water-wall shear stresses calculated from a two-fluid model before and after adding the polymer are presented in section 9.3. In section 9.4, the effect of polymer concentration on flow patterns and pressure drop is reported. Finally, a summary is given in section 9.5.

9.1 Introduction

Extensive studies on adding very small amounts of polymer particularly on single but also on multiphase flows have reported the appearance of *drag reduction*, a decrease in the pressure drop. For this reason the added polymers are also called *drag reducing polymers* (DRP). Recently, limited number of multiphase flow studies has also shown a change in the configuration of the phases after adding the polymer. Almost all of these studies refer to gas-liquid systems while a small number deals with three phase gas-liquid-liquid systems where the change in pressure drop is noted. There is currently no work available on the effect of DRPs on the flow patterns and pressure drop in liquid-liquid flows.

It has been shown that adding DRPs in gas-liquid flows damps the waves in the gas-liquid interface and delays the transition from stratified to annular and slug flow

patterns (Oliver and Young Hoon, 1968, Al-Sarkhi and Hanratty, 2001(a,b), Soleimani et al., 2002) (for details see section 2.7.2). This observation motivated the investigations carried out as part of this project on the effect of drag reducing polymers (DRPs) on the transition from stratified to dual continuous flow that is the main objective of this work. If, in a manner similar to gas-liquid systems, interfacial waves are damped then this would delay the initiation of drop formation (see Chapter 4) and the transition to dispersed patterns. As oil-water mixtures are difficult to separate at the end of the pipeline, preserving the stratified pattern for a wider range of conditions will facilitate oil-water separation. In fact stratification of the two liquids has been suggested as a means of separating water from oil in the pipe line (Haheim, 2001).

As described in section 3.4.2, a DRP (Magnafloc 1011 which is a very high molecular weight anionic polyacrylamide) was added in the water phase at two different concentrations (50 ppm and 20 ppm) during oil-water flow in order to investigate its effect on flow pattern boundaries and drop formation. 1000 ppm of master solution is used in this study. The investigations were carried out in the small scale facility at the department of Chemical Engineering at UCL (see section 3.2.2). A high speed video camera was used to monitor the flow before and after the injection of the polymer. From the high speed images the average height of the water interface before and after the addition of the polymer and the phase hold-up were found. The pressure drop was also measured.

9.2 Effect of DRP on Oil-Water Flow Properties

9.2.1 Onset of entrainment

Onset of drop entrainment from the stratified pattern occurs when one or more drops of one phase are found to flow continuously into the other phase. The conditions for the onset of entrainment were obtained from visual observations and the analysis of the pictures from the high speed video camera and are shown in Fig. 9.1 in terms of oil and water superficial velocities without and with DRP in water.

When no DRP was present, drops were found to form at U_{so} = 0.30 m/s and higher. At lower oil superficial velocities, no drops were found and the stratified wavy pattern

changed with increasing water velocity to either slug or bubbly flow. When drag reducing polymer is added at a concentration of 50 ppm in the water phase, drop formation was delayed and the flow remained stratified up to higher velocities (see Fig. 9.1). At U_{so} less than 0.37 m/s, no drops appeared in the flow for all the conditions investigated. It is quite possible that drops may have formed at higher water velocities.

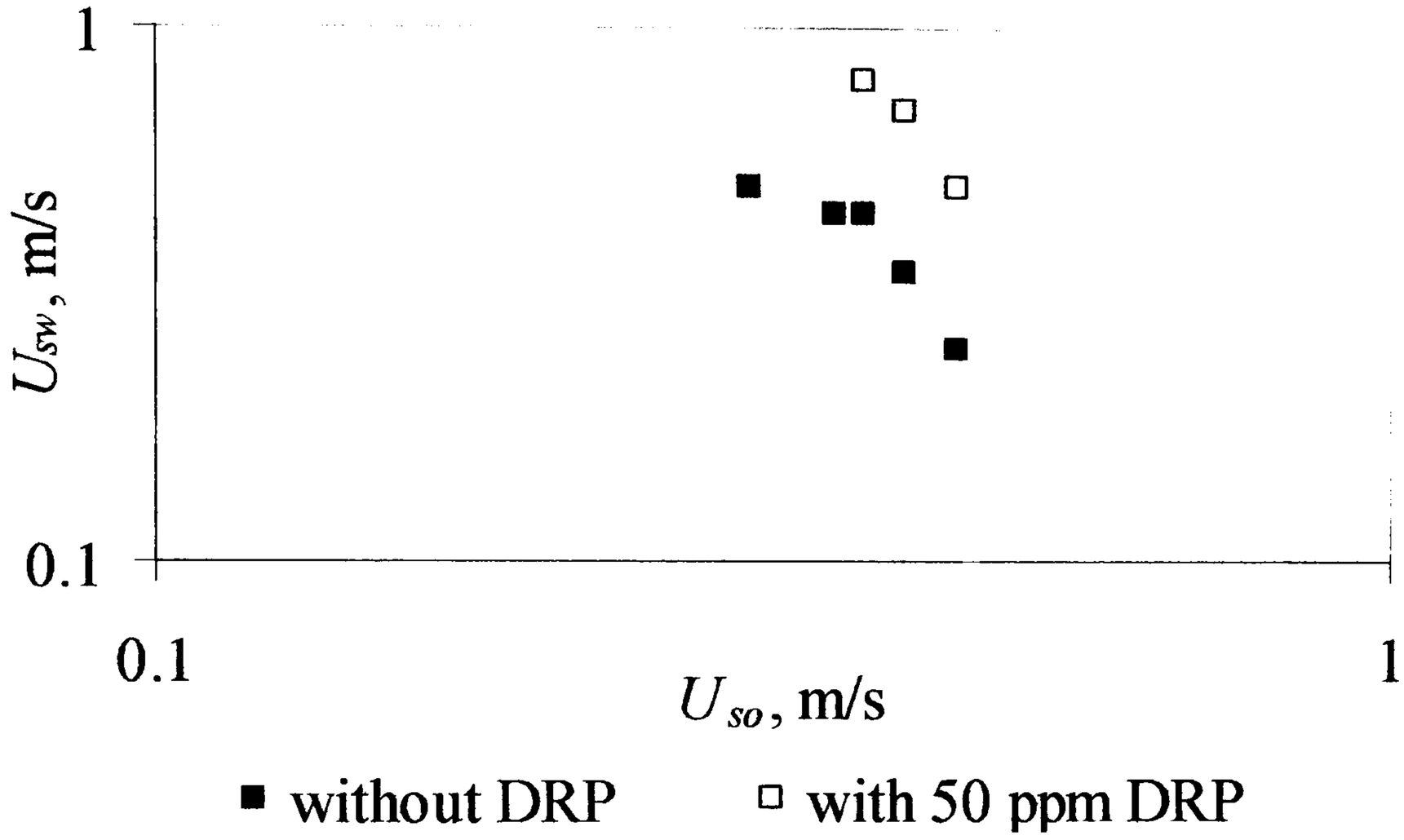

Fig. 9.1 Onset velocities for the dual continuous flow pattern with and without DRP in the 14mm ID test pipe.

Fig. 9.2a shows the oil-water flow without DRP at the onset of drop formation (U_{so} = 0.30 m/s). The interface is wavy and drops of oil clearly appear in the water phase. With the addition of 50 ppm DRP the oil-water interface becomes relatively smooth (Fig. 9.2b). At U_{so} = 0.37 m/s, drop formation is delayed from U_{sw} = 0.50 m/s without DRP to U_{sw} = 0.80 m/s with DRP (see Fig. 9.3). For all the cases investigated at the onset of drop formation, with the addition of the polymer the interface became smoother and drops disappeared. Al-Sarkhi and Hanratty (2001a) suggested that the polymer damps the unstable waves which are the source of drop formation. As was discussed in Chapter 4 no drops form when the interface is smooth or the amplitude of the waves is small. The waves should reach a finite height before drop formation is possible.

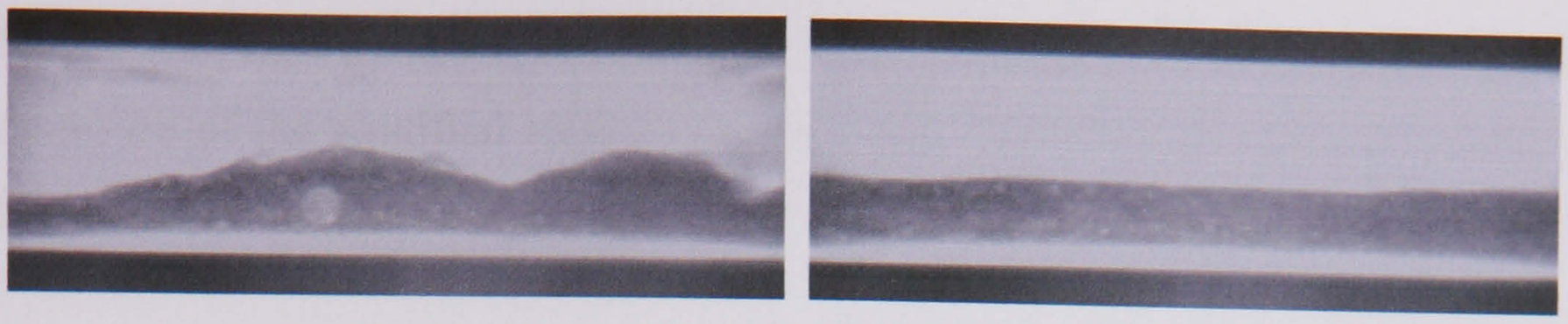

(a) (b)

Fig. 9.2 (a) Flow at the onset of drop formation without DRP, (b) Flow after adding 50 ppm DRP at U_{so} = 0.37, U_{sw} = 0.50 m/s.

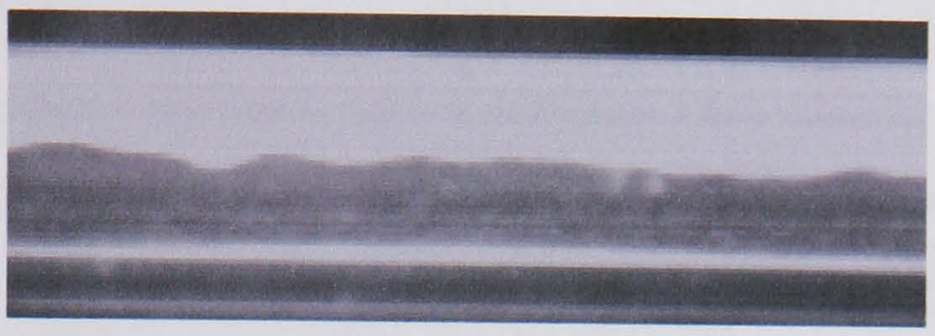

Fig. 9.3 Onset of drop formation after the addition of 50 ppm DRP at U_{so} = 0.37, U_{sw} = 0.80 m/s

9.2.2 Flow pattern transitions

Five flow patterns were identified for the range of conditions investigated during the oil-water flow in the 14 mm ID acrylic horizontal pipe. These are:

Stratified (*stratified smooth, SS, and stratified wavy, SW*): where both fluids flow in layers at the top and bottom of the pipe respectively.

Dual continuous (*DC*): where both oil and water form continuous layers at the top and bottom of the pipe respectively but drops of one phase appear into the continuum of the other phase.

Annular (*AN*): where water forms an annular film and oil is in the pipe core.

Slug (*SG*): where the oil flows in elongated bubbles (slugs) close to the top of the pipe

Bubbly (*B*): where the oil appears in the form of elongated drops (smaller than the bubbles) inside the water continuous phase.

The corresponding flow pattern map with and without drag reducing polymer (DRP) is shown in Fig. 9.4. The points represent flow patterns with 50 ppm DRP while the lines represent the pattern boundaries without DRP. The map indicates a strong effect of polymer on the flow patterns transitions. In general, with the addition of the polymer the region of both *stratified smooth* and *wavy* flow is extended over a wider range of conditions, the *annular* flow disappears completely for the conditions investigated while

the transition to *bubbly* flow is not affected. These changes in the boundaries, especially the extension of the stratified region, are very important for transporting oil and water and for their separation.

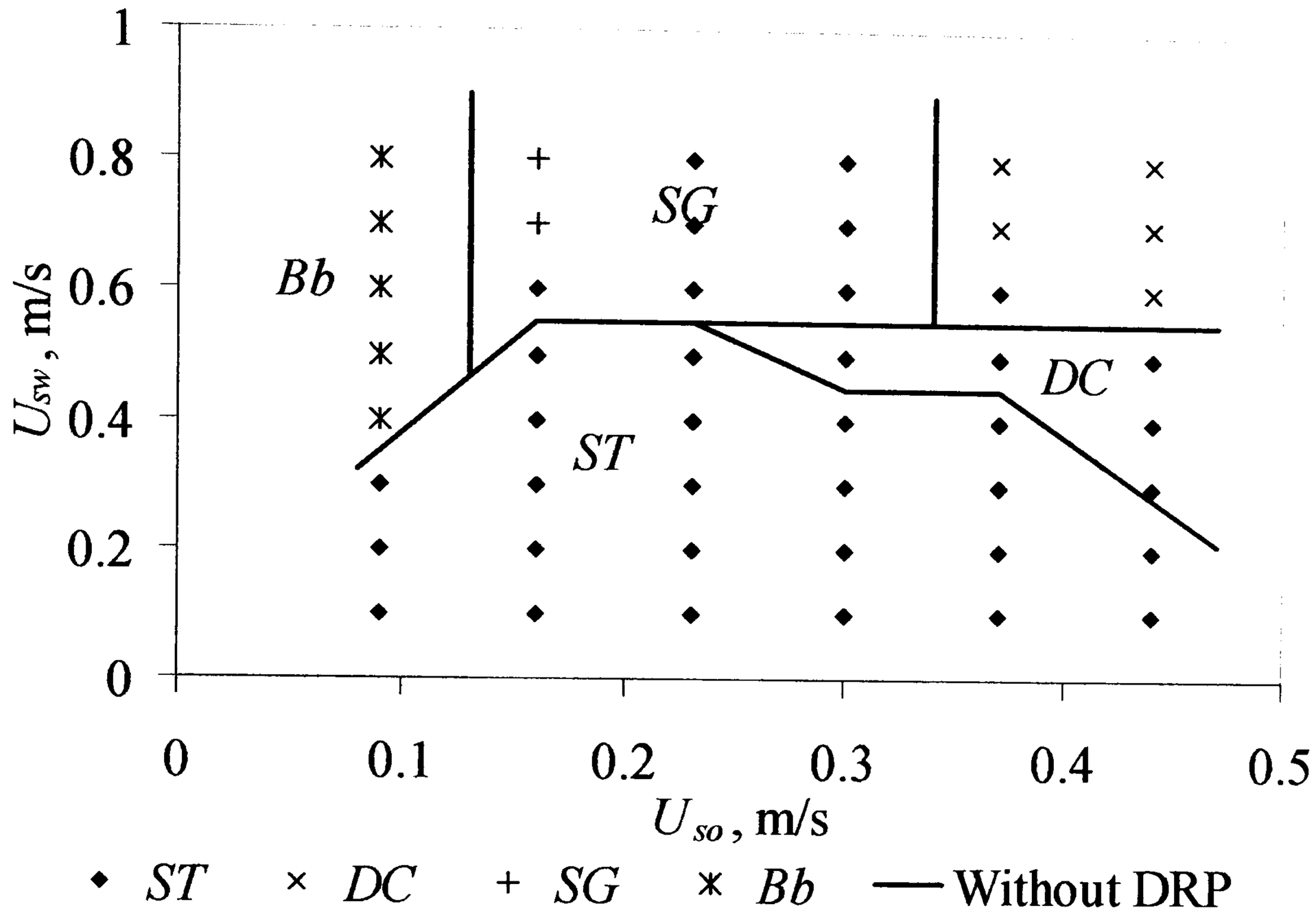

Fig. 9.4 Comparison of flow patterns with 50 ppm DRP with the flow pattern boundaries without DRP in horizontal oil-water flows in the 14 mm ID test pipe. The flow pattern (*AN*) that does not appear when 50 ppm DRP is added is written on the map in grey.

(a) *Stratified flow*

In stratified flow the interface is either smooth or wavy with small and large amplitude waves. For the smooth interface the pattern is not expected to change when adding the DRP (see Figs. 9.5a and b). However, as will be discussed later, a reduction in pressure drop is observed which means that the polymer does have an effect on the flow. In the stratified wavy pattern, the interface becomes either smooth or relatively smooth with very small amplitude waves after adding the polymer. At $U_{so} = 0.23$ m/s, $U_{sw} = 0.50$ m/s for example the oil-water interface is wavy with quite large amplitude waves when there is no polymer (Fig. 9.6a). These waves are completely damped by adding the polymer as can be seen in Fig. 9.6b and a fairly smooth interface appears instead. The

experimental results from chapter 4 showed that no drops form when the oil-water interface is smooth or the amplitude of the waves is small. The reduction in the amplitude of the waves with the addition of DRP will, therefore, delay drop formation from the oil-water interface and the transition from stratified to dispersed patterns. Al-Sarkhi and Hanratty (2001a) also suggested that the polymer damps the unstable waves which are the source of drop formation.

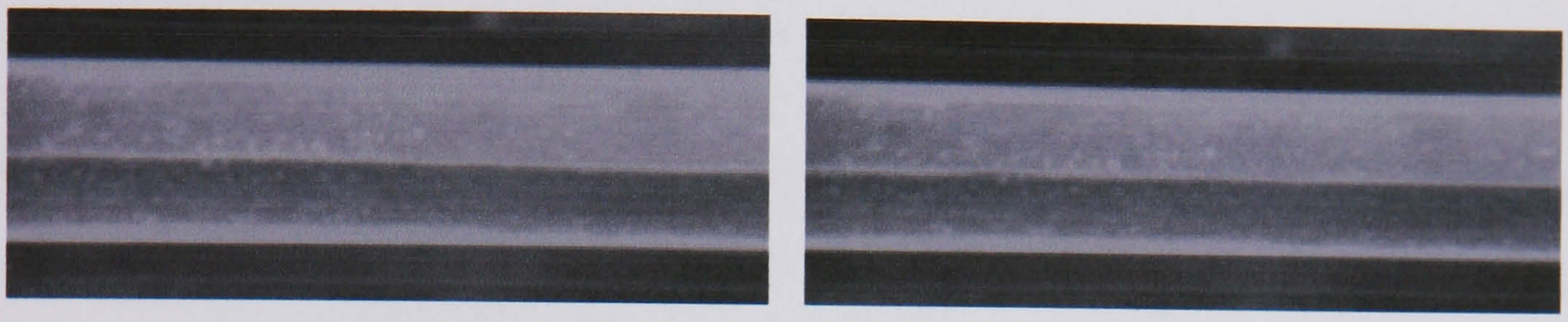

(a) (b)

Fig. 9.5 (a) *Stratified smooth* flow at $U_{so} = 0.09$, $U_{sw} = 0.20$ m/s without DRP. (b) Flow after adding 50 ppm DRP.

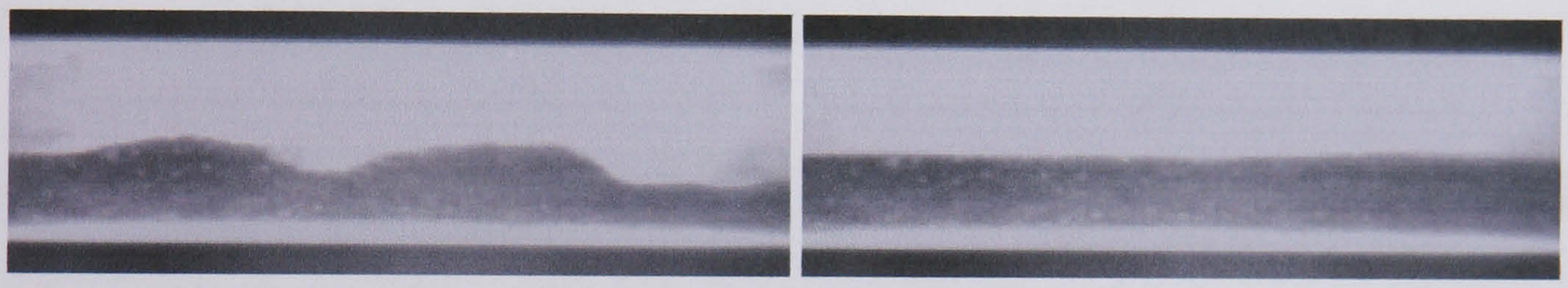

(a) (b)

Fig. 9.6 (a) *Stratified wavy* flow at $U_{so} = 0.23$, $U_{sw} = 0.50$ m/s without DRP. (b) Flow becomes s*tratified smooth* after adding 50 ppm DRP.

(b) *Dual continuous flow*

Dual continuous flow appeared only for a limited range of conditions. For all the conditions investigated, the *dual continuous* flow changes completely when DRP is added to *stratified smooth* or *wavy* with small amplitude waves. Fig. 9.7a shows the flow before adding the polymer at $U_{so} = 0.44$ m/s, $U_{sw} = 0.50$ m/s. The interface is wavy with drops appearing on both phases. The addition of the polymer changes the pattern to *stratified* flow as shown in Fig. 9.7b where the drops have completely disappeared. Al-Sarkhi and Hanratty (2001a) suggested that the disturbance waves can be considered as patches of turbulence that will be destroyed as a result of the decrease in turbulence in the presence of the polymer.

(a) (b)

Fig. 9.7 (a) *Dual continuous* flow at U_{so} = 0.44, U_{sw} = 0.50 m/s without DRP. (b) Flow becomes *stratified wavy* after adding 50 ppm DRP.

(c) *Annular flow*

At higher oil and water velocities, *annular* flow appears. In this pattern, a thin layer of water is seen at the top of the pipe. The interface is disturbed and drops of oil are visible within the water. The flow appears to be more disturbed as the water velocities increase. Visual observations revealed that addition of polymer changes the *annular* flow to either *stratified wavy* or *dual continuous* flow. In the example shown in Fig. 9.8 *annular* flow with very disturbed wavy interface and drops of oil within the water changes to *dual continuous* flow after the addition of polymer.

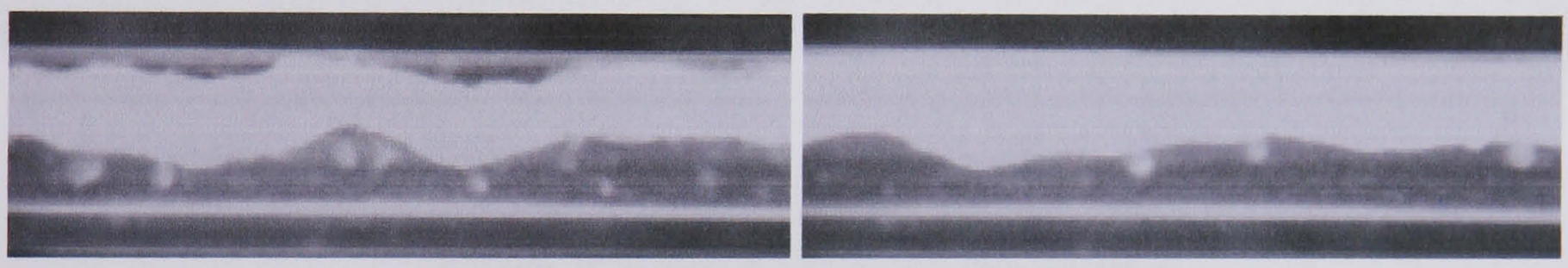

(a) (b)

Fig. 9.8 (a) *Annular* flow at U_{so} = 0.44, U_{sw} = 0.80 m/s without DRP. (b) Flow becomes *dual continuous* after adding 50 ppm DRP.

(d) *Slug flow*

As the oil superficial velocity decreases to U_{so} = 0.16-0.30 m/s, oil *slug* patterns form with increasing water velocity instead of *dual continuous* or *annular* flows, which appeared at higher oil velocities. The breakage of the oil layer continuity and the formation of slugs could be attributed to the reduced thickness of the oil layer at these high water velocities and medium oil to water ratios. In addition, oil tends to wet the acrylic pipe and cover a large cross sectional area relative to its volume. Therefore, as the oil to water ratio decreases the thickness of the oil layer decreases relatively more because of its tendency to wet a large area of the pipe. At increased water velocity its turbulence will be increased and the interface will be wavier. The probability of the

waves to touch the upper pipe wall and break up the thin oil layer to slugs is therefore high. The slug length was found to reduce as the oil to water ratio decreases.

The addition of the polymer in *slug* flow either changes completely the pattern to *stratified* flow at the high oil velocities (U_{so} = 0.30 m/s, U_{so} = 0.23 m/s) or to small slugs and bubbles that are closely packed at the low oil velocity (U_{so} = 0.16 m/s). Fig. 9.9a shows an example of *slug* flow at the high oil velocity (U_{so} = 0.30, U_{sw} = 0.80 m/s). Slugs are very long and can reach up to 15-20 times the pipe diameter while in some cases the pattern appears like annular flow but with discontinuities. When DRP is added to the water phase, the flow changes from *slug* to *stratified wavy* (see Fig. 9.9b). This can be explained by arguing that the polymers destroy turbulence in the water phase and damp the large amplitude waves at the interface which in turn decreases the capability of the water to break up the oil layer.

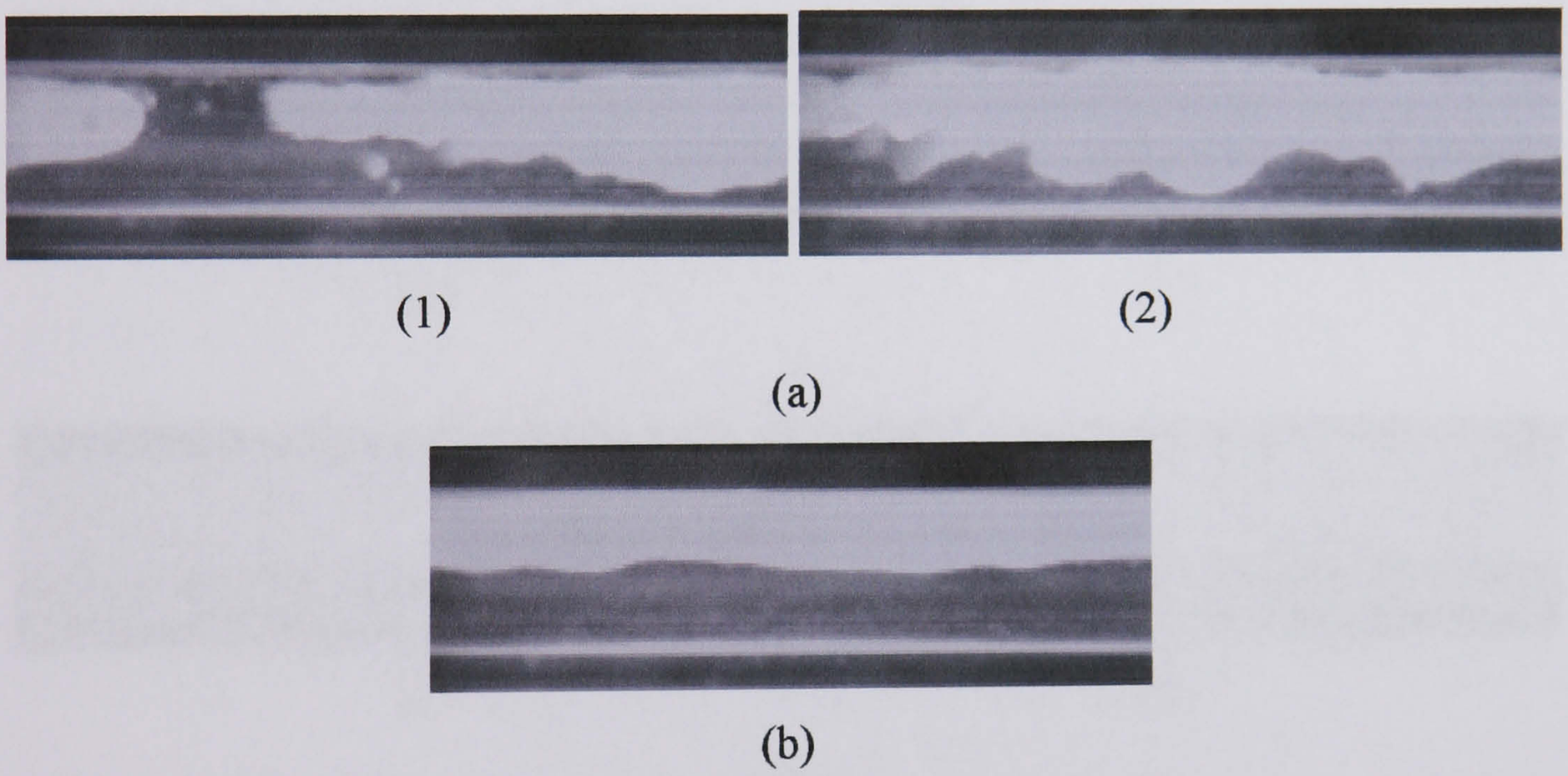

Fig. 9.9 (a) *Slug* flow at U_{so} = 0.30, U_{sw} = 0.80 m/s without DRP. (b) Flow becomes *stratified wavy* after adding 50 ppm DRP.

At lower oil velocity (U_{so} = 0.23, U_{sw} = 0.80 m/s), the slug lengths decrease and can fluctuate between 3-15 times the pipe diameter as shown in Figs. 9.10a and b. In this case, the addition of the polymer to the flow changes the pattern to *stratified wavy* (see Fig. 9.10c). However, sometimes a discontinuity in the stratified oil layer is found and the pattern appears similar to long slugs touching each other. This may happen because of discontinuities in the polymer.

At even lower oil velocity (at U_{so} = 0.16 m/s), slug lengths further decrease. At U_{sw} = 0.60 m/s, *slug* flow changes to *stratified* when polymer is added. However, this not the case at the higher superficial water velocities. At U_{so} = 0.16, U_{sw} = 0.80 m/s, the *slug* pattern persists even after the polymer is added but slugs are smaller than when there is no polymer and close to each other (see Figs. 9.11a and b). Although the polymer reduces the turbulence in water, slug flow still exists because the thin oil layer at this low oil to water ratio can still be broken up by water. Thus, the addition of the polymer could not prevent the formation of slugs. These slugs are, however, found to be closely packed through the test section. This is because the velocities of the oil slugs increased after the addition of the polymer which increased the shedding rate of the water between them that makes the slugs to flow close together (Soleimani et al., 2002). It is possible that these short slugs would coalesce to a continuous oil layer and form stratified flow if the test section was longer.

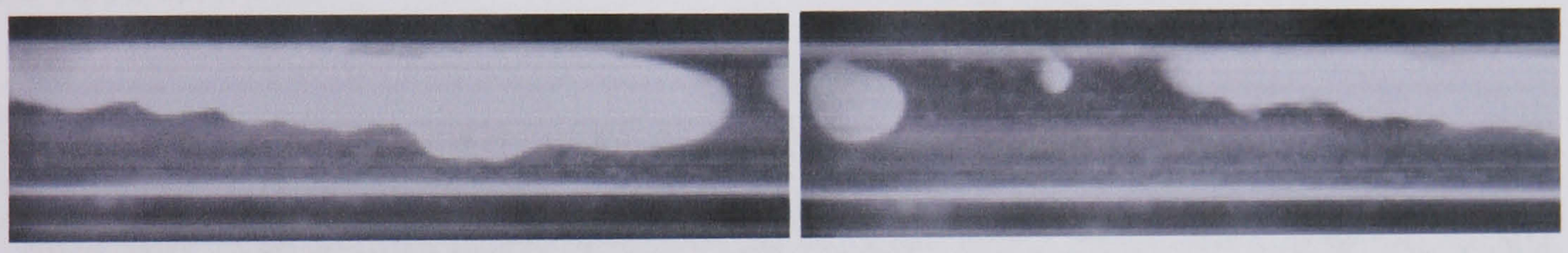

(1) (2)

(a)

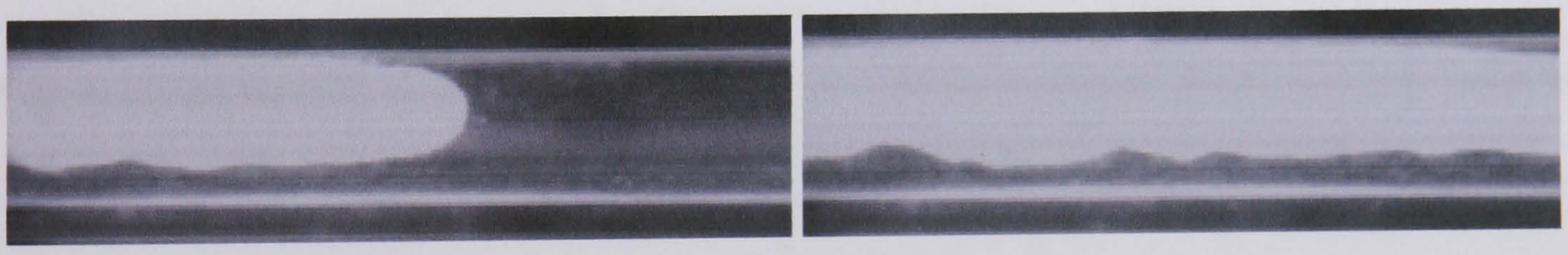

(1) (2)

(b)

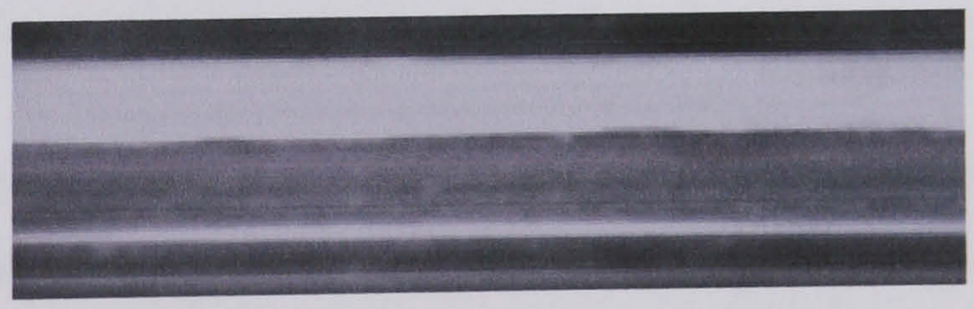

(c)

Fig. 9.10 (a) Short s*lug flow* at U_{so} = 0.23, U_{sw} = 0.80 m/s without DRP. (b) Long s*lug flow* at U_{so} = 0.23, U_{sw} = 0.80 m/s without DRP. (c) Flow becomes s*tratified* after adding 50 ppm DRP.

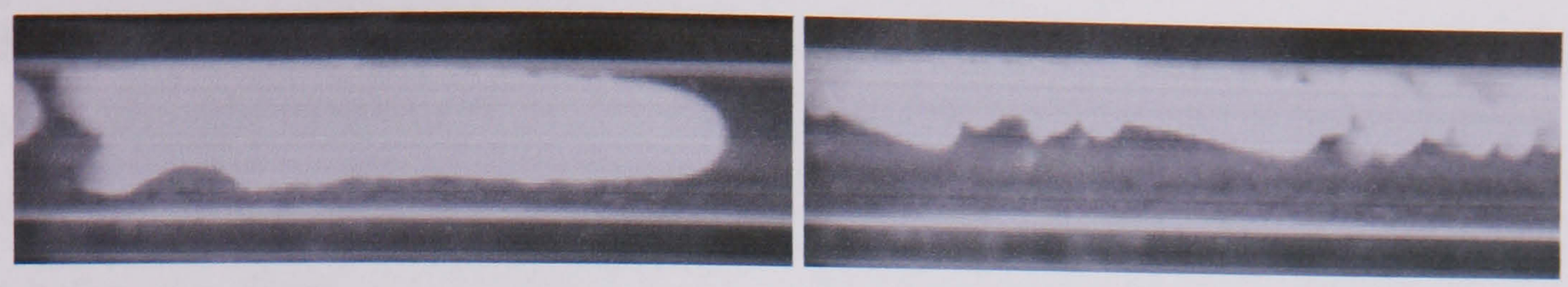

(a) (b)

Fig. 9.11 (a) Short s*lug flow* at $U_{so} = 0.16$, $U_{sw} = 0.80$ m/s without DRP. (b) The slugs can be seen to flow close together after adding 50 ppm DRP.

(d) *Bubble flow*

A further reduction of the oil velocity to $U_{so} = 0.09$ m/s resulted in oil bubbles in water. Figs. 9.12a and b show the flow pattern observed at $U_{so} = 0.09$, $U_{sw} = 0.80$ m/s before and after adding polymer respectively. The addition of the DRP brought the oil bubbles close to each other. It is worth noting again that perhaps a longer distance may have resulted in the coalescence of the bubbles and the change of the pattern to *stratified* or *dual continuous* flow.

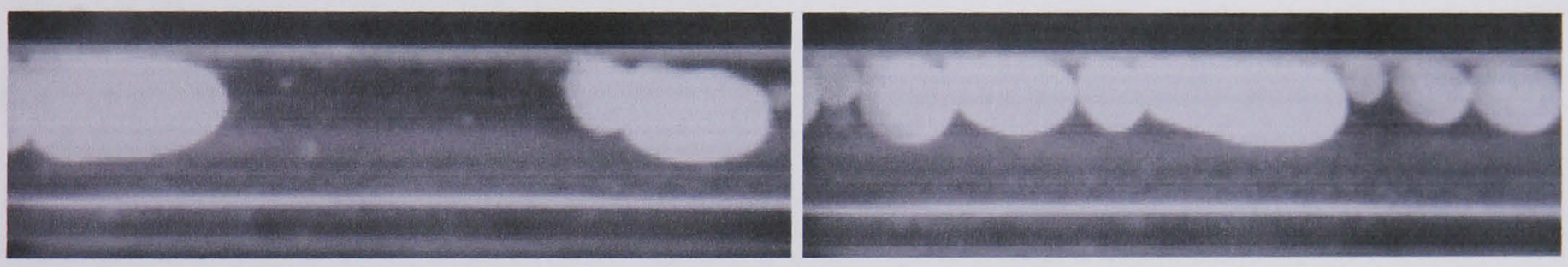

(a) (b)

Fig. 9.12 (a) *Bubble flow* at $U_{so} = 0.09$, $U_{sw} = 0.80$ m/s without DRP. (b) The bubbles can be seen to flow close together after adding 50 ppm DRP.

9.2.3 Pressure drop and drag reduction

The pressure gradient measurements of the oil-water flow before and after the addition of 50 ppm polymer are plotted in Figs. 9.13 and 14. The figures demonstrate that the addition of the polymer reduces the two phase pressure gradient, an effect that becomes very significant as the water velocity increases. It can also be seen that pressure gradient increases as the superficial water and oil velocities increase for both cases of flow without and with DRP.

For the cases when no polymer is present in the flow, the slopes of the pressure drop lines seem to change with the flow pattern transitions. The slopes are small for stratified

and dual continuous flows. At the transition to other flow patterns, the slopes increase and the pressure drop lines become steeper. This can be observed in Fig. 9.13 at U_{so} = 0.09, U_{sw} = 0.40 m/s where flow changes to *bubbly* and at U_{so} = 0.23, U_{sw} = 0.50 m/s just before the change to *slug* flow. The same is also observed in Fig. 9.14 at U_{so} = 0.30, U_{sw} = 0.50 m/s and at U_{so} = 0.44, U_{sw} = 0.50 m/s, just before the change to *slug* and *annular* flows respectively.

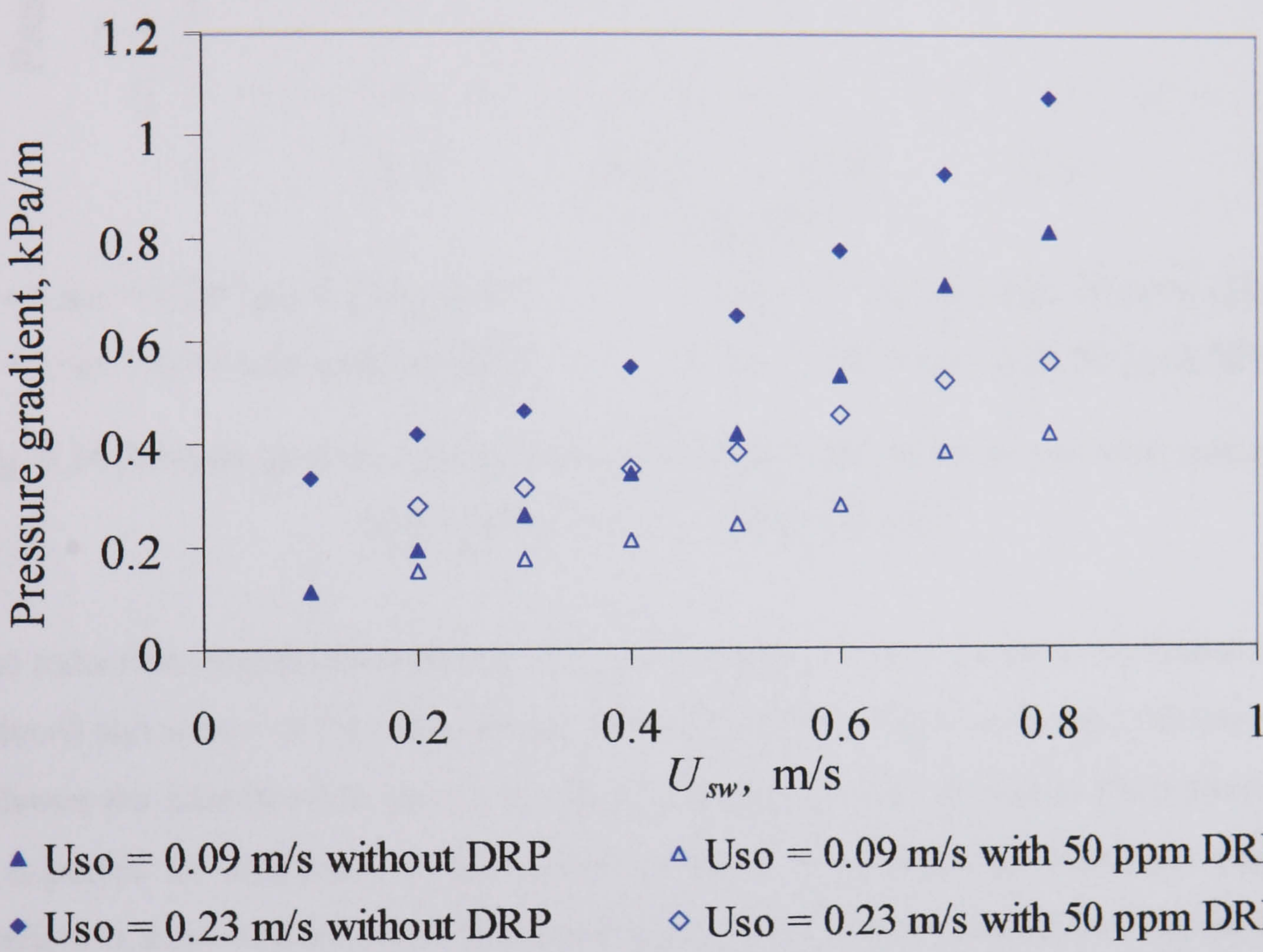

Fig. 9.13 Pressure gradient against superficial water velocity before and after adding 50 ppm DRP at U_{so} = 0.09 and 0.23 m/s.

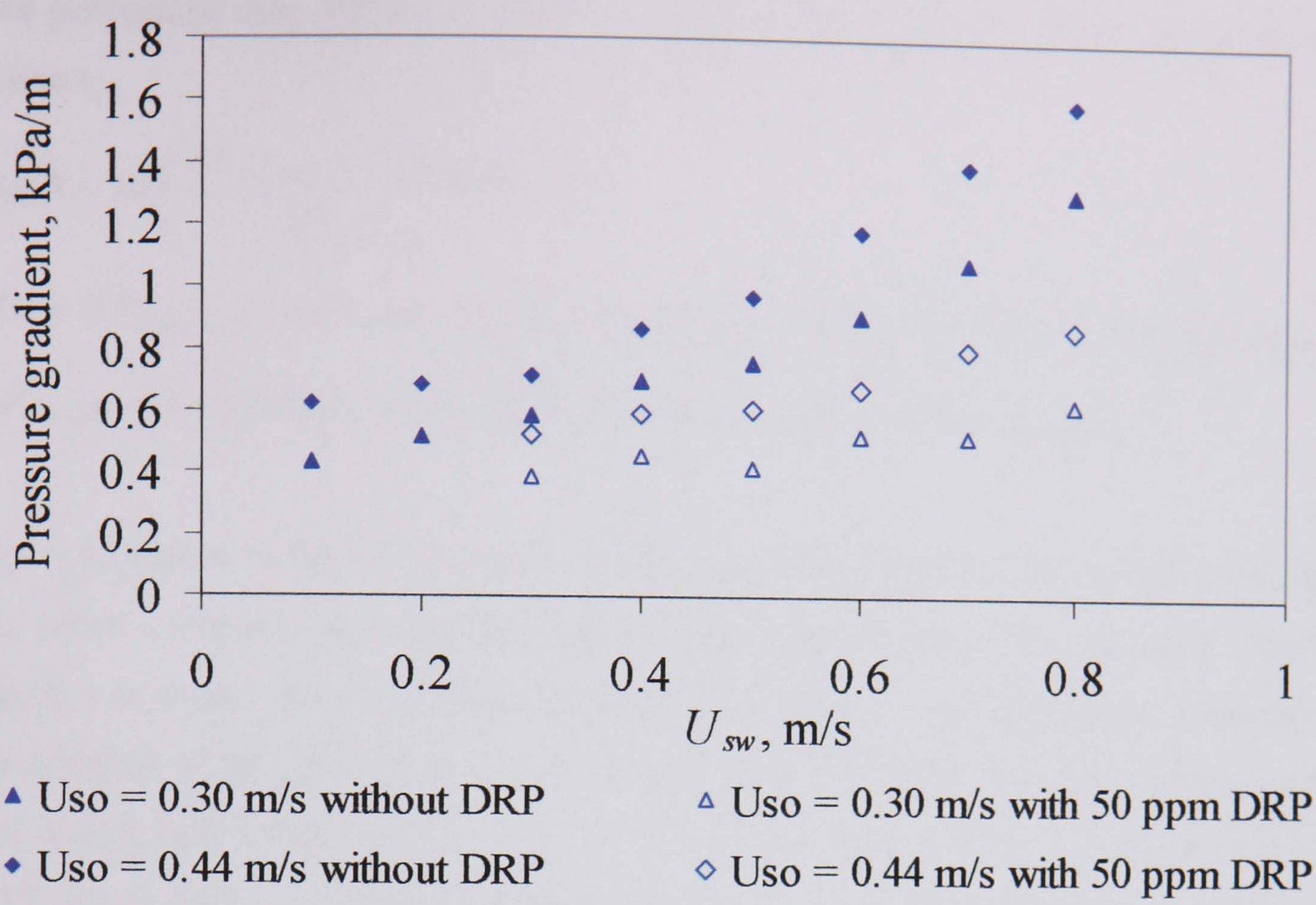

Fig. 9.14 Pressure gradient against superficial water velocity before and after adding 50 ppm DRP at U_{so} = 0.30 and 0.44 m/s.

The reduction in pressure gradient after the addition of the polymer is attributed to the reduced turbulence in the water phase. In stratified flow, where with the addition of the polymer the interface becomes less rough, a decrease in the interfacial shear stress (τ_i), is expected to contribute to the overall pressure drop decrease. However, pressure gradient is seen to reduce more during the other flow patterns perhaps because the effect of the polymer is greater at high velocities where turbulence is stronger and also because in most cases these patterns change to stratified flow.

In most cases in Figs. 9.13 and 14 when polymer is present there is little variation of the pressure gradient slope with increasing water velocity as the pattern remains stratified. For U_{so} = 0.09 m/s (Fig. 9.13) an increase in the slope is seen at U_{sw} = 0.50 m/s, where the flow, even after the addition of the polymer, still changes from stratified to bubbly. Fig. 9.14 shows little variation of pressure drop when polymers are added except for U_{so} = 0.44 at U_{sw} = 0.70 and 0.80 m/s where the flow is dual continuous flows while in the other U_{so} it is stratified for the whole range of U_{sw}.

The percentage drag reduction effected by the addition of the polymer can be found as follows:

$$\%DR = 100\left(\frac{\Delta P_{without\ DRP} - \Delta P_{with\ DRP}}{\Delta P_{without\ DRP}}\right) \tag{9.1}$$

where $\Delta P_{without\ DRP}$ is the pressure drop measured without the drag reducing polymer and $\Delta P_{with\ DRP}$ is the pressure drop measured with the drag reducing polymer.

Fig. 9.15 shows a plot of the $\%DR$ versus the water superficial velocities at different U_{so} when a concentration of 50 ppm of drag reducing polymer was used. From the figure it is noted that the highest drag reductions occur when the pattern changes with the addition of the DRP from slug or annular flow to stratified or dual continuous flow and during bubble flow at U_{sw} = 0.6 – 0.8 m/s. The highest $\%DR$ is calculated at U_{so} = 0.37, U_{sw} = 0.60 m/s which is greater than 50 %. This could be because at this point despite the high velocities the flow with the polymer is still stratified; any further increase in the velocities changes the pattern to dual continuous, where the disturbed interface increases the overall pressure gradient.

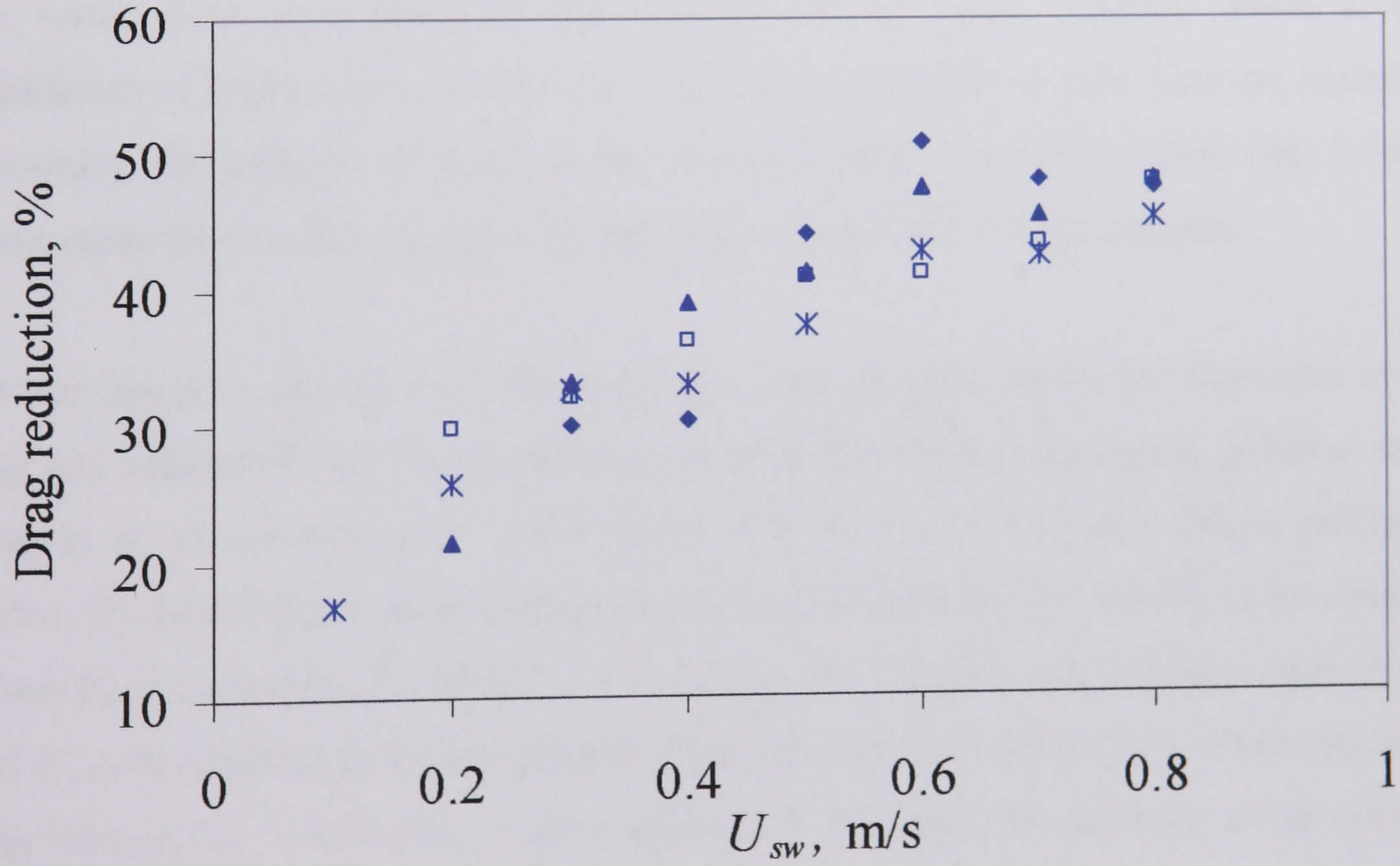

Fig. 9.15 Drag reduction against water superficial velocity at different oil superficial velocities when 50 ppm DRP is added in the water phase.

9.3 Hold-up Measurements and the Calculated Stresses

From the still pictures of the high speed video images the average height of the water interface (h_w) was calculated in the stratified and dual continuous patterns. In a particular picture the height was measured at different locations and an average value was found. The same method was repeated for 20 different pictures selected at different times for the same flowrates and an overall average height was found. It should be noted here that there is some ambiguity in the measurement of the interface height since this is recorded from outside the pipe and represents the value of the height at the wall rather than in the middle of the pipe. Since the acrylic material of the pipe is oil wetted the interface is likely to be slightly concave rather than flat. The dimensionless average interface height, h_w/D with and without polymer in the flow is shown in Fig. 9.16 as a function of U_{sw} for U_{so} = 0.23 and 0.44 m/s. Only cases where the pattern is stratified or dual continuous are shown.

In the stratified wavy and dual continuous flows, the addition of the polymer slightly increases at the higher water velocities the h_w/D at U_{so} = 0.23 m/s while the increase is more pronounced at U_{so} = 0.44 m/s. This could be due to the increase in the thickness of the water layer as a result of the damping of the wavy interface which is more significant at higher oil velocity. At U_{sw} = 0.10 and 0.20 m/s for both oil superficial velocities, the addition of the polymer does not affect the hold-up (see Fig. 9.16). In these cases the interface is smooth even before the addition of the polymer.

As was noted in section 9.2.2 the addition of the polymer delays the transition to both slug and annular flows. The transition to annular flow before adding the polymer occurs roughly at an average h_w/D = 0.32 at U_{so} = 0.44, U_{sw} = 0.50 m/s. When polymer is added, the flow from annular changes to dual continuous for all conditions investigated, where h_w/D increases to 0.50 at U_{sw} = 0.80 m/s. It is possible that higher values of h_w/D and U_{sw} are required to initiate annular flow when DRP is present. For the transition to slug flow at U_{so} = 0.23 m/s, h_w/D is equal to 0.48 before the addition of the polymer. When polymer is added, the flow remains stratified for the conditions investigated and h_w/D reaches a value of 0.57. This shows that the required h_w/D to initiate slug flow should be higher than this value. At U_{so} = 0.16 m/s, the critical h_w/D prior to slug formation is equal to 0.53 before adding the polymer. This critical h_w/D for slug formation increases to 0.65 (at U_{sw} = 0.6 m/s), when polymer is added. The increase in

the water hold up reflects a decrease in the water velocity while the oil velocity should increase because of the accompanying decrease in the oil hold up.

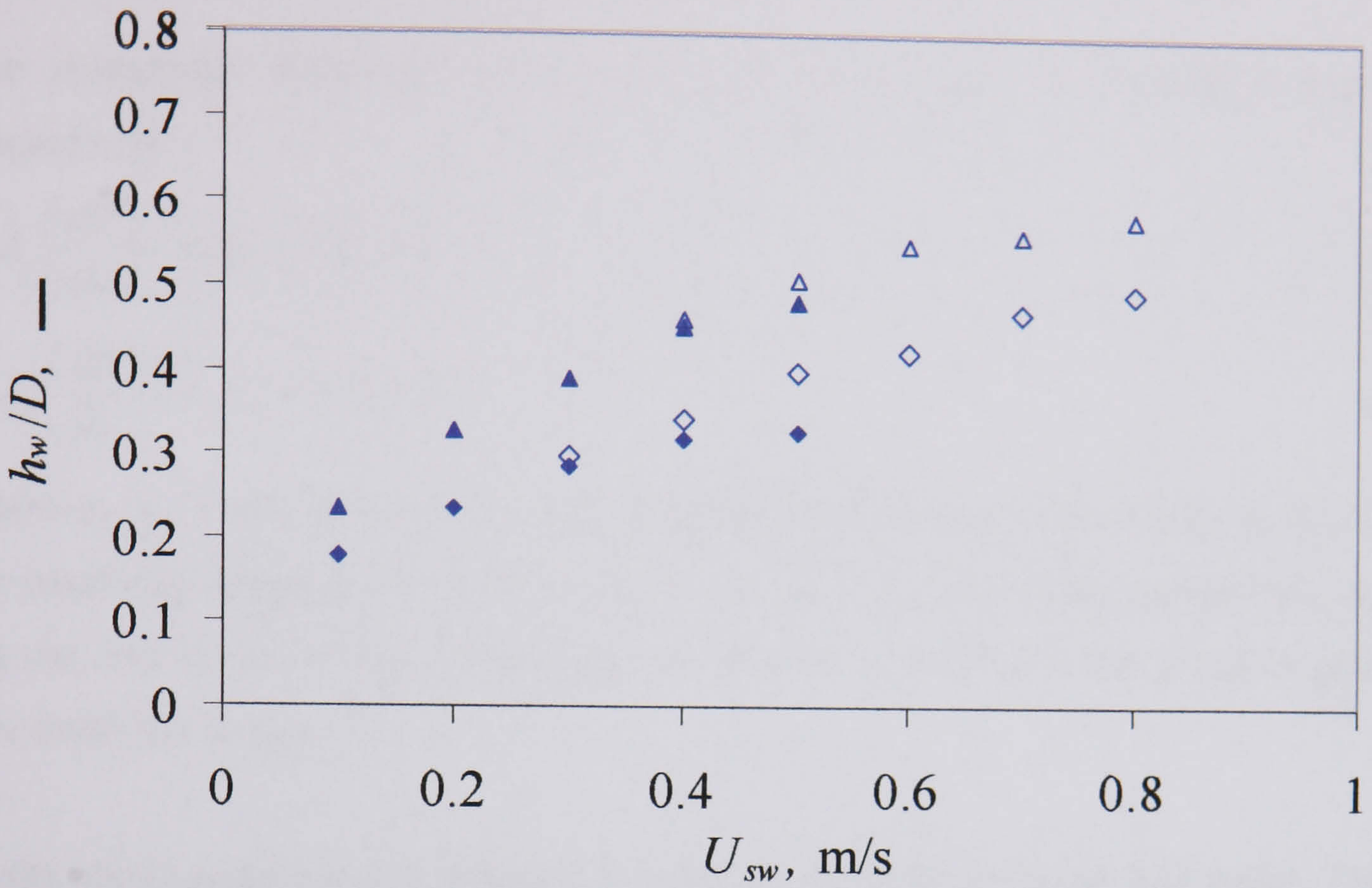

Fig. 9.16 Water hold-up against superficial water velocity before and after adding 50 ppm DRP at U_{so} = 0.23 and 0.44 m/s.

In stratified flows, the polymer is expected to have a significant effect on the interfacial shear stress as it was shown to smoothen the oil-water interface. It was also shown above that the addition of the polymer to the water phase increases the water hold up and as a result may decreases the water velocity if a flat interface is assumed (the effect on water velocity depends on the interface shape). Combined with the reduced turbulence in the water phase the addition of the polymer is expected to decrease the water wall shear stress as well. The interfacial and water wall shear stresses can be calculated from a two-fluid model using the experimentally measured overall pressure drop and interface height (details of the model can be found for example in the classical work by Taitel and Dukler, 1976; Brauner and Moalem Maron, 1989). In the current model it is assumed that the interface is flat and there is no entrainment of one phase into the other. Developments of the model including non-flat interfaces and entrainment of one phase into the other have also been suggested (see for example Brauner et al.,

1998; Lovick, 2004) but given the lack of additional information on interface shape and entrainment, the simple model used here is considered sufficient to indicate changes in the shear stresses when polymer is added in the flow.

The momentum equations for the oil and water layers in horizontal flow are respectively:

$$-A_o\left(\frac{dP}{dz}\right)-\tau_o S_o-\tau_i S_i=0 \tag{9.2}$$

$$-A_w\left(\frac{dP}{dz}\right)-\tau_w S_w+\tau_i S_i=0 \tag{9.3}$$

where τ_w, τ_o, τ_i are the water, oil and interfacial shear stresses respectively, S_i, S_o, S_w are the interfacial length and the wall perimeter of oil and water phase respectively, A_o, A_w are the area of the oil and water phase respectively and dP/dz is the pressure gradient (for detail see chapter 5).

In the above equation it is assumed that the oil phase flows faster than water. The oil wall shear stress, τ_o, is expressed in terms of the corresponding fluid friction factor, f_o. The oil wall friction factor, f_o, is Fanning type and the pipe is considered smooth.

Using the above equations, the interfacial shear stresses (τ_i) can be calculated from Eq.(9.2), using the measured pressure gradient and hold-up values while the water wall shear stress values (τ_w) are calculated from Eq.(9.3), using the calculated interfacial shear stresses.

The effect of adding polymer on the interfacial shear stress (τ_i) is presented in Fig. 9.17. Again only those cases where the flow is *stratified* and *dual continuous* are shown. Before the addition of the polymer, it is clear that the interfacial shear stress increases with the superficial water velocity. The increase is clearer for U_{so} = 0.44 m/s especially at the points where drops start forming at the interface after U_{sw} = 0.3 m/s and 0.44 m/s. As expected the interfacial shear stress values at U_{so} = 0.44 m/s are higher than those at U_{so} = 0.23 m/s since the interface is more wavy at the higher oil velocity. The addition of the polymer causes a dramatic decrease in the interfacial shear stress values especially for U_{so} = 0.44 m/s. This reduction is a result of damping the wavy oil-water

interface as was shown in section 3.1.2. It can also be seen that the sign of the interfacial stress term changes for U_{so} = 0.23 m/s which means that the water phase now becomes slightly faster than the oil.

The values of the water wall shear stress before and after the addition of polymer are plotted in Fig. 9.18. The plot shows a decrease in the shear stress when polymer is added. The decrease for the lower water velocities occurs mainly as a result of the damping of the turbulence in the water phase while at higher water velocities, where water hold up was found to increase, the decrease could also be related to a decrease in the water velocity if flat interface is assumed.

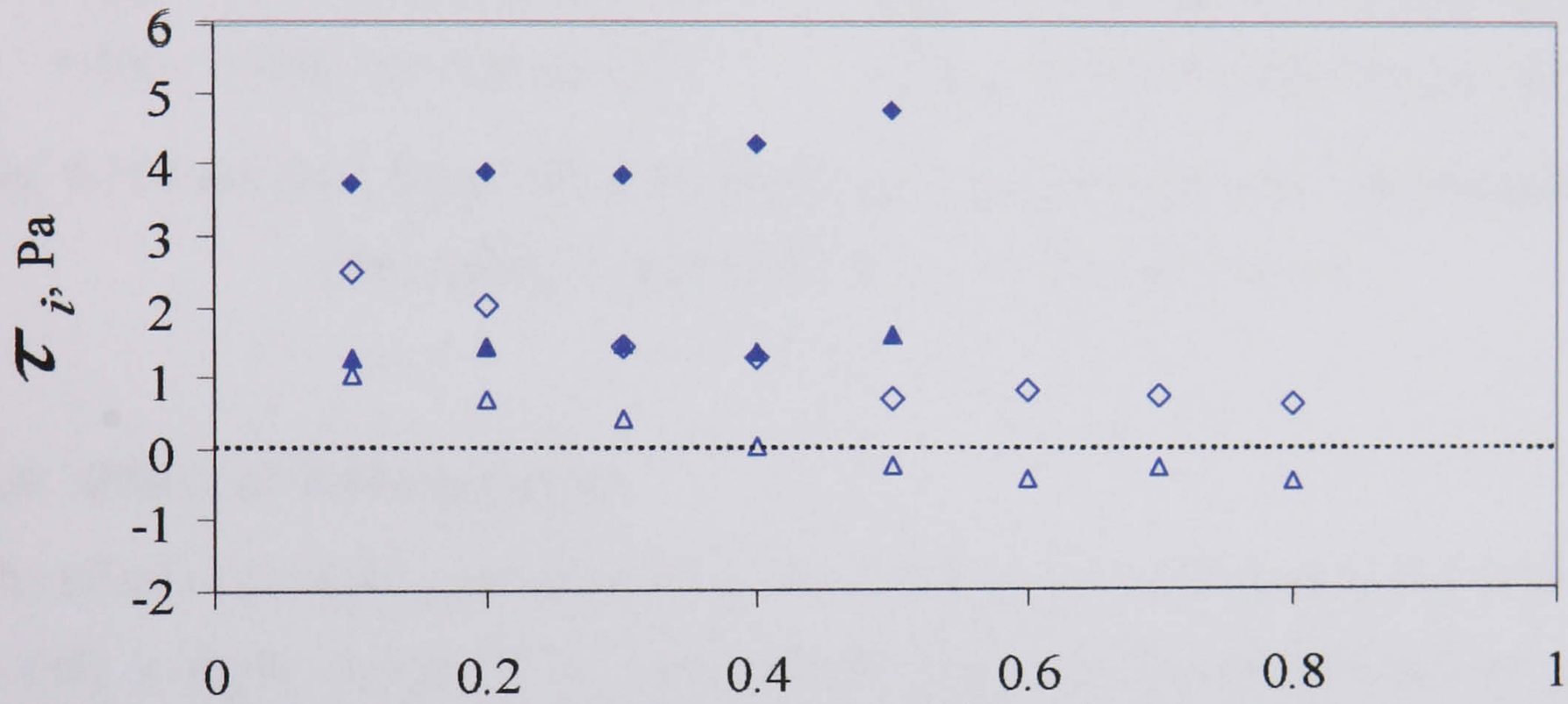

Fig. 9.17 Calculated interfacial shear stress against superficial water velocity before and after adding 50 ppm DRP at U_{so} = 0.23 and 0.44 m/s.

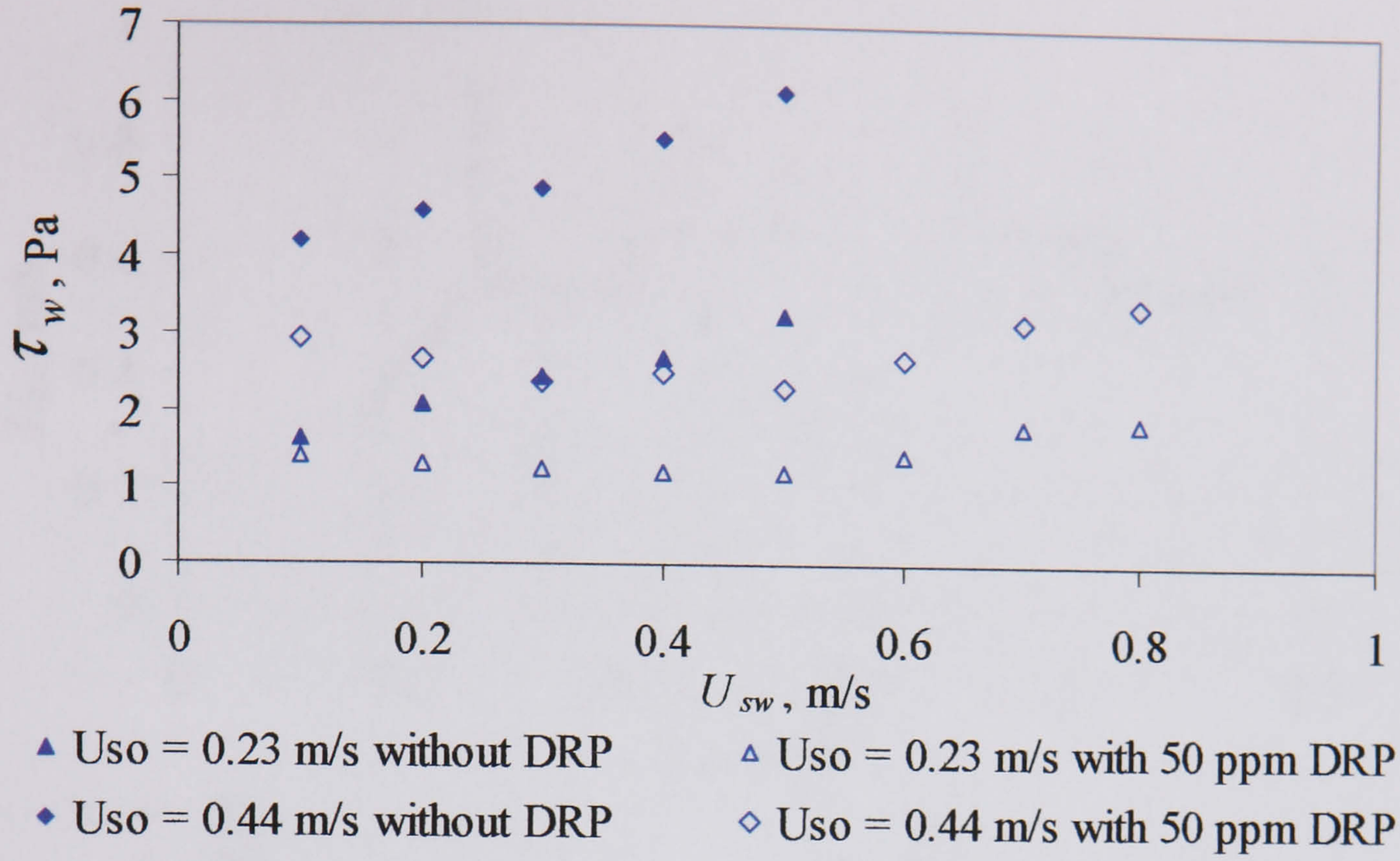

Fig. 9.18 Calculated water wall shear stress against superficial water velocity before and after adding 50 ppm DRP at U_{so} = 0.23 and 0.44 m/s.

9.4 Effect of Concentration

The effect of polymer concentration on the flow pattern is presented in Fig. 9.19. There is only a slight change in the flow pattern transitions between 20 and 50 ppm of polymer. An earlier transition to slug flows occurs at U_{so} = 0.16 and 0.23 m/s with 20 ppm of polymer than with 50 ppm.

Although the comparison does not show a significant change in the flow pattern boundaries, careful analysis of the pictures reveals a significant difference in the appearance of the flow patterns between these two concentrations. For the stratified wavy flows, especially those prior to transition to other flow patterns, the damping of the waves is more pronounced when 50 ppm is used instead of 20 ppm. Fig. 9.20 shows the flow at U_{so} = 0.23, U_{sw} = 0.50 m/s before and after adding 20 ppm of DRP. In Fig. 9.20a, the oil-water interface is wavy with quite large amplitude waves. These waves are only partially damped by the addition of polymer (Fig. 9.20b) and the level of the disturbance at the interface is reduced. However, with 50 ppm, the damping of the waves is more significant and the interface becomes smooth (see Fig. 9.6).

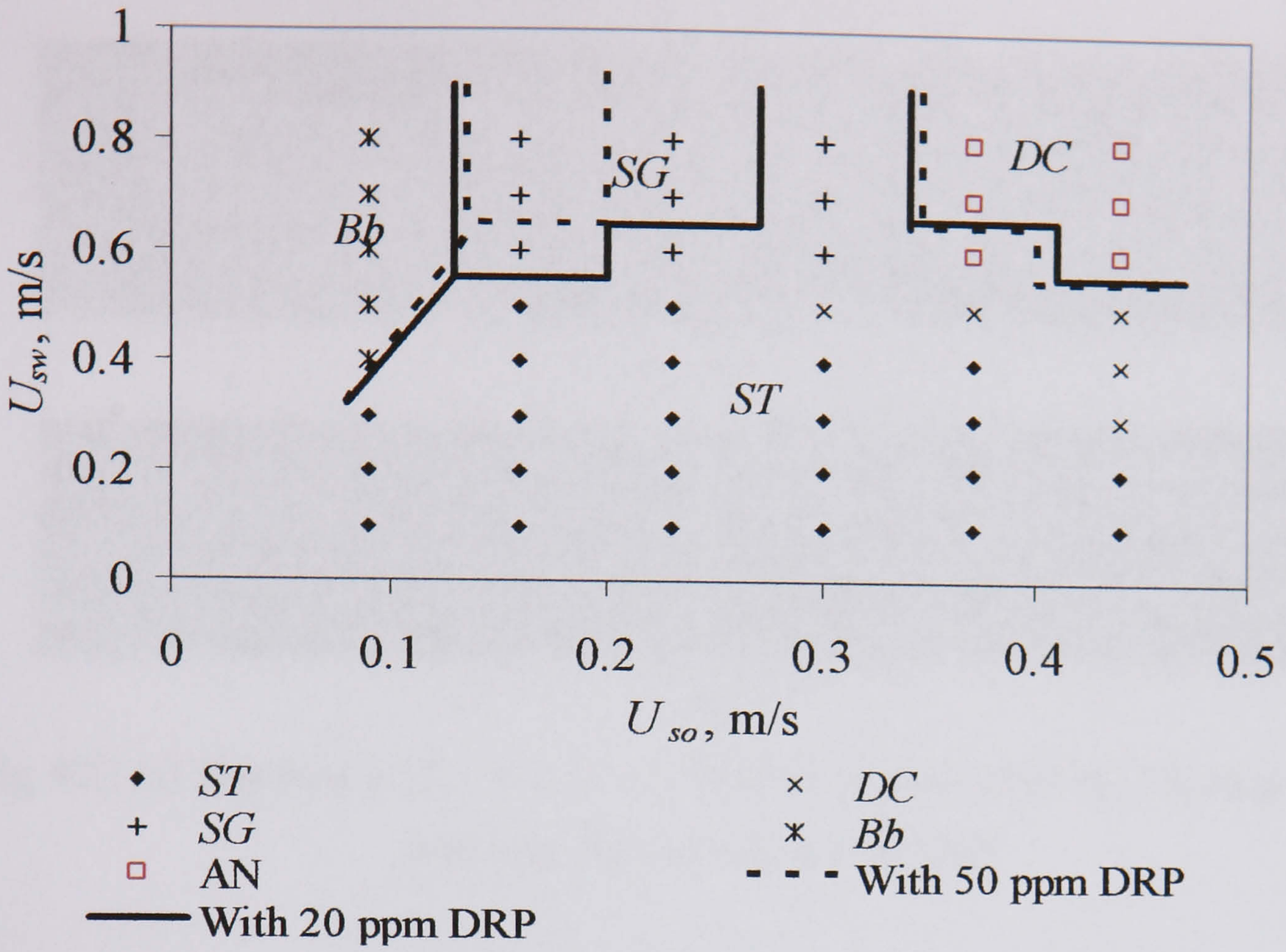

Fig. 9.19 Comparison of flow patterns without DRP against the flow pattern boundaries with 20 and 50 ppm DRP in water for horizontal oil-water flows in the 14 mm ID test section.

At $U_{so} = 0.23$, $U_{sw} = 0.80$ m/s, slug flow is observed before the addition of the polymer (Fig. 9.21a). After adding 20 ppm polymer into the water phase, very long slugs appear and the pattern looks like stratified flow but with discontinuities (Fig. 9.21b). In this study, this pattern is classified as slug flow. For the same conditions but with 50 ppm polymer, it was seen that slug flow changes to stratified (Fig. 9.10). The decrease in water turbulence with 20 ppm is apparently not as high as with 50 ppm, and the water can still break up the oil layer in slugs. It is possible that if a longer test section were available the closely packed slugs seen with 20 ppm polymer would coalesce to form a continuous layer resulting in stratified flow as with the higher concentration polymer.

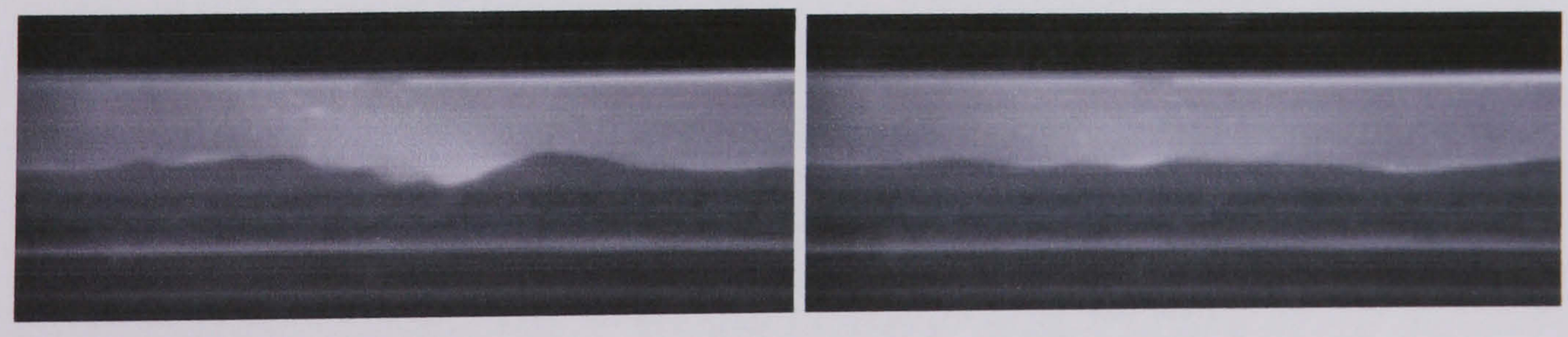

(a) (b)

Fig. 9.20 (a) *Stratified wavy* flow at $U_{so} = 0.23$, $U_{sw} = 0.50$ m/s without DRP. (b) Flow becomes *stratified* after adding 20 ppm DRP.

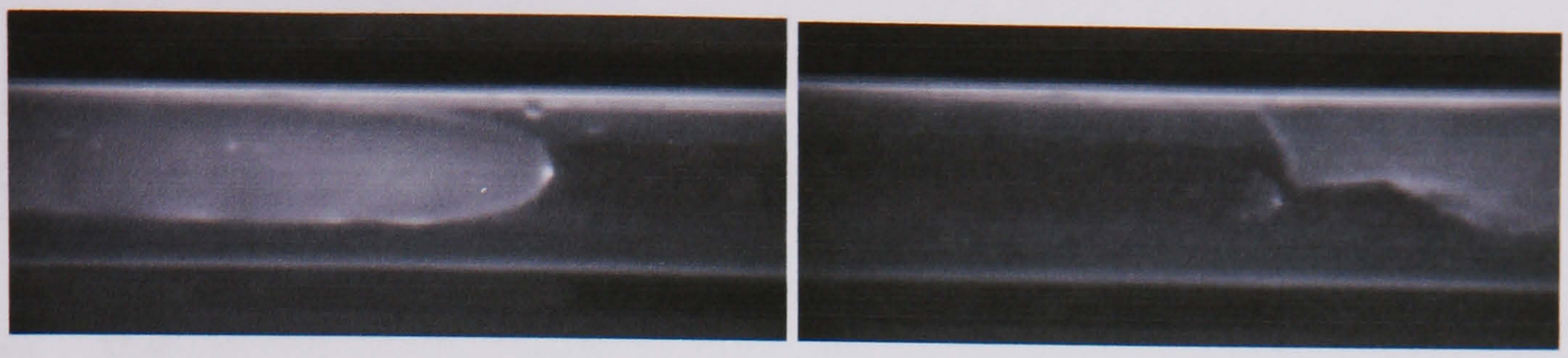

(a)

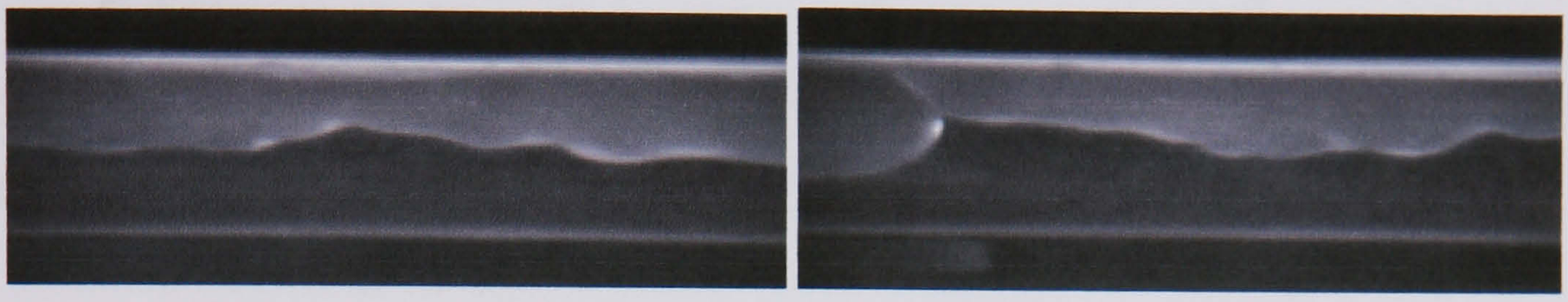

(b)

Fig. 9.21 (a) *Slug* flow at U_{so} = 0.23, U_{sw} = 0.80 m/s without DRP. (b) The slugs become very long after adding 20 ppm DRP.

The effect of polymer concentration on pressure gradient is given in Figs. 9.22, 23 and 24 for U_{so} = 0.09 m/s (transition from stratified to bubble flow), 0.23 m/s (transition from *stratified* to *slug* flow) and 0.44 m/s (transition from *stratified* and *dual continuous* to *annular* flow) respectively. All the figures show that the pressure gradients with polymer of any concentration added are less than those without polymer. At U_{so} = 0.09 m/s, the pressure gradients with 20 ppm DRP are slightly higher than those with 50 ppm especially in the bubble region (U_{sw} = 0.5 – 0.7 m/s). The same is seen at U_{so} = 0.23 m/s especially in the slug region. It is worth noting that with the 20 ppm polymer slug flow appears after U_{sw} = 0.6 m/s while for 50 ppm polymer there is no slug flow at this U_{so}. For U_{so} = 0.44 m/s, the difference between the pressure gradients for 20 and 50 ppm is almost negligible.

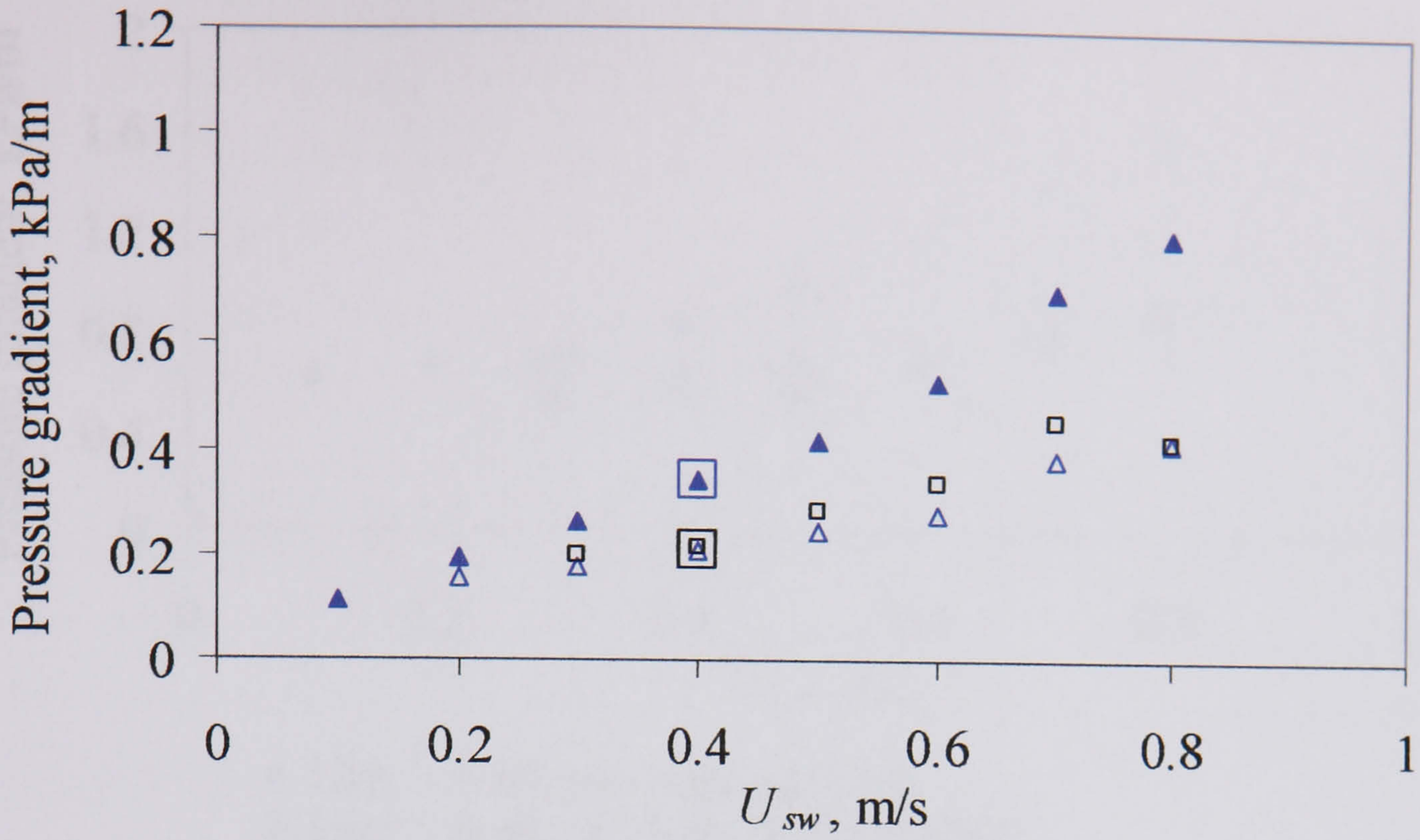

Fig. 9.22 Pressure gradient against superficial water velocity before and after adding 20 and 50 ppm DRP at U_{so} = 0.09 m/s.

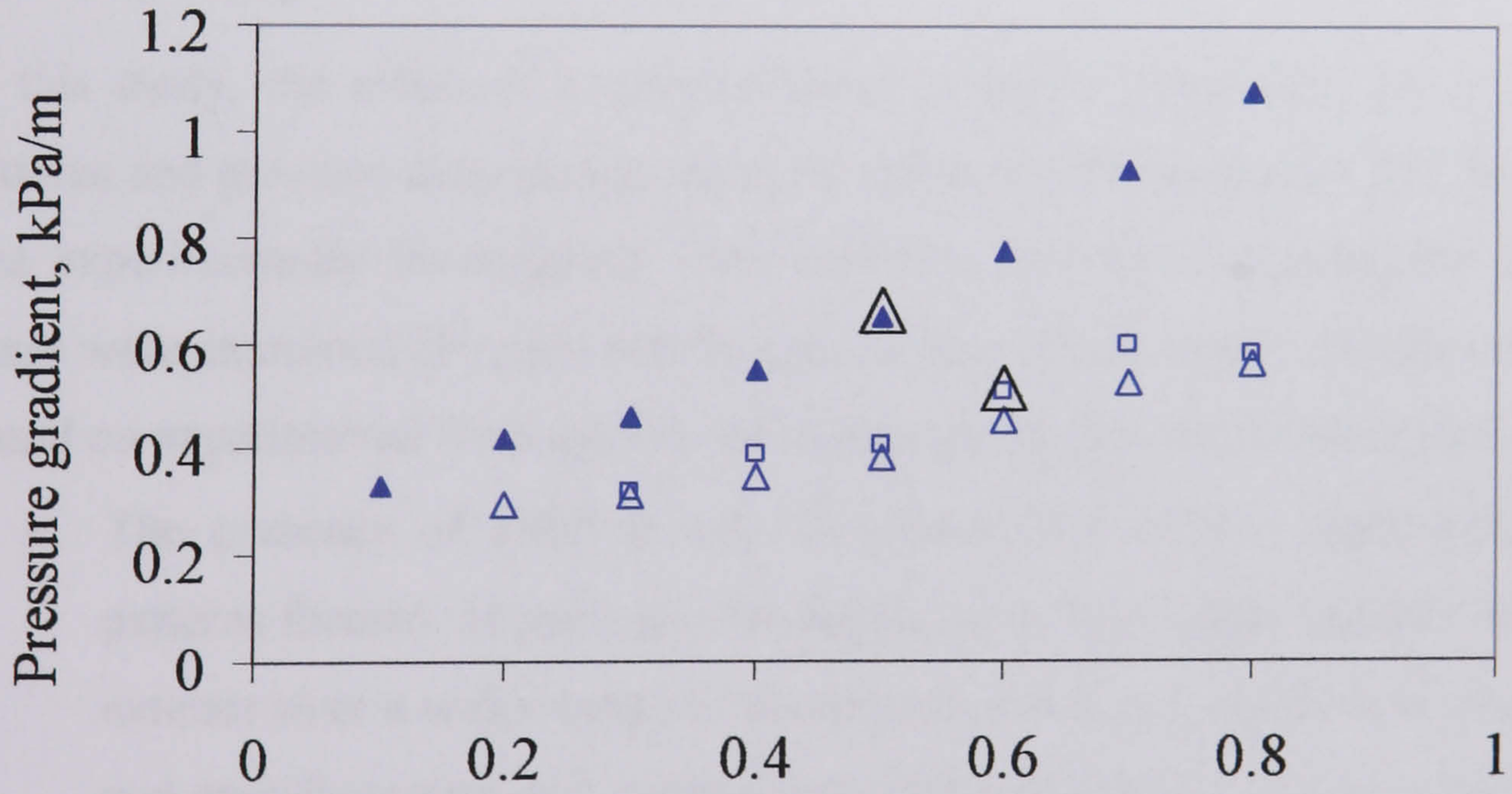

Fig. 9.23 Pressure gradient against superficial water velocity before and after adding 20 and 50 ppm DRP at U_{so} = 0.23 m/s.

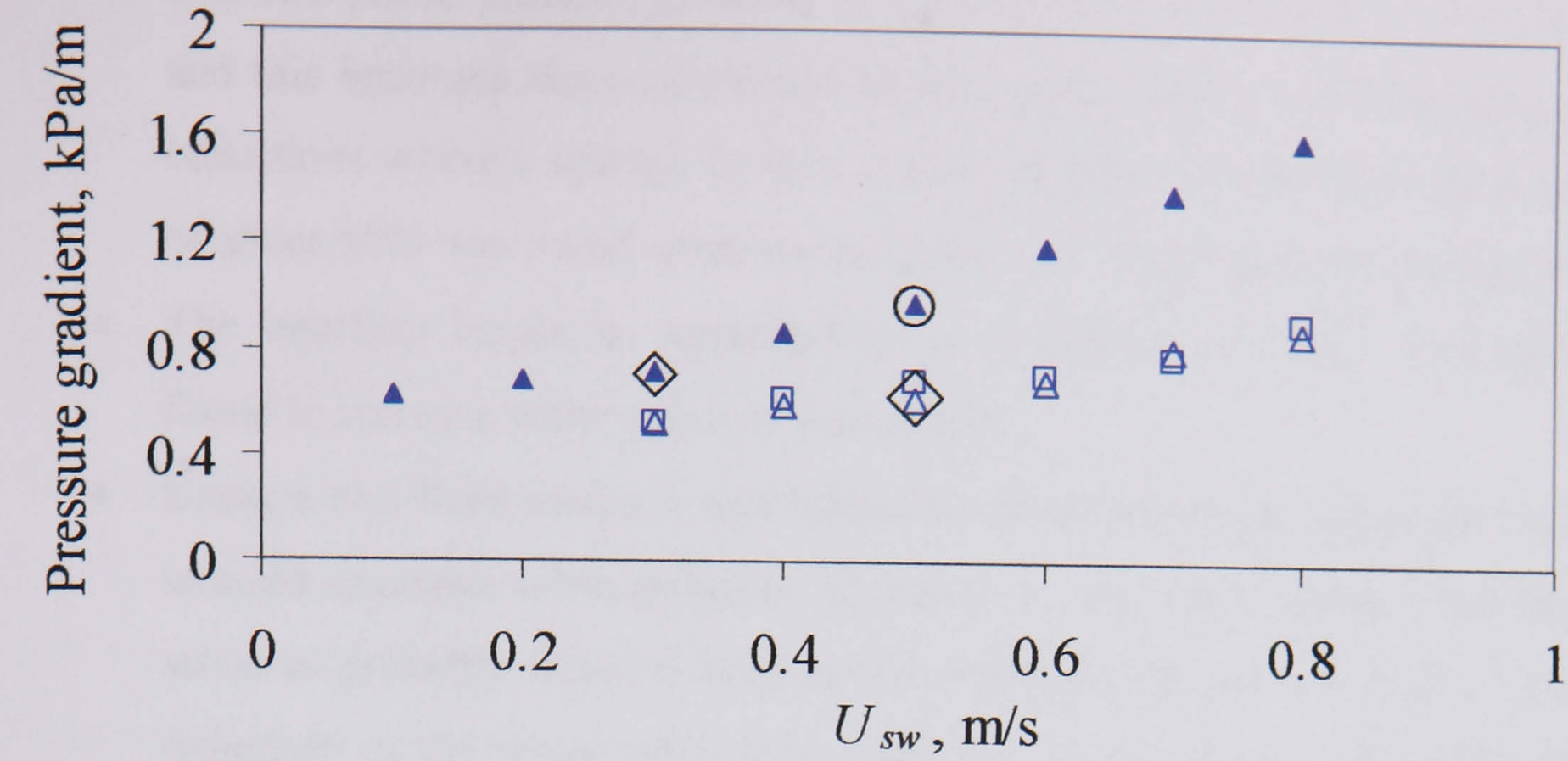

Fig. 9.24 Pressure gradient against superficial water velocity before and after adding 20 and 50 ppm DRP at U_{so} = 0.44 m/s.

9.5 Summary

In this study, the effect of a drag reducing polymer (Magnafloc 1011) on the flow patterns and pressure drop during oil-water flows in a horizontal 14 mm ID acrylic pipe was experimentally investigated. Two different polymer concentrations in the water phase were examined (50 ppm and 20 ppm) using a fixed master solution of 1000 ppm. Based on experimental findings, the following conclusion can be concluded:

- The presence of DRP in the two-phase flow affects significantly the flow patterns formed. In particular the region of both *stratified smooth and wavy* flow extends over a wider range of conditions. The wavy interface is clearly damped and drop formation and transition to dispersed patterns is delayed when polymer is present. *Annular* flow changes to either *stratified* or *dual continuous* while the very disturbed interface becomes smoother. *Slug* flow changes to *stratified* in most conditions, apart from low superficial oil velocities where oil slugs still exist but tend to flow close together. The oil drops in *bubbly* flow remain after the addition of DRP but flow closer together.

- The two-phase pressure gradient is reduced with the addition of the polymer, and this becomes more significant as the water velocity increases especially at conditions where a change in flow pattern happened. Maximum drag reduction of about 50% was found when the polymer was introduced into annular flow.
- The interface height in separated flows (stratified and dual continuous) was found to increase when polymer was added.
- Using a two-fluid model it was found that both interfacial and water wall shear stresses decrease when polymer is present in the water phase. The interfacial stress is probably reduced because the interface becomes smoother, while the reduction in the water wall stress could be a combination of decreased water velocity (because of increased height) and turbulence.
- There was no significant difference on flow patterns or pressure drop between the two polymer concentrations used. However, the higher polymer concentration appears to damp more the interfacial waves.

The findings of this study point to the significant effect of polymers into oil –water flows. Further measurements are needed to quantify the changes in the interfacial shape or the effect of master solution and polymer concentration during flow. Of course the more fundamental questions on the origin of drag reduction (still disputed in single phase flows) will also have to be addressed in liquid-liquid flows where the presence of the interface increases the complexity of the system.

CHAPTER 10

Conclusions and Recommendations

The aim of this project was to study phenomena related to *dual continuous* during liquid-liquid flow which is a pattern continuously occurring but little understood and studied. The insufficient experimental information about this pattern, the lack of understanding the mechanism of drop formation and the difficulties in identifying the interface in this pattern compared to *stratified* flow are the main reasons for not having adequate theoretical models for dual continuous flow. In order to develop such models, a better understanding of this type of flow is needed. This is done by acquiring new data in the dual continuous region of horizontal liquid-liquid flow and by developing models that can predict the stability of the interface, the onset of drop formation and the entrained fraction of each phase into the other.

10.1 Experimental Program-Instrumentation

The experimental work of this project was performed in a 14 mm and 38 mm diameter, horizontal, acrylic and stainless steel test sections respectively, using water and oil (5.5 mPa s viscosity and 828 kg/m^3 density) as test fluids. The flow facility with the small test section was made as part of this project. The liquid-liquid flow facilities are located in the department of Chemical Engineering at University College London. The inlet geometry of the large test section was modified to introduce better stratification to the flow. Flow patterns, mechanism of drop formation and onset velocities of entrainment were investigated using a high speed video camera. The wave characteristics before and at the onset of entrainment were studied by measuring the instantaneous fluctuation of the interface between the oil and water using a wire conductivity probe. The entrained fraction of each phase into the other was found from the phase distribution data produced using the high frequency impedance probe developed by Lovick (2004). A dual impedance probe developed by Lovick (2004) was used to obtain drop velocities and drop chord length distribution at different location in a pipe cross section.

A wire conductivity probe was developed in this project to acquire detailed data about the structure of the waves before and at the onset of entrainment. The results helped to gain insight on the size of the waves just before breakup. They were also used to validate a model on wave stability that was developed in this project. Visual observation although important, was not able to quantify exactly the size of the waves and especially the wavelengths. The data were gathered using a data acquisition program that was developed using HPVee software.

10.2 Experimental Results

10.2.1 Visual observation of the flow

High speed video camera was used to monitor and record the flow at different conditions of oil and water superficial velocities. Both available test sections were used to investigate wave characteristics before and at the transition from stratified to non-stratified flows (mainly dual continuous flow). The experiments in the 38 mm ID pipe were carried out with two different inlet sections (Y-and T-junctions) at 7 m from the inlet while at 2 m the experiments were conducted with the Y-junction only. The following conclusions can be drawn:

- The flow pattern map by Lovick and Angeli (2004) was used for the 38 mm ID pipe, and a new flow pattern map was obtained for the 14 mm ID.
- In the 14 mm ID pipe, *dual continuous* flow occurs at a small range of superficial velocities compared to the large pipe. At low oil velocities, *stratified* flow changes to either *slug* or *bubble* flow (due may be to the small thickness of the oil layer) in the test section. These patterns were not found in the 38 mm ID pipe. Also, apart from the works of Charles et al. (1961) and Russell et al. (1959), none of the other studies available in the literature have reported *bubble* or *slug* flow. This could be mainly due to the smaller pipe diameter and oil viscosity used.
- The results from both the 38 mm and 14 mm ID pipes indicate that no drops are formed when interfacial waves are absent. Also, the amplitudes of the waves increase as both the superficial oil and water velocities increase. As a result the required U_{sw} for the onset of entrainment decreases as U_{so} increases

- The pictures that were taken at 2 m from the inlet in the 38 mm ID pipe showed that no drops were found at this location for the onset velocities obtained 7 m from the inlet. Such observation showed that all the drops observed in the downstream part of the pipe were evolved from the waves only as they propagate through it. It also means that the new inlet section introduced a better stratification to the flow and diminished entrance effects.
- *Annular* flow pattern with water at the wall was clearly observed in the present experiments at low oil superficial velocities and high water superficial velocities for the 38 mm and 14 mm ID pipe. The *annular* flow continued to form as the water superficial velocities increased. However, the top layer of water became a little bit thicker while the oil layer became more dispersed.
- For the effect of inlet geometry in the 38 mm ID pipe, it is believed that the bend after the T-junction increases the mixing of the phases since larger drops are observed with this inlet compared to the Y-junction inlet.
- The conditions and mechanism leading to drop formation from the wave crests in wavy stratified oil-water flow and to the transition to dual continuous flow were also investigated in this study. Drops were found to form as a result of the relative movement between the oil and water phases. The faster phase will undercut the other one until a drop is detached from the wave crest.

10.2.2 Onset of entrainment

The water superficial velocities, U_{sw}, at which droplets are first observed in the oil-water flow in each oil superficial velocity, were obtained using the high speed camera for both the 38 mm and 14 mm ID pipes. Based on experimental findings, the following conclusions can be drawn:

- The measurements from the two test sections showed that the onset appears at decreasing water superficial velocities as the oil superficial velocities increase.
- Lovick and Angeli (2004) found the onset of dual continuous flow pattern at 0.80 m/s mixture velocity using visual observation. Using the same fluid properties and the same condition in the present study, the onset occurred at slightly different conditions. The differences could be due to the fact that visualization by Lovick and Angeli (2004a)was done by naked eye while in the present study, a high speed video camera was used. Also, in this study a more

strict definition was used to define the where onset was considered to have happened when a single drops was flowing continuously in the opposite phase rather than many drops.

- The effect of inlet geometry on the onset of entrainment at 7 m from the inlet was almost negligible. The onset velocities measured when the fluids go through a bend after the inlet were found to be close in most cases to those when oil and water were introduced in a stratified manner (Y-junction). At $U_{so} = 0.50$ and $U_{so} = 0.55$ m/s drops were formed at lower superficial water velocities when bend was present in the inlet. This could be due to the effect of mixing in the bend.
- The VKH model developed by Trallero (1995) was unable to predict the onset velocities of entrainment obtained in the present study.

10.2.3 Experimental wave characteristics using a conductivity probe

The transition between stratified and non-stratified flows both at 7 m from the inlet and close to the inlet at 2m was investigated with a wire conductivity probe. The conductivity probe was used to measure wave characteristics (by measuring the fluctuation of the water layer) before and at the onset of entrainment in the 38 mm ID stainless steel test section. In all cases the Y-junction inlet was used that minimize entrance effects. From the experimental measurements, the following summarize the conclusions:

- In accordance with the visual observations, the results from the conductivity probe showed an increase in the amplitude of the waves as the superficial velocities increase.
- The experimental results showed that the required wave amplitude to form a drop increases as the difference between oil and water velocities decreases. This is because the shear between the two phases is smaller at reduced phase velocity difference and waves have to grow to large amplitudes before drop formation is possible. It is also clear that wavelength increases as the velocity difference between the two phases decreases.
- At 2 m downstream the inlet, the measurements of the wave characteristics at the onset velocities showed that the amplitude of the waves increased as the superficial oil velocities increase. Also, the wavelengths are longer than those measured at 7 m from the inlet and the amplitudes are smaller. These waves are

expected to grow in amplitude and decrease in wavelength so the drops observed at 7 m from the inlet can form.

10.2.4 Entrained fraction

The impedance probe was used to measure local volume fraction distribution in a pipe cross section. The integration of these results gives the phase distribution in that pipe cross section. From the phase distribution, the entrained fraction of each phase into the other was calculated. All the measurements were obtained in the 38 mm ID pipe and the following conclude the experimental findings:

- The phase distributions of the different conditions measured showed that dispersion concentrated at the interface and the degree of dispersion increased as the superficial water velocity increased.
- The entrained fraction of water in oil ($E_{w/o}$) increased as the input water flow rates increased at constant oil superficial velocity. On the other hand, the entrained fraction of oil in water ($E_{o/w}$) increased as the oil flow rates increased at a constant water superficial velocity.
- Similar trends were found while using both the T-junction with a bend and the Y-junction at the inlet for the test section. However, the entrained fractions when the bend was used were higher than those obtained with the Y-junction. The difference between the values became more significant at higher velocities. Therefore, for the range of conditions covered in this research, the effect of the bend in the inlet is found to be more significant on the entrained fractions of each phase into the other at higher velocities and could initiate an early transition from dual continuous to dispersed flow.

10.2.5 Drop size distribution

Drop velocities and chord lengths were measured along a vertical diameter in the 38 mm ID pipe 7 m from the inlet with a dual impedance probe. All measurements were done in the dual continuous pattern. In all measurements, water is consider continuous below 68 % input oil percentage while above that oil is considered to be the continuous phase. The following summarize the conclusions:

- From the chord length measurements, chord lengths up to 20mm were measured.
- Drop concentration and chord length decreased with increasing distance from the interface.
- Oil drops were found to be larger than water drops since oil tends to lose continuity at relatively high oil volume fraction compared to water.
- From the average chord length distributions, it was found that the number density of large drops decrease as the water superficial velocities increase at each oil superficial velocity.
- In *DC* flow, water drops were in general faster than the velocity of the upper layer while oil drops could be either faster or slower than the lower layer.
- Although there is no clear trend on the effect of velocity on the chord length in general it can be reported that the average L_{32} is constant for the oil drops while it tends to decrease for the water drops as the corresponding layer velocity increases. For the average L_{10}, both oil and water drops tend to decrease as the layer velocity increases.
- The chord length distribution was also transformed to drop size distribution using a method developed by Hu et al. (2006). The results show that the drop size distribution is smaller than the corresponding chord length distribution.
- There is no clear trend on the effect of oil velocity on the drop size and this is due to two competing phenomena. In other words, as the increase in oil velocity tends to decrease the size of the water drops, the increase in water entrained tends to increase the drop size.

10.2.6 Effect of DRP on horizontal oil-water flow

A drag reducing polymer (Magnafloc 1011) was injected in a horizontal oil-water flow using a fixed master solution of 1000 ppm. All experiments were carried out in the 14 mm ID acrylic pipe with two different polymer concentrations in the water phase (50 ppm and 20 ppm). The influence of polymer on flow patterns and pressure drop was investigated. Based on the experimental results, the following conclusions can be drawn:

- The addition of the polymer had a significant effect on the flow patterns formed. The region of stratified flow (*stratified smooth and wavy*) extended over a wider

range of conditions and *annular* flow changes to either *stratified* or *dual contimuous*. The wavy interface in the stratified, dual continuous and annular flows was clearly damped and the interface became smoother. This would delay drop formation and transition to dispersed patterns. *Slug* flow changed to *stratified* in most conditions, apart from low superficial oil velocities where oil slugs still existed but tended to flow closer together. The oil drops in *bubbly* flow remained after the addition of DRP but similar to slugs were also found to flow closer together.

- The presence of DRP reduced the two-phase pressure drop. The reduction became more significant as the water velocity increased especially at conditions where a change in flow pattern happened. Maximum drag reduction of about 50% was found when the polymer was introduced into annular flow.
- The interface height in separated flows (stratified and dual continuous) was found to increase when polymer was added.
- Using a two-fluid model it was found that both interfacial and water wall shear stresses decrease when polymer is present in the water phase. The interfacial stress is probably reduced because the interface becomes smoother, while the reduction in the water wall stress could be a combination of decreased water velocity (because of increased water layer height) and turbulence.
- There was no significant difference on flow patterns or pressure drop between the two polymer concentrations used. However, the higher polymer concentration appeared to damp more the interfacial waves.

10.3 Theoretical Results

10.3.1 Stability analysis and prediction of the onset of entrainment

A criterion for the transition between stratified stable and unstable liquid-liquid flows was derived theoretically based on Kelvin-Helmholtz (K-H) instability and finite wavelength that relates critical amplitude and wavelength at the onset of instability. The following points summarize the findings:

- The model predicted well the VKH line developed by Trallero (1995) assuming very long wavelengths.
- The model satisfactory predicted whether waves with certain amplitudes and lengths are stable or not. According to the model the required amplitudes and

lengths for waves to become unstable decrease as the superficial water velocity increases for a given superficial oil velocity. At higher water velocities, any disturbance in the oil-water interface will become unstable.

- In comparison with experimental results it was found that the onset of drop formation with higher viscosity oils coincides with the appearance of unstable waves, while with lower viscosity oils, the onset of drop formation appears at higher velocity than the transition to unstable waves.
- The results revealed that critical amplitudes to initiate instability decrease as the viscosity ratio increases. This agrees with published experimental results which show that onset velocities for drop formation decrease as the viscosity ratio increases.
- It was also found from the model that for low viscosity oils the critical amplitude to initiate instability acquired maximum value at almost zero slip velocity while for high viscosity oils the maximum value was reached for water velocity higher than the oil one.
- The experimental results of interfacial wave characteristics that were studied experimentally before and at the onset of entrainment (see chapter 4) showed satisfactory agreement when compared with the model predictions.
- The stability model can predict transition from stable to unstable waves but not the conditions for drop formation. Another criterion should be implemented based on the mechanism of drop formation to determine whether unstable waves will form drops. However, the required amplitudes and lengths of the waves for drop formation would need to be above the critical ones for transition to instability. Based on this and on current experimental data an empirical amplitude and wavelength were selected to predict the onset of entrainment and the transition from stratified to other mixed flow regimes. These predictions agreed well with experimental observations from a number of studies from the literature using both low and high viscosity oils.

10.3.2 Mechanism of drop formation

A model was developed which assumes that a drop will detach from a wave when the drag force acting on the wave exceeds the stabilizing surface tension force in the flow direction. In the suggested entrainment equation (Eq. 6.12) the critical wave length for

droplet formation was related to wave amplitude. This equation can be used together with Eq. (5.19) on wave stability (see chapter 5) to define three regions in a wave amplitude against length graph. In summary the following can be concluded:

- In the region below both lines (*stable waves region*) the waves are stable and no drops can form. In the region above both lines (*entrainment region*) the waves are unstable and also drag force exceeds the surface tension force so that drops can form from the wave crests. Finally in the region between the two lines (*unstable waves region*) the waves are unstable but would need to grow further in amplitude before any drops can detach from them.
- The critical minimum amplitudes and wavelengths required for drop formation, found from the intersection of the two lines (Eqs. (5.19) and (6.12)), agreed well with experimental data when a new correlation for the drag coefficient on the waves was used.
- In stratified flow it was found that all waves measured experimentally had characteristics below the entrainment line while in dual continuous flow some (but not all) waves had characteristics above the entrainment line; these would be the waves that produce drops.
- Amplitudes and lengths of waves that were experimentally observed to form drops were found to be within the predicted entrainment region.

Thus the model can predict satisfactorily the critical amplitudes for specific wavelength required to form drops at the onset of entrainment. Knowing the amplitudes and lengths of the waves, the model can predict the transition between stratified wavy and dual continuous flow.

10.3.3 Entrainment model

A model for predicting the entrainment of one phase into the other phase in dual continuous horizontal oil-water flows was developed theoretically based on the balance between the rates of drop entrainment and of drop deposition. The model was further modified with the use of experimental data from the present work. Comparisons were made with experimentally determined entrained fractions from the literature. The predictions were reasonable in many cases taking into consideration the uncertainties in both experimental entrained fraction measurements and in the model development (most

notably the calculation of the deposition rate). It was demonstrated that the model can also be used to predict the transition between dual continuous and dispersed flow patterns.

10.4 Recommendations for Future Work

- All the experimental investigations in this work were carried out with one pair of fluids. As information regarding the *dual continuous* pattern and the transition to it is still insufficient detailed investigations involving fluids with different properties are needed. Obtaining new data on the onset of entrainment, wave structures, mechanism of drop formation at the transition to dual continuous flow and more data on entrained fraction of each phase into the other and drop size distribution will lead to more generalised models for describing liquid-liquid flow.
- Further detailed investigation of the wave structure and wave velocities with conductivity probes are indeed needed to understand and better predict the onset of drop formation.
- The findings of this study point to the significant effect of polymers into oil – water flows. Further measurements are needed to quantify the changes in the interfacial shape or the effect of master solution and polymer concentration during flow. Of course the more fundamental questions on the origin of drag reduction (still disputed in single phase flows) will also have to be addressed in liquid-liquid flows where the presence of the interface increases the complexity of the system.
- The prediction of the onset of drop formation can be significantly improved if a correlation that relates the wave amplitudes to the wavelength is developed.
- The entrainment onset velocities can be predicted using Eq. 5.9 while the entrainment model can be used to describe the transition between dual continuous flow and other dispersed patterns. Further investigations of flow pattern transitions with these two models are needed.

References

- Alkaya, B., 2000, Oil-water flow patterns and pressure gradients in slightly inclined pipes. M.S. Thesis, University of Tulsa.
- Al-Sarkhi, A., Hanratty, T. J., 2001a. Effect of drag reducing polymer on annular gas-liquid flow in a horizontal pipe, Int. J. Multiphase Flow., 27, 1151-1162.
- Al-Sarkhi, A., Hanratty, T. J., 2001b. Effect of pipe diameter on the performance of drag reducing polymer in annular gas-liquid flows. Trans IChemE., 79, Part A, 402-408.
- Al-Sarkhi, A., Soleimani, A., 2004. Effect of drag reducing polymer on two-phase gas-liquid flows in a horizontal pipe. Trans IChemE., 82, Part A, 1583-1588.
- Andritsos, N., Williams, L., Hanratty, T.J., 1989. Effect of liquid viscosity on the stratified-slug transition in horizontal pipe flow. Int. J. Multiphase Flow, 15, 877-892.
- Angeli, P. A., 1996. Liquid-liquid dispersed flows in horizontal pipes. PhD. Thesis, Imperial College, University of London.
- Angeli, P. and Hewitt, G.F., 2000a. Flow structure in horizontal oil-water flow. Int. J. Multiphase Flow, 24, 1183-1203.
- Angeli, P., and Hewitt, G.F, 2000b. Drop size distributions in horizontal oil-water dispersed flows. Chem. Eng. Sci., 55, 3133-3143.
- Arirachakaran, S., Oglesby, K. D., Shoham, O., and Brill, J. P., 1989. An investigation of oil water flow phenomena in horizontal pipes, SPE Proc. Prod. Operation Symp., SPE 18836, 155-167.
- Astria, G., 1969. A phenomenological interpretation and correlation of drag reduction. AIChE J., 14, 564-567.
- Azzopardi, B.J., 1983. Mechanisms of entrainment in annular two-phase flow, UKAEA, Report AERE-R 11068.
- Azzopardi, B.J., 1997. Drops in annular two-phase flow, Int. J. Multiphase Flow, 23, 1-53.

- Azzopardi, B.J., Whalley, P.B., 1980. Artificial waves in annular two-phase flow, ASME Winter Annual Meeting, Chicago. Published in Basic Mechanisms in Two-Phase Flow and Heat Transfer, 165-173.
- Bai, R., 1995. Traveling waves in a high viscosity ratio and axisymmetric core annular flow. PhD thesis, University of Minnesota.
- Bai, R., Joseph, D.D., 2000. Steady flow and interfacial shapes of a highly viscous dispersed phase. Int. J. Multiphase Flow., 26, 1469-1491.
- Baik, S., Hanratty, T.J., 2003. Effects of drag reducing polymer on stratified gas-liquid flow in a large diameter horizontal pipe. Int. J. Multiphase Flow., 29, 1749-1757.
- Bannwart, A.C., 1998. Wavespeed and volumetric fraction in core annular flow. Int. J. Multiphase Flow., 24, 961-974.
- Barnea, D., 1991. On the effect of viscosity on stability of stratified gas-liquid flow: Application to flow pattern transition at various pipe inclinations. Chem. Eng. Sci. 46, 2123-2131.
- Barnea, D., Taitel, Y., 1993. Kelvin-Helmholtz stability criteria for stratified flow: Viscous versus non-viscous (inviscid) approaches. Int. J. Multiphase flow.19, 639-649.
- Barnea, D., Taitel, Y., 1994. Nonlinear interfacial instability of separated flow. Chem. Eng. Sci. 49, 2341-2349.
- Brauner, N., Moalem Maron, D., 1989. Two-phase liquid-liquid stratified flow. PhysicoChem Hydrodynamics. 11, 487-506.
- Brauner, N., Moalem Maron, D., 1992a. Stability analysis of stratified liquid-liquid flow. Int. J. Multiphase Flow, 18, 103-121.
- Brauner, N., Moalem Maron, D., 1992b. Flow pattern transitions in two-phase liquid-liquid flow in horizontal tubes. Int. J. Multiphase Flow, 18, 123-140.
- Brauner, N., and Ullmann, A., 2002. Modelling of phase inversion phenomenon in two-phase pipe flows. Int. J. Multiphase Flow, 28, 1177-1204.
- Brooke, J.W., Hanratty, T.J., 1993. Origin of turbulence-producing eddies in a channel flow. Phys. Fluids A 5 (4), 1011-1022.
- Choi, H. J., Jhon, M. S., 1996. Polymer induced turbulent drag reduction. Ind. Eng. Chem. Res., 35, 2993-2998.

- Clay P.H., 1940. The mechanism of emulsion formation in turbulent flow, Proceedings, Akademie van Wetenschappen, Amsterdam, 43, 852-965.
- Collins, S.B., and Knudsen, J.G., 1970. Drop size distribution produced by turbulent pipe flow of immiscible liquids, AIChE J., 6, 1072-1080.
- Cox, A. L., 1985. A study of horizontal and downhill two-phase oil-water flow, M.S. Thesis. The University of Texas.
- Dallman, J. C., Laurinat, J. E. Hanratty, T.J., 1979. Interpretation of entrainment measurements in annular gas-liquid flows. In: Durst, F., Tsiklauri, G. V., Afgan, N.H. (Eds.), Two-Phase Momentum, Heat and Mass Transfer, vol.2. Hemisphere, Washington, DC, pp. 681-693.
- Dallman, J. C., Laurinat, J. E. Hanratty, T.J., 1984. Entrainment for horizontal annular gas-liquid flow. Int. J. Multiphase Flow 10, 677-690.
- Das, R. K., Pattanayak, S., 1993. Electrical impedance method for flow regime identification in vertical upward gas-liquid two-phase flow. Meas. Sci. Technology 4, 1457-1463.
- De Gennes, P., 1990. Introduction to polymer dynamics. Cambridge University Press, New York.
- El-Hamouz, A.M., Stewart, A.C., 1996. On-line drop size distribution measurements of oil-water dispersions using a Par tec M300 laser backscatter instrument. Proceedings of. SPE annual technical conf. and exhibition, SPE 36672, 785-796.
- Elseth, G., 2001. An experimental study of oil-water flow in horizontal pipes, PhD. Thesis, Telemark University College, Norway.
- Fan, Z., Lusseyran, F., Hanratty, T.J., 1993. Initiation of slugs in horizontal gas-liquid flows. AIChE J., 39, 1741-1753.
- Fairuzov, Y. V., Arenas-Medina, P., Verdejo-Fierro, J. and Gonzalez-Islas, R., 2000. Flow pattern transitions in horizontal pipelines carrying oil-water mixtures: full-scale experiments. J Energy Resources Technology. 122, 169-176.
- Fortuna, G., Hanratty, T.J., 1971. Use of electrochemical techniques to study the effect of drag reducing polymers on flow in the viscous sublayer. AIChE Symp. Series, 67, 90-97.
- Greskovich, E.J., Shrier, A.L., 1971. Pressure drop and hold up in horizontal slug flow. AIChE J, 17, 1214-1219.

- Guzhov, A. I., Grishan, A. L., Medredev, V. F., Medredeva, O. P., 1973. Emulsion formation during the flow of two immiscible liquids in a pipe. Neft Khoz. 8, 58-61 (in Russian).
- Guzhov, A. I., and Medvedev, O. P., 1971. Pressure losses in flow of two mutually immiscible liquids, Int. Chem. Eng. 11, 104-106.
- Gyr, A., Bewersdorff, H.-W., 1995. Drag reduction of turbulent flows by additives. Kluwer Academic publishers, Dordrecht.
- Haheim, S. A., 2001. Oil-water slip in inclined pipes and application to downhole separation. Proc. 10th Int. Conf. Multiphase, Cannes, France.
- Hay, K. J., Liu, Z. C. Hanratty, T. J., 1996. Relation of deposition to drop size when the rate law is nonlinear. Int. J. Multiphase Flow 22, 829-848.
- Hewitt, G., Hall-Taylor, N., 1970. Annular two-phase flow. Pergamon Press, New York.
- Hewitt, G. and Govan, D., 1990. Phenomenological modeling of non-equlibrium flows with phase change. Int. J. Heat and Mass Transfer, 33, 229-241.
- Hewitt, G. and Pulling, D., 1969. Liquid entrainment in adiabatic steam-water flow. AERE-R-5374, Harwell, England.
- Hinze, J. O., 1955. Fundamentals of the hydrodynamic mechanism of splitting in dispersion processes, AIChE J., 1, 289-295.
- Holowach, M.J., Hochreiter, L.E., Cheung, F.B., 2002. A model for droplet entrainment in heated annular flow. Int. J. Heat & Fluid Flow 23, 807-822.
- Hoyt, J., 1986. Drag Reduction, in Encyclopedia of Polymer Science and Engineering, 5, 2nd ed. Wiley, New York.
- Hu, B., 2006. Experiemntal and theoretical investigation of phase inversion in liquid-liquid dispersions, PhD. Thesis. University College London, University of London.
- Hu, B., Angeli, P., Matar, O.K., Lawrence, C.J., Hewitt, G.F., 2006. Evaluation of drop size distribution from chord length measurements. AIChE J., 52, 931-939.
- Hughmark, G.A., 1971. Drop breakup in turbulent pipe flow, AIChE J., 17, 1000.
- Hussain, A., 2004. Experimental and computational studies of liquid-liquid dispersed flows, PhD. Thesis, Imperial College, University of London.

- Hutchinson, P., Whalley, P.B., 1973. A possible characterization of entrainment in annular flow. Chem. Engineering Sci. 28, 974-975.
- Hutchinson, P., Hewitt, G.F., and Dukler, A.E., 1971. Deposition of liquid or solid dispersions flow turbulent gas streams: a stochastic model, Chem. Eng. Sci., 26, 419-439.
- Ishii, M., Grolmes, M., 1975. Inception criteria for droplet entrainment in two-phase concurrent film flow. AICHE Journal 21 (2).
- Ishii, M., Mishima, K., 1989. Droplet entrainment correlation in annular two-phase flow. Int. J. Heat & Mass Transfer 32, 1835-1846.
- Jurman, Bruno, K., McCready, M.J., 1989. Periodic and solitary waves of thin horizontal, gas-sheared liquid films. Int. J. Multiphase Flow 15, 371-384..
- Kataoka, I., Ishii, M., Mishima, K., 1983. Generation and size distribution of droplet in annular two-phase flow. . J. Fluids Eng. 105, 230-238.
- Kataoka, I., Ishii, M., 1982. Mechanism and correlation of droplet entrainment and deposition in annular two-phase flow. NUREG/CR-2885, ANL-82-44.
- Kataoka, I., Ishii, M., Nakayama, A., 2000. Entrainment and deposition rates of droplets in annular two-phase flow. Int. J. Heat & Mass Transfer 43, 1573-1589.
- Keeys, R., Ralph, J., and Roberts, D., 1970. Liquid entrainment in adiabatic steam-water flow at 500 and 1000 psia. AERE-R-6293, Harwell, England.
- Karabelas, A.J., 1978. Droplet size spectra generated in turbulent pipe flow of dilute liquid-liquid dispersions. AIChE J., 24, 170-180.
- Kolmogorov, AN., 1949. On the breaking of drops in turbulent pipe flow of dilute liquid-liquid dispersions, AIChE J., 24, 170-180.
- Kubie, J., and Gardner, G.C., 1977. Drop sizes and drop dispersion in straight horizontal tubes and helical coils, Chem. Eng. Sci., 32, 195-202.
- Laflin, G. C., and Oglesby, K. D., 1976. An experimental study on the effects of flow rate, water fraction and gas-liquid ratio on air-oil-water flow in horizontal pipes, B.S. Thesis. The University of Tulsa.
- Langston, P.A., Burbidge, A.S., Jones, T.F., Simmons, M.J., 2001. Particle and droplet size analysis from chord measurements using Bayes' theorem. Powder Technology 116, 33-42.
- Lin, P. Y., Hanratty, T. J., 1986. Prediction of the initiation of slugs with linear stability theory. Int. J. Multiphase flow. 20, 79-98.

- Lopez de Bertodano, M., Assad, A. and Beus, S., 2001. Experiments for entrainment rate of droplets in the annular regime. Int. J. Multiphase Flow 27, 685-699.
- Lovick, J., 2004, Horizontal oil-water flows in the dual continuous flow regime, PhD. Thesis. University College London, University of London.
- Lovick, J., and Angeli, P., 2001. Two-phase liquid flow at the partially dispersed flow regime. Proc. 4th Int. Conference on Multiphase Flow. New Orleans, USA.
- Lovick, J., and Angeli, P., 2004a. Experimental studies on the dual continuous flow pattern in oil-water flows. Int. J. Multiphase flow. 30, 139-157.
- Luchik, T. S., Tiederman, W. G., 1988. Turbulent structure in low-concentration drag-reducing channel flows. J. Fluid Mech., 198, 241-263.
- Lum, J., 2002. Inclined oil-water flow in the dual continuous flow regime, MPhil Thesis. University College London.
- Lum, J.Y.-L., Lovick, J., Angeli, P., 2004. Low inclination oil-water flows. Canad. J. Chem. Eng. 82, 303-315.
- Lum, J.Y.-L., Al-Wahaibi, T., Angeli, P., 2006. Upward and downward inclination oil-water flows. Int. J. Multiphase flow. 32, 413-435.
- Lumley, J.L., 1969. Drag reduction by additives. Annual Review of Fluid Mechanics, 1, 367-384.
- Malinowsky, M. S., 1975. An experimental study oil water and air-water flowing mixtures in horizontal pipes. MS thesis, The University of Tulsa.
- Manfield, C. J., Lawrence, C., Hewitt, G., 1999. Drag-reduction with additive in multiphase flow: A literature survey. Multiphase Sci. Tech., 11, 197-221.
- Manolis, I. G., 1996. High pressure gas-liquid slug flow. PhD thesis, Imperial College, University of London.
- Massey, B. S., 1989. Mechanics of fluids, 6th edition, Chapman and Hall.
- McCoy, D. D. and Hanratty, T. J., 1977. Rate of deposition of droplets in annular two-phase flow. Int. J. Multiphase Flow 3, 319-331.
- Mishima, K., Ishii, M., 1980. Theoretical prediction of onset of horizontal slug flow. J. Fluids Eng. 102, 441-445.

- Mowla, D., Naderi, A., 2006. Experimental study of drag reduction by a polymeric additive in slug two-phase flow of crude oil and air in horizontal pipes. Chem. Eng. Sci., 61, 1549-1554.
- Nadler, M. and Mewes, D., 1997. Flow induced emulsification in the flow of two immiscible liquids in horizontal pipes, Int. J. Multiphase flow. 23(1), 55-68.
- Nigmatulin, R. I., 1991. Dynamics of multiphase media, vol. 2. Hemisphere, New York.
- Ng, T. S., 2002. Interfacial structure of stratified pipe flow. Ph.D Thesis. Imperial College, University of London.
- Ng, T. S., Lawrence, C. J., Hewitt, G. F., 2004. Evolution of interfacial structures in wavy stratified two-phase pipe flow. 5th Int. Conf. on Multiphase Flow, Yokohama, Japan, paper no. 389.
- Oglesby, K. D., 1979, An experimental study on the effects of oil viscosity, mixture velocity, and water fractions on horizontal oil-water flow, MS Thesis. The University of Tulsa.
- Oliemans, R. V.A., 1986. The lubricating-film model for core-annular flow, PhD thesis, Delft University, The Netherlands.
- Oliver D. R., Young Hoon A., 1968. Two-phase non-newtonian flow. Trans. Instn. Chem. Engrs., 46, T106.
- Otten, L., Fayed, A.S., 1976. Pressure drop and drag reduction in two phase non-Newtonian slug flow. Can. J. Chem. Eng., 54, 111-114.
- Ousaka, A., Kariyasaki, A., 1992, Distribution of entrainment flow rate for air-water annular two-phase flow in a horizontal tube. JSME International Journal. 35 (3), 354-360.
- Pacek, A.W., Man, C.C. and Nienow, A.W., 1998. On the Sauter mean diameter and size distributions in turbulent liquid-liquid dispersions in a stirred vessel. Chem. Eng. Sci., 53, 2005-2011.
- Paleev, I. I. and Filippovich, 1966. Phenomena of liquid transfer in two-phase dispersed annular flow, Int. J. Heat Mass Transfer. 9, 1089.
- Pan, L. and Hanratty, T, J., 2002a. Correlation of entrainment for annular flow in vertical pipes. Int. J. Multiphase Flow 28, 363-384.
- Pan, L. and Hanratty, T, J., 2002b. Correlation of entrainment for annular flow in horizontal pipes. Int. J. Multiphase Flow 28, 385-408.

- Raj, T.S., Chakrabarti, D.P., Das, G., 2005. Liquid-liquid stratified flow through horizontal conduits. Chem. Eng. Technol., 28, 899-907.
- Rosehart, R.G., Scott, D., Rhodes, E., 1972. Gas-liquid slug flow with drag reducing polymer solutions. AIChE J, 18, 744-750.
- Saether, G., Kubberud, K., Nuland, S., Lingelem, M.N., 1989. Drag reduction in two phase flow. Proc. 4th Int. Conf. on Multiphase Flow, 171-184.
- Schadel, S. A. and Hanratty, T. J., 1989. Interpretation of atomization rates of the liquid film in gas liquid annular flow. Int. J. Multiphase flow. 15, 893-900.
- Schadel, S. A., Leman, G. W., Binder, J. L. and Hanratty, T. J., 1990. Rates of atomization and deposition in vertical annular flow. Int. J. Multiphase flow. 16, 363-374.
- Scott, G. M., 1985, A study of two-phase liquid-liquid flow at variable inclinations, M.S. Thesis. University of Texas at Austin.
- Shinnar R., 1961. On the behaviour of liquid dispersions in mixing vessels, J. Fluid Mech., 10, 259-275.
- Simmons, M.J., Langston, P.A., Burbidge, A.S., 1999. Particle and droplet size analysis from chord distributions. Powder Technology 102, 75-83.
- Simmons, M.J., Azzopardi, B.J., 2001. Drop size distribution in dispersed liquid-liquid pipe flow. Int. J. Multiphase flow. 27, 843-859.
- Simmons, M.J., Zaidi, S.H., and Azzopardi, B.J., 2000. Comparison of laser-base drop size measurement techniques and their application to dispersed liquid-liquid pipe flow. Opt. Eng., 32, 505-509.
- Sleicher, CA. Jr., 1982. Maximum stable drop size in turbulent flow, AIChE J., 8, 471-477.
- Srichai, S., 1994. High pressure separated two-phase flow. PhD thesis, Imperial College, University of London.
- Soleimani, A., 1999. Phase Distribution and Associated Phenomena in Oil-Water Flows in Horizontal Tubes, PhD. Thesis, Imperial College, University of London.
- Soleimani, A., Al-Sarkhi, A., Hanratty, T. J., 2002. Effect of drag reducing polymers on pseudo-slugs-interfacial drag and transition to slug flow. Int. J. Multiphase Flow., 28, 1911-1927.

- Sprow F.B., 1967. Distribution of drop sizes produced in turbulent liquid-liquid dispersions. Chem. Eng. Sci., 22, 435-442.
- Su, H.T., and Hanzevack, E.L., 1998. A model of drop size distribution and maximum drop size in two phase liquid-liquid flow, AIChE Annual Meeting Washington DC.
- Sylvester, N.D., Brill, J.P., 1976. Drag reduction in two-phase annular mist flow of air and water. AIChE J, 22, 615-617.
- Taitel, Y., Dukler, A. E., 1976. A model for predicting flow regime transitions in horizontal and near horizontal gas-liquid flow. AIChE J. 22, 47-55.
- Tennekes H., and Lumley JL., 1972. A first course in turbulence, The MIT Press, Cambridge, Mass.
- Thomas RM., 1981. Bubble coalescence in turbulent flows, Int. J. Multiphase Flow, 7, 709-717.
- Thwaites, G.R., Kulov, N.N., Nedderman, N.M., 1976. Liquid film properties in two phase annular flow. Chem. Eng. Sci., 31, 481
- Trallero, J. L., 1995, Oil-water flow patterns in horizontal pipes, PhD. Thesis. University of Tulsa.
- Toms, B.A., 1948. Some observations on the flow of linear polymer solutions through straight tubes at large Reynolds numbers. Proc. 1st Inter. Congress in Reheology, North Holland publication company, Amsterdam, 135-141.
- Tsouris, C., Tavlarides, L.L., 1994. Breakage and coalescence models for drops in turbulent dispersions. AIChE J, 40, 395-406.
- Valentas K.J., Bilous O., and Amundson NR., 1966. Breakage and coalescence in dispersed phase systems, Ind. Eng. Chem. Fundamentals, 5, 533-542.
- Valle. A., 2000. Three phase gas-oil-water pipe flow. PhD Thesis. Imperial College.
- Valle, A. and Kvandal, H., 1995, Pressure drop and dispersions characteristics of separated oil-water flow. Proc. Int. Symp. On Two-Phase Flow Modelling and Experimentation. Rome, Italy. 583-591.
- Vedapuri, D., Bessette, D. and Jepson, W. P., 1997. A segregated flow model to predict water layer thickness in oil-water flows in horizontal and slightly inclined pipelines. Proc. Multiphase'97, Cannes, France. 75-105.

- Wallis, G.B., 1969. One dimensional Two-Phase Flow. McGraw-Hill, New York.
- Ward JP., and Knudsen, JG., 1967. Turbulent flow of unstable liquid-liquid dispersions: drop sizes and velocity distributions, AIChE J., 13, 356-365.
- Warholic, M.D., Massah, H., Hanratty, T.J., 1999. Influence of drag reducing polymers on turbulence: effects of Reynolds number, concentration and mixing. Exp in Fluid, 27, 461-472.
- Wei, T., Willmarth, W.W., 1992. Modifying turbulence structure with drag reducing polymer additives in turbulent channel flows. J. Fluid. Mech., 245, 619-641.
- Wicks, M. and Dukler, A. E., 1960. Entrainment and pressure drop in concurrent gas-liquid flow. AIChE J. 6, 463-468.
- Williams, L.R., Dykhno, L. A. and Hanratty, T. J., 1996. Droplet flux distributions and entrainment in horizontal gas-liquid flows. Int. J. Mutiphase Flow 22, 1-18.
- Woodmansee, D. E. and Hanratty, T. J., 1969. Mechanism for the removal of droplets from a liquid surface by a parallel air flow. Chem. Eng. Sci. 24, 299-307.

Nomenclature

Symbols	Description
Roman letters	
a	Wave amplitude
A	Cross section area of the pipe
A_{cv}	Area of the control volume
A_o	Cross section area of the oil above the smooth interface
A_{o1}	Cross section area of the oil above the peak of the sinusoidal wave
A_{o2}	Cross section area of the oil above the trough of the sinusoidal wave
A_w	Cross section area of the water below the smooth interface
A_{w1}	Cross section area of the water below the peak of the sinusoidal wave
A_{w2}	Cross section area of the water below the trough of the sinusoidal wave
A_{oil_wave}	Cross section area of the trough of the wave (oil wave)
A_{water_wave}	Cross section area of the peak of the wave (water wave)
$A(h_o)$	Function of film thickness in Eq. (2.65)
C_1	Constant in Eq. (2.43)
C_1	Constant in Eq. (2.51)
C_2	Constant in Eq. (2.55)
C_3	Constant in Eq. (2.66)
C_B	Bulk concentration
C_d	Drag coefficient
C_D	Concentration of droplets in the unit of mass per unit volume
C_{Do}	Concentration of oil droplets in the lower water phase
C_{Dw}	Concentration of water droplets in the upper oil phase
C_e	Equilibrium concentration
C_F	Concentration of the salt in the film
C_H	Tunable constant in Eq. 2.63

C_{MC}		Mixing cup concentration
C_s		Sheltering coefficient
C_{iv}		Critical wave velocity
C_v		Wave velocity
C_w		Concentration at the wall
d		Diameter of a drop
d_{init}	I	Initial drop diameter
d_{max}	I	Maximum drop diameter
d_{min}		Minimum diameter for which separation of drops after collision is still possible
d_{10}	I	Linear mean drop diameter
d_{32}	I	Sauter mean drop diameter
d^*		Drop diameter corresponding to $V_{cum} = 0.3679$
D		Pipe diameter
D_i		Equivalent phase hydraulic diameters
D_{Lf}		Hydraulic diameter of the film
DC		Dual continuous
Do/w		Dispersed oil-in-water
Dw/o		Dispersed water-in -oil
$\left(\frac{dp}{dz}\right)_g$		Pressure gradient for the gas phase
$\left(\frac{dp}{dz}\right)_{Lf}$		Pressure gradient for the liquid film
E		Entrainment fraction
E_a		Adhesion energy for two drops of equal diameter
E_{ci}		In-situ phase fraction of continuous phase i
E_{di}		In-situ phase fraction of dispersed phase i
E_M		Maximum entrainment fraction
$E_{o/w}$		Entrainment of oil in water
E_{th}		Theoretical entrainment limit if all the excess liquid was entrained
$E_{w/o}$		Entrainment of water in oil

f	Friction factor for flow over smooth wall
$f(h)$	Attraction force per square centimetre between two infinite parallel plates surfaces separated by distance h
F	Force pressing the drops together (Eq. 2.67)
F_g	Gravity force acting on an individual drop
F_d	Drag force acting on a wave crest
F_D	Drag force acting on an individual drop
F_T	Net driving force acting on an individual drop due to turbulent fluctuation
F_σ	Surface tension resists the wave deformation
g	Acceleration due to gravity
h_g	Thickness of the gas phase
h_{gl}	Thickness of the gas phase up to the peak of the liquid wave
h_L	Thickness of the liquid phase
h_{L1}	Thickness of the liquid phase including the peak of the wave
h_o	Thickness of the oil phase
h_w	Thickness of the water phase
j_L	Total liquid volumetric flux (superficial velocity), m/s
j_{Lf}	Liquid film volumetric flux, m/s
j_g	Gas volumetric flux (superficial velocity), m/s
J_η	Viscous term in Eq. 2.6
J_u	Velocity term in Eq. 2.6
J_g	Gravity term in Eq. 2.6
J_σ	Surface tension term in Eq. 2.6
J_s	Sheltering effect term in Eq. 2.6
h_{cr}	Critical distance between the drop and the interface
H_L	Liquid hold-up
H_o	Oil hold-up

H_w		Water hold-up
k		Mass transfer coefficient
k		Wave number
k_A		Atomization rate constant
k_D		Deposition rate constant
k_{Do}		Oil deposition rate constant
$k_{Do-corr}$		Corrected oil deposition rate constant
k_{Dw}		Water deposition rate constant
$k_{Dw-corr}$		Corrected water deposition rate constant
l		Length scale
l_e		Length scale of the energy containing the eddies
l_k		Kolmogoroff length scale
L_{max}		Maximum chord length
L_{10}	I	Linear mean chord length
L_{32}	I	Sauter mean chord length
K		Bernoulli constant
K		von Karman constant
m		interfacial mobility parameter
m		Average film height around the pipe circumference
n_d		Number of drops at the interface
N_μ		Viscosity number
N_{vi}		Viscosity group
$N_{w,cv}$		Number of waves in the control volume
P		Pressure above the smooth interface
P_1		Pressure above the peak of the wave
P_{o1}		Pressure above the peak of the sinusoidal wave
P_{o2}		Pressure above the trough of the sinusoidal wave
P_{w1}		Pressure below the peak of the sinusoidal wave
P_{w2}		Pressure below the trough of the sinusoidal wave
Q_g		Volumetric flow of the gas
Q_L		Flow rate of the lower layer

Q_u	Flow rate of the upper layer
R	Interface principal radius of curvature
R_A	Rate of entrainment
R_{Ao}	Rate of entrainment of oil
R_{Aw}	Rate of entrainment of water
R_D	Rate of deposition
R_{Do}	Rate of deposition of oil
R_{Dw}	Rate of deposition of water
Re_L	Total Liquid film Reynolds number
Re_{Lf}	Liquid film Reynolds number
Re_{Lfc}	Critical liquid film Reynolds number
S	Ratio of drop velocity to gas velocity.
S_i	Wetted perimeter of the interface
S_o	Wetted perimeter of the oil
S_w	Wetted perimeter of the water
SM	Stratified mixed flow
SS	Stratified smooth
ST	Stratified flow
SW	Stratified wavy
$u_f^{'}$	Fluctuating turbulent velocity
U_c	Average axial velocity of the continuous phase
U_d	Drop velocity
U_i	Equivalent phase hydraulic diameters
U_{Lf}	Liquid film velocity
U_{sco}	Superficial velocity when oil is the continuous phase
U_{sco}	Superficial velocity when water is the continuous phase
U_{sd}	Dispersed phase superficial velocity
U_{sg}	Superficial gas velocity
U_g	In-situ gas velocity above the smooth interface

U_{gc}	Gas core velocity
U_{g1}	In-situ gas velocity above the peak of the wave
U_{sL}	Superficial liquid velocity
U_{so}	Superficial oil velocity
U_{o}	In-situ oil velocity above the smooth interface
U_{o1}	In-situ oil velocity above the peak of the sinusoidal wave
U_{o2}	In-situ oil velocity above the trough of the sinusoidal wave
U_{sw}	Superficial water velocity
U_{w}	In-situ water velocity below the smooth interface
U_{w1}	In-situ water velocity below the peak of the sinusoidal wave
U_{w2}	In-situ water velocity below the trough of the sinusoidal wave
V_{cum}	Cumulative volume fraction
ν_{c}	Kinematic viscosity of the continuous phase
ν_{d}	Initial drop velocity normal to the interface
v_{df}	Final velocity for a drop in the oil-water interface
$\langle v'^{2} \rangle$	Mean of the square of the velocity fluctuation v'
VKH	Viscous Kelvin-Helmholtz
IKH	Inviscid Kelvin-Helmholtz
$V_{entr,w}$	Volume of liquid entrained from the wave
Δv	Velocity difference across the drop
We	Weber number
We_{c}	Critical Weber number
We_{crit}	Critical Weber number that gives the maximum drop size (Eq. 2.51)
We_{g}	Gas Weber number
W_{oc}	Mass flow rate of the when oil is the continuous phase
W_{wc}	Mass flow rate of the when water is the continuous phase
W_{L}	Total liquid mass flow rate.
W_{Le}	Droplets mass flow rate
W_{Lf}	Liquid film mass flow rate

W_{Lfc}	Critical liquid film mass flow rate
W_{od}	Mass flow rate of the oil drops
W_{wd}	Mass flow rate of the water drops
ZRC	Zero real characteristics
ZNC	Zero neutral stability

Greek symbols

δ	Film thickness
δ	Parameter of the log normal distribution (Eq. 2.71) which affects the distribution height
ε	Rate of energy dissipation per unit mass
ε_l	Local energy dissipation per unit mass
ε_M	Mean energy rate per unit mass
ζ	Parameter of the log normal distribution (Eq. 2.71) which affects the distribution width
λ	Wavelength
μ_i	Phase viscosity
μ_c	Continuous phase viscosity
μ_d	Dispersed phase viscosity
μ_g	Gas viscosity
μ_{Lf}	Liquid film viscosity
μ_o	Oil viscosity
μ_w	Water viscosity
ρ	Total density
ρ_c	Continuous phase density
ρ_d	Dispersed phase or drop density
ρ_{Lf}	Liquid film density
ρ_g	Gas density
ρ_{gc}	Gas core density in annular flow
ρ_i	Phase density

ρ_L	Liquid density
ρ_o	Oil density
ρ_w	Water density
$\Delta\rho$	Density difference
σ	Oil-water interfacial tension
σ	Surface tension
τ	Viscous stress or dynamic pressure force in Eq. (2.48)
$\tau_{w,cv}$	Period of the entrainment phenomena in the control volume
τ_i	Interfacial shear stress
τ_o	Wall shear stress in the oil phase
τ_w	Wall shear stress in the water phase
ϕ	Velocity potential
φ	Parameter of the log normal distribution (Eq. 2.71)

Subscripts

g	Gas Phase
i	Phase i in the pipe
L	Liquid Phase
o	Oil Phase
s	Superficial
w	Water Phase

Appendix A

Program for Predicting the Transition between Stable and Unstable Waves

The program was written to process the stability equation (Eq. 5.19) developed to predict the wave amplitude required to destabilize the wave at certain wavelength. A program was also written for the two-fluid model and wave velocity calculation.

A.1 Stability Equation Eq. (5.19)

```
% Program to solve the stability equation (Eq. 5.19 in chapter 5)
% prediction of wave amplitudes required to destabilize waves with certain wavelength

% Fluid properties (Input the properties)
% density of oil (denso), density of water (densw)
denso=828; densw=1000;
% viscosity of oil (viso), viscosity of water (visw)
viso=5.5*0.001; visw=1.0*0.001;
% gravity (g), surface tension (ST), diameter (D)
g=9.81; ST=40*.001; D=0.038;

% Input the oil and water superficial velocities
Uso=0.1;Usw=0.25

% Defining the transition to turbulent (Reynolds Number)
ReNu=2000;

% Calculate the cross sectional area of the pipe (A)
A=pi*D^2/4;
```

% Height of the water interface from the two-fluid model assuming stratified smooth (see two-fluid model calculation)

```
hwnew = two_fluid(Usw, ReNu, Uso, denso, densw, g, ST, D, viso, visw)
H=2*(hwnew/D)-1;
Si=D*((1-H^2)^(1/2));
So=D*acos(H);
Sw=(D*pi-So);
A=pi*D^2/4;
Ao=D*((So)-(Si*H))/4;
Aw=A-Ao;
Hw=Aw/A;
Ho=Ao/A;
denst=densw/Hw+denso/Ho;
Uw=Usw/Hw;
Uo=Uso/Ho;
```

% wave velocity calculation (see wave velocity calculation)

```
Cv = wave_velocity(Hw,hwnew, Usw, ReNu, Uso, denso, densw, g, ST, D, viso, visw)
```

% prediction of wave amplitudes required to destabilize waves at certain wavelength

```
output = [i i];
```

% Wavelength (lamda)

```
lamda=0.0;

for j=1:100
 if lamda <= 5*D
    lamda=lamda+.1*D;
 else
    lamda=lamda+1*D
end
```

```
% amplitude (a)
a=0.00;

k=(D-hwnew)/0.0001;
% finding amplitude (a) at each wavelength (lamda)
for m=1:k
   a=a+0.0001;
   % parameters with the peak
   Hapeak=2*((hwnew+a)/D)-1;
   Soapeak=D*acos(Hapeak);
   Siapeak=D*((1-Hapeak^2)^(1/2));
   Aoapeak=D*((Soapeak)-(Siapeak*Hapeak))/4;
   Awapeak=A-Aoapeak;

   % parameters with the trough
   Hatrough=2*((hwnew-a)/D)-1;
   Siatrough=D*((1-Hatrough^2)^(1/2));
   Soatrough=D*acos(Hatrough);
   Aoatrough=D*((Soatrough)-(Siatrough*Hatrough))/4;
   Awatrough=A-Aoatrough;

   % see chapter 5 for the definition of Aw1, Aw2, Ao1, Ao2
   Aw1=Awapeak;
   Aw2=Awatrough;
   Ao1=Aoapeak;
   Ao2=Aoatrough;

   % Stability equation (Eq. 5.19)
   Term1=0.5*densw*((Uw-Cv)^2*((Aw/Aw2)^2-(Aw/Aw1)^2));
   Term2=0.5*denso*((Uo-Cv)^2*((Ao/Ao1)^2-(Ao/Ao2)^2));
   Term3=2*g*a*(densw-denso);
   Term4=2*(4*pi^2*a/lamda^2)*ST;
   Total=Term1+Term2-Term3-Term4;
   if Total >=0
```

```
      break
    end
end
output=[output;lamda a];
end

% writing the output file
wk1write('output',output)
```

A.2 Two-Fluid model

A.2.1 Main Program

```
% Two-fluid model calculation;
% finding the height of the water interface
% Function to calculate height of the water interface and return it to the stability
model file
function hwnew = two_fluid(Usw, ReNu, Uso, denso, densw, g, ST, D, viso, visw)

% Calculate the cross sectional area of the pipe (A)
A=pi*D^2/4;

% Defining epsilon
E1=0.0;

% Defining the minimum and maximum height of water interface
hwmin=0.00001; hwmax=0.0379;

% check the validity of the initial point
if hwmin==hwmax
   'error1'
   break
end
```

```
% check the validity of epsilon
if E1 < 0.0
   'error2'
   break
end

% F is the two-fluid model at equilibrium
% calculate the min F
hwinput=hwmin
Fhw = hwF(hwinput, Usw, ReNu, Uso, denso, densw, g, ST, D, viso, visw);
Fmin=Fhw;
% ************************************************************

% calculate the max F
hwinput=hwmax
Fhw = hwF(hwinput, Usw, ReNu, Uso, denso, densw, g, ST, D, viso, visw);
Fmax=Fhw;
% ************************************************************
if Fmin>Fmax
hw_1=hwmin;
Fmin_1=Fmin;
hwmin=hwmax;
Fmin=Fmax;
hwmax=hw_1;
Fmax=Fmin_1;
end

for k=1:1000
   if Fmin==Fmax
      'error3'
      root=hwmax;
      break
   end
```

```
hwnew=hwmin-Fmin*(hwmax-hwmin)/(Fmax-Fmin);


H=2*(hwnew/D)-1;
Si=D*((1-H^2)^(1/2));
So=D*acos(H);
Sw=(D*pi-So);
A=pi*D^2/4;
Ao=D*((So)-(Si*H))/4;
Aw=A-Ao;
Hw=Aw/A;
Ho=Ao/A;
denst=densw/Hw+denso/Ho;
Uw=Usw/Hw;
Uo=Uso/Ho;
% **********************************************************************
% calculate the new F
hwinput=hwnew;
Fhw = hwF(hwinput, Usw, ReNu, Uso, denso, densw, g, ST, D, viso, visw);
Fnew=Fhw;
% **********************************************************************


   if abs(Fnew)<=abs(E1)
      error = 0
      root = hwnew;
       i;
      break
   end


% update the points
hwmin=hwmax;
Fmin=Fmax;
hwmax=hwnew;
```

```
Fmax=Fnew;
end

H=2*(hwnew/D)-1;
Si=D*((1-H^2)^(1/2));
So=D*acos(H);
Sw=(D*pi-So);
A=pi*D^2/4;
Ao=D*((So)-(Si*H))/4;
Aw=A-Ao;
Hw=Aw/A;
Ho=Ao/A;
denst=densw/Hw+denso/Ho;
Uw=Usw/Hw;
Uo=Uso/Ho;
```

A.2.2 Calculating the two-fluid model at equilibrium (F)

```
% Calculating the F equation (F is the two-fluid model at equilibrium)
% Function to calculate F and return to the two-fluid model file
function Fhw = hwF(hwinput, Usw, ReNu, Uso, denso, densw, g, ST, D, viso, visw)

hw=hwinput;
Uso=Uso;
Usw=Usw;
H=2*(hw/D)-1;
Si=D*((1-H^2)^(1/2));
So=D*acos(H);
Sw=(D*pi-So);
A=pi*D^2/4;
Ao=D*((So)-(Si*H))/4;
Aw=A-Ao;
Hw=Aw/A;
Ho=Ao/A;
denst=densw/Hw+denso/Ho;
```

```
Uw=Usw/Hw;
Uo=Uso/Ho;

if Uo/Uw >=0.98 & Uo/Uw <1.05
  Dw=4*Aw/(Sw); Do=4*Ao/(So);
elseif Uo > Uw
  Dw=4*Aw/(Sw); Do=4*Ao/(So+Si);
else
  Dw=4*Aw/(Sw+Si); Do=4*Ao/So;
end

% calculating Reynolds number of water
Rew=Dw*Uw*densw/visw;
if Rew <= ReNu
  Cw=16; m=1;
  else
  Cw=0.046; m=0.2;
end

% calculating Reynolds number of oil
Reo=Do*Uo*denso/viso;
if Reo <= ReNu
  Co=16; n=1;
  else
  Co=0.046; n=0.2;
end

% calculating Reynolds number of interface
if Uo > Uw
  Rei=Si*Uo*denso/(pi*viso); densf=denso;
  else
  Rei=Si*Uw*densw/(pi*visw); densf=densw;
end
```

```
if Rei <= ReNu
   Ci=16; p=1;
   else
   Ci=0.046; p=0.2;
end

% calculation of the friction factors
fi=Ci*Rei^-p;
fw=Cw*Rew^-m;
fo=Co*Reo^-n;

% calculation of oil and water wall and interfacial shear stress
Tw=fw*densw*Uw*abs(Uw)/2;
To=fo*denso*Uo*abs(Uo)/2;
if Uo/Uw >=0.98 & Uo/Uw <1.05
   Ti=0
else
Ti=fi*densf*(Uo-Uw)*abs(Uo-Uw)/2;
end

% calculating the two fluid model
Fhw=To*So/Ao+Ti*Si*(1/Aw+1/Ao)-Tw*Sw/Aw;
```

A.3 Wave velocity

A.3.1 Main Program

% Calculating wave velocity (Cv is the continuity wave velocity)

% Function to calculate Cv and return to the stability model file

function Cv = wave_velocity(Hw, hwnew,Usw, ReNu, Uso, denso, densw, g, ST, D, viso, visw)

% calculating the continuity wave velocity

% ----------

% Calculating dfHw (derivative of F with respect to water hold-up, Hw)

% ----------

Hwinput=Hw+0.001*Hw;

Hwinput=Hwinput;

FHw= HF(Hwinput, hwnew, Usw, ReNu, Uso, denso, densw, g, ST, D, viso, visw);

F3=FHw;

Hwinput=Hw-0.001*Hw;

FHw= HF(Hwinput, hwnew, Usw, ReNu, Uso, denso, densw, g, ST, D, viso, visw);

F33=FHw;

dfHw=(F3-F33)/(2*0.001*Hw);

% ----------

% Calculating dfUso2 (derivative of F with respect to superficial oil velocity, Uso)

% ----------

Uso1=Uso+0.001*Uso;

Usoinput=Uso1;

Uswinput=Usw;

FdfUs= dfUs(hwnew, Uswinput, ReNu, Usoinput, denso, densw, g, ST, D, viso, visw);

F2=FdfUs;

Uso1=Uso-0.001*Uso;

Usoinput=Uso1;

Uswinput=Usw;

FdfUs= dfUs(hwnew, Uswinput, ReNu, Usoinput, denso, densw, g, ST, D, viso, visw);

F22=FdfUs;

dfUso=(F2-F22)/(2*0.001*Uso);

```
% -----------------
% Calculating dfUsw1 (derivative of F with respect to superficial water velocity, Usw)
% -----------------
Usw1=Usw+0.001*Usw;
Usoinput=Uso;
Uswinput=Usw1;
FdfUs= dfUs(hwnew, Uswinput, ReNu, Usoinput, denso, densw, g, ST, D, viso, visw);
F1=FdfUs;


Usw1=Usw-0.001*Usw;
Usoinput=Uso;
Uswinput=Usw1;
FdfUs= dfUs(hwnew, Uswinput, ReNu, Usoinput, denso, densw, g, ST, D, viso, visw);
F11=FdfUs;
dfUsw=(F1-F11)/(2*0.001*Usw);

% .....
% wave velocity calculation
v=dfHw/(dfUso-dfUsw);
```

A.3.2 Change in F with respect to water hold-up Hw

```
% Calculating derivative of F with respect to water hold-up , Hw (either oil or water)
% Function to calculate F with respect to a change in water hold-up and return it to the wave velocity file
function FHw= dfHw(Hwinput, hwnew, Usw, ReNu, Uso, denso, densw, g, ST, D, viso, visw)


hw=hwnew;
Uso=Uso;
Usw=Usw;
Hw=Hwinput;
```

```
% check the validity of the initial point
hwmin=0.00001; hwmax=0.0379;E1=0.0000;
if hwmin==hwmax
   'error1'
   break
end
% check the validity of epsilon
if E1 < 0.0
   'error2'
   break
end
% .....
% calculate the min F
% .....
Hmin=2*(hwmin/D)-1;
Simin=D*((1-Hmin^2)^(1/2));
Somin=D*acos(Hmin);
Swmin=(D*pi-Somin);
A=pi*D^2/4;
Aomin=D*((Somin)-(Simin*Hmin))/4;
Awmin=A-Aomin;
Hwmin=Awmin/A;
Homin=Aomin/A;
Fmin=Hwmin-Hw;
% Finish calculating F min
% .....
% calculate the max F
% .....
Hmax=2*(hwmax/D)-1;
Simax=D*((1-Hmax^2)^(1/2));
Somax=D*acos(Hmax);
Swmax=(D*pi-Somax);
```

```
A=pi*D^2/4;
Aomax=D*((Somax)-(Simax*Hmax))/4;
Awmax=A-Aomax;
Hwmax=Awmax/A;
Homax=Aomax/A;
Fmax=Hwmax-Hw;
% Finish calculating F max

if abs(Fmin)<abs(Fmax)
hw_1=hwmin;
Fmin_1=Fmin;
hwmin=hwmax;
Fmin=Fmax;
hwmax=hw_1;
Fmax=Fmin_1;
end

for k=1:1000
   if Fmin==Fmax
      'error3'
      root=hwmax
      break
   end

   hwnew=hwmin-Fmin*(hwmax-hwmin)/(Fmax-Fmin)

% .....
% calculate the new F
% .....
Hnew=2*(hwnew/D)-1;
Sinew=D*((1-Hnew^2)^(1/2));
Sonew=D*acos(Hnew);
Swnew=(D*pi-Sonew);
A=pi*D^2/4;
```

```
Aonew=D*((Sonew)-(Sinew*Hnew))/4;
Awnew=A-Aonew;
Hwnew=Awnew/A;
Honew=Aonew/A;
Fnew=Hwnew-Hw;
% Finish calculating F new
   if abs(Fnew)<=abs(E1)
      error = 0
      root = hwnew
       i;
      break
   end

% .....
% updates the points
hwmin=hwmax;
Fmin=Fmax;
hwmax=hwnew;
Fmax=Fnew;
end

H=2*(hwnew/D)-1;
Si=D*((1-H^2)^(1/2));
So=D*acos(H);
Sw=(D*pi-So);
A=pi*D^2/4;
Ao=D*((So)-(Si*H))/4;
Aw=A-Ao;
Hw=Aw/A;
Ho=Ao/A;
denst=densw/Hw+denso/Ho;
Uw=Usw/Hw;
Uo=Uso/Ho;
```

```
if Uo/Uw >=0.98 & Uo/Uw <=1.05
  Dw=4*Aw/(Sw); Do=4*Ao/(So);
elseif Uo > Uw
  Dw=4*Aw/(Sw); Do=4*Ao/(So+Si);
else
  Dw=4*Aw/(Sw+Si); Do=4*Ao/So;
end
```

% calculating Reynolds number of water

```
Rew=Dw*Uw*densw/visw;
if Rew <= ReNu
  Cw=16; m=1;
else
  Cw=0.046; m=0.2;
end
```

% calculating Reynolds number of oil

```
Reo=Do*Uo*denso/viso;
if Reo <= ReNu
  Co=16; n=1;
else
  Co=0.046; n=0.2;
end
```

% calculating Reynolds number of interface

```
if Uo > Uw
  Rei=Si*Uo*denso/(pi*viso); densf=denso;
else
  Rei=Si*Uw*densw/(pi*visw); densf=densw;
end

if Rei <= ReNu
  Ci=16; p=1;
else
```

```
  Ci=0.046; p=0.2;
end

% calculation of the friction factors
fi=Ci*Rei^-p;
fw=Cw*Rew^-m;
fo=Co*Reo^-n;

% calculation of oil and water wall and interfacial shear stress
Tw=fw*densw*Uw*abs(Uw)/2;
To=fo*denso*Uo*abs(Uo)/2;
if Uo/Uw >=0.98 & Uo/Uw <=1.05
   Ti=0;
else
Ti=fi*densf*(Uo-Uw)*abs(Uo-Uw)/2;
end

% calculating the two fluid model
FHw=To*So/Ao+Ti*Si*(1/Aw+1/Ao)-Tw*Sw/Aw;
```

A.3.3 Change in F with respect to superficial velocity (Uso or Usw)

```
% Calculating derivative of F with respect to superficial velocity, Us (either oil or
water)
% Function to calculate F with respect to a change in superficial velocity and
return it to the wave velocity file
function FdfUs = dfUs(hwnew, Uswinput, ReNu, Usoinput, denso, densw, g, ST, D,
viso, visw)

hw=hwnew;
Uso=Usoinput;;
Usw=Uswinput;;
H=2*(hw/D)-1;
Si=D*((1-H^2)^(1/2));
So=D*acos(H);
```

```
Sw=(D*pi-So);
A=pi*D^2/4;
Ao=D*((So)-(Si*H))/4;
Aw=A-Ao;
Hw=Aw/A;
Ho=Ao/A;
denst=densw/Hw+denso/Ho;
Uo=Uso/Ho;
Uw=Usw/Hw;

if Uo/Uw >=0.98 & Uo/Uw <=1.05
   Dw=4*Aw/(Sw); Do=4*Ao/(So);
elseif Uo > Uw
   Dw=4*Aw/(Sw); Do=4*Ao/(So+Si);
else
   Dw=4*Aw/(Sw+Si); Do=4*Ao/So;
end
```

% calculating Reynolds number of water

```
Rew=Dw*Uw*densw/visw;
if Rew <= ReNu
   Cw=16; m=1;
else
   Cw=0.046; m=0.2;
end
```

% calculating Reynolds number of oil

```
Reo=Do*Uo*denso/viso;
if Reo <= ReNu
   Co=16; n=1;
else
   Co=0.046; n=0.2;
end
```

% calculating Reynolds number of interface

```
if Uo > Uw
  Rei=Si*Uo*denso/(pi*viso); densf=denso;
else
  Rei=Si*Uw*densw/(pi*visw); densf=densw;
end

if Rei <= ReNu
  Ci=16; p=1;
else
  Ci=0.046; p=0.2;
end
```

% calculation of the friction factors

```
fi=Ci*Rei^-p;
fw=Cw*Rew^-m;
fo=Co*Reo^-n;
```

% calculation of oil and water wall and interfacial shear stress

```
Tw=fw*densw*Uw*abs(Uw)/2;
To=fo*denso*Uo*abs(Uo)/2;
if Uo/Uw >=0.98 & Uo/Uw <=1.05
   Ti=0;
else
Ti=fi*densf*(Uo-Uw)*abs(Uo-Uw)/2;
end
```

% calculating the two fluid model

```
FdfUs=To*So/Ao+Ti*Si*(1/Aw+1/Ao)-Tw*Sw/Aw;
```

Appendix B

Program for the Mechanism of Drop Formation

The program was written to process the force balance equation (Eq. 6.12) developed to predict the wave amplitude required for drop formation at certain wavelength.

% Program to solve the force balance equation (Eq. 6.12 in chapter 6)
% Prediction of wave amplitudes required for drop formation with certain wavelength

% Fluid properties (Initialize the fluid properties)

denso=0.0; densw=0.0; g=0.0; ST=0.0;

D=0.0; viso=0.0; visw=0.0;Cs=0.0;lamda=0.0;

% Fluid properties (Input the properties)

% density of oil (denso), density of water (densw)

denso=828; densw=1000;

% viscosity of oil (viso), viscosity of water (visw)

viso=5.5*0.001; visw=1.0*0.001;

% gravity (g), surface tension (ST), diameter (D)

g=9.81; ST=40*.001; D=0.038;

% Input the oil and water superficial velocities

Uso=0.1;Usw=0.25

% Defining the transition to turbulent (Reynolds Number)

ReNu=2000;

% Calculate the cross sectional area of the pipe (A)

A=pi*D^2/4;

% Height of the water interface from the two-fluid model assuming stratified smooth (see two-fluid model calculation)

hwnew = two_fluid(Usw, ReNu, Uso, denso, densw, g, ST, D, viso, visw)

H=2*(hwnew/D)-1;

Si=D*((1-H^2)^(1/2));

So=D*acos(H);

Sw=(D*pi-So);

A=pi*D^2/4;

Ao=D*((So)-(Si*H))/4;

Aw=A-Ao;

Hw=Aw/A;

Ho=Ao/A;

denst=densw/Hw+denso/Ho;

Uw=Usw/Hw;

Uo=Uso/Ho;

if Uo/Uw >=0.98 & Uo/Uw <1.05

  Dw=4*Aw/(Sw); Do=4*Ao/(So);

elseif Uo > Uw

  Dw=4*Aw/(Sw); Do=4*Ao/(So+Si);

else

  Dw=4*Aw/(Sw+Si); Do=4*Ao/So;

end

% calculating Reynolds number of water

Rew=Dw*Uw*densw/visw;

if Rew <= ReNu

```
  Cw=16; m=1;
  else
  Cw=0.046; m=0.2;
end

% calculating Reynolds number of oil
Reo=Do*Uo*denso/viso;
if Reo <= ReNu
  Co=16; n=1;
  else
  Co=0.046; n=0.2;
end

% Drag coefficient
Cd=2.7e-7*Reo^(0.77)*Rew^(0.86);

output = [1 100]

% Wavelength (lamda)
lamda=0.0;
for j=1:100
   if lamda <= 5*D
      lamda=lamda+.1*D;
   else
      lamda=lamda+1*D
   end

% amplitude (a)
a=0.00;

k=(D-hwnew)/0.0001;
   for m=1:k
      a=a+0.0001;
      Hapeak=2*((hwnew+a)/D)-1;
```

```
Soapeak=D*acos(Hapeak);
Siapeak=D*((1-Hapeak^2)^(1/2));
Aoapeak=D*((Soapeak)-(Siapeak*Hapeak))/4;
Awapeak=A-Aoapeak;

Hatrough=2*((hwnew-a)/D)-1;
Siatrough=D*((1-Hatrough^2)^(1/2));
Soatrough=D*acos(Hatrough);
Aoatrough=D*((Soatrough)-(Siatrough*Hatrough))/4;
Awatrough=A-Aoatrough;

Aw1=Awapeak;
Aw2=Awatrough;
Ao1=Aoapeak;
Ao2=Aoatrough;

Uo1=Uo*(Ao/Ao1);
    Uw1=Uw*(Aw/Aw1);

% Drag force (Fd)
Fd=0.5*denso*(Aw1-Aw)*Cd*(Uw1-Uo1)^2;

% Surface tension force (Fst)
L=(a^2+(lamda/2)^2)^0.5;
Fst=2*Si*ST*(lamda/2)/L;
Total=Fd-Fst;
        if Total>=0
          break
      end
  end
```

```
output=[output;lamda a];
end
end

% writing the output file
wk1write('output',output)
```

Appendix C

Program for Entrainment Fraction Calculation

```
% Program to solve the entrainment fraction of water in oil and oil in water (see
chapter 8)
% Fluid properties (Initialize the fluid properties)
denso=0.0; densw=0.0; g=0.0; ST=0.0;
D=0.0; viso=0.0; visw=0.0;Cs=0.0;lamda=0.0;

% Fluid properties (Input the properties)
% density of oil (denso), density of water (densw)
denso=828; densw=1000;
% viscosity of oil (viso), viscosity of water (visw)
viso=5.5*0.001; visw=1.0*0.001;
% gravity (g), surface tension (ST), diameter (D)
g=9.81; ST=40*.001; D=0.038;

% Defining the transition to turbulent (Reynolds Number)
ReNu=2000;

% Calculate the cross sectional area of the pipe (A)
A=pi*D^2/4;

% Define the critical amplitude at the onset of entrainment
a_oil=3.8/1000;
a_water=3.8/1000;
```

% Input the oil and water superficial velocities

Uso=0;Usw=0

% start calculating the entrainment fraction

% water_frac is the input water fraction

% Entw_o is the entrainment fraction of water in oil

% Ento_w is the entrainment fraction of oil in water

% Um is the mixture velocity

water_frac=0.0;

output1 = [i i];

while water_frac < 0.95

Entw_o=0;

Ento_w=0;

frac=frac+0.05;

Um=1.5;

Usw=frac*Um;

Uso=Um-Usw;

% Height of the water interface from the two-fluid model assuming stratified smooth (see two-fluid model calculation)

hwnew = two_fluid(Usw, ReNu, Uso, denso, densw, g, ST, D, viso, visw)

H=2*(hwnew/D)-1;

Si=D*((1-H^2)^(1/2));

So=D*acos(H);

Sw=(D*pi-So);

A=pi*D^2/4;

Ao=D*((So)-(Si*H))/4;

Aw=A-Ao;

Hw=Aw/A;

Ho=Ao/A;

denst=densw/Hw+denso/Ho;

Uw=Usw/Hw;

Uo=Uso/Ho;

```
if Uo/Uw >=0.98 & Uo/Uw <1.05
   Dw=4*Aw/(Sw); Do=4*Ao/(So);
elseif Uo > Uw
   Dw=4*Aw/(Sw); Do=4*Ao/(So+Si);
else
   Dw=4*Aw/(Sw+Si); Do=4*Ao/So;
end

% calculating Reynolds number of water
Rew=Dw*Uw*densw/visw;
if Rew <= ReNu
   Cw=16; m=1;
   else
   Cw=0.046; m=0.2;
end

% calculating Reynolds number of oil
Reo=Do*Uo*denso/viso;
if Reo <= ReNu
   Co=16; n=1;
   else
   Co=0.046; n=0.2;
end

% Drag coefficient
Cd=2.7e-7*Reo^(0.77)*Rew^(0.86);

% Wavelength (lamda)
lamda=1*D;

% Prediction of the entrainment fraction of oil in water (Ento_w)
% Calculating the critical amplitude of oil waves at the new condition
% amplitude (a)
a=0.00;
```

```
k=(D-hwnew)/0.0001;
    for m=1:k
    a=a+0.0001;
    Hapeak=2*((hwnew+a)/D)-1;
    Soapeak=D*acos(Hapeak);
    Siapeak=D*((1-Hapeak^2)^(1/2));
    Aoapeak=D*((Soapeak)-(Siapeak*Hapeak))/4;
    Awapeak=A-Aoapeak;

    Hatrough=2*((hwnew-a)/D)-1;
    Siatrough=D*((1-Hatrough^2)^(1/2));
    Soatrough=D*acos(Hatrough);
    Aoatrough=D*((Soatrough)-(Siatrough*Hatrough))/4;
    Awatrough=A-Aoatrough;

    Aw1=Awapeak;
    Aw2=Awatrough;
    Ao1=Aoapeak;
    Ao2=Aoatrough;

    Uo2=Uo*(Ao/Ao2);
    Uw2=Uw*(Aw/Aw2);

% Drag force (Fd)
Fd=0.5*densw*(Aw-Aw2)*Cd*(Uw2-Uo2)^2;

% Surface tension force (Fst)
L=(a^2+(lamda/2)^2)^0.5;
Fst=2*Si*ST*(lamda/2)/L;
Total=Fd-Fst;
        if Total>=0
           break
        end
  end
```

```
% calculating the amount of oil transfer to the water Phase
% Vent_o is the amount of oil waves transfer to the water phase
Vent_o=0.5*((a_oil-a)*lamda*Si/(pi));

%vdfo_old is the oil drops deposition rate constant from McCoy and Hanratty
(1977)
vdfo_old=0.17*(Tw/densw)^0.5

%vdfo is the modified deposition rate constant using present study experimental
data
vdfo=vdfo_old*0.3*(Uso/Um)^-2.08;

% Calculation of the entrainment fraction of oil in water (Ento_w)
C_oil=Vent_o*denso*abs(Uw2-Uo2)/(Si*lamda^2*vdfo);
Ento_w=((densw)-((densw)^2-4*(densw-denso)*C_oil)^0.5)/(2*(densw-denso));

% Prediction of the entrainment fraction of water in oil (Entw_o)
% Calculating the critical amplitude of water waves at the new condition
% amplitude (a)
a=0.00;
k=(D-hwnew)/0.0001;
   for m=1:k
      a=a+0.0001;
      Hapeak=2*((hwnew+a)/D)-1;
      Soapeak=D*acos(Hapeak);
      Siapeak=D*((1-Hapeak^2)^(1/2));
      Aoapeak=D*((Soapeak)-(Siapeak*Hapeak))/4;
      Awapeak=A-Aoapeak;


      Hatrough=2*((hwnew-a)/D)-1;
      Siatrough=D*((1-Hatrough^2)^(1/2));
      Soatrough=D*acos(Hatrough);
      Aoatrough=D*((Soatrough)-(Siatrough*Hatrough))/4;
      Awatrough=A-Aoatrough;
```

```
Aw1=Awapeak;
Aw2=Awatrough;
Ao1=Aoapeak;
Ao2=Aoatrough;

Uo1=Uo*(Ao/Ao1);
Uw1=Uw*(Aw/Aw1);

% Drag force (Fd)
Fd=0.5*denso*(Aw1-Aw)*Cd*(Uw1-Uo1)^2;

% Surface tension force (Fst)
L=(a^2+(lamda/2)^2)^0.5;
Fst=2*Si*ST*(lamda/2)/L;
Total=Fd-Fst;
        if Total>=0
            break
        end
    end

% calculating the amount of water transfer to the oil Phase
% Vent_w is the amount of water waves transfer to the oil phase
Vent_w=0.5*((a_water-a)*lamda*Si/(pi));

%vdfw_old is the water drops deposition rate constant from McCoy and Hanratty
(1977)
vdfw_old=0.17*(To/denso)^0.5

%vdfw is the modified deposition rate constant using present study experimental
data
vdfw=vdfw_old*0.45*(Usw/Um)^-1.8;
```

```
% Calculation of the entrainment fraction of water in oil (Entw_o)
C_water=Vent_w*densw*abs(Uw1-Uo1)/(Si*lamda^2*vdfw);
Entw_o=((denso)-((denso)^2-4*(denso-densw)*C_water)^0.5)/(2*(denso-densw));

output1=[output1;100*Ento_w 100*Entw_o];
end
wk1write('entrainment',output1)
```

Appendix D

Phase Distribution

Oil volume fraction distribution in a pipe cross section were obtained with the high frequency impedance probe in the way described in section 3.3.2, and the result were converted into phase distribution diagram using Matlab. The full sets of phase distributions investigated in this study are presented in the following figures for two different inlet geometries (T-junction with bend and Y-junction).

D.1 Inlet section: T-junction with 90° bend

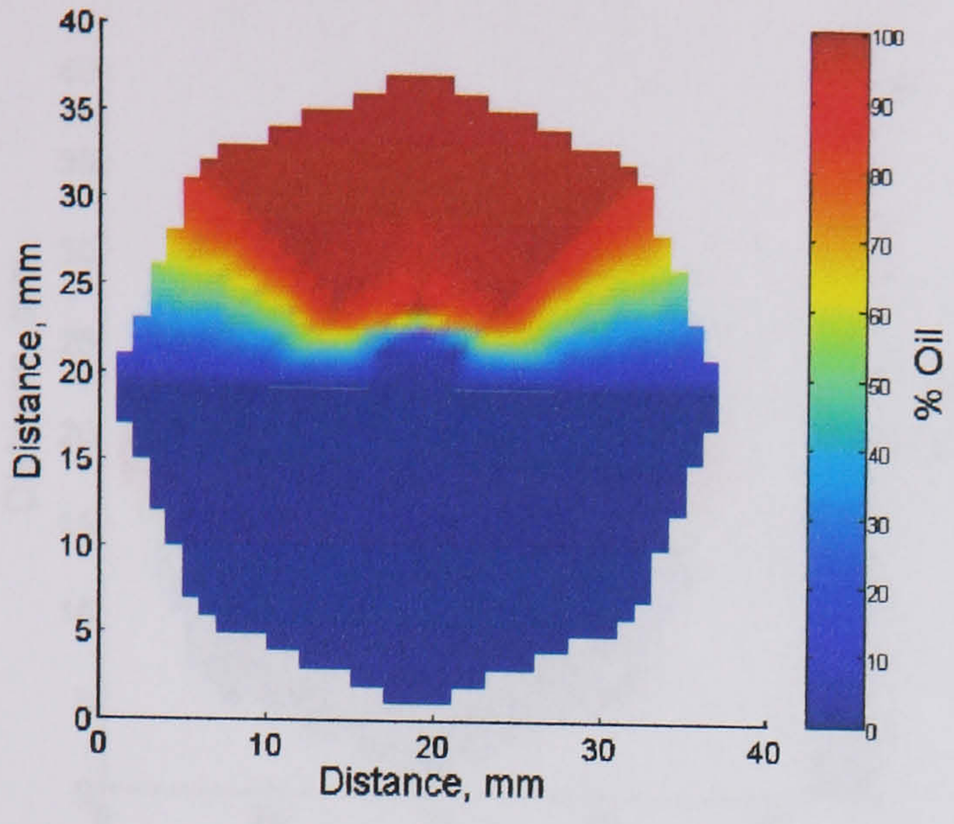

(a)

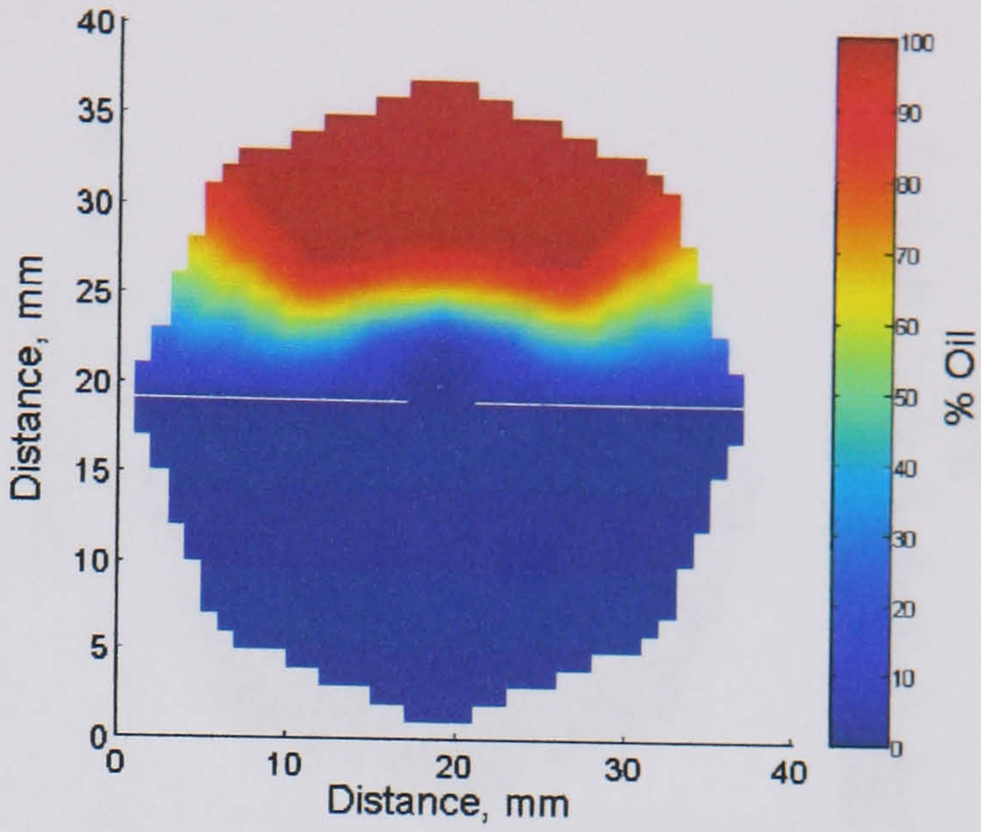

(b)

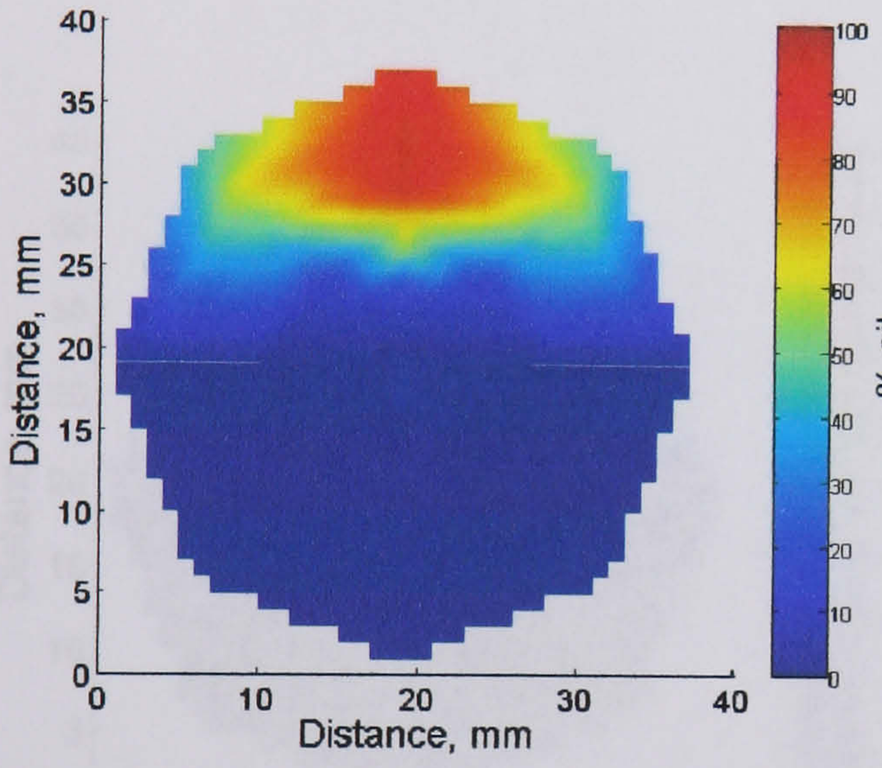

(c)

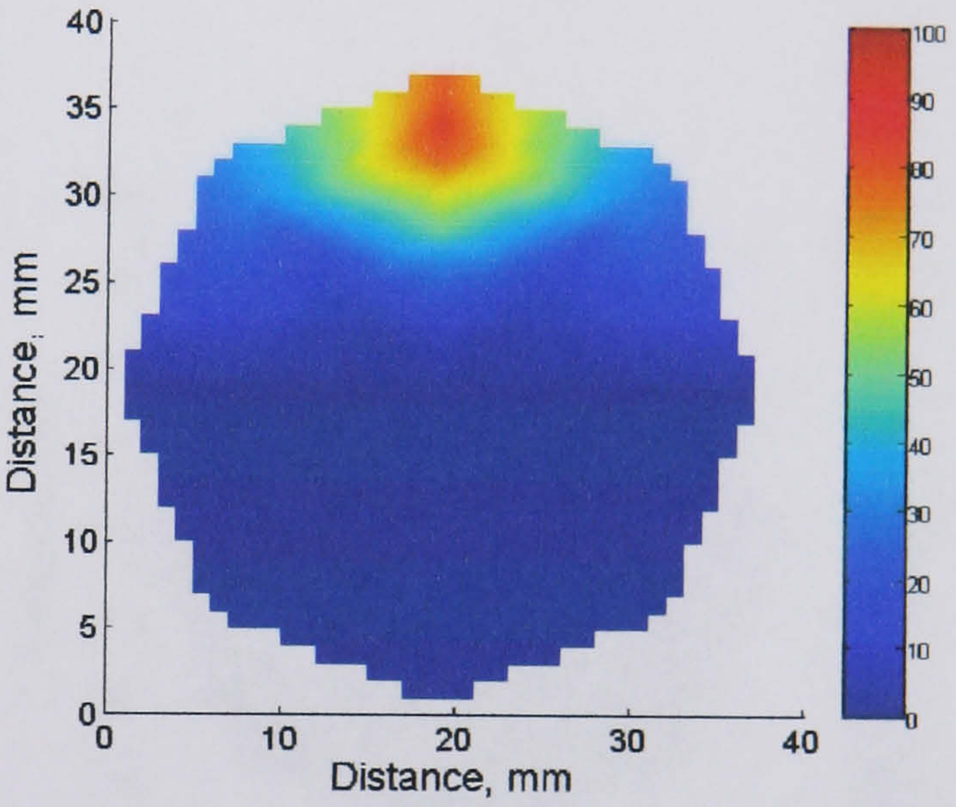

(d)

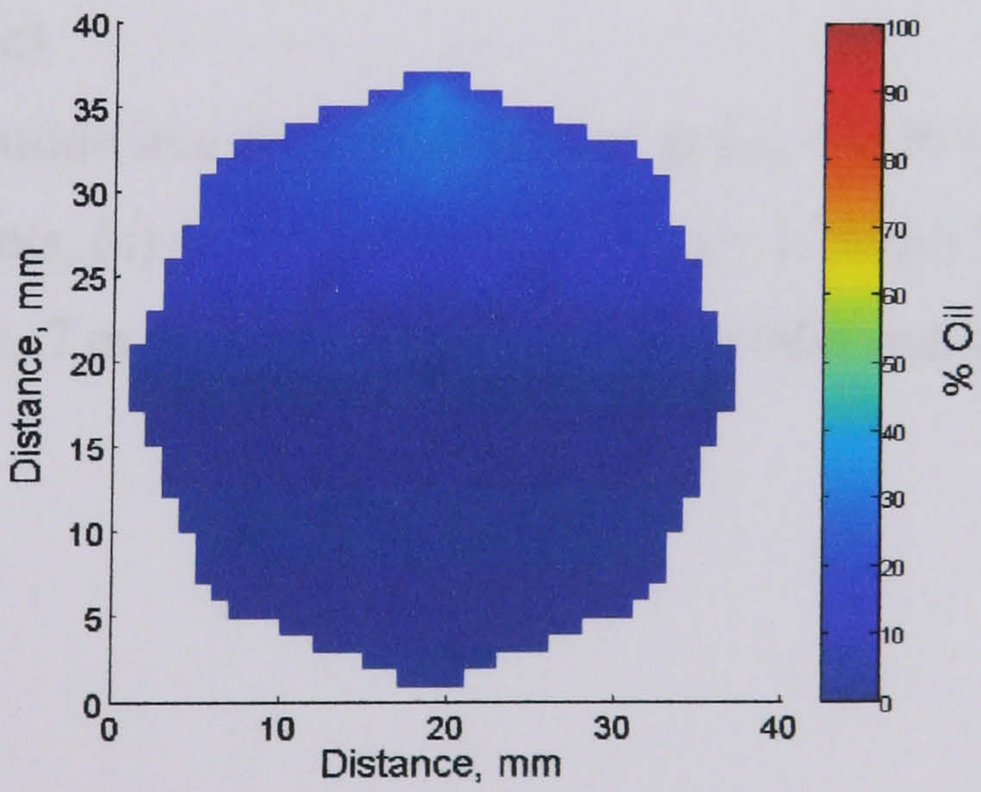

(e)

Fig. D.1 Phase distribution in a pipe cross section at $U_{so} = 0.35$ m/s and (a) $U_{sw} = 0.50$ m/s, (b) $U_{sw} = 0.60$ m/s, (c) $U_{sw} = 0.80$ m/s, (d) $U_{sw} = 1.10$ m/s, (e) $U_{sw} = 0.50$ m/s in the 38 mm ID test pipe, 7 m from the inlet (T-junction inlet section).

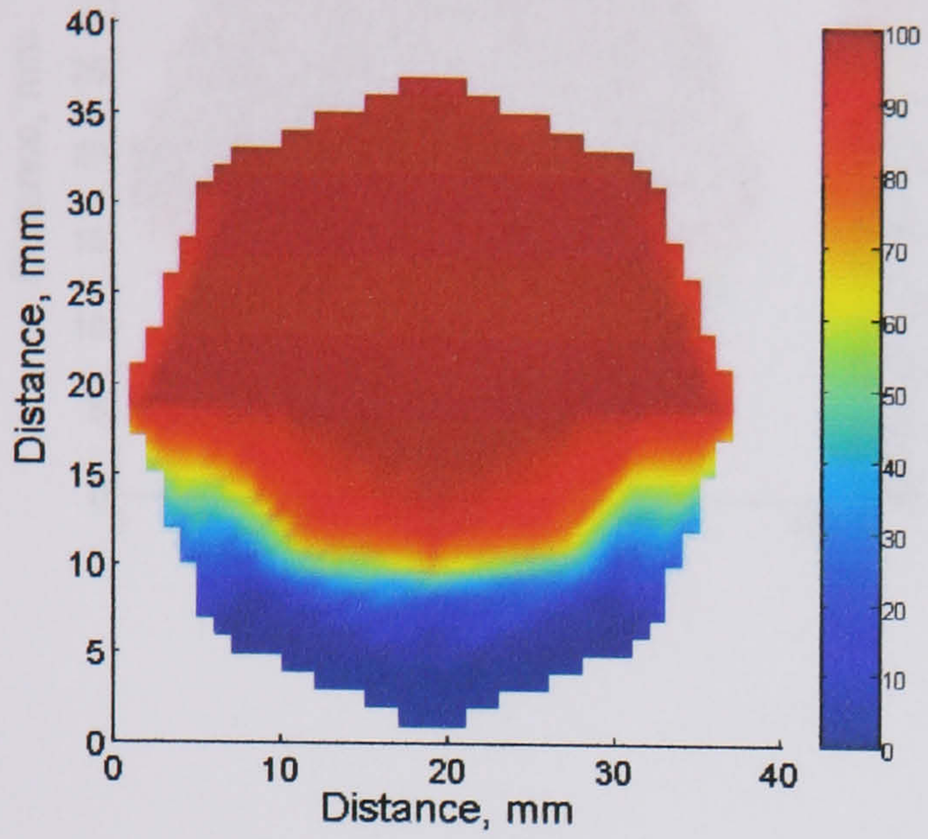

(a)

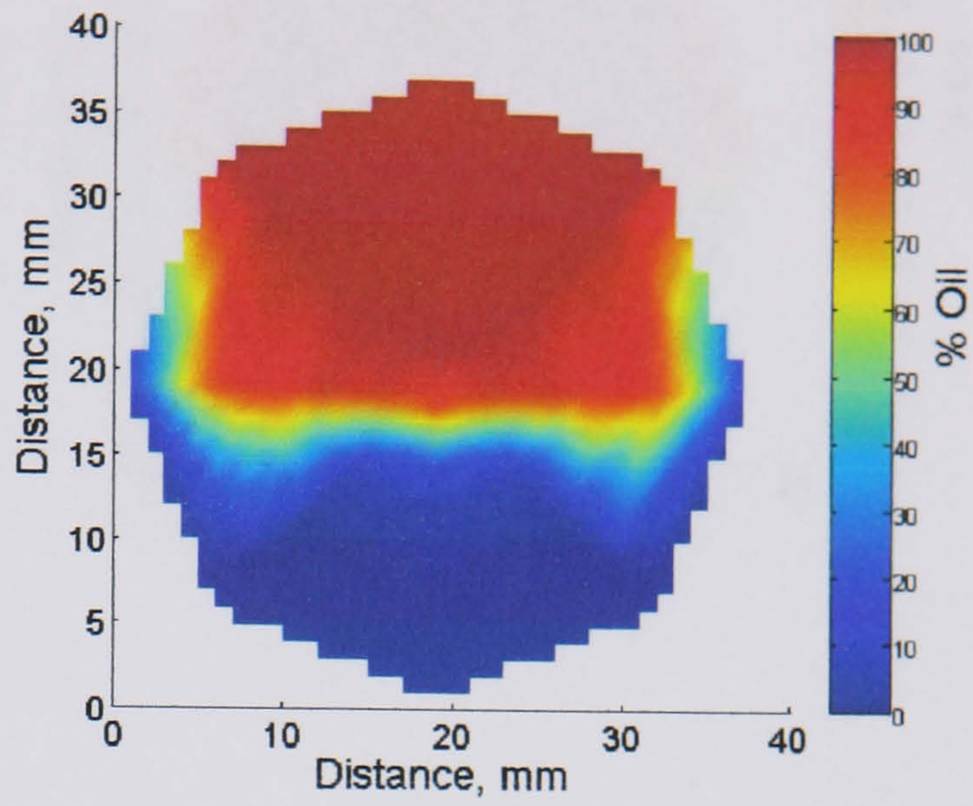

(b)

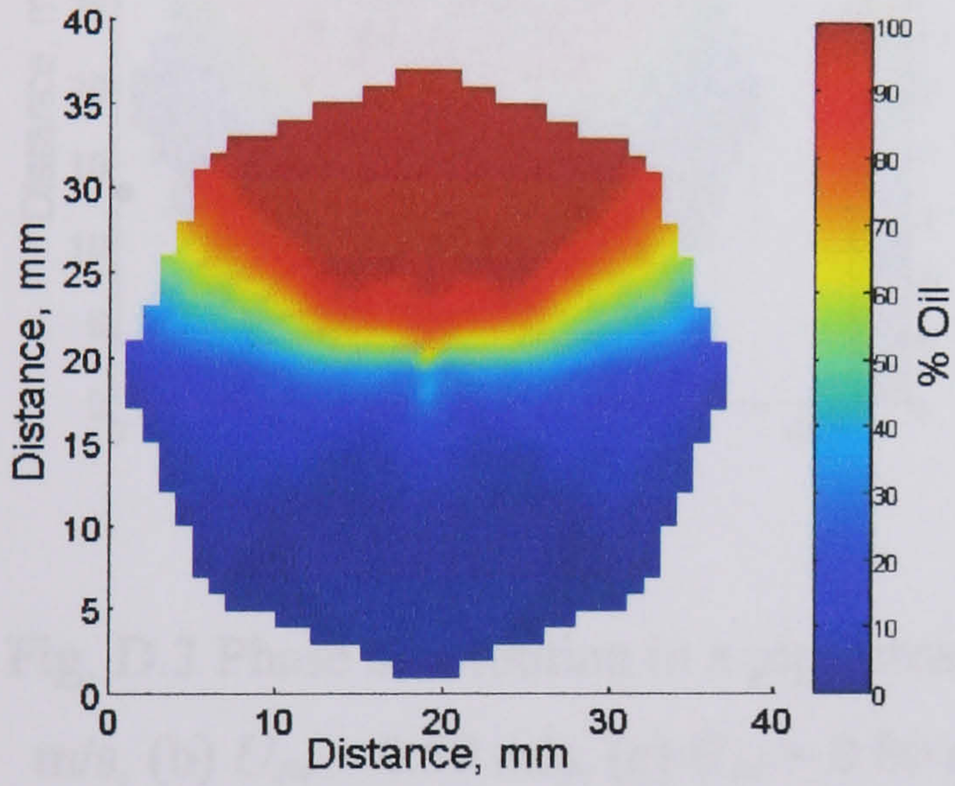

(c)

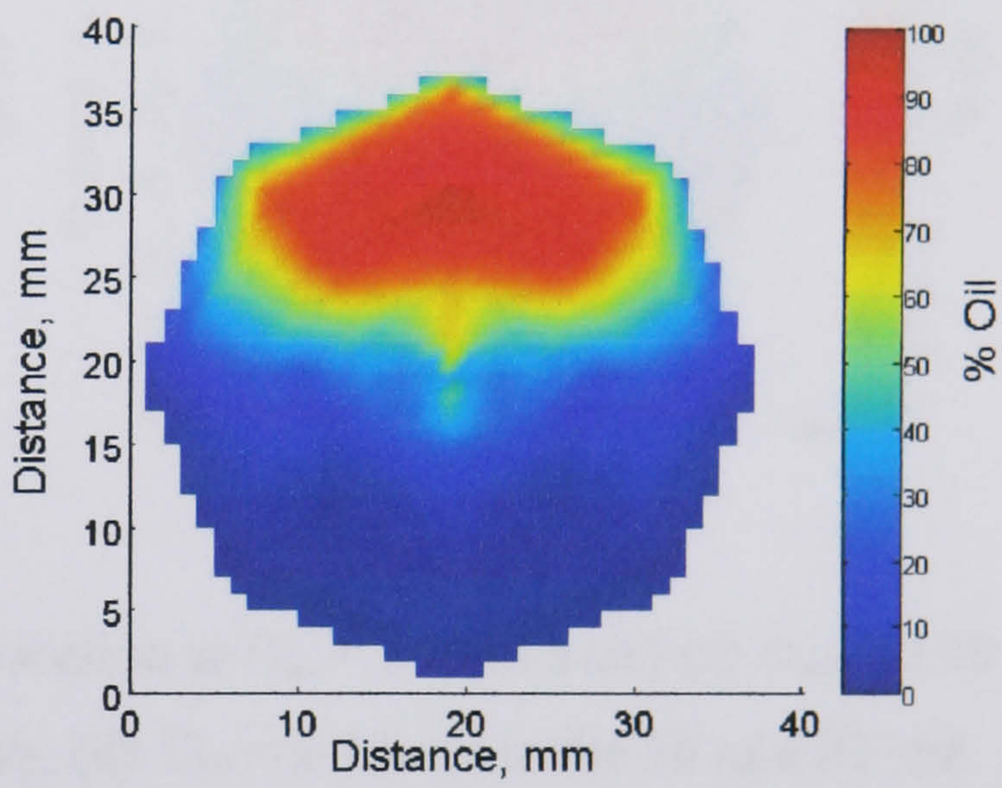

(d)

Fig. D.2 Phase distribution in a pipe cross section at U_{so} = 0.80 m/s and (a) U_{sw} = 0.20 m/s, (b) U_{sw} = 0.50 m/s, (c) U_{sw} = 0.80 m/s, (d) U_{sw} = 1.10 m/s in the 38 mm ID test pipe, 7 m from the inlet (T-junction inlet section).

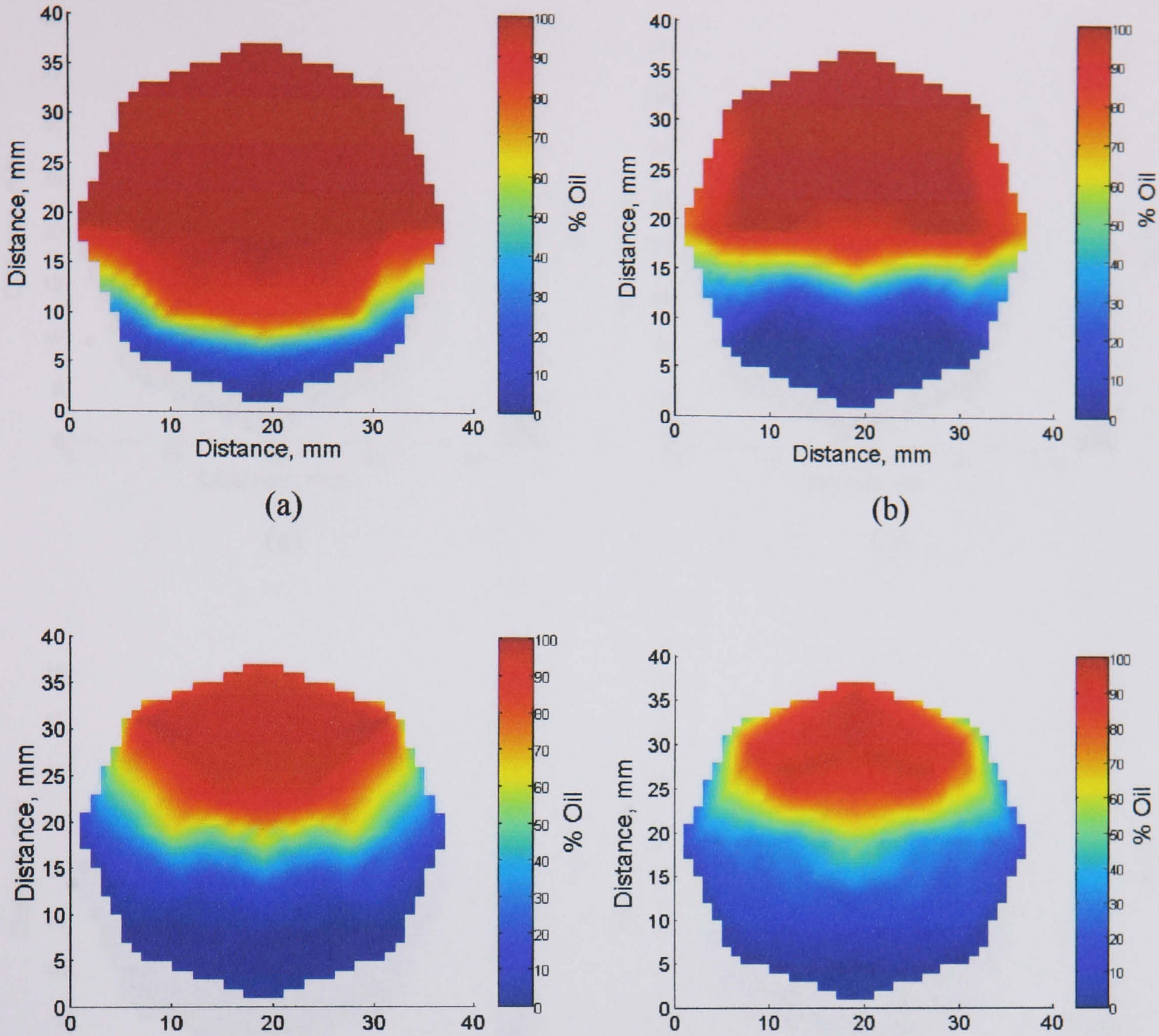

Fig. D.3 Phase distribution in a pipe cross section at U_{so} = 1.10 m/s and (a) U_{sw} = 0.20 m/s, (b) U_{sw} = 0.50 m/s, (c) U_{sw} = 0.80 m/s, (d) U_{sw} = 1.10 m/s in the 38 mm ID test pipe, 7 m from the inlet (T-junction inlet section).

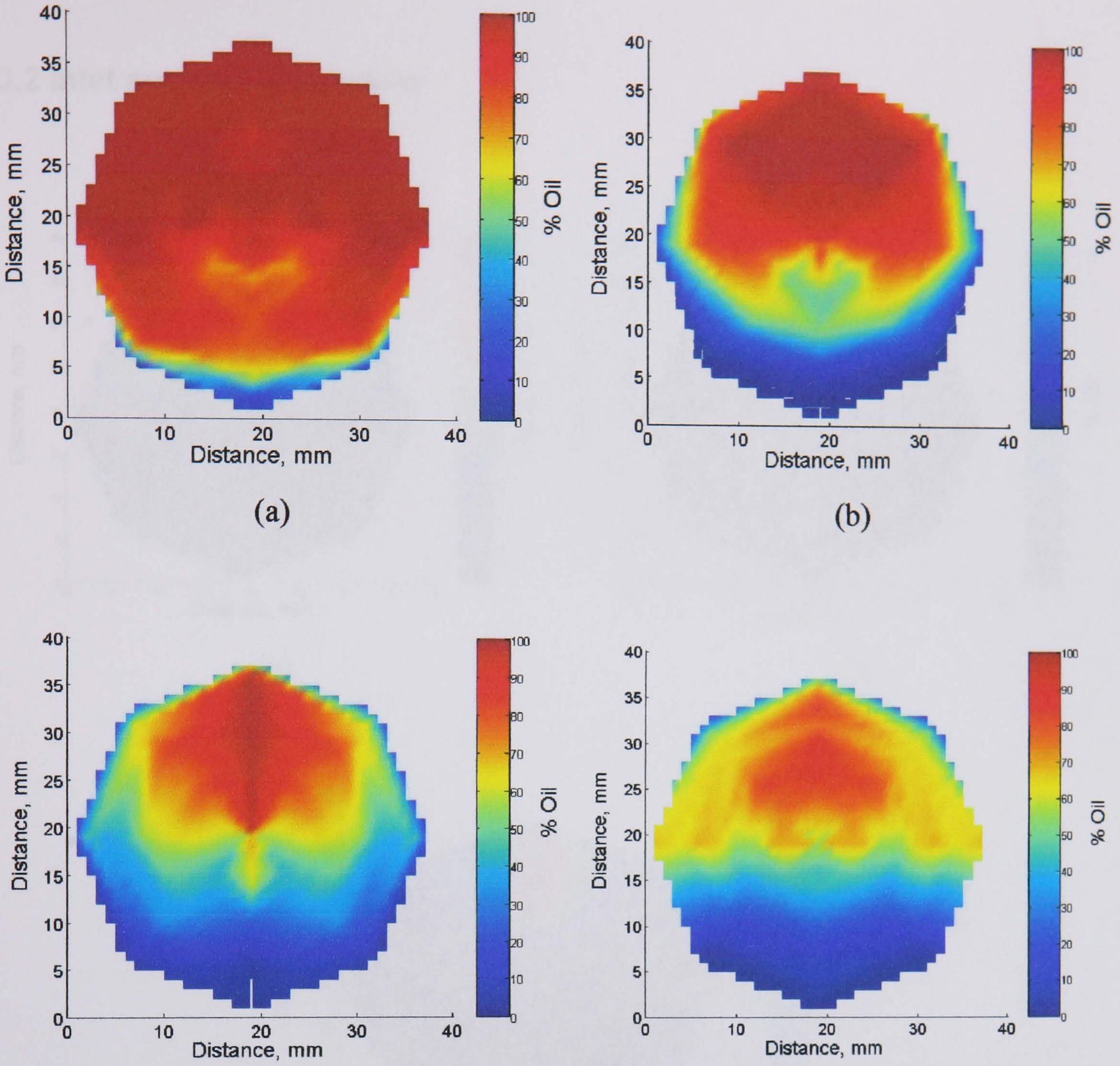

Fig. D.4 Phase distribution in a pipe cross section at U_{so} = 1.40 m/s and (a) U_{sw} = 0.20 m/s, (b) U_{sw} = 0.50 m/s, (c) U_{sw} = 0.80 m/s, (d) U_{sw} = 1.10 m/s in the 38 mm ID test pipe, 7 m from the inlet (T-junction inlet section).

D.2 Inlet section: Y-junction

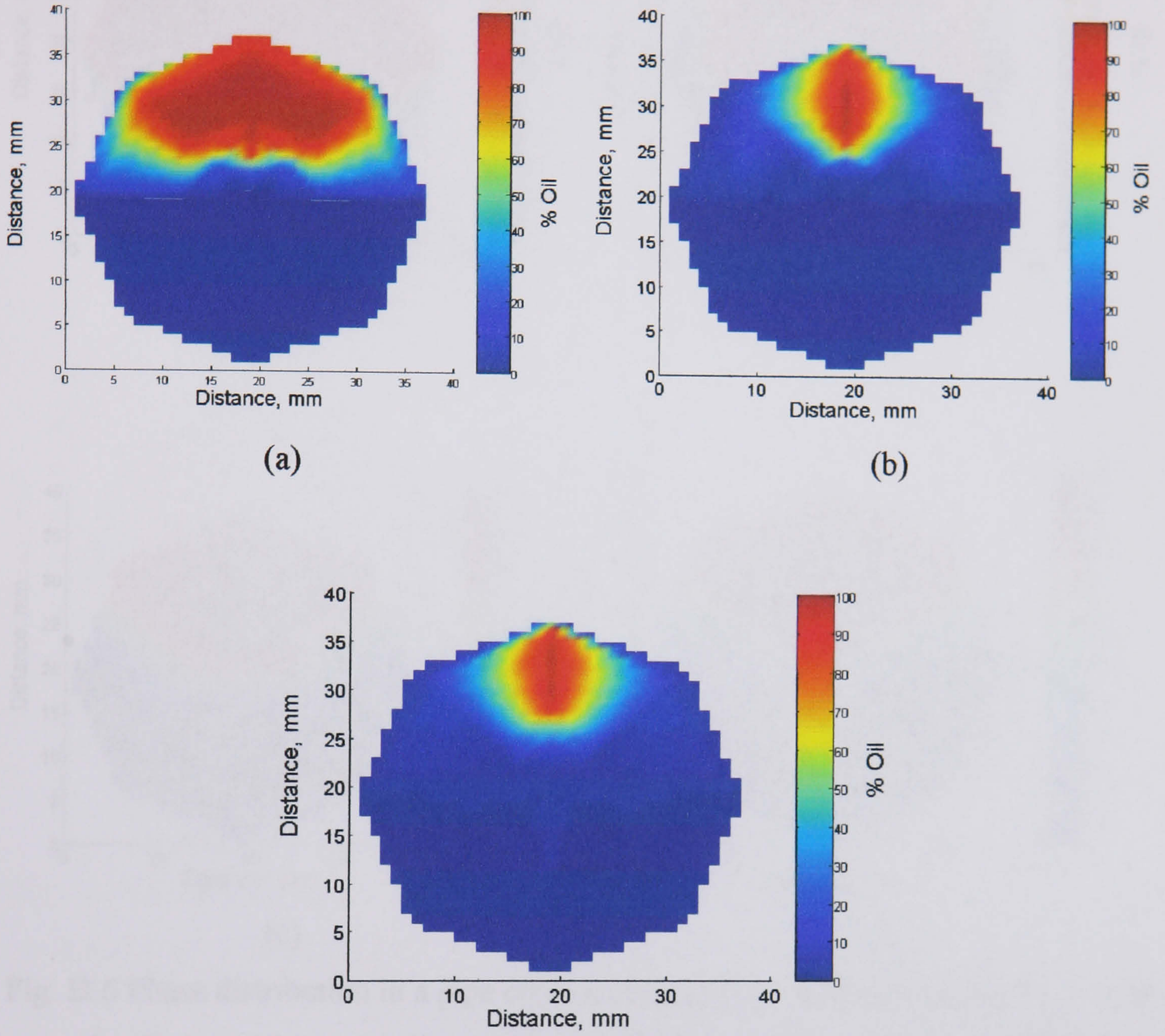

(a) (b)

(c)

Fig. D.5 Phase distribution in a pipe cross section at U_{so} = 0.35 m/s and (a) U_{sw} = 0.60 m/s, (b) U_{sw} = 0.80 m/s, (c) U_{sw} = 1.10 m/s in the 38 mm ID test pipe, 7 m from the inlet (Y-junction inlet section).

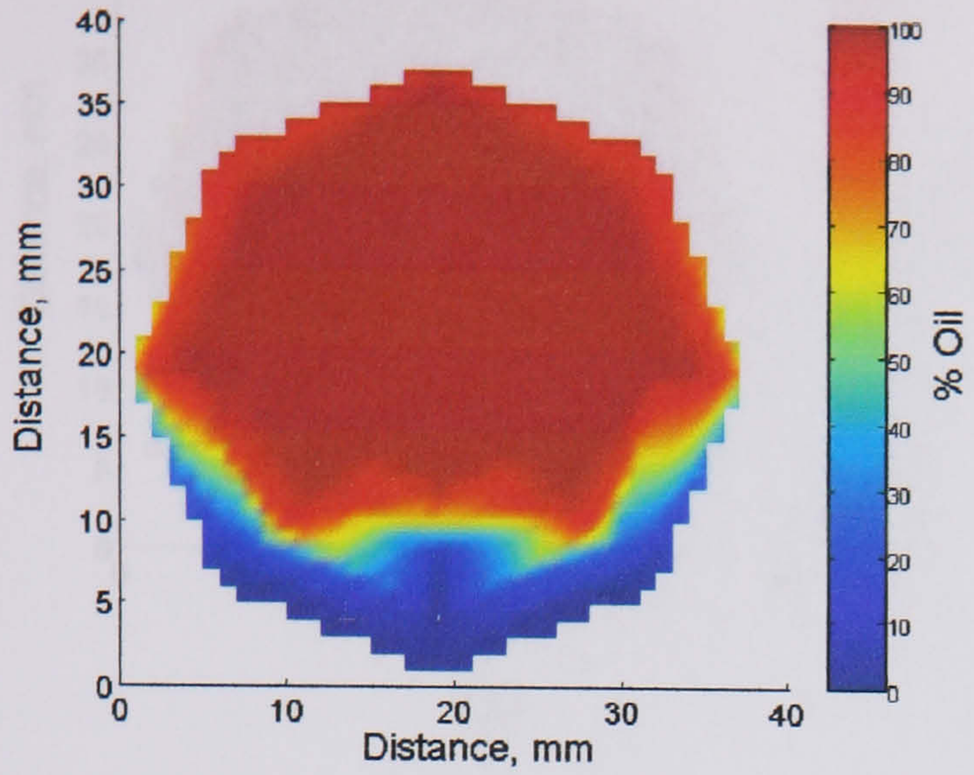

(a)

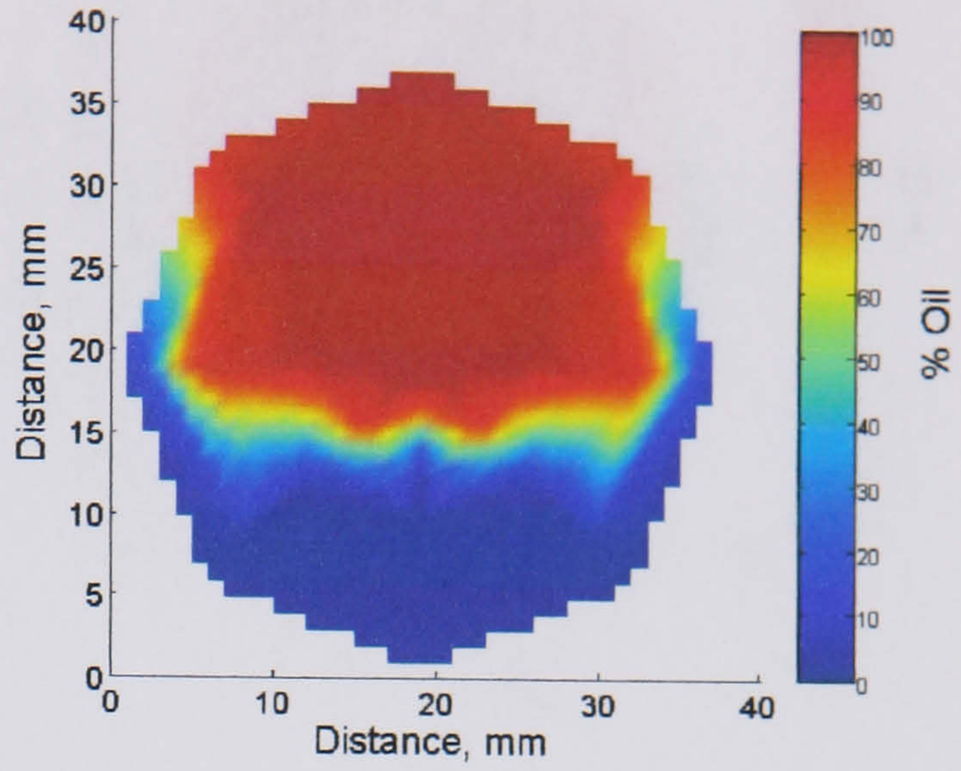

(b)

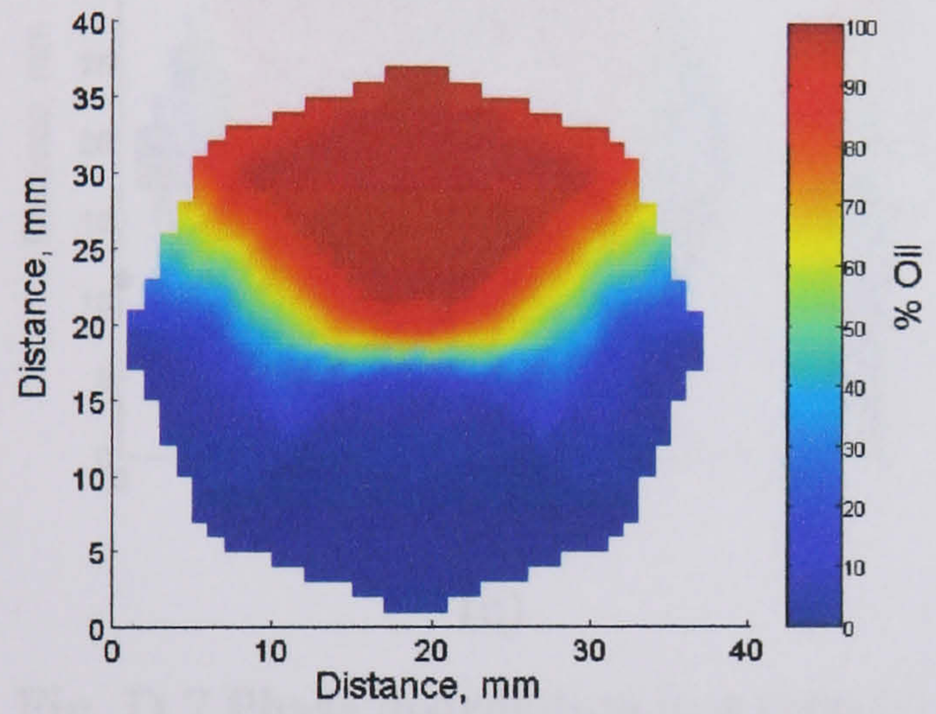

(c)

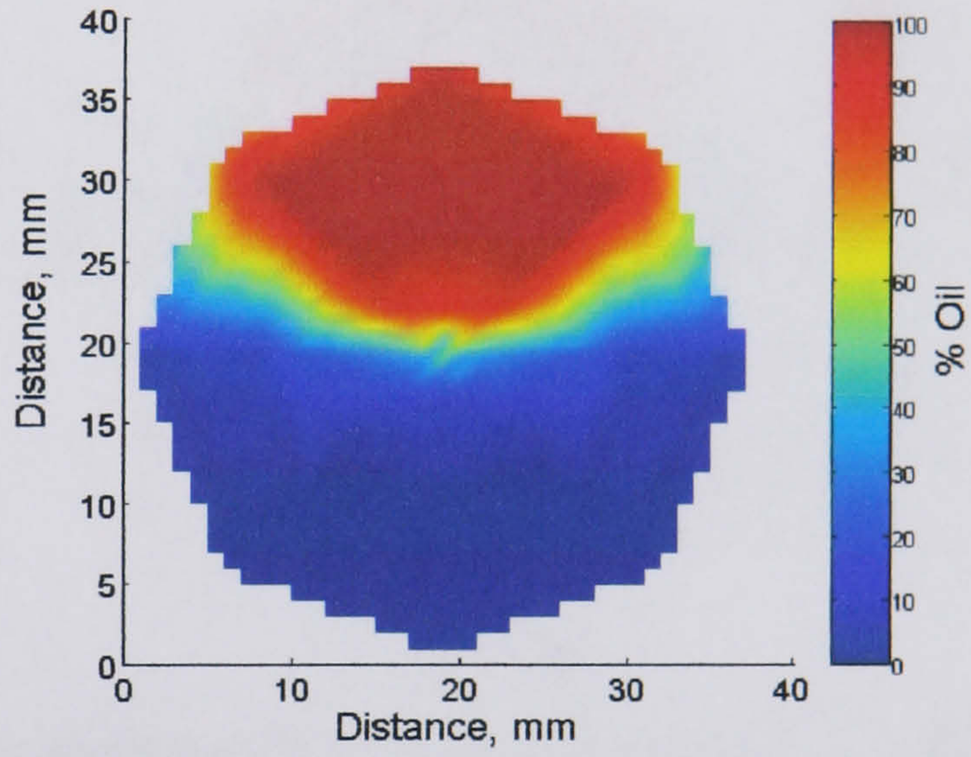

(d)

Fig. D.6 Phase distribution in a pipe cross section at $U_{so} = 0.80$ m/s and (a) $U_{sw} = 0.20$ m/s, (b) $U_{sw} = 0.50$ m/s, (c) $U_{sw} = 0.80$ m/s, (d) $U_{sw} = 1.10$ m/s in the 38 mm ID test pipe, 7 m from the inlet (Y-junction inlet section).

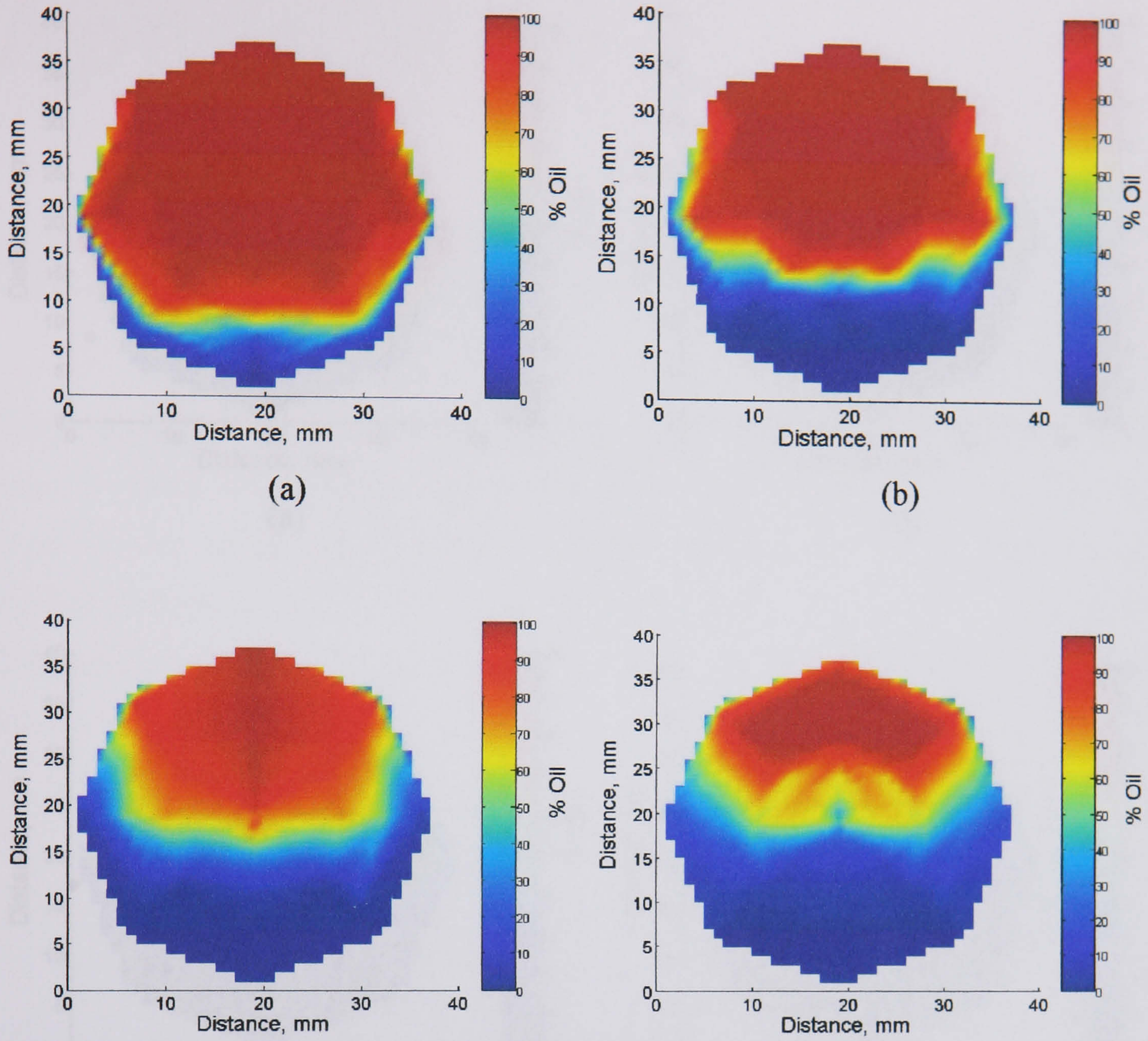

Fig. D.7 Phase distribution in a pipe cross section at U_{so} = 1.10 m/s and (a) U_{sw} = 0.20 m/s, (b) U_{sw} = 0.50 m/s, (c) U_{sw} = 0.80 m/s, (d) U_{sw} = 1.10 m/s in the 38 mm ID test pipe, 7 m from the inlet (Y-junction inlet section).

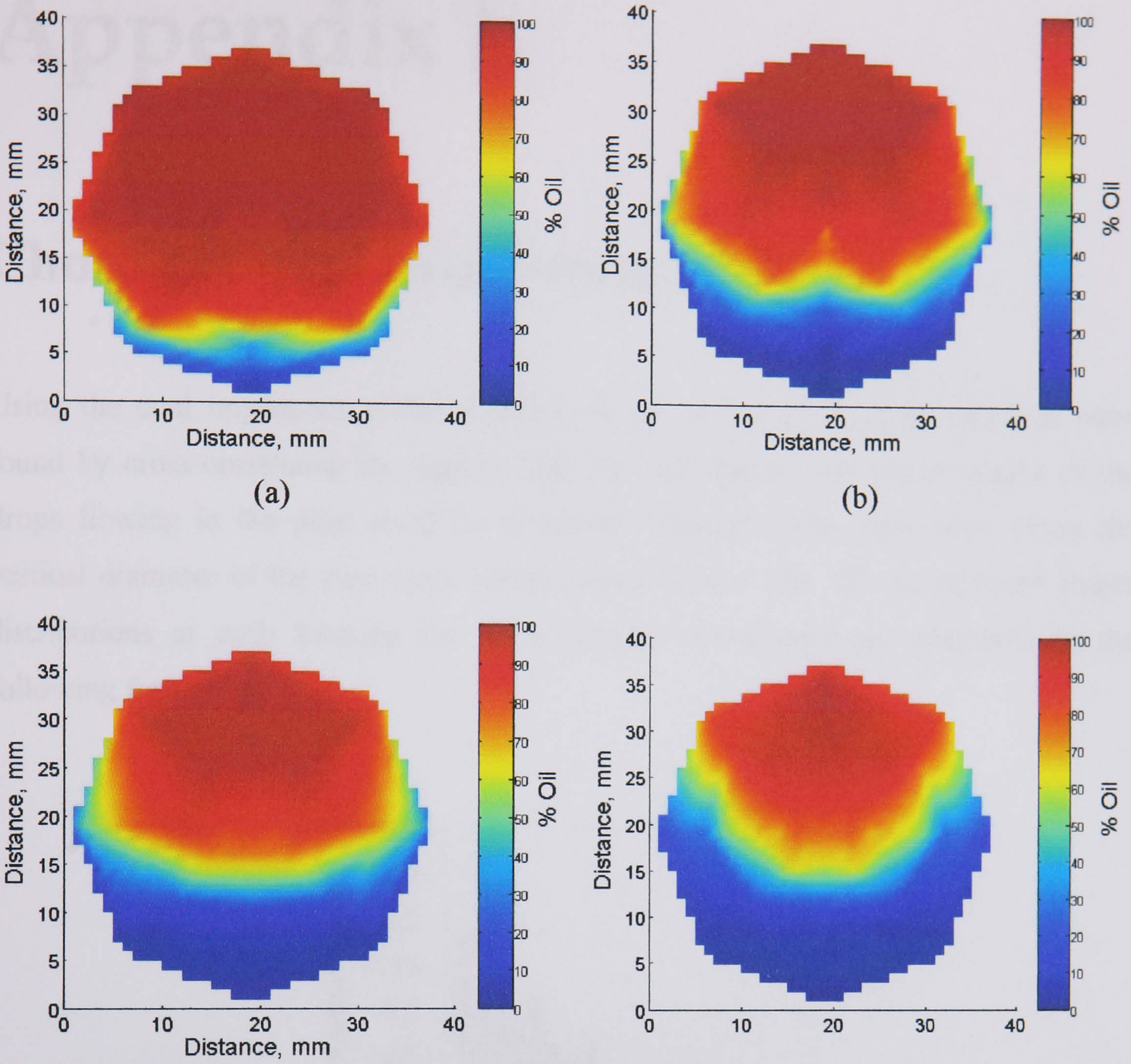

Fig. D.8 Phase distribution in a pipe cross section at U_{so} = 1.40 m/s and (a) U_{sw} = 0.20 m/s, (b) U_{sw} = 0.50 m/s, (c) U_{sw} = 0.80 m/s, (d) U_{sw} = 1.10 m/s in the 38 mm ID test pipe, 7 m from the inlet (T-junction inlet section).

Appendix E

Chord Length Distribution

Using the dual impedance probe as illustrated in section 3.3.3, drop velocities were found by cross-correlating the signals from the two sensors and chord lengths of the drops flowing in the pipe could be measured. Measurements were taken along the vertical diameter of the pipe cross section, every 2 mm. The full set of chord length distributions at each location for all conditions investigated are presented in the following figures.

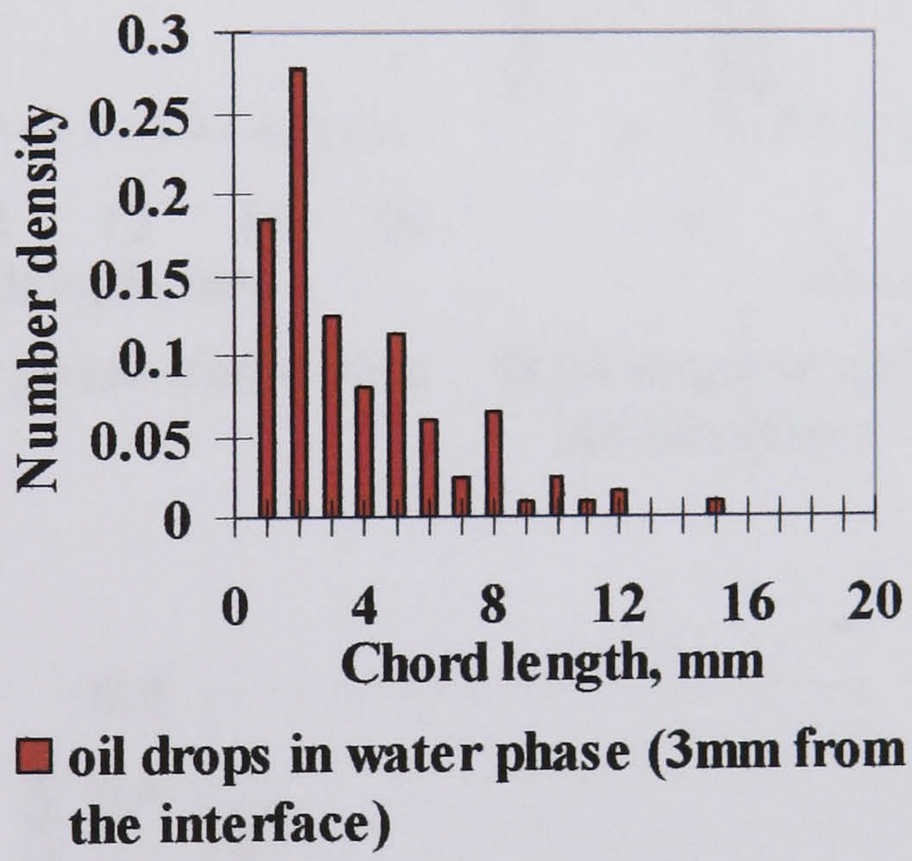

Fig. E.1 Chord length distributions of water drops in oil and oil drops in water at different locations along the vertical diameter at U_{so} = 0.35, U_{sw} = 0.80 m/s in the 38 mm ID test pipe, 7 m from the inlet (no water drops were found above the 3 mm from the interface).

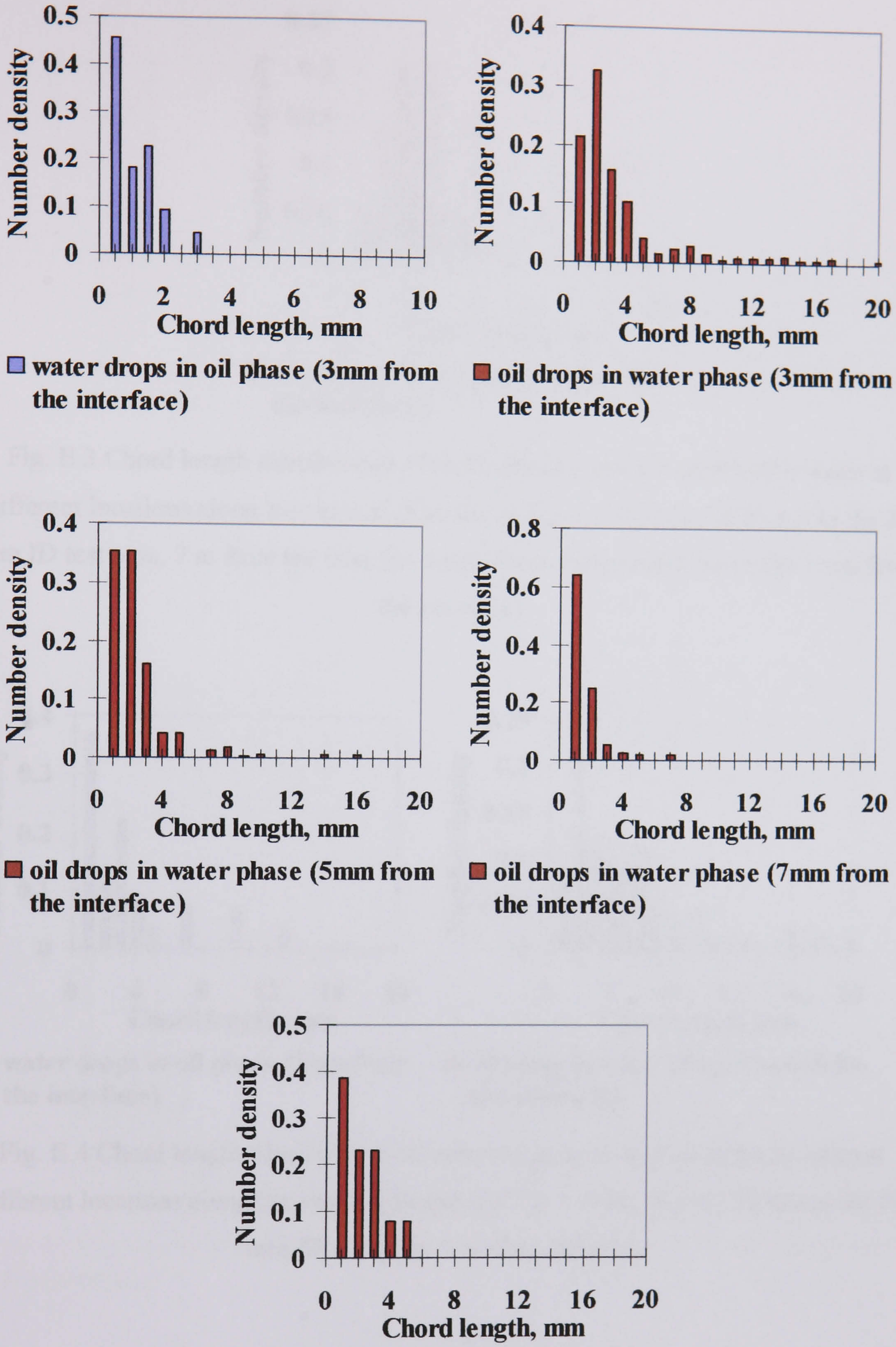

Fig. E.2 Chord length distributions of water drops in oil and oil drops in water at different locations along the vertical diameter at U_{so} = 0.35, U_{sw} = 1.10 m/s in the 38 mm ID test pipe, 7 m from the inlet.

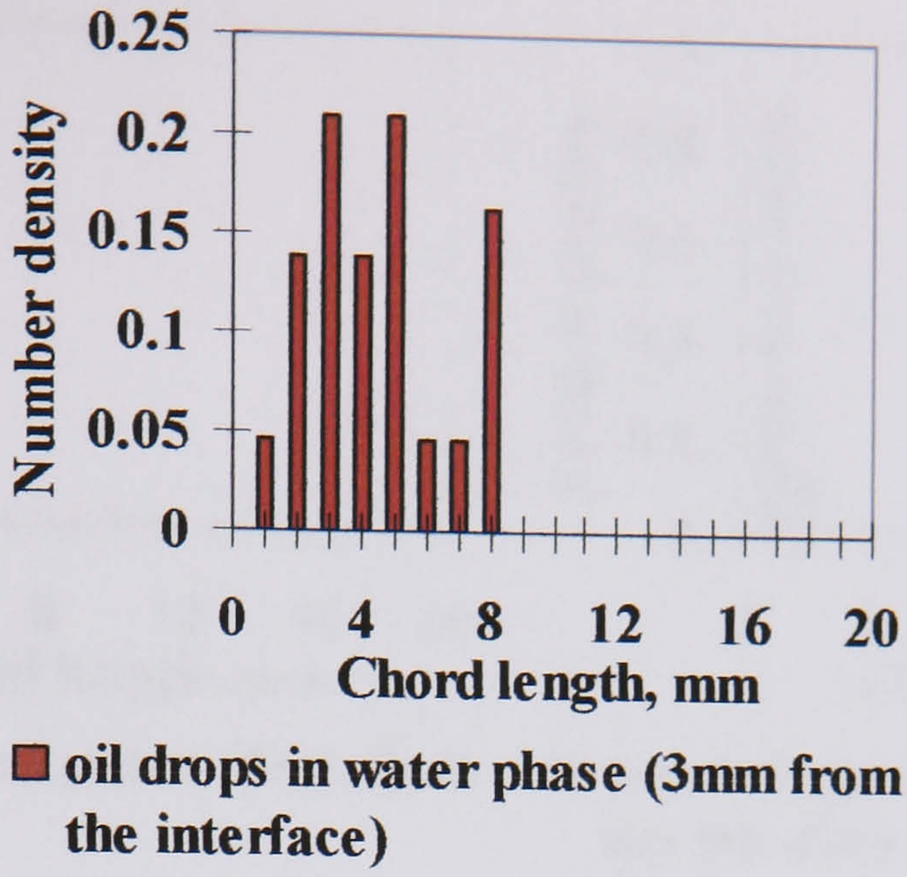

Fig. E.3 Chord length distributions of water drops in oil and oil drops in water at different locations along the vertical diameter at $U_{so} = 0.80$, $U_{sw} = 0.20$ m/s in the 38 mm ID test pipe, 7 m from the inlet (no water drops were found above the 3 mm from the interface).

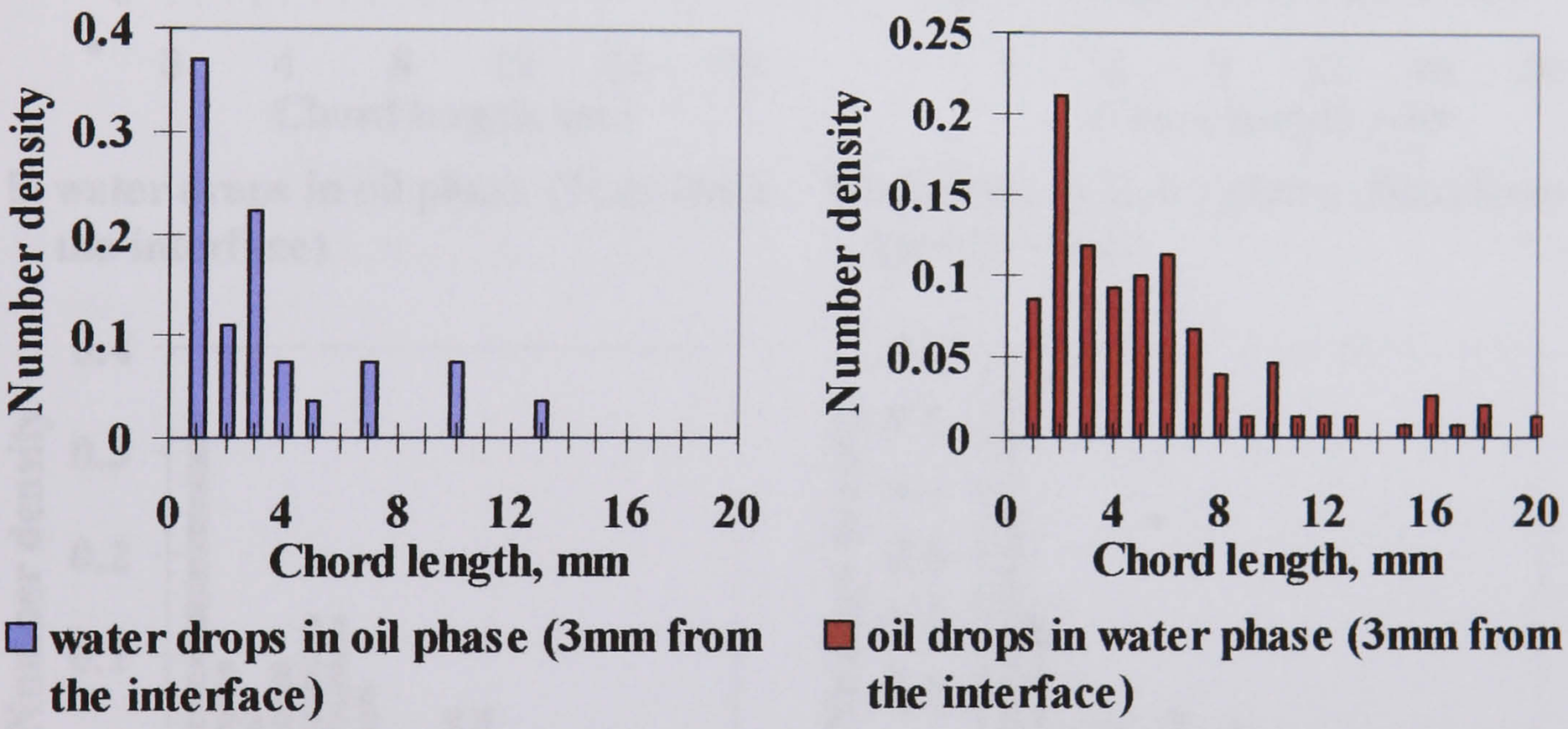

Fig. E.4 Chord length distributions of water drops in oil and oil drops in water at different locations along the vertical diameter at $U_{so} = 0.80$, $U_{sw} = 0.50$ m/s in the 38 mm ID test pipe, 7 m from the inlet.

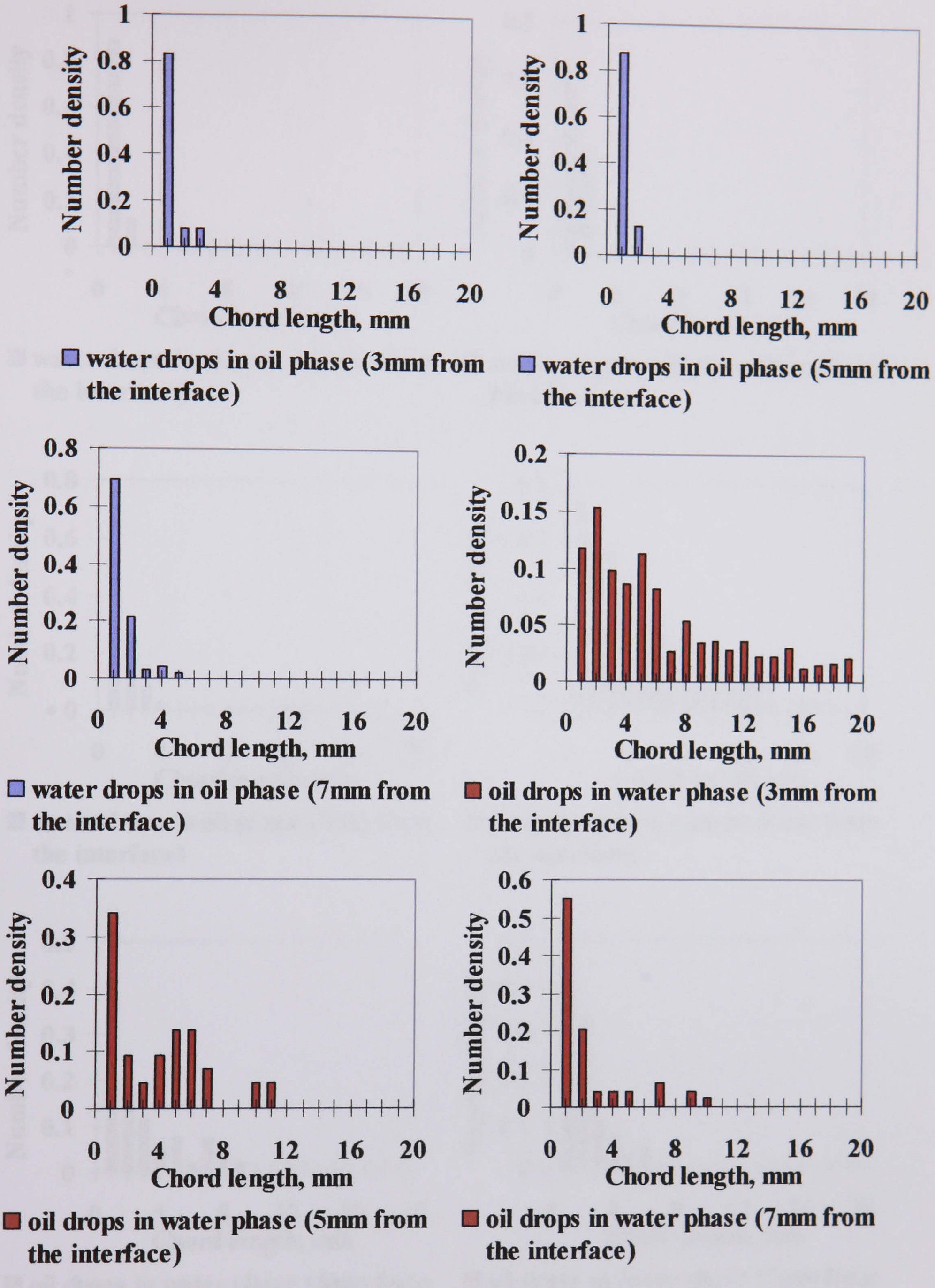

Fig. E.5 Chord length distributions of water drops in oil and oil drops in water at different locations along the vertical diameter at $U_{so} = 0.80$, $U_{sw} = 0.80$ m/s in the 38 mm ID test pipe, 7 m from the inlet.

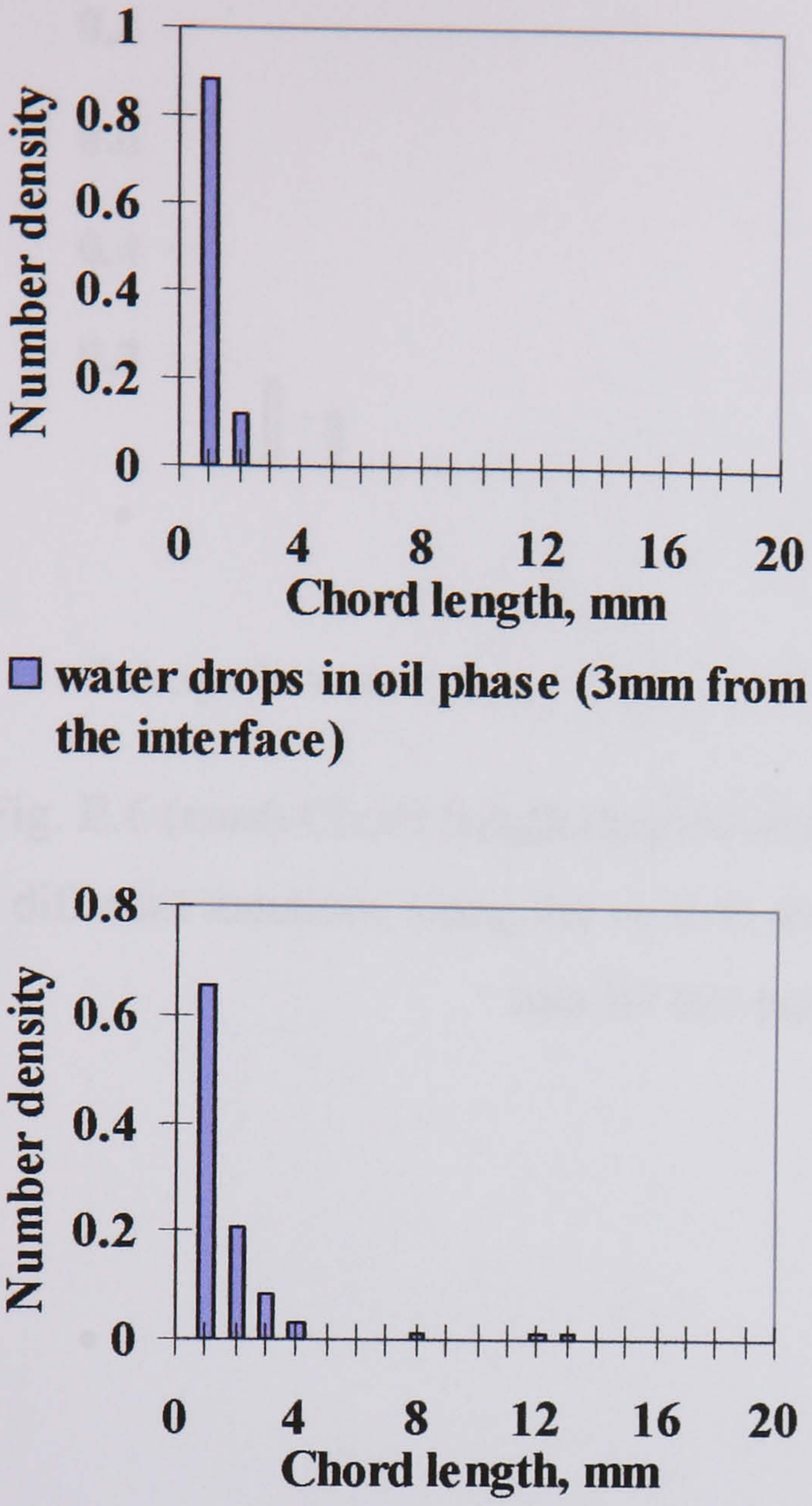

water drops in oil phase (3mm from the interface)

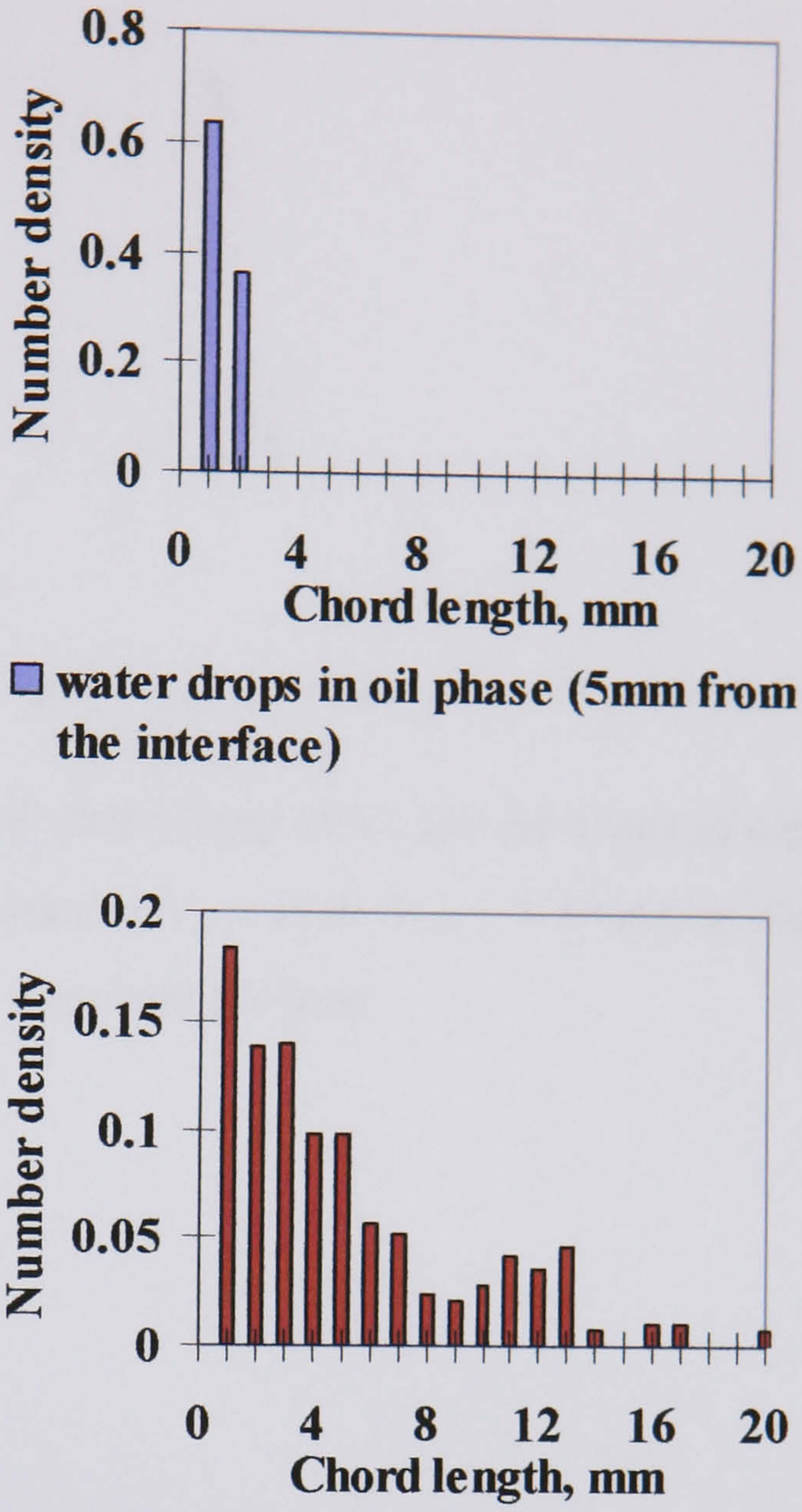

water drops in oil phase (5mm from the interface)

water drops in oil phase (7mm from the interface)

oil drops in water phase (3mm from the interface)

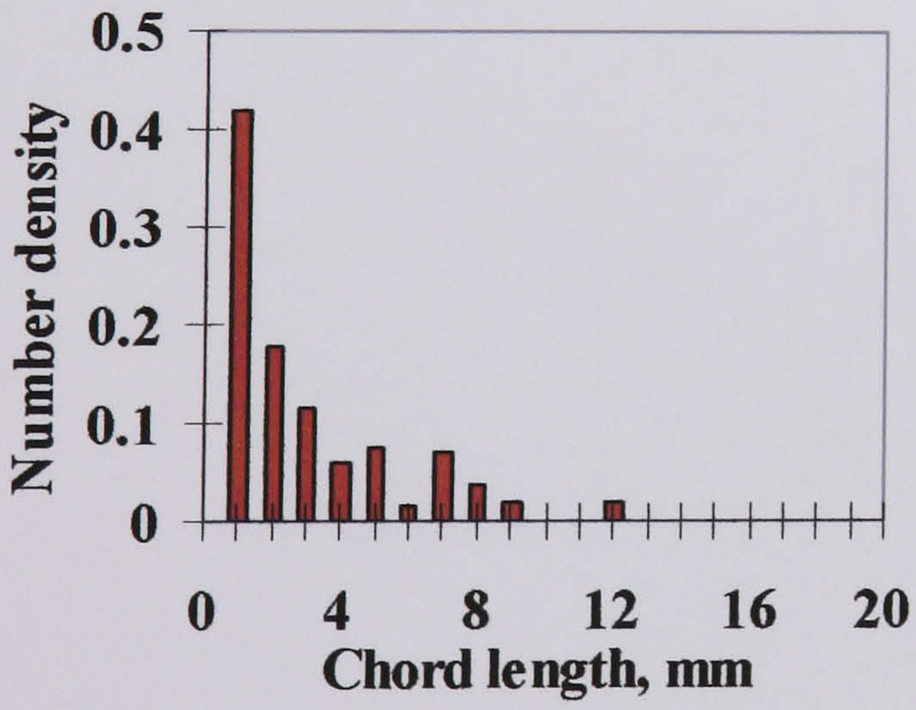

oil drops in water phase (5mm from the interface)

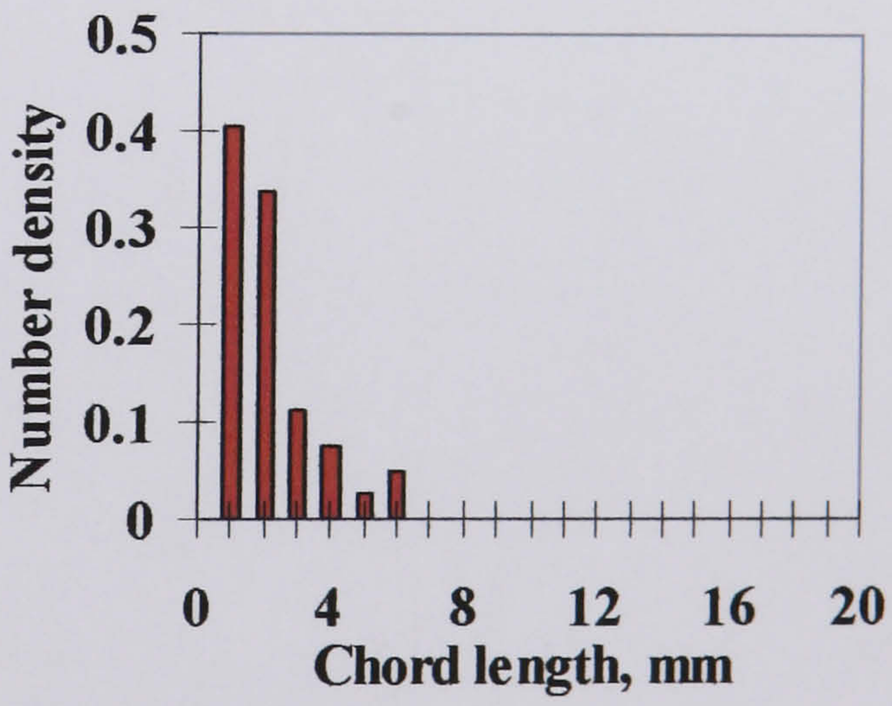

oil drops in water phase (7mm from the interface)

Fig. E.6 Chord length distributions of water drops in oil and oil drops in water at different locations along the vertical diameter at U_{so} = 0.80, U_{sw} = 1.10 m/s in the 38 mm ID test pipe, 7 m from the inlet.

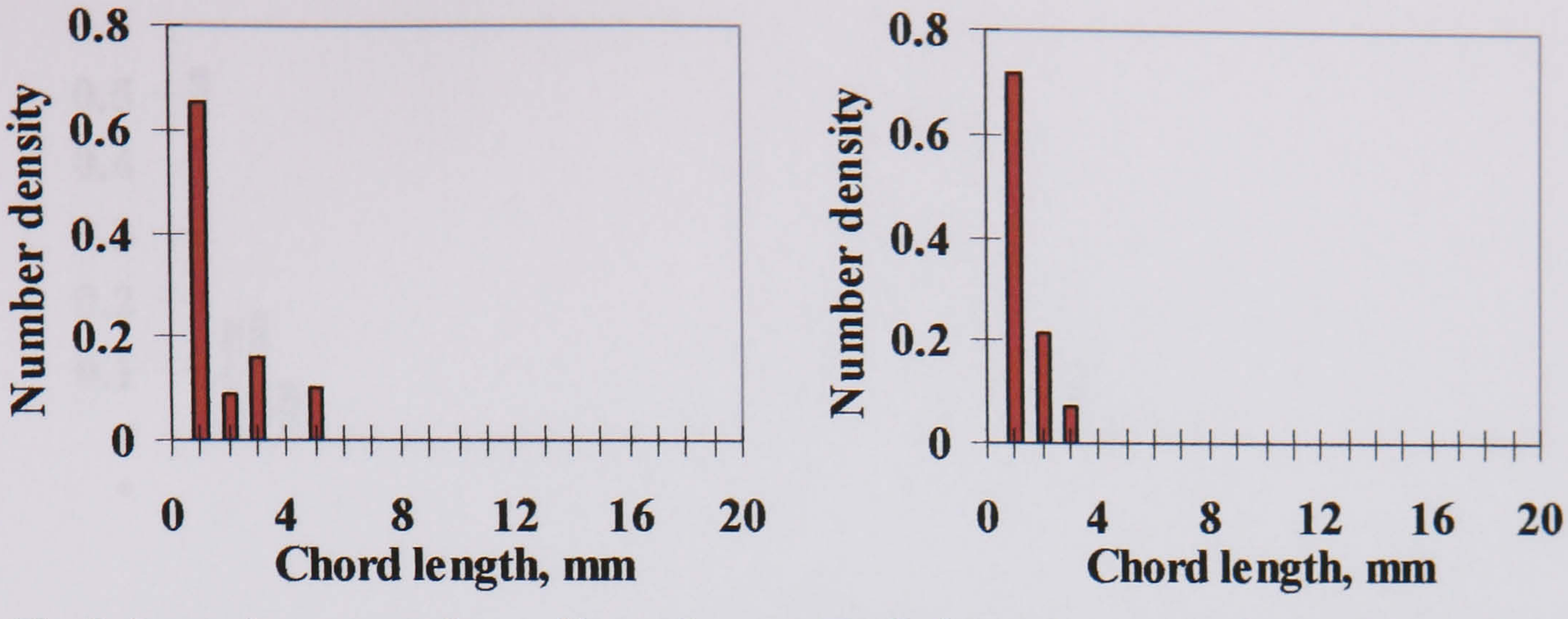

■ **oil drops in water phase (9mm from the interface)**

■ **oil drops in water phase (11mm from the interface)**

Fig. E.6 (*cont*) Chord length distributions of water drops in oil and oil drops in water at different locations along the vertical diameter at U_{so} = 0.80, U_{sw} = 1.10 m/s in the 38 mm ID test pipe, 7 m from the inlet.

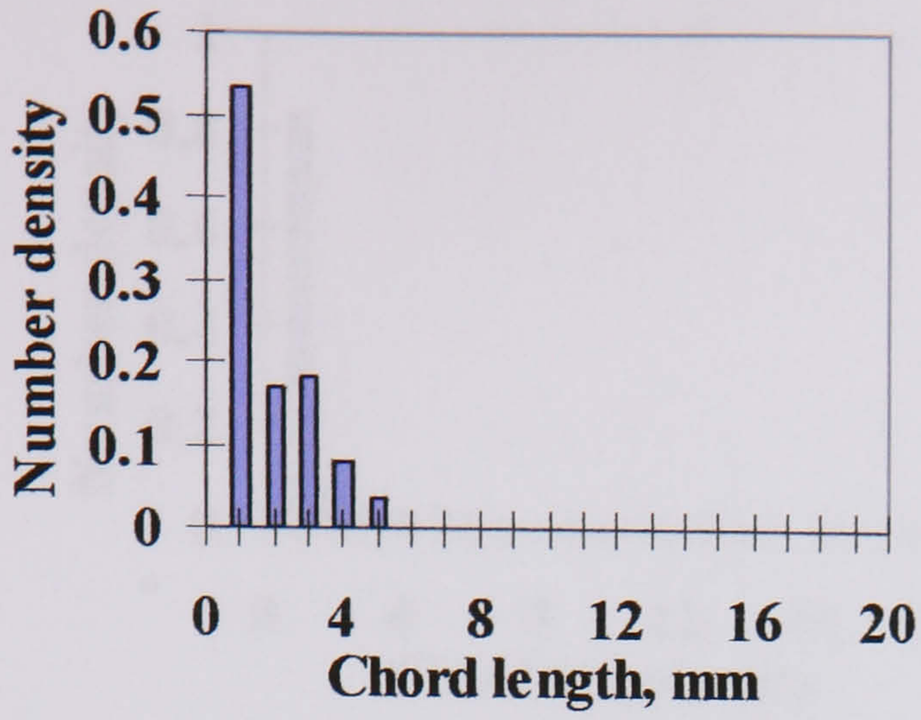

■ water drops in oil phase (3mm from the interface)

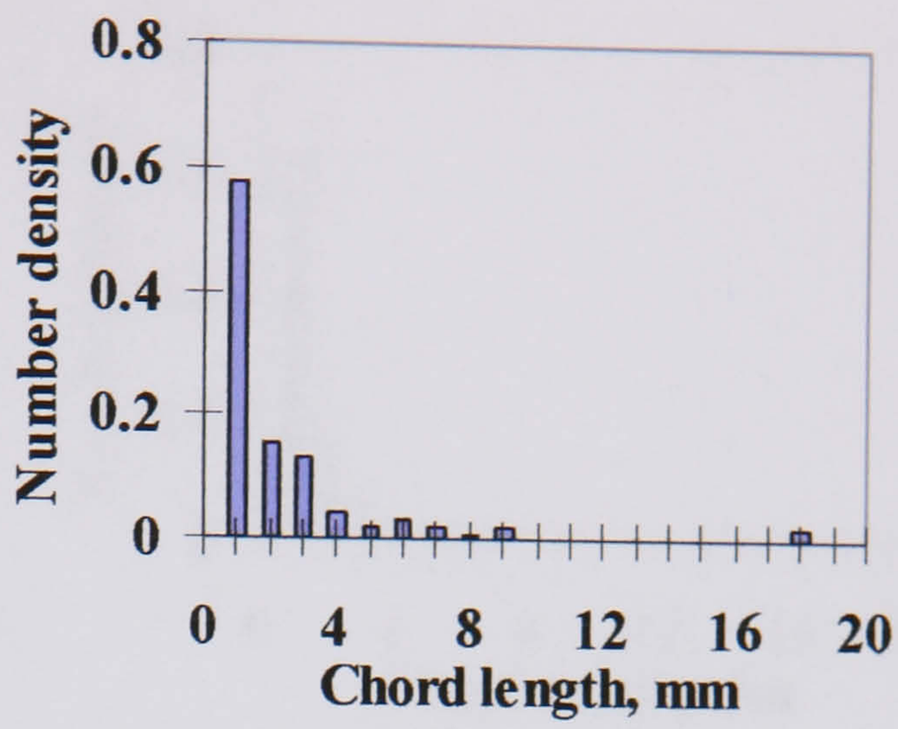

■ water drops in oil phase (5mm from the interface)

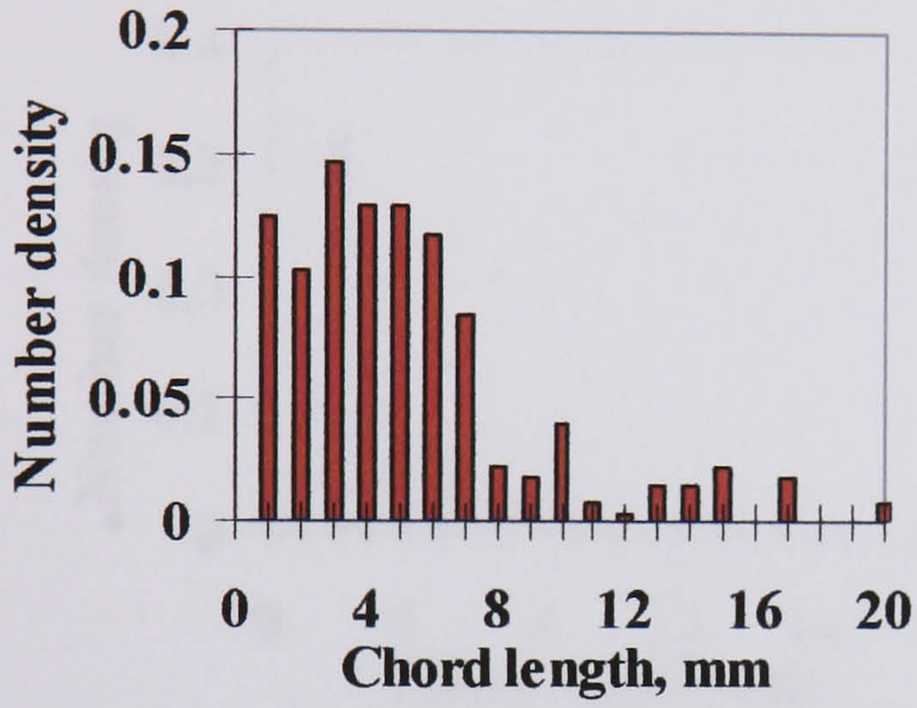

■ oil drops in water phase (3mm from the interface)

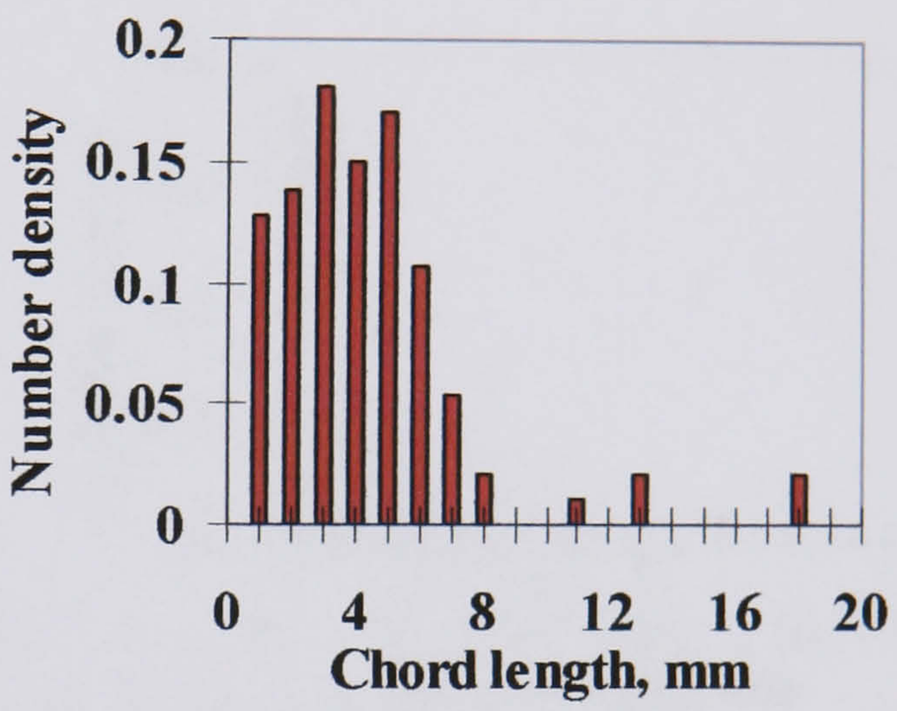

■ oil drops in water phase (5mm from the interface)

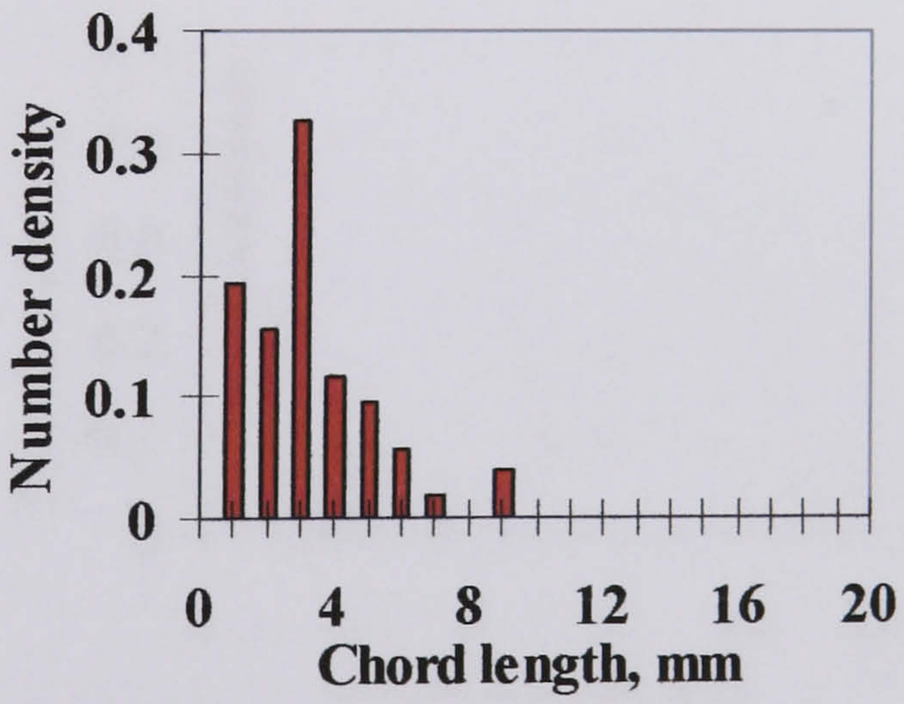

■ oil drops in water phase (7mm from the interface)

Fig. E.7 Chord length distributions of water drops in oil and oil drops in water at different locations along the vertical diameter at U_{so} = 1.10, U_{sw} = 0.20 m/s in the 38 mm ID test pipe, 7 m from the inlet.

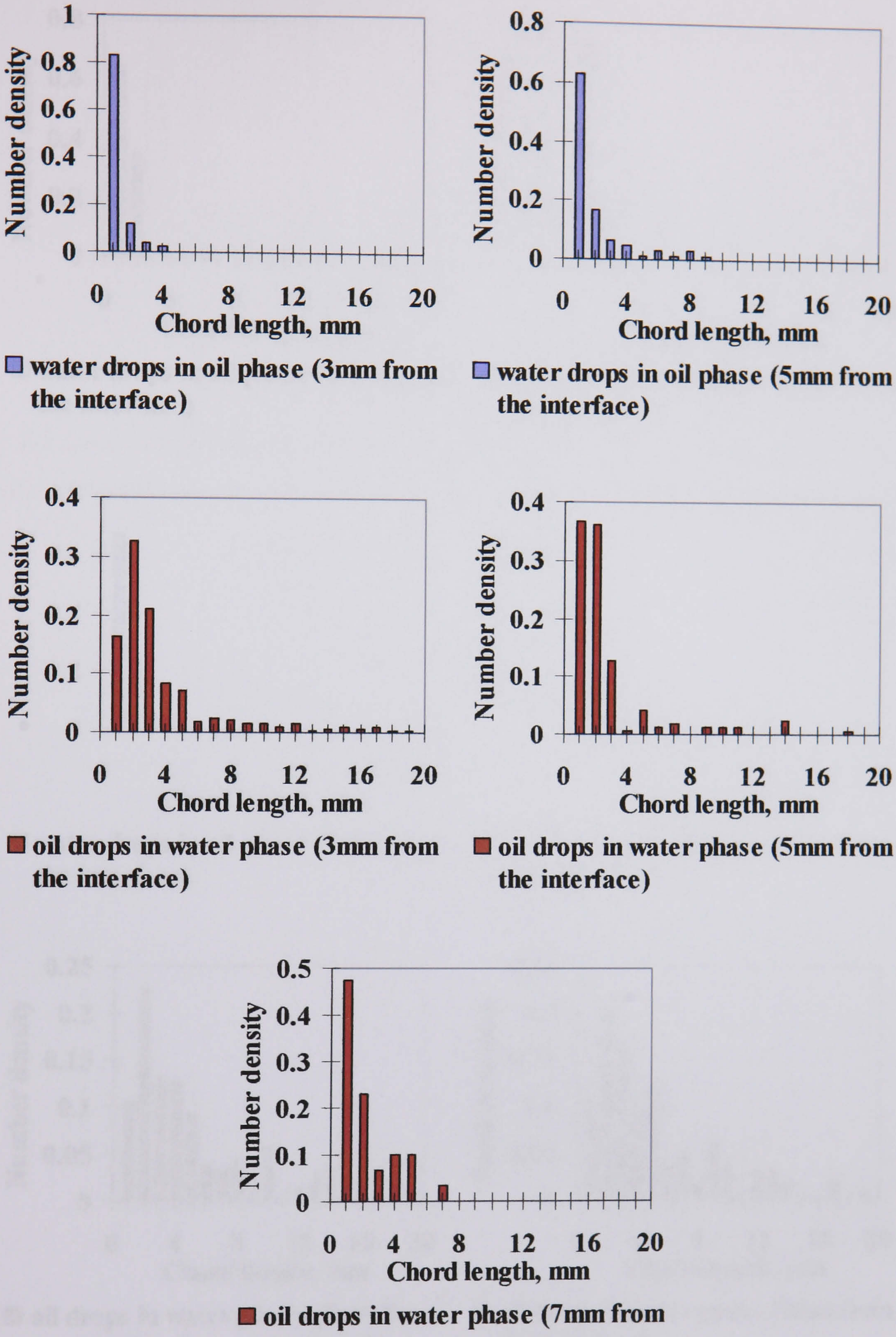

Fig. E.8 Chord length distributions of water drops in oil and oil drops in water at different locations along the vertical diameter at U_{so} = 1.10, U_{sw} = 0.50 m/s in the 38 mm ID test pipe, 7 m from the inlet.

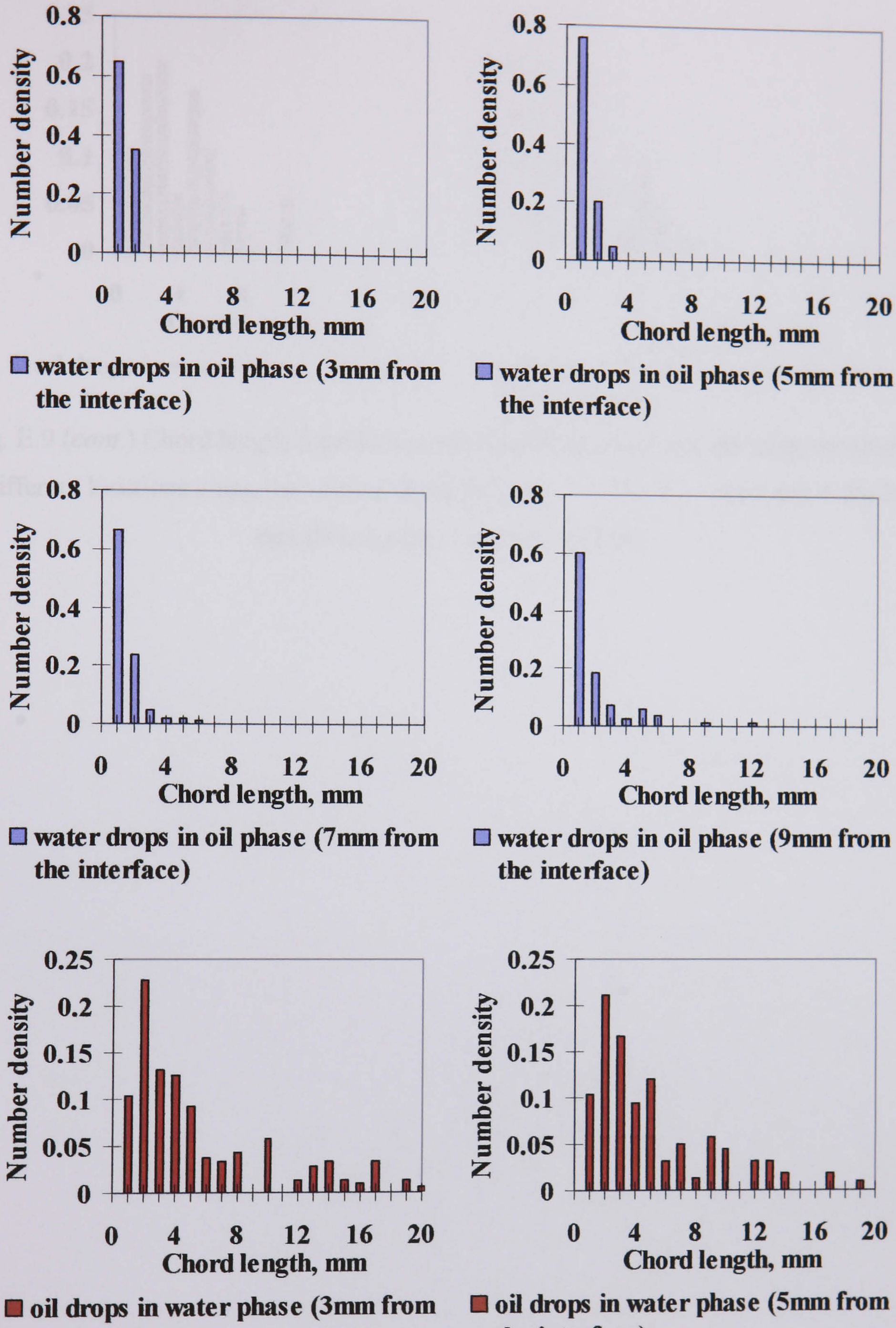

Fig. E.9 Chord length distributions of water drops in oil and oil drops in water at different locations along the vertical diameter at U_{so} = 1.10, U_{sw} = 0.80 m/s in the 38 mm ID test pipe, 7 m from the inlet.

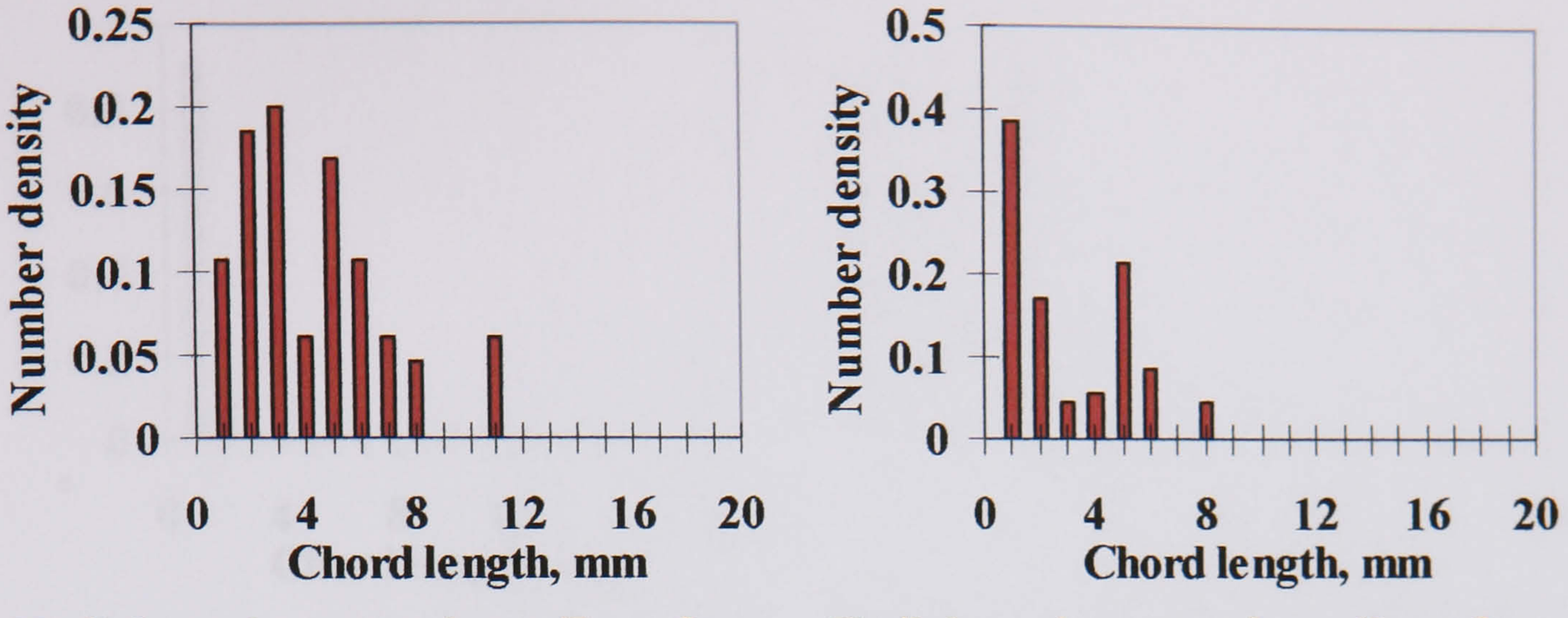

oil drops in water phase (7mm from the interface)

oil drops in water phase (9mm from the interface)

Fig. E.9 (*cont.*) Chord length distributions of water drops in oil and oil drops in water at different locations along the vertical diameter at U_{so} = 1.10, U_{sw} = 0.80 m/s in the 38 mm ID test pipe, 7 m from the inlet.

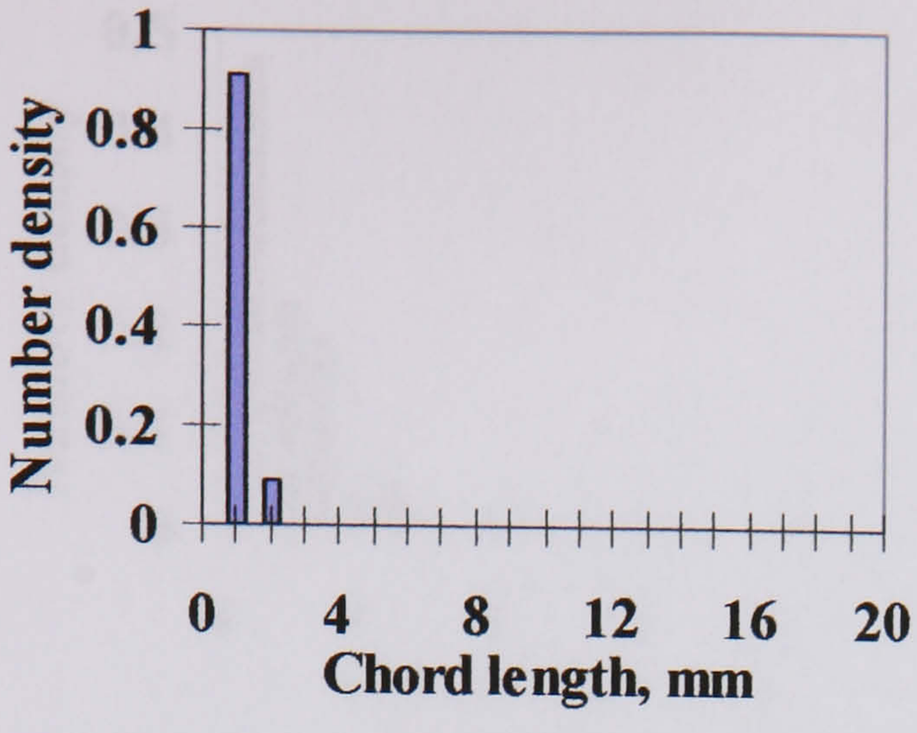

water drops in oil phase (3mm from the interface)

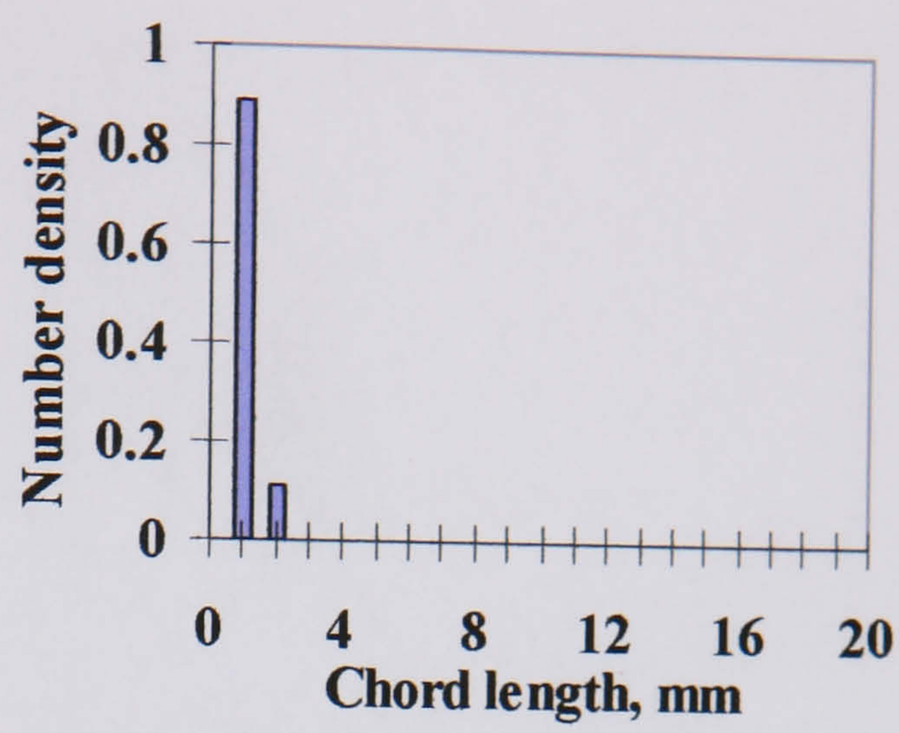

water drops in oil phase (5mm from the interface)

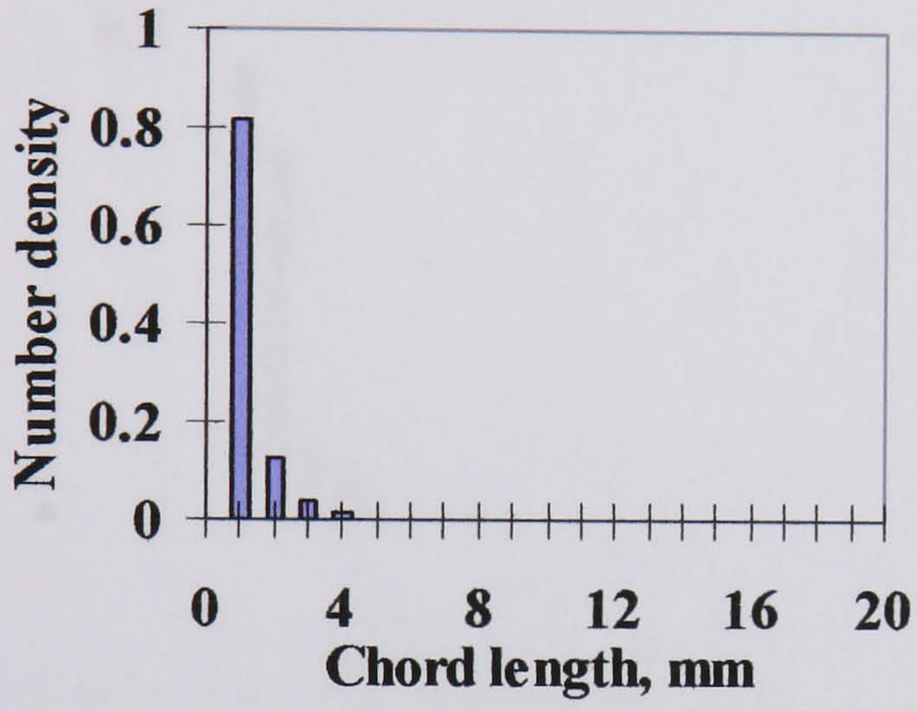

water drops in oil phase (7mm from the interface)

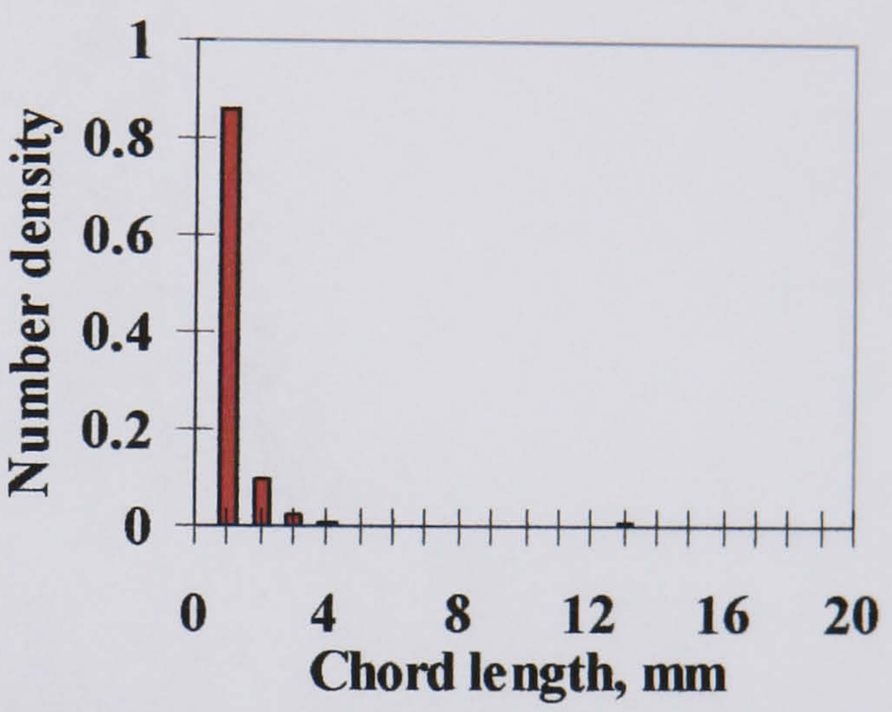

oil drops in water phase (3mm from the interface)

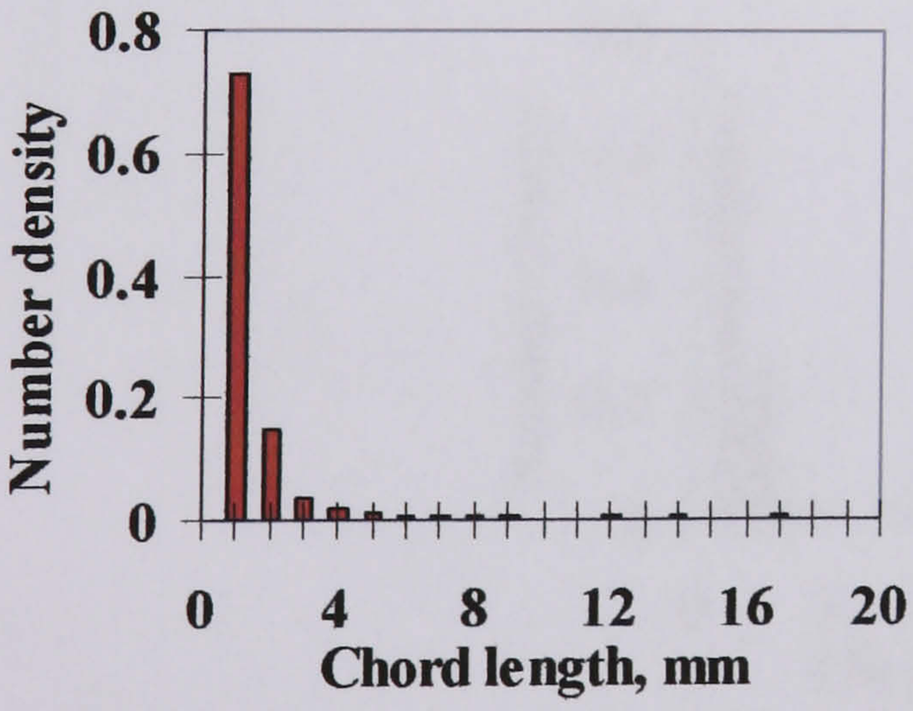

oil drops in water phase (5mm from the interface)

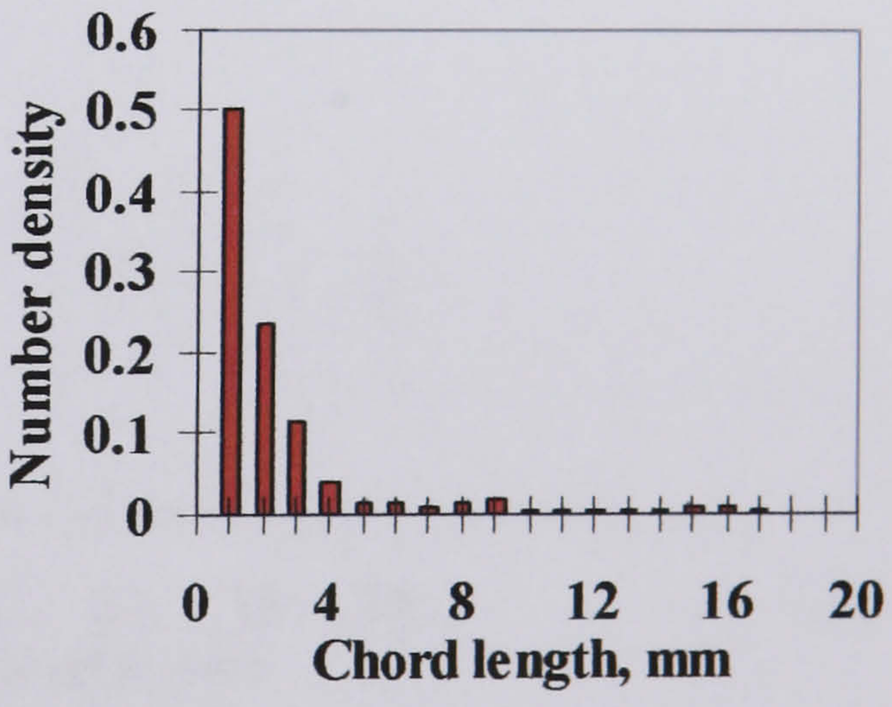

oil drops in water phase (7mm from the interface)

Fig. E.10 Chord length distributions of water drops in oil and oil drops in water at different locations along the vertical diameter at U_{so} = 1.10, U_{sw} = 1.10 m/s in the 38 mm ID test pipe, 7 m from the inlet.

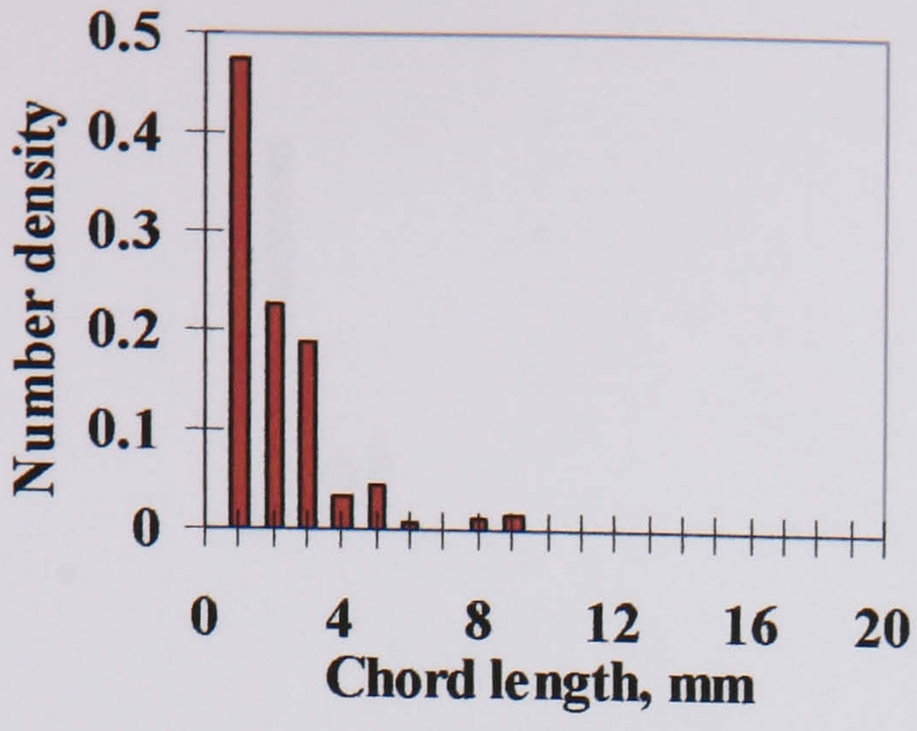

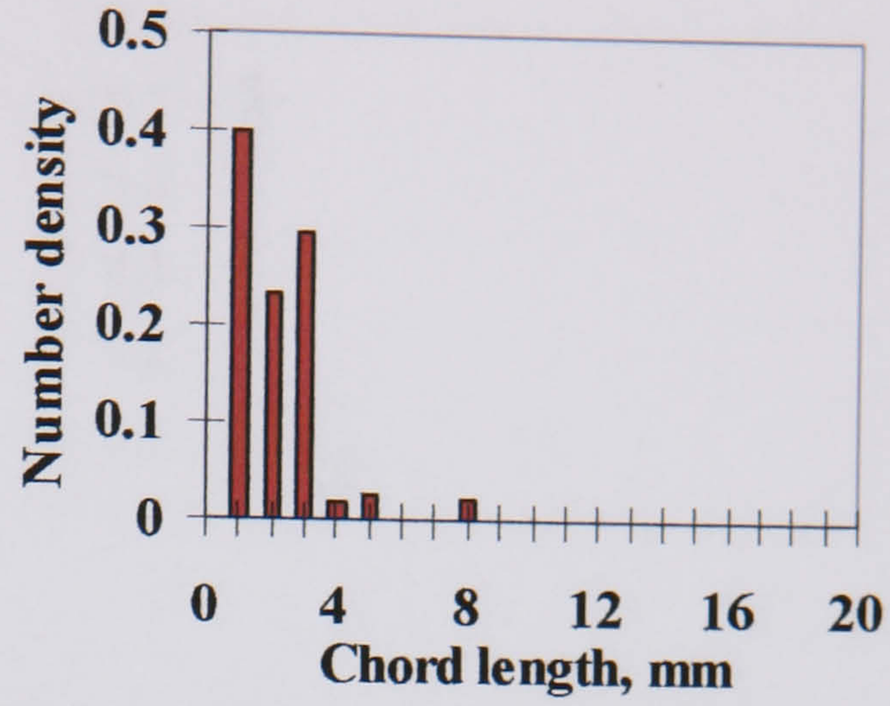

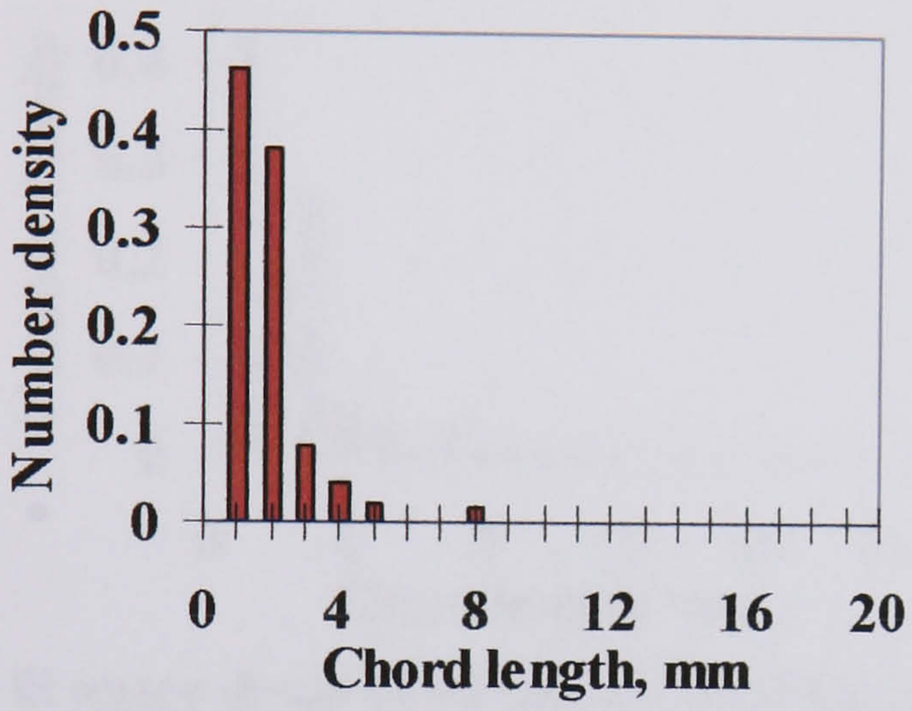

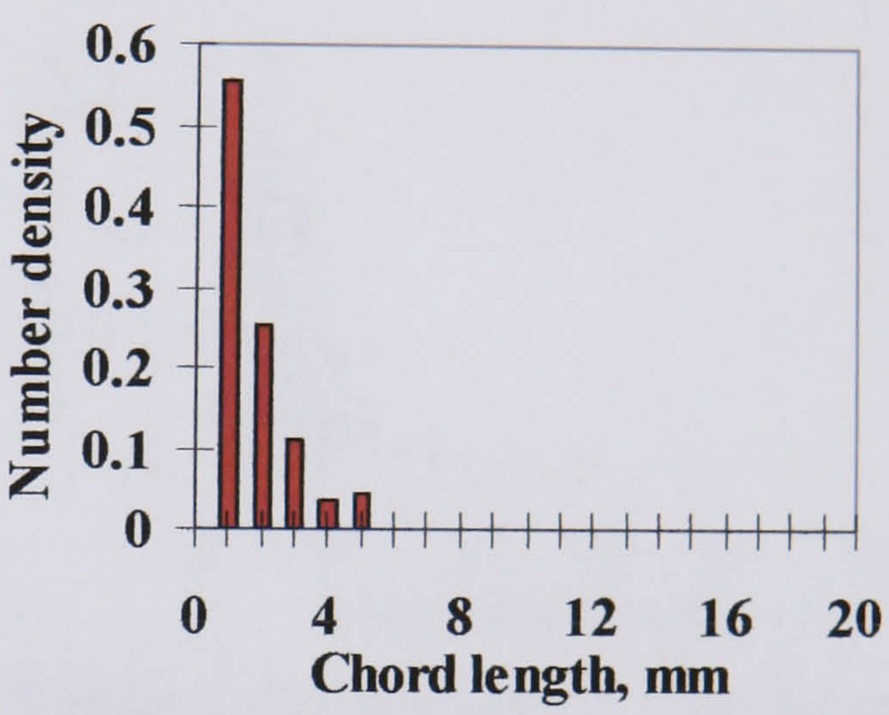

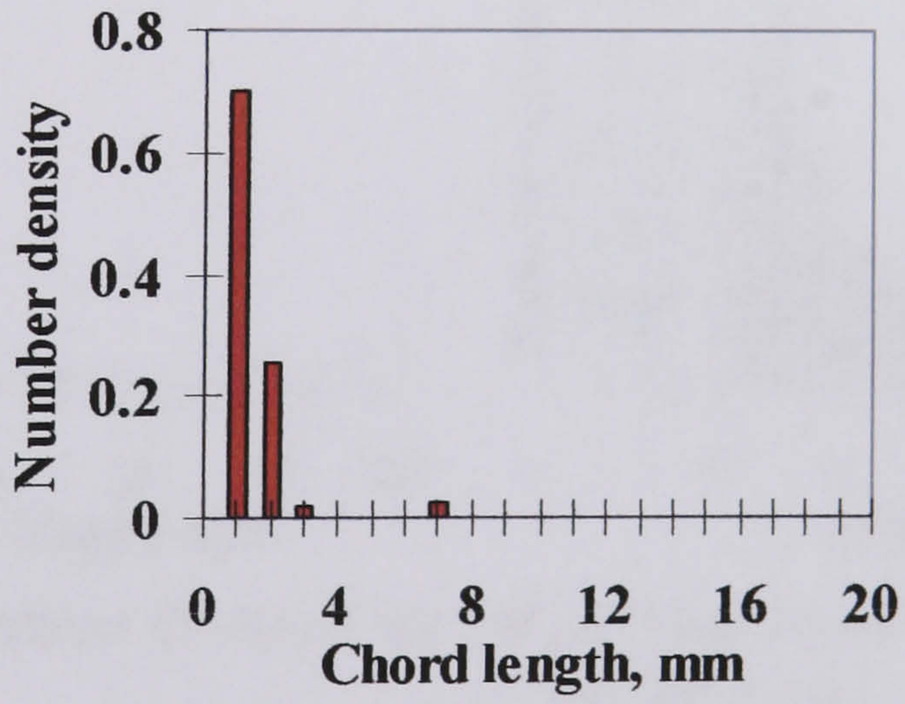

Fig. E.10 (*cont.*) Chord length distributions of water drops in oil and oil drops in water at different locations along the vertical diameter at U_{so} = 1.10, U_{sw} = 1.10 m/s in the 38 mm ID test pipe, 7 m from the inlet.

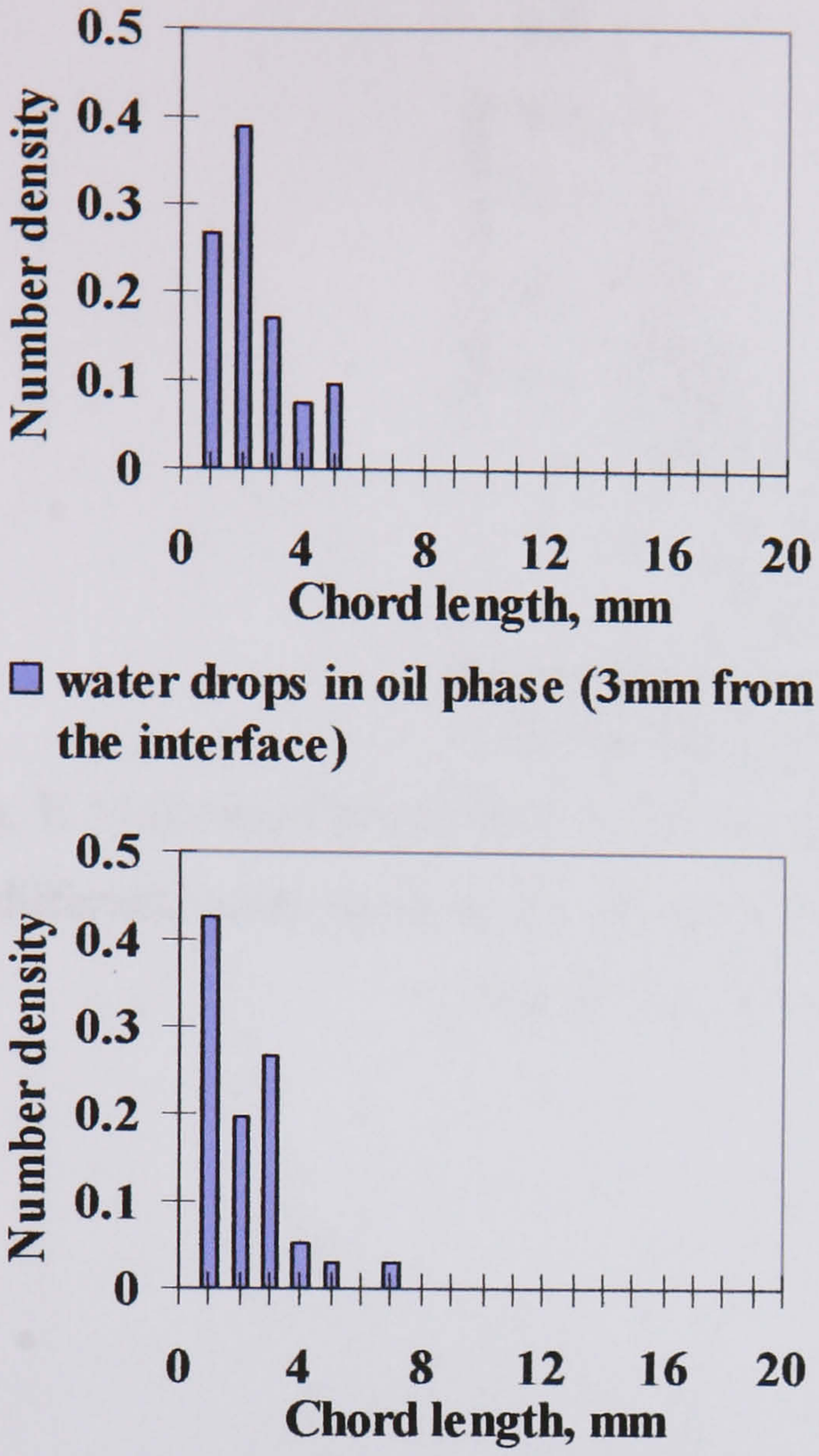

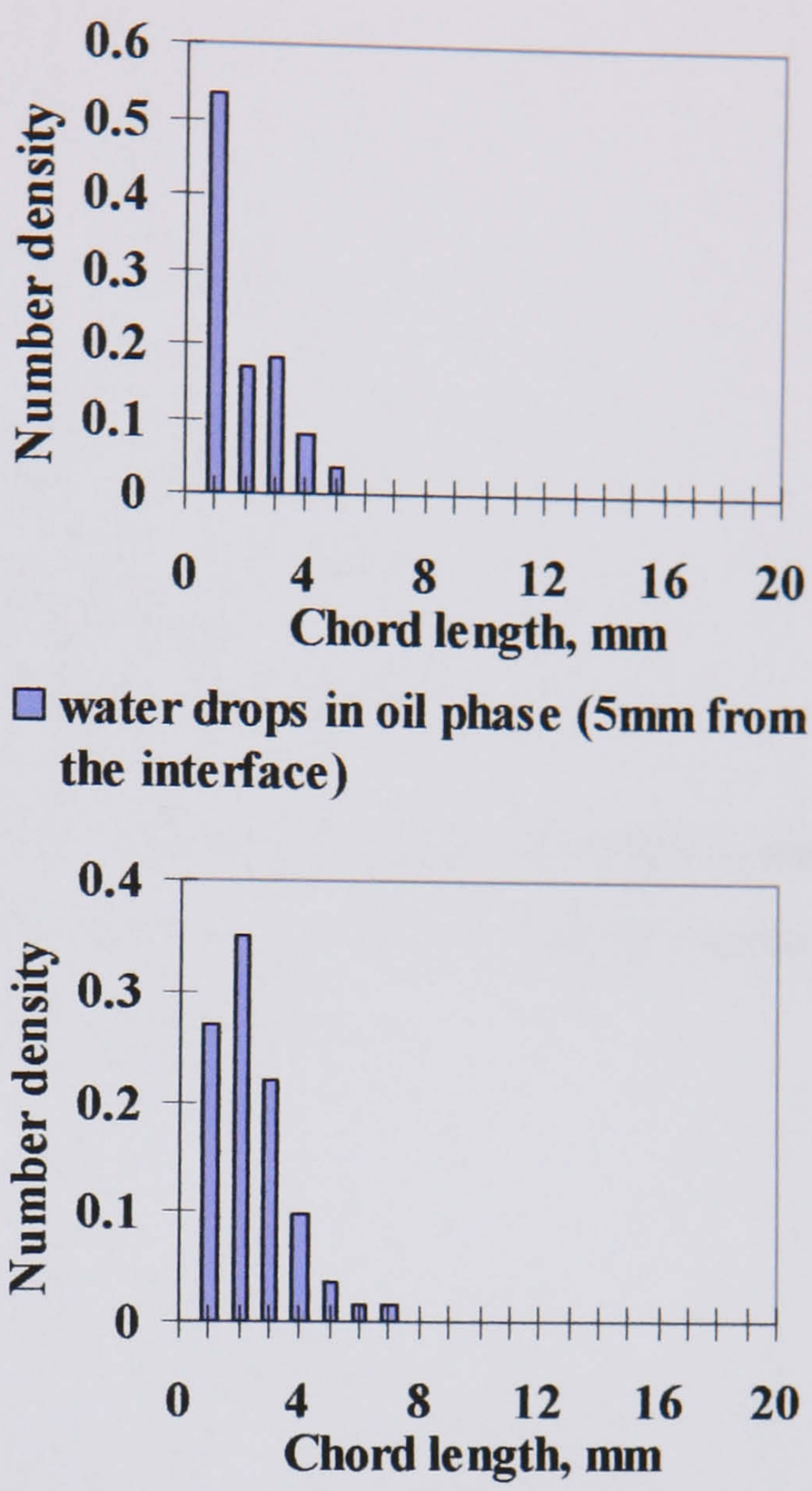

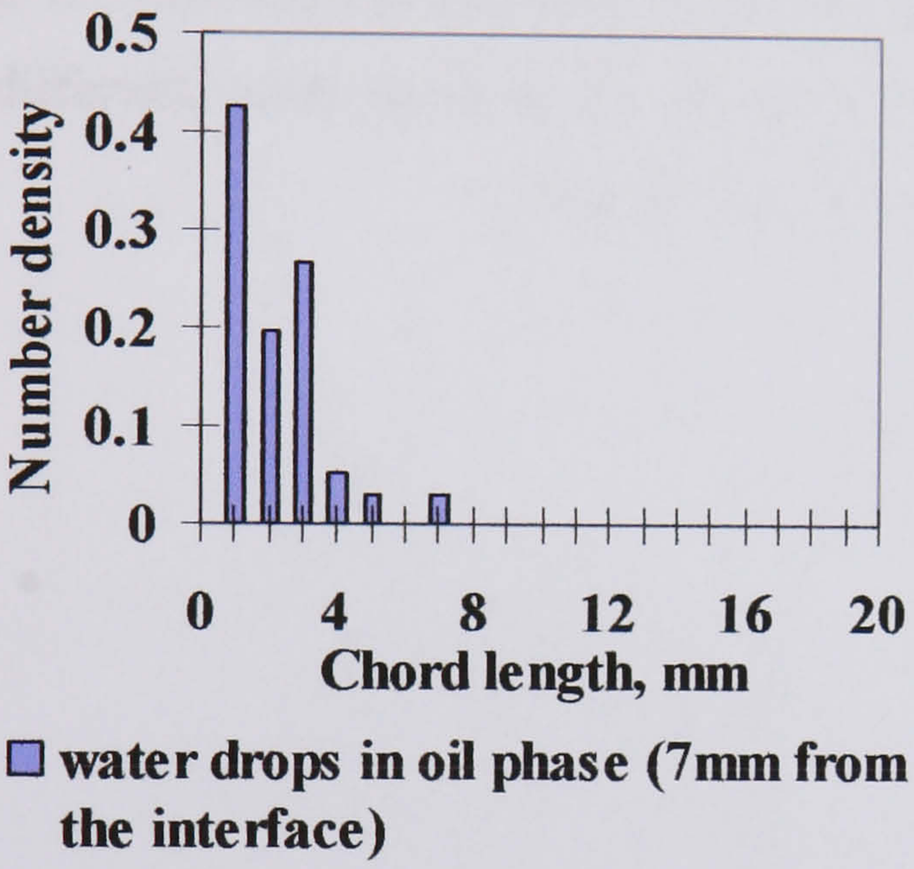

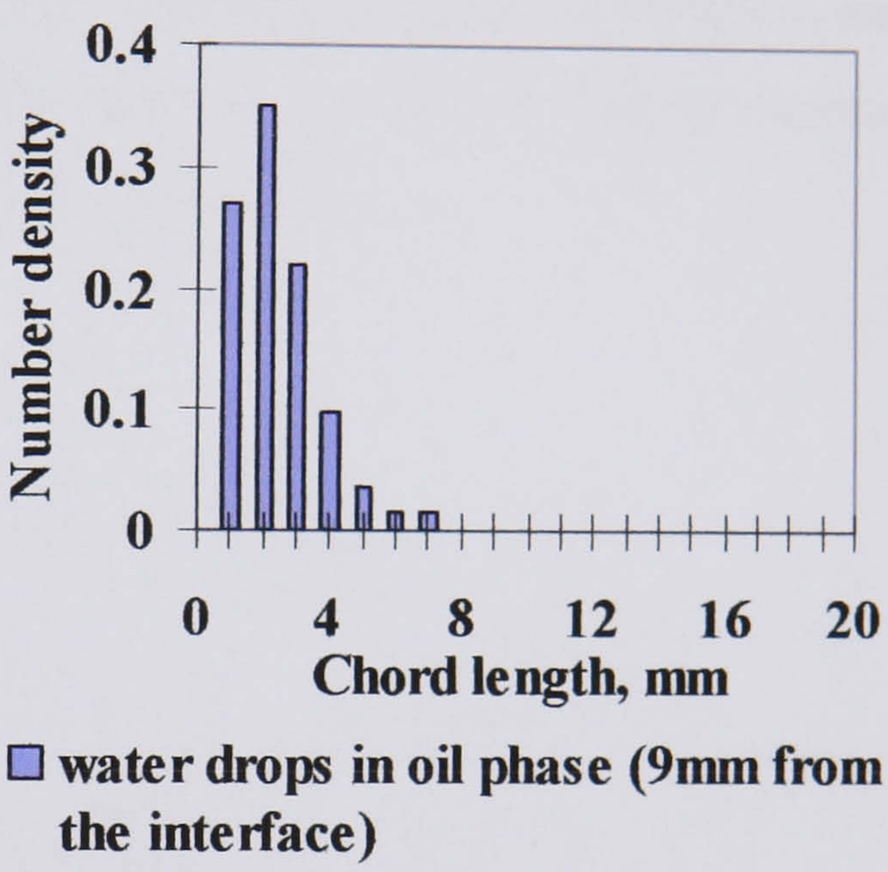

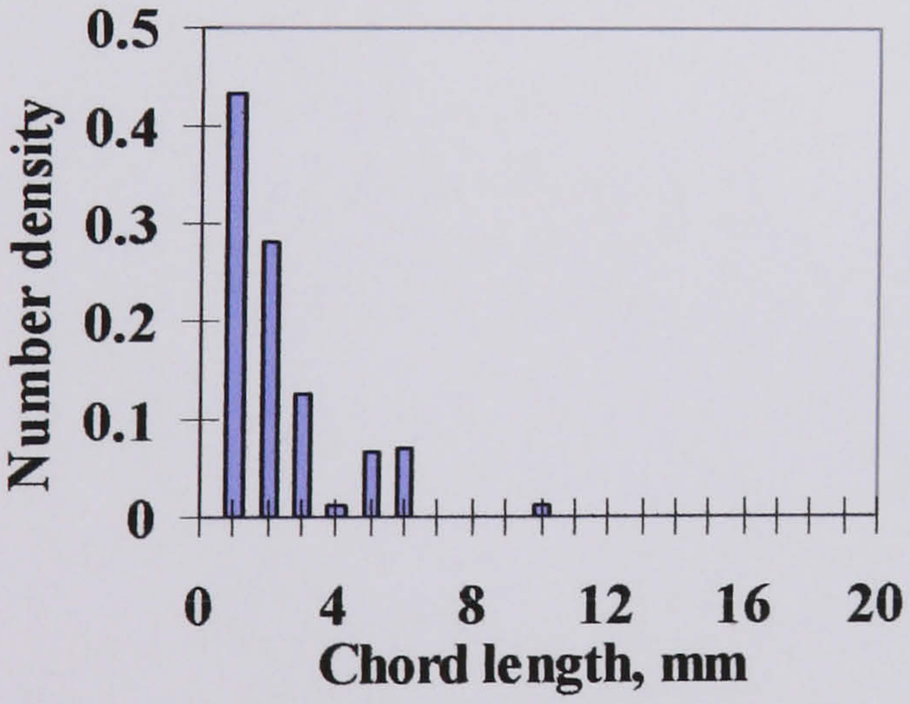

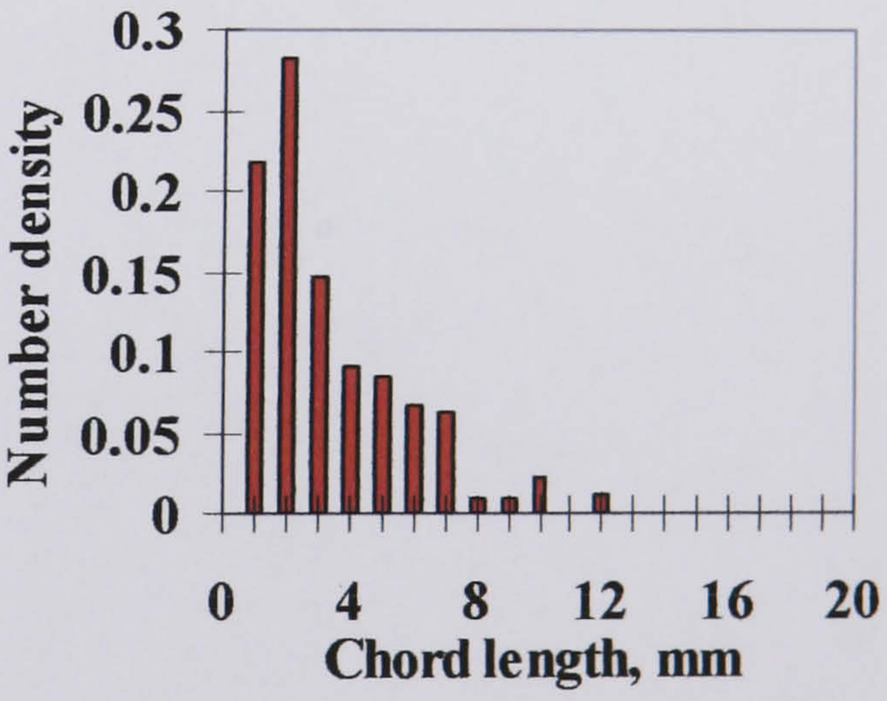

Fig. E.11 Chord length distributions of water drops in oil and oil drops in water at different locations along the vertical diameter at U_{so} = 1.40, U_{sw} = 0.20 m/s in the 38 mm ID test pipe, 7 m from the inlet.

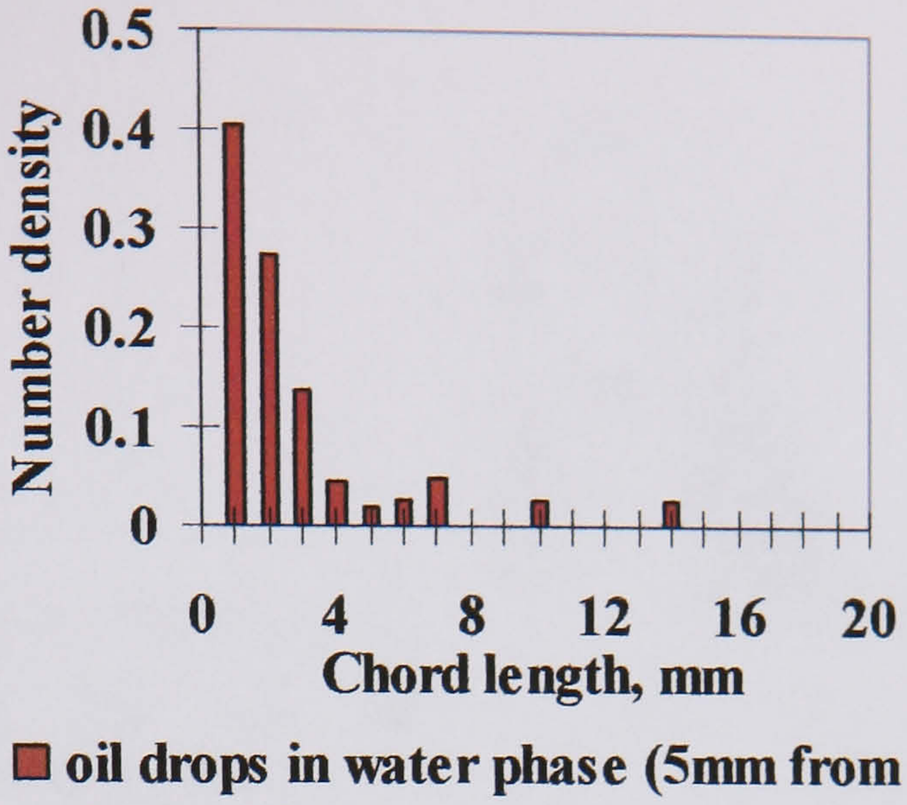

Fig. E.11 (*cont.*) Chord length distributions of water drops in oil and oil drops in water at different locations along the vertical diameter at U_{so} = 1.40, U_{sw} = 0.20 m/s in the 38 mm ID test pipe, 7 m from the inlet.

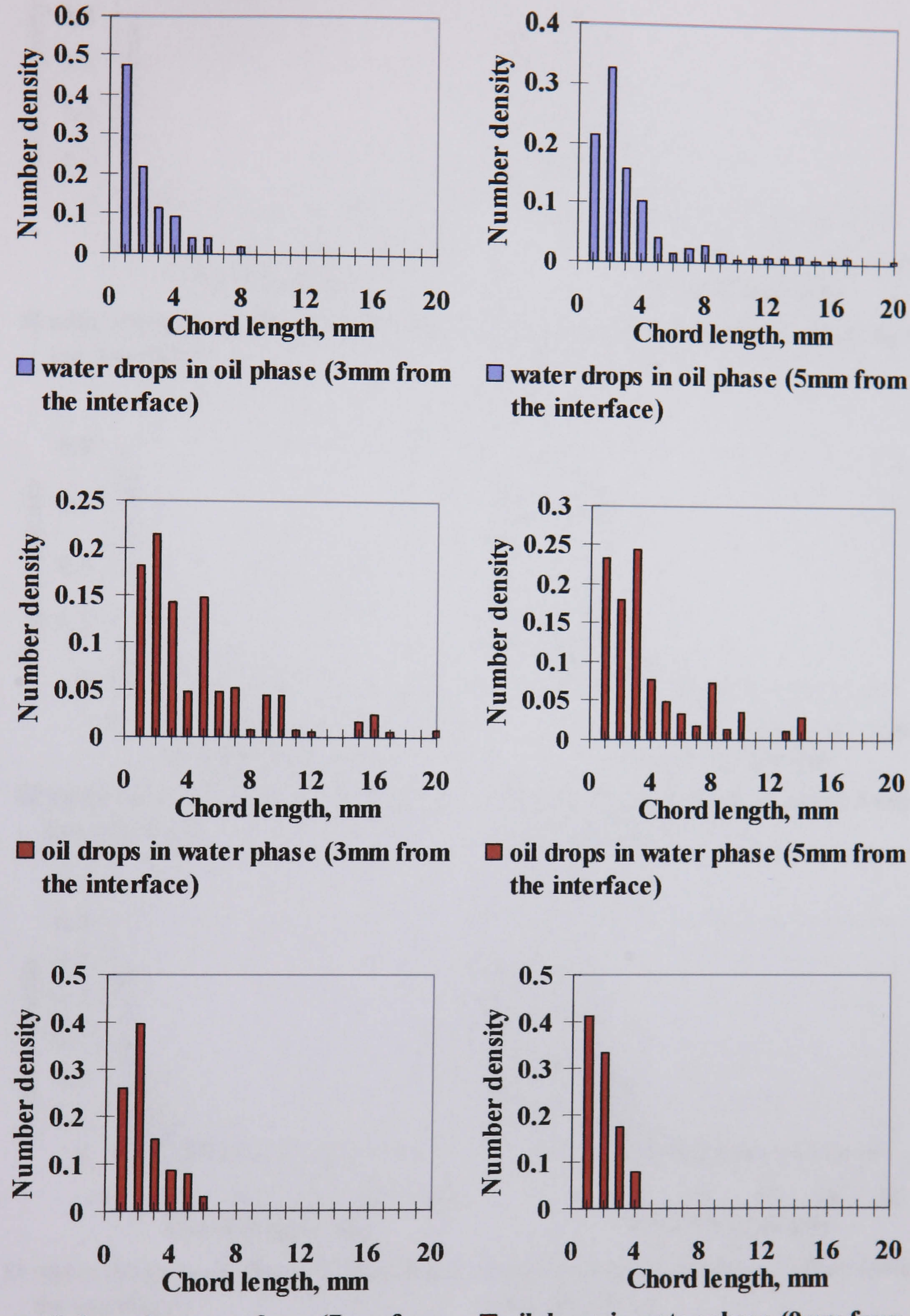

Fig. E.12 Chord length distributions of water drops in oil and oil drops in water at different locations along the vertical diameter at U_{so} = 1.40, U_{sw} = 0.50 m/s in the 38 mm ID test pipe, 7 m from the inlet.

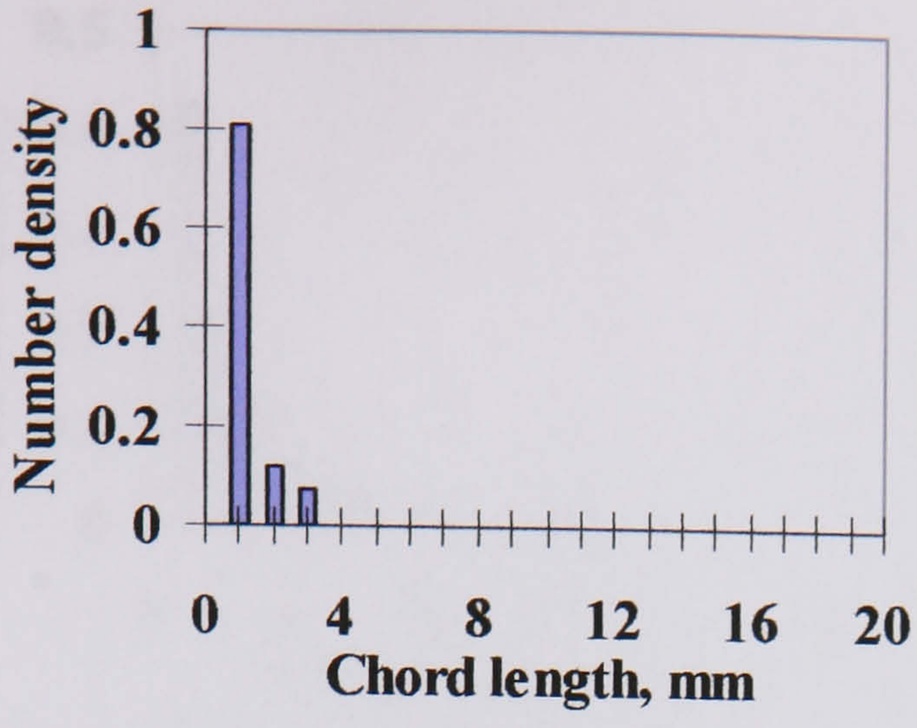

water drops in oil phase (3mm from the interface)

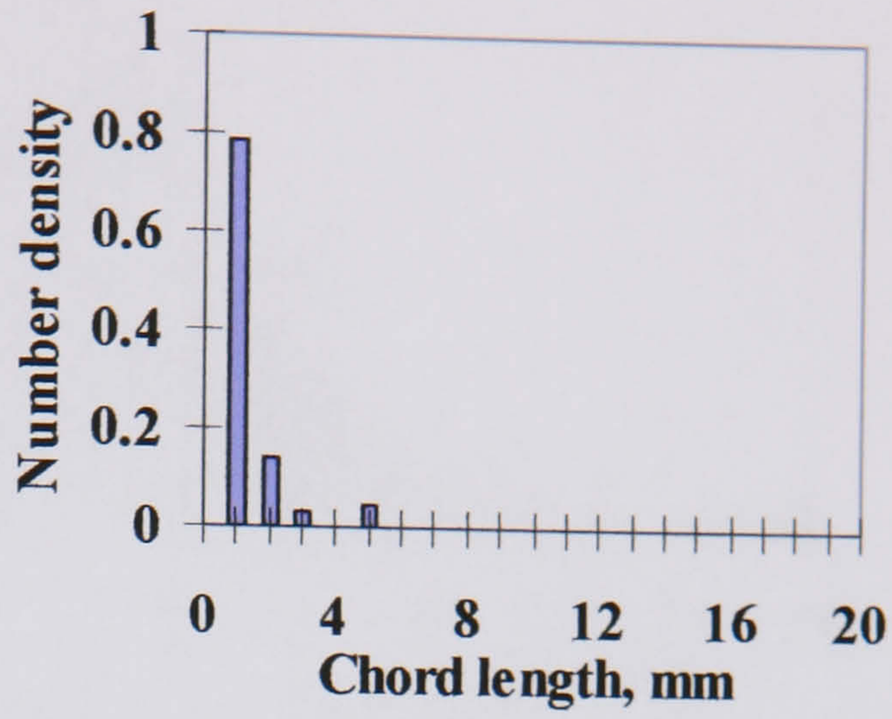

water drops in oil phase (5mm from the interface)

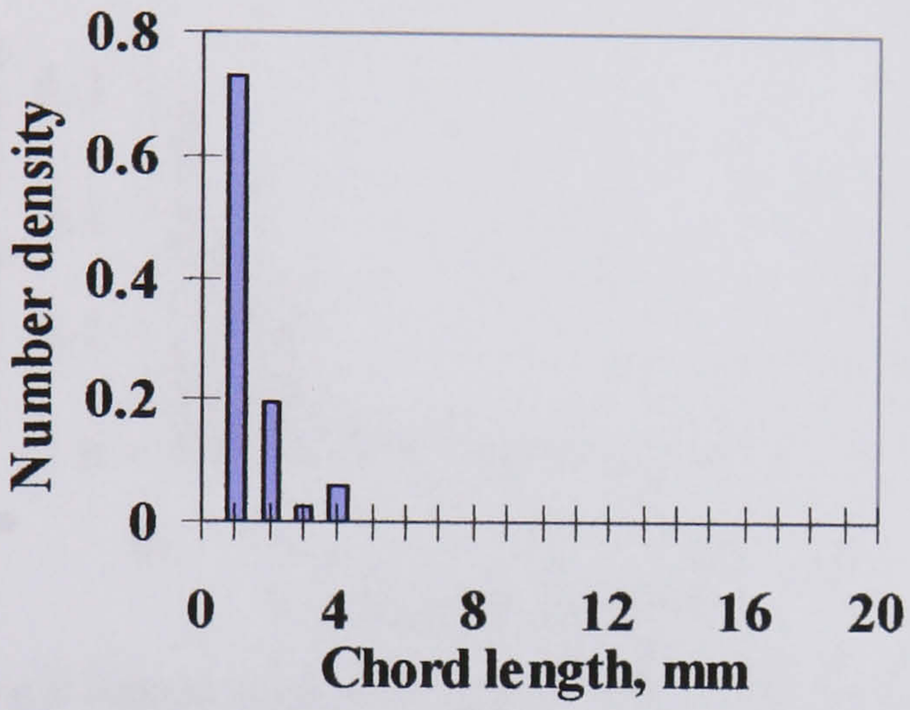

water drops in oil phase (7mm from the interface)

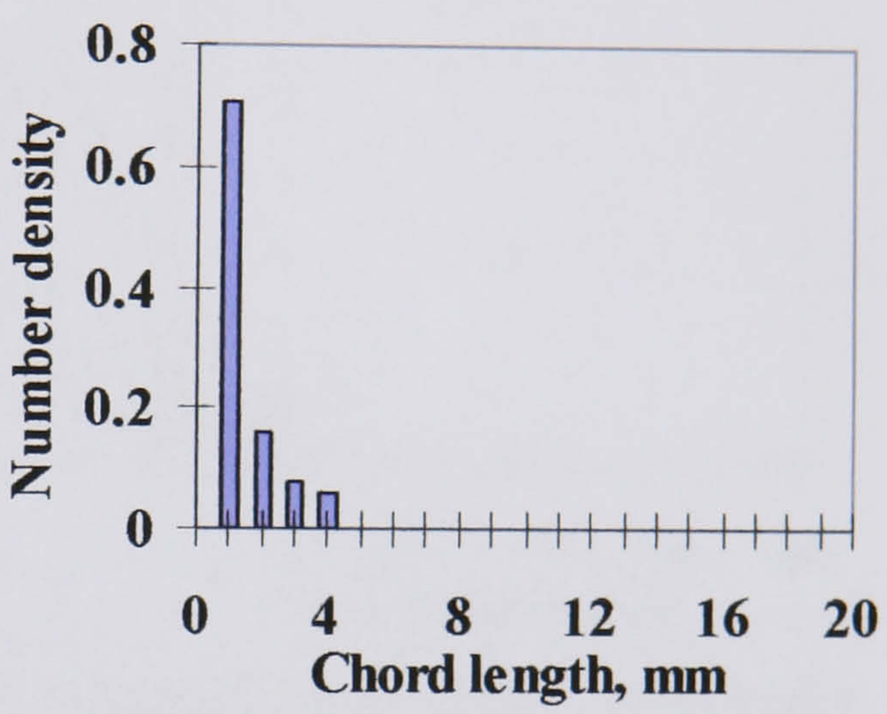

water drops in oil phase (9mm from the interface)

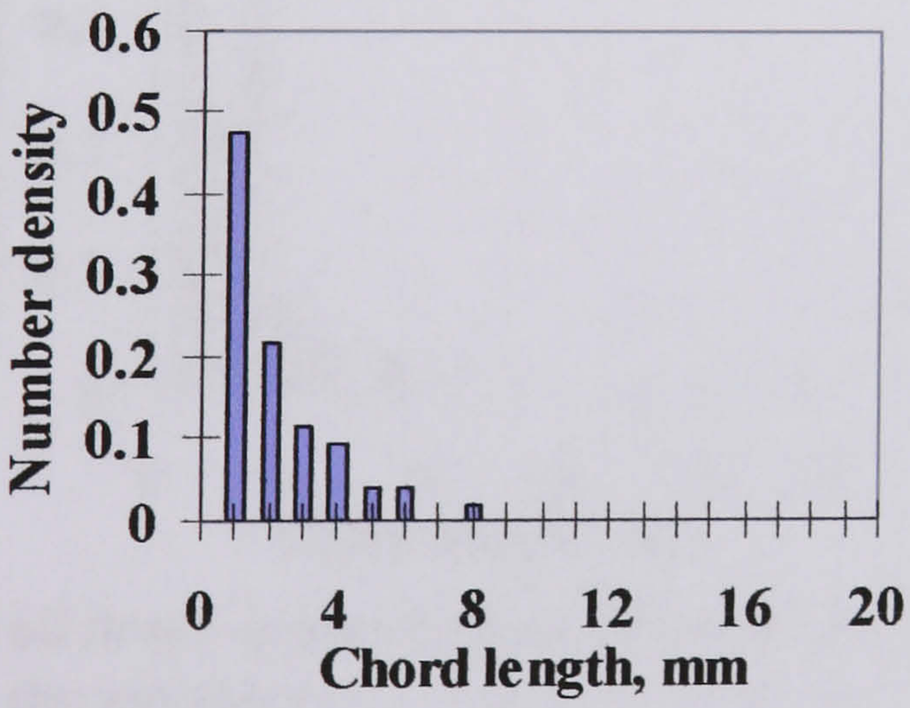

water drops in oil phase (11mm from the interface)

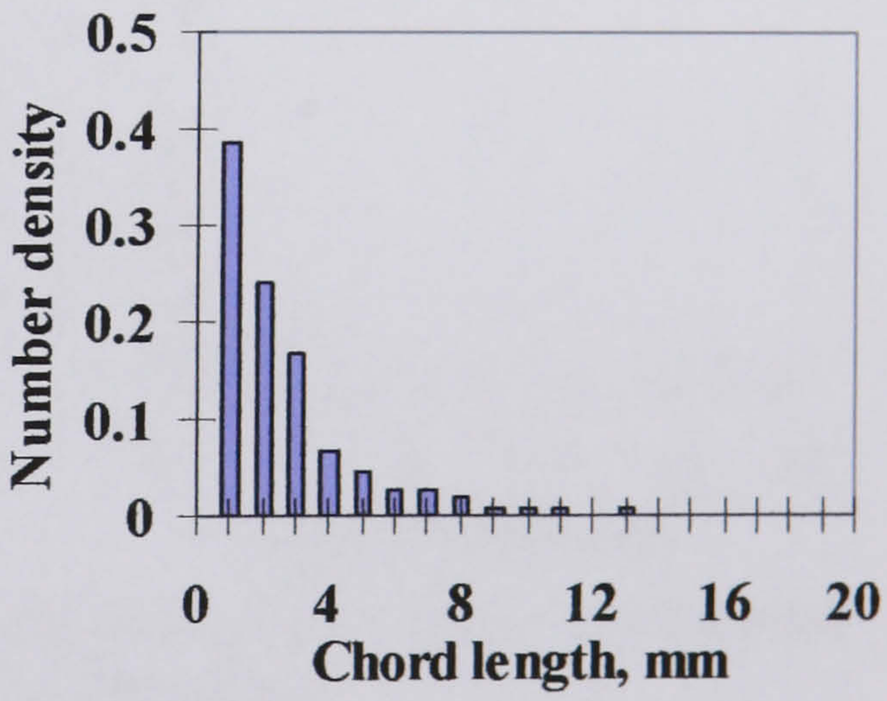

water drops in oil phase (13mm from the interface)

Fig. E.13 Chord length distributions of water drops in oil and oil drops in water at different locations along the vertical diameter at U_{so} = 1.40, U_{sw} = 0.80 m/s in the 38 mm ID test pipe, 7 m from the inlet.

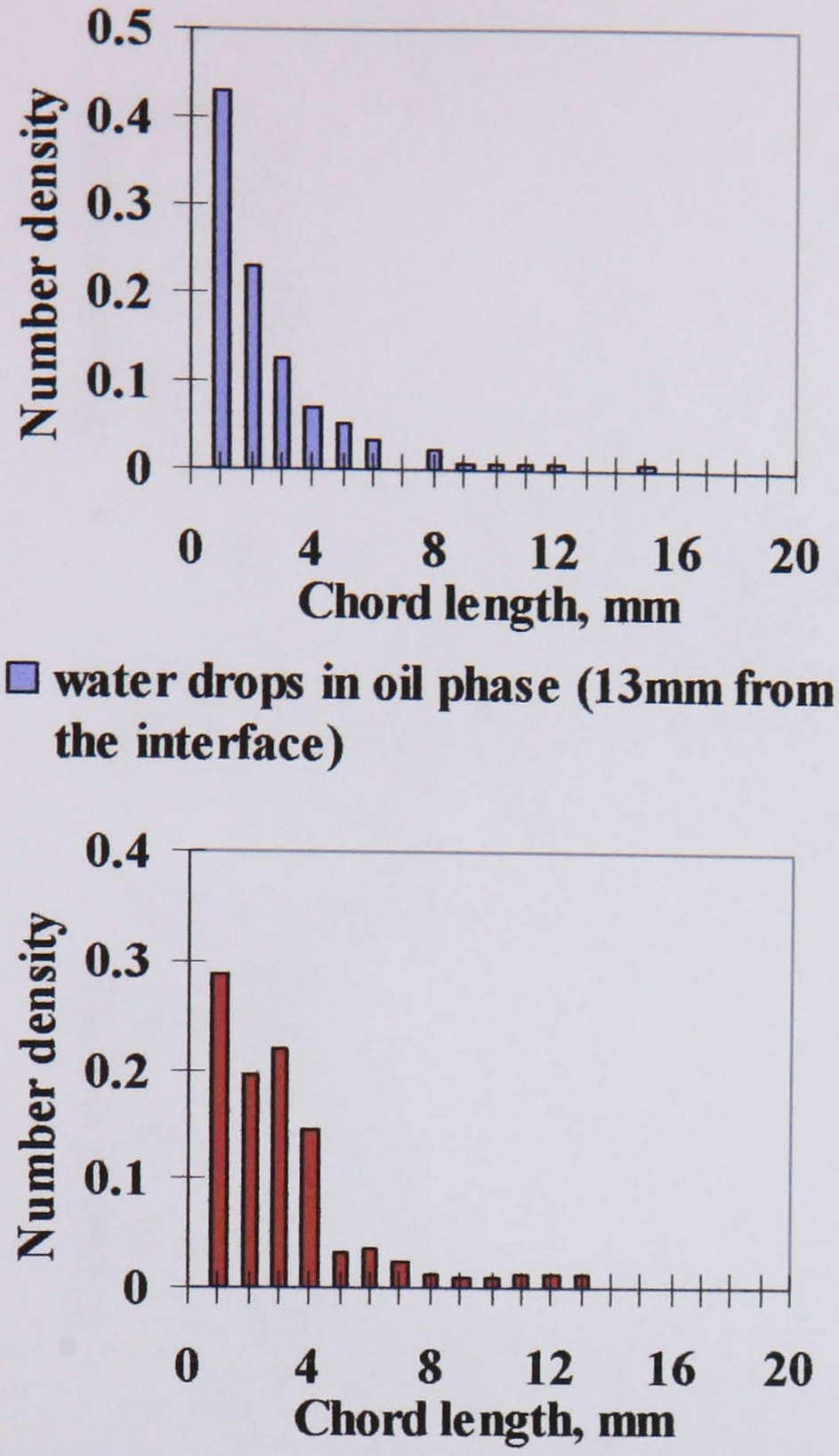

water drops in oil phase (13mm from the interface)

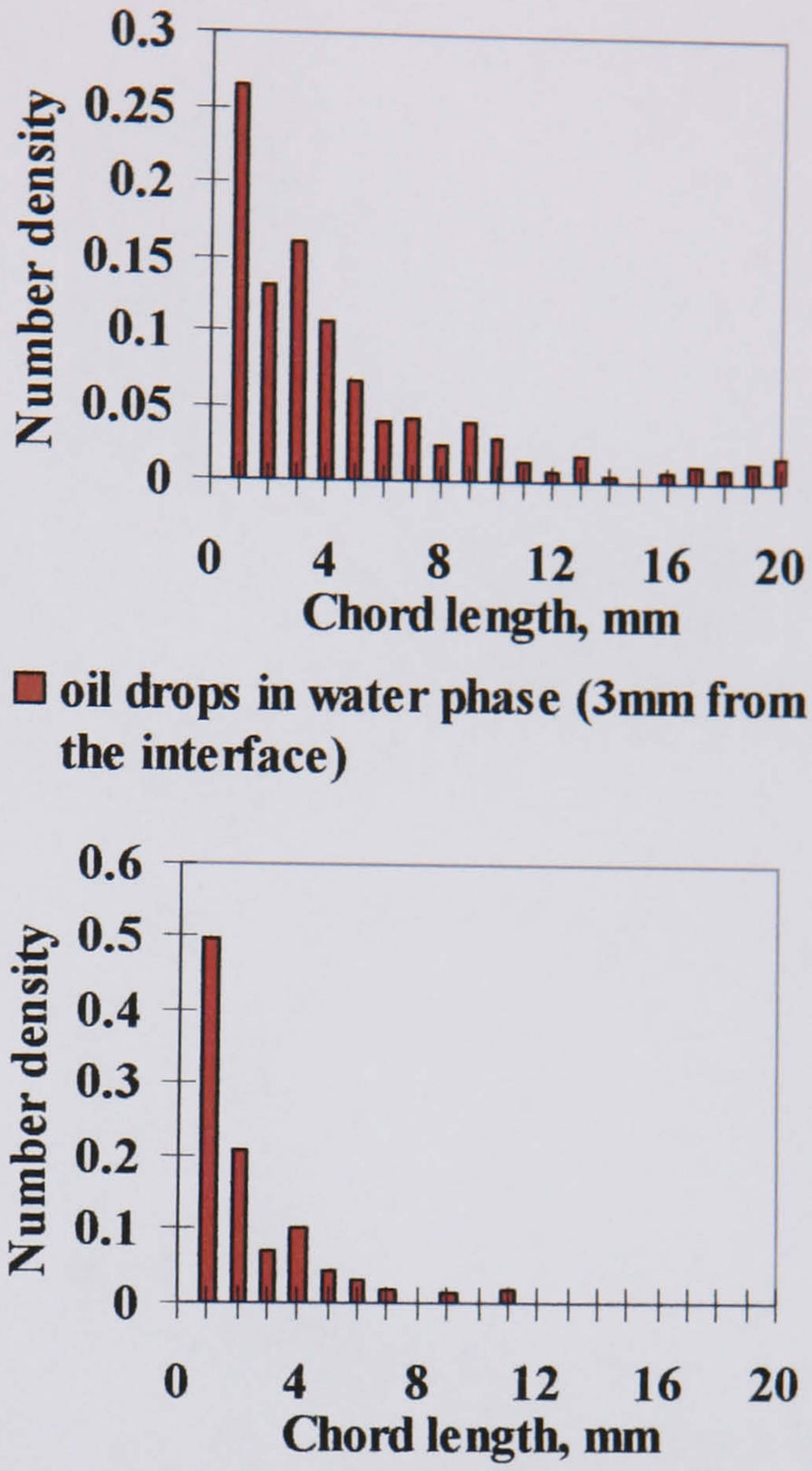

oil drops in water phase (3mm from the interface)

oil drops in water phase (5mm from the interface)

oil drops in water phase (7mm from the interface)

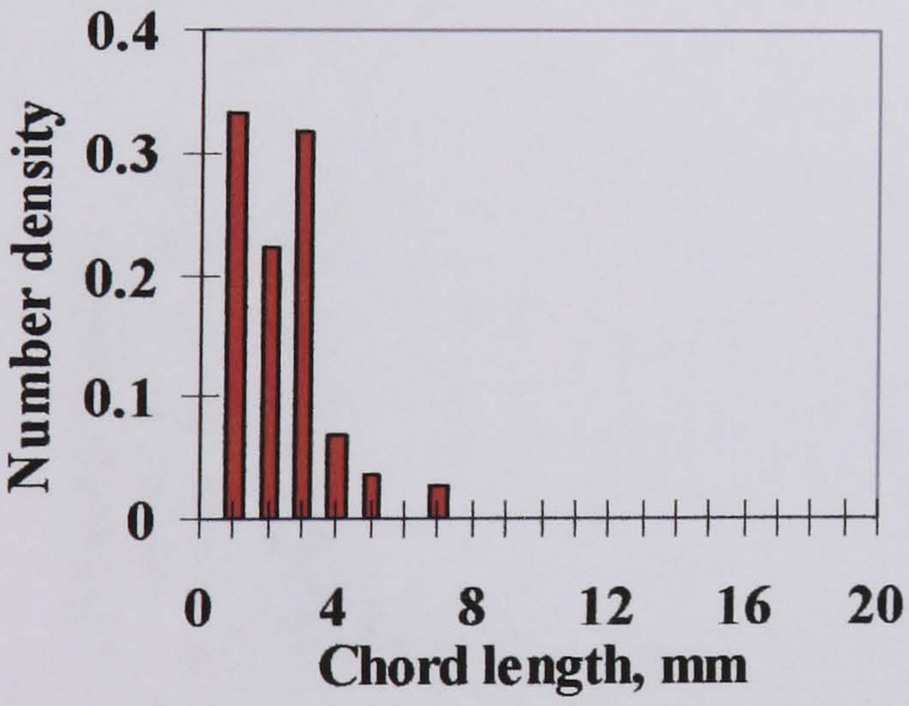

oil drops in water phase (9mm from the interface)

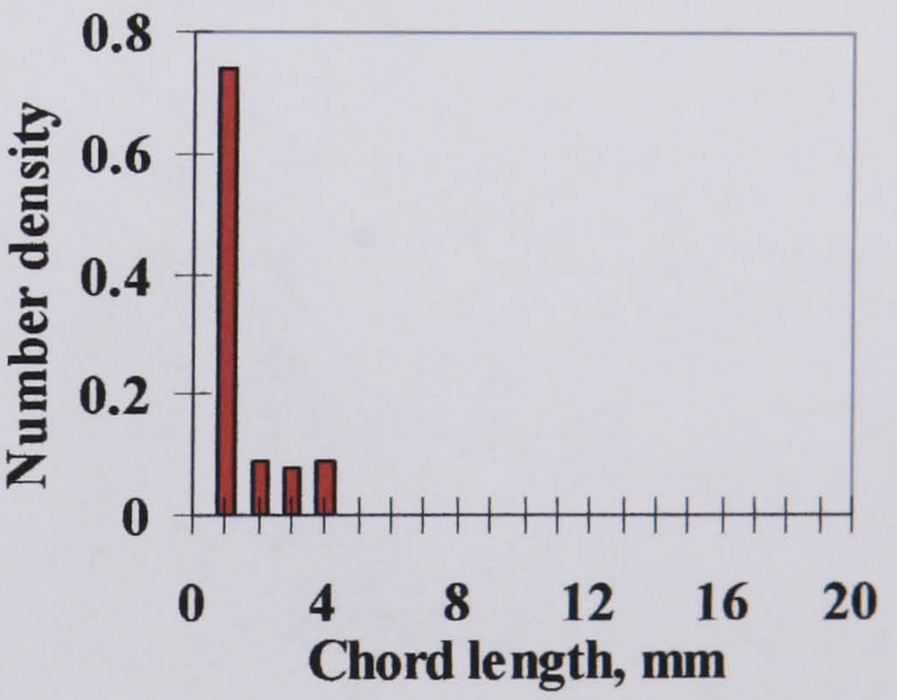

oil drops in water phase (11mm from the interface)

Fig. E.13 (*cont.*) Chord length distributions of water drops in oil and oil drops in water at different locations along the vertical diameter at U_{so} = 1.40, U_{sw} = 0.80 m/s in the 38 mm ID test pipe, 7 m from the inlet.

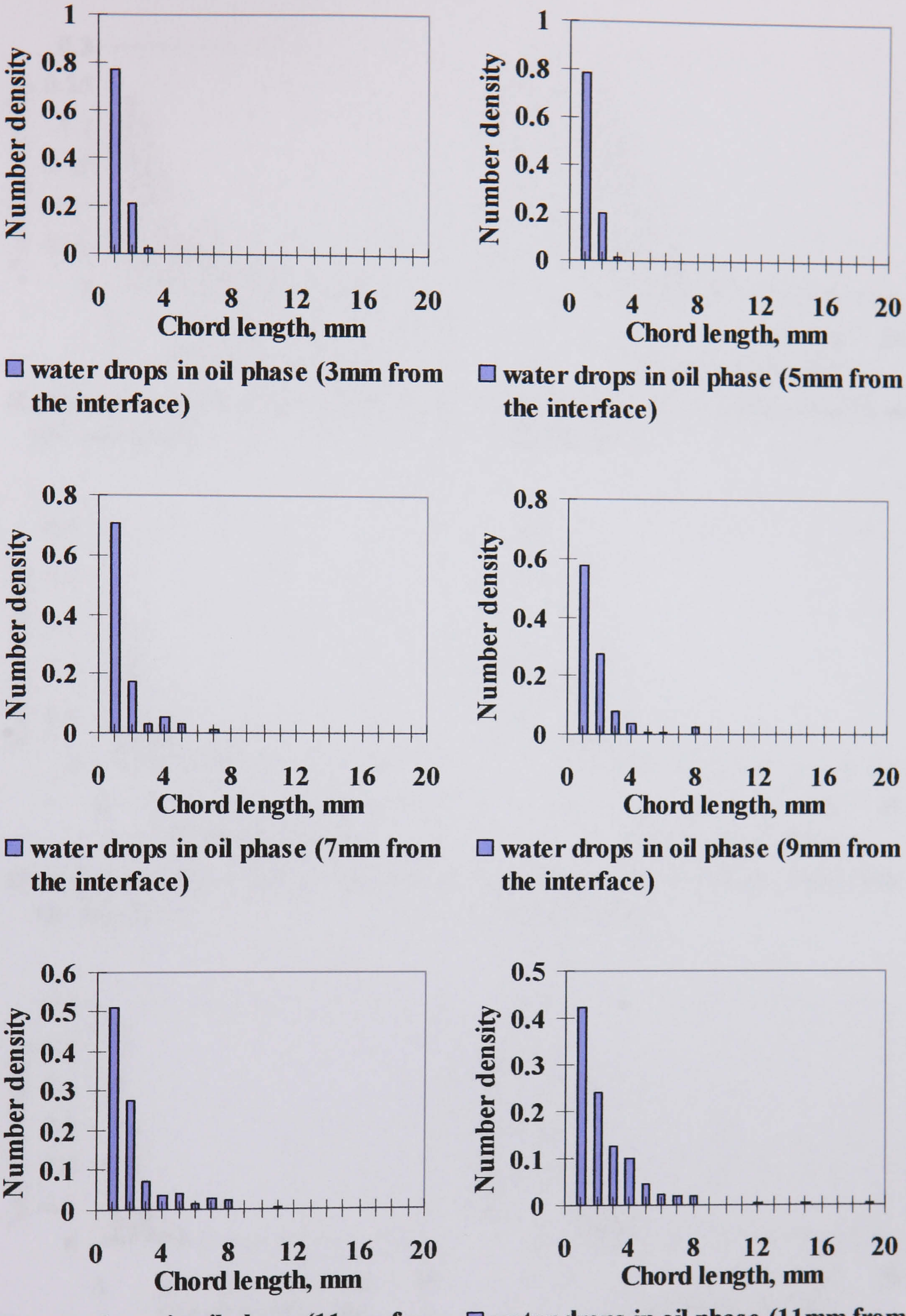

Fig. E.14 Chord length distributions of water drops in oil and oil drops in water at different locations along the vertical diameter at U_{so} = 1.40, U_{sw} = 1.10 m/s in the 38 mm ID test pipe, 7 m from the inlet.

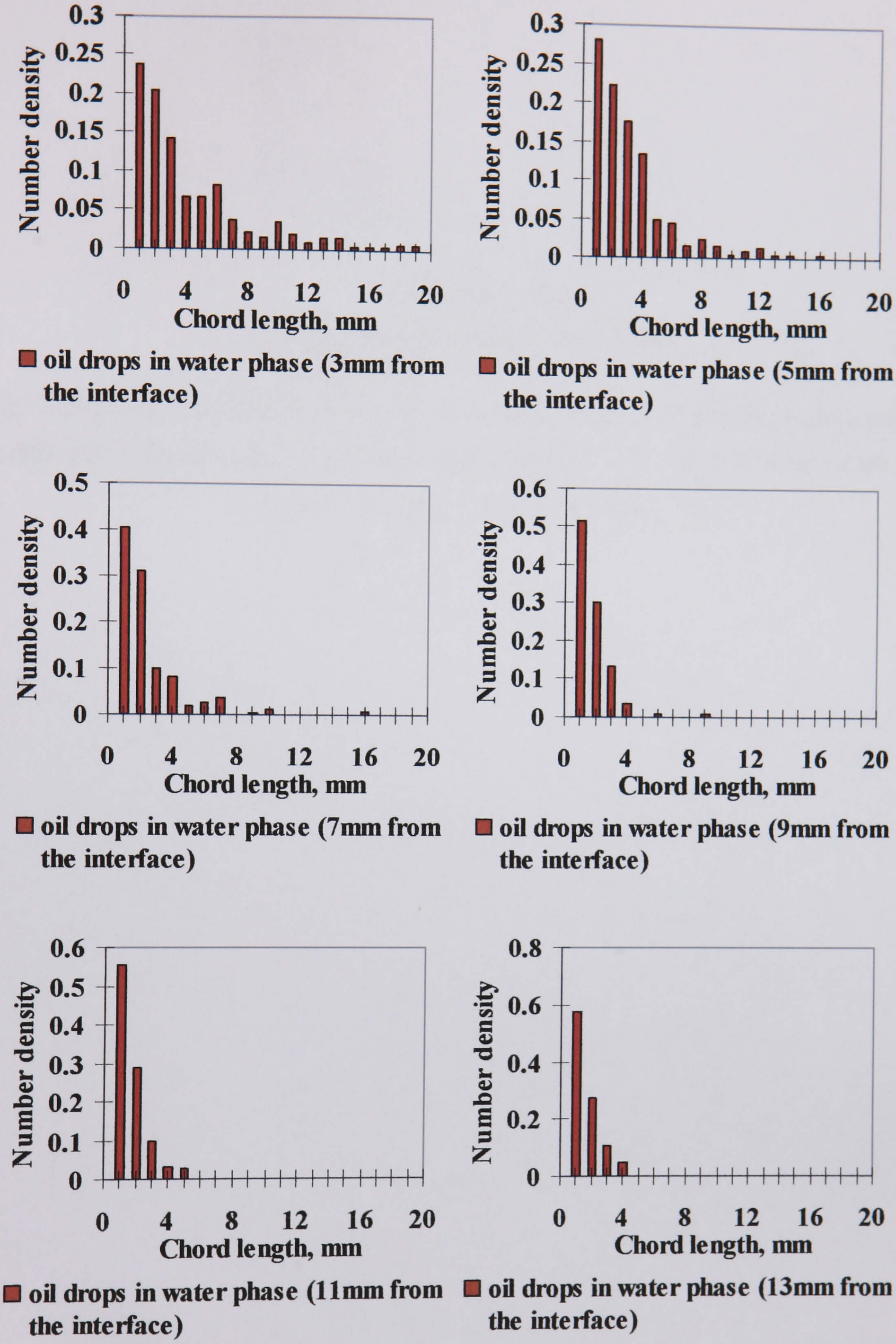

Fig. E.14 (*cont.*) Chord length distributions of water drops in oil and oil drops in water at different locations along the vertical diameter at U_{so} = 1.40, U_{sw} = 1.10 m/s in the 38 mm ID test pipe, 7 m from the inlet.

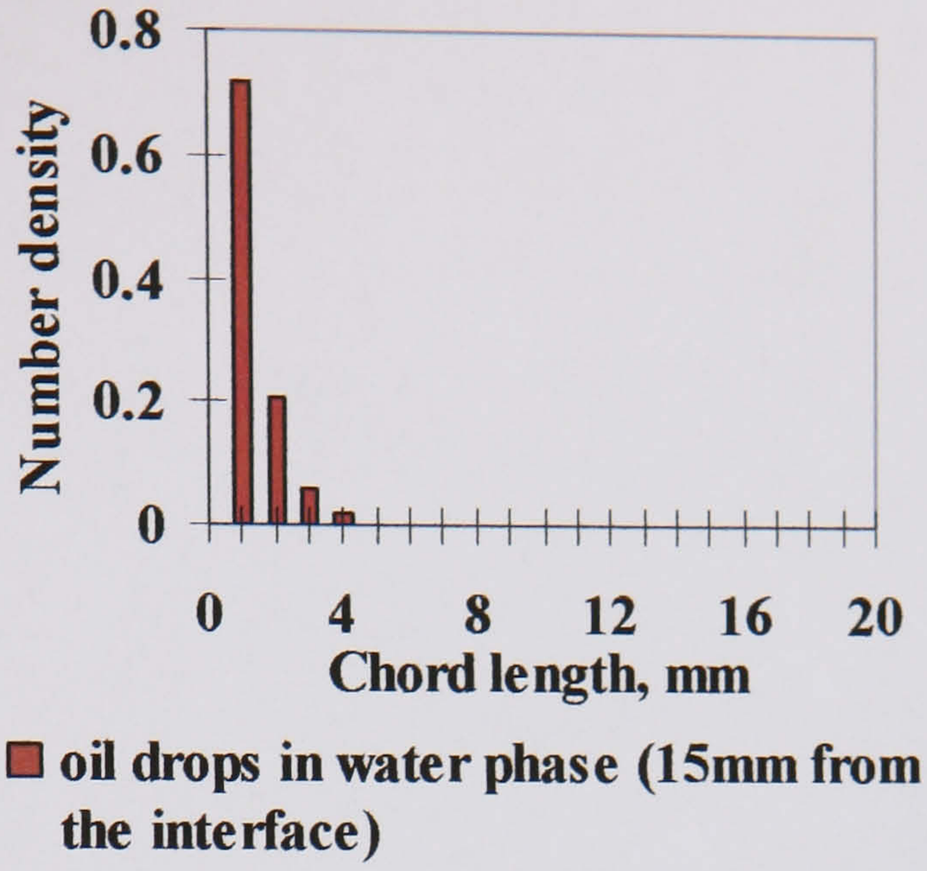

Fig. E.14 (*cont.*) Chord length distributions of water drops in oil and oil drops in water at different locations along the vertical diameter at U_{so} = 1.40, U_{sw} = 1.10 m/s in the 38 mm ID test pipe, 7 m from the inlet.